STUDY OF DRIFT LIMITS FOR HIGH-STRENGTH CONCRETE COLUMNS

BY

ADOLFO BENJAMIN MATAMOROS

Ing. Civ., University of Costa Rica, 1989
M.S., University of Illinois, 1994

THESIS

Submitted in partial fulfillment of the requirements
for the degree of Doctor of Philosophy in Civil Engineering
in the Graduate College of the
University of Illinois at Urbana-Champaign, 1999

Urbana, Illinois

UNIVERSITY OF ILLINOIS AT URBANA-CHAMPAIGN

THE GRADUATE COLLEGE

OCTOBER 1999
(date)

WE HEREBY RECOMMEND THAT THE THESIS BY

ADOLFO BENJAMIN MATAMOROS

ENTITLED STUDY OF DRIFT LIMITS FOR HIGH-STRENGTH CONCRETE COLUMNS

BE ACCEPTED IN PARTIAL FULFILLMENT OF THE REQUIREMENTS FOR

THE DEGREE OF DOCTOR OF PHILOSOPHY

Director of Thesis Research

Head of Department

Committee on Final Examination†

Chairperson

David Pecknold

William F. Gamble

Gabriel Fernandez P

† Required for doctor's degree but not for master's.

O-517

Abstract

A series of experiments was carried out to investigate the behavior of columns made with high-strength concrete subjected to shear reversals. Specimens comprised two column members framing into a common joint. The main variables of the experimental study were axial load and concrete strength. Column dimensions and the amount of transverse reinforcement did not vary between specimens. The transverse reinforcement ratio was set at 1%. Columns were square with dimensions of 8 x 8 in.

A constant axial load was applied to the specimens by means of hydraulic rams. Columns were deformed by applying anti-symmetric loads at inflection points. The displacement history consisted of cycles with increasing maximum deflections, until failure occurred. The applied displacement history was selected to simulate the effect of repeated load reversals typically induced by earthquakes.

The investigation focused on three problems about the behavior of reinforced concrete columns made with high-strength concrete. (1)The series of tests studied the influence of concrete strength on drift capacity and provided a factual base for projecting available theory to columns with high-strength concrete. (2) The tests were instrumented to obtain information about the relationship between normal/shear strains and rotation at yield and at drifts exceeding yield. (3) Tests were designed to provide an improved basis for determining the amount of reinforcement required for adequate drift capacity of high-strength concrete members.

The effect of the controlled variables on the behavior of the specimens is discussed and a simple theoretical approach to calculate the critical coordinates for the load-displacement response is presented.

Dedication

To my parents, sisters, and brother whose support and encouragement made this thesis possible.

Acknowledgments

This study was part of a research program sponsored by the National Science Foundation under grant 9320150-CMS. The experimental study was carried out at Kettelhut Laboratory, Purdue University.

The writer would like to express his gratitude to Brian J. Malone and Robert J. Peterman for their valuable advice, their assistance in the erection of the reaction frames, and their help casting the specimens. The writer benefitted in numerous instances from their experience operating scientific equipment at the Kettelhut Laboratory.

The writer would like also to acknowledge fellow students Santiago Pujol, Cemaletin Donmez, JoAnn Browning, Amy Grider, Lisa Samples and Alejandro Bonilla for their help casting the specimens, preparing test logs, and operating the data acquisition equipment.

Laboratory assistants David Gatchel, Timothy Nuetzel, Brian Chen, Michael Stewart, Jenny Smits, and Laboratory Technician Harry S. Tidrick participated in the construction and casting of the specimens, their instrumentation, and the test setup. They also assisted in the process of recording deformation measurements made with the electronic gages.

The writer expresses his gratitude to Mrs. Linda Vail who offered her generous help with administrative duties at Purdue University. The assistance of Professor David A. Pecknold and Mrs. Deidre Bever was essential to achieve a successful cooperative effort between the University of Illinois and Purdue University.

The writer benefitted from the advice and experience of Professor Mete A. Sozen, who’s help was instrumental for the completion of this study.

Table of Contents

Section Page

Chapter 3

Chapter 4

Section Page

Section Page

List of Tables

Table Page

Table Page

List of Figures

Figure Page

Figure Page

Figure Page

Figure Page

Figure Page

Figure Page

Figure Page

Figure Page

Figure Page

Figure Page

Figure Page

Figure Page

Figure Page

Figure Page

Figure Page

Figure Page

Figure Page

Figure Page

Figure Page

Figure Page

Figure Page

Figure Page

Figure Page

Figure Page

Chapter 1

Introduction

1.1 Background

The use of high-strength concrete in structural members has many advantages. High-strength concrete makes smaller structural sections possible. It has higher stiffness, and lower permeability than lower-strength concrete (American Concrete Institute, 1984). Because of its sudden and sometimes explosive failure in compression tests, high-strength concrete is considered a brittle material. This perception, along with the paucity of experimental data, has created concern about its use on earthquake resistant structures, where toughness under cyclic loading and the capability to dissipate energy are important requirements.

In a reinforced concrete member subjected to axial load and bending, an increase in compressive strength, without a change in cross section and axial load, results in a lower ratio of applied axial to balanced load (combination of axial force and bending moment compatible with the reaching of assumed limit of compressive strain in the concrete and yield strain in the reinforcement in tension at the same time). Preliminary analyses indicated that such a reduction would lead to an increase the ability of the column to deform, and it would improve its toughness. This is currently a controversial issue among engineers, and some of them refrain from the option of obtaining ductility by increasing concrete strength because of the lack of experimental evidence to support it.

This study focuses on the use of high-strength concrete in columns subjected to cyclic loading and explores the possibility of adequate drift capacity with a reasonable amount of transverse reinforcement.

1.2 Objectives

Three problems about the behavior of reinforced concrete columns with high-strength concrete were investigated:

(1) Theoretical relationships among section properties, axial load magnitude, and drift indicated that, for a given section and axial load, increasing the strength of concrete would enable higher drift capacity. Current practice precludes this option because experimental work on columns made with high-strength concrete is scarce. Tests of columns with high and normal-strength concrete were carried out to study the influence of concrete strength on drift capacity and to provide experimental data for projecting the available theory to apply to columns with high-strength concrete.

(2) Previous studies of reinforced concrete column tests have led to reasonable doubt about the definition and calculation of yield displacement, a parameter of importance for the common definition of ductility (Konwinski, 1996). The tests were instrumented to provide information about the relationship between normal and shear strains and rotations at yield, and at drifts exceeding yield.

(3) The specimens were designed to provide an improved basis for determining the amount of transverse reinforcement required for adequate drift capacity.

1.3 Scope of the Research

A series of experiments was carried out using specimens made with normal-strength and high-strength concrete. Results from the tests provided information about the behavior of high-strength columns subjected to axial loads below the balanced failure condition. The behavior of elements made with high-strength concrete was compared with that of similar specimens made with normal-strength concrete, subjected to the same axial load and mean axial stress.

Specimens were instrumented to allow detailed mapping of the deformation throughout the loading history. The instrumentation was selected to capture the magnitude of the components of the total displacement and the distribution of mean curvature along the length of the structural members.

Nonlinear deformations in the plastic hinge and rotations induced by slip of the reinforcement complicate the analysis of columns subjected to lateral loads. The specimens were instrumented to measure in detail the deformation near the joint and the distribution of strain along the anchorage region to capture the effect of slip.

Measured deformations were used to study the relationship between the components of the total displacement, and to calculate the coordinates for critical points of the load-displacement relationship.

1.4 Previous research

Early research on high-strength concrete focused on material properties. A research program carried out at Cornell University (Nilson, 1985) investigated such properties as the modulus of elasticity, tensile strength, shrinkage, long term deformations and Poisson's ratio. Other studies that also addressed material properties were carried out by the Portland Cement Association (Farny and Paranese, 1994), Swamy (Swamy, 1985), and Larrad (Larrad, 1990). Information on this subject is well documented in the state of the art report by ACI committee 363, on high-strength concrete (American Concrete Institute, 1984).

The main concern about the use of high-strength concrete in earthquake-resistant structures is the ability of structural members to sustain inelastic deformations and repeated load reversals without significant loss in strength. Experiments with axially loaded specimens have indicated that confinement is less effective for high-strength concrete (Bjerkeli, Tomaszewicz and Jensen, 1990), (Young, Nour and Nawy, 1987), (Martinez, Nilson and Slate, 1984), (Li, 1994).

1.4.1 Shear Strength of High-Strength Concrete Members

A study on shear capacity of high-strength beams without transverse reinforcement (Thorenfeldt and Drangsholt, 1990) showed that the diagonal cracking load remained almost constant in spite of an increase in compressive strength from 11.31 ksi to 14.21 ksi.

A more extensive series of tests conducted in Japan looked at the shear strength of high-strength members (Sakaguchi, Yamanobe, Kitada, Kawachi and Koda, 1990). It comprised six beams and ten columns with different amounts of transverse reinforcement

and was intended to determine their diagonal cracking and ultimate shear capacities. For beam specimens, concrete strength was maintained constant at about 13 ksi. The principal variable was transverse reinforcement capacity $\rho_s f_y$, ranging from 0 to 1.15 ksi. In beams with $\rho_s f_y$ lower than 260 psi ($\rho_s f_y / f'_c = 2\%$) diagonal cracking propagated rapidly leading to a quick and sudden shear failure. In specimens with $\rho_s f_y$ of 725 and 1145 psi ($\rho_s f_y / f'_c$ higher than 5.5%) both the shear and longitudinal reinforcement yielded before failure, exceeding considerably the diagonal cracking capacity.

High-strength column specimens with an axial load of $0.40\ f'_c\ A_g$ were more sensitive to $\rho_s f_y$. Lateral reinforcement below $\rho_s f_y$ of 815 psi ($\rho_s f_y / f'_c = 6\%$) resulted in brittle failures after diagonal cracking. Transverse reinforcement $\rho_s f_y$ of 1625 psi ($\rho_s f_y / f'_c = 12\%$) provided enough shear capacity to prevent propagation of diagonal cracking, resulting in failure caused by crushing of the concrete in the compression zone. The ACI equation for shear strength provided by concrete in members subjected to shear, flexure and compression (American Concrete Institute, 1983) underestimated test results.

1.4.2 Drift Capacity of High-Strength Concrete Members

Based on a series of beam tests conducted at Cornell University Nilson observed that although the ultimate compressive strain was smaller for high-strength concrete, section and member displacement ductility was larger than in normal strength elements (Nilson, 1985). However, Nilson also observed that spiral reinforcement was less effective in high-strength columns, resulting in a smaller displacement ductility.

A study on the flexural ductility of high-strength beams (Shin, Kamara and Ghosh, 1990) indicated that ductility ratios increased with concrete strength for specimens with similar amounts of longitudinal and transverse reinforcement. This was observed for monotonic as well as cyclic loading.

A study on the properties of high-strength concrete members (Bjerkeli, Tomaszewicz and Jensen, 1990) concluded that if properly confined, columns can have ductile behavior and sustain large axial strains. Both the effectiveness of confinement and the ultimate strain decreased with increases in concrete strength. According to the authors,

specimens with a confining reinforcement ratio of 1.1% resulted in inadequate ductility, while behavior of specimens with 3.1% transverse reinforcement was satisfactory.

An extensive study on the behavior of concrete members with high-strength materials was sponsored by the Ministry of Construction in Japan (Aoyama, Murota, Hiraishi and Bessho, 1990). Because the maximum number of stories in high rise buildings is limited by concrete strength, Japanese engineers felt that strengths higher than 6000 psi would be essential to the construction of buildings taller than 30 stories.

Tests conducted in Japan focused on columns subjected to axial loads mostly above 0.3 $f'_c A_g$ (Aoyama, et al, 1990), (Sakaguchi et al, 1990), (Muguruma and Watanabe, 1990), (Sugano et al, 1990), (Kimura et al, 1995), (Hibi et al, 1991). These tests showed a strong correlation between axial load, amount of confinement and the drift capacity of columns. A large amount of transverse reinforcement was required in order to obtain ductile behavior in columns subjected to axial loads greater than the balanced load. Japanese researchers addressed this problem by incorporating the use of high-strength steel in their specimens.

Muguruma and Watanabe tested eight specimens varying the transverse reinforcement yield stress between 48 and 115 ksi (Mugumura and Watanabe, 1990), while maintaining a constant volumetric ratio of 1.6%. Four tests were conducted on specimens with a strength of 12,400 psi at axial loads of 0.4 and 0.6 $f'_c A_g$. For these specimens, ultimate drifts ranged from 1.5 to 10%, showing a strong correlation between drift, axial load and the yield stress of the transverse reinforcement. The remaining four specimens had a strength of 16,800 psi, and were tested at axial loads of 0.25 and 0.41 $f'_c A_g$. Ultimate drifts in this case varied between 3.0 and 8.5%. The authors concluded that high ductility could be achieved with the use of high yield transverse reinforcement.

Motivated by the need to use high-strength materials in high rise structures, a research program was carried out by Takenaka Corporation in Tokyo. It comprised a first series of eight column and ten beam tests (Sugano, Nagashima, Kimura, Tamura and Ichikawa, 1990), and a second series of five column tests (Kimura, Sugano and Nagashima, 1995). The first series showed excellent behavior for specimens with an axial load of 0.3 $f'c A_g$, attaining drifts of 4%. Ultimate drift increased in proportion to the lateral reinforcement capacity normalized by concrete strength. The authors suggest a minimum

value for $\rho_s f_y / f'_c$ of 0.10 to achieve drifts of 2% at an axial load of 0.6 $f'_c A_g$. Beams showed little influence of the amount of transverse reinforcement or concrete strength on ultimate drift.

The second study concludes that ductility of high-strength columns was strongly affected by both the level of axial compression and lateral reinforcement capacity. The authors stated that lateral reinforcement capacity normalized by concrete strength was an appropriate index to evaluate ductility.

A series of 5 test at the University of Tokyo focused on column behavior after flexural yielding (Hibi, Mihara, Otani and Aoyama, 1991). The columns had axial loads of 0.30 and 0.45 $f'_c A_g$, varying the amount and strength of the lateral reinforcement while maintaining the quantity $\rho_s f_y$ almost constant. The tests showed a strong correlation between deformability and axial load. For specimens with an axial load of 0.3 $f'_c A_g$ behavior was very ductile, achieving drift ratios exceeding 4%. Specimens with higher axial load failed in shear with drift ratios in the order of 3.5%.

For drift ratios below 2% the University of Tokyo tests indicate that the shear component of the lateral deflection is similar for all specimens within the plastic hinge region, regardless of axial load. However, it must be pointed out that none of the specimens reached yielding of the transverse reinforcement, thus limiting the degradation of the confined core within the plastic hinge region

Thompsen and Wallace tested 12 specimens with a compressive strength of approximately 12,000 psi (Thompsen and Wallace, 1992). The cross section dimensions were 6x6 in. Tests variables were spacing and configuration of the transverse reinforcement, yield stress of the transverse reinforcement (115 and 185 ksi) and the level of axial load (0, 0.1 and 0.2 $f'_c A_g$). Measurements indicated that the longitudinal reinforcement started to yield at a drift ratio of 1%. Strength deteriorated at drift levels beyond 2% and severe damage occurred at drift levels higher than 4%. The longitudinal reinforcement buckled in specimens with axial loads of 0.2 $f'_c A_g$, for drift ratios greater than 4 %.

Razvi and Saatcioglu conducted an investigation on the strength and deformability of high-strength columns (Razvi and Saatcioglu, 1994) based on results from 250 tests. They concluded that the volumetric ratio required for confinement of high-strength columns may be reduced with the use of high-strength steel, particularly for high axial loads. They indicate that the use of high-strength steel did not improve behavior when low axial loads were present. They also observed that column deformability decreased with axial compression. A specimen tested under axial tension showed reduced strength but improved deformability.

1.4.3 Constitutive Relationships for High-Strength Concrete

Constitutive relationships for concrete provide the base for analytical models to calculate the load-deflection response of structural members. proposed a simple stress-strain model for normal strength concrete (Hognestad, 1951). This model provides a good representation of behavior from zero up to the strain at which the maximum stress occurs, which is in the order of 0.002 for normal-strength concrete. Later, Roy proposed an expression to quantify the influence of transverse reinforcement at larger strains (Roy and Sozen, 1964). A large number of stress-strain models for normal-strength concrete were proposed later (Soliman and Yu, 1967), (Popovics, 1970), (Sargin, Gosh and Handa, 1971), (Kent and Park, 1971), (Vallenas, Bertero and Popov, 1977), (Sheik and Uzumeri, 1982), (Sheikh, 1982), (Park, Priestley and Gill, 1982), (Mander, Priestley and Park, 1988).

Some of the stress-strain expressions for normal-strength concrete were modified to account for the difference in behavior of high-strength concrete, mainly that the maximum stress occurs at a different strain and that there is a reduction in the effectiveness of confining reinforcement (Young, Nour and Nawy, 1987), (Hsu and Hsu, 1994), (Azizinamini et al, 1994), (Cusson and Paultre, 1995). New expressions have also surfaced (Martinez, Nilsoon and Slate, 1984), (Fafitis and Shah, 1985), (Bjerkeli, Tomaszewicz and Jensen, 1990), (Muguruma and Watanabe, 1990), (Li, 1994).

1.4.4 Analytical Procedures to Calculate Deformations due to Lateral Loads

Different analytical procedures have attempted to model column deformation due to lateral loads. Early studies on beams assumed a linear curvature distribution up to yield, and a plastic hinge zone where the inelastic deformations occur (Baker and Amarakone,

1964), (Mattock, 1964), (Corley, 1966), (Burns and Siess, 1966). Deformations in the plastic hinge region of beams have been studied in depth (Thomas and Sozen, 1965). This approach provides a good estimate for the yield and ultimate displacements in beams, without requiring complicated calculations. In columns, lateral deformations are increased by slip of the reinforcement (Priestley and Park, 1987), (Konwinski, 1996). Otani proposed a simple equation to estimate deflections related to slip at any stage of loading (Otani and Sozen, 1972).

With the appearance of digital computers, analysis evolved towards more complex methods. Wight used a constitutive model proposed by Karlson (Karlson, 1973) to calculate moment curvature relationships under cyclic loading (Wight and Sozen, 1973). Load-deflection curves were obtained by integrating the calculated curvature through the length of the specimen. Suharwardy and Pecknold used an assumed curvature distribution throughout the column which was integrated in order to find the displacement (Suharwardy and Pecknold, 1978).

Methods based on section properties are simple and in general do not imply large amounts of calculations. Finite element procedures that account for the nonlinear behavior of concrete provide an lengthier alternative (Kaba and Mahin, 1984), (Fardis, 1991), (De La Colina, 1993). The main difficultly of this type of analysis is to obtain a numerically stable solution with a reasonable amount of calculations.

Chapter 2

Experimental Program

2.1 Introduction

A series of eight experiments was carried out using reinforced concrete specimens designed to simulate a beam-column connection (Fig 2.1). Specimens consisted of two column elements spanning in opposite directions, from a central stub, to assumed "inflection points" (Fig. 2.1). Each column element and the central stub had a length of 2 ft., for a total distance between "inflection points" of 6 ft. Specimens are described in detail in the Appendix.

The controlled variables for the experimental study were axial load and concrete strength. Specimens were tested with constant axial loads of 0, 32, 64 and 128 kips. To study the influence of the material on the lateral deformation capacity, specimens were cast using both normal-strength and high-strength concrete. Concrete mixes were proportioned to have a nominal strength of 10,000 psi for the high-strength specimens and 5,000 psi for their normal-strength counterparts. Proportions for the two mixes used in the study are presented in Table A.2.

Specimen designations indicate the two variables of the study, compressive strength and axial load. The first part of the name is preceded by the letter C to indicate that it is related to the compressive strength of the concrete. Designations starting with C5 refer to specimens with a nominal compressive strength of 5,000 psi, and designations starting with C10 were given to specimens with a nominal compressive strength of 10,000 psi. The second part of the designation indicates the amount of axial load as a fraction of the product $f'_c A_g$. Material properties are presented in detail in section A.2 of the Appendix.

The fabrication of the specimens and their dimensions are described in section A.3. Because of the large forces required to test high-strength materials, specimen cross section

was set at 8 by 8 in. (Fig A.17). Longitudinal reinforcement consisted of 4 No.5 bars, which was approximately 2 % of the total gross area of the elements (section A.2.2, Fig. A.17).

The amount and distribution of confining steel was the same for all specimens (section A.2.2, Fig. A.17). The transverse reinforcement ratio was 1%. This is slightly below the amount of transverse reinforcement required by the Building Code Requirements of the American Concrete Institute (American Concrete Institute, 1995) for columns with a compressive strength of 10,000 psi, in regions of high seismicity (Eq. 21-3 and 21-4).

The test procedure is described in section A.4. The two column elements of each specimen were subjected to equal but opposite deformations (Fig. A.32) at the "inflection points". The applied displacement history induced deformations in the columns well into the nonlinear range, while also providing the effect of cyclic loading typical of earthquakes.

For the first two specimens, which had little or no axial load, emphasis was placed in recording deformation data with the Whittemore strain gages near the yield condition (Fig 2.2). The displacement history consisted of four cycles with increasing maximum displacements (from 0.6 in. for the first cycle to 1-¼ in. for the fourth). After four cycles were completed, the specimen was subjected to a monotonically increasing deformation up the maximum allowed by the test configuration (approximately 3 in. corresponding to a drift ratio of 12.5% for the specimens).

Subsequent tests were submitted to a different deformation history emphasizing the effect of repeated cycles up to increasing levels of deformation (Fig 2.3). It consisted of pairs of loading cycles with the same maximum displacement. After each pair was completed, the maximum displacement was increased by ¼ in. This type of displacement history intensified the damaging effect that load reversals had on the elements.

2.2 Instrumentation

A detailed description of the instrumentation used in the tests is presented in section A.4.3. Specimens were instrumented to measure strain, deformation and force.

Deflections at various points in the column elements were measured using displacement transducers (Fig. A.34). Deformations in the column and the central stub, near the joint, were mapped using an electronic gage that was developed and built for this experimental program. Its design was based on a similar gage built at the University of Toronto. The electronic gage is referred to in this study as “electronic Whittemore gage” because it is similar in principle to the mechanical Whittemore gage. A displacement transducer connected to the data acquisition system measured the deformation between two anchor points attached to the surface of the specimen (Fig. A.37). Three gages of different sizes were built for this study, to monitor deformations over gage lengths of 4.75, 7.0 and 8.5 in.

Longitudinal and transverse reinforcement were instrumented using ¼ in. electrical resistance strain gages. Locations where strain gages were attached to the reinforcing cage are shown in Fig. A.36. The type of gage used and the installation procedure are described in section A.4.3.

There were slight variations in the instrumentation plan of the specimens. Figure A.35 shows a basic layout for the location of electronic Whittemore gage anchor points. The specific layout used in each test is shown in Figs. 2.4 to 2.7. Similarly, Fig. A.36 shows a general layout for the location of electrical resistance strain gages. The first four specimens that were tested had a more extensive array of strain gages in order to study of the effect of slip on the stress in the longitudinal reinforcement, along the anchorage zone (Fig. 2.8). This first group included specimens C10-00, C5-10, C10-05 and C5-20.

Chapter 3

Test Results

3.1 Introduction

This chapter describes the force and deformation measurements made during the tests. Instrumentation, described in the Appendix, consisted of load cells, displacement transducers, strain gages and electronic Whittemore gages.

Displacement readings at preselected stations near the joint were obtained using electronic Whittemore gages. The location of the stations is described in chapter 2 (Figs. 2.4 to 2.7) and the Appendix (Figs. A.30 and A.35). In order to refer to the figures in this chapter in a simple and clear manner, the three stations on each element for the seven-inch electronic Whittemore gage were numbered from inside the joint towards the "inflection point". According to that convention, station 1 was located inside the joint and station 3 was closest to the "inflection point".

Mean strains (average over 7-in. gage length) were calculated using the displacement readings at each electronic Whittemore gage station. Those strains were then plotted to show the variation of the strain with respect to the distance from the bottom of the element, at each station, and also to calculate mean curvatures and rotations at the same locations.

It is necessary to define the terms limiting drift, toughness and ductility, used to describe the behavior of the test specimens. The limiting drift refers to the drift (or displacement) at which the resisting capacity of the element was reduced to 80% of its maximum capacity. Toughness of a test element refers to the comparison of the limiting drift to the drift at yield. Ductility of a test element refers to the comparison of the drift at which the element was no longer able to carry the applied axial load to the drift at yield.

3.2 Measured Shear-Displacement Curves

Figures 3.1 to 3.8 show the measured relationships between the shear force and displacement at the "inflection point" of each specimen. The terminology associated with the senses of the load and displacements was as follows. Loading involved forces of opposite sense on the north and south elements acting as a couple. A clockwise couple was considered to be positive. For the force-displacement plots for each flexural element, upward loads and displacement were plotted as positive.

A brief description of the behavior of each specimen follows.

Specimen C10-00 (load schedule A, P = 0, high-strength): Its displacement history consisted of four cycles with maximum displacements less than 1-¼ in. At the end of the first quarter cycle, with a maximum displacement of approximately 0.55 in., damage to the concrete of the shell was barley noticeable, and limited to the surface of the surface of the column. At the end of the fourth cycle, with a maximum displacement of 1 in., observed damage to the concrete of the shell was still very light.

During the first quarter of the fifth cycle the specimen was subjected to a deformation of 3 in. (drift ratio of 12.5%) without reaching the failure criterion (Fig. 3.17). Spalling of the shell became noticeable at a drift ratio of 8%. At a drift of 3.25 in., the maximum allowed by the test setup, the shell had spalled off completely. However, the core was in good condition and the measured shear force remained over 90% of the maximum value (Fig. 3.17). Loads recorded at peak displacements for specimen C10-00 are summarized in Table 3.2.

Specimen C10-05 (load schedule B, P = 32 kips, high-strength) : It was the first to be tested under displacement history B, shown in Fig. 2.3, which consisted of pairs of loading cycles with the same maximum displacement. After each pair was completed, the maximum displacement was increased by ¼ in. This type of displacement history intensified the damaging effect that load reversals had on the elements.

The specimen developed a limiting drift ratio of 5.5%. The hysteresis curves (Figs. 3.3 and 3.4) show a small pinching effect, attributable to the fact that the axial load was small compared with the axial capacity of the column. Crushing of the concrete was

observed on the surface of the column at a displacement of ½ in. At the end of the fourth cycle, which had a maximum drift ratio of 3% (drift of ¾ in.), a thin layer of concrete had spalled off. At a drift ratio of 5% (1.25 in. drift) damage to the concrete in the shell concrete was very severe.

At a displacement of 1-½ in. the shell had spalled off, but the specimen was still able to carry approximately 80% of the maximum shear force (Table 3.3). During the two subsequent cycles, with a maximum displacement of 1-¾ in., members had a decrease in the shear carrying capacity, which dropped to 66% of the initial value. During the first quarter of cycle 13, which had an intended maximum displacement of 2 in. (drift ratio of 8%), the north element had a large drop in shear and the test was stopped (Fig. 3.18).

Specimen C10-10 (load schedule B, P = 64 kips, high-strength) : The measured load-displacement response for this specimen was characterized by a large capacity to dissipate energy (Figs. 3.5 and 3.6). Damage to the concrete was first observed during the first cycle, at a drift of 0.5 in. After cycle 3, which had a maximum drift of ¾ in., damage to the concrete in the shell was still very light. At a drift of 1 in., during cycle 5, spalling was noticeable. The concrete of the shell had spalled off at a drift of 1 ½ in.

At cycles 9 and 10, which had a maximum deformation of 1-¾ in., the shear force remained close to 80 % of the initial in both elements (Fig 3.19, Table 3.4). At the point of positive peak displacement of cycle eleven the top bars on the north element started to show signs of buckling, although there was not a noticeable effect on the measured shear force. During the last quarter of cycle 12, the south element showed a considerable reduction in the shear force. At this point, the compression reinforcement on both elements had buckled. Cycle 13 was started with an intended maximum displacement of 2 in. After reaching a displacement of 1.8 in., there was a drop in the axial load followed by out-of-plane deformation of the elements, towards the west side. The test was stopped at that time.

Specimen C10-20 (load schedule B, P = 128 kips, high-strength) : Crushing of the concrete on the surface of the column was first observed at a drift of ½ in. Spalling was visible at a drift of ¾ in. and the concrete of the shell had spalled off completely at a drift of 1 in.

Hysteresis curves for specimen C10-20 (Figs. 3.7 and 3.8) show that both elements sustained deformations of 1- ¼ in. without a significant drop in the shear force (Table 3.5). However, failure was rather abrupt, as occurred in the case of specimen C5-40, which was also subjected to an axial load of 128 kips. The shear force dropped below 55% of the initial value at the maximum negative displacement of cycle 10, and the axial load could no longer be carried by the element (Fig. 3.20).

Specimen C5-00 (load schedule B, P = 0 kips, normal-strength) : The response of specimen C5-00 was characterized by large toughness, (Figs. 3.9 and 3.10), reaching a drift ratio of 6% while carrying approximately 85% of the maximum shear. The hysteresis curves for both elements show the effect of pinching, related to the lack of axial load necessary to close the flexural crack during a reversal of loading. Specimen C5-00 had a very ductile failure in which large displacements were sustained while maintaining the axial load carrying capacity.

Crushing of the concrete was barely visible on the surface of the columns at the end of cycle 4, which had a maximum drift of ¾ in. Spalling was observed during cycles 5 and 6, which had a maximum drift of 1 in. By the end of the tenth cycle, with a maximum drift ratio of 6 %, the south element had totally lost its shell, leaving the longitudinal reinforcement exposed on both faces of the column. It was during cycle 11, the first with a maximum displacement of 1-¾ in., that the shear force dropped below 70 % of the initial (Table 3.6).

During cycle 12, which also had a maximum drift of 1-¾ in., the south element suffered severe damage, although it did not translate into a further decrease of the shear force. At this point the longitudinal reinforcement on both elements was fully exposed. Cycle 13 was the first with a maximum displacement of 2 in. At the peak positive displacement the shear force was comparable to that of cycle 12, slightly below 70 % of the initial value (Fig. 3.21). After unloading the specimen the test had to be stopped because the damage to the elements was too severe.

Specimen C5-10 (load schedule A, P = 32 kips, normal-strength) : Testing was interrupted by a power failure, that also led to the loss of some data. The displacement schedule was similar to that of specimen C10-00, consisting of four and one quarter cycles.

Observed behavior (Figs. 3.11 and 3.12) was also similar to that of specimen C10-00 (Figs 3.1 and 3.2) .

Crushing of the concrete on the surface of the column was noticed during the first cycle. Damage to the concrete of the shell did not increase considerably during cycles 2, 3, and 4. This was reflected by the fact that the measured shear force remained above 85% of the maximum at the peak displacement of each of these cycles (Table 3.7).

The most severe damage occurred during the fifth cycle. At a drift ratio of 10% most of the concrete in the shell had spalled off. However, the confined core was still in very good condition and the specimen was able to sustain such large deformation without a sudden drop in its load carrying capacity (Fig. 3.22).

Although there was not an abrupt drop in the shear capacity, second order effects caused a reduction in the shear force to 80% of the maximum measured value, at a displacement slightly larger than 1-½ in. (Table 3.7, Fig. 3.22).

Specimen C5-20 (load schedule B, P = 64 kips, normal-strength) : The axial load corresponded to approximately 50% of the balanced load of the normal-strength specimens. The increase in axial load from 32 to 64 kips had a detrimental effect on the soundness of the elements, particularly for displacement cycles with large maximum displacements (Figs. 3.13 and 3.14).

Crushing of the concrete was first observed at a displacement of 0.4 in. At the end of the first cycle, damage to the shell concrete was very light and mostly limited to the surface of the column. By the third cycle, which had a maximum displacement of ¾ in., damage of the shell concrete was severe. After cycle 5, which had a maximum displacement of 1 in., most of the shell concrete had spalled off. At this point, the shear force had dropped down to approximately 75% of the initial value (Table 3.8).

During cycle nine, which had a maximum displacement of 1-½ in., the shell concrete had spalled off and the shear force in the south element had dropped below 55% of initial (Fig. 3.23). It was observed that during cycle 9 the inclined cracks on both members widened considerably. By cycle ten, the width of the inclined cracks had surpassed 1/8 in. The test was stopped during cycle eleven, close to a displacement of 1-¾

in., because the south element had deteriorated so much that it made the axial load equipment unstable (Fig. 3.13).

Specimen C5-40 (load schedule B, P = 128 kips, normal-strength) : This specimen was subjected to the maximum value of axial load that was used in the entire test series. The applied axial load was slightly above the load corresponding to the "balanced point" on the interaction diagram. Both elements (Figs. 3.15 and 3.16) started to exhibit crushing of the concrete in the surface of the column during the first cycle, at a displacement of 0.3 in. At a drift of 0.4 in. spalling of the shell concrete was clearly visible, and, at a drift of 0.5 in. damage to the concrete of the shell was severe. The most damage was incurred during cycles 5 and 6, which had maximum displacement of 1 in. After these two cycles, the shell concrete had spalled off.

On the third quarter of cycle six, while increasing the displacement from -0.97 to -1.0 in., the bottom bars of the south element buckled, giving rise to a large out-of-plane motion. Up to this point, the measured shear capacity had been above 70% of the maximum (Fig 3.24, Table 3.9).

3.3 Comparison of Measured Shear-Displacement Curves

The maximum shear force in the test elements was affected by the repeated load reversals and the large nonlinear compressive strains imposed on the concrete. Envelope curves, based on the maximum values of shear while loading in the positive or clockwise direction (Figs. 3.17 to 3.24), show that the shear force had a tendency to drop with increasing displacement.

The values of limiting drift, defined as the largest displacement at which an element was able to carry at least 80% of its maximum shear, are summarized in Table 3.1. Because each specimen had two elements (columns), the results from the first element to reach the failure criterion were included in Table 3.1. Values between successive points of the envelope curve were determined by interpolation.

In general, all the specimens were able to sustain drift ratios of 4% or more before failure. Considering that the amount of transverse reinforcement used in normal-strength specimens was higher than that required by the Building Code Requirements of the

American Concrete Institute (American Concrete Institute, 1995), the large deformation capacity observed was not surprising. Among normal-strength specimens subjected to displacement history B, drift capacity decreased with increasing axial load (Figs. 3.21, 3.23 and 3.24).

High-strength specimens had improved behavior compared with that of the normal-strength counterparts. They were able to attain larger deformations while sustaining higher shear than similarly loaded normal-strength specimens. The drift limit of high-strength specimens with axial loads of 32 and 64 kips was comparable (Figs. 3.18 and 3.19), while the specimen subjected to 128 kips (Fig. 3.20) had a slightly lower limit of 1.25 in. However, there was a noticeable difference in the shape of the load-displacement envelope curves (Figs. 3.18 to 3.20), where axial load had a detrimental effect on behavior.

A comparison of the limiting drift values based on the deformation schedule (Table 3.1) shows that the displacement history had an important effect on the deformation limit of the specimens. Both specimens tested with displacement history A (Figs. 3.17 and 3.22) sustained drift ratios exceeding 6.9% without reaching the failure criterion. Specimen C5-10 was able to reach a drift ratio of 15% without losing its ability to carry the full axial load (Fig. 3.22). For the group of specimens subjected to displacement schedule B the maximum value of limiting drift was that of specimen C5-00, with 1.6 in., which corresponds to a drift ratio of 6.5%.

There were two cases in which a direct comparison could be established because the displacement schedule and the axial load were the same while concrete strength varied. The first comparison is between the results from specimens C5-20 and C10-10, both tested with an axial load of 64 kips. The concrete in specimen C5-20 had a mean compressive strength of 7,000 psi, while concrete in specimen C10-10 had a mean compressive strength of 9,830 psi.

There was a measurable difference in the limiting drifts for these two specimens. The maximum shear force in specimen C5-20 dropped to 80% of the initial by cycle 5, which had a maximum displacement of 1 in. or a drift ratio of 4%. Specimen C10-10 reached the failure criterion during cycle 9 after sustaining deformations of 1.45 in. without a significant decrease in the shear force (Table 3.1).

The second pair of specimens tested under a similar displacement schedule and axial load were C5-40 and C10-20. The difference in compressive strength was larger in this case. Concrete in specimen C5-40 had a mean compressive strength of 5,520 psi, while that in C10-20 had a mean compressive strength of 9,500 psi.

The axial load acting on specimen C5-40 was close to that associated with balanced failure of the unconfined section, while specimen C10-20 was subjected to an axial load of approximately half the balanced load. Specimen C5-40 reached the failure criterion after cycle 5, which had a limiting drift of 1.0 in. The limiting drift for specimen C10-20 was 1.25 in., between cycles 7 and 9 (Table 3.1).

The use of high-strength concrete resulted in increased shear and deformation capacities compared to those of normal-strength concrete. The increase in maximum shear force was proportional to the axial load. It was negligible for specimens without axial load and highest for those subjected to 128 kips. The area inside the hysteresis loops of high-strength specimens was larger, indicating a better capacity to dissipate energy.

3.4 Measured Moment-Curvature Relationships

This section describes the moment-curvature relationships measured at three stations along the length of each element. Deformation readings taken with electronic Whittemore gages were divided by the initial distance between anchor points to obtain the mean strains in each station. The two values of mean strain closest to the top and bottom face of the element, were added algebraically and then divided by the vertical distance between them to obtain the mean curvature.

All graphs containing moment-curvature relationships were plotted to the same scale in order to make comparisons easier. Because joints were constrained against rotation with externally applied force (Fig. 2.1) it is not appropriate to talk about a bending moment inside the joint, where the stress distribution is very complex. However, for the purpose of comparing the deformation that occurs inside the joint to that in the column, the calculated curvature inside the joint was plotted against the moment at the face of the joint.

Specimen C10-00 (load schedule A, P = 0, high-strength): Figure 3.25 shows the calculated bending moment vs the measured mean curvature for specimen C10-00. The

location of each measurement is indicated next to the moment-curvature plot. The curvature in station 1 of the south element (Fig 3.25), located inside the joint, was comparable in magnitude to that in the adjacent station 2, located in the column. Both curves showed signs of large nonlinear deformations, associated with yielding of the longitudinal reinforcement. Curvatures measured in station 3 of the south element had linear behavior during the entire test, and were much smaller in magnitude than curvatures recorded in stations 1 and 2.

The north element of specimen C10-00 (Fig. 3.25) had a similar behavior, although the deformations inside the joint (station 1) were much smaller than those in the south element. Another difference was that for the north element most of the nonlinear behavior occurred in the column, outside the joint.

Figure 3.25 indicates that most of the deformation on this specimen was associated with the flexural cracks, located at approximately 1.5 in. from the face of the joint in both directions.

Specimen C10-05 (load schedule B, P = 32 kips, high-strength): Moment-curvature plots for specimen C10-05 (Fig. 3.26) indicate that most of the deformation occurred in station 2 for both test elements, within a distance equivalent to the effective depth from the face of the joint. At station 3, closer to the "inflection point", behavior was mostly linear, which was consistent with the behavior of all other specimens.

Specimen C10-10 (load schedule B, P = 64 kips, high-strength): The behavior of specimen C10-10 (Fig. 3.27) was similar to that of specimen C10-05 (Fig. 3.26). The measured curvatures in stations 1 and 3 of both elements were much smaller than those in station 2. Curvatures in stations 1 and 3 remained in the linear range, with all nonlinear deformation concentrated in station 2.

Specimen C10-20 (load schedule B, P = 128 kips, high-strength): The behavior of specimen C10-20 (Fig. 3.28) was comparable to that of C5-40 (Fig. 3.32), which was also tested with an axial load of 128 kips. The increase in compressive strength with respect to C5-40 resulted in the ability to sustain larger curvatures and higher moments than the normal-strength counterpart. When compared with the results of specimen C10-10 (Fig.

3.27) a decrease in maximum curvature and an increase in maximum moment were observed.

Specimen C5-00 (load schedule B, P = 0, normal-strength): Behavior of specimen C5-00 (Fig. 3.29) was similar to that of C10-00 (Fig. 3.25). The absence of axial load resulted in flexural cracks forming inside the joint, where considerable inelastic deformations occurred. There was a pinching effect in the curve which can be attributed to the absence of axial load, that would allow the flexural crack to close sooner after a load reversal. The specimen showed toughness and a very ductile failure.

Specimen C5-10 (load schedule A, P = 32 kips, normal-strength): Figure 3.30 shows the moment-curvature relationships for specimen C5-10. For this specimen, electronic Whittemore gage readings were stopped after the second cycle because of experimental exigencies, so the curvature plots do not report what occurred at large displacements. Specimen C5-10 showed less deformation within the joint than C10-00. As it was the case for specimen C10-00, most of the nonlinear behavior in the north element occurred outside the joint. Deformations in station 1of the north element were negligible. Deformations in station 1 of the south element were also small, although the moment-curvature plot shows some indication of nonlinear behavior.

Specimen C5-20 (load schedule B, P = 64 kips, normal-strength): Specimen C5-20 (Fig 3.31) had a curvature distribution similar to that of C10-05 (Fig. 3.26). Deformations inside the joint were negligible, with the nonlinear behavior concentrated within a distance d (effective depth) from the face of the joint.

Specimen C5-40 (load schedule B, P = 128 kips, normal-strength): Specimen C5-40 had the lowest drift at failure. The moment-curvature plots (Fig. 3.32) show that the deformation inside the joint was negligible, with nonlinear deformations concentrated within a distance d from the face of the joint as well. However, when compared with the data from specimens C5-20, C10-10 and C10-05, the maximum curvatures were smaller, consistent with the fact that the drift at failure was smaller. Smaller curvatures at ultimate indicate that axial load had a detrimental effect on the toughness of the core.

3.5 Comparison of Measured Moment-Curvature Relationships

There were several characteristics of the moment-curvature relationships that were repeated in all the specimens. Mean curvatures in station 2 were the largest of the three stations, while at station 3, the closest to the "inflection point", curvatures were smaller and behavior was mostly linear. In station 1, located inside the joint, the mean curvatures were the smallest, indicating that the deformation inside the joint was negligible for most cases.

In the two specimens without axial load (C5-00 and C10-00), flexural cracks developed inside the joint, very close to the face. Because of the deformations in those cracks, curvatures in station 1 were comparable in magnitude to those in station 2, and also had excursions into the nonlinear range.

The boundary condition of the joint affected the curvature distribution of these two specimens (C5-00 and C10-00). The reaction force at the bottom of the joint was provided by the high-strength concrete pedestal. The joint was clamped at the top using a thick steel plate, which was more flexible than the concrete pedestal. The stiffer pedestal provided a more effective constraint to motion inside the joint. This is why during the first quarter cycle, the north element, which reacted against the concrete pedestal, developed flexural cracks in the element (station 2), while the south element, which reacted against the steel plate, developed a flexural crack inside the joint.

Interesting conclusions can be drawn by comparing the behavior of specimens C10-20, C5-40, C10-10 and C5-20. The increase in load from 64 to 128 kips in the normal-strength specimens resulted in a significant reduction in deformation capacity. A similar increase of load in high-strength specimens also had a detrimental effect on the limiting drift, although not as large as in the normal-strength case.

Considering that inelastic deformations were concentrated within a short distance from the face of the joint, specimens C5-20, C10-10 and C10-05 exhibited toughness in their confined cores. The magnitude of the maximum curvatures and the area inside each loop of the moment curvature plot are comparable for these three specimens, indicating that ductility and toughness were not diminished by the use of high-strength concrete.

Comparing the behavior of all specimens tested with displacement schedule B, an increase in compressive strength led to higher shear and deformation capacities. The increase was larger for an axial load of 128 kips.

3.6 Measured Moment-Rotation Curves

Rotations were based directly on the deformation readings at each station and plotted against the bending moment in Figs. 3.33 to 3.40, following a similar format to that of the moment-curvature relationships. Because the calculated change in rotation is proportional to the mean curvature, the trends observed in these plots are similar to those of the moment-curvature plots described in section 3.3

3.7 Measured Strain Distributions

Figures 3.41 to 3.48 show the variation of the strain distribution for each specimen of the test series during the first quarter cycle, intended to take the specimens slightly past yield.

Electronic Whittemore gage stations were located to measure the variation of the mean strain through the height of the cross section and along the length of the elements. Top and bottom stations were located near the positions of the longitudinal reinforcement. These measurements provided information about the magnitude of the compressive strains in the concrete, the depth of the neutral axis, the linearity of the strain distribution and the deformations of the tensile reinforcement. The sign convention is such that tensile strains were plotted with a positive sign.

Figure 3.41 shows the strain distribution for specimen C10-00 at increasing displacements during the first quarter cycle. A larger number of Whittemore readings were taken for specimens C10-00 and C5-10, so the evolution of the strain distribution during the first quarter cycle is presented in greater detail.

The cracks that developed inside the joint affected the strain distribution, leading to a deformation pattern that is consistent with the curvatures determined from electronic Whittemore gage measurements (Fig. 3.25). Deformation in the south element was distributed to two cracks on both sides of the face of the joint. Extrapolating the mean

compressive strain to the face of the element, the maximum mean compressive strain on the shell of the south element was estimated to be approximately 0.002, during the first quarter cycle. Deformations in the north element were mostly concentrated outside the joint, leading to a maximum mean compressive strain of 0.004.

Maximum mean tensile strains at the level of the steel for both north and south elements were above 0.005 and some reached as high as 0.01, clearly above the measured yield strain of the longitudinal steel. Mean tensile strains at the level of the steel for station 3 on both elements were on the order of 0.0025, which is close to the measured yield strain of the steel. However, moment-curvature plots for this station indicate that behavior was mostly linear. The mean neutral axis depth, in station 2 of both elements, was approximately 1.5 in.

Strain distributions for specimen C5-10 are presented in Fig. 3.46. During the first quarter cycle the mean strains for the south element were similar in magnitude at all three stations. The north element shows a different behavior, with little deformation occurring inside the joint and the largest strains located in station 2. The mean compressive strains on the shell of both elements was approximately 0.0025. Mean tensile strains at the level of the reinforcement were approximately 0.005 for all stations of the south element. In the north element, the largest mean tensile strains at the level of the reinforcement occurred in station 2 with a value of approximately 0.010. Station 1 of the south element showed negligible mean strains at the level of the reinforcement.

Because of the axial load, the mean neutral axis depth for this specimen was closer to 2.0 in. Strains at station 3 had a distribution that appears to deviate from linear. This is attributable in part to an inclined crack, which crossed only the top three lines (in tension) of the Whittemore point array. Another way of interpreting the effect of the inclined crack in station 3 is to say that deformations associated with it create a distortion of the element reflected by the nonlinear strain distribution.

Figures 3.41 and 3.46 show that during the first quarter cycle the depth of the neutral axis, measured from the compression face, was larger for the south element than for the north. The smaller depth of the neutral axis on the north element originated tensile strains at the levels corresponding to both layers of longitudinal reinforcement.

Figures 3.42 to 3.45 and 3.47 to 3.48 show the strain distributions for the remaining specimens. The maximum mean compressive strain for specimens C10-05 (Fig 3.42) and C10-10 (Fig. 3.43) were close to 0.003. Specimens C5-20 (Fig. 3.47) and C5-40 (Fig. 3.48) showed a maximum mean compressive strain of approximately 0.005.

Specimens C5-10 (Fig. 3.46), C5-20 (Fig. 3.47) and C5-40 (Fig. 3.48) had a progressive increase in the neutral axis depth, proportional to the increase in axial load. The larger depth of the neutral axis implied larger compressive strains acting on the shell of the concrete, and therefore, more damage to it. A similar trend was observed comparing specimens C10-05 (Fig. 3.42), C10-10 (Fig. 3.43) and C10-20 (Fig. 3.44).

The use of high-strength concrete resulted in a reduction of the neutral axis depth. This was particularly clear for specimens C5-40 (Fig. 3.48) and C10-20 (Fig. 3.44).

Figures 3.49 to 3.56 show the variation of the strain distribution during peak positive displacements for each cycle. The maximum deformation during the first cycle was close to the yield displacement. Subsequent cycles generated increasing incursions into the nonlinear range.

The distribution of mean strains had a similar pattern to that observed during the first quarter cycle. The largest mean strains occurred in station 2 for both the north and south elements. Station 3 registered very small mean strains (Figs. 3.49 to 3.56) compared to station 2, indicating that the rotation of the normal to the cross section between station 2 and the inflection point was negligible.

Strains in station 3 also appeared to have a nonlinear distribution (Figs. 3.52, 3.53, 3.54 and 3.56), which again can be attributed to inclined cracks crossing only some lines of the Whittemore point array. However, during the latter cycles the magnitude of the mean strains in station 3 remained similar to those for the first cycle, while the mean strains in station 2 increased considerably.

For both specimens without axial load, C10-00 (Fig. 3.49) and C5-00 (Fig. 3.53), mean strains in station 1 were of similar magnitude than those of station 2. In all other specimens mean strains in station 1 (Figs. 3.50 to 3.52 and 3.54 to 3.56) of the south element were very small or negligible compared to those of station 2.

The maximum mean strains at the level of the tensile reinforcement, as shown in Figs. 3.49 to 3.56, were recorded in station 2, and were on the order of 4 %. Because the Whittemore readings were stopped before the end of some tests, it is likely that some specimens sustained larger mean strains in station 2.

In general, the behavior of all specimens was dominated by the deformation of the longitudinal reinforcement, with the exception perhaps of specimen C5-40. Because the axial load acting on specimen C5-40 was close to the "balanced load" for the normal-strength specimens, a significant part of the cross section was in compression, and the properties of the concrete had a stronger influence on the overall response.

As the axial load increased, larger compressive strains were imposed on the concrete, resulting in more damage to the shell of the element. The concrete inside the core was adequately confined by the transverse reinforcement, allowing the specimen to sustain large deformations while having ductile and tough behavior. For specimens tested with 128 kips of axial load, the ultimate drift was limited by buckling of the longitudinal reinforcement.

3.8 Measured Mean Curvature Distributions

Figures 3.57 to 3.64 present the mean curvature distribution along the length of the specimens, for successive displacements during the first quarter cycle. Abscissae represent the distance from the center of the specimen to the center of gaged length, and ordinates the mean curvature.

Mean curvature values were calculated using deformation readings obtained with electronic Whittemore Gages, using a procedure similar to that described in section 3.4. According to the distribution of anchor points for the electronic Whittemore gage, the calculated mean curvatures corresponded to points located at distances of 1.1 in. and 4.6 in., on both sides of the face of the joint. An additional data point corresponded to a location 10.5 in. from the face of the joint, towards the inflection point.

Figure 3.57 shows the mean curvature distribution for specimen C10-00. Even near yield, deformations in the flexural cracks resulted in high values of mean curvature

near the face of the joint. At distances further from the joint face, mean curvatures showed a linear distribution and much lower magnitudes.

The north element showed large curvatures concentrated in the flexural crack located outside the joint, closest to the joint face. Mean curvatures measured inside the joint were negligible. The south element showed somewhat different behavior. Rotations were concentrated in the two cracks located on both sides of the face of the joint. Therefore, the largest measured mean curvatures for the south element were within the first 2.25 in. of the joint. Mean strains and thus curvatures were very small at distances further than 2.25 in into the joint. This observation was consistent with the mean strain distribution.

The mean curvature distribution of specimen C5-10 (Fig. 3.62) was similar to that of C10-00 (Fig. 3.57). The south element showed the effect of two flexural cracks, one of them inside the joint and very close to its face. On the north element only one crack, located outside of the joint, generated most of the deformation in the element.

Specimens C5-10 and C10-00 were subjected to displacement history A (Fig. 2.2, chapter 2), which had a larger maximum displacement during its first cycle than displacement history B (Fig. 2.3, chapter 2). Therefore, the maximum mean curvatures for specimens C5-10 and C10-00 were larger than those for all subsequent specimens. For the same reason, nonlinear deformations during the first quarter cycle in specimens C5-10 and C10-00 were also larger than those for all other specimens.

Figures 3.58 to 3.61 and 3.63 to 3.64 show the evolution of the curvature distribution during the first quarter cycle for specimens C10-05, C10-10, C10-20, C5-00, C5-20 and C5-40. Behavior was similar among the aforementioned specimens. The largest curvatures were recorded at the location of the flexural crack that formed closest to the face of the joint. On the remainder of the element, the curvature distribution was close to linear and proportional to the distance from the “inflection point”. Strains inside the joint, and therefore mean curvatures, were very small.

Figs. 3.65 to 3.72 show a progression of the curvature distribution at the peak positive displacement of each measured cycle. Specimens C10-00 (Fig. 3.65) and C5-00

(Fig. 3.69) correspond to the two cases without axial load. Both plots indicate that at deformations larger than yield, unlike all other specimens with axial load, a flexural crack inside the joint and very close to its face contributed considerably to the overall deformation.

There were some common trends in the behavior of the specimens. Because cracks are discontinuities in the material with very high localized values of strain, their position had a definite effect on the curvature distribution. As mentioned earlier, flexural cracks often coincided with the location of the two stirrups closest to the face of the joint, 1.5 in. in both directions. The deformation from those cracks had a strong effect on the calculated mean curvature at 1.1 in. from the face of the joint.

During the first quarter cycle and after cracking occurred, deformation across the crack closest to the face of the joint increased at a faster rate than in the remaining part of the specimen. The deformation was related to strains in the reinforcement at the location of the crack, and also slip of the reinforcement. Lower values of axial load resulted in deformations being more concentrated at the location of the first flexural crack.

Large curvature values were measured near the face of the joint Curvatures at distances larger than 7 in. from the face of the joint were small compared to those measured near the face, and remained in the linear range throughout the entire duration of the tests.

3.9 Measured Stirrup Strains

The first three stirrups of each element were instrumented using electric resistance strain gages. In some specimens each instrumented stirrup had two gages and in other cases four. The recorded stirrup strain vs load point displacement is presented in Figs. 3.73 to 3.92. A horizontal line in each plot indicates the yield strain measured as described in the Appendix. The location of the strain gage is indicated in each plot.

Specimen C10-00 (load schedule A, P = 0, high-strength): Figures 3.73 and 3.74 show stirrup strains in specimen C10-00. Strain values recorded in the stirrups of both elements were much lower than the measured mean yield throughout the entire test. This could be attributed in part to the fact that the number of full cycles of load history A (Fig. 2.2) was limited to 4. Wight observed in his tests that as the concrete core deteriorated, the

fraction of the shear force carried by the steel increased (Wight, 1973). In the case of specimen C10-00 the increase in the maximum stirrup strain between successive cycles was rather small, indicating that there was little change in the force carried by the steel.

Because the strain, and therefore the stress, in the transverse reinforcement were at all times below yield, adequate confinement to the core was provided, allowing the concrete to sustain large strains while preserving the integrity of the core. Because the transverse reinforcement prevented severe damage to the core, the specimen was able to endure drift ratios exceeding 15% during the last cycle without a large drop in its shear carrying capacity.

Specimen C10-05 (load schedule B, P = 32 kips, high-strength): Specimen C10-05 (Figs. 3.75 and 3.76) had two strain gages on each of the first three stirrups. The strain in the instrumented stirrups of the south element was at all times below yield (Fig. 3.75), and there was no significant increase between successive cycles. The fact that the strain in the steel remained nearly constant with cycling indicates that the damage to the core due to the repeated load reversals did not diminish its ability to carry the shear force.

The maximum strain in the stirrups of the north element remained nearly constant during the first six cycles, all of them with a maximum load point displacement below 1 in. After the sixth cycle, strain on the second stirrup started to increased on every cycle, reaching yield at a negative peak displacement of 1-¼ in. (Fig. 3.76). Although the variation in the total shear was small, there was a redistribution of internal forces within the section, and progressively the steel carried a larger fraction of the total shear force. During the first quarter of cycle 13, which had a maximum displacement of 2 in., a large increase in strain occurred after reaching a displacement of approximately 1 in. Soon after the specimen was no longer able to sustain the axial load.

Specimen C10-10 (load schedule B, P = 64 kips, high-strength): Figures 3.77 and 3.78 show the strain in the stirrups of specimen C10-10. This specimen showed extremely good behavior under cyclic loading, enduring a drift ratio of 6% while maintaining 80% of the initial shear. Figure 3.77 shows that the strain remained below yield for every instrumented stirrup in the south element.

Figure 3.78 shows a slightly different scenario for the north element. As in previous specimens, the largest strains were recorded in the second stirrup. During the first eight cycles the maximum strain in the stirrups did not vary considerably. As cycling up to 1-½ in. began, maximum strains increased with cycling, reaching values close to yield. However, for specimen C10-10 the strain displacement curve did not become almost vertical. In this case, the limiting factor was most likely buckling of the longitudinal bars.

Specimen C10-20 (load schedule B, P = 128 kips, high-strength): Behavior of specimen C10-20 (Figs. 3.79 and 3.80) resembles that of specimen C5-40 (Figs. 3.91 and 3.92). Strains surpassed yield in both elements, showing larger increases between cycles during the latter stages of the test.

In the south element, the strain in the second stirrup exceeded yield during the ninth cycle (Fig. 3.79). The third stirrup did the same earlier, but it did not develop large strains at the end of the test. In the north element, the first stirrup exceeded yield during the seventh cycle, with a maximum drift of 1-½ in. The second and third stirrups yielded for the first time between the seventh and ninth cycles.

Specimen C5-00 (load schedule B, P = 0, normal-strength): By contrast, strains in the stirrups of specimen C5-00 remained below yield for the entire test (Figs. 3.81 and 3.82). Behavior of this specimen was extremely ductile. Although the load had dropped below 80% of the initial during the eleventh cycle, which had a maximum drift of 1-¾ in., the specimen was able to sustain larger deformations until the thirteenth cycle, with a maximum displacement of 2 in.

Specimen C5-10 (load schedule A, P = 32 kips, normal-strength): Specimen C5-10 had four strain gages on each stirrup (Figs. 3.83 to 3.86). Behavior was similar to that of specimen C10-00. In this case however, strains in the second stirrup of the south element reached yield near the end of the test, at a drift ratio of approximately 12% (Figs. 3.83 and 3.84), indicating perhaps a higher amount of damage to the concrete core. As described in section 3.1, during the fifth cycle the maximum shear force in the south element dropped to approximately 80% of the initial, after surpassing a displacement of approximately 1-½ in.

Specimen C5-20 (load schedule B, P = 64 kips, normal-strength): Figures 3.87 to 3.90 show strains in the first three stirrups for both elements of specimen C5-20. Each stirrup had 4 strain gages, 2 on each leg. Strain gages in the south element (Fig. 3.87 and 3.88) show that the second stirrup reached yield at the negative peak displacement of 1.25 in., during the seventh cycle. It was at that point, that the shear in the south element dropped to approximately 65% of the initial, indicating substantial damage. Once again, there was a pattern of increasing strains with cycling in the second stirrup. After the seventh cycle, was the measured yield strain had been surpassed, strain increases between cycles became larger. During the negative loading portion of cycle 10, the strain displacement curve became almost vertical and the shear carrying capacity of the north element dropped to approximately 40% of the initial.

Figures 3.89 and 3.90 shows that the first stirrup of the north element behaved similarly. Strains began to have considerable increases during cycle 9, to a maximum displacement of 1-½ in. During loading in the negative direction for cycle 10, a large increase in strain was recorded, and the test had to be stopped soon after that because the specimen could no longer sustain the axial load.

Specimen C5-40 (load schedule B, P = 128 kips, normal-strength): Specimen C5-40 (Figs. 3.91 and 3.92) had the highest axial load and the lowest drift at failure. The second stirrup recorded the largest strain values of the south element (Fig. 3.91). Both the first and second stirrups (Fig. 3.92) recorded strains above yield in the north element. In both elements, the maximum recorded strains reached yield during the fifth cycle, much earlier than in previous specimens.

3.10 Comparison of Measured Stirrup Strains

Strains in the stirrups of all specimens were below yield during the first few cycles. As the maximum displacement increased further, the confined core deteriorated, causing the demand on the stirrups, indicated by the strain, to increase. For higher values of axial load, the increase in stirrup strains began at lower drifts.

An increase in concrete strength resulted in improved behavior of the core, as shown by comparing the strain displacement curves of specimens C5-40 (Figs. 3.91 and

3.92) and C10-20 (Figs. 3.79 and 3.80). In specimens without axial load (Figs. 3.73, 3.74, 3.81 and 3.82), strain remained below yield during the entire test, which resulted in very ductile behavior.

After the strain in the stirrups exceeded yield, the rate of increase in the strain became very large, and failure of the specimens ensued.

3.11 Measured Strains in Longitudinal Bars

Longitudinal bars were instrumented following two different schemes. For the first four tests, strain gages were located at the face of the joint and at several points near by in order to study the variation of stresses throughout the bar. The second group of four specimens had strain gages only at the face of the joint. Specimens with little or no axial load developed very large strains immediately after yield, usually causing the gages to malfunction. Strains plotted are those obtained while the gages were functioning properly.

Specimen C10-00 (load schedule A, P = 0, high-strength): Figures 3.93 to 3.97 show strain vs load-point-displacement for different locations along the top longitudinal bars. The horizontal line indicates the yield strain for No. 5 bars, measured as described in the Appendix. Because the top face of the south element was subjected to compression during the first quarter cycle, strain readings on the face of the south element were negative (Fig. 3.93). However, near the peak positive displacement strains became positive again, although very close to 0. During the first two cycles, the shell was able to carry the total compression force in the section and both layers of steel were in tension.

When loading in the negative direction, the top bars in the south element were subjected to tension (Figs. 3.93 and 3.94). Strains at the negative peak displacements of the first two cycles just reached yield. During the third cycle, while loading in the negative direction, there was a large increase in strain after yield, which caused the gages to malfunction.

At 3 in. into the joint, the first four cycles recorded strains at or below yield. At 6 in. from the face of the joint strains were at all times below yield, showing that anchorage reduced the stress in the bar inside the joint (Figs. 3.93 and 3.94). Strains recorded at the center of the specimen remained very close to 0 through the entire test (Figs. 3.94 and

3.95), indicating that 20 bar diameters were sufficient to fully develop the bar. This was the case for all four specimens instrumented to measure such strains.

Strains in the top bars of the north side showed a similar trend (Figs. 3.95 and 3.96). At the face of the joint, top bars yielded during the first cycle reaching strains in the order of 0.5%. Readings inside the joint showed lower values of strain than the south element. This is attributable to the fact that the south element developed a flexural crack inside the joint as indicated by the measured strains and curvatures.

Gages in the bottom bar showed similar trend. Strains in the longitudinal reinforcement suffered a large increase soon after yield, and the strain at the center of the specimen was very small (Figs. 3.96 and 3.97).

Specimen C10-05 (load schedule B, P = 32 kips, high-strength): Strains in the top bars of the south element are shown in Figs. 3.98. Top bars were close to the compression face during the first quarter cycle, and because the shell had not been affected at this point, the neutral axis depth was small enough to cause the bars to go into tension at and near the face of the joint. During the second half of the cycle, top bars acted as the main tension reinforcement and the strains surpassed yield. At the peak displacement of -0.5 in., measured strains were larger than yield at the joint and at 3 in. from it in both directions. Measurements taken 6 in. into the joint indicate a strain of 1500 which is slightly more than half the measured yield strain. The maximum strain at that location increased with cycling, reaching values as high as 2500 microstrain during cycles 3 and 4, with a maximum displacement of 0.75 in.

When loading in the positive direction during the second cycle, damage to the shell incurred during the first cycle caused the top bars to remain in compression (Fig. 3.98).

Figure 3.99 shows the strain in the top bars of specimen C10-05 also. Strain gages in the north side of the joint recorded lower measurements than in the south side. At 6 in. into the joint, the strain reached 1000 micro strain during the first cycle and up to 1500 at a displacement of 1.75 in. Gages located 3 in. into the joint recorded close to 2000 microstrain during the first cycle and barely reached yield at the end of the test.

Once again, at the joint face, strain registered an extremely large increase soon after yield, causing the failure of the strain gages.

Figures 3.101 and 3.102 show the strain recorded in the bottom bars of specimen C10-05. In this case, one of the two bottom bars recorded values near 1000 at the center of the specimen, showing that anchorage was less effective for this particular bar. Bottom bars in the north element showed behavior similar to that of the top bars. Soon after yield, strain increased considerably causing the gages to malfunction.

Specimen C10-10 (load schedule B, P = 64 kips, high-strength): Strains in the top bars of specimen C10-10 (Fig. 3.103) yielded in tension during the first cycle, and the recorded strain increased up to values of 25000 soon after exceeding the yield strain. Compressive strains in the bars were very small and there was no indication of yielding in compression up to a maximum displacement of 1 in. (Figs. 3.103 to 3.105) Readings in the bottom bars (Figs. 3.104 and 3.105) showed a similar pattern to those of top bars (Figs. 3.103 and 3.104).

Specimen C10-20 (load schedule B, P = 128 kips, high-strength): Figures 3.106 to 3.108 show strain-displacement readings for specimen C10-20. During the first three cycles behavior of the top bars was similar to that of specimens with small axial loads. Tensile strains reached values on the order of 2 to 3% (Fig. 3.106), while compressive strains remained below yield. While loading during the third cycle, tensile strains became so large that they caused the strain gages to cease working.

At bottom bars, compressive strains were larger (Figs. 3.107 and 3.108). During the third cycle one of the bars at the south element yielded in compression, reaching close to -7000 . Strain readings in the north element (Fig. 3.108) also indicated yielding in compression with peak values close to -8000 microstrain for a displacement of 1-½ in.

Specimen C5-00 (load schedule B, P = 0 kips, normal-strength): Behavior of specimen C5-00 (Figs. 3.109 and 3.110) was similar to that of other specimens with low values of axial loads. During the first cycle, as soon as the bars reached yield, strains exceeding 2 % were developed at the face of the joint, causing the strain gages to

malfunction in most cases. Compressive strains recorded during this first cycle were very small (Fig. 3.110).

Specimen C5-10 (load schedule A, P = 32 kips, normal-strength): Readings from strain gages in the longitudinal bars of specimen C5-10 are presented in Figs. 3.111 to 3.115. The presence of axial load reduced the magnitude of the strains after yielding. Figure 3.111 shows that strain gages located 3 in. from the face of the south element in both directions, recorded yielding of the top longitudinal bars. Of the two afore mentioned locations, strain in the column was higher than that inside the joint.

The strain recorded in the center of the specimen was very small (Fig. 3.112). Top bars in the north element were subjected to tension during the first quarter cycle (Fig. 3.113). After reaching yield, the strain in the face of the joint increased to values larger than 1%. The same behavior was observed for the gages located three in. into the column (Fig. 3.100). Figs. 3.114 and 3.115 show strains in the bottom bars for specimen C5-10.

Specimen C5-20 (load schedule B, P = 64 kips, normal-strength): In this case, bottom bars were instrumented extensively. The two horizontal lines in the plot indicate the yield strain measured as indicated in the Appendix (A.2.2). Fig. 3.116 shows the strain in the top bars of the south element. During the first three cycles, strain in the south element reached values slightly above yield. Starting on the third cycle the maximum compressive strain began to increase. As cycling progressed and the shell deteriorated, the reinforcement absorbed an increasing fraction of the compression force in the section, eventually causing the longitudinal bars to yield in compression at a displacement of 1 in. At this point, the longitudinal reinforcement was yielding in tension and compression during each cycle.

Strain in the top bars of the north element (Fig. 3.117) was recorded up to a displacement of 0.75 in., and behavior was similar to that of the south element.

Bottom bars in the south element (Figs. 3.118 and 3.119) were instrumented with greater detail. They yielded in compression during the third cycle (Fig. 3.118) at a location 3 in. into the column. Strains at the face of the joint were smaller in compression and higher in tension for the third cycle. Strains within the south side of the joint (Fig. 3.119)

showed values just below yield during the entire test. Similar readings in the north side of the joint (Figs. 3.120 and 3.121) showed that the bottom bars did yield, reaching large strains at a location 3 in. into the joint.

Specimen C5-40 (load schedule B, P = 128 kips, normal-strength): Strain-displacement plots for specimen C5-40 (Figs. 3.122 to 3.124) resemble those of specimen C5-20 (Figs. 3.116 to 3.121). Top bars in the south element yielded in compression during the third cycle (Fig. 3.122). In the north element one of the bars yielded in compression during the first cycle (Fig. 3.124).

3.12 Observed Crack Patterns

During the tests, at different stages of loading, cracks were transcribed to transparencies which were later digitized.

Figure 3.125 shows the crack pattern for specimen C10-00 at the end of the test. The diagram shows that a flexural crack formed inside of the south element, approximately 0.5 in. from the face. This correlates with observations from the strain and curvature plots which indicated that a significant fraction of the total rotation originated within the first 2 in. of the south element. At a distance of 7 in. from the face of the joint, cracks started in the vertical direction, consistent with flexure strains, and then dipped towards the compression zone near the face of the joint. The north element showed greater damage to the concrete in the shell as indicated by the hatched area (Fig. 3.125). The flexural crack in the element was the main source of deformation, although there was a contribution from a second flexural crack inside the joint.

Figures 3.126 to 3.128 show the evolution of cracks at increasing levels of displacement for specimen C10-05. During the first cycle, which had a maximum displacement of 0.5 in., flexural cracks formed starting at small displacements. As displacement increased, cracks located at a distance d from the joint dipped and formed inclined cracks. Fig. 3.126 shows the crack pattern at the end of the first two cycles, both of them with a maximum displacement of ½ in. Horizontal cracks located in the element and near the joint are attributable to the crushing of the shell, which was slightly damaged at this point.

During subsequent cycles (Figs. 3.127 and 3.128), the crack pattern did not change considerably. The main difference was that as cycling damaged the shell, the extent of the horizontal cracks grew (Fig. 3.127) and later caused sections of the shell to fall (Fig. 3.128).

Figures 3.129 to 3.131 show the evolution of cracks for specimen C10-10, with an axial load of 64 kips. Figs. 3.129 and 3.130 show the progression of cracks during the first quarter cycle. Figure 3.123 shows cracks after the direction of loading was reverted. At larger displacements, the main difference in the crack pattern was originated by the loss of the shell.

The crack pattern for specimen C10-20 is presented in Figs. 3.132 to 3.135. The higher axial load imposed on specimen C10-20 had an adverse effect on the soundness of the shell. Fig. 3.135 indicates that at the end of the first cycle small sections of shell had already been lost.

Figures 3.136 to 3.139 show the location of the cracks for specimen C5-00 at different points during the first cycle. Most of the deformation in this specimen occurred near the joint face.

Figures 3.140 and 3.141 show crack patterns for specimens C5-10 and C5-20 at different stages of loading.

3.13 Failure Mechanism

Considering that the test parameters varied between specimens, it is reasonable to conclude that their behavior varied accordingly. However, there were common elements of behavior which are presented in this section (Fig. 3.146). Background is provided about the parameters that affect the shear and deformation capacities of a column and a plausible failure mechanism is described.

During the early stages of loading, before the appearance of the flexural cracks, the strain in the transverse reinforcement was barely measurable (Fig. 3.146). Flexural cracks formed at very small displacements, corresponding to a shear force of approximately 700 lbs. in the case of specimen C10-00, which had no axial load.

Flexural cracks propagated as the shear force increased. After cracking, at a displacement of approximately ¼ in., the flexural cracks started to dip towards the compression zone at the face of the joint. Once the flexural cracks started to propagate in an inclined direction, the strain in the transverse reinforcement increased proportionally with the displacement.

At a displacement slightly lower than ½ in., the longitudinal reinforcement yielded at the face of the joint, immediately reaching strains on the order of 1 to 2%. At approximately the same displacement, crushing of the concrete was first observed at surface of the column and the the shear-displacement curve registered a change in slope, indicating the initiation of yielding in the element.

After yielding, the increasing deformations and the cyclic loading had a debilitating effect on the elements. The high compressive strains imposed on the concrete resulted in spalling and subsequent loss of the unconfined shell. Repeated movement along the inclined cracks consistent with both directions of loading had an abrasive effect on the concrete inside the confined core.

The maximum strain in the stirrups continued to increase with load-point deflection. The slope of the strain-displacement curve was proportional to the axial load. In specimen C5-00, without axial load, the force in the transverse reinforcement had a very small increase with cycling and remained at all times below yield, even for a drift ratio of 8%. For specimens with axial loads of 32 and 64 kips, the critical stirrup reached the measured yield strain at drift ratios ranging from 5% to7 %. For an axial load of 128 kips strain in the critical stirrup of the normal-strength specimen reached yield at a drift ratio of 4%. Once the transverse reinforcement yielded, the core suffered cumulative damage with cycling and the axial capacity of the column was lost soon after.

Equations 21-3 and 21-4 in the Building Code Requirements of the American Concrete Institute (American Concrete Institute, 1995) were developed based on the premise that adding spiral reinforcement to a reinforced concrete section induces a tri-axial state of stress in the concrete inside the core. Confining pressure provided by the transverse reinforcement improves the ability to deform and compressive strength of the concrete inside the core. Because the confining stress and the increase in compressive

strength of the core are proportional to the amount of transverse reinforcement, the capacity that is lost because of crushing of the unconfined shell concrete can be compensated by the increased strength of the core, if sufficient reinforcement is provided.

The maximum shear force that a column with adequate transverse reinforcement can sustain is limited by its flexural capacity. If enough shear reinforcement is provided to prevent the occurrence of a shear failure, the column should be able to sustain deformations up to its flexural limit. However, subjecting a column to load reversals causes deterioration of the core inside the stirrups, as inclined cracks open in both directions. Wight observed in a study using normal-strength columns that as the core deteriorated the shear force carried by the transverse reinforcement increased (Wight, 1973). Once the transverse reinforcement yielded, damage to the confined core occurred at a much faster rate, leading to failure.

Another way to present this phenomenon is to assume that the effectiveness of the confining pressure decreases as damage to the core progresses. Because the axial load demand remains nearly constant, strains in the transverse steel must increase in order to maintain the "effective confining pressure" constant, and compensate for the loss in area of the cross section.

Once the increased demand is enough to make stirrups yield, the problem becomes more complicated. In order to carry the axial load, concrete within the damaged core needs to redistribute some force to the longitudinal steel, which also acts as an important source of confinement to the core. Several effects combine in detriment of the longitudinal steel. First, the longitudinal bars are subject to an outward pressure generated by the damaged core. Also, because of the damage to the concrete, they must carry a larger fraction of the compression force, while the lateral support provided by the transverse reinforcement has weakened due to yielding. All of these factors combine to make the longitudinal reinforcement more susceptible to buckling. For these reasons the section loses its capacity to carry the axial load soon after yielding of the stirrups.

3.14 Effect of Test Variables

There were three parameters that were varied during the course of the experimental investigation: displacement schedule, axial load, and compressive strength of the concrete. This section discusses the effects those three variables had on the test results.

The displacement history had a dominant effect on behavior. The two displacement schedules used in the tests differed in their number of cycles and the maximum displacement of each cycle. For schedule A, the maximum displacement of each cycle had a progressive increase up to a value of 1-¼ in., applied during the fourth cycle. The displacement was subsequently increased up to the maximum value allowed by the test setup (three in.). For schedule B, the maximum cycle displacement started at a value of ½ in. and increased by ¼ in. every two cycles, until it was no longer possible for the specimen to sustain the axial load.

The shear-displacement response was closely related to the type of displacement schedule. Figures 3.147 and 3.148 show the shear-displacement curves for normal-strength and high-strength specimens respectively. In both graphs, the limiting drift of the specimen subjected to displacement schedule A (specimens C5-10 and C10-00) exceeded 1.6 in. The limiting drifts of the specimens subjected to displacement schedule B were much lower, all of them equal to or below 1.6 in. (Table 3.1).

The behavior of the two specimens subjected to displacement schedule A, C10-00 and C5-10, was characterized by large toughness and ductility. For displacements larger than yield, the shear force in the specimen made with high-strength concrete (C10-00, Fig. 3.148) was insensitive to the displacement, while the shear force in the normal-strength specimen (C5-10, Fig. 3.147) had a slight tendency to drop with increasing displacements. Specimen C5-10, the only one of the two subjected to displacement schedule A to have axial load acting on it, was still able to carry the full axial load at the end of the test.

The displacement schedule also had a strong effect on stirrup strains. Figure 3.149 shows the relationships between the maximum strain in the stirrups and the load-point displacement for the normal-strength specimens. Figure 3.150 shows similar relationships for the high-strength specimens.

Between 0 and 1 in., strain increased proportionally with the load-point displacement. At larger deformations, there was a distinct difference in behavior dependent on the displacement history. For specimens subjected to schedule B, the maximum strain continued to increase in proportion to the load-point displacement until the stirrups yielded. Conversely, strain in both specimens subjected to displacement schedule A (C5-10 and C10-00) was not affected by the increase in load-point displacement and remained nearly constant until the end of the test (Figs. 3.149 and 3.150).

Based on the trends observed in the load-displacement curves for the elements and the strain-displacement curves for the stirrups, it is clear that the number of cycles in the displacement history had a determining effect on the toughness and ductility of the elements.

The second parameter to be varied within the experimental study was the axial load. There were four different values of axial load applied to the specimens: 0, 32, 64 and 128 kips. To dismiss the effect of the load history, attention is centered on the specimens that were subjected to displacement schedule B. Among normal-strength elements the limiting drift (Fig. 3.147) had an unambiguous tendency to decrease with axial load. The toughness also had a clear decreasing trend with respect to axial load.

The effect of axial load on the behavior of high-strength specimens was not as significant (Fig. 3.148). Specimen C10-20, subjected to an axial load of 128 kips, had lower a limiting drift and toughness than specimens C10-05 and C10-10. The limiting drift of specimens C10-05 and C10-10 was similar, with values of approximately 1.3 in. for C10-05 and 1.45 in. for C10-10.

Comparing the shear-displacement relationships of normal and high-strength specimens, the axial load had a noticeable effect on behavior for those specimen in which its magnitude was larger than half the balanced load.

The slope of the strain-displacement curve for the critical stirrups of normal-strength specimens was proportional to the axial load (Fig. 3.149). While in specimen C5-00 the increase in stirrup strain was small and never reached the measured

yield value, the strain-displacement curve for the critical stirrup of specimen C5-40 had a much larger slope that led to yield at a displacement of ¾ in.

In high-strength specimens the pattern was not as consistent (Fig. 3.150). The behavior of specimens C10-20 and C10-05 indicated an increase in the slope of the strain-displacement curve proportional to the increase in axial load. However, the strain-displacement curve for the critical stirrup of specimen C10-10 falls out of this pattern because it had the largest slope of the three specimens.

The third variable of the study was the compressive strength of the concrete. There were two pairs of specimens that were subjected to the same axial load and displacement schedule while having different concrete properties. The first pair consisted of specimens C5-20 and C10-10, tested with an axial load of 64 kips. The second pair was tested with an axial load of 128 kips and it consisted of specimens C5-40 and C10-20.

Figure 3.151 shows the shear-displacement relationships for the two pairs of specimens. In both cases, the increase in concrete strength led to increases in the limiting drift and toughness of the elements. The increase in limiting drift was most significant for the two specimens tested with an axial load of 128 kips.

A comparison of the relationships between stirrup strain and displacement is shown in Fig. 3.152. For the two specimens subjected to 128 kips of axial load the increase in compressive strength was associated with a significant reduction of the slope in the strain-displacement curve. However, the behavior of specimen C10-10 was again inconsistent with this pattern because the slope of its strain-displacement curve was higher than that of specimen C5-20. In the case of specimen C10-20 the measured yield strain was reached at a displacement of approximately 1-¼ in., and the slope of its strain-displacement curve remained constant, indicating linear elastic behavior, up to a displacement of 1-¾ in. The critical stirrup of specimen C5-20 reached the measured yield strain at a displacement of approximately 1-½ in., and immediately suffered a large increase, indicating that at this point the stirrup yielded.

In conclusion, the effect of the three variables on behavior was as follows:

- An increase in the number of displacement cycles resulted in a reduction of the limiting drift, toughness and ductility of the elements.

- Increasing the axial load had an adverse effect on the limiting drift, toughness and ductility of the elements. For specimens subjected to load values below one half the balanced load, the effect of axial load was not very significant and even beneficial.

- The use of high-strength concrete increased the limiting drift and improved the toughness and ductility of the elements.

Chapter 4

Calculation of Displacement Components

4.1 Introduction

Internal deformations in the elements were recorded by means of Whittemore strain gages using the array of stations and procedure described in Chapter 2. The current Chapter presents an analysis of those readings with the object of calculating vertical deflections and their components based on internal deformations. Deflection values inferred from the electronic Whittemore gage readings were then compared with those measured directly with displacement transducers.

Based on the deformed configurations mapped with the electronic Whittemore gages, the total deformation was separated into components related to flexure, shear, rigid body motion and slip. The magnitude of the components at different stages of loading is discussed.

4.2 Calculated Deflections Based on Whittemore Readings

Each element had three stations for measuring deformations (Fig 4.1) beginning at a distance of 7 in. into the joint up to 14 in. towards the load-point. Each station consisted of a rectangle in which both horizontal, vertical and diagonal distances were measured. The internal angles were calculated based on one of the diagonals (Fig. 4.1) for each deformed configuration that was mapped using the laws of sines and cosines, i.e.

$$\beta_2 = \text{acs}\left(\frac{L_1^{\,2} + L_3^{\,2} - L_2^{\,2}}{2L_1L_3} \right) \qquad (4.1)$$

$$\beta_1 = \text{asn}\left(\frac{L_1}{L_2} \sin\beta_2 \right) \qquad (4.2)$$

$$\beta_3 = \text{asn}\left(\frac{L_3}{L_2}\sin\beta_2\right) \tag{4.3}$$

$$\beta_5 = \text{acs}\left(\frac{L_4^{\,2} + L_5^{\,2} - L_2^{\,2}}{2L_4L_5}\right) \tag{4.4}$$

$$\beta_4 = \text{asn}\left(\frac{L_4}{L_2}\sin\beta_5\right) \tag{4.5}$$

$$\beta_6 = \text{asn}\left(\frac{L_5}{L_2}\sin\beta_5\right) \tag{4.6}$$

Once the internal angles were determined for each station, the vertical deflection and the rotation with respect to the vertical at each point in the station were calculated using simple geometry. The vertical line of station 1 closest to the center of the specimen was assumed to remained vertical to establish a reference point.

Deflection values were calculated based on each of the two diagonals and then compared. The results showed very good agreement.

4.3 Comparison of Vertical Deflections at Station 3

A first comparison was established between the vertical deflections calculated at station 3 (Fig. 4.1) and those recorded using displacement transducers.

The deflections inferred from the electronic Whittemore gage readings include components related to flexure, shear and slip. However, because they were recorded directly on the elements using the undeformed configuration as a reference, their coordinate system was fixed to the specimens and was not affected by the rigid body motion of the specimens.

The deflections measured with displacement transducers referred to the strong floor of the laboratory, so they include the rigid displacement and rotation of the specimen with respect to the floor. Therefore the displacements inferred from the Whittemore readings

had to be corrected to account for the effects of rigid body motions before a comparison could be established.

The location of the displacement transducers is shown in Fig. 4.2. Measurements from transducers designated in Fig. 4.2 as RB_{1s} and RB_{1n} were used to calculate the rigid body motion of the specimens. These two transducers were located within the joint, were as observed in Chapter 3 the deformations were negligible compared to those that occurred in the elements.

The rigid body rotation and vertical displacement at the center of the specimen were calculated using Eq. 4.7 and 4.8.

$$\theta_{\text{Rigid Body}} = \frac{\left(RB_{1s} + RB_{1n}\right)}{10} \tag{4.7}$$

where RB_{1s} and RB_{1n} are given in in.

$$\delta_{\text{Rigid Body}} = \frac{\left(RB_{1s} + RB_{1n}\right)}{2} \tag{4.8}$$

Knowing the rotation and displacement at the center of the specimen, the displacement related to the rigid body motion of the specimen at the location of any transducer was calculated using equation 4.9.

$$RB_n = \delta_{\text{Rigid Body}} + \theta_{\text{Rigid Boody}}\, d_n \tag{4.9}$$

where d_n is the distance from the center of the specimen to the location of the transducer.

The calculated rigid body component at station 3 was added to the displacement inferred from the electronic Whittemore gage readings at the same location and their total was compared with the deflections obtained directly with displacement transducers. Plots showing the comparison between calculated and measured displacement at station 3 for each specimen are presented in Figs. 4.3 to 4.18.

Figures 4.3 to 4.18 indicate that there was very good agreement between measured and calculated displacements. There were however three specimens in which there was a noticeable difference between the measured and calculated response. For specimen C5-10 (Figs. 4.13 and 4.14) the transducers recording rigid body motion did not function properly. Without measurements of rigid body motion, it was not possible to calculate the rigid body component, which very likely amounts to the difference between measured and calculated displacement observed in Figs. 4.13 and 4.14.

The second problem arose with both specimens subjected to an axial load of 128 kips. The motion of the joint was restrained by the mechanism fixing the specimen to the base block. This mechanism behaved as a very stiff rotational spring, so the rigid body rotation of each specimen was proportional to the shear force in its elements. Because the maximum shear force in the elements increased proportionally to the axial load, the largest rigid body rotations occurred in both specimens subjected to an axial load of 128 kips. In these two specimens, C5-40 and C10-20, one of the transducers recording the displacements within the joint was saturated while loading with a negative couple. Because of this, the calculated rigid body component was slightly overestimated in the south element and considerably underestimated in the north (Figs. 4.9, 4.10, 4.17 and 4.18).

For all other specimens the difference between the calculated and measured response is very small, indicating that the procedure used to infer the vertical deflections based on the electronic Whittemore gage readings yielded good results.

4.4 Load-Point Displacements

The displacements presented in section 4.3 correspond to a point located 26 in. from the center of the specimen, in station 3. Because there were no electronic Whittemore gage measurements in the 10 in. distance between station 3 and the load-point, certain assumptions were made to extrapolate the vertical displacements inferred from the electronic Whittemore gages to the load-point.

The total displacement at station 3 was separated into components following the procedure outlined in section 4.5. As observed in Chapter 3, the mean curvature distribution is such the inelastic behavior occurs within a distance equivalent to the

effective depth from the face of the joint. Hence, it was assumed that the mean curvature varied linearly from none at the load-point to the inferred mean curvature at the center of station 3 (Fig. 4.19). Based on this assumption, the mean curvature at 5 in. from the load-point was determined by interpolation. Knowing the mean curvature, the rotation and subsequently the displacement related to flexure for the last 10 in. of the specimen were calculated and added to the deformation at station 3. Because the interpolated mean curvature was small, the main contribution to the flexural component over the last 10 in. of the element originated from the rotation at the end of station 3.

A similar approach was followed to estimate the deformations related to shear. It was assumed that the mean shear strain in station 3 was similar to that between station 3 and the load-point (Fig. 4.19). The deformation related to shear was then calculated as the mean strain multiplied by the distance between station 3 and the load-point.

The additional displacement components related to shear and flexure were added to those inferred from the electronic Whittemore gages at station 3 to obtain the displacement at the load-point. The rigid body displacement at the load-points were also calculated based on the readings from the transducers located inside the joint (Fig. 4.2). The comparison between measured and calculated deflections at the load-point are presented in Figs 4.20 to 4.35.

Results were similar to those obtained at station 3, indicating that the assumptions used to extrapolate the displacements were adequate. Calculated and measured deflections show a very close match, with the same exceptions indicated in section 4.4 (Specimens C5-10, C5-40 and C10-20). For the remaining five specimens there was good agreement between measured and calculated results.

For specimens C5-10, C5-40 and C10-20 the error was traced to the measurement of the rigid body component of the displacement, establishing that the displacements inferred from the electronic Whittemore gage readings were reliable. Because of this, the rigid body displacements were calculated as the difference between the displacements inferred from the Whittemore readings (which include the components related to shear, flexure and slip) and the total displacement measured with respect to the laboratory floor. Figures 4.36 to 4.51 show the magnitude of the displacement components during the tests.

The dotted line shows the total displacement at the load-point measured by means of a displacement transducer. The solid line shows the total of the components related to flexure, shear and slip, which were calculated based on the electronic Whittemore gage readings. Finally, the dashed line shows the component related to the rigid body motion of the specimen which was calculated as the difference between the other two.

4.5 Calculation of Components Related to Shear, Flexure and Slip

The internal angles for each station were calculated using the electronic Whittemore gage readings following the procedure outlined in section 4.2. However, it is of interest to study not only the load-displacement response, but also the variation of the displacement components during the tests.

To separate the components of the displacement related to flexure and shear, the total deformation in each station was expressed as the linear combination of two mode shapes (Fig. 4.52). The first of these modes represents the deformation related to flexure. Plane sections remain plane after deforming and the mean strain is proportional to the distance from the neutral axis. This mode was characterized by the parameter α which is one half of the rotation between the two vertical lines.

The second mode represents the deformation related to shear, where a rectangle in the undeformed configuration is distorted without a change in length of the horizontal lines. The distortion is characterized by the parameter γ, which is equivalent to twice the mean shear strain.

Adding both deformation modes, the internal angle change is expressed as a combination of the deformations related to flexure and the deformations related to shear (Fig. 4.52). The value of α was obtained calculating the mean angle change for the top two angles. The value of γ was obtained by calculating the mean angle change of the bottom left and top right angles.

The displacements related to flexure were calculated by integrating the rotations for each station, and later extrapolated to the load-point as described in section 4.4. For this set

of calculations the rotation at station 2 includes the rotation related to the slip of the reinforcement.

The displacements related to shear for each station were calculated based on the distortion angle γ. To verify that the calculations were consistent, both components were added and the total was compared with the displacements obtained previously using simple geometry. The comparison showed very close match.

Figures 4.53 to 4.68 show the deflection related to shear vs the deflection related to flexure and slip, at the load-point. For the majority of the specimens, the relationship between both components was approximately linear with the shear deflection being very small compared to the deflection related to flexure and slip.

For specimen C5-00 (Figs. 4.61 and 4.62), without axial load, the behavior differs. During each cycle, most of the shear deformation occurred while the specimen was unloading. Once loading in the opposite direction started and the crack closed, the deformation related to shear was negligible. This behavior was more evident as the maximum deformation of the cycle increased.

Figures 4.69 to 4.84 show the envelopes for the displacement components while loading in the positive direction. These figures show the relative magnitude of the displacement components.

4.6 Displacements Related to Shear

Although the deflection related to shear was a small fraction of the total, it was much larger than calculated from theory of elasticity. For a rectangular beam, fixed in one end and a subjected to a point load V at the other end, the elastic deformation related to shear is given by

$$\delta_s = \frac{6LV}{5AG} \qquad (4.10)$$

Assuming $A = bd$ and $G = E/2.5$ and substituting into equation 4.10,

$$\delta_s = \frac{3 L V}{b d E} \qquad (4.11)$$

Equation 4.11 was evaluated for L = 7 in. and compared with the displacements related to shear inferred from the Whittemore readings at stations 2 and 3. The results are presented in Figs. 4.85 to 4.100.

The displacements related to shear at stations 2 and 3 were much larger than those calculated using elastic beam theory (shown by the dotted line in Figs. 4.85 to 4.100). Shear deformations in station 2, indicated by the dashed line in Figs. 4.85 to 4.100, were typically larger than those in station 3 (solid line). They also show a tendency to increase with cycling, while the maximum deformation related to shear at station 3 remained approximately constant. This is consistent with the fact that the element remained in the elastic range of response at station 3. The larger displacements that were induced as cycling progressed, were originated by increasing inelastic deformations of the element near the face of the joint.

4.7 Displacements Related to Slip

The most difficult challenge in the analysis of the displacement readings was to calculate the component of the total displacement related to slip. Figure 4.101 shows the model that was adopted in the calculation of the displacement at the load-point. The slip, obtained by integrating the strain distribution along the reinforcing bar in the anchorage region, is indicated by the distance s. The rotation related to slip is given by

$$\theta_s = \frac{s}{h_s} \qquad (4.12)$$

and the displacement at the load point is obtained by multiplying the rotation times the distance from the face of the joint to the load-point.

Specimens C10-00, C10-05, C5-10 and C5-20 were instrumented so the strain in the reinforcement at several locations within the joint would be recorded (Fig. 4.102). Strain gages were attached at the face of the joint and at distances of 3, 6, and 12 in. toward the center of the specimen from the face of the joint.

Strains recorded at the bars that were instrumented inside the joint are presented in Figs. 4.103 to 4.110. Typically two bars were instrumented in each specimen, on opposite faces of the column. Upon first loading, one of the bars was subjected to tension and the other to compression.

For convenience it is commonly assumed that bond stress along the anchorage length is constant (Otani, 1972). This assumption results in a linear strain distribution along the reinforcing bar. Following this assumption, a linear regression was carried out for every group of strain readings at 0, 3 and 6 in. from the face of the joint. Each fitted straight line provided the basis for calculating a development length and a mean bond stress.

The variation of the calculated mean bond stress with load-point displacement is presented in Figs. 4.111 to 4.114. Data are provided up to yielding of the bar or to the level at which the strain gages failed. Calculated values of mean bond stress at yield for the high-strength specimens were approximately 1500 psi (Figs. 4.111 and 4.113). Specimens made with normal-strength concrete had lower values of bond at yielding of the longitudinal reinforcement, of approximately 1000 psi.

A previous study compiled experimental data on bond tests (Matamoros, 1994). Bond strength for tests reported in this study ranged from 240 to 1277 psi for specimens with mean compressive strengths mostly between 3 and 7 ksi. Treece and Jirsa reported a test with a bond strength of 920 psi for a specimen without transverse reinforcement and concrete compressive strength of 10,500 psi (Treece and Jirsa, 1989). DeVries and Moehle reported a bond strength of 1050 psi for a specimen with some confinement and concrete compressive strength of 13,000 psi (DeVries and Moehle, 1989).

The values of mean bond stress calculated for specimens C10-00, C5-10, C10-05 and C5-20, were high compared with results from previous bond tests (Matamoros, 1994). The higher bond strength can be attributed to the fact that bars in the afore mentioned specimens had cover exceeding 3 bar diameters and also a large amount of confining reinforcement. Both factors contributed to prevent failure because of splitting of the concrete. No sign of splitting was observed at the surface of the concrete in any one of the tests.

Figures 4.115 to 4.118 show the calculated development length based on the linear-regression analysis of the strain data. The four instrumented specimens show a common trend. As the load-point displacement increased, the calculated development length tended toward a constant value. This observation is not consistent with the assumption of a constant value for the bond stress, which would result in the development length varying proportionally to the stress being developed by the bar. Given this inconsistency a new model to calculate the strain distribution along the anchorage zone of the bar was deemed desirable. This model is described in chapter 5.

Chapter 5

A Model to Estimate Slip

5.1 Introduction

Strain gage measurements recorded on the longitudinal reinforcement along the anchorage length were described in chapter 4. A linear-regression analysis was performed on the strain readings to estimate the development length and the bond stress at different stages of loading.

The results of the linear regression analysis were described in detail in section 4.7. It was observed that as the stress in the reinforcing bar increased, the calculated development length tended to remain constant. This observation was inconsistent with the conventional assumption of a constant bond stress acting on the surface of the bar. Therefore, a conceptual model based on the principles of mechanics was developed to investigate the deformation of the reinforcement inside the anchorage zone.

5.2 Equilibrium Equation for Reinforcing Bar

A segment of reinforcing bar was considered. The forces assumed to be acting on the bar are shown in Fig. 5.1. The equilibrium equation for the segment of bar is given by,

$$-\sigma(x)\,A + \left(\sigma(x) + \frac{\partial\sigma(x)}{\partial x}\Delta x\right)A - b(x)\,\Delta x\,P = 0 \qquad (5.1)$$

where A is the area of the bar, P the perimeter, and b(x) is the unit shear stress acting on the surface of the bar. The first two terms cancel one another, resulting in the differential equation

$$\left(\frac{\partial\sigma(x)}{\partial x}\,A - b(x)\,P\right)\Delta x = 0 \qquad (5.2)$$

To satisfy Eq. 5.2 for $\Delta x \neq 0$, the term inside the parentheses must be equal to 0. Thus,

$$\frac{\partial \sigma(x)}{\partial x} - \frac{P}{A} b(x) = 0 \qquad (5.3)$$

From the constitutive equation for the bar, neglecting Poisson's effect,

$$\sigma(x) = C\, \varepsilon(x) \qquad (5.4)$$

From the compatibility equations, assuming that displacements are small and second order effects negligible,

$$\varepsilon(x) = \frac{\partial u(x)}{\partial x} \qquad (5.5)$$

Substituting Eq. (5.4) and (5.5) into Eq. (5.3),

$$C \frac{\partial^2 u}{\partial x^2} - \frac{P}{A} b(x) = 0 \qquad (5.6)$$

5.3 Solution of Equilibrium Equation

In order to solve Eq. 5.6 it is necessary to define the variation of the bond stress with distance, along the surface of the bar. Traditionally, b(x) has been assumed to be constant and equal to the mean shear stress. For the case of $b(x) = b_o$ equation 5.6 is resolved by direct integration. The displacement is given by a second order polynomial, and the variation of strain and stress in the bar is linear with respect to x.

Other mechanical models for bond can be derived by assuming different types of functions for b(x). A plausible choice is to add a term to b(x) that is proportional to the displacement of the bar. Stress is transmitted from the bar to the surrounding concrete by direct bearing of the bar deformations. If linear behavior is assumed, the bearing stress is proportional to the deformation. Therefore,

$$b(x) = k_s\, u(x) + b_o \qquad (5.7)$$

Substituting Eq. (5.7) into Eq. (5.6),

$$\frac{\partial^2 u}{\partial x^2} - \frac{P\, k_s}{A\, C}\, u - \frac{P\, b_o}{A\, C} = 0 \tag{5.8}$$

Defining k_p as

$$k_p = \sqrt{\frac{P\, k_s}{A\, C}} \tag{5.9}$$

and

$$k_b = \frac{P\, b_o}{A\, C} \tag{5.10}$$

substituting Eq. 5.9 and 5.10 into Eq. 5.8

$$\frac{\partial^2 u}{\partial x^2} - k_p{}^2\, u - k_b = 0 \tag{5.11}$$

Equation 5.11 represents a boundary value problem. After the solution to the second order differential equation is found, two boundary conditions are necessary to solve for the values of the integration constants (Fig 5.2). The first boundary condition is obtained by choosing the coordinate system so that the displacement of the bar at x = 0 is also 0. The second boundary condition is obtained from equilibrium at the loaded end of the bar, located at a distance L from the origin. The stress in the bar at x = L is σ_s. Thus, the two boundary conditions are,

$$u(0) = 0 \tag{5.12}$$

$$u'(L) = \frac{\sigma_s}{C} \tag{5.13}$$

Solving Eq. 5.11 and evaluating the boundary conditions 5.12 and 5.13, the displacement u is given by,

$$u(x) = \frac{\sigma_s}{C\ k_p} \frac{e^{k_p L\,(1 - x/L)}(e^{2k_p L\, x/L} - 1)}{(e^{2k_p L} + 1)} - \frac{k_b}{k_p{}^2} \frac{e^{-k_p x}(e^{k_p x} - 1)(e^{k_p x} - e^{2k_p L})}{(1 + e^{2k_p L})} \qquad (5.14)$$

The strain is obtained by taking the derivative of the displacement with respect to x, as indicated by Eq. 5.5

$$\varepsilon(x) = \frac{\sigma_s}{C} \frac{e^{k_p L\,(1 - x/L)}(e^{2k_p L\, x/L} + 1)}{(e^{2k_p L} + 1)} + \frac{k_b}{k_p} \frac{(e^{k_p x} - e^{k_p (2L - x)})}{(1 + e^{2k_p L})} \qquad (5.15)$$

and the stress along the bar is obtained by substituting Eq. 5.15 into 5.4,

$$\sigma(x) = \sigma_s \frac{e^{k_p L\,(1 - x/L)}(e^{2k_p L\, x/L} + 1)}{(e^{2k_p L} + 1)} + \frac{C\,k_b}{k_p} \frac{(e^{k_p L\, x/L} - e^{k_p L\,(2 - x/L)})}{(1 + e^{2k_p L})} \qquad (5.16)$$

The first term in Eq. 5.15 (strain) and 5.16 (stress) is the product of the value of the stress at the loaded end of the bar and a shape function. The shape function depends solely on the parameter k_p L and the variable x.

The constant k_p, defined by Eq. 5.9, is proportional to the constant k_s, which is a property related to the stiffness of the material surrounding the bar. A reinforcing bar embedded in a very flexible material would have a very small value of k_p . Conversely a bar embedded in a very stiff material would have a large value of k_p. The constant k_p is also inversely proportional to the modulus of elasticity of the bar material and the diameter of the bar.

To study the effect of k_pL on the stress along the bar k_b (Eq. 5.10) is assumed to be 0. If k_b = 0, the second term of the right-hand side of Eq. 5.15 drops out and the strain in the bar (and also the stress) varies exponentially with x. The variation of the stress along the bar with respect to k_pL is presented in Fig. 5.3. As the value of k_p tends to 0, the stress in the bar tends to remain constant along its length and equal to the value at the loaded end. As a result of the negligible change of stress along the bar, the development length tends to infinity. Conversely, for a very large value of k_p the stress in the bar drops to 0 over a very short distance, and as a result the development length tends to 0.

Figure 5.4 presents the variation of the second term in Eq. 5.15 and 5.16 , related to k_b, with respect to the parameter k_pL. The negative sign indicates that the contribution from the term related to k_b must be subtracted from that calculated with the first term, related to k_pL and the stress at the loaded end, to obtain the total. The bar stress at any x is the algebraic sum of the stresses indicated in Fig. 5.3 and 5.4 albeit in different scales

As k_pL goes to 0, the first term, related solely to k_pL, tends to remain constant with a value equal to the stress at the loaded end (Fig. 5.3). Figure 5.4 indicates that the term related to k_b becomes linear with respect to x, proportional to the value of k_b, but opposite in sign to the first term, thus subtracting from it. The net stress variation in the bar is then linear, with a slope proportional to the constants C, k_b, and L. This is consistent with the solution for a bar subjected to a constant bond stress.

As the value of k_pL increases relative to k_b, the effect of term related to k_b becomes less significant at the loaded end of the bar. Its effect is most significant at the anchored end, where the stress related to the first term, related to k_pL, is small.

5.4 Development Length

To determine the development length in terms of the parameter k_p the stress at x = 0 is defined as $n\,\sigma_s$. Therefore, from Eq. 5.16,

$$\sigma(0) = \sigma_s \frac{2\,e^{k_pL} - \frac{k_bC}{k_p\sigma_s}(e^{2k_pL} - 1)}{(e^{2k_pL} + 1)} = n\,\sigma_s \qquad (5.17)$$

Thus,

$$n = \frac{2\,e^{k_pL} - k_1(e^{2k_pL} - 1)}{(e^{2k_pL} + 1)} \qquad (5.18)$$

Where

$$k_1 = \frac{k_bC}{k_p\sigma_s} = \frac{b_o}{\sigma_s}\sqrt{\frac{P\,C}{A\,k_s}} \qquad (5.19)$$

In order to solve Eq. 5.18 substitute $a = e^{kpL}$ into 5.19 and the result is a quadratic equation in terms of a and the constant n,

$$(n + k_1)\, a^2 - 2a + n - k_1 = 0 \tag{5.20}$$

Solving 5.20 for a,

$$a = \frac{1 \pm \sqrt{1 + k_1 - n^2}}{k_1 + n} = e^{k_p L} \tag{5.21}$$

Taking the positive root and solving for k_pL,

$$k_p L = \ln\left(\frac{1 + \sqrt{1 + k_1 - n^2}}{k_1 + n} \right) \tag{5.22}$$

From Eq. 5.22 it is possible to determine the constant k_p if L and n are known. Therefore, the value of k_p for different types of surrounding material can be determined experimentally. Conversely, if the value of k_p is known, then the value of L can be determined using Eq. 5.22.

5.5 **Bond Stress**

To determine the bond stress b(x), the constant k_s is determined using Eq. 5.9.

$$k_s = \frac{k_p^{\,2} A C}{P} \tag{5.23}$$

For a circular bar,

$$k_s = \frac{k_p^{\,2} d_b C}{4} \tag{5.24}$$

Substituting Eq. 5.24 and 5.14 into 5.7,

$$b(x) = \left[\frac{d_b k_p \sigma_s}{4} \frac{e^{k_p L (1 - x/L)} (e^{2k_p L \, x/L} - 1)}{(e^{2k_p L} + 1)} - b_o \frac{(1 - e^{-k_p x})(e^{k_p x} - e^{2k_p L})}{(1 + e^{2k_p L})} \right] + b_o \quad (5.25)$$

The peak bond stress occurs at x = L and its magnitude is given by

$$b(L) = \frac{d_b \sigma_s k_p}{4} \frac{(e^{2k_p L} - 1)}{(e^{2k_p L} + 1)} - b_o \frac{(e^{k_p L} - 1)^2}{(e^{2k_p L} + 1)} + b_o \quad (5.26)$$

Because bond stress was assumed to be proportional to the displacement of the bar, the peak value obtained using Eq. 5.26 was approximately twice that calculated assuming a constant bond stress.

5.6 Calculation of Slip

It is assumed that the displacement of the bar at the loaded end, or at x = L, is equal to the slip. The slip, u(L) is obtained evaluating Eq. 5.14 at x = L,

$$u(L) = \frac{\sigma_s}{C \, k_p} \frac{(e^{2k_p L} - 1)}{(e^{2k_p L} + 1)} - \frac{k_b}{k_p^{\,2}} \frac{(e^{k_p L} - 1)^2}{(e^{2k_p L} + 1)} \quad (5.27)$$

5.7 Calculation of Model Parameters for Test Specimens

Constant k_p was calculated using Eq. 5.22 for each specimen that was instrumented. Because Eq. 5.22 depends also on the constants L, k_1 (which depends on b_o) and n, it was necessary to define them in order to calculate k_p. The main goal was to select values for the constants so that the calculated strains would match those measured inside the joint of each instrumented specimen.

The first step was to define b_o, the constant term of b(x). Because this term is independent of bar deformation, it can be related to the static friction force, or cohesion, between the bar surface and the concrete. This is the main mechanism for transfer of stress between the bar and the surrounding medium in undeformed bars (Abrams 1913). For this reason, bond tests of undeformed bars provided a frame of reference. A reasonable value was assumed to be

$$b_o = 4\sqrt{f'_c} \qquad (5.28)$$

where b_o and the compressive strength are given in units of psi (Fig. 5.6).

Values of L and n were determined for various loading stages based on the strain measured along the anchored length. The distance between the face of the joint and the point where the strain had dropped to 10% of that at the face was calculated using a linear regression of the strain data. The value of k_p was then inferred using Eq. 5.22. This procedure was repeated, at various loading stages during the firs quarter-cycle, for all four specimens that had strain gages on the bars inside the joint region.

The value of k_p is related to the stiffness of the medium surrounding the bar, which is in turn affected by the modulus of elasticity of the concrete, and to a lesser degree, other variables such as bar cover, and the amount of transverse reinforcement. The only parameter that varied between specimens and could have had an impact on k_p was the compressive strength of the concrete. Assuming that k_s, related to k_p by Eq. 5.24, would be a function of the compressive strength of the concrete, the best fit was found to be given by Eq. 5.29.

$$k_s = \frac{f'c}{40} \qquad (5.29)$$

where k_s and the compressive strength are given in units of psi (Fig. 5.7). This result was not expected on the basis of hypotheses based on compressive deformation of the concrete, but the measurements did not permit an interpretation based on the mechanical model.

5.8 Comparison Between Measured and Calculated Bar Strains

The strain along the anchorage length was calculated using Eq. 5.15. The calculated strains (solid lines) are compared with the measured strains (dashed lines) in Figs. 5.8 to 5.11. The data from the two high-strength specimens (Figs. 5.8 and 5.10) showed a very close match to calculated strains at all ranges of loading.

For normal-strength specimens (Figs. 5.9 and 5.11) the proposed bond model showed good results while the strains at the face of the joint remained below 0.15%. At larger strains, the bond stress near the face of the joint showed a tendency to decreased with increasing strain. The result was that the strain in the bar decreased at a smaller rate with respect to distance within the region that had a reduced bond. A plausible explanation for this phenomenon is that the material surrounding the bar surpassed its linear range of response. Based on this observation a limit of 1,600 psi was set for the maximum bond stress that the material could sustain in the case of the normal-strength specimens.

For the distance over which Eq. 5.27 resulted in bond stresses higher than the limit of 1,600 psi, it was assumed that the bond stress was constant and equal to 5/8 of b_{lim}. Given the scarcity of information, a more elaborate criterion was deemed inappropriate.

This assumption improved the calculated strains for specimen C5-10 (Fig 5.12). However, the behavior of specimen C5-20 (Fig. 5.13) differed from that of C5-10. The bond stress near the face of the joint was much lower than that of specimen C5-10, making it impossible to capture the behavior of both specimens by applying the same equations.

No limit was specified for the maximum bond strength of the high-strength specimens (Figs. 5.8 and 5.10) because there was a very close match to the experimental results without any modification to Eq. 5.25.

The variation of bond stress along the anchored length is presented in Figs. 5.14 to 5.17. Because the bond stress was assumed to vary with the deformation of the bar, the calculated stresses were much higher than those calculated assuming a uniform bond distribution (described in section 4.7).

The relationship between slip and stress was calculated using Eq. 5.25 and modified according to the limit in maximum bond stress for the normal strength specimens. Three curves are presented in Fig. 5.18 for the different compressive strengths of specimens in this study. Figure 5.18 shows that the slip decreased as the compressive strength of the concrete increased. Another factor that affected slip was that the strain distribution along the length of the bar varied with the magnitude of the stress being developed for the

normal-strength specimens. This was not the case for specimens made with high-strength concrete.

Inferred stress-slip relationships are compared to that obtained with the proposed model to calculate slip in Figs. 5.19 to 5.21. The measured stress was calculated using readings from the strain gage attached to the longitudinal bar at the face of the joint. Measured slip was inferred following a procedure used by Wight (Wight, 1973). It was assumed that the distribution of strain in the longitudinal reinforcement was linear along the length of the element, varying from zero at the load-point, to the measured value at the face of the joint. To calculate slip, strain in the reinforcement was integrated over the 7 in. gage-length closest to the face of the joint, and subtracted from the extension reading obtained with the electronic Whittemore gage. Good agreement was observed between the proposed stress-slip relationship and inferred values.

A comparison between development length obtained using linear regression of the strain data along the anchorage zone and that from the slip model is presented in Figs. 5.22, 5.23 and 5.24.

Chapter 6

Calculated Load-Displacement Response

6.1 Introduction

The main objective of this chapter is to provide a procedure, based on the principles of mechanics, to estimate the load-displacement response of the test specimens. There are several plausible approaches to achieve this goal. In this case, a methodology based on the moment-curvature relationship of the cross section was selected.

Rather than trace the strains and stresses through the entire displacement history of each element, emphasis was placed on estimating the response at certain points of the load-displacement envelope. These critical points are shown in Fig. 6.1, which is a typical envelope for a measured load-displacement curve of a specimen.

The behavior of the specimens was described in detail in chapter 3. The largest member stiffness was measured upon first loading, before flexural cracks formed. The stiffness decreased after flexural cracking occurred. For elements without axial load, stiffness remained nearly constant with increasing displacement, until yielding of the longitudinal reinforcement occurred. In specimens with axial load, the tangential stiffness decreased gradually with displacement (Fig 6.1).

As the displacement increased beyond yield, the load increased as the slope of the load-displacement envelope decreased. The load reached a maximum value and, at larger displacements, the load decreased with increasing displacement. The limiting drift was defined as the displacement corresponding to 80% of the maximum shear (Fig. 6.1).

The behavior of the specimens was characterized by defining the coordinates of flexural cracking, yielding of longitudinal reinforcement, maximum shear, and the limiting drift.

6.2 Components of the total displacement

A detailed analysis of the measured displacement components was presented in chapter 4. The total deflection was defined as the sum of the components related to the rigid body motion of the specimens, shear, slip, and flexure.

The displacement component related to the rigid body motion of the specimens originates from the flexibility of the setup used to fix the specimen to the laboratory floor. Its magnitude was proportional to the flexibility of the setup, and was unrelated to the properties of the specimen. Therefore, for the purpose of comparing measured and calculated displacements, the rigid body component was subtracted from the total measured deflection and excluded from the calculations.

6.3 Displacement related to shear

Section 4.6 presented a discussion on the variation of the displacement component related to shear with respect to drift. It was observed that the mean shear strains measured throughout the elements were larger than those calculated from theory of elasticity. It was also observed that the mean shear strains measured in the plastic hinge region were larger than those measured in the remaining portion of the elements. A typical distribution of measured mean shear strains is presented in the top diagram of Fig 6.2.

The shear strain along the element was assumed constant, in order to calculate the displacement component related to shear by means of a simple procedure. An equivalent shear strain was defined such that the calculated deformation related to shear was equal to that obtained from the measured distribution. The equivalent constant shear strain is indicated by the dashed lined in the bottom diagram of Fig. 6.2.

According to beam theory, the deformation related to shear of a rectangular beam fixed in one end and subjected to a point load V on the other is given by:

$$\delta_s = \frac{6LV}{5AG} \qquad (6.1)$$

In an undamaged element, the area A is the full gross area of the cross section and the material constant G is proportional to the modulus of elasticity. As displacement increases and the element degrades because of repeated load reversals, the material cracks and is no longer a continuum. The area of the cross section decreases as the shell is lost and the cracked member has different material properties than it did before loading began.

The shear displacement, as defined by Eq. 6.1, is the product of the cross section properties L, A and G, and the shear force V applied to the beam. The cross section properties for each specimen are summarized in Table 6.1.

A moment-curvature analysis was performed for each specimen. The procedure used to calculate the moment-curvature relationship is explained in detail in section 6.6. The moment that corresponded to yielding of the longitudinal reinforcement and the maximum moment were obtained from the calculated moment-curvature relationship. The shear force at yield and at the limiting drift conditions were then calculated neglecting second order effects.

Using the shear force obtained from the moment-curvature analysis and the section properties from Table 6.1, the displacement related to shear was calculated according to Eq. 6.1, for the drift at yield (Table 6.2) and the limiting drift (Table 6.3).

Based on the mean ratios of measured to calculated displacement at yield and at the limiting drift, a relationship between shear force and the shear displacement was proposed (Fig 6.3). This relationship was used to calculate the displacement component related to shear for the group of specimens.

6.4 Displacement related to slip of the longitudinal reinforcement

A model to calculate the slip of the longitudinal reinforcement in the anchorage zone was presented in chapter 5. This model was calibrated using data from the tests (section 5.7) and a relationship was derived for the slip as a function of the stress in the longitudinal reinforcement (Fig. 6.4).

For each point of the moment-curvature relationship, the stress in the longitudinal reinforcement was calculated. Knowing the stress, slip was determined using the curves

shown in Fig. 6.4. The slip was divided by the distance between the two layers of longitudinal reinforcement (Table 6.4) to obtain the rotation and multiplied by the length of the element to obtain the displacement.

6.5 Displacement related to the deformation of the joint

As described in chapters 2 and 3, the configuration of anchor points for the electronic Whittemore gage extended into the central stub (Figs. 2.4 to 2.7). The measured deflections within the central stub were negligible compared to those at the load-point. This was expected because the central stub was strongly attached to the base block, and also because its flexibility was much lower than that of the two column elements.

However, the compression stress exerted by each of the two column elements on the stub and the tensile stresses along the anchorage zone of the longitudinal reinforcement, gave rise to a rotation at the face of the joint. This rotation, albeit small, had a noticeable contribution to the total deflection.

Using the electronic Whittemore gage readings, the mean strain was determined over a distance of 7 in. from the face of the joint toward the center of the stub (Station 1, Fig. 4.1). Table 6.5 summarizes the mean of the measured rotations at both sides of the stub, for the yield displacement. The displacement at the load-point associated with the distortion at the face of the joint was approximately 15% of the total displacement at yield. At the limiting drift its contribution was less than 5% of the total deflection.

Calculating the deformations within the stub is a very complex problem. A linearly elastic finite element model was created to provide insight into the problem. Figure 6.5 shows the mesh, composed of eight-node brick elements.

Loads and boundary conditions are shown in Fig. 6.6. Displacements in all nodes at the bottom of the stub were restrained in all three directions. The nodes located at the top of the stub were restrained from moving in the vertical direction, but allowed to move on the horizontal direction.

The forces applied to the stub in the finite element model, attempted to simulate the compression stresses exerted by the column elements and the bond stresses along the

surface of the longitudinal reinforcement. The magnitude of the compressive forces was determined by estimating the total force in the tension reinforcement at yield and distributing it along the face of the stub. The force was applied over a length of 2 in., approximately equal to the neutral axis depth calculated from the moment-curvature analysis at yielding of the longitudinal reinforcement, in a specimen without axial load.

Tensile forces were applied at nodes located inside the stub, along a line defined by the location of the longitudinal reinforcement. The total yield force of a bar was distributed over a length of 9 in., which was approximately the observed development length for the high-strength specimens. Because the distance between nodes was longer toward the center of the stub, the force per unit of length was larger near the face of the joint. This is consistent with the observed behavior along the anchorage zone. The modulus of elasticity for the material was set at 4.5 million psi, approximately equal to the values measured for high-strength concrete mixes.

Figure 6.7 shows a frontal view of the deformed mesh obtained from the finite element analysis. The combination of the compression forces imposed by the column elements and the tensile forces from the anchorage of the longitudinal reinforcement, result in a distortion of the vertical boundary of the stub. This behavior was consistent with the pattern of deformations measured with the electronic Whittemore gage.

The calculated displacement field, along the longitudinal direction, is shown in Figs. 6.8 and 6.9. The maximum deformation in the longitudinal direction was calculated to be approximately 0.007 in. (Figs. 6.8 and 6.9), in the zone where the column element imposes compressive forces on the stub.

An approximation of the rotation at the face of the joint was obtained based on the calculated displacement field. An extension of 0.002 in. at the level of the tensile reinforcement and a contraction of 0.005 in. at the level of the compressive reinforcement were assumed (Fig 6.8). For a separation of 4.5 in. between layers of reinforcement, the resulting rotation is 0.0015. This value is very close to those summarized in Table 6.5, although slightly lower. Larger deformations would be expected from an analysis that accounts for the nonlinear behavior of the concrete.

The purpose of the finite element analysis was to obtain an estimate of the effect that the deformation of the joint had on the load-point deflection, particularly at the yield point. Based on the finite element analysis and the measurements summarized in Table 6.5, the rotation at the face of the joint, at yield, was assumed to be 0.002 for the high-strength specimens and 0.003 for the normal-strength specimens. A linear variation was assumed between zero and yield loads.

6.6 Displacements related to flexure

The component of the displacement related to flexure was calculated based on the calculated moment-curvature relationship for the specimens. A computer program was developed to carry out the calculations. The cross section was modeled allowing the use of two different material models for the concrete of the shell and the core. The total area was divided into layers (Fig. 6.10), and a linear strain distribution was assumed, fixing the strain at the centroid of each layer of concrete and steel. Stresses were obtained from material models (Fig. 6.11) and integrated over the section. This procedure was repeated for a specified value of compressive strain in the extreme fiber, until the depth of the neutral axis was such that the sum of tensile and compressive forces were equal.

Several material models were incorporated into the program both for steel and concrete. For the concrete, a simple model proposed by Hognestad was used for the ascending part of the stress-strain curve (Hognestad, 1951).

For $0 < \varepsilon < \varepsilon_o$

$$f_c = f''_c \left[\frac{2\varepsilon}{\varepsilon_o} - \left(\frac{\varepsilon}{\varepsilon_o} \right)^2 \right] \qquad (6.2)$$

Taking the derivative of Eq. 6.2 and evaluating at $\varepsilon = 0$,

$$\varepsilon_o = \frac{2 f''_c}{E_c} \qquad (6.3)$$

The value for ε_o was obtained using Eq. 6.3 and the measured values for compressive strength and modulus of elasticity for each specimen. Values of ε_o used in the analysis are summarized in Table 6.6.

The descending branch was modeled using a straight line (Roy and Sozen, 1964). For $\varepsilon > \varepsilon_o$

$$f_c = f''_c [1 - z(\varepsilon - \varepsilon_o)] \qquad (6.3)$$

The parameter z, which controls the slope of the descending branch, was kept constant for all specimens. For the concrete in the confined core, following the approach by Roy, the value of z was 50. For the unconfined shell, the slope was set to that suggested by Hognestad in his model, which was approximately 75. The actual stress-strain curves for concrete used in the analysis are shown in Figs. 6.12 to 6.14.

The steel was modeled using a tri-linear curve (Fig. 6.11). In the strain hardening range, the adopted model differed from the results obtained with coupons (Fig. 6.15). However, the tri-linear curve resulted in a better fit for the measured moment-curvature relationship. The parameters for the steel model are presented in Table 6.7.

The calculated moment-curvature relationship is compared with the measured history for each specimen in Figs. 6.16 to 6.27.

After the moment-curvature relationship was calculated, the curvature along the element was integrated to obtain the rotation, which was integrated again to obtain the displacement.

In order to carry out the integration, it was necessary to know the curvature distribution along the length of the element. The bending moment diagram was determined using the equations of equilibrium, and the curvature interpolated from the moment-curvature relationship (Fig. 6.28). This approach provided good results for displacements from zero load to yielding of the longitudinal reinforcement.

The measured curvature distribution along the specimens, for the yield displacement, is shown in Figs. 6.30 to 6.36. The broken line shows a theoretical

distribution in which curvature varies linearly, from 0 at the load-point, to the calculated yield curvature at the face of the joint. The theoretical distribution shows very good agreement with the measured values along the member. The disturbance at the face of the joint is attributed to the effect of slip.

For displacements larger than that associated with the maximum moment, the procedure described in the previous paragraphs resulted in calculated values much smaller than measured. The difficulty lies in determining the curvature distribution at the location of the plastic hinge. A simple solution was to assume that the curvature was constant along the plastic hinge and linear through the remainder of the element (Fig. 6.29).

6.7 Displacement at cracking

The cracking moment was calculated using the measured tensile strength and the gross section properties

$$M_{cr} = \left(\sigma_{cr} + \frac{P}{A} \right) \frac{I}{c} \qquad (6.4)$$

At this range of displacements, a linear distribution of curvature (Fig. 6.30) was observed to provide adequate results for the displacements related to flexure. The curvature at cracking is given by

$$\varphi_{cr} = \frac{M_{cr}}{E\,I} \qquad (6.5)$$

The displacement components related to shear and the deformation of the joint were calculated and added to the component related to flexure. Values are presented in Table 6.8. The displacement component related to shear was negligible. The deformation related to slip was assumed to be zero.

6.8 Displacement at yielding of the longitudinal reinforcement

The displacement at yield was determined for each member based on the shape of the measured load-displacement curve and readings from the strain gages attached to the longitudinal reinforcement. The coordinates for yield are shown by the broken lines in

Figs. 6.37 to 6.50. Values for measured displacement, moment, and shear are presented in Table 6.9. Shear values in Table 6.9 were corrected for second order effects.

Figures 6.51 and 6.52 show the variation of the measured displacement at yield with respect to compressive strength of the concrete and axial load. There was no appreciable trend with either variable. Within the accuracy of the measurements, the yield displacement was insensitive to compressive strength and axial load.

Calculated yield displacements are shown in Table 6.10. The moment and curvature at yielding of the longitudinal reinforcement were obtained from the moment-curvature relationships (section 6.6). The displacement related to flexure was calculated assuming a linear curvature distribution (section 6.6, Fig 6.30).

The shear was obtained from the calculated moment at yield, neglecting second order effects. The displacement related to shear was then calculated following the procedure outlined in section 6.3. Displacement components related to slip and deformation of the joint were calculated as indicated in sections 6.3, 6.4 and 6.5.

Calculating the displacement at yield of a reinforced concrete member is a difficult task because of the inherent variability of the displacement components related to slip and deformation of the joint. The sum of these constitute an important fraction of the total displacement in scaled specimens. Measured and calculated displacements at yield for the test series are compared in Fig. 6.53. The mean ratio of measured to calculated yield displacement was 0.98, with a standard deviation of 0.13 (Table 6.10). The standard deviation is provided to give an approximate measure for the scatter.

A similar comparison was made for the moments at yield (Table 6.11, Fig 6.54). Better agreement was observed between measured and calculated moments than in the case of displacements. The mean ratio of measured to calculated moment was 0.97, with a standard deviation of 0.05 (Table 6.11).

A computer program was developed to calculate the displacement at the load-point as indicated in sections 6.3 to 6.6. The displacement related to flexure was determined by calculating the moment diagram for the member and interpolating the curvature from the moment-curvature relationship. Several iterations were carried out to account for second

order effects. A comparison of measured and calculated load-displacement curves from zero load to yielding of the longitudinal reinforcement is presented in Figs. 6.55 to 6.68.

6.9 Flexural Strength

Table 6.12 lists the maximum moment calculated using moment-curvature analysis and the maximum measured moment for each member. The ratio of measured to calculated moment vs. the axial load for each member are shown in Fig. 6.69. There was very good agreement between measured and calculated values. The mean ratio of measured to calculated maximum moment was 0.97, with a standard deviation of 0.05.

Flexural strengths calculated using the Building Code Requirements of the American Concrete Institute (American Concrete Institute, 1995) were also very close to measured values (Table 6.13, Fig. 6.70). The mean ratio of measured to calculated maximum moment was 1.01, with a standard deviation of 0.05.

6.10 Limiting Drift

The imposed displacement history subjected the specimens to load reversals up to increasing levels of drift. In specimens subjected to low axial loads the depth of the neutral axis was small. As a result, strains much larger than the elastic limit were required of the tension reinforcement, in order to sustain the increasing drift demand. After the direction of loading changed, similar strains were required from the opposing layer of reinforcement. Meanwhile, the compression stress was not large enough to offset the permanent extension of the bars (Fig. 6.85). As cycling progressed, both layers of reinforcement continued to extended as rotation increased. This trend can be observed in Figs. 6.71 to 6.84. They show the mean strain at the level of the reinforcement, over a distance of 7 in. from the face of the joint. This behavior was more evident as the axial load decreased.

In a cross section subjected to monotonic loading, the compression reinforcement is not affected by reversal of the load. Because reinforcing bars subjected to compression were not previously extended by loading in the opposite direction, the percentage of the total compression force carried by the steel is less than in the case of cyclic loading. A higher compression force sustained by the concrete implies a higher strain, and the effect of confinement becomes more important.

Because the cyclic nature of the loading affects the behavior of the members, a solution for monotonic loading will provide an approximation of curvature and strain at ultimate.

In specimens subjected to an axial load below half the balanced load, the transverse reinforcement provided was sufficient to control the width of the inclined crack. Their moment capacity did not deteriorate significantly with cycling (Figs. 6.16 to 6.28), and the members were able to sustain very large drifts. The stress-strain relationship of the steel was the controlling factor in their behavior.

Figures 6.86 to 6.99 show envelopes for the measured load, inferred strain at the extreme compressive fiber, inferred neutral axis depth and measured mean strain at the level of the tensile reinforcement. Values for strain at the extreme fiber, position of the neutral axis and tensile strain at the level of the reinforcement were determined using readings from the electronic Whittemore gages for station 2 (Fig. 4.1).

The legend SP in Figs. 6.86 to 6.99 points to the displacement at which the first indications of spalling were observed. In most specimens this occurred near the end of the first quarter cycle. The inferred values of strain range approximately from 0.002 to 0.005.

The legend SD indicates the displacement for which spalling was clearly observed, and part of the shell had been lost. This occurred after several load reversals, so the calculated values reflect the nonlinear deformation of the reinforcement.

Displacement components related to shear, slip, and deformation of the joint were calculated according to sections 6.3 to 6.5 and subtracted from the total. Assuming that, at ultimate, the curvature is constant over the length of the plastic hinge (section 6.6, Fig. 6.29), the component of the limiting drift related to flexure is approximately given by

$$\Delta_{u\,flexure} = (\varphi_u - \varphi_y)\, Lp\, L + \frac{\varphi_y L^2}{3} \qquad (6.6)$$

Solving Eq. 6.6 for the curvature at ultimate

$$\varphi_u = \varphi_y + \frac{1}{Lp\,L}\left(\Delta_{u\,flexure} - \frac{\varphi_y L^2}{3}\right) \qquad (6.7)$$

The length of the plastic hinge Lp was assumed equal to the effective depth. Limiting drift values determined in chapter 3 and calculated yield curvatures were substituted into Eq. 6.7 to obtain the ultimate curvature. The strain at the extreme compression fiber of the shell and the core were then interpolated from the moment-curvature relationships. Results are presented in Figs 6.100 to 6.103.

Figures 6.100 and 6.101 show the calculated strain at the extreme compression fiber of the shell for normal-strength and high-strength specimens respectively. A limiting compressive strain of 0.008 provides a safe lower bound for both groups of specimens.

Figures 6.102 and 6.103 show the calculated strain at the extreme compression fiber of the shell. In this case values of compressive strain seemed to be strongly influenced by the calculated depth of the neutral axis.

The limiting drift question was approached from the viewpoint of conventional practice. The standard method for determining the contribution of plastic deformation to drift in reinforced concrete elements involved the calculation of a plastic rotation defined by the product of $(\varphi_u - \varphi_y)\,d$, where φ_u is the limiting curvature, φ_y is the yield curvature, and d is the effective depth.

The observed scatter of the measured results for limiting drift did not support introducing a new approach. Therefore, the quantity φ_u was calculated using a stress-strain curve for the concrete shown in Fig. 6.11. The parameter z in Eq. 6.3 was taken as 50, while values of strain at the extreme compression fiber varied from zero to 0.01. The displacement was then calculated using Eq. 6.6 and compared with measured values. The ratio of calculated to measured displacement vs the strain at the extreme compression fiber is shown in Figs. 6.104 and 6.105. A limiting strain of 0.008 led to a safe estimate of the limiting drift for the test series.

The behavior of the two specimens subjected to 128 kips of axial load (Figs. 6.92, 6.93, 6.98 and 6.99) is of interest because they were least affected by permanent set in the

longitudinal reinforcement (Figs. 6.77, 6.78, 6.83 and 6.84). The curvature at ultimate can be expressed as

$$\varphi_u = \frac{\varepsilon_c}{na} \qquad (6.8)$$

where na is the neutral axis depth.

For specimen C5-40, the measured mean neutral axis depth for station 2 at ultimate (Fig. 6.98) was approximately 3.7 in. The measured mean strain at the extreme compression fiber was approximately 0.01 (Figs. 6.83 and 6.84). Evaluating Eq. 6.8, the measured curvature at ultimate was approximately 0.0027 1/in. The calculated curvature at ultimate for specimen C5-40 (Table 6.14) was 0.0021, showing excellent agreement between measured and calculated values.

Similarly, for specimen C10-20, the measured mean neutral axis depth for station 2 at ultimate (Fig. 6.92) was approximately 2.1 in. The measured mean strain at the extreme compression fiber was approximately 0.008 (Fig. 6.77). Once again, evaluating Eq. 6.8, the measured curvature at ultimate was approximately 0.0038 1/in. The calculated curvature at ultimate for specimen C10-20 (Table 6.14) was 0.0036 1/in.

The displacement component related to flexure was calculated using the same material model for the core and the shell, using a value of compressive strain in the extreme fiber of 0.008. Calculated limiting drifts are summarized in Table 6.14. A comparison is established with measured values in Table 6.15. The mean ratio of measured to calculated limiting drift (Fig. 6.106) was 1.16 with a standard deviation of 0.12.

Chapter 7

Summary and Conclusions

7.1 Summary

7.1.1 Object and Scope

A series of eight tests was carried out to investigate the behavior under shear reversals of reinforced concrete column members made with high-strength concrete. Each test specimen comprised two column elements framing into the same joint (Fig. 2.1). The controlled variables of the experimental study were axial load and concrete compressive strength.

The axial compressive stress on the columns, maintained throughout each test, was 0, 500, 1000 or 2000 psi (Table A.1, Appendix). Results from the tests provided information about the behavior of high-strength columns subjected to axial loads below the balanced failure condition (Fig. 7.1). Compressive strength of the concrete used in the specimens ranged from 5,500 to 10,000 psi (Table A.3, Appendix).

Column dimensions and the amount of transverse reinforcement were kept constant. The cross section was square with dimensions of 8 x 8 in. (Fig. A.12, Appendix). The distance from the face of the joint to the load-point was 24 in. (Fig. A.11, Appendix), resulting in a shear span to depth ratio of approximately 3.4.

The transverse reinforcement ratio was set to 1% (Fig. A.12, Appendix). The measured yield stress of the transverse reinforcement ranged from 60 to 75 ksi (Tables A.4 and A.5, Figs. A.12 and A.13, Appendix).

The longitudinal reinforcement consisted of four No. 5 bars, which corresponds to 2% of the gross section area. The measured yield strength of the longitudinal reinforcement was 84 ksi (Tables A.4 and A.5, Figs. A.9, A.10 and A.11, Appendix).

Axial load was applied to the specimens by means of external hydraulic rams (Fig A.13, Appendix). Columns were deformed by applying lateral anti-symmetric loads. The displacement history consisted of cycles of increasing maximum deflections, until failure occurred (Figs. 2.2 and 2.3). The applied displacement history was selected to induce the detrimental effect of repeated load reversals typically caused by earthquakes.

The investigation focused on three problems about the behavior of column elements:

(1) Current practice tends to make the use of high-strength concrete in earthquake resistant structures difficult because of a lack of adequate experimental support and filed evidence. The series of tests studied the influence of concrete strength on drift capacity and provided a factual basis for projecting available theory to columns with high-strength concrete.

(2) Previous studies of reinforced concrete column tests have led to reasonable doubt about the definition and calculation of yield displacement, a parameter of importance for the common definition of ductility. The tests were instrumented to obtain information about the relationship between normal/shear strains and rotation at yield and at drifts exceeding yield.

(3) Tests were designed to provide an improved basis for determining the amount of transverse reinforcement required for adequate drift capacity of columns made with high-strength concrete.

7.1.2 **Observed Behavior**

Specimens were subjected to two different displacement schedules. Limiting drift ratios for the specimens subjected to displacement schedule B (Fig. 2.3) ranged from 4 to 6.5%. The two specimens that were subjected to displacement schedule A (Fig. 2.2) had a limiting drift exceeding 6.9%.

Measured moment-curvature relationships (Figs. 6.16 to 6.27) showed that, while the transverse reinforcement had not reached yield, the moment capacity of the members was not affected significantly by shear reversals. The reduction in measured moment was

associated with the P-Δ effect and not with the reduction of the moment capacity of the section.

Behavior of the specimens was dominated by the deformation of the longitudinal reinforcement, with the exception of specimen C5-40 (f'c = 5,500 psi, P=128 kips). Damage to the shell concrete with cycling increased with axial load. Concrete inside the core was observed to be adequately confined by the amount of transverse reinforcement provided.

Although the shear force started to decrease soon after yielding of the longitudinal reinforcement, strains in the transverse reinforcement continued to increase. This behavior indicated that as the core deteriorated, a larger fraction of the total shear force was carried by the transverse reinforcement. Specimens were able to sustain the axial load while the transverse reinforcement was in the linear range. Soon after yielding of the transverse reinforcement, the longitudinal reinforcement buckled, which led to the collapse of the members.

Displacement history had a dominant effect on behavior. The two specimens subjected to displacement schedule A (Fig. 2.2), with a lower number of cycles, had the highest limiting drift. Measurements from the critical stirrups in these specimens (C10-00 and C5-10) indicated that the rate of increase for the strain with respect to displacement, was lower when the specimens were subjected to monotonically increasing displacements than in the case of cyclic loads.

7.1.3 Effect of Test Variables

As expected, limiting drift decreased with axial load. Measurement from strain gages in the transverse reinforcement showed that the rate of strain increase with displacement was proportional to axial load. Yielding of the transverse reinforcement was observed to be followed, after a small or no increase in drift, by the collapse of the members.

For the range of axial loads used in this test series, the use of high- strength concrete improved shear capacity, drift capacity, and the ability to dissipate energy of the

structural members. The increase in displacement ductility (Fig 7.2) was largest for the two specimens subjected to an axial load of 128 kips (axial stress of 2000 psi).

Compressive strength also affected the distribution of strains along the anchorage zone. A linear regression analysis of the strains recorded along the anchorage zone indicated that development length tended towards a constant while the mean bond stress increased, with increasing displacement. The calculated mean bond stress at yielding of the longitudinal reinforcement was approximately 1500 psi, for high-strength specimens. In the case of normal-strength specimens, the mean bond stress at yielding of the longitudinal reinforcement was approximately 1000 psi.

7.1.4 Displacement Components

Lateral displacement was assumed to have four components related to (1) flexure, (2) slip of the reinforcement, (3) shear, and (4) distortion of the joint face.

Measured displacements related to shear were larger than those calculated using elastic beam theory. A comparison of the measured and calculated shear displacements (using elastic beam theory), at yielding of the longitudinal reinforcement, was presented in Table 6.2. The shear distortion based on uncracked gross section varied from 0.003 to 0.007 in. The distortion based on triangulation of measured displacements over gage-lengths of 7 to 8.5 in. ranged from 0.01 to 0.08 in. The variation of the measured shear deformation had weak correlations with the experimental parameters (Figs. 7.3 and 7.4). It would appear that the inferred shear deformation depended on if, where, and how the inclined cracks formed.

Displacements related to shear increased as the displacement increased, without an increase in the shear force. At the limiting drift, the ratio of measured to calculated shear displacement using elastic beam theory, ranged approximately from 15 to 60. Ratios increased with decreasing axial load (Table 6.3, Figs. 7.5 and 7.6).

Given the shear span to depth ratio of the specimens, and based on elastic theory, it was expected that shear displacements be small compared with the total drift. At yielding of the longitudinal reinforcement, measured shear displacements (Table 7.1) ranged from 2 to 20% of the total displacement (corrected for rigid body motions). At the drift limit, the

shear displacement (Table 7.2) was approximately 10% of the total deflection (corrected for rigid body motions).

Because it was difficult to make a direct measurement of the displacement related to slip, the relative magnitude of each displacement component is presented in terms of the calculated values (Table 7.3).

At yielding of the longitudinal reinforcement, the flexural displacement ranged from 40 to 50% of the total. Components related to slip and deformation of the joint had approximately similar magnitudes, approximately 15 to 25% of the total displacement. The calculated displacement related to shear was approximately 10% of the total (Figs. 7.7 and 7.8, Table 7.3).

At the limiting drift, the displacement related to flexure represented a higher percentage of the total, approximately 60 to 85% of the total. Calculated displacement components related to the deformation of the joint and slip were each approximately 5 to 10% of the total (Figs. 7.9 and 7.10, Table 7.3).

The measured displacement, at yielding of the longitudinal reinforcement, was not sensitive to compressive strength or axial load. Limiting drift decreased with axial load and increased with compressive strength.

7.1.5 Evaluation of Test Results

An envelope for the load-displacement curves was obtained by evaluating the contribution of all displacement components at critical stages of loading. The displacement related to flexure was calculated by integrating the curvature distribution along the length of the members.

Moment-curvature relationships were calculated using the conventional assumptions of equilibrium, linear strain distribution, and constitutive models for the materials. Several material models were investigated, and a reasonable envelope for the measured moment-curvature relationships was obtained using simple material models for the steel and concrete (Fig. 6.11). Calculated yield and maximum moments from the moment-curvature analysis showed good agreement with measured values.

At yielding of the longitudinal reinforcement, measured curvature profiles indicated that the distribution of curvature along the length of the member was approximately linear.

Drift limits were calculated assuming a constant curvature along the length of the plastic hinge (Fig. 6.29). Estimates for the drift limit were based on a limiting strain of 0.008.

7.2 Conclusions

The conclusions below relate strictly to the domain of the experimental variables defined in chapter 2 and the Appendix.

The main objective of the study was to answer the question, “Is the use of higher-strength concrete an option in earthquake resistant design, in order to increase the drift capacity of reinforced concrete columns?”. The answer was affirmative. It was observed that increasing the strength of concrete from 5,000 to 10,000 psi increased the drift capacity of the column.

Figure 7.1 illustrates the measured and calculated increases in capacity for all test specimens. Two examples comparing the measured shear displacement are shown in Fig. 7.2

Safe estimates of the limiting drift for the specimens made with high-strength concrete were obtained using conventional methods, with the limiting compressive strain for the concrete set at 0.008.

Various specific observations are listed below.

- The amount of transverse reinforcement required by the Building Code Requirements of the American Concrete Institute, in Eq. 21.3 and 21.4, (American Concrete Institute, 1995), was sufficient to enable the specimens to reach limiting drift ratios exceeding 4%. There was no decrease in member toughness associated with the use of high-strength concrete.

• Consistent with conventional theory, flexural strength increased with axial load and compressive strength of the concrete. Liming drift decreased with axial load, for axial loads more than half the balanced load, and increased with the use of high-strength concrete. The difference in limiting drift related to concrete strength was largest for the two specimens subjected to an axial load of 128 kips (Fig 7.1).

• A model was developed to estimate the stress-slip relationship for the longitudinal reinforcement (chapter 5). It provided a good estimate of the strain distribution along the anchorage zone, particularly for high-strength specimens.

• Calculating the displacement at yield was a difficult task because of the inherent variability of the displacement components related to slip and shear. At this stage of loading, the component related to flexure was approximately 50% of the total.

• At ultimate, the displacement component related to flexure was successfully estimated using simple material models for steel and concrete. An estimate of the limiting drift was obtained using a liming strain of 0.008. The limiting strain was not sensitive to compressive strength of the concrete.

• Shear displacements were larger than those estimated using elastic beam theory. As the integrity of the core was affected by load reversals and increasing drift, the shear displacement increased, even though the shear force decreased. The measured displacement related to shear was largest at the location of the plastic hinge, decreasing in magnitude towards the load-point point. This was consistent with the distribution of inclined cracks along the length of the members.

• Deformation within the joint led to a rotation at the face of the member that affected the total drift. Measured rotation magnitudes were consistent with results from a three-dimensional finite element model of the joint.

• Yielding of the transverse reinforcement was observed to be the trigger for column collapse under shear reversals.

List of References

1.- Abrams, D., "Tests of Bond Between Concrete and Steel" Bulletin No. 71. Engineering Experiment Station, University of Illinois, Urbana, December 1913.

2.- American Concrete Institute, Committee 442, "Response of Buildings to Lateral Forces", ACI Journal, Proceedings, Vol.68, No. 2, February 1971, pp. 81-106.

3.- American Concrete Institute, Committee 363, "State of the Art Report on High Strength Concrete", ACI Journal, Proceedings, V. 81, No. 4, July-August 1984. pp. 364-411.

4.- Aoyama, H., Murota, T., Hiraishi, H. and Bessho, S., "Outline of the Japanese National Project on Advanced Reinforced Concrete Buildings with High-Strength and High-Quality Materials", Proceedings, Second International Symposium on High Strength Concrete, SP-121, American Concrete Institute, Detroit, Michigan, 1990, pp. 21-32.

5.- Aoyama, H., "Moment-Curvature Characteristics of Reinforced Concrete Members Subjected to Axial Load and Reversal of Bending", Proceedings, International Symposium on Flexural Mechanics of Reinforced Concrete, Miami, Fla., November, 1964, pp. 183-205.

6.- Aschheim, M., and Moehle, J., "Shear Strength and Deformability of R/C Bridge Columns Subjected to Inelastic Cyclic Displacements". Report No. UCB/EERC-92/04, Earthquake Engineering Research Center, College of Engineering, University of California, Berkeley, March 1992.

7.- Azizinamini, A., Baum Kuska, S., Brungardt, P., and Hatfield, E., "Seismic Behavior of Square High-Strength Concrete Columns", ACI Structural Journal, Vol. 91, No. 3, May-June 1994, pp. 336-345.

8.- Baker, A. L. and , A. M., "Inelastic Hyperstatic Frames Analysis", Proceedings, International Symposium on Flexural Mechanics of Reinforced Concrete, Miami, Fla., November, 1964, pp. 85-142.

9.- Bertero, V. V. and Felippa, C., "Discussion of "Ductility of Concrete" by H. E. Roy and M. A. Sozen". Proceedings, International Symposium on Flexural Mechanics of Reinforced Concrete, Miami, Fla., November, 1964, pp. 227-234.

10.- Bjerkeli, L., Tomaszewicz, A. and Jensen A. A., "Deformation Properties and Ductility of High Strength Concrete", Proceedings, Second International Symposium on High-Strength Concrete, SP-121, American Concrete Institute, Detroit Michigan, 1990, pp. 215-238.

11.- Bjerkeli, E. G. and Hilsdorf, H. K., "Behavior of Laterally Reinforced Concrete Columns" Journal of the Structural Division, Proceedings of the American Society of Civil Engineers, Vol. 97, No. ST2, February 1971, pp. 587-602.

12.- Burns, N. and Siess, C. P., "Repeated and Reversed Loading in Reinforced Concrete". Journal of the Structural Division. Proceedings of the American Society of Civil Engineers. Vol. 92, No. ST5, October, 1966, pp. 65-78.

13.- Burns, N. H. and , C. P., "Plastic Hinging in Reinforced Concrete". Journal of the Structural Division. Proceedings of the American Society of Civil Engineers. Vol.92, No. ST5, October, 1966, pp.45-64.

14.- Chung, H., , S. and Kokusho, S., "Reinforced High Strength Columns Subjected to Axial Force, Bending Moments, and Shear Forces", Transactions of the Japan Concrete Institute, V. 2, 1980. pp 335-342.

15.- Corley, W. G., "Rotational Capacity of Reinforced Concrete Beams" Journal of the Structural Division. Proceedings of the American Society of Civil Engineers. Vol 92, No. ST5, October, 1966, pp. 121-146.

16.- Cusson, D. and Paultre, P., "Stress-Strain Model for Confined High-Strength Concrete", Journal of Structural Engineering, American Society of Civil Engineers, Vol. 121, No. 3, March 1995, pp. 468-477.

17.- DeVries, R. A. "Lap Splice Strength of Plain and Epoxy-Coated Reinforcement: an

Experimental Study Considering Concrete Strength, Casting Position, and Anti-Bleeding Additives". Structural Engineering, Mechanics and Materials, School of Civil Engineering, University of California at Berkeley, June 1989.

18.- Fafitis, A. and Shah, S. P., "Lateral Reinforcement for High Strength Concrete Columns", High Strength Concrete, SP-87, American Concrete Institute, Detroit, 1985, pp. 213-232.

19.- Ghee, A. B. "Seismic Shear Strength of Circular Bridge Piers", Research Report 85-5. Department of Civil Engineering, University of Canterbury, Christchurch New Zealand, 1985.

20.- Gill, W. D., Park, R., and Priestley, N., "Ductility of Rectangular Reinforced Concrete Columns with Axial Load" Department of Civil Engineering, University of Canterbury, Christchurch, New Zealand, February 1979.

21.- Hibi, J., Mihara, Y., Otani, S. and Aoyama H., "Behavior of Reinforced Concrete Columns Using High Strength Concrete after Flexural Yielding", Transactions of the Japan Concrete Institute, Vol. 13, 1991, pp. 395-402.

22.- Hoedajanto, D., "A Model to Simulate Lateral-Force Response of Reinforced Concrete Structures with Cylindrical and Box Sections" PhD Thesis, Department of Civil Engineering, University of Illinois at Urbana-Champaign, Urbana, Illinois, 1983.

23.- Hsu, L. S. and Hsu, C. T., "Complete stress-strain behavior of high-strength concrete under compression". Magazine of Concrete Research, Vol. 46, No. 169, December 1994, pp. 301-312.

24.- Ibrahim, H. and MacGregor, J., "Tests of Eccentrically Loaded High-Strength Concrete Columns", ACI Structural Journal, Vol. 93, No. 5, September-October 1996.

25.- Kaba, S. A., and Mahin, S. A., "Refined Modelling of Reinforced Concrete Columns for Seismic Analysis". Report No. UCB/EERC-84/03, Earthquake Engineering Research Center, College of Engineering, University of California, Berkeley, April 1984.

26.- Kabeyasawa, T., Li, K. N. and Huang, K., "Experimental Study on Strength and Deformability of Ultrahigh Strength Concrete Columns", Transactions of the Japan Concrete Institute, V. 12, 1990, pp. 315-322.

27.- Kabeyasawa, T., Shen, F., Kuramoto, H. and Rubiano, N., "Experimental Study on the Behavior of Ultra-High-Strength Reinforced Concrete Columns under Tri-Axial Forces", Transactions of the Japan Concrete Institute, V. 13, 1991, pp. 279-286.

28.- Karlsson, B., Aoyama, H., and Sozen, M., "Spirally Reinforced Concrete Columns Subjected to Loading Reversals", Fifth World Conference on Earthquake Engineering, Session 2-D, Rome, Italy, 1973.

29.- Kent, D. C. and Park, R., "Flexural Members with Confined Concrete" Journal of the Structural Division, Proceedings of the American Society of Civil Engineers, Vol. 97, No. ST7, July 1971, pp. 1970-1990.

30.- Kimura, H., Sugano, S., and Nagashima, T., "Study of Flexural Strength and Ductility of R/C Columns Using High Strength Concrete", Takenaka Technical Research Report, No. 51, November 1995, pp. 161-178.

31.- Kuramoto, H., Kabeyasawa, T. and Shen, F., "Influence of Axial Deformation on Ductility of High-Strength Reinforced Concrete Columns under Varying Triaxial Forces" ACI Structural Journal, V. 92, No. 5, September-October 1995. pp. 610-618.

32.- Lai, S., Will, G., and Otani, S., "Model for Inelastic Biaxial Bending of Concrete Members", Journal of Structural Engineering, Vol. 110, No. 11, November 1984, pp. 2563-2584.

33.- Li, Bing., "Strength and Ductility of Reinforced Concrete Members and Frames Constructed Using High Strength Concrete", Research Report 94-5, Department of Civil Engineering, University of Canterbury, Christchurch, New Zealand, May 1994.

34.- Low, S. and Moehle, J., "Experimental Study of Reinforced Concrete Columns Subjected to Multi-Axial Cyclic Loading". Report No. UCB/EERC-87/14, Earthquake Engineering Research Center, College of Engineering, University of California, Berkeley, September 1987.

35.- Mander, J. B., Priestley, J. N. and Park, R., "Theoretical Stress-Strain Model for Confined Concrete". Journal of Structural Engineering, Vol. 114, No. 8, August 1988, pp. 1804-1826.

36.- Matamoros, A., "Study of Bond Data Using Neural-Networks". M.S. Thesis, Department

of Civil Engineering, University of Illinois at Urbana-Champaign, May 1994.

37.- Mattock, A., "Rotational Capacity of Hinging Regions in Reinforced Concrete Beams", Proceedings, International Symposium on Flexural Mechanics of Reinforced Concrete, Miami, Fla., November, 1964, pp. 143-180.

38.- Measurements Group, Inc., "Strain Gage Installations with M-Bond 200 Adhesive", Instruction Bulletin B-127-9, Raleigh, NC., 1979.

39.- Measurements Group, Inc., "Strain Gage Applications with M-Bond AE-10/15 and M-Bond GA-2 Adhesive Systems", Instruction Bulletin B-137-15, Raleigh, NC., 1979.

40.- Mizoguchi, M., Arakawa, T. and Arai, Y., "Strength Behavior of High Strength R/C Columns under Biaxial Bending-Shear and Varying Axial Load", Transactions of the Japan Concrete Institute, V. 13, 1991, pp. 387-394.

41.- Muguruma, H., Nishiyama, M., Watanabe, F. and Tanaka, H., "Ductile Behavior of High Strength Concrete Columns Confined y High Strength Transverse Reinforcement", Evaluation and Rehabilitation of Concrete Structures and Innovations in Design, SP-128, American Concrete Institute, Detroit, 1991, pp. 877-891.

42.- Muguruma, H. and Watanabe, F., "Ductility Improvement of High-Strength Concrete Columns with Lateral Confinement", Proceedings, Second International Symposium on High-Strength Concrete, SP-121, American Concrete Institute, Detroit Michigan, 1990. pp. 47-60.

43.- Otani. S. and Sozen, M. A., "Behavior of Multistory Reinforced Concrete Frames During Earthquakes". Civil Engineering Studies. Structural Research Series No. 392. University of Illinois at Urbana-Champaign, Urbana, Illinois, 1972.

44.- Ozcebe, G. and Saatcioglu, M., "Confinement of Concrete Columns for Seismic Loading", ACI Structural Journal, V. 84, No. 4, July-August 1987. pp. 308-315.

45.- Park, R. and Paulay, T., "Reinforced Concrete Structures", John Wiley and Sons, New York, 1975.

46.- Park, R., , N. M. and Gill, W. D., "Ductility of Square-Confined Concrete Columns" Journal of the Structural Division, Proceedings of the American Society of Civil

Engineers, Vol. 108, No. ST4, April 1982, pp. 929-950.

47.- Popovics, S., "A review of Stress-Strain Relationships for Concrete". Journal of the American Concrete Institute, Vol. 67, No. 3, March 1970, pp. 243-248.

48.- Razvi, S. and Saatcioglu, M., "Strength and Deformability of Confined High-Strength Concrete Columns". ACI Structural Journal, V. 91, No. 6, November-December 1994. pp. 678-687.

49.- Roy, H. E. and Sozen, M. A., "Ductility of Concrete". Proceedings, International Symposium on Flexural Mechanics of Reinforced Concrete, Miami, Fla., November, 1964, pp. 213-224.

50.- Saatcioglu, M., "Deformability of Reinforced Concrete Columns", Earthquake Resistant Structures, Inelastic Response and Design, SP 127, American Concrete Institute, Detroit, 1991, pp. 421-452.

51.- Saatcioglu, M. and Ozcebe, G., "Response of Reinforced Concrete Columns to Simulated Seismic Loading", ACI Structural Journal, V. 86, No. 1, January-February 1989, pp. 3-12.

52.- Saatcioglu, M. and Razvi, S., "Strength and Ductility of Confined Concrete", Journal of Structural Engineering, ASCE, V. 118, No. 6, 1992, pp. 1590-1607.

53.- Sakaguchi, N., Yamanobe, K., Kitada, Y., Kawachi, T. and Koda, S., "Shear Strength of High-Strength Concrete Members", Proceedings, Second International Symposium on High-Strength Concrete, SP-121, American Concrete Institute, Detroit Michigan, 1990. pp. 155-178.

54.- Sakai, K. and Sheikh, S., "What Do We Know about Confinement in Reinforced concrete Columns? (A Critical Review of Previous Work and Code Provisions)" ACI Structural Journal, Vol. 86, No. 2, March-April 1989, pp. 192-207.

55.- Sakai, Y., Hibi, J., Otani, S. and Aoyama, H., "Experimental Study of Flexural Behavior of Reinforced Concrete Columns Using High Strength Concrete", Transactions of the Japan Concrete Institute, V. 12, 1990, pp. 323-330.

56.- Sargin, M. T., Gosh, S. K., and Handa, V. K., "Effects of Lateral Reinforcement upon the

Strength and Deformation Properties of Concrete", Magazine of Concrete Research, Vol. 23, No. 75-76, June-September, 1971, pp. 99-110.

57.- Scott, B. D., Park, R. and Priestley, N. J., "Stress-Strain Behavior of Concrete Confined by Overlapping Hoops at Low and High Strain Rates", Journal of the American Concrete Institute, Proceedings V. 79, No. 1, January-February 1982, pp.13-27.

58.- Sheikh, S. A., "A Comparative Study of Confinement Models". Journal of the American Concrete Institute, Proceedings V. 79, No. 4, July-August 1982. pp. 296-306.

59.- Sheikh, S. A. and Uzumeri, S. M., "Analytical Model for Concrete Confinement in Tied Columns". Journal of the Structural Division, Proceedings of the American Concrete Society of Civil Engineers, Vol. 108, No. ST12, December, 1982.

60.- Sheikh, S. A. and Yhe, C., "Tied Concrete Columns under Axial Load and Flexure" Journal of Structural Engineering, Vol. 116, No. 10, October 1990. pp. 2780-2800.

61.- Sheikh, S. A. and Uzumeri, S. M., "Strength and Ductility of Tied Concrete Columns" Journal of the Structural Division, Proceedings of the American Society of Civil Engineers, Vol. 106, No. ST5, May, 1980. pp. 1079-1102.

62.- Sheikh, S. A., Shah, D. and Khoury, S., "Confinement of High-Strength Concrete Columns" ACI Structural Journal, V. 91, No. 1, January-February, 1994. pp. 100-111.

63.- Shin, S. W., Kamara, M. and Gosh, S. K., "Flexural Ductility, Strength Prediction, and Hysteretic Behavior of Ultra-High-Strength Concrete Members", Proceedings, Second International Symposium on High-Strength Concrete, SP-121, American Concrete Institute, Detroit Michigan, 1990. pp. 239-264.

64.- Soliman, M. T., and Yu, C. W., "The flexural stress-strain relationship of concrete confined by rectangular transverse reinforcement". Magazine of Concrete Research. Vol. 19, No. 61, December 1967, pp. 223-238.

65.- Sugano, S., Nagashima, T., Kimura, H., Tamura, A. and Ichikawa, A., "Experimental Studies on Seismic Behavior of Reinforced Concrete Members of High Strength Concrete", Proceedings, Second International Symposium on High-Strength Concrete, SP-121, American Concrete Institute, Detroit Michigan, 1990. pp. 61-87.

66.- Suharwardy, M. I. and Pecknold, D. A., "Inelastic Response of Reinforced Concrete Columns Subjected to Two-Dimensional Earthquake Motions" Civil Engineering Studies, Structural Research Series No. 455, University of Illinois at Urbana Champaign, October, 1978.

67.- Thomas, K. and Sozen, M. A., "A Study of the Inelastic Rotation Mechanism of Reinforced Concrete Connections". Structural Research Series No. 301. University of Illinois at Urbana-Champaign, Urbana, Illinois, 1965.

68.- Thompsen, J. and Wallace, J., "Lateral Load Behavior of Reinforced Concrete Columns Constructed Using High-Strength Materials" ACI Structural Journal, V. 91, No. 5, September-October 1994. pp. 605-615.

69.- Thorenfeldt, E. and Drangsholt, G., "Shear Capacity of Reinforced High-Strength Concrete Beams", Proceedings, Second International Symposium on High-Strength Concrete, SP-121, American Concrete Institute, Detroit Michigan, 1990. pp. 129-154.

70.- Treece, R. A. and Jirsa, J. O. "Bond Strength of Epoxy-Coated Reinforcing Bars". ACI Materials Journal, March-April 1989, pp. 167-174.

71.- Vallenas, J., Bertero, V., and Popov, E. P., "Concrete Confined by Rectangular Hoops and Subjected to Axial Loads". Report No. UCB/EERC-77/13, Earthquake Engineering Research Center, College of Engineering, University of California, Berkeley, August 1977.

72.- Watanabe, F., Mugumura, H., Matsutani, T. and Sanda, D., "Utilization of High Strength Concrete for Reinforced Concrete High-Rise Buildings in Seismic Area", Utilization of High Strength Concrete Proceedings, Stavenger, Norway, Tapir Publishers, 1987, pp. 655-666.

73.- Wight, J. K. and Sozen, M. A., "Shear Strength Decay in Reinforced Concrete Columns Subjected to Large Deflection Reversals" Civil Engineering Studies. Structural Research Series No. 403. University of Illinois at Urbana-Champaign, Urbana, Illinois, 1973.

74.- Yong, Y. K., Nour, M. G. and Nawy, E. G., "Behavior of Laterally Confined High-Strength Concrete under Axial Loads", Journal of Structural Engineering, Proceedings of the American Society of Civil Engineers, Vol. 114, No. 2, February 1982.

pp. 332-351.

75.- Zahn, F. A., "Design of Reinforced Concrete Bridge Columns for Strength and Ductility" Research Report 86-7. Department of Civil Engineering, University of Canterbury, Christchurch New Zealand, 1986.

Tables

Table 3.1

Limiting Drift *

Specimen	Axial Load, kips	Limiting Drift, in.	Limiting Drift ratio, %	Cycle	Displacement History
C10-00	0	> 3	> 15	5	A
C10-05	32	1.3	5.5	7 - 9	B
C10-10	64	1.5	6.1	7 - 9	B
C10-20	128	1.3	5.2	5 - 7	B
C5-00	0	1.6	6.5	9 - 11	B
C5-10	32	1.7	6.9	5	A
C5-20	64	1.0	4.0	3 - 5	B
C5-40	128	1.0	4.1	5 - 7	B

* Largest displacement at which an element was able to carry at least 80 % of its maximum shear.

Table 3.2

Peak Loads and Displacements for Specimen C10-00

Displacement in.		Load kips		V/Vmax		Cycle
South	North	South	North	South	North	
Positive Direction						
0.56	-0.57	12.8	-13.0	1.00	1.00	1+
0.75	-0.78	12.3	-12.4	0.96	0.96	3+
0.99	-0.99	12.0	-12.1	0.94	0.94	4+
2.87	-2.90	12.1	-12.3	0.95	0.95	5+
3.25	3.25	11.9	-12.1	0.93	0.93	5+
Negative Direction						
-0.52	0.70	-10.4	10.4	1.00	0.98	1-
-0.82	0.83	-10.4	10.6	1.00	1.00	3-
-1.01	1.01	-10.3	10.5	0.99	0.99	4-

Table 3.3

Peak Loads and Displacements for Specimen C10-05

Displacement in.		Load kips		V/Vmax		Cycle
South	North	South	North	South	North	
Positive Direction						
0.49	-0.52	15.1	-15.5	0.98	0.98	1+
0.75	-0.75	14.6	-15.0	0.95	0.95	3+
0.98	-0.98	13.8	-14.1	0.90	0.90	5+
1.26	-1.26	12.7	-12.8	0.83	0.81	7+
1.50	-1.52	11.4	-11.4	0.74	0.73	9+
1.75	-1.76	10.3	-10.4	0.67	0.66	11+
1.63	-1.95	6.5	-7.3	0.43	0.46	12+
Negative Direction						
-0.49	0.51	-14.9	14.9	1.00	1.00	1-
-0.75	0.75	-14.4	14.4	0.97	0.97	3-
-1.00	1.01	-13.7	13.7	0.92	0.92	5-
-1.25	1.27	-12.4	12.6	0.84	0.85	7-
-1.50	1.50	-11.3	11.6	0.76	0.77	9-
-1.76	1.76	-9.8	10.1	0.66	0.68	11-

Table 3.4

Peak Loads and Displacements for Specimen C10-10

Displacement in.		Load kips		V/Vmax		Cycle
South	North	South	North	South	North	
Positive Direction						
0.50	-0.51	20.7	-21.3	0.99	0.99	1+
0.75	-0.76	20.1	-20.7	0.96	0.96	3+
1.00	-1.02	19.3	-19.8	0.92	0.92	5+
1.25	-1.25	18.0	-18.5	0.86	0.86	7+
1.50	-1.50	16.8	-17.3	0.81	0.81	9+
1.75	-1.75	15.6	-16.1	0.75	0.75	11+
Negative Direction						
-0.50	0.50	-21.0	21.0	0.99	0.99	1-
-0.75	0.77	-20.3	20.2	0.96	0.96	3-
-1.00	1.00	-19.3	19.3	0.91	0.91	5-
-1.25	1.25	-18.1	18.1	0.86	0.86	7-
-1.51	1.50	-16.7	16.9	0.79	0.80	9-
-1.76	1.75	-15.1	15.1	0.72	0.72	11-
-1.76	1.75	-12.7	12.2	0.60	0.58	12-

Table 3.5

Peak Loads and Displacements for Specimen C10-20

Displacement in.		Load kips		V/Vmax		Cycle
South	North	South	North	South	North	
Positive Direction						
0.50	-0.51	22.4	-23.4	0.98	0.97	1+
0.75	-0.75	21.9	-23.2	0.95	0.96	3+
1.00	-1.00	20.6	-21.8	0.90	0.90	5+
1.25	-1.25	18.3	-19.4	0.80	0.81	7+
1.50	-1.50	15.5	-16.6	0.67	0.69	9+
1.50	-1.50	14.4	-15.6	0.63	0.65	10+
Negative Direction						
-0.50	0.50	-22.1	21.9	0.95	0.96	1-
-0.75	0.76	-23.2	22.5	0.99	0.99	3-
-1.01	1.01	-21.4	20.8	0.92	0.91	5-
-1.25	1.25	-19.3	18.7	0.83	0.82	7-
-1.50	1.51	-16.1	15.6	0.69	0.68	9-

Table 3.6

Peak Loads and Displacements for Specimen C5-00

Displacement in.		Load kips		V/Vmax		Cycle
South	North	South	North	South	North	
Positive Direction						
0.50	-0.51	12.7	-12.9	0.97	0.97	1+
0.74	-0.76	13.1	-13.2	1.00	1.00	3+
1.02	-1.01	12.8	-13.0	0.98	0.98	5+
1.27	-1.25	12.6	-12.7	0.96	0.96	7+
1.53	-1.53	10.9	-11.0	0.83	0.83	9+
1.73	-1.73	8.5	-8.6	0.65	0.65	11+
2.00	-2.00	8.7	-8.8	0.66	0.67	13+
Negative Direction						
-0.49	0.51	-12.4	12.6	0.97	0.98	1-
-0.74	0.77	-12.7	12.9	1.00	1.00	3-
-1.02	1.00	-12.7	12.9	1.00	1.00	5-
-1.28	1.29	-12.4	12.5	0.97	0.97	7-
-1.54	1.58	-10.6	10.8	0.83	0.84	9-
-1.79	1.82	-9.1	9.5	0.72	0.74	11-

Table 3.7

Peak Loads and Displacements for Specimen C5-10

Displacement in.		Load kips		V/Vmax		Cycle
South	North	South	North	South	North	
Positive Direction						
0.70	-0.72	13.2	-13.3	0.89	0.89	1+
1.01	-1.02	13.2	-13.3	0.89	0.89	3+
1.23	-1.25	12.6	-12.8	0.86	0.86	4+
2.74	-2.81	9.6	-9.9	0.65	0.66	5+
Negative Direction						
-0.69	0.70	-12.0	11.6	0.93	0.90	1-
-1.00	1.01	-12.9	12.9	1.00	1.00	3-
-1.22	1.28	-12.5	12.6	0.97	0.97	4-

Table 3.8

Peak Loads and Displacements for Specimen C5-20

Displacement in.		Load kips		V/Vmax		Cycle
South	North	South	North	South	North	
Positive Direction						
0.50	-0.50	15.4	-16.0	0.99	1.00	1+
0.75	-0.75	14.9	-15.6	0.96	0.97	3+
1.01	-1.01	11.8	-12.2	0.76	0.76	5+
1.26	-1.27	10.5	-10.7	0.67	0.67	7+
1.51	-1.51	8.5	-8.6	0.55	0.54	9+
1.50	-1.50	8.3	-8.3	0.53	0.52	10+
Negative Direction						
-0.50	0.50	-15.6	15.5	0.96	0.95	1-
-0.75	0.75	-15.2	14.9	0.93	0.91	3-
-1.00	1.03	-13.5	13.3	0.82	0.82	5-
-1.26	1.27	-11.0	11.2	0.67	0.69	7-
-1.50	1.54	-9.4	9.7	0.57	0.59	9-
-1.50	1.55	-7.1	6.8	0.43	0.42	10-

Table 3.9

Peak Loads and Displacements for Specimen C5-40

Displacement in.		Load kips		V/Vo		Cycle
South	North	South	North	South	North	
Positive Direction						
0.50	-0.50	18.97	-19.04	1.00	1.00	1+
0.73	-0.73	15.72	-15.84	0.83	0.83	3+
1.00	-1.01	15.56	-15.63	0.82	0.82	5+
1.00	-1.01	13.64	-13.49	0.72	0.71	6+
Negative Direction						
-0.50	0.50	-17.4	17.9	1.00	1.00	1-
-0.72	0.72	-14.4	14.8	0.83	0.83	3-
-1.00	1.04	-14.3	14.6	0.82	0.82	5-
-0.97	0.98	-11.5	11.6	0.66	0.65	6-

Table 6.1

Section Properties for Calculation of Shear Deflection

Specimen	E	G *	L	As	$\frac{6\ L}{5\ As\ G}$
	psi	psi	in.	$in.^2$	in./lb
C5-00	4.30E+06	1.79E+6	24	56	2.87E-07
C5-20	4.50E+06	1.88E+6	24	56	2.74E-07
C5-40	4.60E+06	1.92E+6	24	56	2.68E-07
C10-00	4.90E+06	2.04E+6	24	56	2.52E-07
C10-05	3.50E+06	1.46E+6	24	56	3.53E-07
C10-10	3.50E+06	1.46E+6	24	56	3.53E-07
C10-20	5.20E+06	2.17E+6	24	56	2.37E-07

* The shear modulus G was calculated as

$$G = \frac{E}{2\ (1+\nu)}$$

Poisson's ratio was assumed to be 0.20.

Table 6.2

Displacements Related to Shear at Yield

	Shear at Yield		Calculated Displacement Related to Shear		Measured Displacement Related to Shear		Measured/Calculated	
Specimen	South	North	South	North	South	North	South	North
	kips	kips	in	in	in	in		
C5-00	11.9	-12.0	0.003	-0.003	0.06	-0.06	18.6	18.5
C5-20	15.4	-15.9	0.004	-0.004	0.02	-0.03	5.8	7.2
C5-40	18.9	-18.7	0.005	-0.005	0.04	-0.04	8.6	8.6
C10-00	11.6	-11.2	0.003	-0.003	0.01	-0.01	2.2	5.2
C10-05	15.0	-15.3	0.005	-0.005	0.04	-0.04	6.9	6.9
C10-10	20.2	-20.3	0.007	-0.007	0.05	-0.08	7.7	11.3
C10-20	22.7	-23.1	0.005	-0.005	0.02	-0.04	3.6	7.0
						Mean	7.6	9.2

Table 6.3

Displacements Related to Shear at Ultimate

	0.8 x Calculated Maximum Shear		Calculated Displacement Related to Shear		Measured Displacement Related to Shear		Measured/Calculated	
Specimen	South	North	South	North	South	North	South	North
	kips	kips	in	in	in	in		
C5-00	10.5	10.6	0.003	0.003	0.18	0.18	56.1	55.4
C5-20	12.4	12.8	0.004	0.004	0.08	0.08	22.6	21.9
C5-40	15.2	15.2	0.004	0.004	0.06	0.06	15.3	15.3
C10-05	12.3	12.6	0.005	0.005	0.16	0.16	36.1	35.1
C10-10	16.7	17.2	0.006	0.006	0.13	0.13	21.2	20.7
C10-20	18.4	19.3	0.005	0.005	0.09	0.09	19.7	18.7
						Mean	28.5	27.8

Table 6.4

Distance Between Top and Bottom Reinforcement

Specimen	Distance between top and bottom layers of reinforcement in.
C5-00	5.4
C5-10	4.0
C5-20	4.0
C5-40	5.2
C10-00	4.0
C10-05	4.0
C10-10	5.2
C10-20	5.4

Table 6.5

Mean Rotation Measured at the Face of the Joint, for Yield Displacement

Specimen	Mean Rotation at the Face of the Joint	Load Point Displacement in.
C5-00	0.0021	0.05
C5-10	0.0024	0.06
C5-20	0.0019	0.05
C5-40	0.0023	0.05
C10-00	0.0040	0.10
C10-05	0.0023	0.06
C10-10	0.0025	0.06
C10-20	0.0024	0.06

Table 6.6

Values of ε_o used in Analysis

Specimen	f"c psi	Ec psi	ε_o Eq. 6.3	ε_o Analysis
C5-00	5500	3.50E+06	0.0031	0.003
C5-10	6900	4.70E+06	0.0029	0.003
C5-20	7000	4.60E+06	0.0030	0.003
C5-40	5520	3.50E+06	0.0032	0.003
C10-00	10000	4.30E+06	0.0047	0.004
C10-05	10100	4.50E+06	0.0045	0.004
C10-10	9830	4.90E+06	0.0040	0.004
C10-20	9500	5.20E+06	0.0037	0.004

Table 6.7

Parameters used in Material Model for Steel

E	29000 ksi
σ_y	84 kips
σ_u	90 kips
ε_{sh}	0.015
ε_u	0.2

Table 6.8

Calculated Displacement at Cracking

Specimen	Cracking								
	Axial Load	Tensile Strength	E	Moment	Load	Curvature	Shear Displacement	Displacement Deformation of Joint	Total Displacement
	lbs	psi	psi	kip in	kips	1/in	in.	in.	in.
C5-00	0	780	3.50E+06	67	2.8	0.000056	0.00	0.02	0.03
C5-10	32000	1050	4.70E+06	132	5.5	0.000082	0.00	0.03	0.04
C5-20	64000	995	4.60E+06	170	7.1	0.000108	0.00	0.03	0.05
C5-40	128000	830	3.50E+06	242	10.1	0.000202	0.00	0.03	0.07
C10-00	0	1010	4.30E+06	86	3.6	0.000059	0.00	0.01	0.03
C10-05	32000	990	4.50E+06	127	5.3	0.000083	0.00	0.02	0.03
C10-10	64000	540	4.90E+06	131	5.5	0.000079	0.00	0.01	0.03
C10-20	128000	925	5.20E+06	250	10.4	0.000141	0.00	0.02	0.05

Table 6.9

Measured Loads and Displacements at Yield

Specimen	Displacement		Moment		Shear	
	South	North	South	North	North	South
	in	in	kip in	kip in	kip	kip
C5-00	0.32	-0.35	286	-288	11.9	-12.0
C5-20	0.35	-0.35	402	-412	15.4	-15.9
C5-40	0.35	-0.35	519	-506	18.9	-18.7
C10-00	0.32	-0.32	278	-268	11.6	-11.2
C10-05	0.37	-0.35	373	-380	15.0	-15.3
C10-10	0.32	-0.36	512	-514	20.2	-20.3
C10-20	0.31	-0.33	623	-612	22.7	-23.1

Table 6.10

Calculated Displacement at Yield

Specimen	Curvature	Displacement Component					Measured / Calculated		
		Flexure	Shear	Slip	Joint Deformation	Total	North	South	Mean
	1/in.	in.	in.	in.	in.	in.			
C5-00	0.000652	0.13	0.04	0.09	0.07	0.33	0.98	1.07	1.03
C5-20	0.000973	0.19	0.05	0.12	0.07	0.43	0.81	0.81	0.81
C5-40	0.001114	0.21	0.07	0.09	0.07	0.45	0.78	0.78	0.78
C10-00	0.000735	0.14	0.03	0.07	0.05	0.28	1.12	1.12	1.12
C10-05	0.000815	0.16	0.06	0.07	0.05	0.33	1.14	1.07	1.10
C10-10	0.000769	0.15	0.07	0.05	0.05	0.32	1.00	1.12	1.06
C10-20	0.000901	0.17	0.07	0.05	0.05	0.34	0.92	0.98	0.95
					Mean		0.96	1.00	0.98
					Standard Deviation		0.13	0.13	0.13

Table 6.11

Calculated Moment at Yield

Specimen	Axial Load	Calculated Moment	Measured Moment		Measured / Calculated		
			South	North	South	North	Mean
	kips	kip in	kip in	kip in			
C5-00	0	309	286	-288	0.93	0.93	0.93
C5-20	64	432	402	-412	0.93	0.95	0.94
C5-40	128	575	519	-506	0.90	0.88	0.89
C10-00	0	277	278	-268	1.00	0.97	0.98
C10-05	32	366	373	-380	1.02	1.04	1.03
C10-10	64	486	512	-514	1.05	1.06	1.06
C10-20	128	637	623	-612	0.98	0.96	0.97
			Mean		0.97	0.97	0.97
			Standard Deviation		0.05	0.06	0.05

Table 6.12

Calculated Maximum Moment

Specimen	Axial Load	Calculated Moment	Measured Moment		Measured / Calculated		
			South	North	South	North	Mean
	kips	kip in	kip in	kip in			
C5-00	0	315	314	-318	1.00	1.01	1.00
C5-20	64	440	409	-425	0.93	0.97	0.95
C5-40	128	575	520	-522	0.90	0.91	0.91
C10-00	0	333	306	-311	0.92	0.94	0.93
C10-05	32	406	378	-388	0.93	0.96	0.94
C10-10	64	508	533	-538	1.05	1.06	1.05
C10-20	128	670	639	-669	0.95	1.00	0.98
			Mean		0.95	0.98	0.97
			Standard Deviation		0.05	0.05	0.05

Table 6.13

Strength According to ACI Building Code

Specimen	Axial Load	Calculated Moment	Measured Maximum Moment		Measured / Calculated		
		Moment	South	North	North	South	Mean
	kips	kip in	kip in	kip in			
C5-00	0	317	314	-318	0.99	1.00	1.00
C5-20	64	433	409	-425	0.94	0.98	0.96
C5-40	128	466	520	-522	1.11	1.12	1.12
C10-00	0	314	306	-311	0.98	0.99	0.98
C10-05	32	393	378	-388	0.96	0.99	0.98
C10-10	64	510	533	-538	1.05	1.06	1.05
C10-20	128	663	639	-669	0.96	1.01	0.99
			Mean		1.00	1.02	1.01
			Standard Deviation		0.06	0.05	0.05

Table 6.14

Calculated Limiting Drift

Specimen	Yield Curvature	Ultimate Curvature	Flexural Displacement	Slip Displacement	Displacement Related to Joint Deformation	Shear Displacement	Total Displacement
	1/in.	1/in.	in.	in.	in.	in.	in.
C5-00	0.000652	0.005911	1.01	0.10	0.072	0.09	1.27
C5-10	0.000868	0.004067	0.70	0.14	0.072	0.09	1.01
C5-20	0.000973	0.003518	0.61	0.14	0.072	0.12	0.94
C5-40	0.001114	0.002135	0.39	0.10	0.072	0.15	0.71
C10-00	0.000735	0.005216	0.89	0.07	0.048	0.08	1.10
C10-05	0.000815	0.004669	0.80	0.07	0.048	0.14	1.06
C10-10	0.000769	0.004933	0.85	0.05	0.048	0.18	1.13
C10-20	0.000901	0.003554	0.62	0.05	0.048	0.16	0.87

Table 6.15

Comparison of Measured and Calculated Limiting Drift

Specimen	Calculated Drift Limit	Measured Drift Limit Corrected for Rigid Body Motion				Measured / Calculated				Mean
		South Positive Loading	North Positive Loading	South Negative Loading	North Negative Loading	South Positive Loading	North Positive Loading	South Negative Loading	North Negative Loading	
	in.	in.	in.	in.	in.					
C5-00	1.27	1.33	1.60	1.66	1.48	1.05	1.26	1.31	1.16	1.20
C5-20	0.94	0.79	0.83	0.87	0.93	0.84	0.88	0.92	0.99	0.91
C5-40	0.71	0.80	0.92	0.99	0.87	1.13	1.31	1.40	1.23	1.26
C10-05	1.06	1.26	1.06	1.35	1.51	1.18	0.99	1.26	1.42	1.22
C10-10	1.13	1.39	1.42	1.35	1.37	1.23	1.26	1.20	1.22	1.23
C10-20	0.87	0.96	1.10	1.13	0.89	1.10	1.26	1.29	1.02	1.17
				Mean		1.09	1.16	1.23	1.17	1.16
				Standard Deviation		0.12	0.16	0.15	0.14	0.12

Table 7.1

Measured Shear and Total Displacement at Yield

Specimen	Total		Shear		Shear / Total		Mean
	North	South	North	South	North	South	
	in.	in.	in.	in.			
C5-00	0.32	-0.36	0.06	-0.06	0.20	0.18	0.19
C5-20	0.35	-0.35	0.02	-0.03	0.07	0.09	0.08
C5-40	0.35	-0.35	0.04	-0.04	0.13	0.12	0.12
C10-00	0.32	-0.35	0.01	-0.01	0.02	0.04	0.03
C10-05	0.35	-0.35	0.04	-0.04	0.10	0.11	0.11
C10-10	0.32	-0.36	0.05	-0.08	0.17	0.23	0.20
C10-20	0.32	-0.35	0.02	-0.04	0.06	0.11	0.09
			Mean		0.11	0.12	0.12
			Standard Deviation		0.06	0.06	0.06

Table 7.2

Shear and Total Displacements at Ultimate

Specimen	Shear Displacement	Drift Limits (Corrected for Rigid Body Motions)				Shear Displacement / Drift Limit				
		South Positive Loading	North Positive Loading	South Negative Loading	North Negative Loading	South Positive Loading	North Positive Loading	South Negative Loading	North Negative Loading	Mean
	in.	in.	in.	in.	in.					
C5-00	0.18	1.33	1.60	1.66	1.48	0.12	0.13	0.11	0.11	0.12
C5-20	0.08	0.79	0.83	0.87	0.93	0.07	0.10	0.10	0.09	0.09
C5-40	0.06	0.80	0.92	0.99	0.87	0.08	0.08	0.07	0.07	0.07
C10-05	0.16	1.26	1.06	1.35	1.51	0.13	0.13	0.15	0.12	0.13
C10-10	0.13	1.39	1.42	1.35	1.37	0.10	0.09	0.09	0.10	0.09
C10-20	0.09	0.96	1.10	1.13	0.89	0.09	0.09	0.08	0.08	0.09
				Mean		0.10	0.11	0.10	0.09	0.10
				Standard Deviation		0.02	0.02	0.03	0.02	0.02

Table 7.3

Percentage of the Total Calculated Deflection Associated with each Component

Specimen	Yield				Ultimate			
	Flexure	Slip	Joint Deformation	Shear	Flexure	Slip	Joint Deformation	Shear
C5-00	0.39	0.28	0.22	0.11	0.83	0.07	0.05	0.06
C5-20	0.43	0.28	0.17	0.11	0.70	0.13	0.07	0.11
C5-40	0.48	0.21	0.16	0.14	0.59	0.13	0.09	0.19
C10-05	0.48	0.20	0.15	0.17	0.79	0.06	0.04	0.11
C10-10	0.47	0.16	0.15	0.22	0.79	0.04	0.04	0.13
C10-20	0.52	0.15	0.14	0.19	0.75	0.05	0.05	0.15

Figures

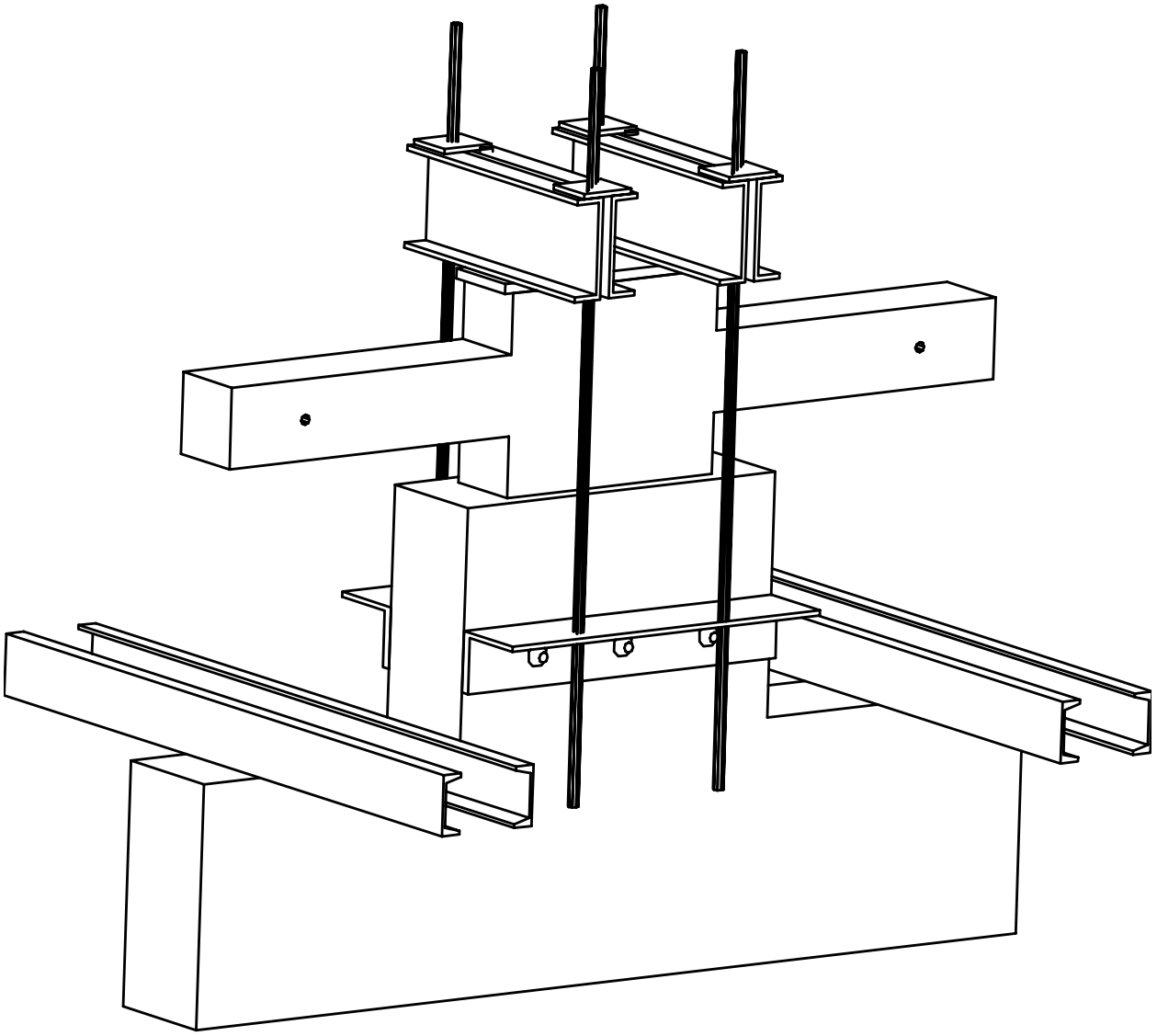

Figure 2.1. Specimen attached to concrete pedestal.

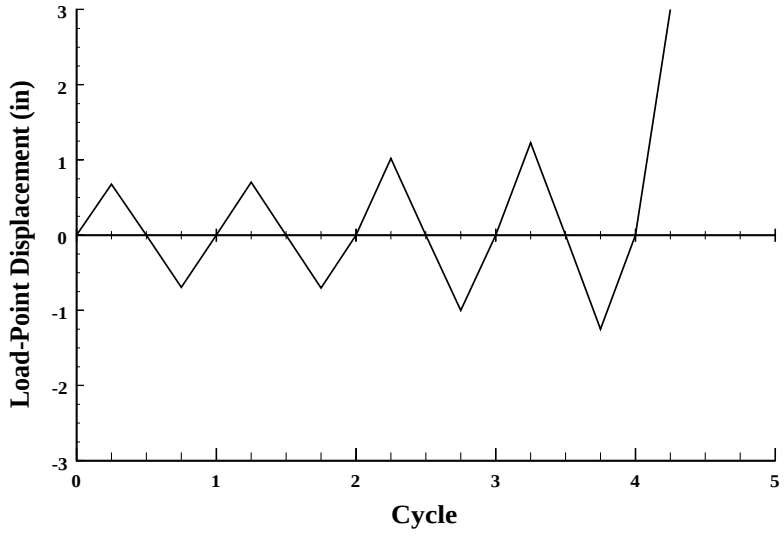

Figure 2.2. Displacement schedule A, used for specimens C10-00 and C5-10.

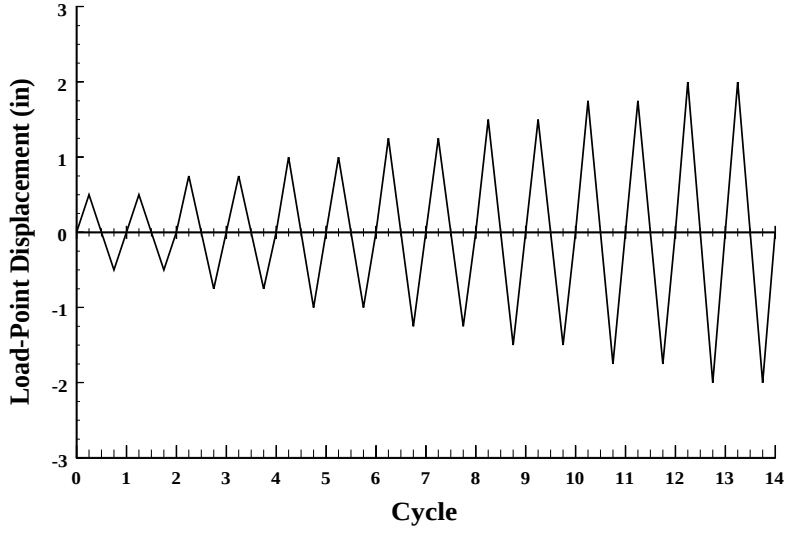

Figure 2.3. Displacement schedule B, used for remaining specimens.

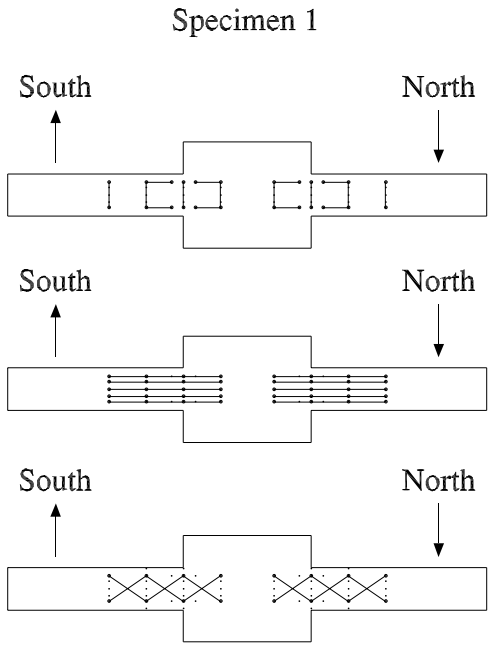

Figure 2.4. Location of anchor points for Whittemore strain gages, specimen C10-00.

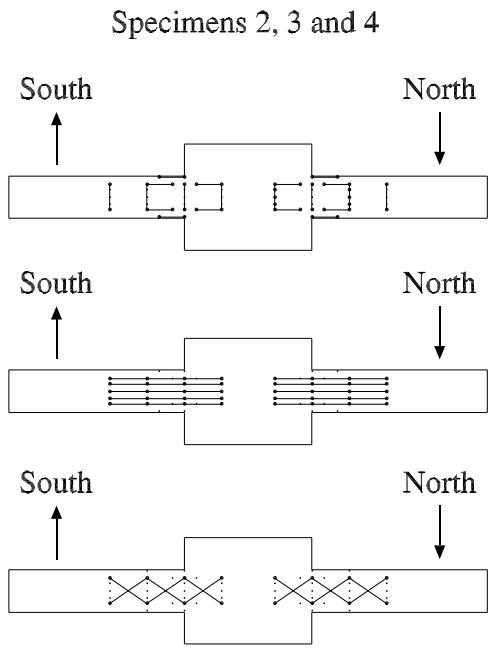

Figure 2.5. Location of anchor points for Whittemore strain gages, specimens C5-10, C5-20 and C10-05.

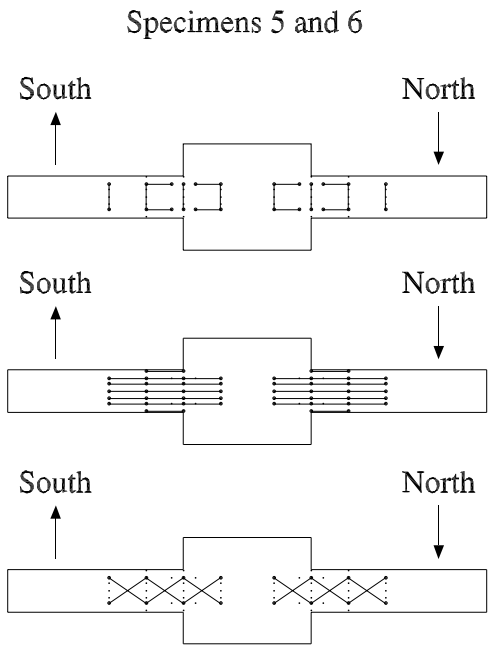

Figure 2.6. Location of anchor points for Whittemore strain gages, specimens C10-10 and C5-40.

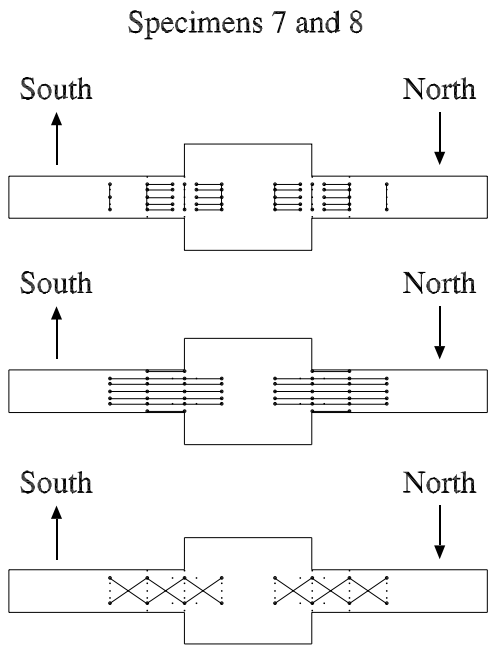

Figure 2.7. Location of anchor points for Whittemore strain gages, specimens C5-00 and C10-20.

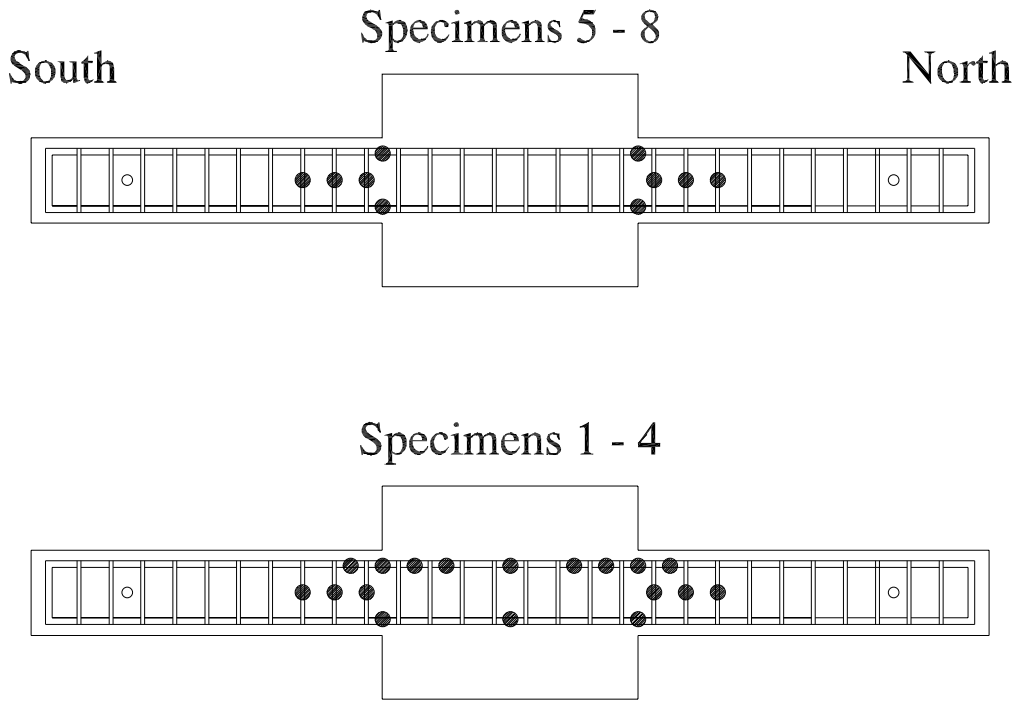

Figure 2.8. Location of strain gages for first and second group of tests. Specimens 1 to 4 are C10-00, C5-10, C10-05 and C5-20.

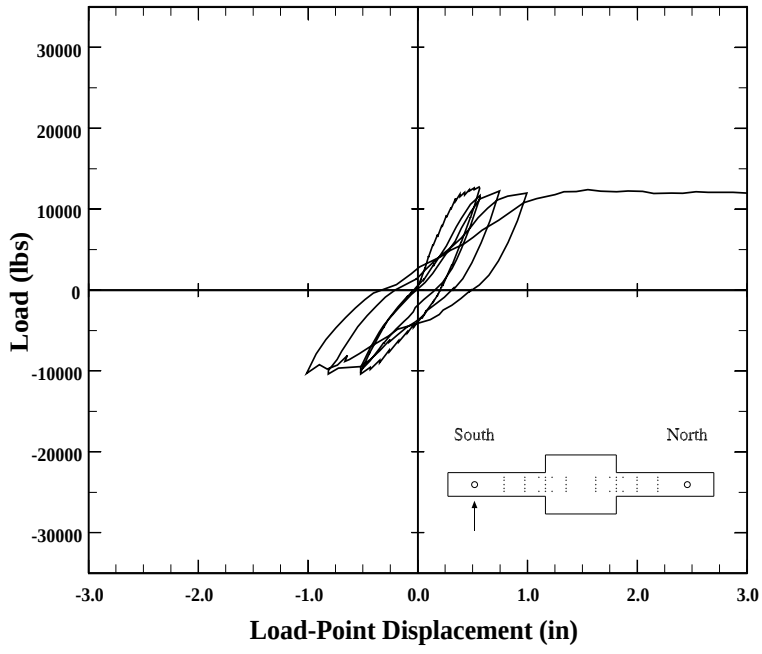

Figure 3.1. Shear force vs load-point displacement for specimen C10-00, south element.

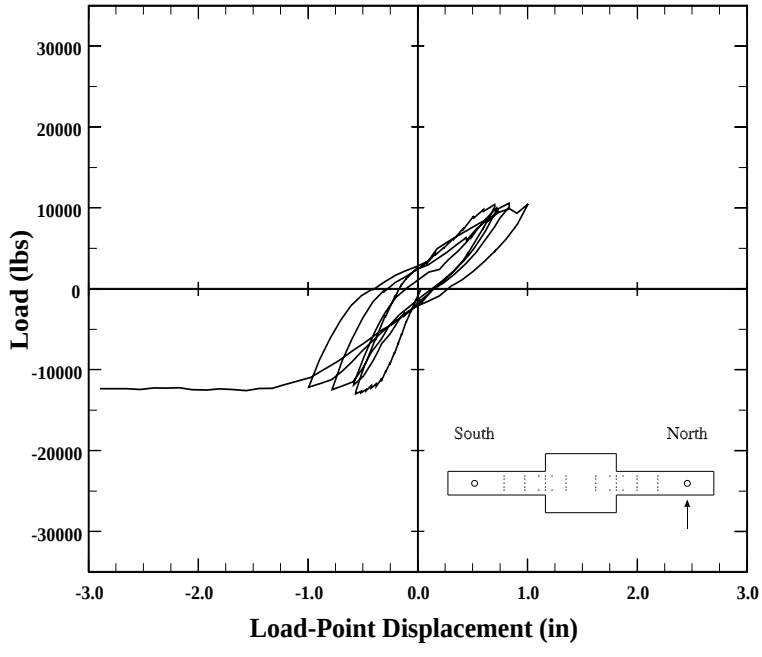

Figure 3.2. Shear force vs load-point displacement for specimen C10-00, north element.

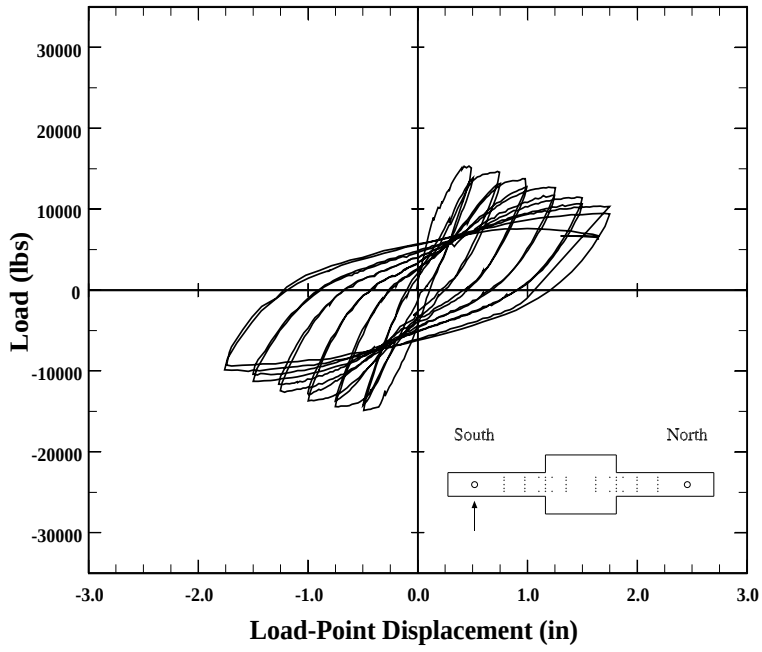

Figure 3.3. Shear force vs load-point displacement for specimen C10-05, south element.

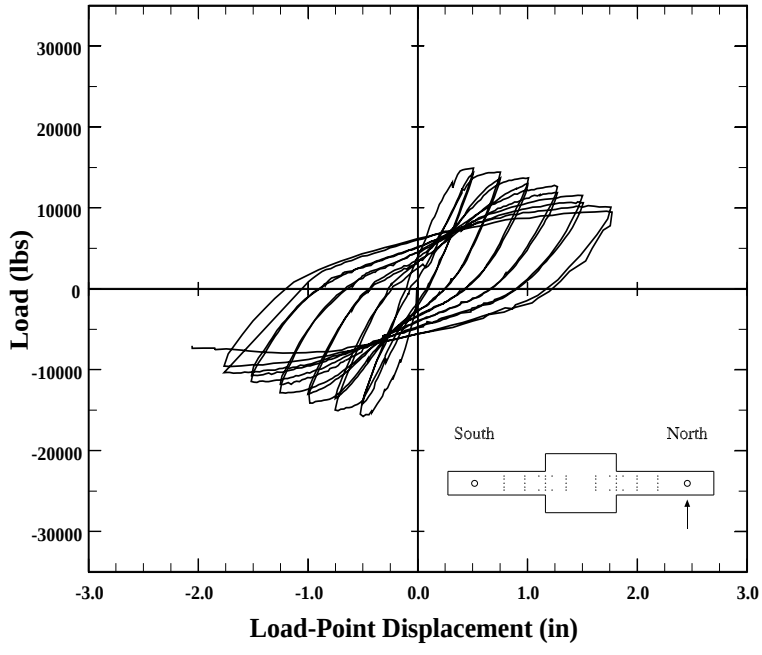

Figure 3.4. Shear force vs load-point displacement for specimen C10-05, north element.

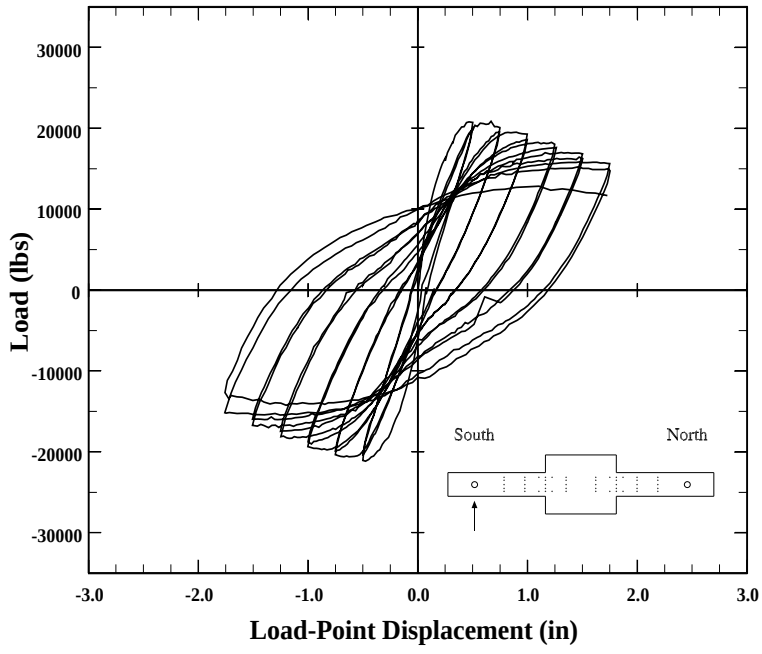

Figure 3.5. Shear force vs load-point displacement for specimen C10-10, south element.

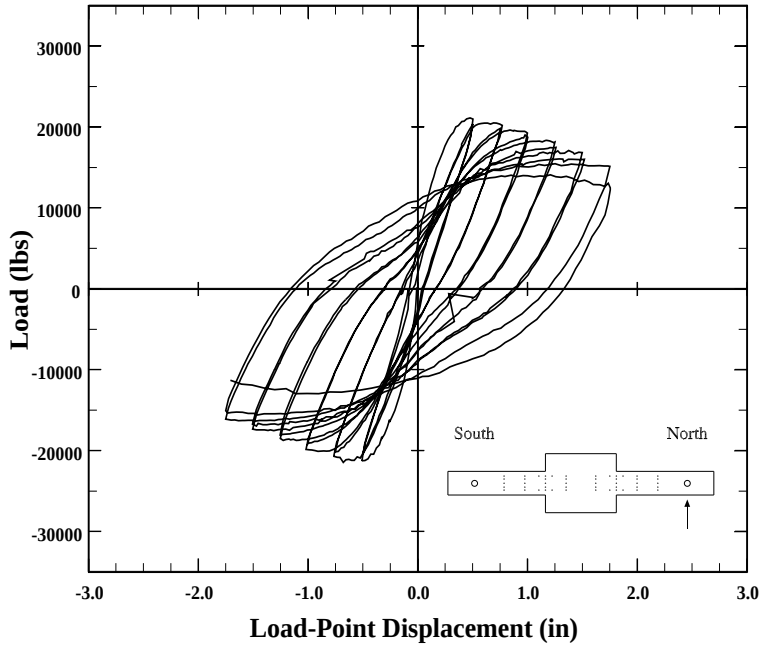

Figure 3.6. Shear force vs load-point displacement for specimen C10-10, north element.

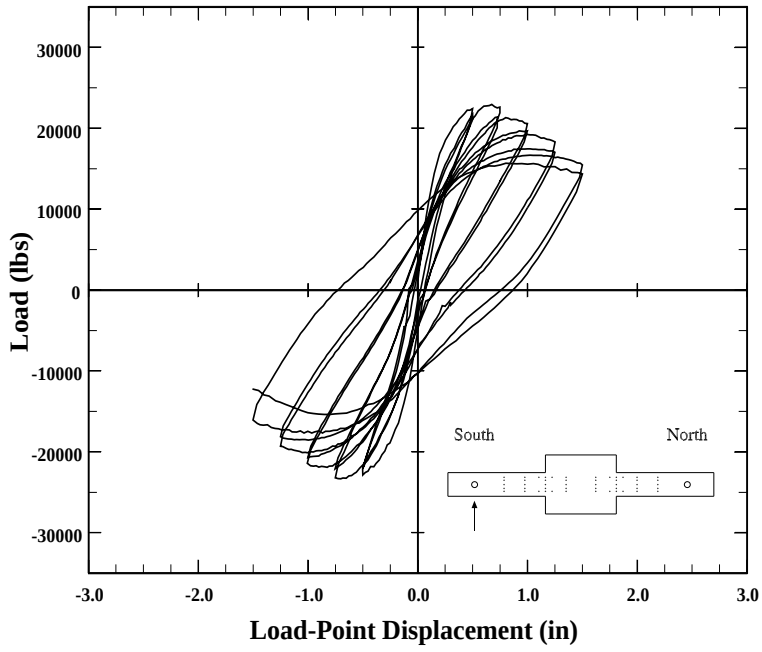

Figure 3.7. Shear force vs load-point displacement for specimen C10-20, south element.

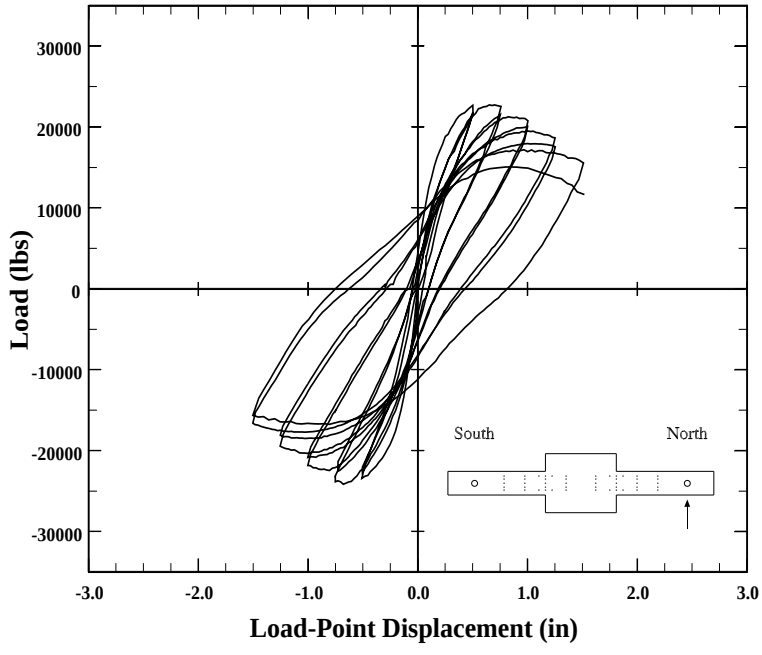

Figure 3.8. Shear force vs load-point displacement for specimen C10-20, north element.

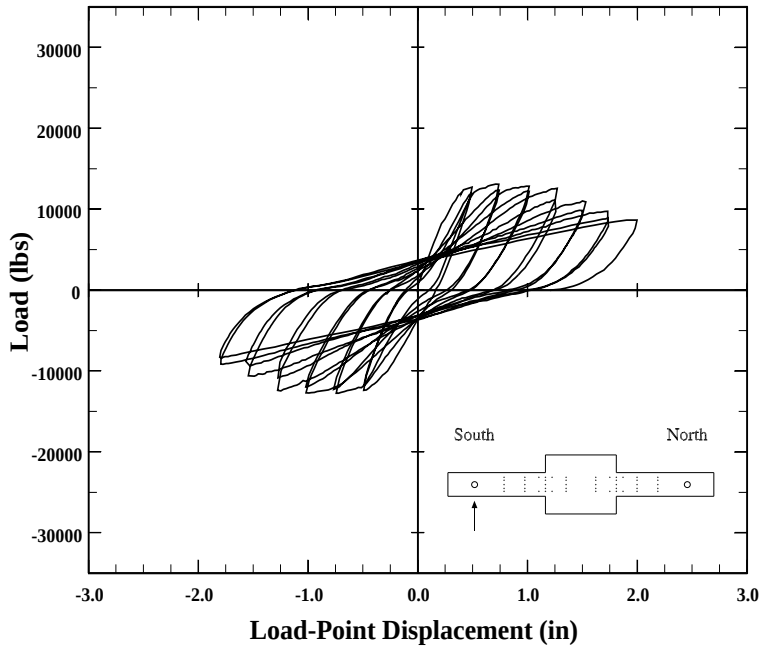

Figure 3.9. Shear force vs load-point displacement for specimen C5-00, south element.

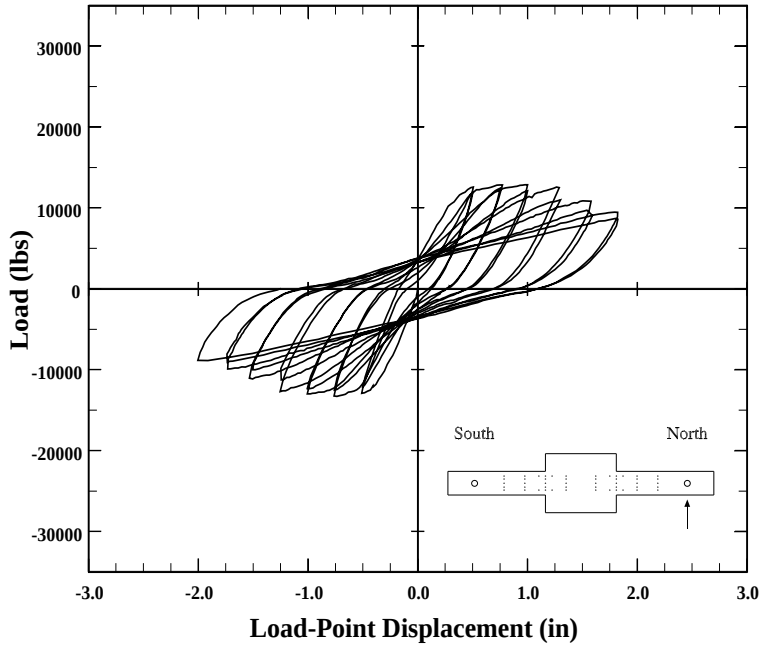

Figure 3.10. Shear force vs load-point displacement for specimen C5-00, north element.

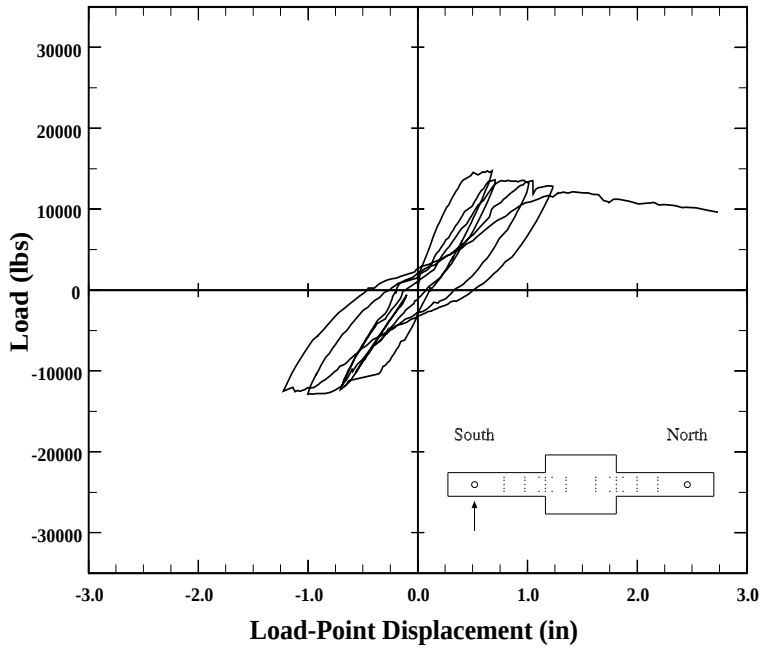

Figure 3.11. Shear force vs load-point displacement for specimen C5-10, south element.

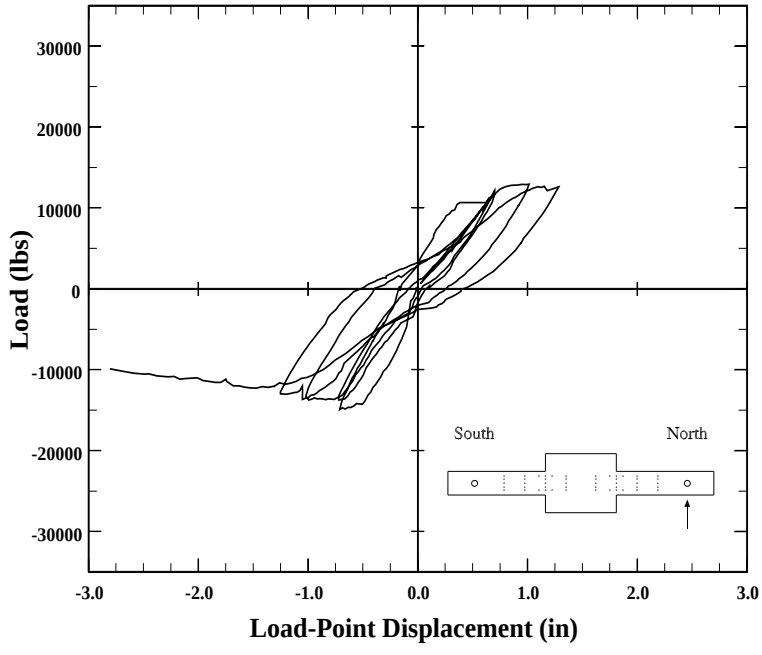

Figure 3.12. Shear force vs load-point displacement for specimen C5-10, north element.

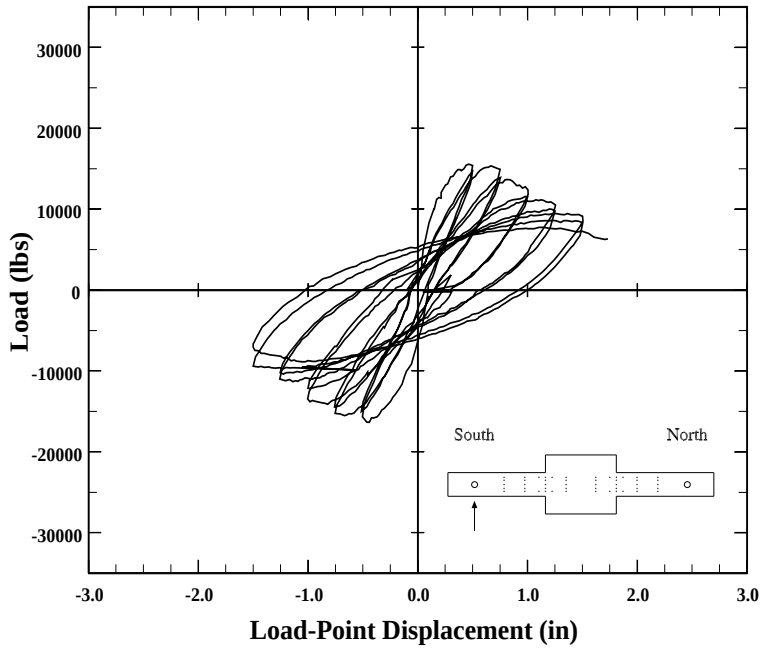

Figure 3.13. Shear force vs load-point displacement for specimen C5-20, south element.

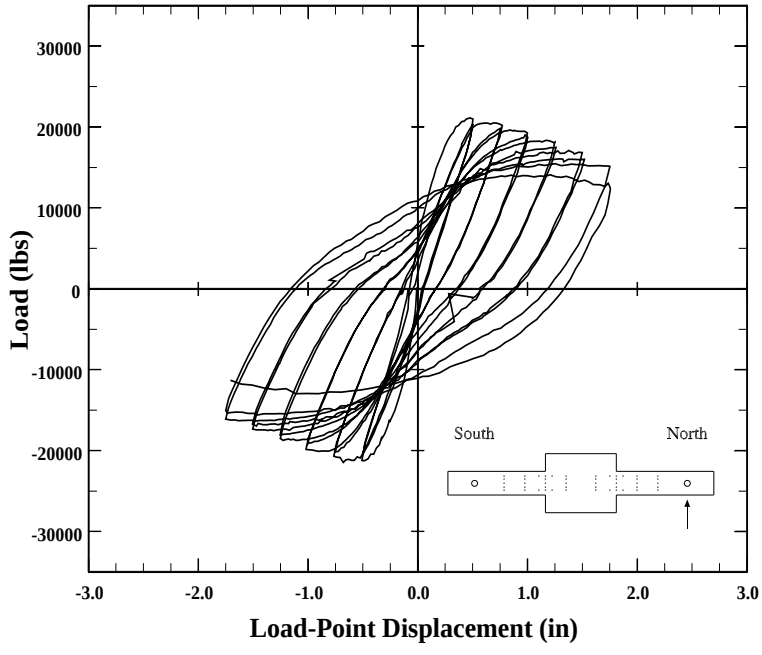

Figure 3.14. Shear force vs load-point displacement for specimen C5-20, north element.

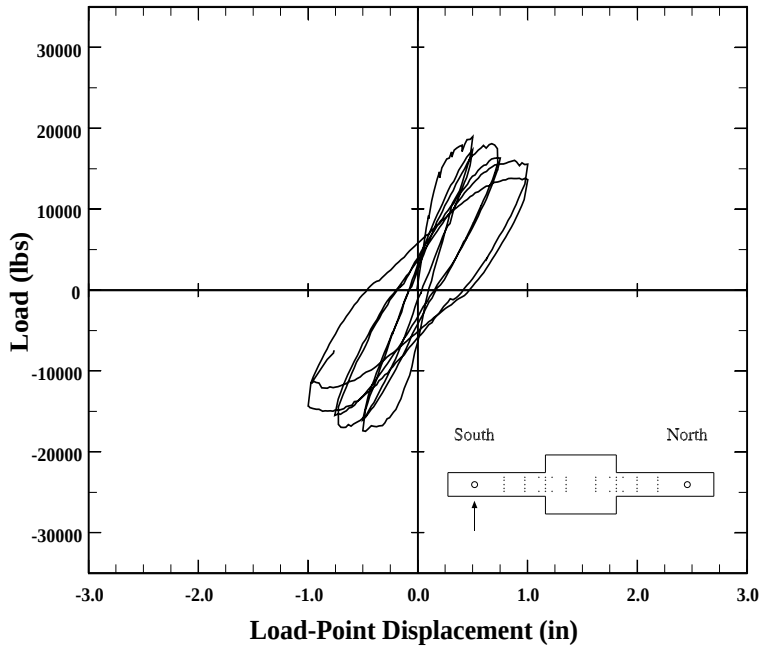

Figure 3.15. Shear force vs load-point displacement for specimen C5-40, south element.

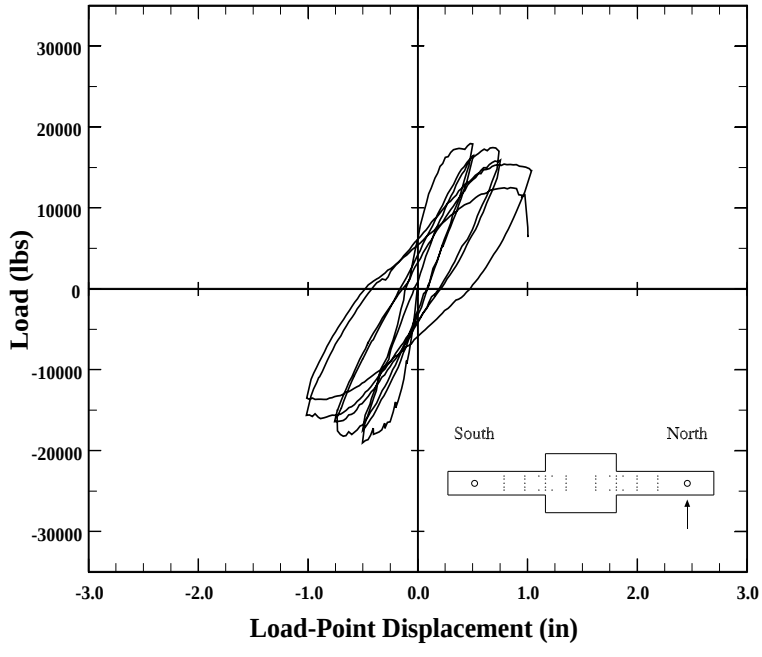

Figure 3.16. Shear force vs load-point displacement for specimen C5-40, north element.

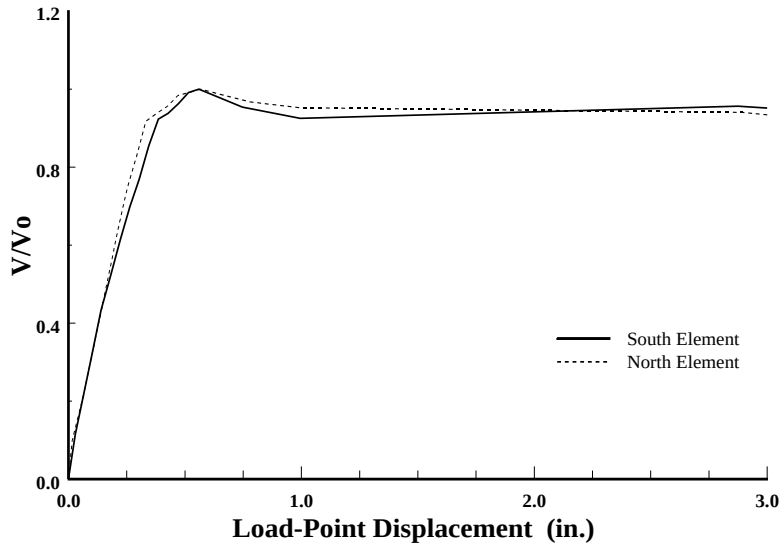

Figure 3.17. Envelope of shear force - load point displacement curve for specimen C10-00.

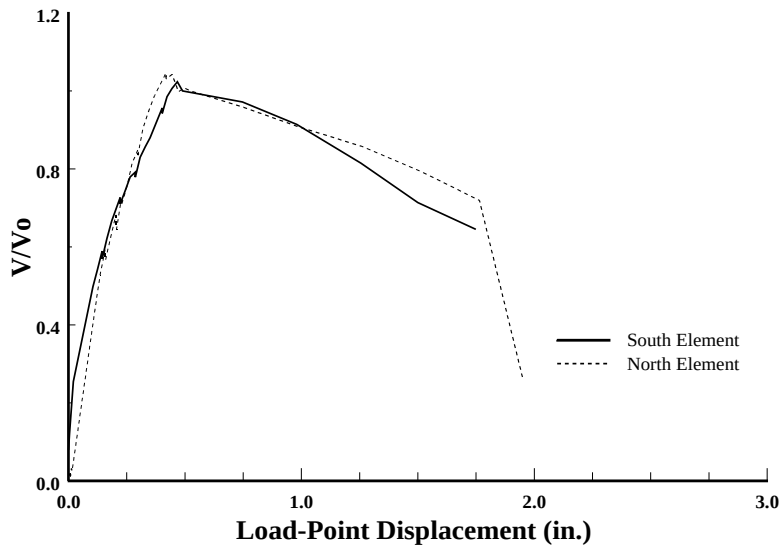

Figure 3.18 Envelope of shear force - load point displacement curve for specimen C10-05

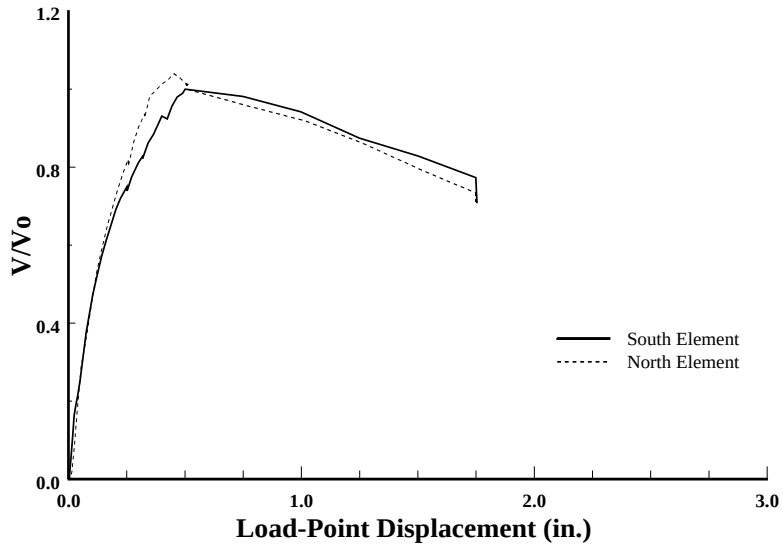

Figure 3.19. Envelope of shear force - load point displacement curve for specimen C10-10.

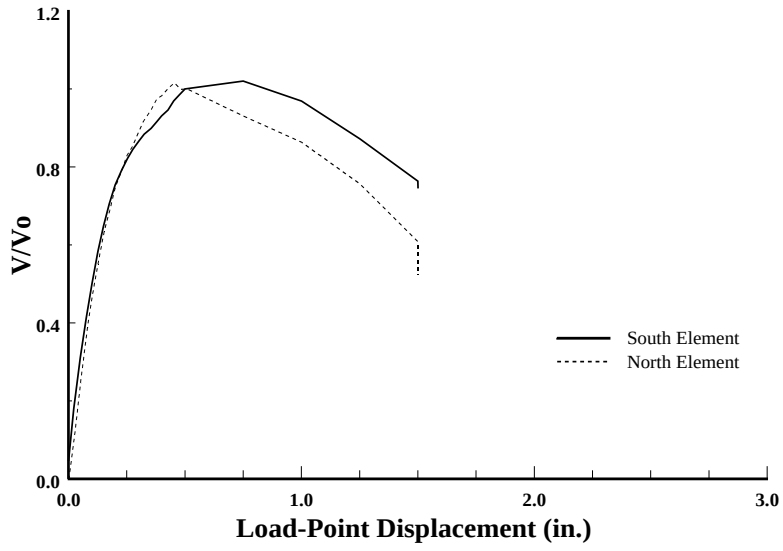

Figure 3.20. Envelope of shear force - load point displacement curve for specimen C10-20.

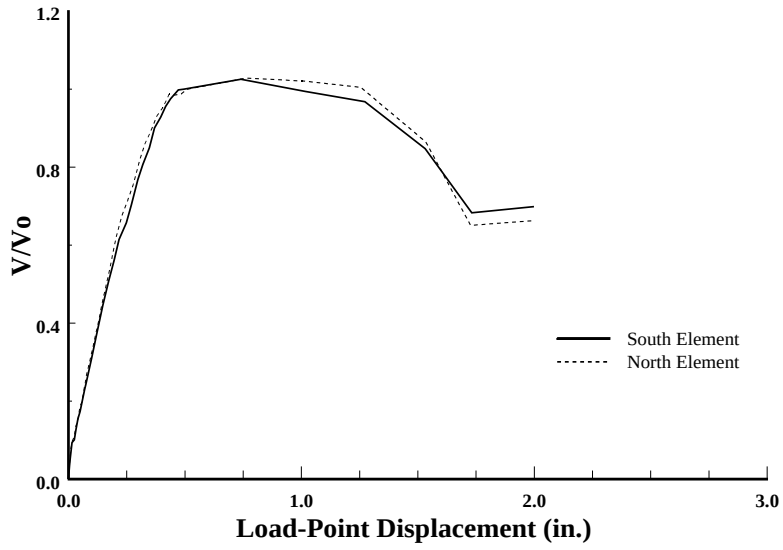

Figure 3.21 Envelope of shear force - load point displacement curve for specimen C5-00.

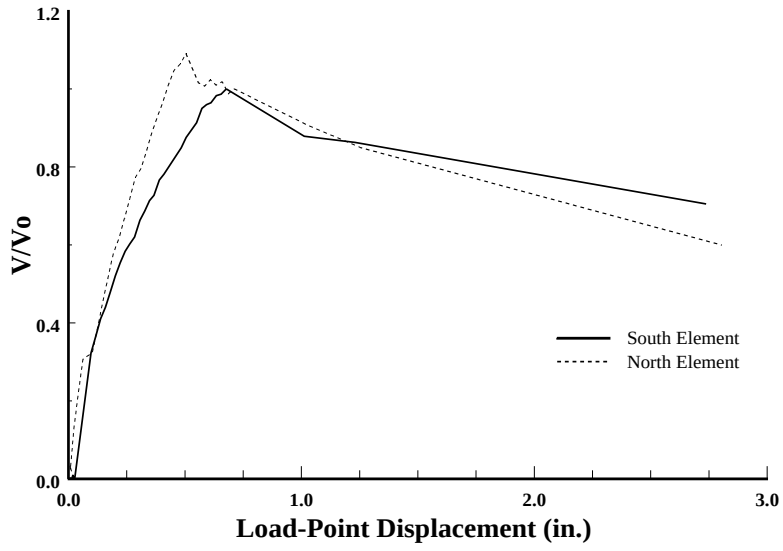

Figure 3.22. Envelope of shear force - load point displacement curve for specimen C5-10.

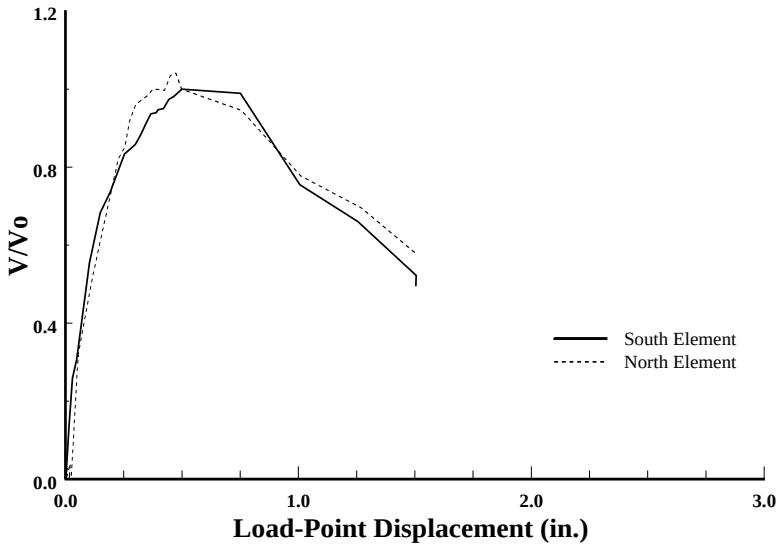

Figure 3.23. Envelope of shear force - load point displacement curve for specimen C5-20.

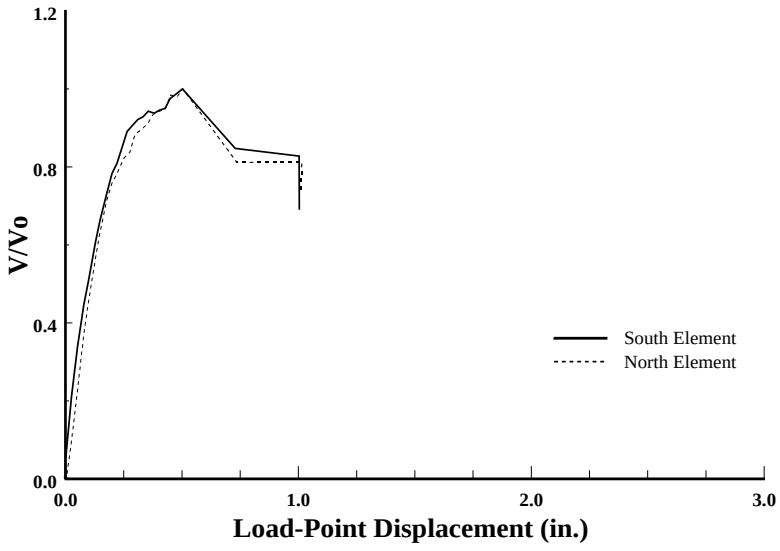

Figure 3.24. Envelope of shear force - load point displacement curve for specimen C5-40.

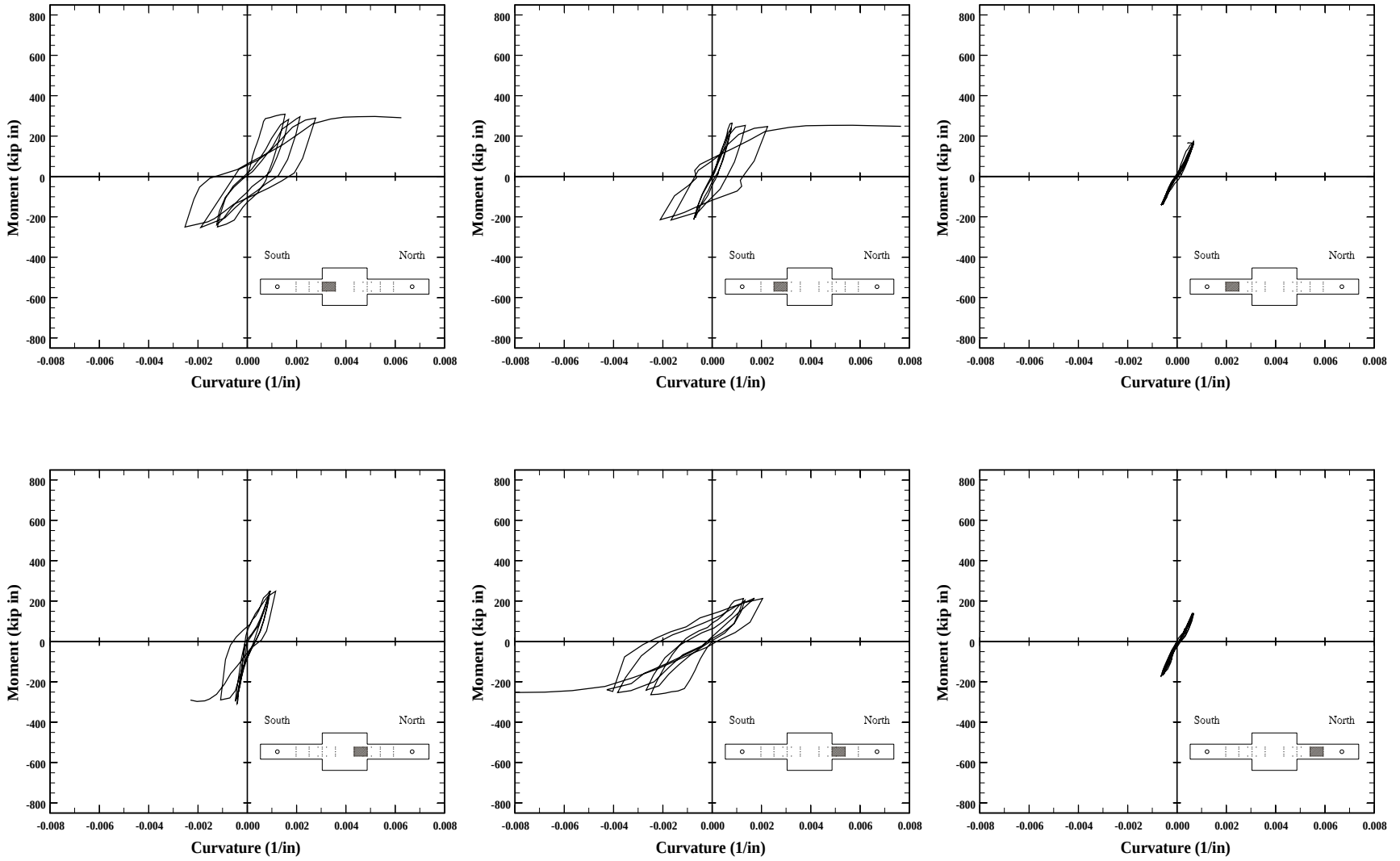

Figure 3.25. Measured moment vs mean curvature in the joint region for specimen C10-00.

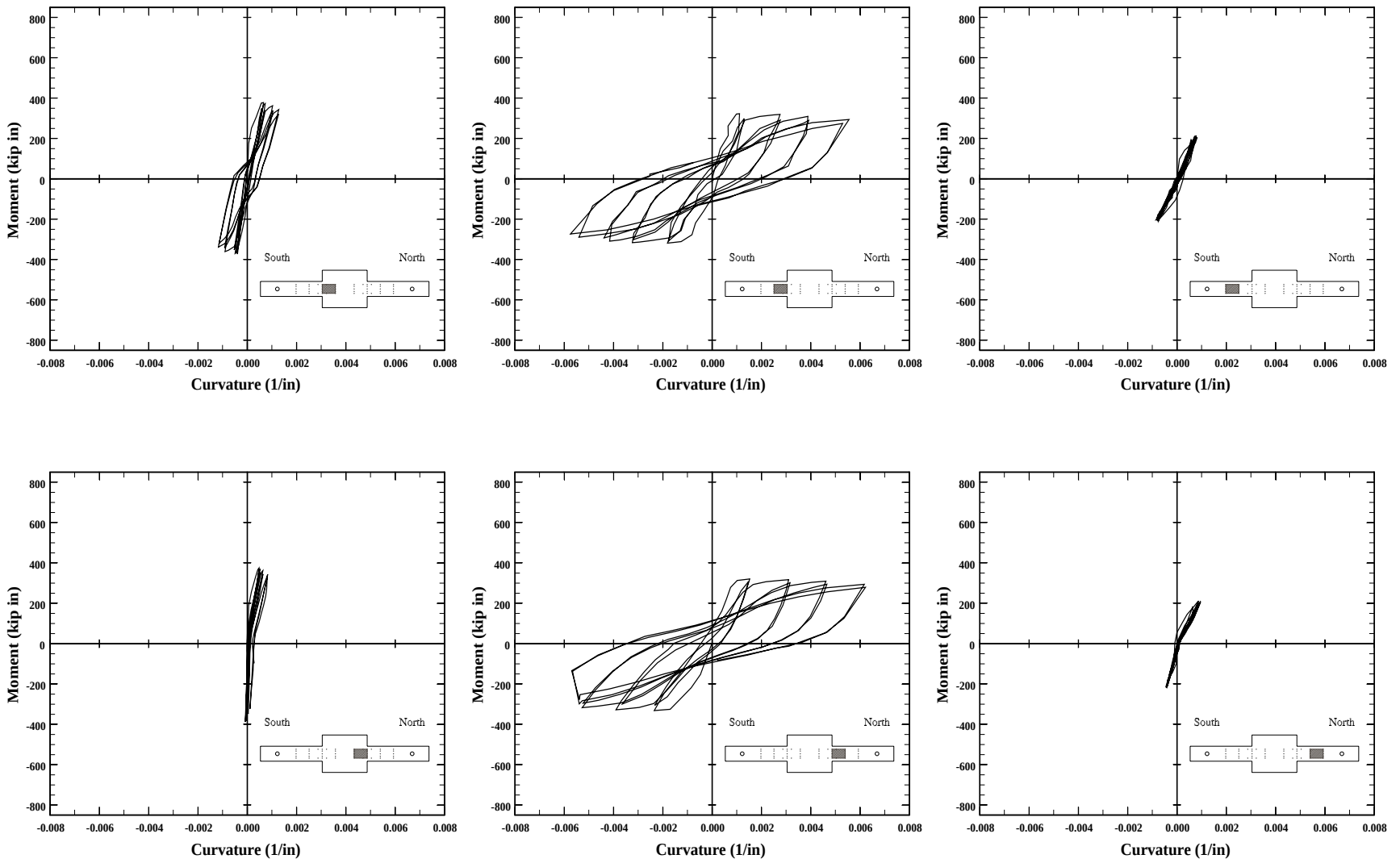

Figure 3.26. Measured moment vs mean curvature in the joint region for specimen C10-05.

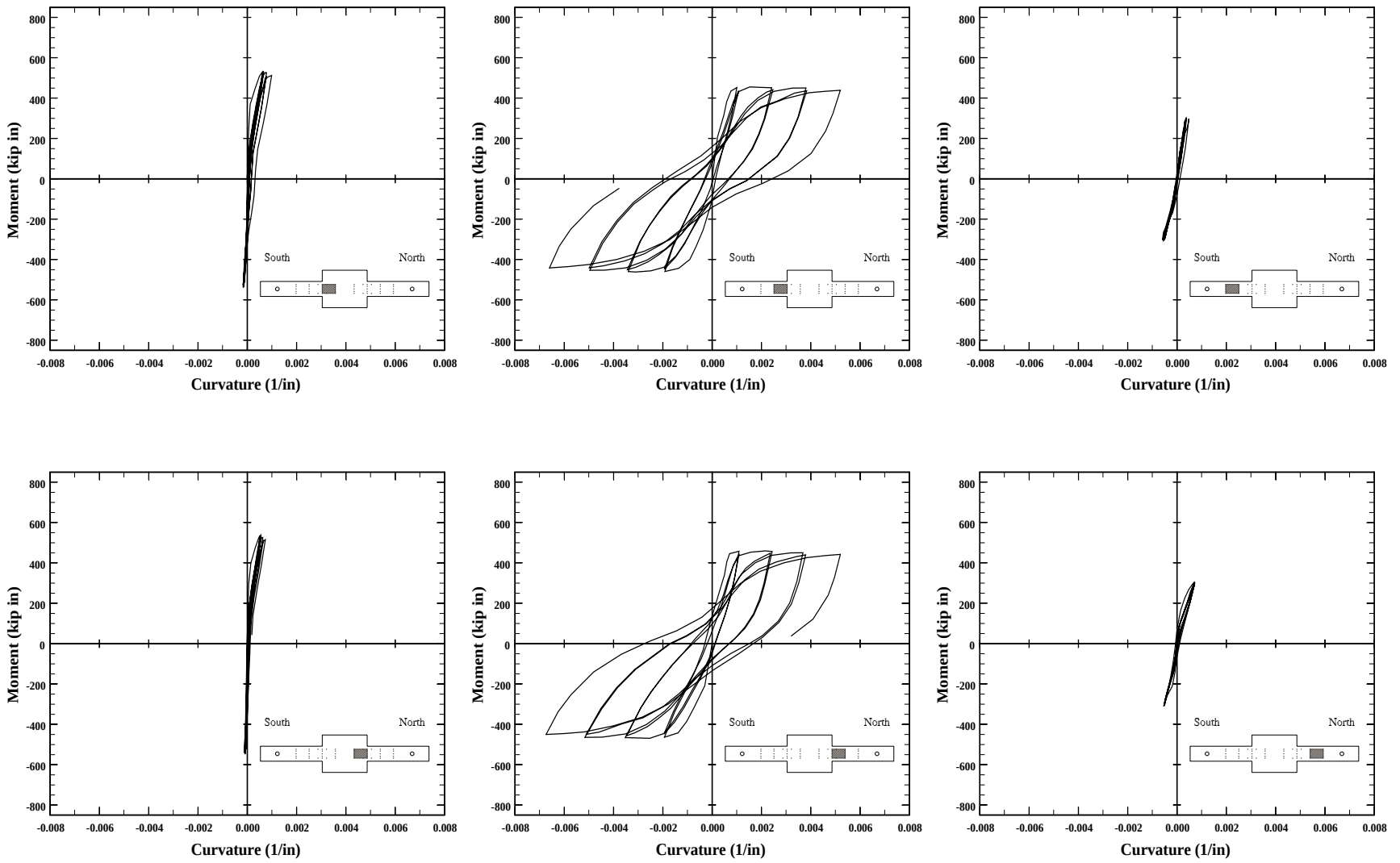

Figure 3.27. Measured moment vs mean curvature in the joint region for specimen C10-10.

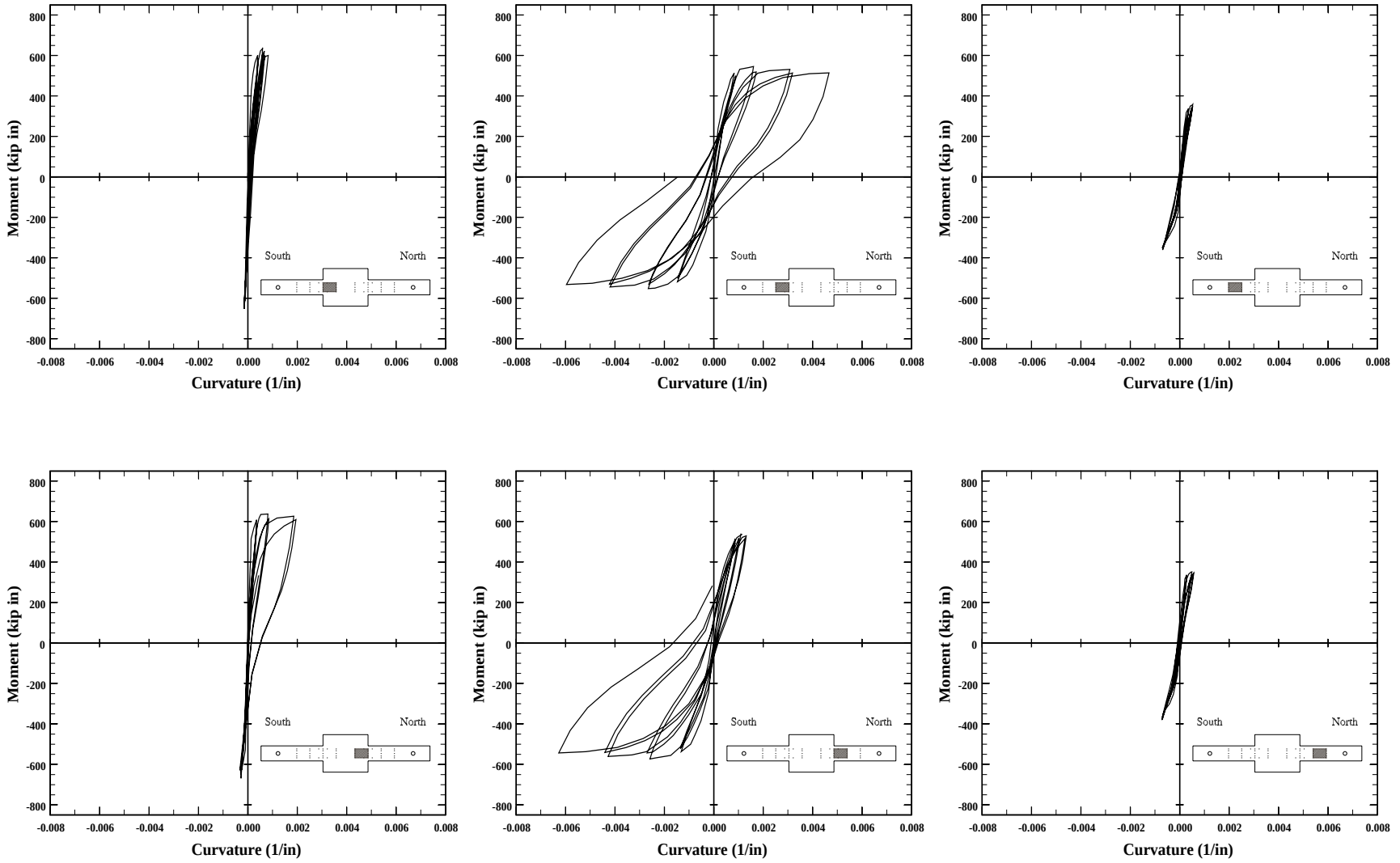

Figure 3.28. Measured moment vs mean curvature in the joint region for specimen C10-20.

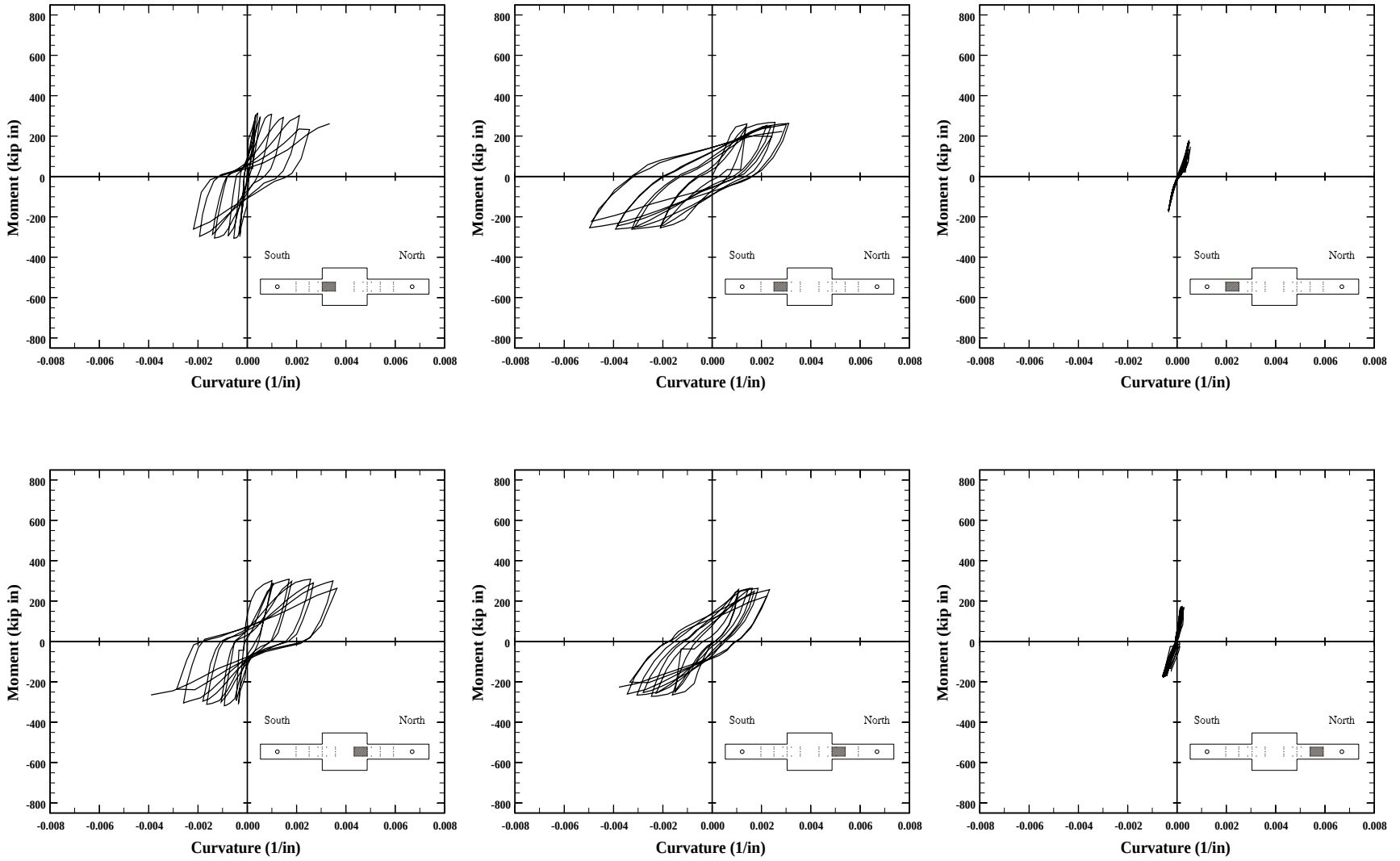

Figure 3.29. Measured moment vs mean curvature in the joint region for specimen C5-00.

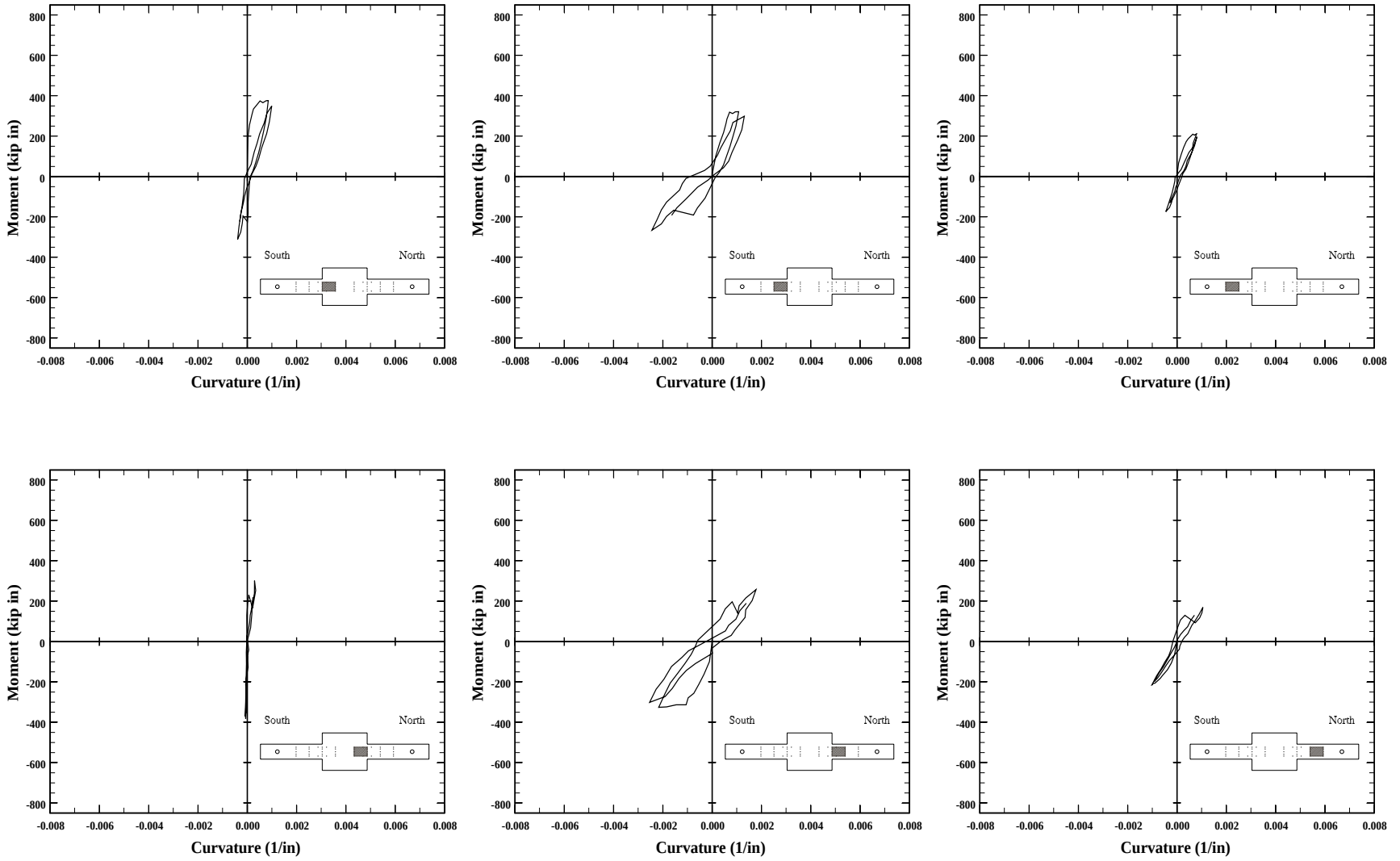

Figure 3.30. Measured moment vs mean curvature in the joint region for specimen C5-10.

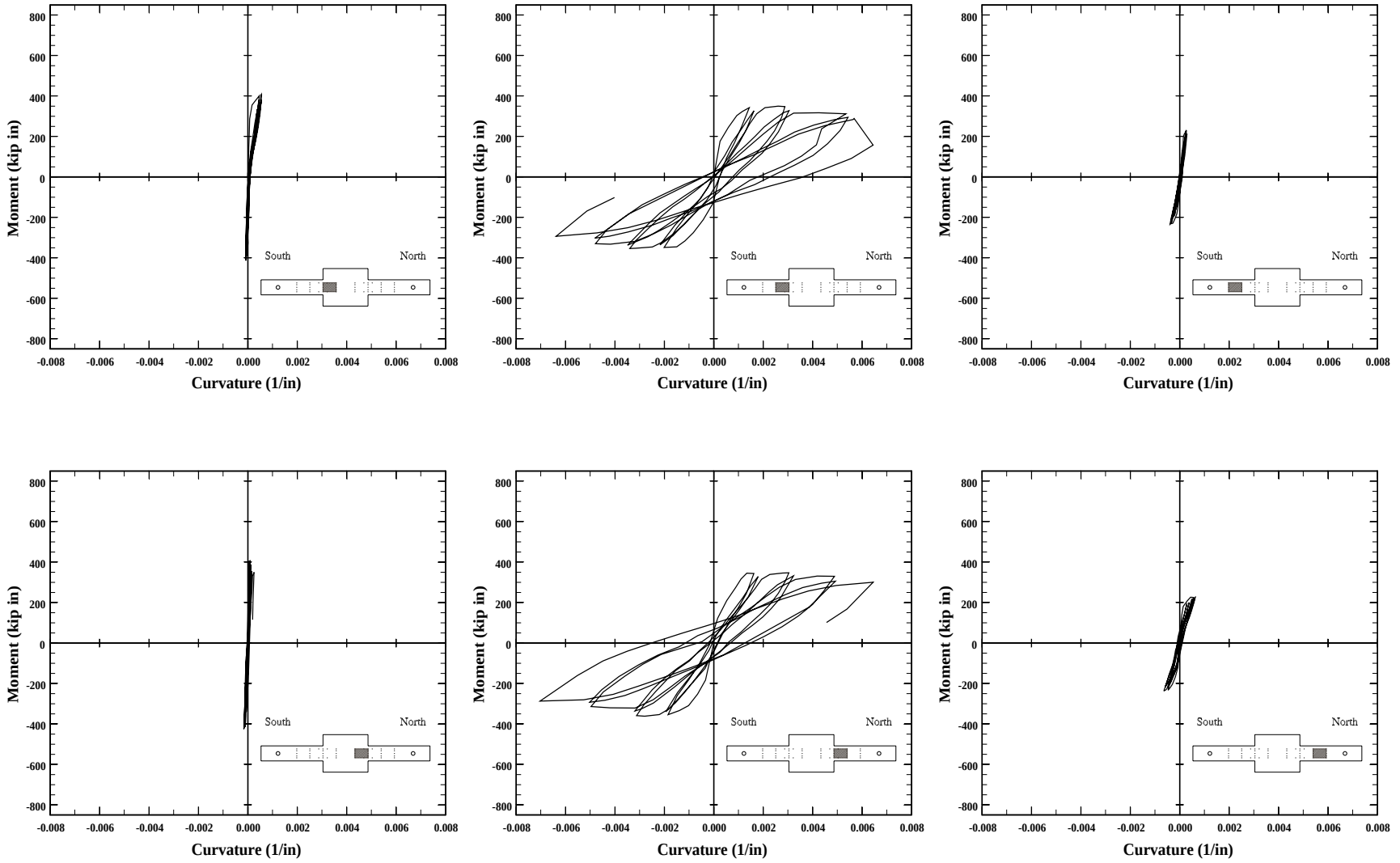

Figure 3.31. Measured moment vs mean curvature in the joint region for specimen C5-20.

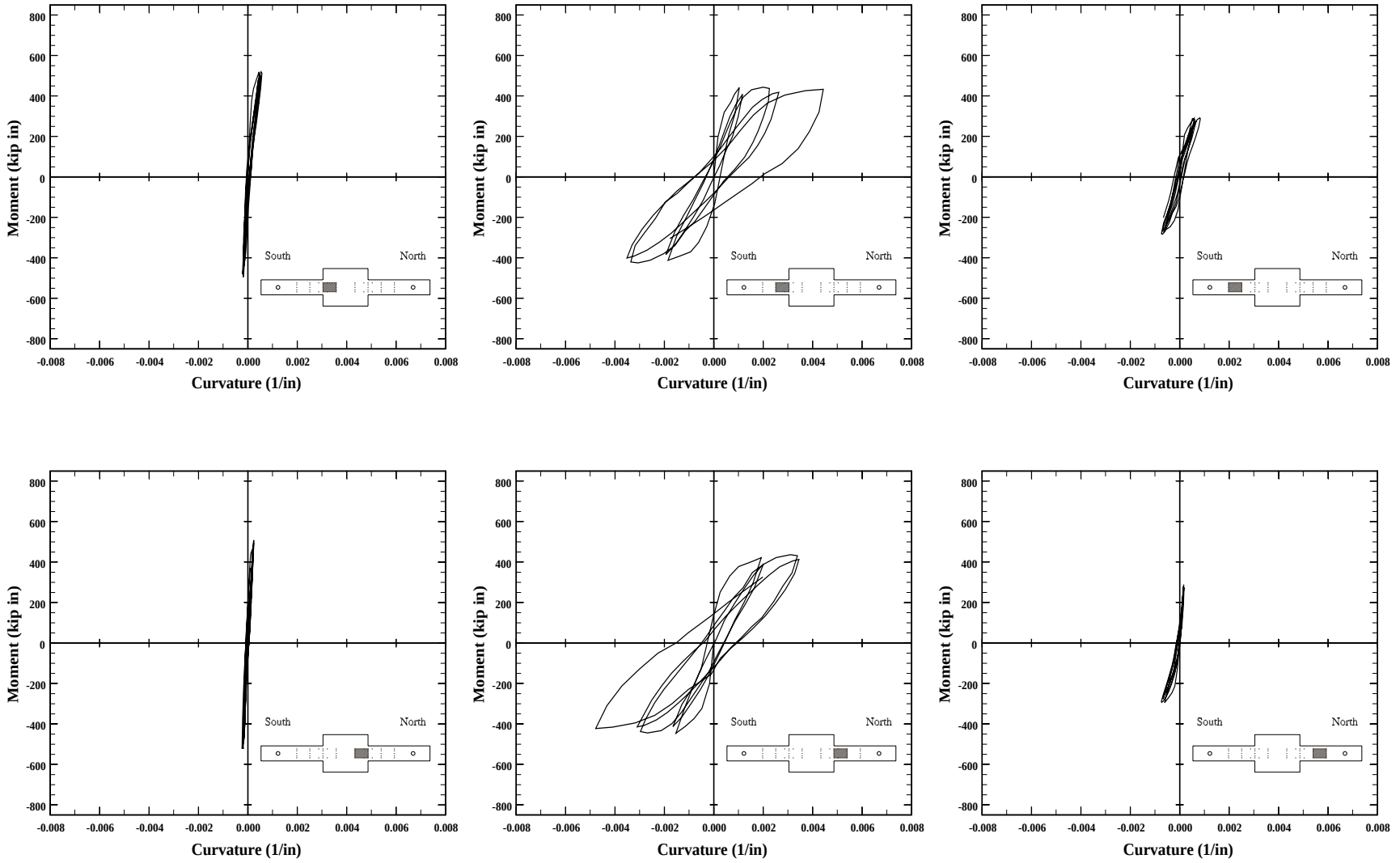

Figure 3.32. Measured moment vs mean curvature in the joint region for specimen C5-40.

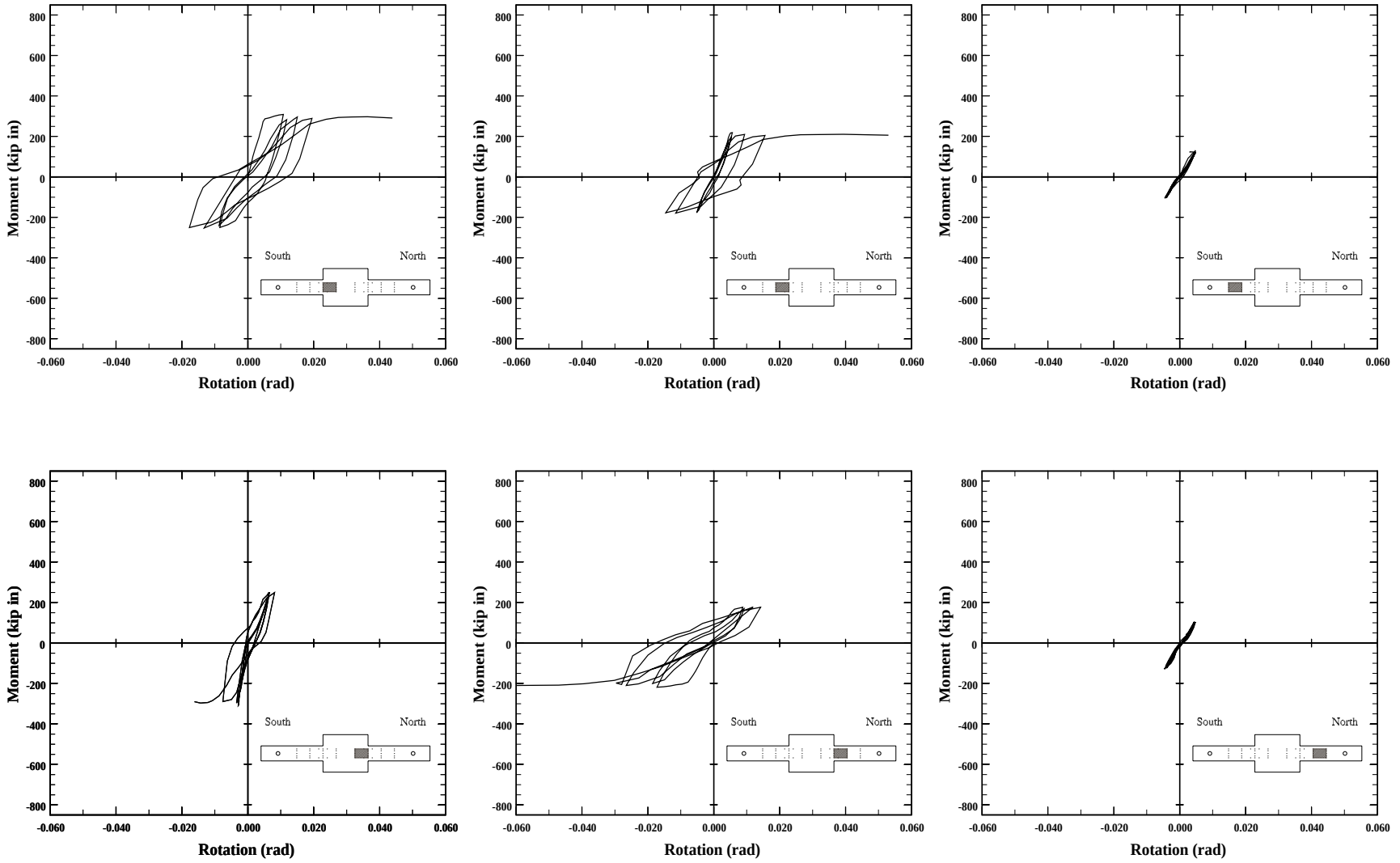

Figure 3.33. Measured moment vs rotation in the joint region for specimen C10-00.

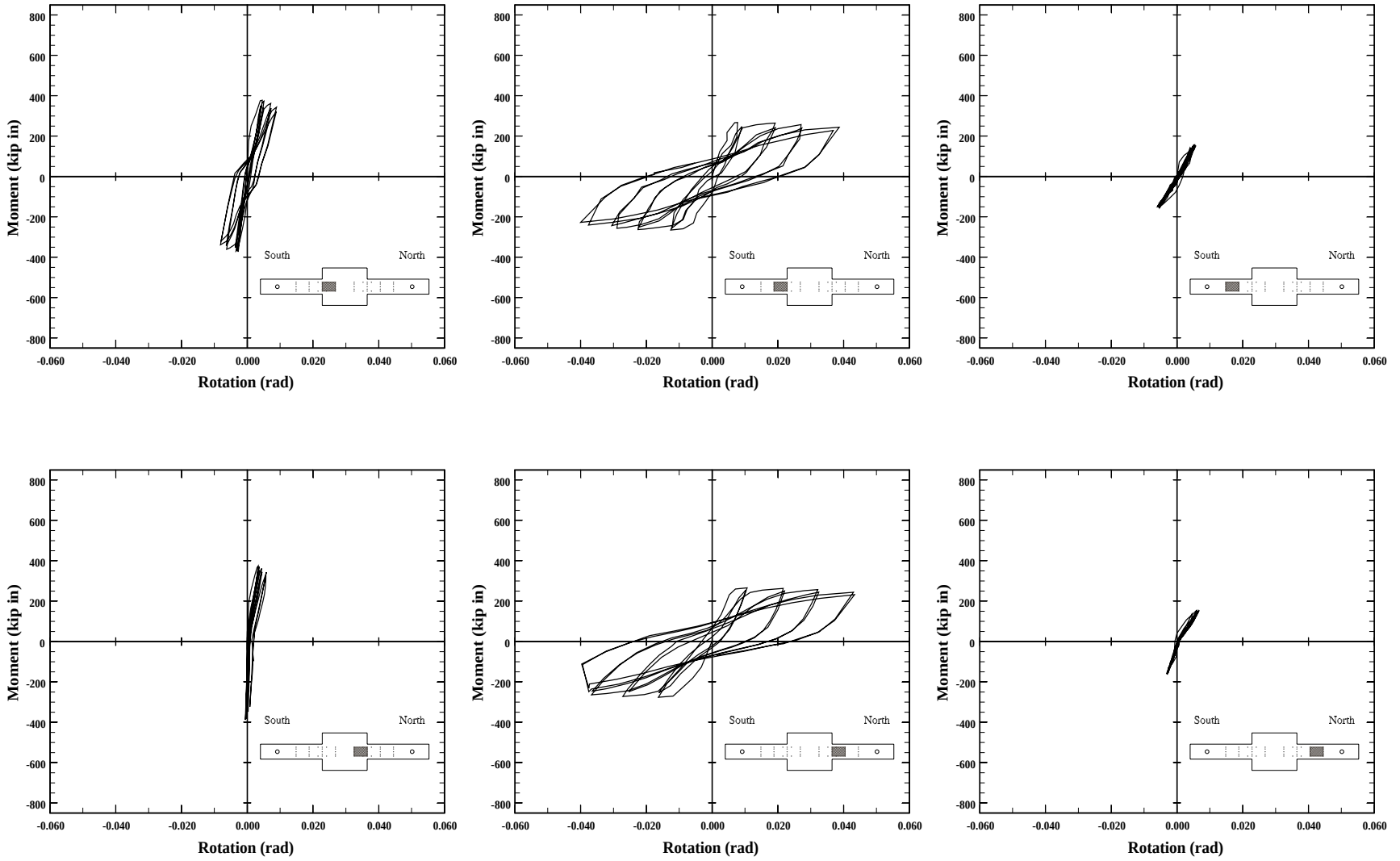

Figure 3.34. Measured moment vs rotation in the joint region for specimen C10-05.

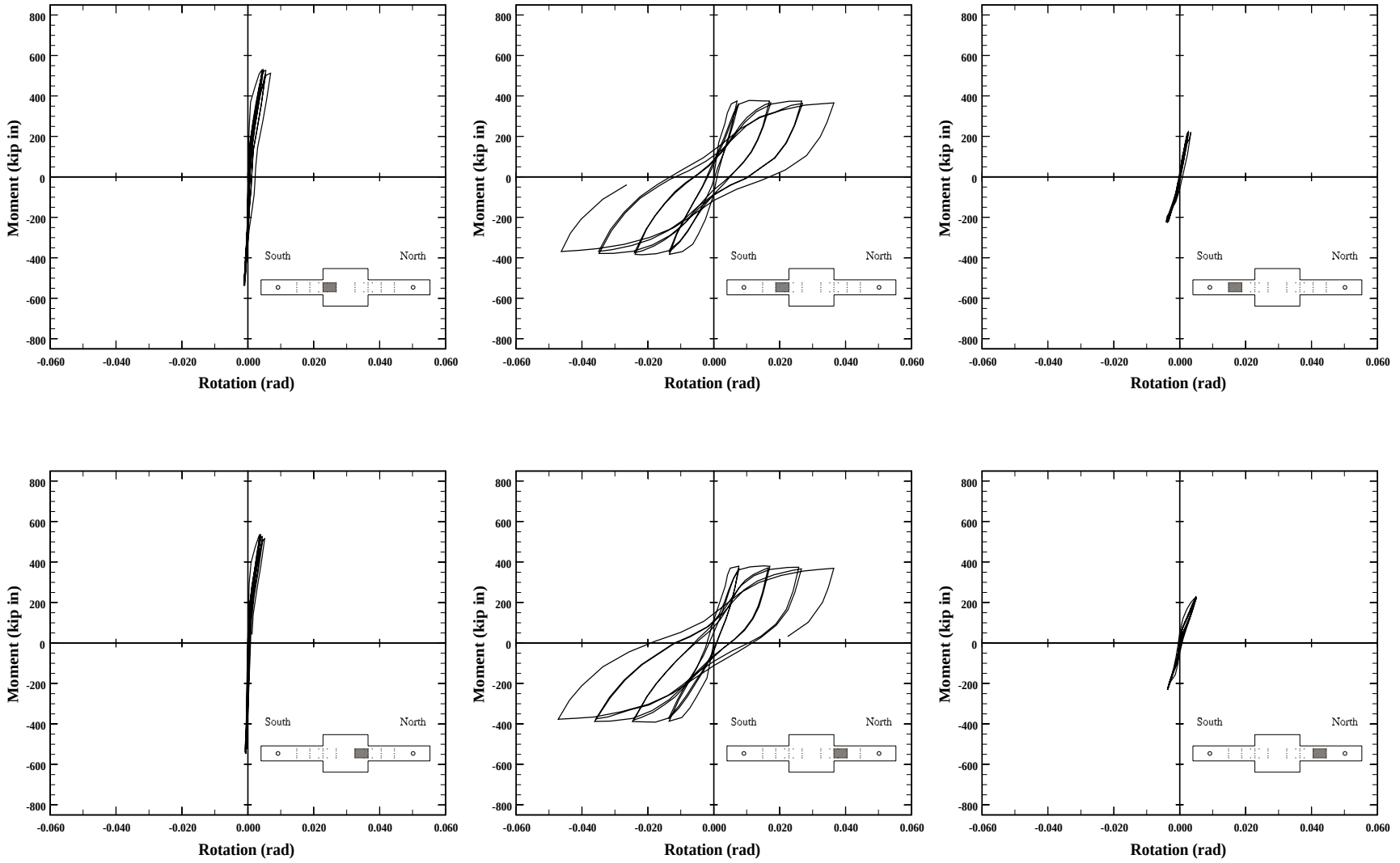

Figure 3.35. Measured moment vs rotation in the joint region for specimen C10-10.

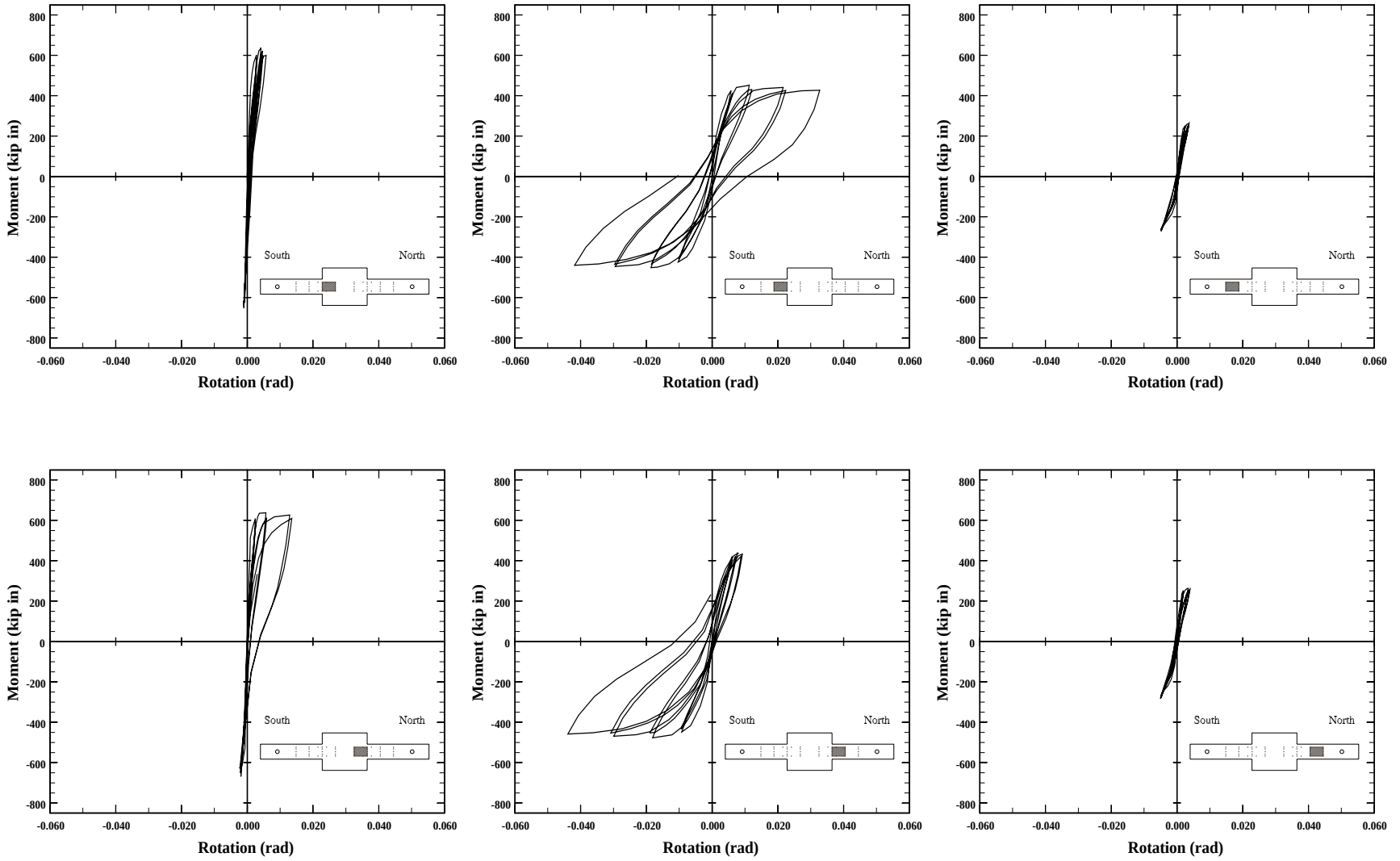

Figure 3.36. Measured moment vs rotation in the joint region for specimen C10-20.

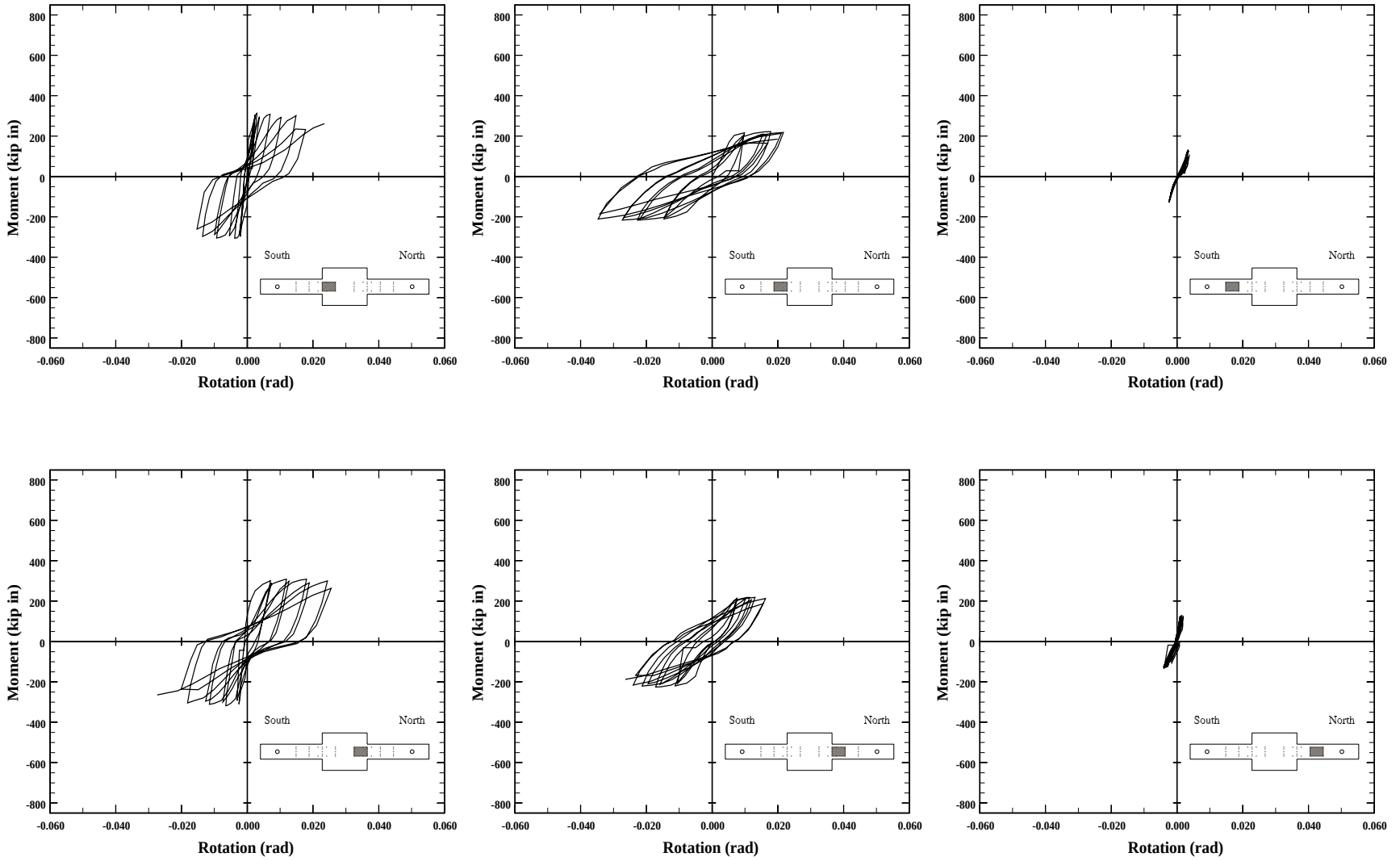

Figure 3.37. Measured moment vs rotation in the joint region for specimen C5-00.

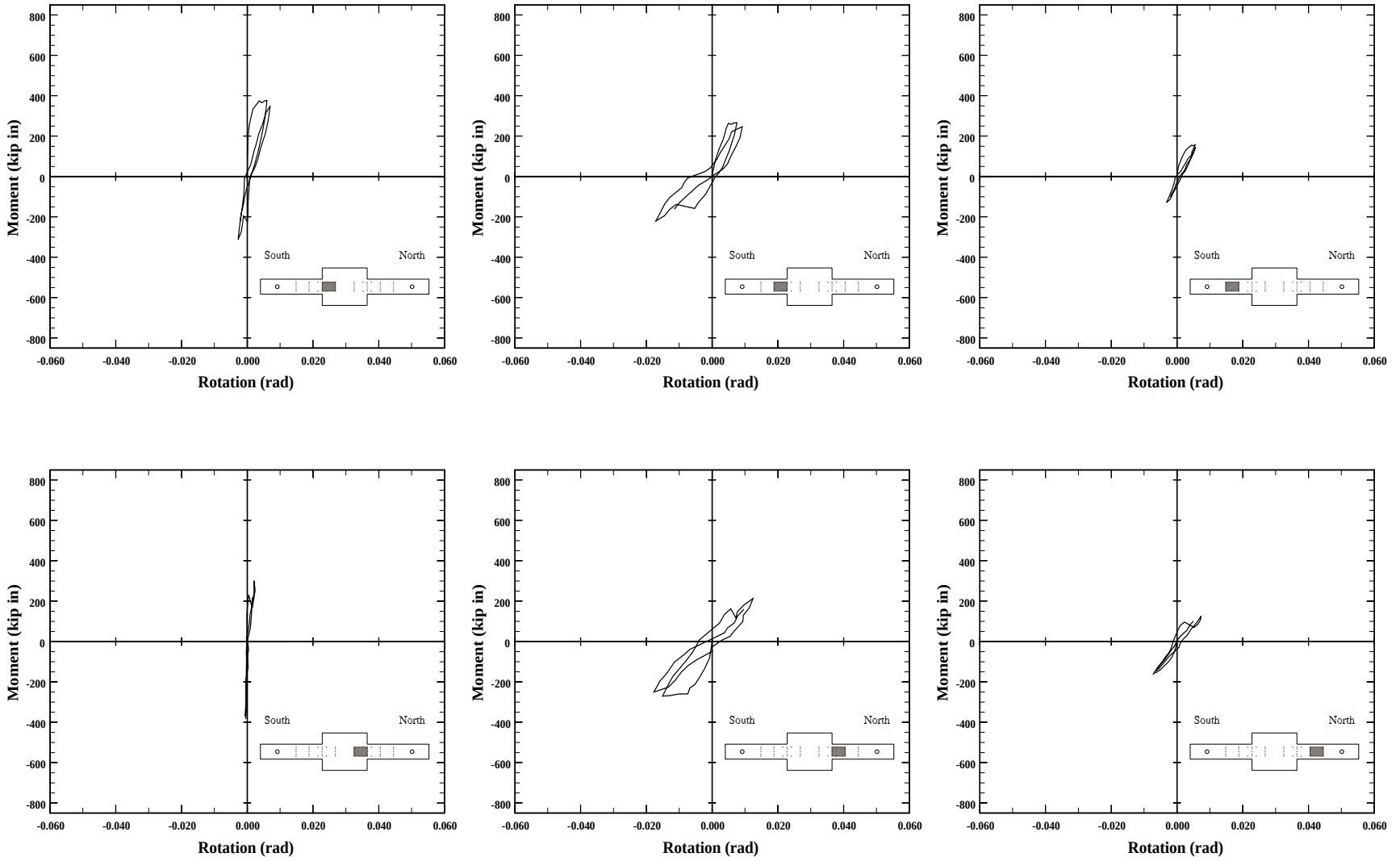

Figure 3.38. Measured moment vs rotation in the joint region for specimen C5-10.

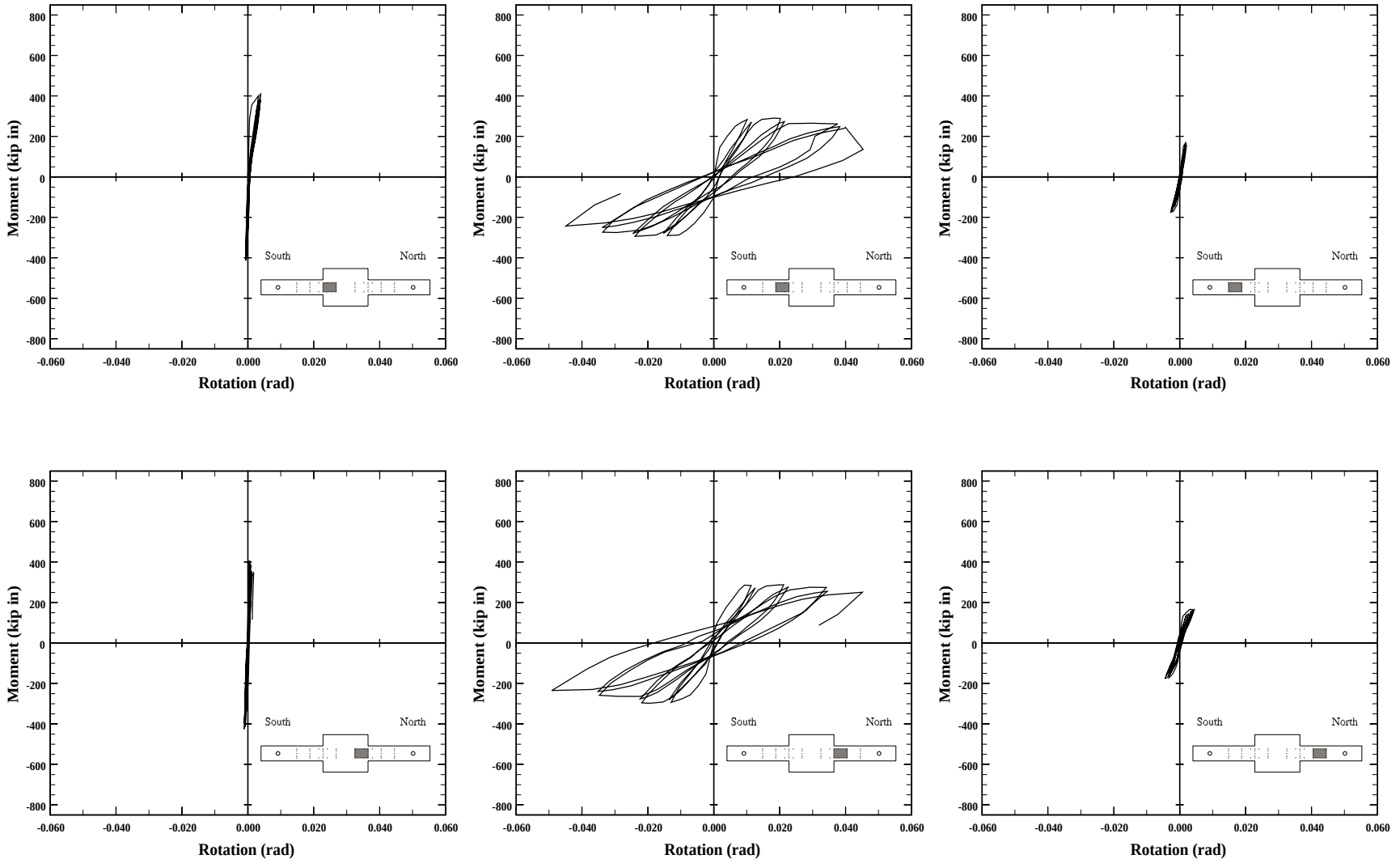

Figure 3.39. Measured moment vs rotation in the joint region for specimen C5-20.

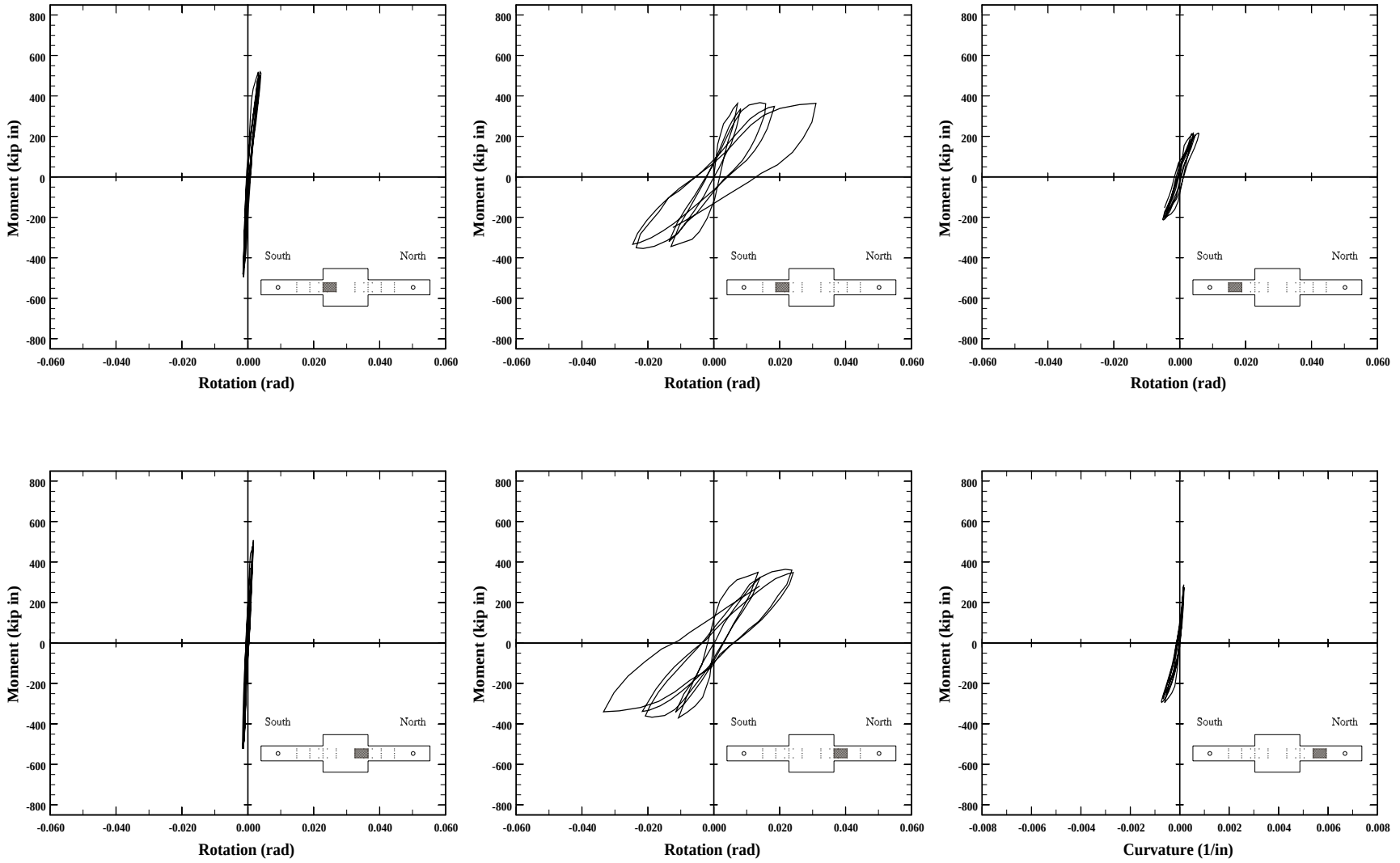

Figure 3.40. Measured moment vs rotation in the joint region for specimen C5-40.

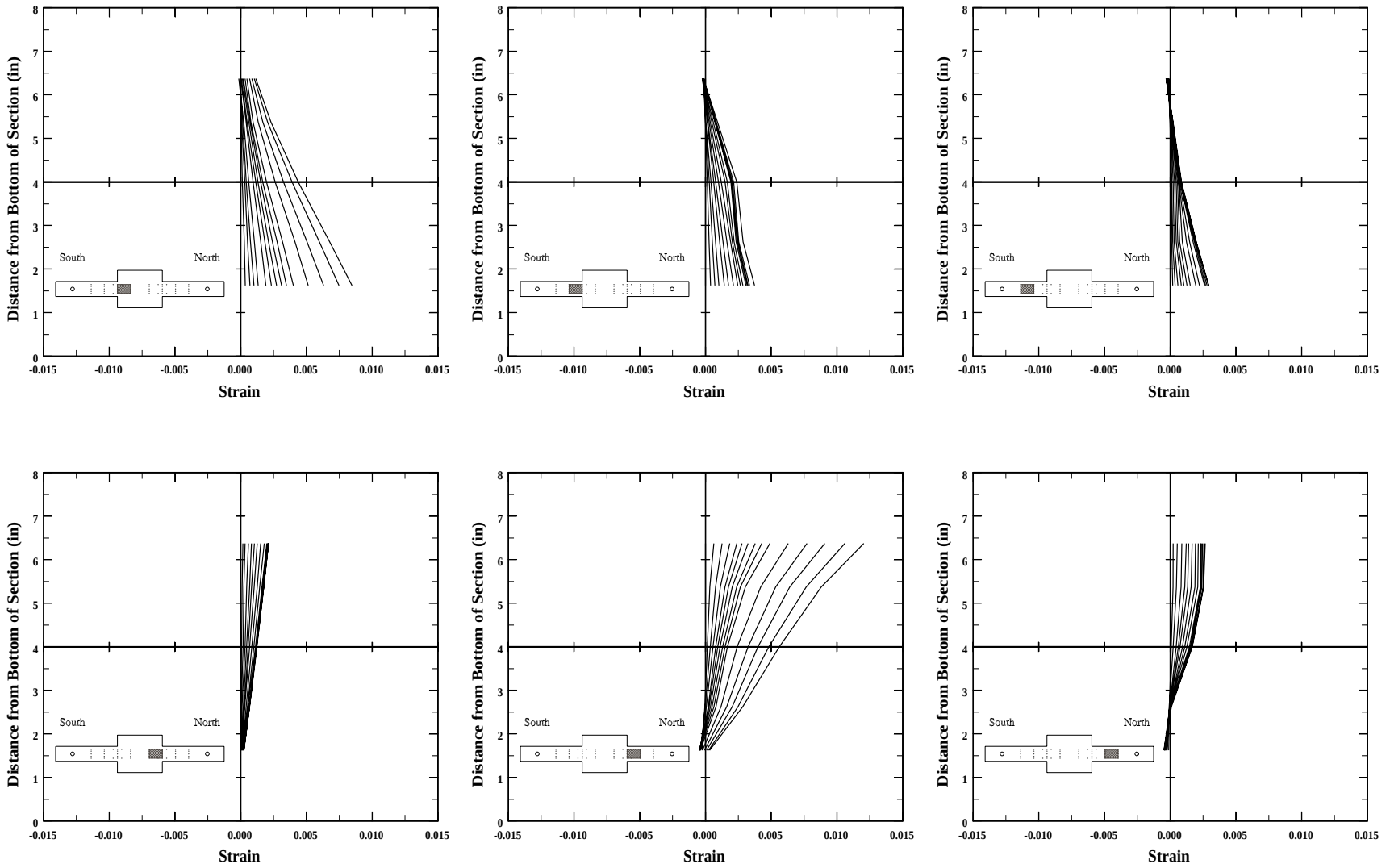

Figure 3.41. Variation of the mean strain distribution in the joint region during the first quarter cycle, for specimen C10-00.

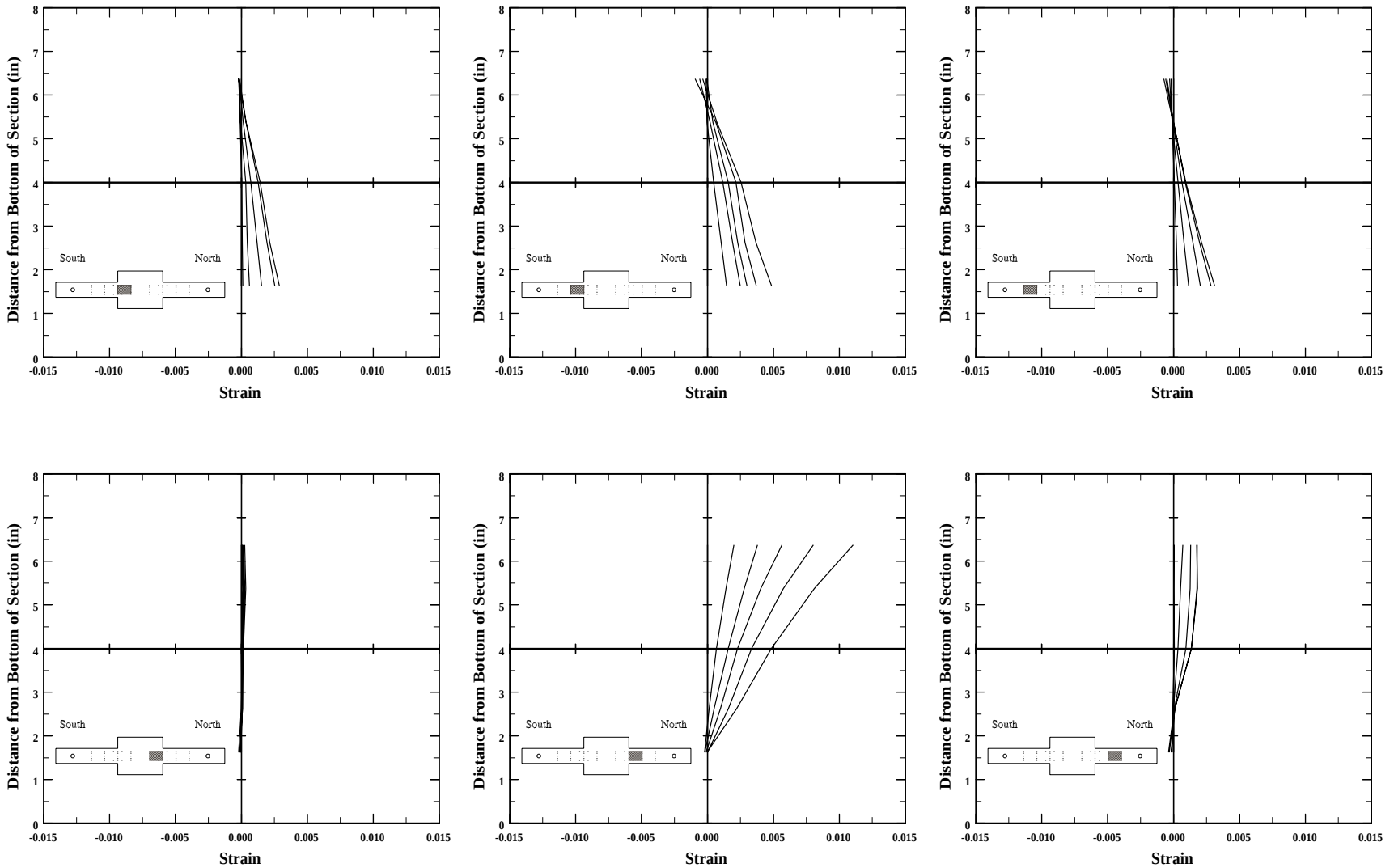

Figure 3.42. Variation of the mean strain distribution in the joint region during the first quarter cycle, for specimen C10-05.

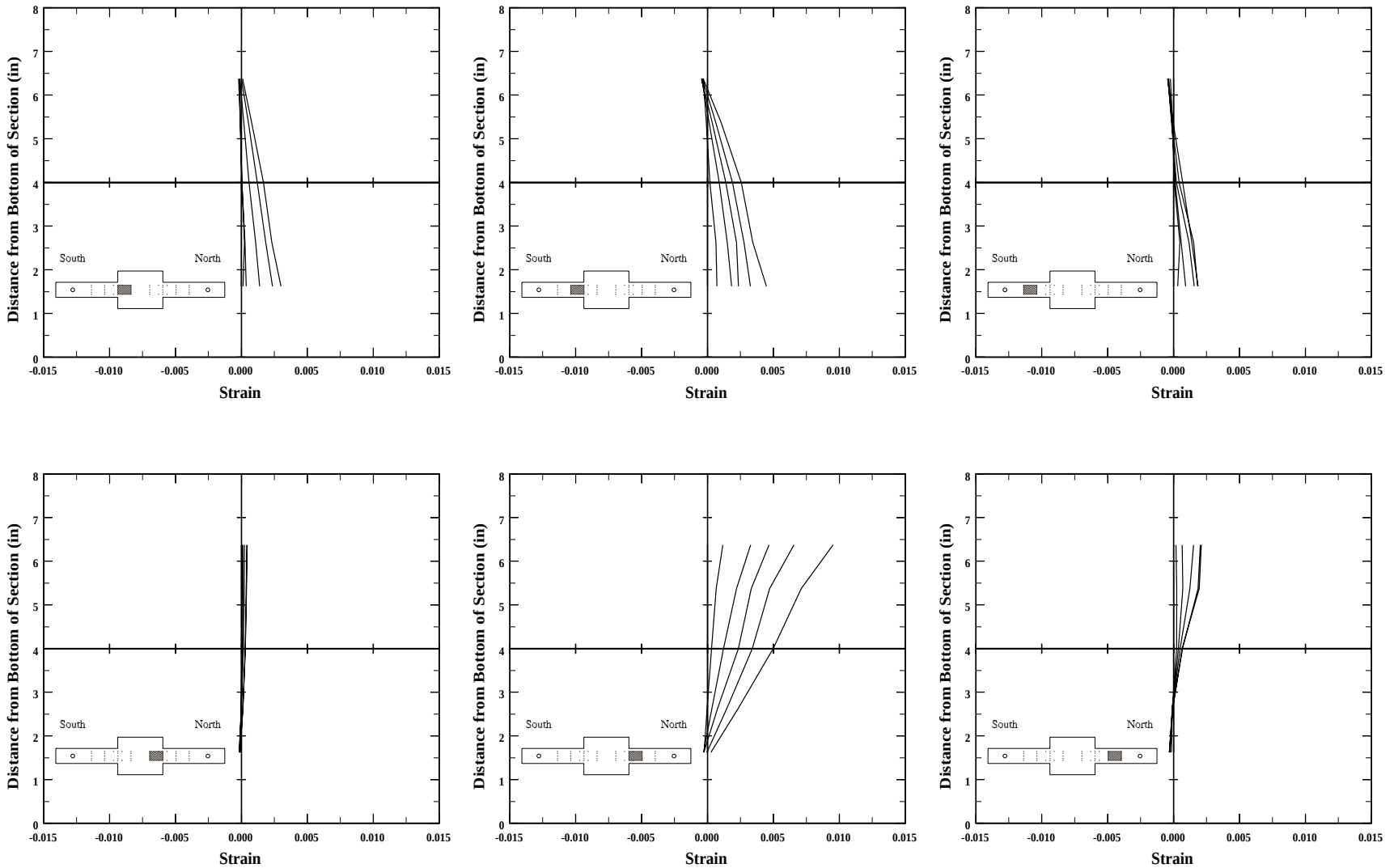

Figure 3.43. Variation of the mean strain distribution in the joint region during the first quarter cycle, for specimen C10-10.

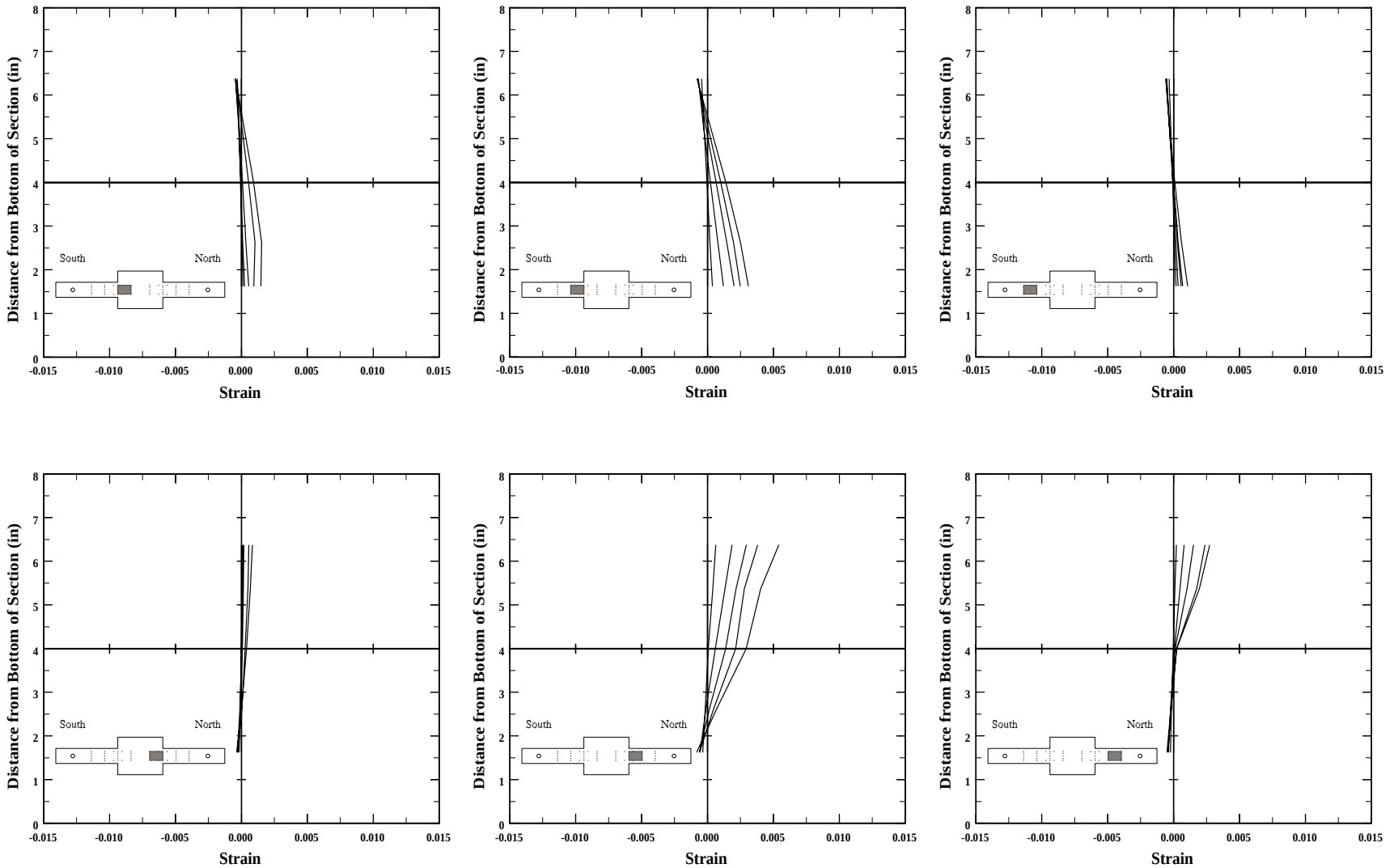

Figure 3.44. Variation of the mean strain distribution in the joint region during the first quarter cycle, for specimen C10-20.

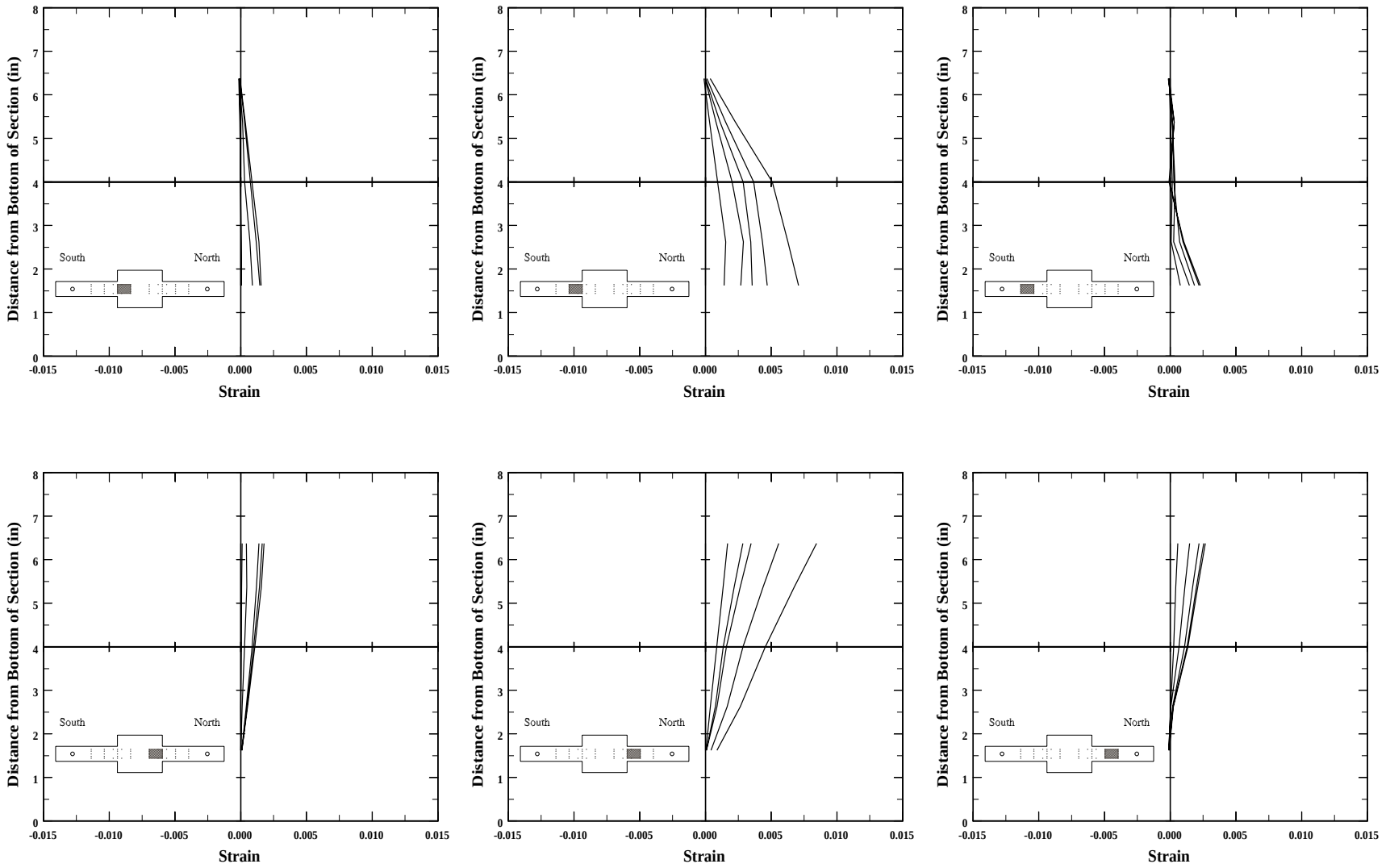

Figure 3.45. Variation of the mean strain distribution in the joint region during the first quarter cycle, for specimen C5-00.

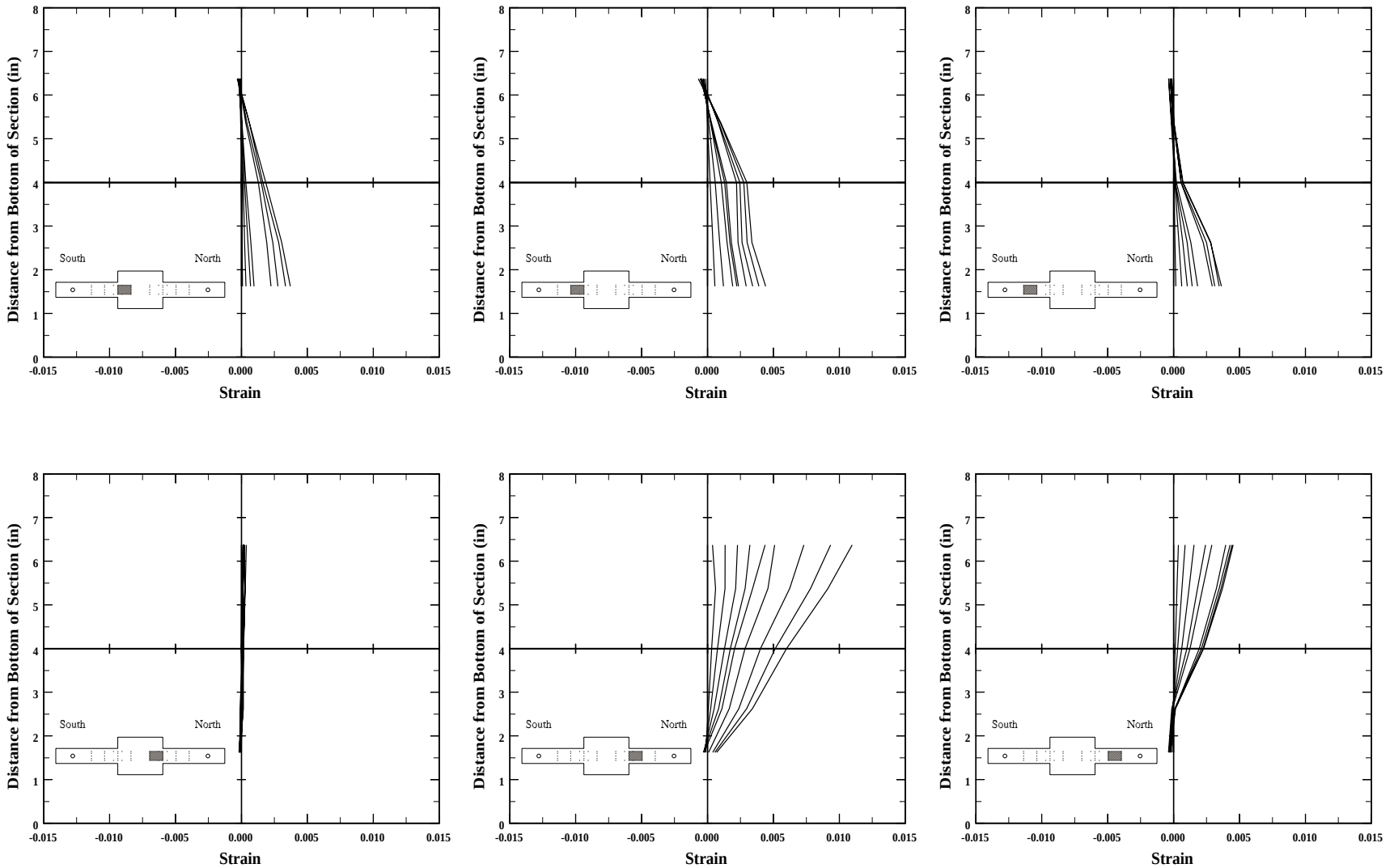

Figure 3.46. Variation of the mean strain distribution in the joint region during the first quarter cycle, for specimen C5-10.

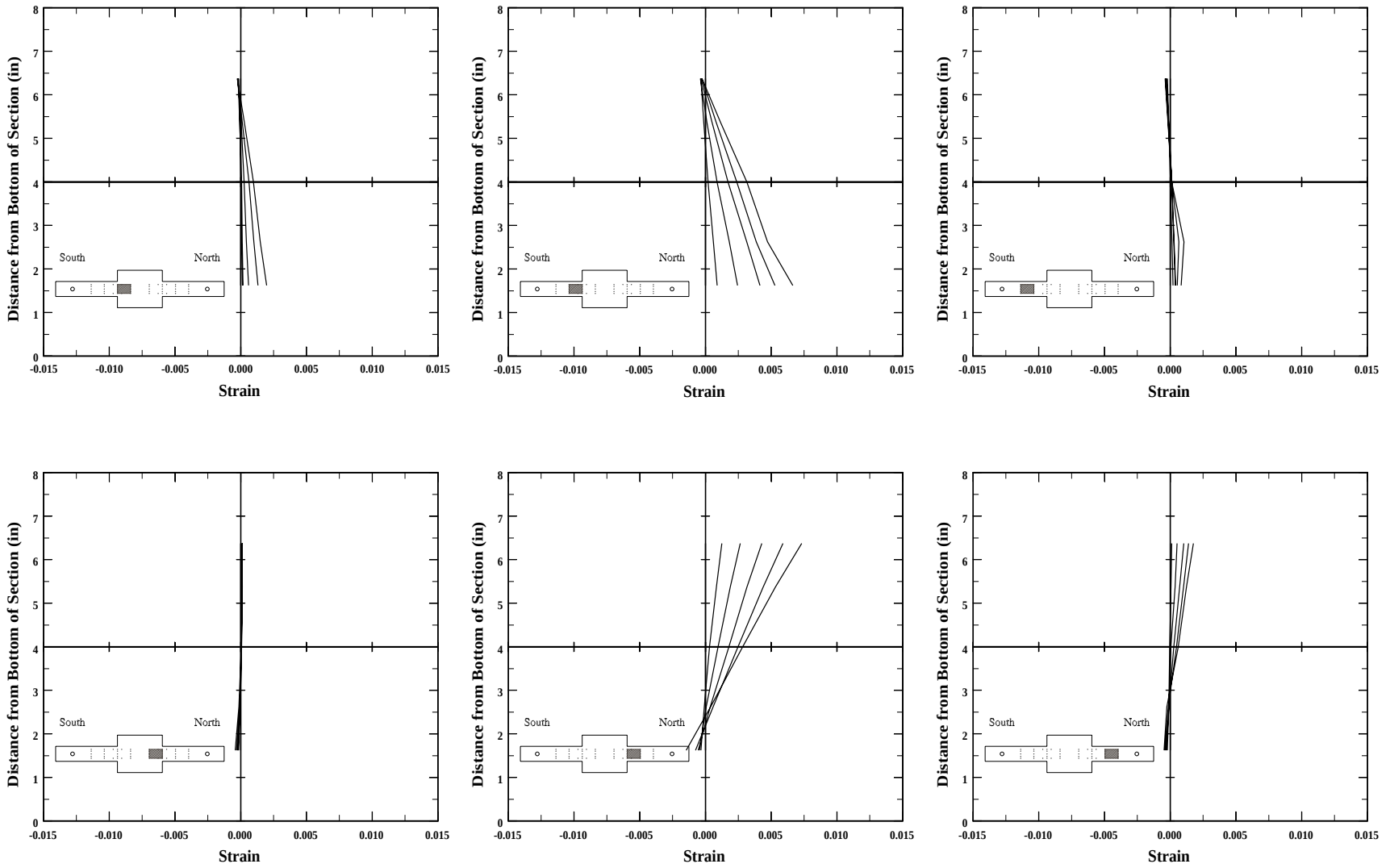

Figure 3.47. Variation of the mean strain distribution in the joint region during the first quarter cycle, for specimen C5-20.

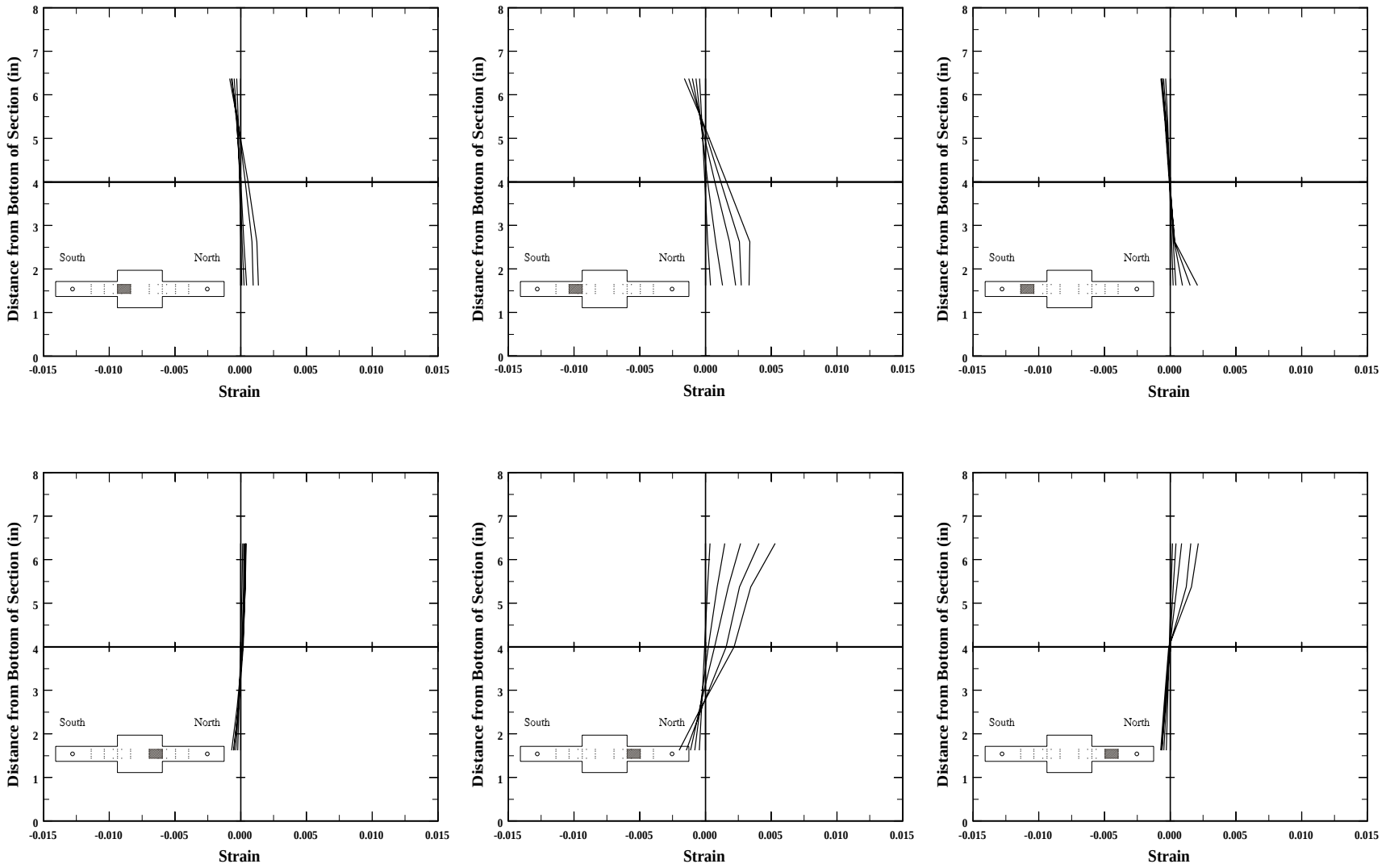

Figure 3.48. Variation of the mean strain distribution in the joint region during the first quarter cycle, for specimen C5-40.

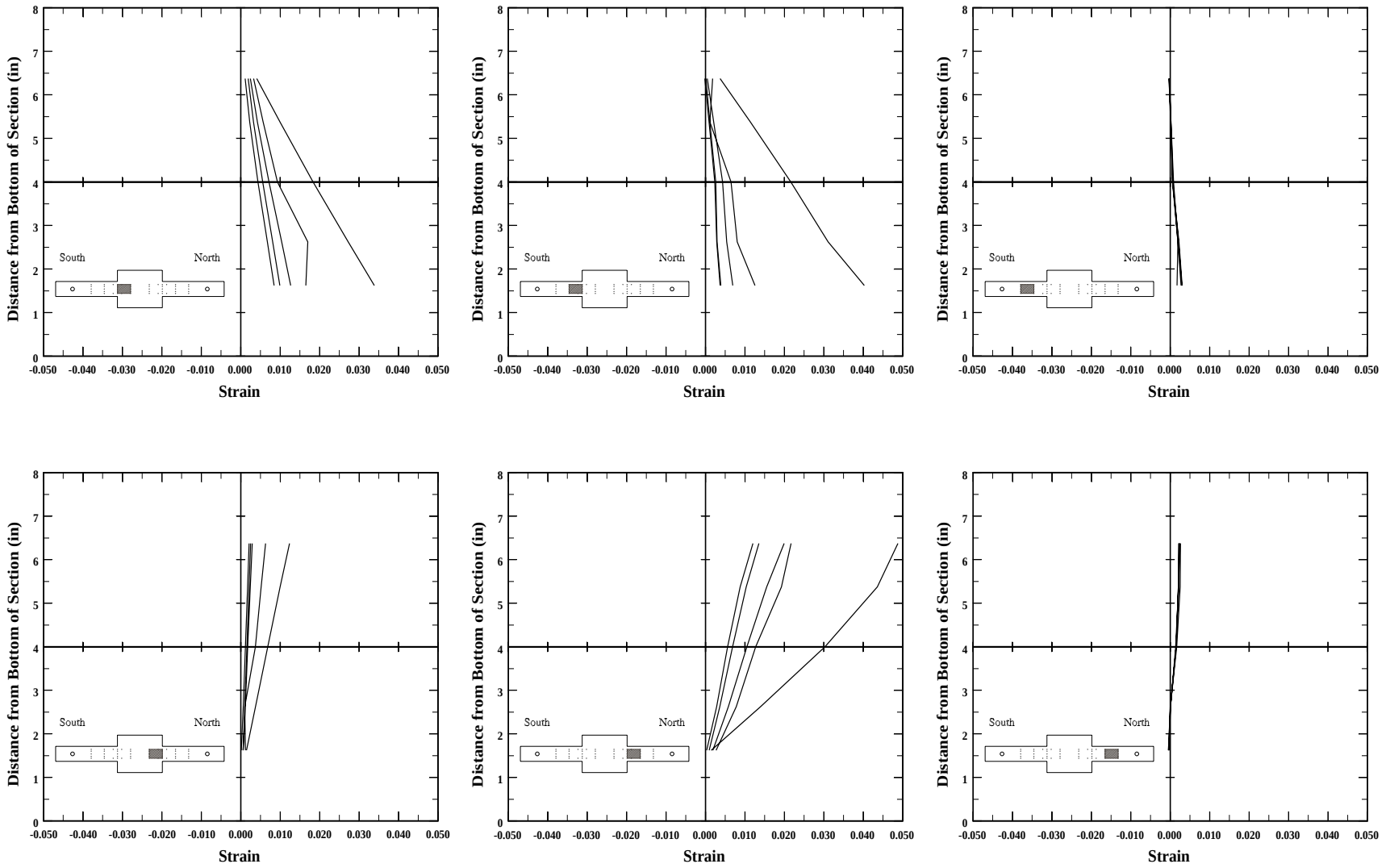

Figure 3.49. Variation of the mean strain distribution in the joint region at peak displacements for each cycle, specimen C10-00.

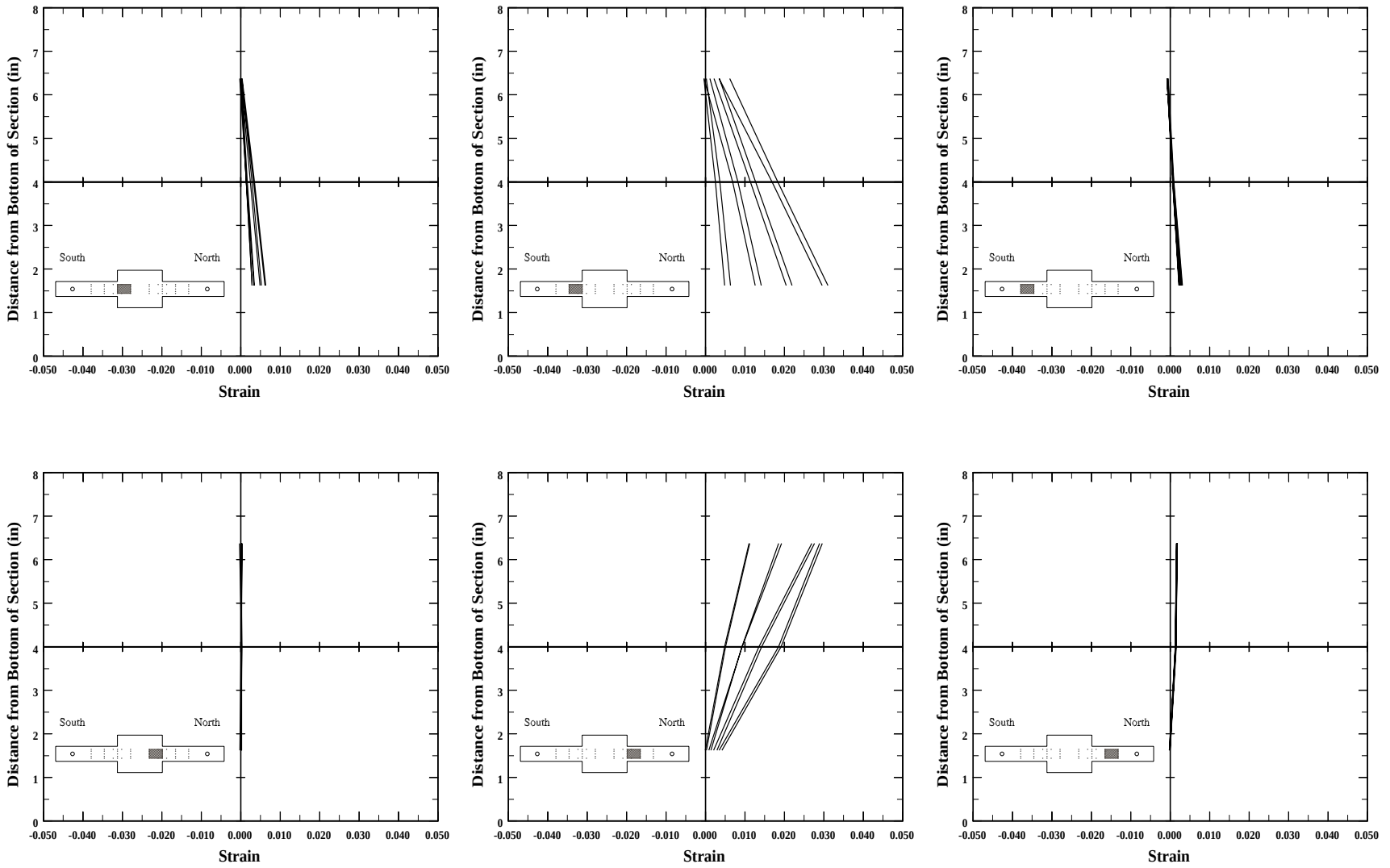

Figure 3.50. Variation of the mean strain distribution in the joint region at peak displacements for each cycle, specimen C10-05.

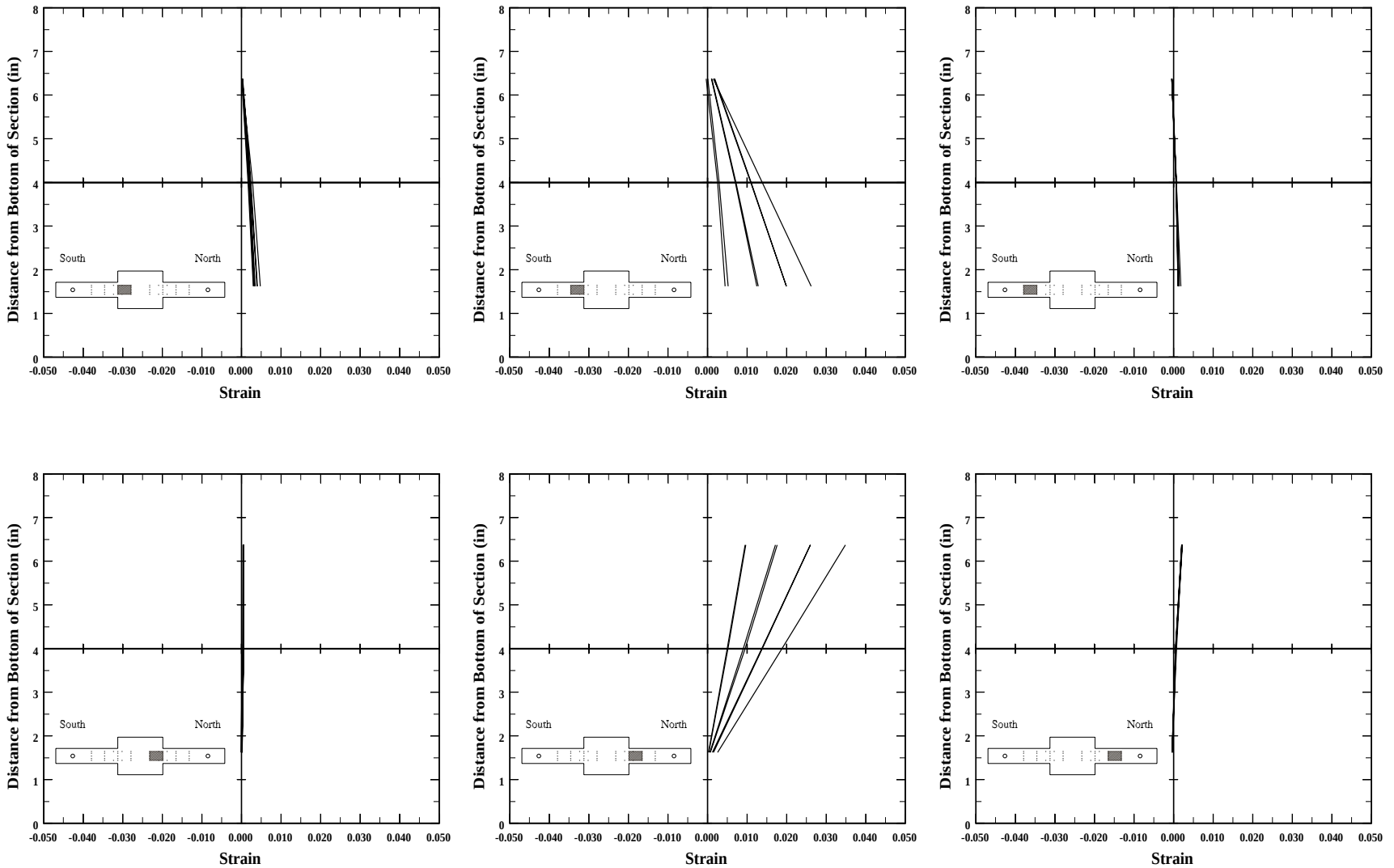

Figure 3.51. Variation of the mean strain distribution in the joint region at peak displacements for each cycle, specimen C10-10.

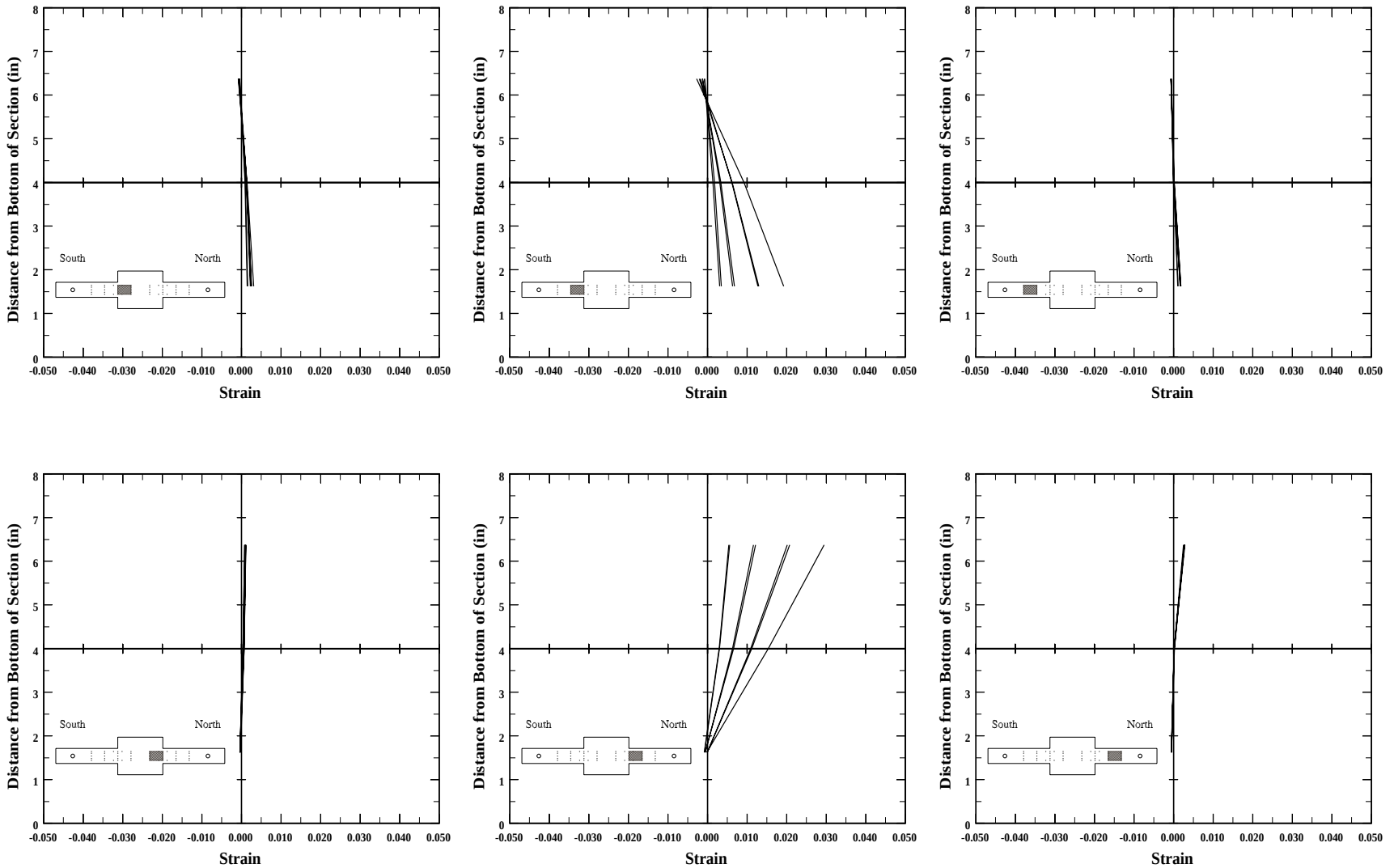

Figure 3.52. Variation of the mean strain distribution in the joint region at peak displacements for each cycle, specimen C10-20.

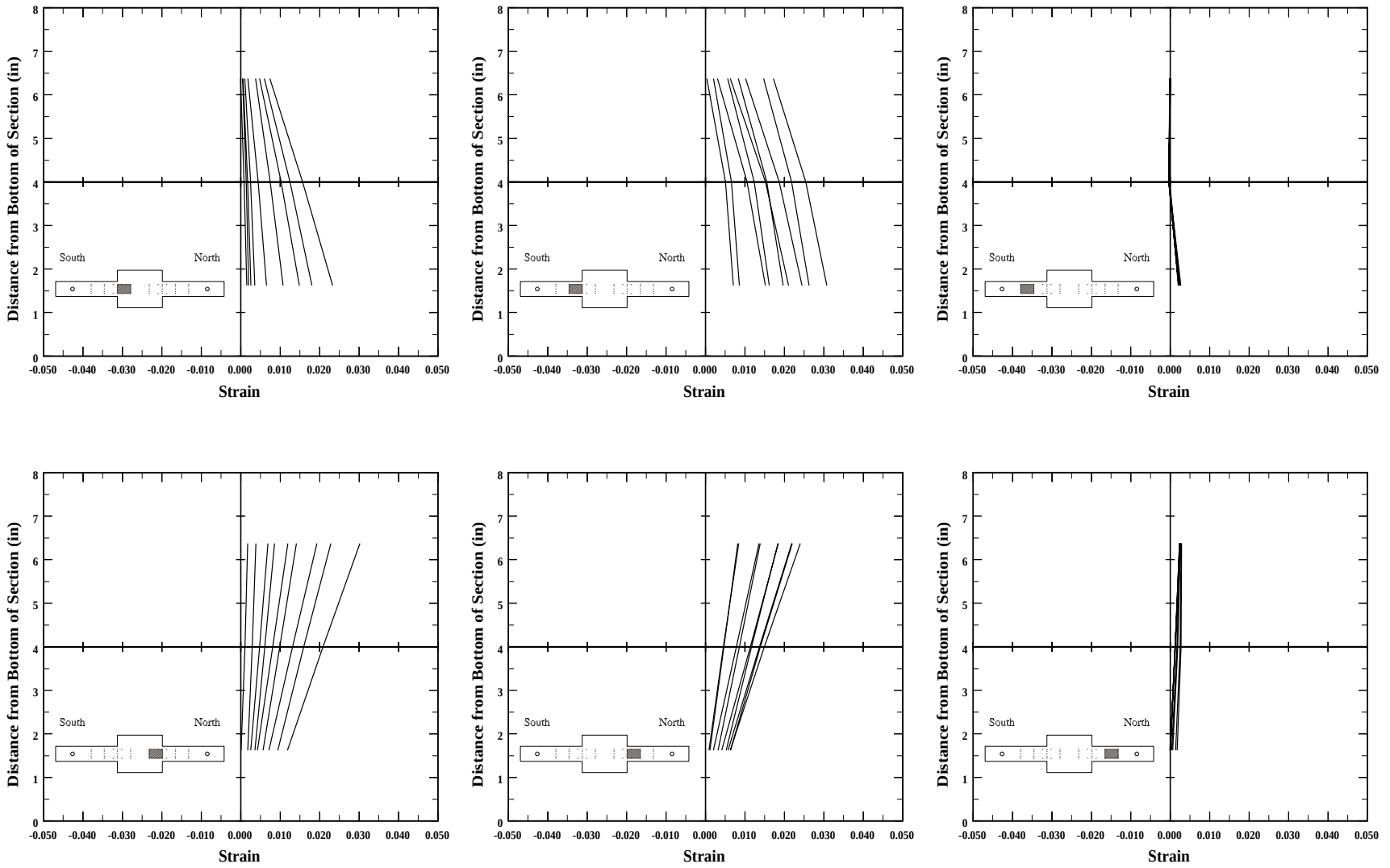

Figure 3.53. Variation of the mean strain distribution in the joint region at peak displacements for each cycle, specimen C5-00.

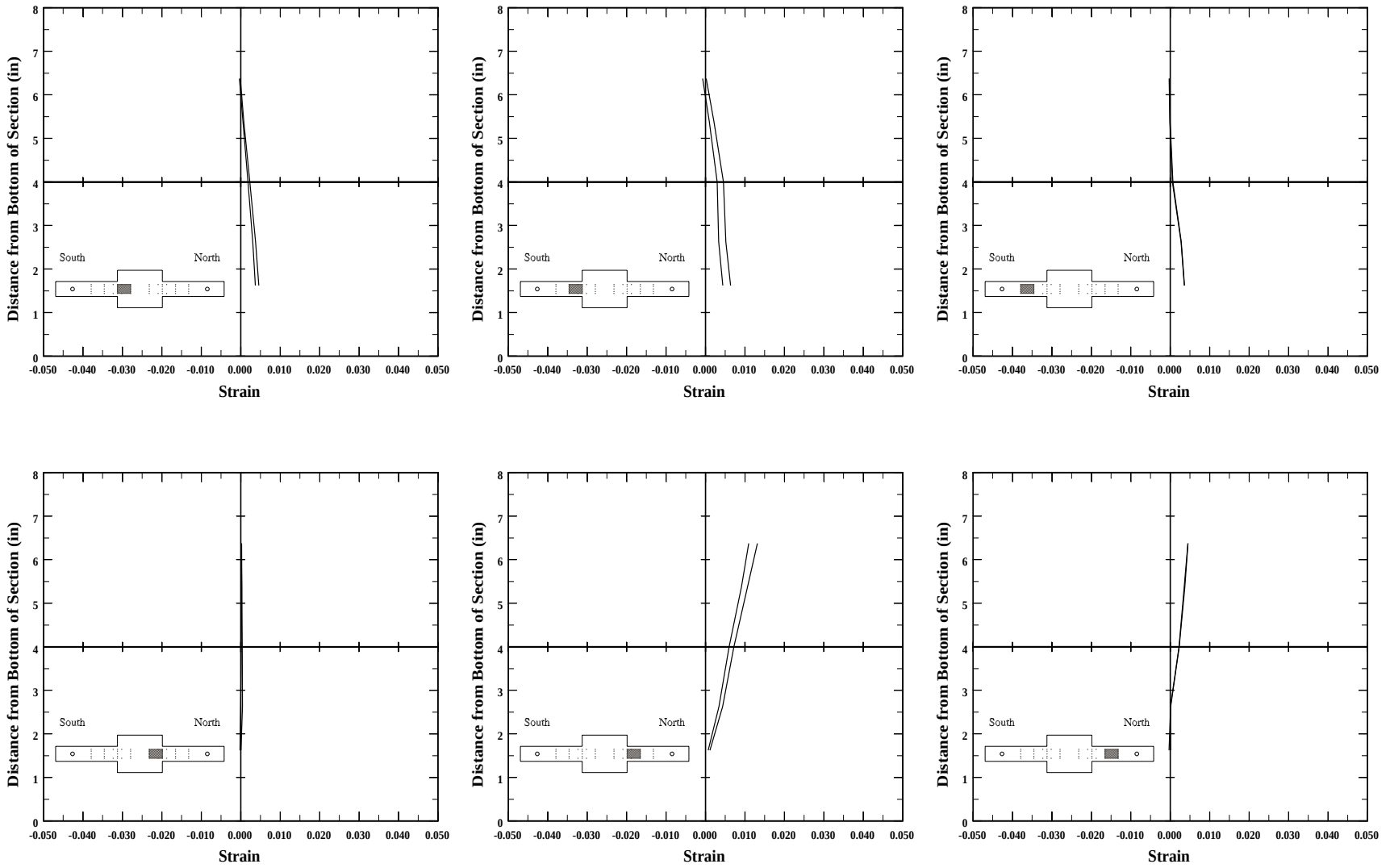

Figure 3.54. Variation of the mean strain distribution in the joint region at peak displacements for each cycle, specimen C5-10.

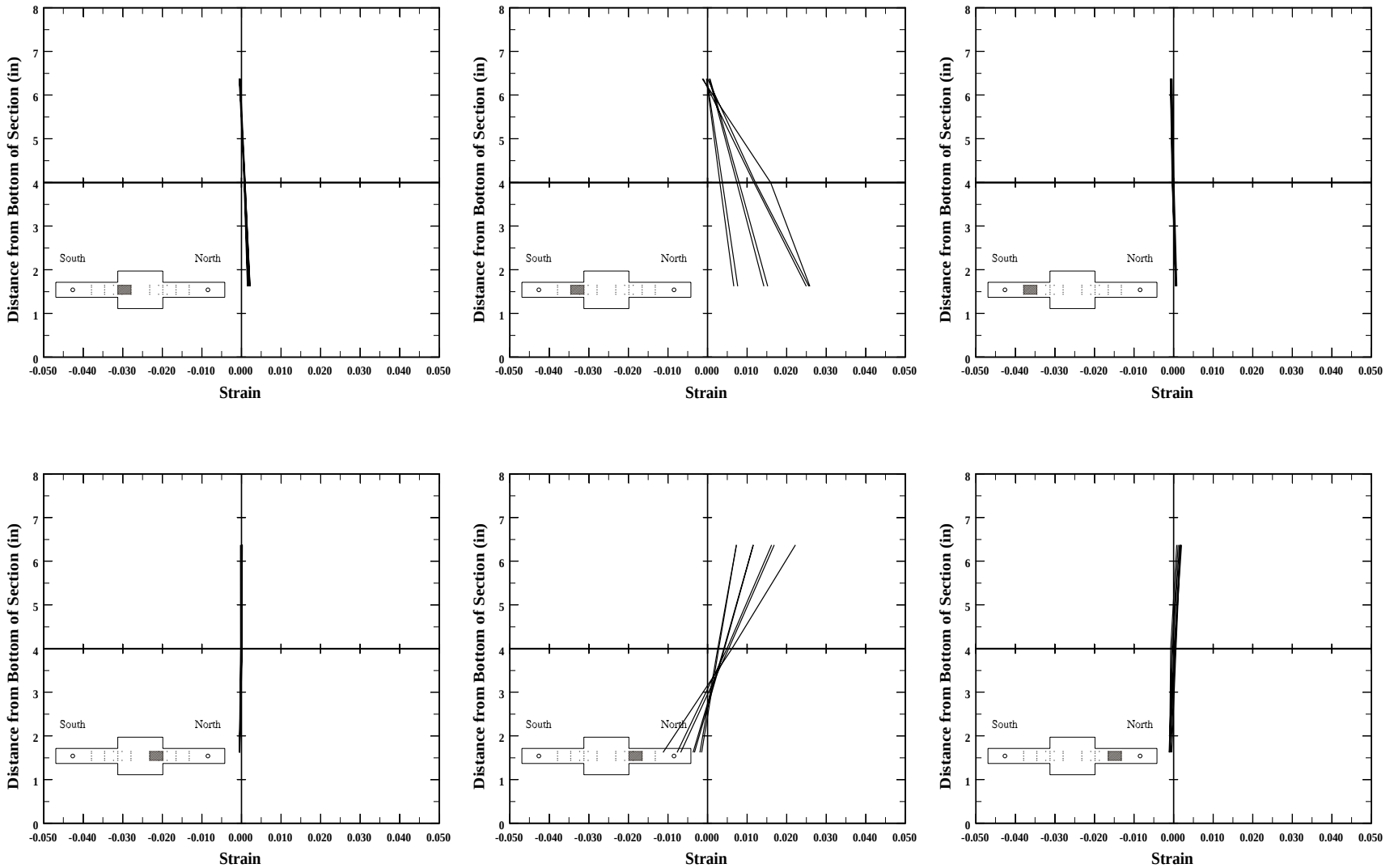

Figure 3.55. Variation of the mean strain distribution in the joint region at peak displacements for each cycle, specimen C5-20.

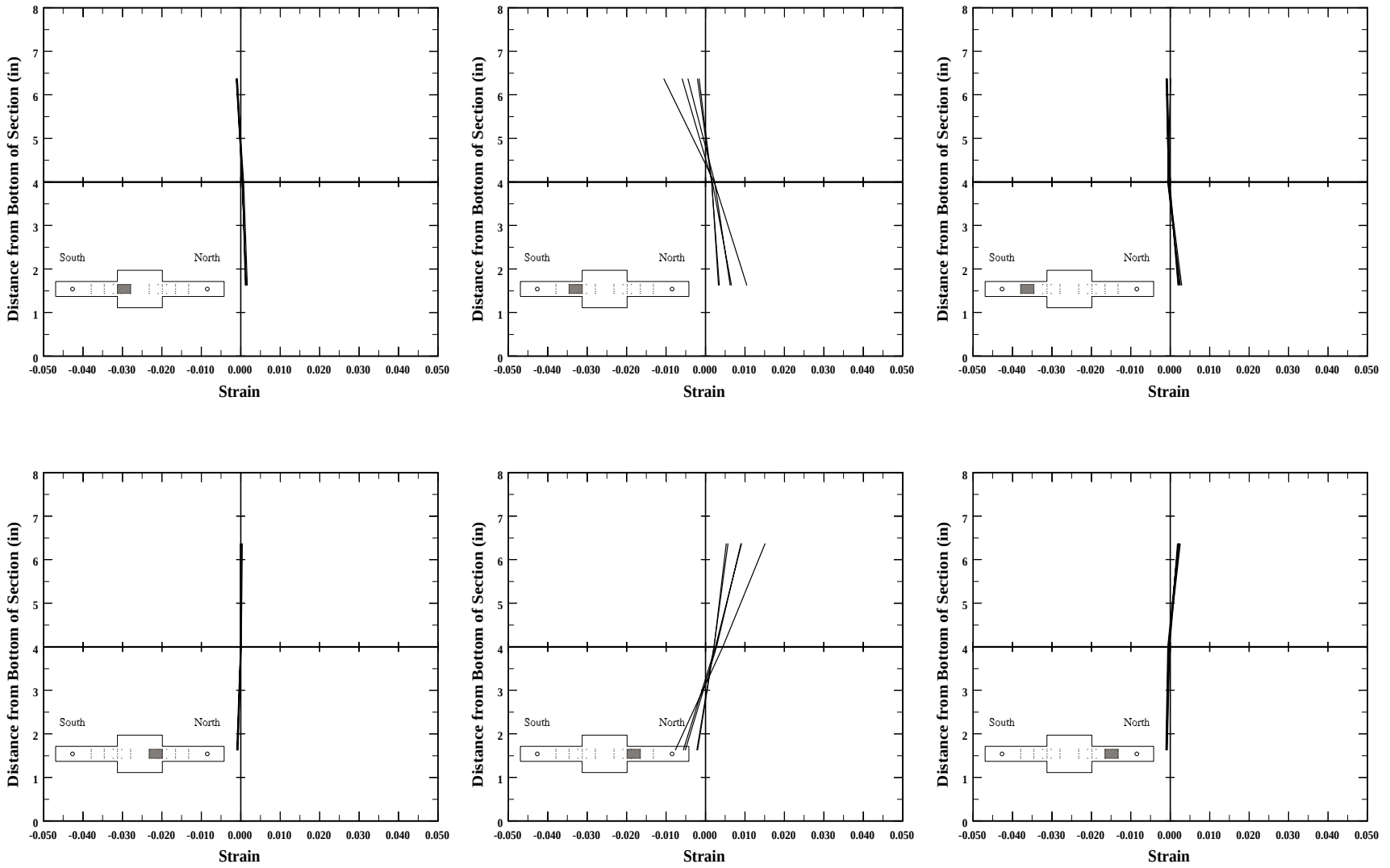

Figure 3.56. Variation of the mean strain distribution in the joint region at peak displacements for each cycle, specimen C5-40.

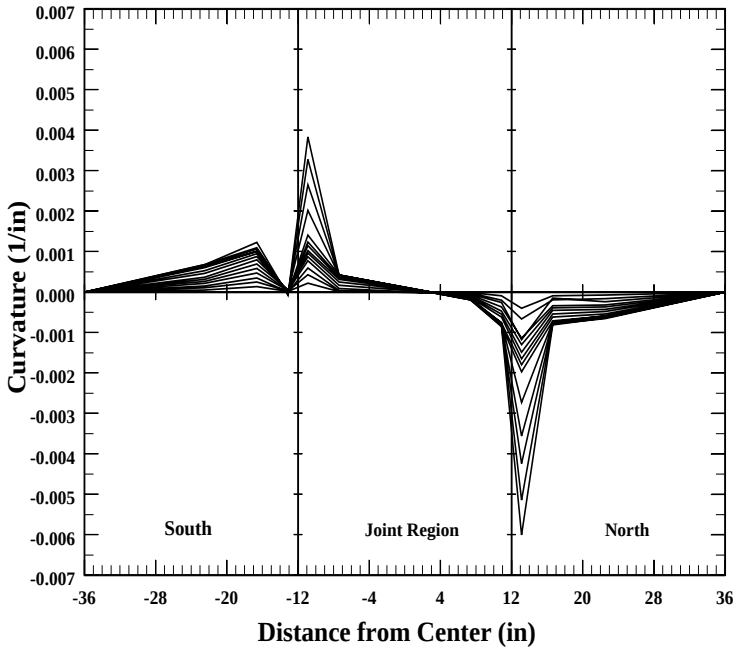

Figure 3.57. Mean curvature distribution throughout the specimen during the first quarter cycle, specimen C10-00.

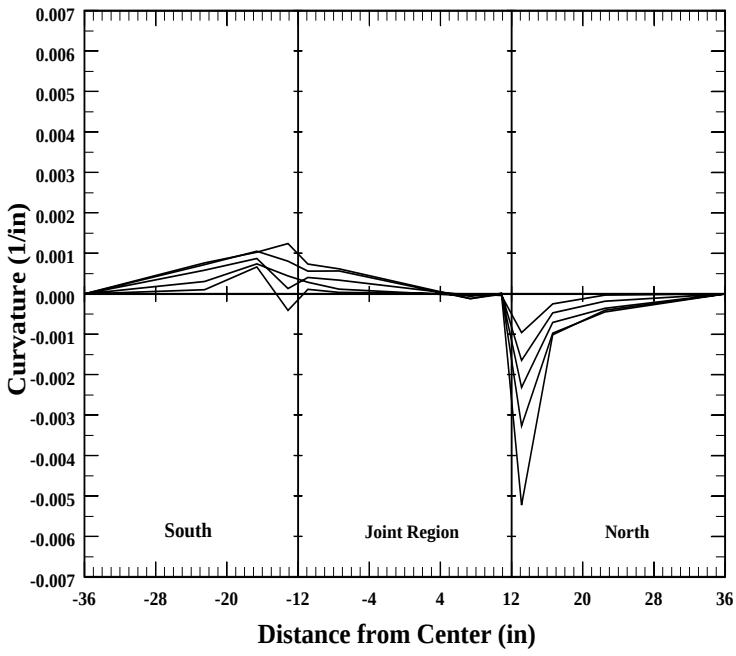

Figure 3.58. Mean curvature distribution throughout the specimen during the first quarter cycle, specimen C10-05.

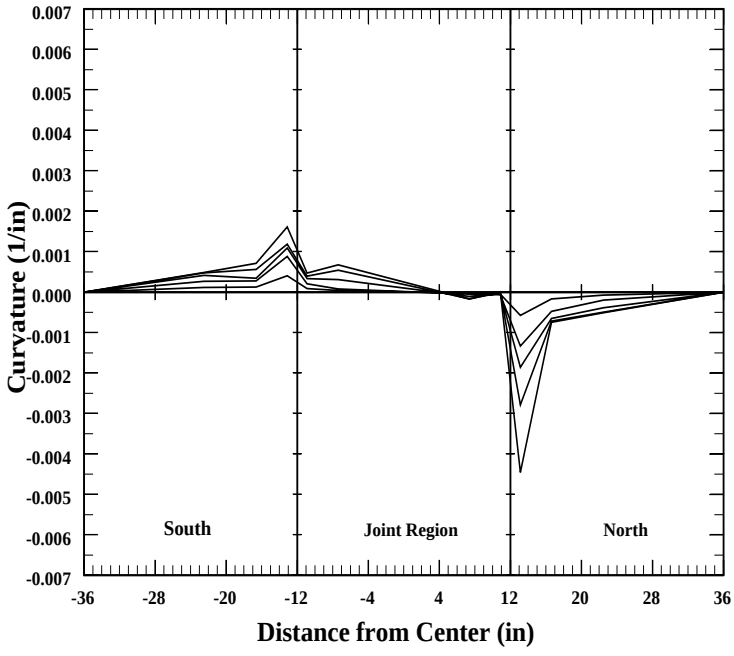

Figure 3.59. Mean curvature distribution throughout the specimen during the first quarter cycle, specimen C10-10.

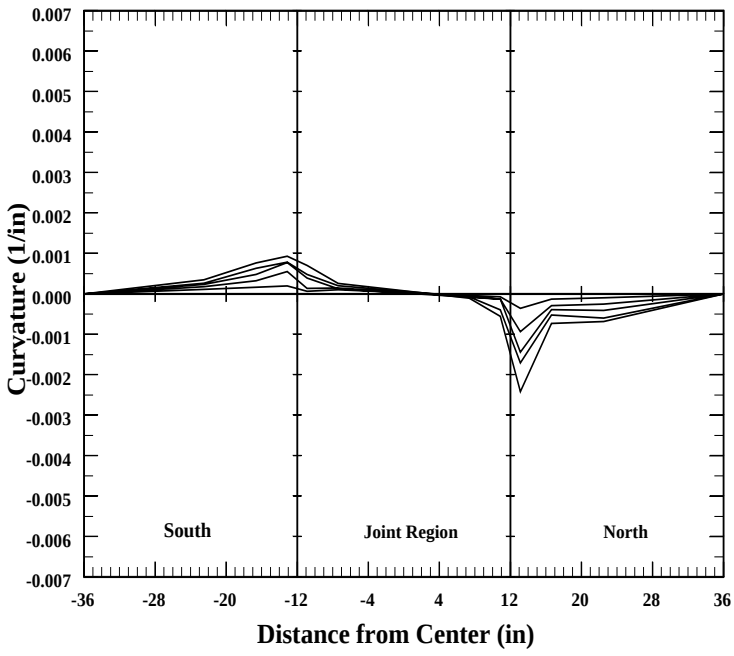

Figure 3.60. Mean curvature distribution throughout the specimen during the first quarter cycle, specimen C10-20.

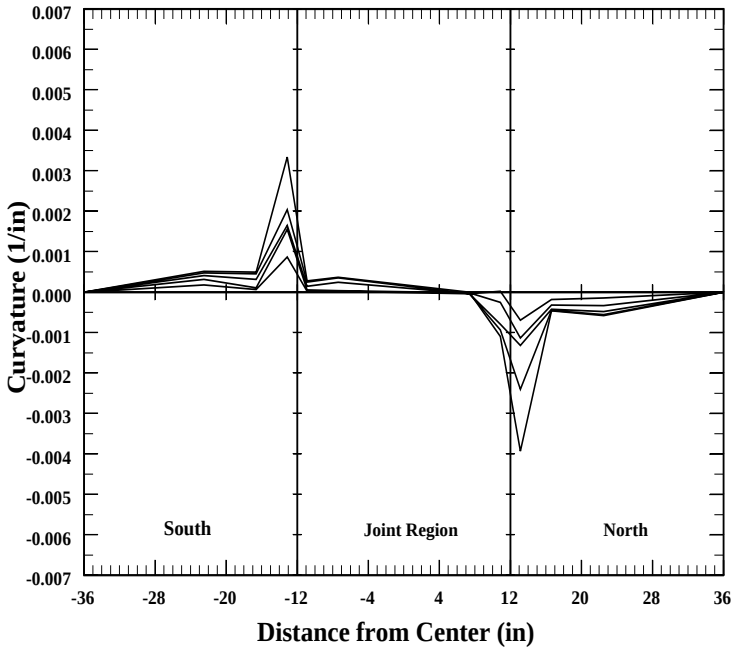

Figure 3.61. Mean curvature distribution throughout the specimen during the first quarter cycle, specimen C5-00.

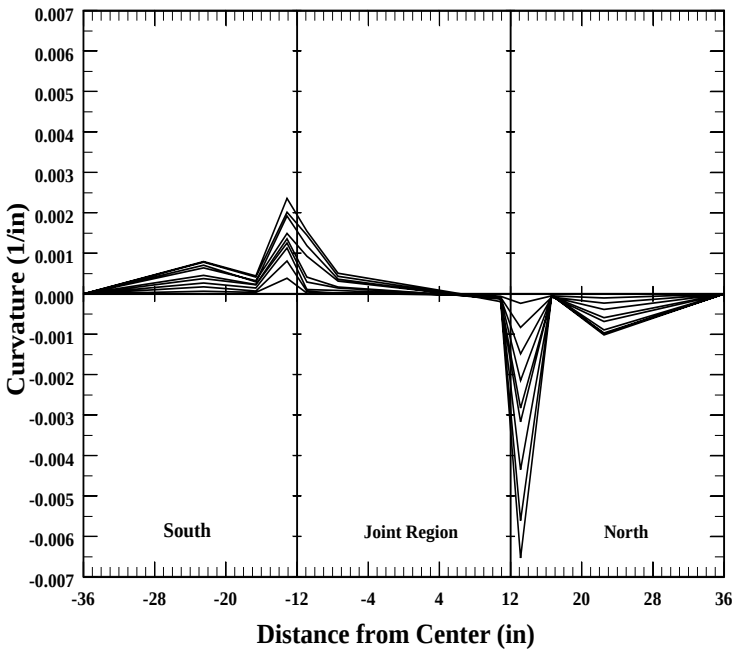

Figure 3.62. Mean curvature distribution throughout the specimen during the first quarter cycle, specimen C5-10.

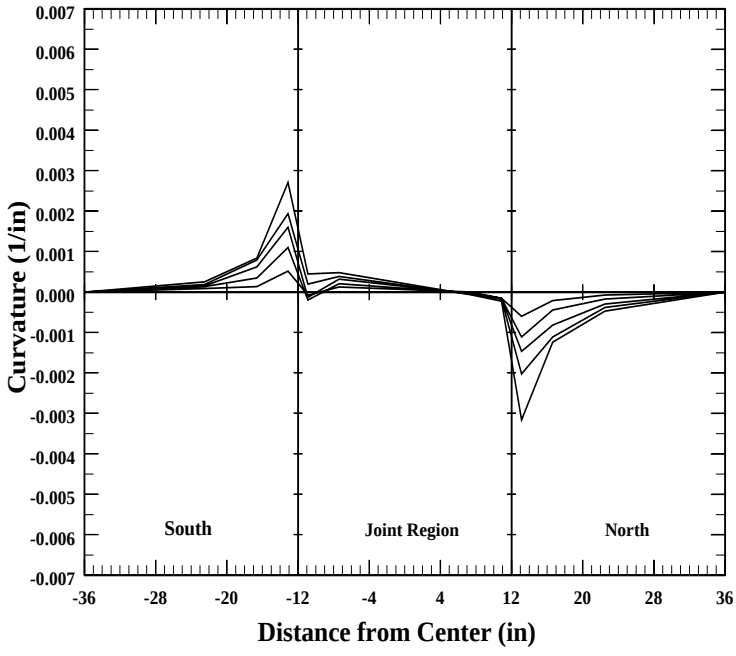

Figure 3.63. Mean curvature distribution throughout the specimen during the first quarter cycle, specimen C5-20.

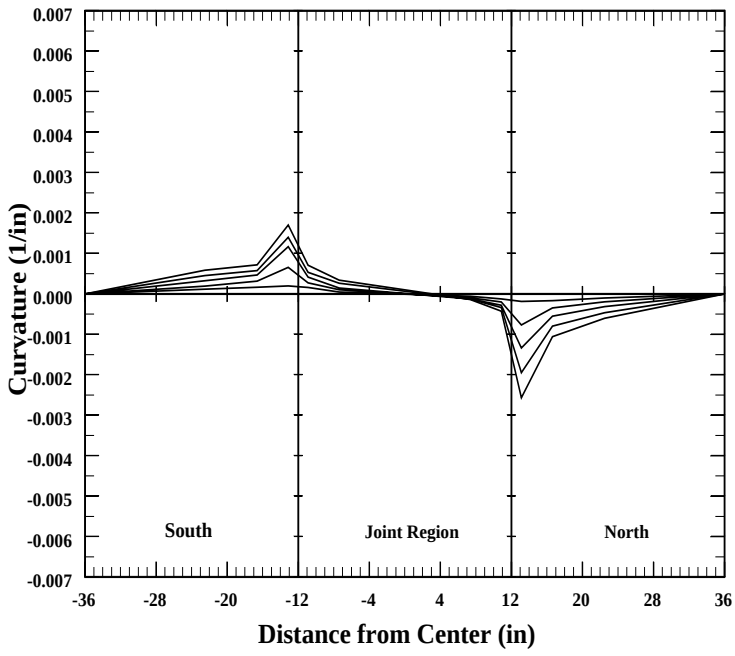

Figure 3.64. Mean curvature distribution throughout the specimen during the first quarter cycle, specimen C5-40.

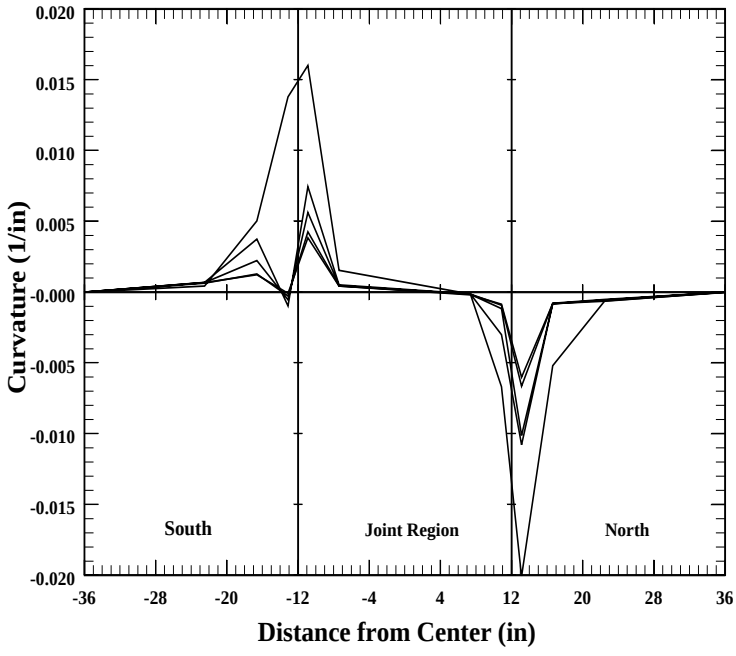

Figure 3.65. Mean curvature distribution throughout the specimen at peak displacements for each cycle, specimen C10-00.

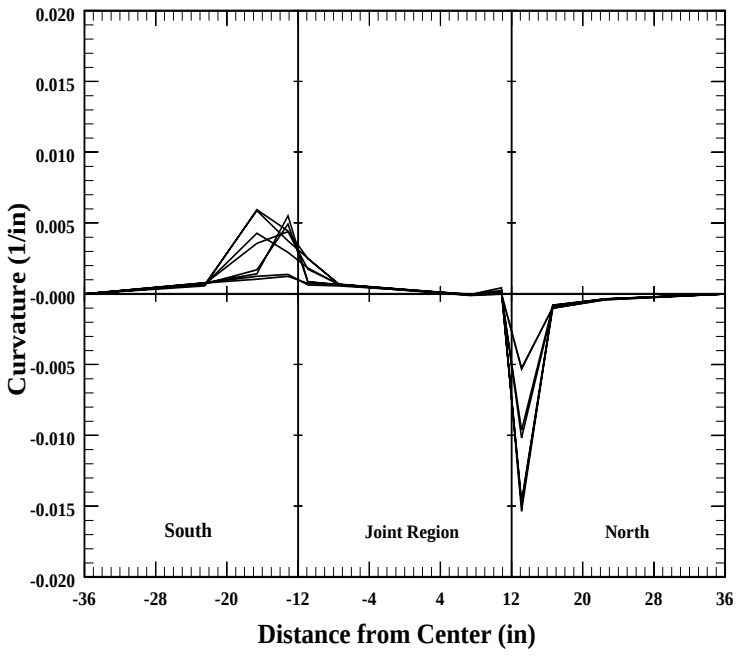

Figure 3.66. Mean curvature distribution throughout the specimen at peak displacements for each cycle, specimen C10-05.

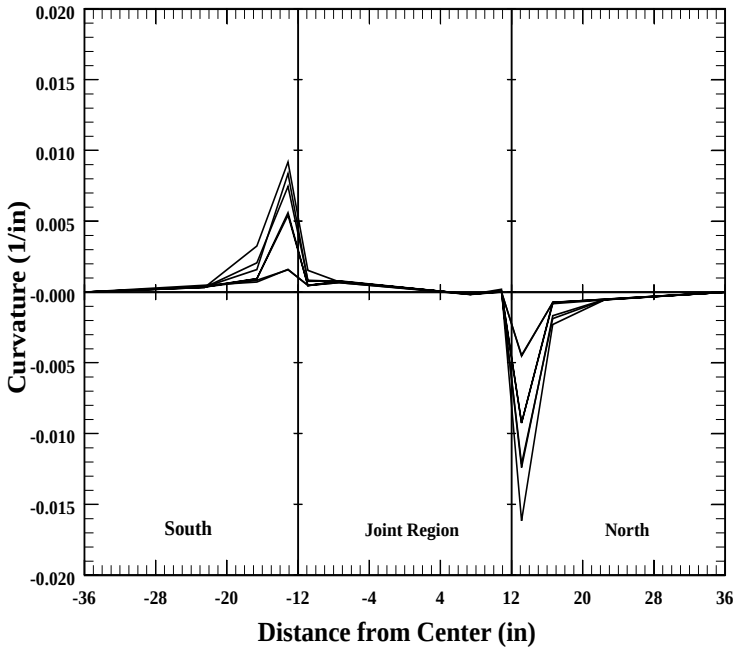

Figure 3.67. Mean curvature distribution throughout the specimen at peak displacements for each cycle, specimen C10-10.

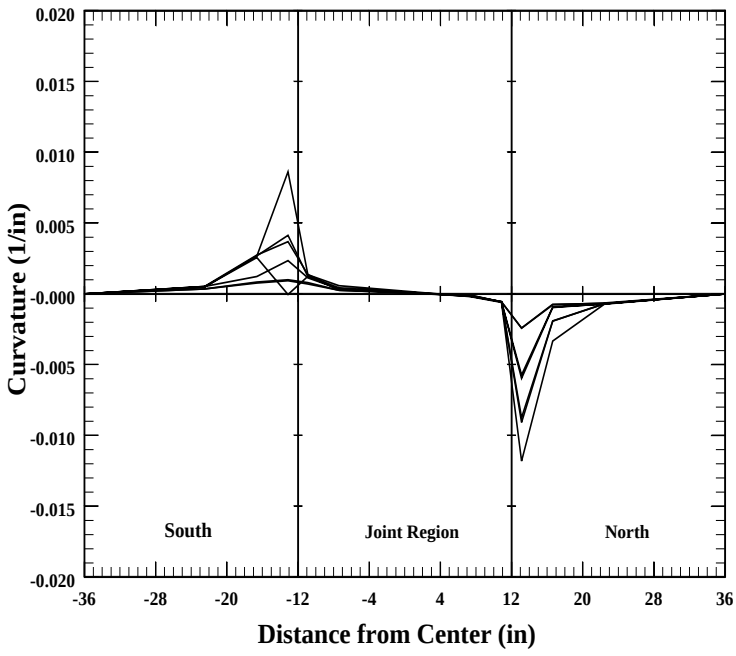

Figure 3.68. Mean curvature distribution throughout the specimen at peak displacements for each cycle, specimen C10-20.

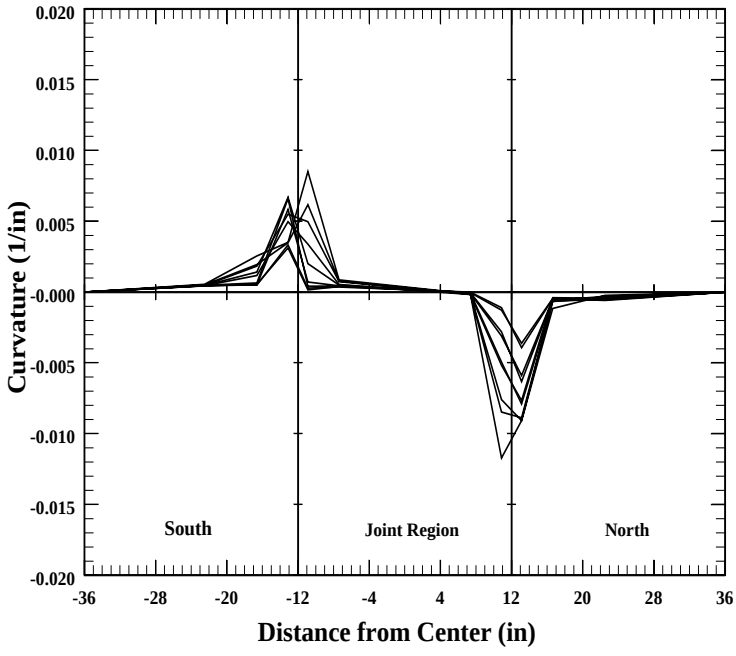

Figure 3.69. Mean curvature distribution throughout the specimen at peak displacements for each cycle, specimen C5-00.

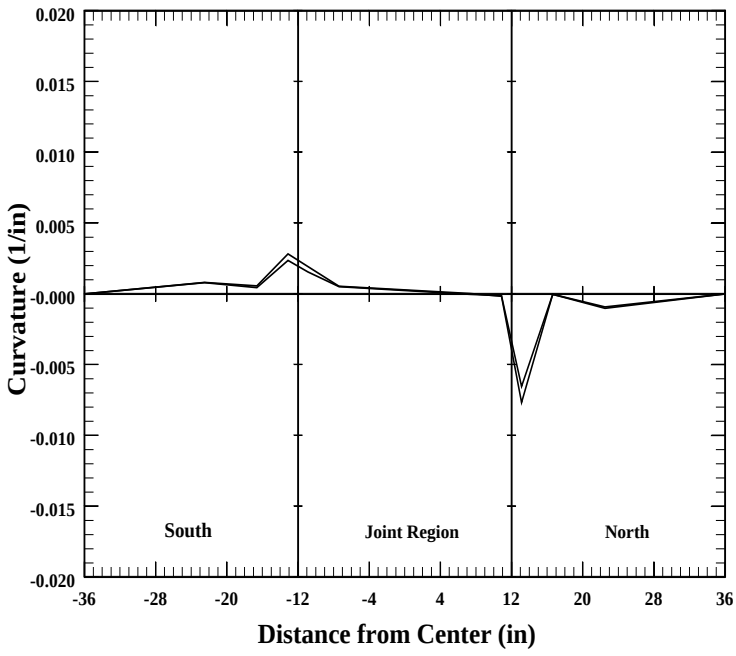

Figure 3.70. Mean curvature distribution throughout the specimen at peak displacements for each cycle, specimen C5-10.

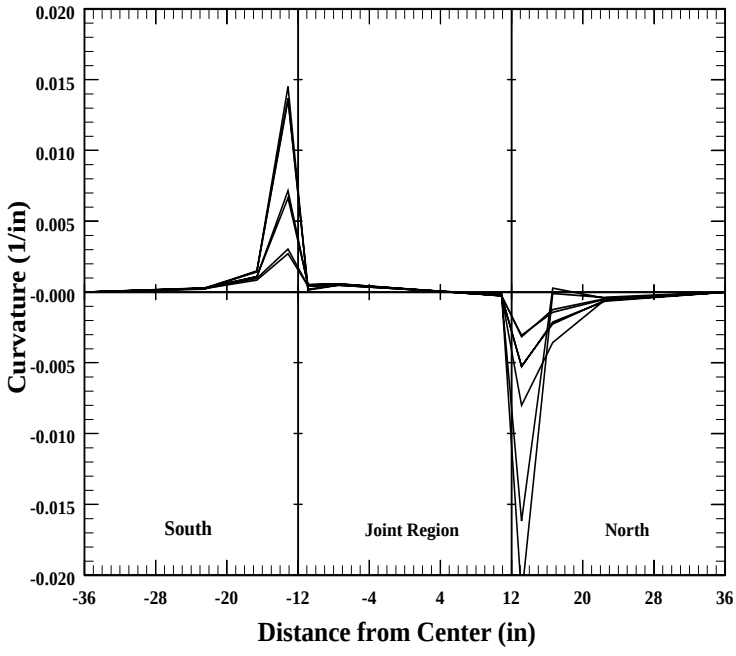

Figure 3.71. Mean curvature distribution throughout the specimen at peak displacements for each cycle, specimen C5-20.

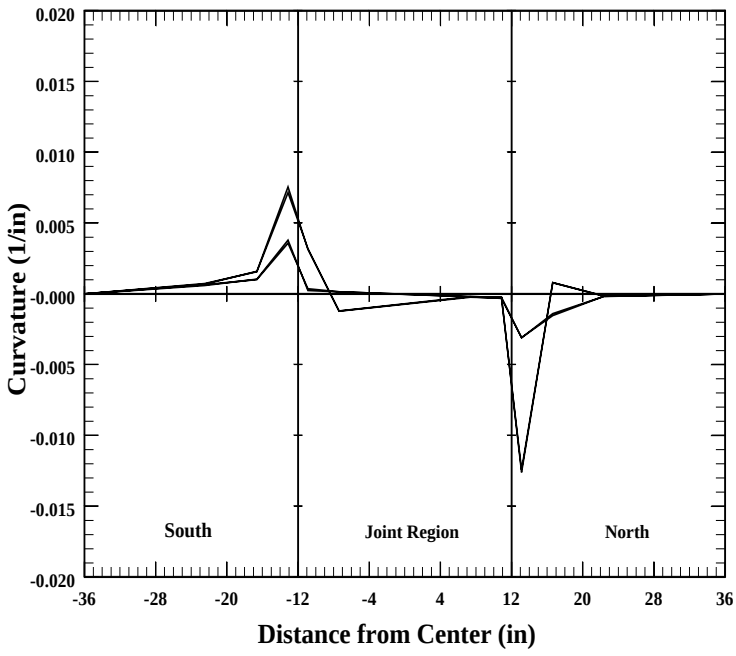

Figure 3.72. Mean curvature distribution throughout the specimen at peak displacements for each cycle, specimen C5-40.

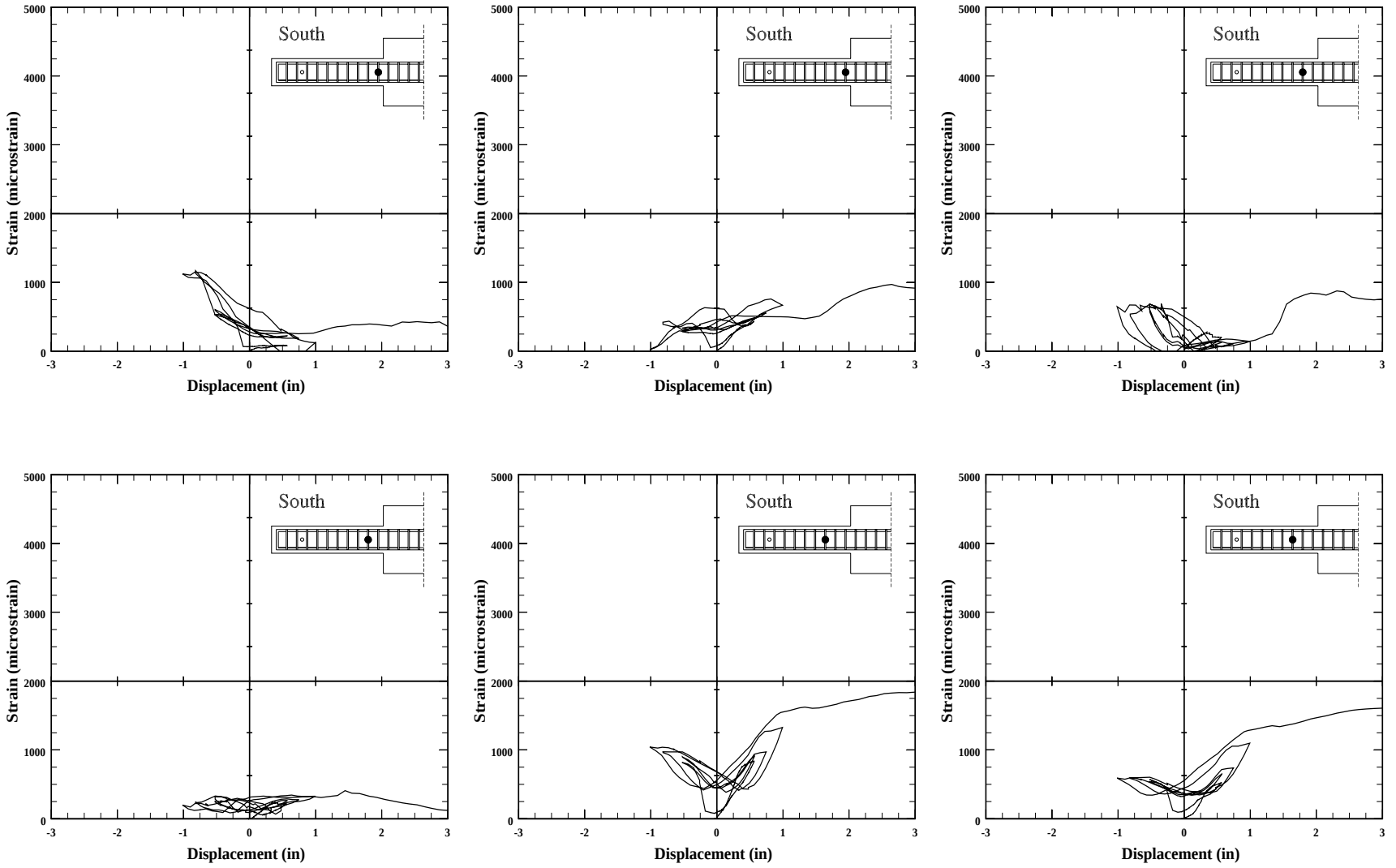

Figure 3.73. Measured stirrup strain vs load-point displacement for specimen C10-00, south element.

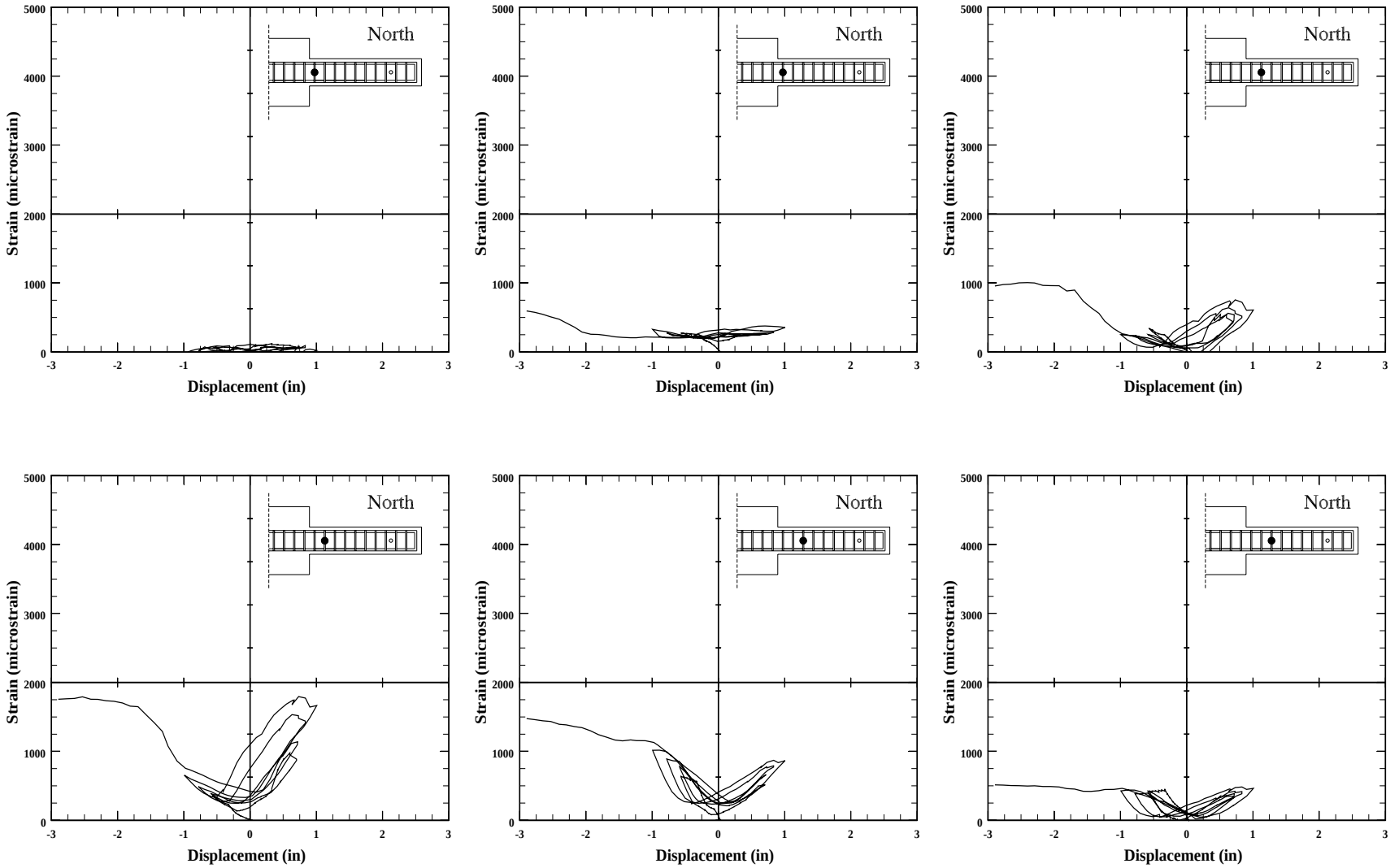

Figure 3.74. Measured stirrup strain vs load-point displacement for specimen C10-00, north element.

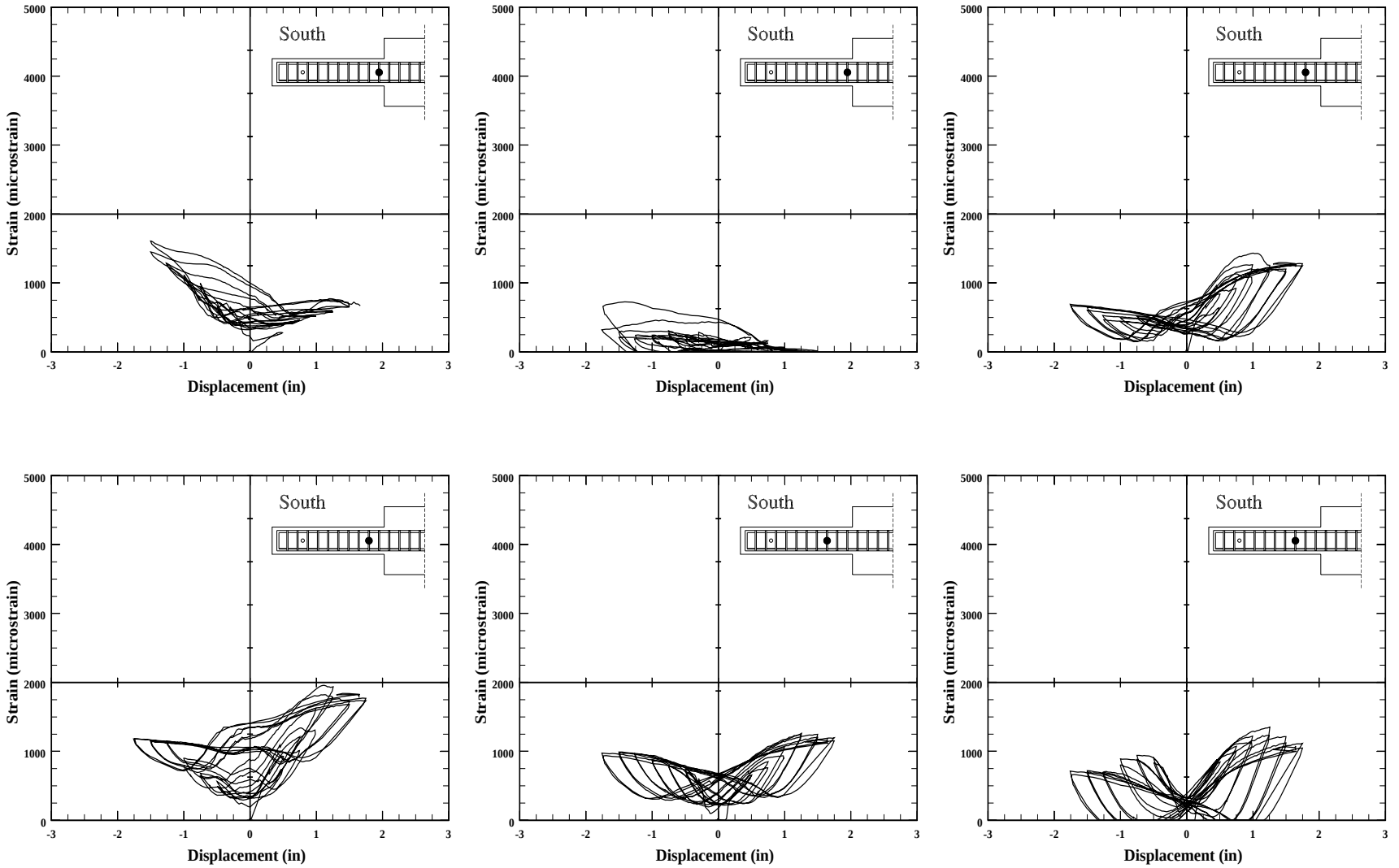

Figure 3.75. Measured stirrup strain vs load-point displacement for specimen C10-05, south element.

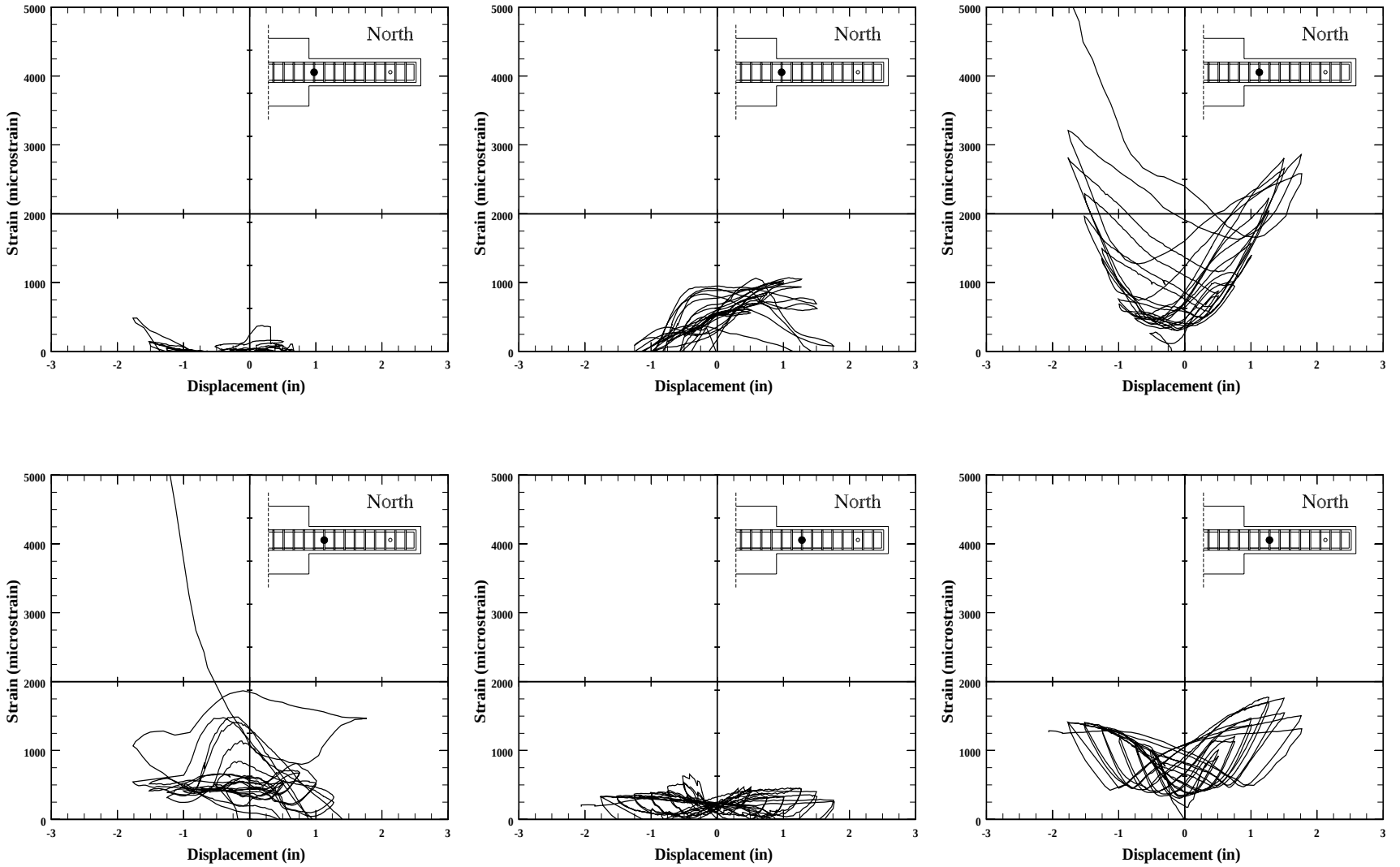

Figure 3.76. Measured stirrup strain vs load-point displacement for specimen C10-05, north element.

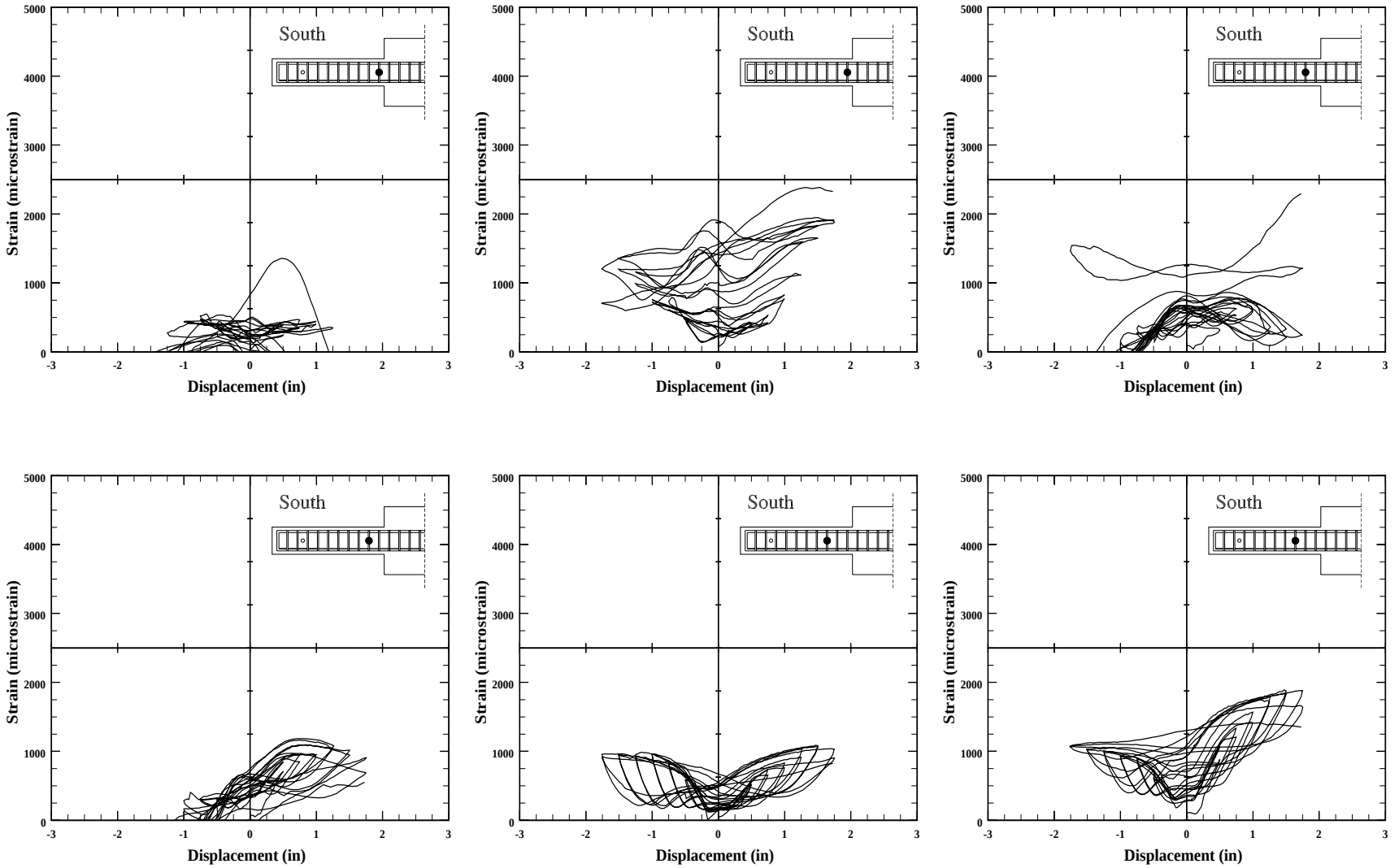

Figure 3.77. Measured stirrup strain vs load-point displacement for specimen C10-10, south element.

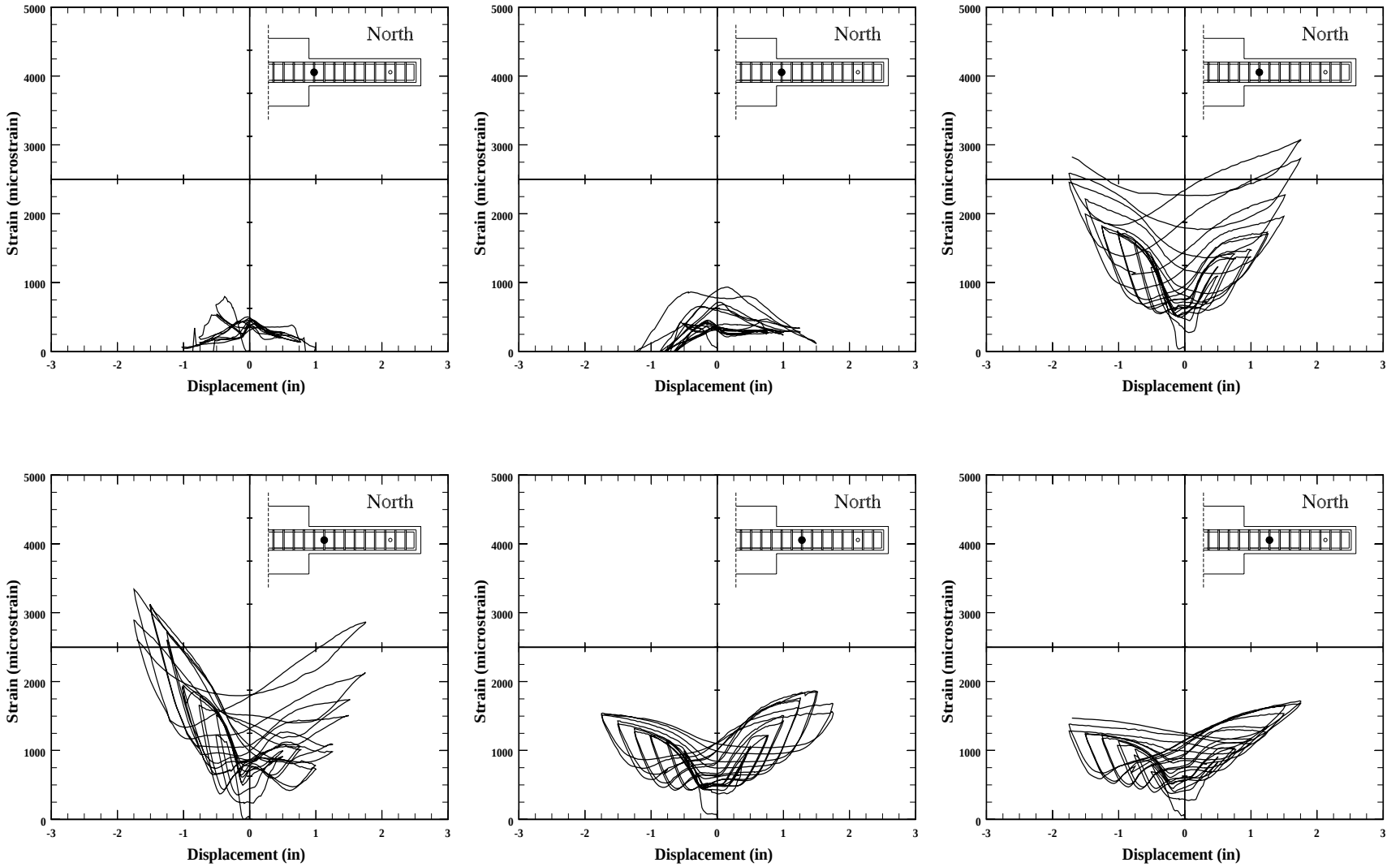

Figure 3.78. Measured stirrup strain vs load-point displacement for specimen C10-10, north element.

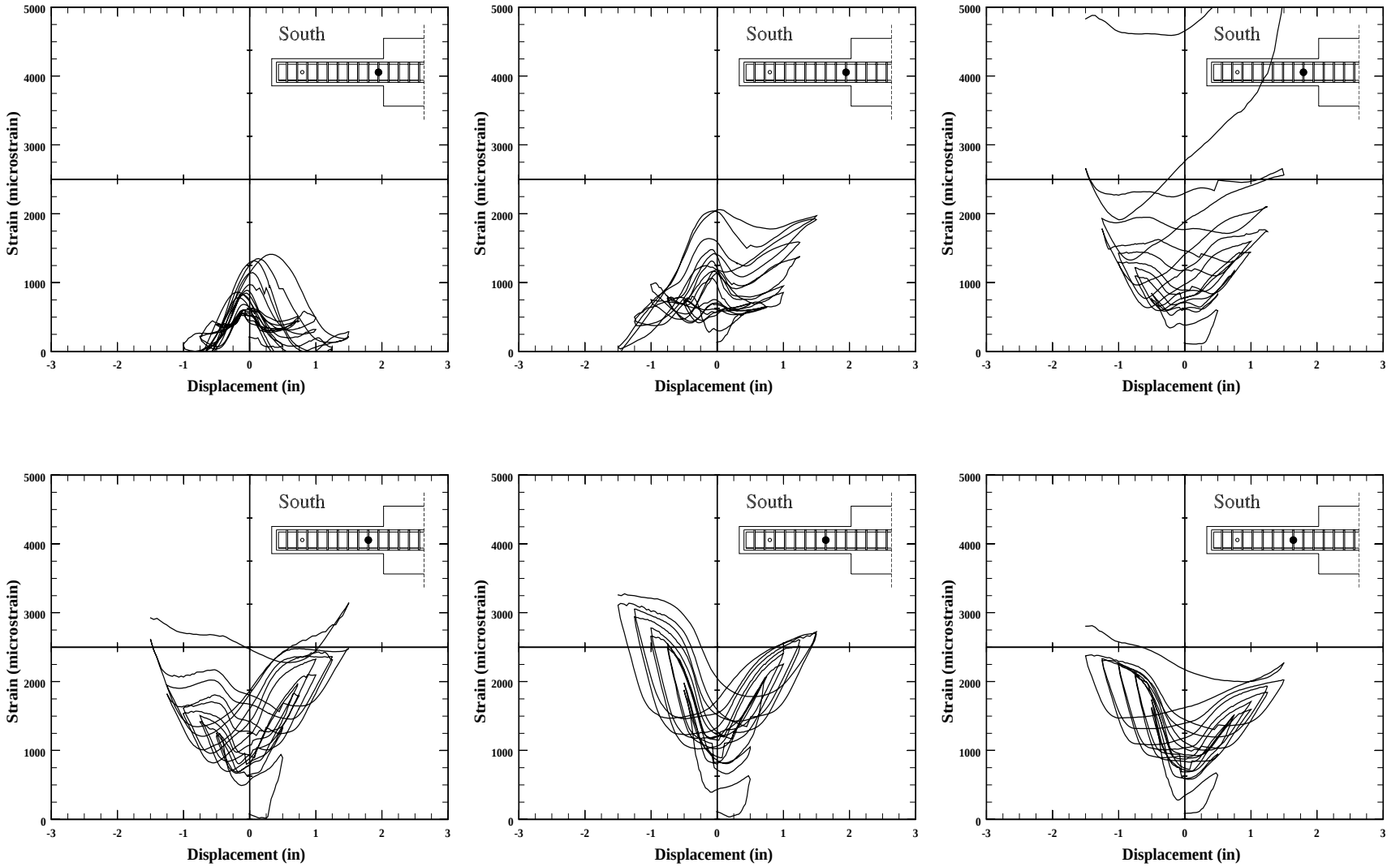

Figure 3.79. Measured stirrup strain vs load-point displacement for specimen C10-20, south element.

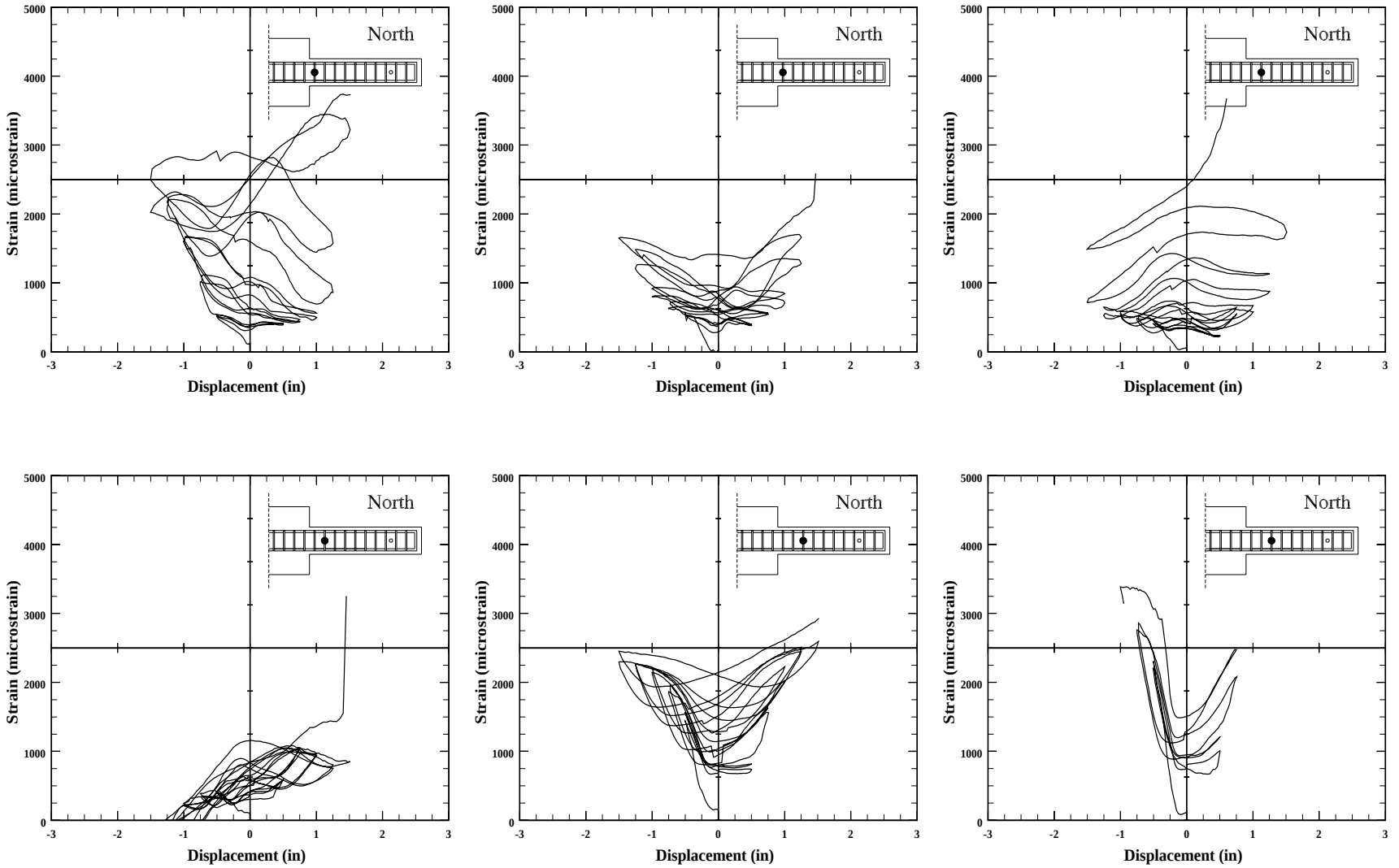

Figure 3.80. Measured stirrup strain vs load-point displacement for specimen C10-20, north element.

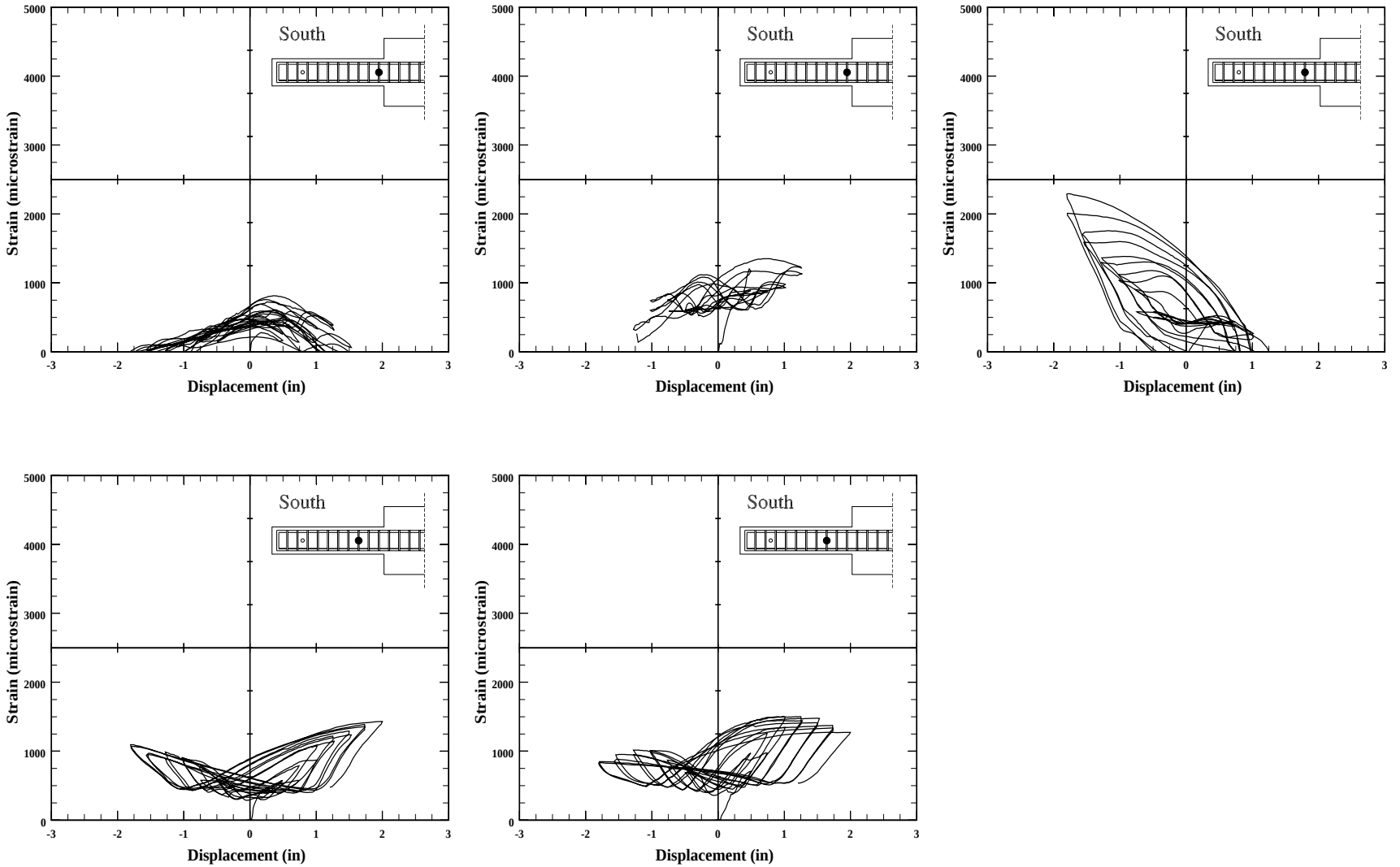

Figure 3.81. Measured stirrup strain vs load-point displacement for specimen C5-00, south element.

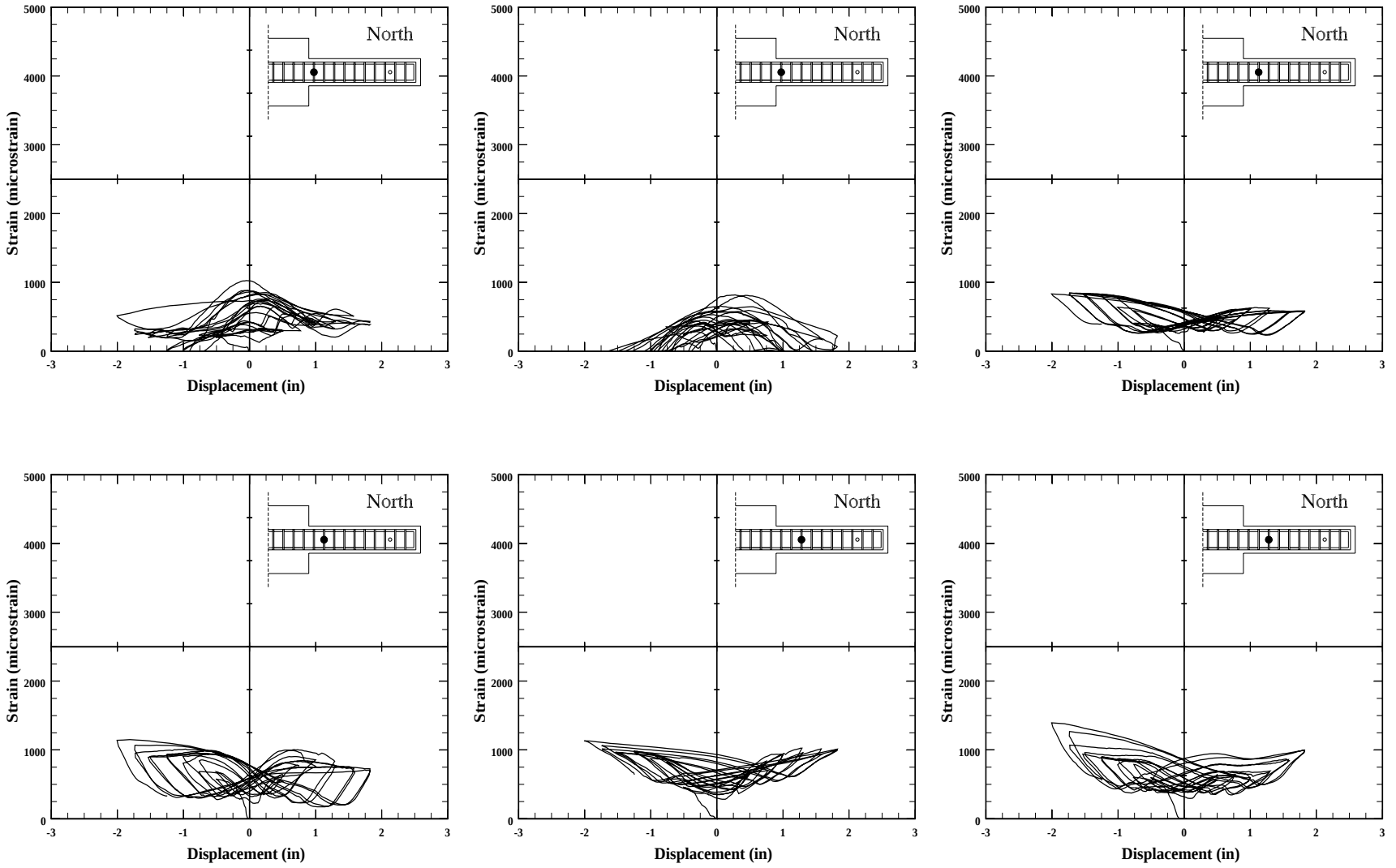

Figure 3.82. Measured stirrup strain vs load-point displacement for specimen C5-00, south element.

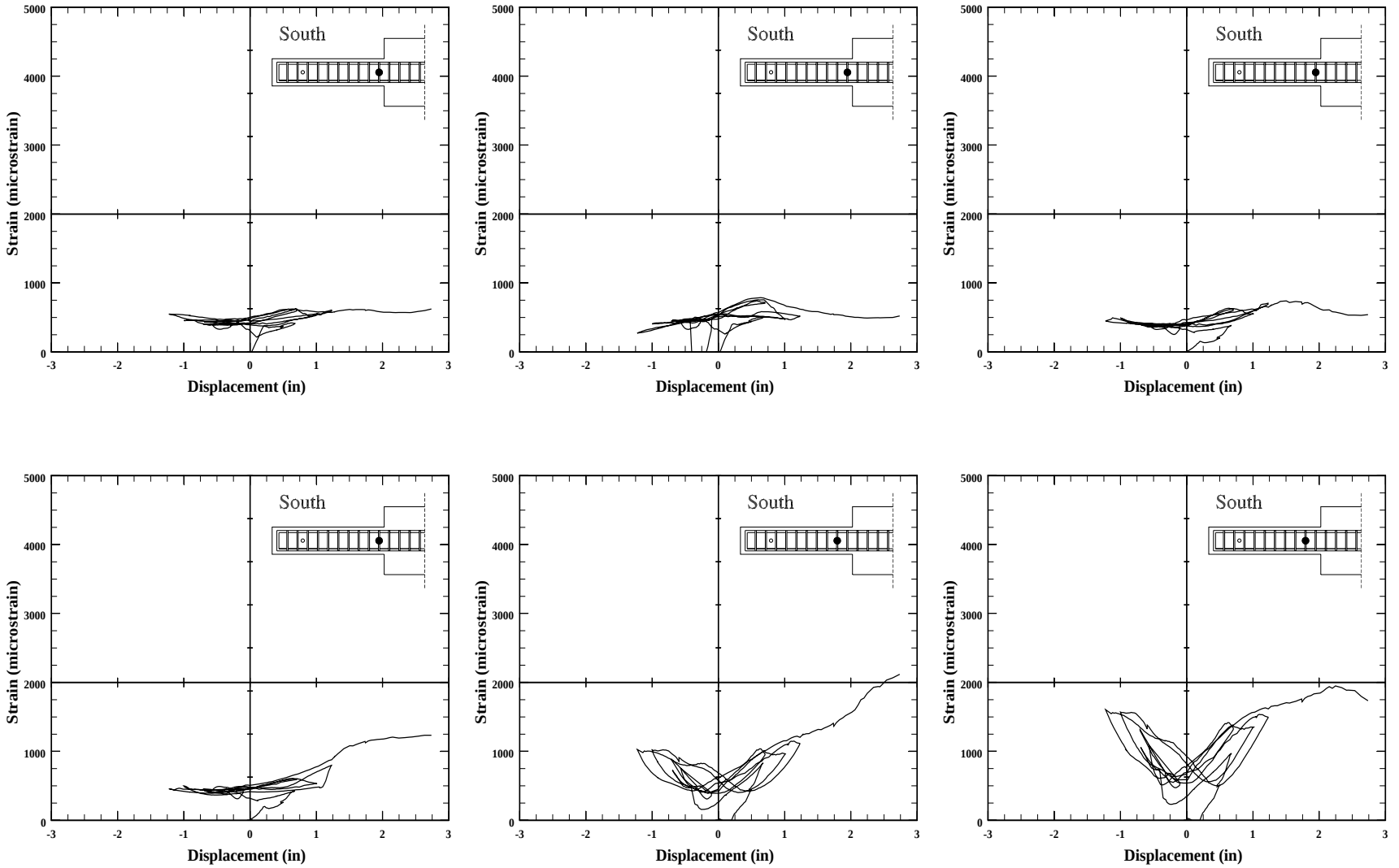

Figure 3.83. Measured stirrup strain vs load-point displacement for specimen C5-10, south element.

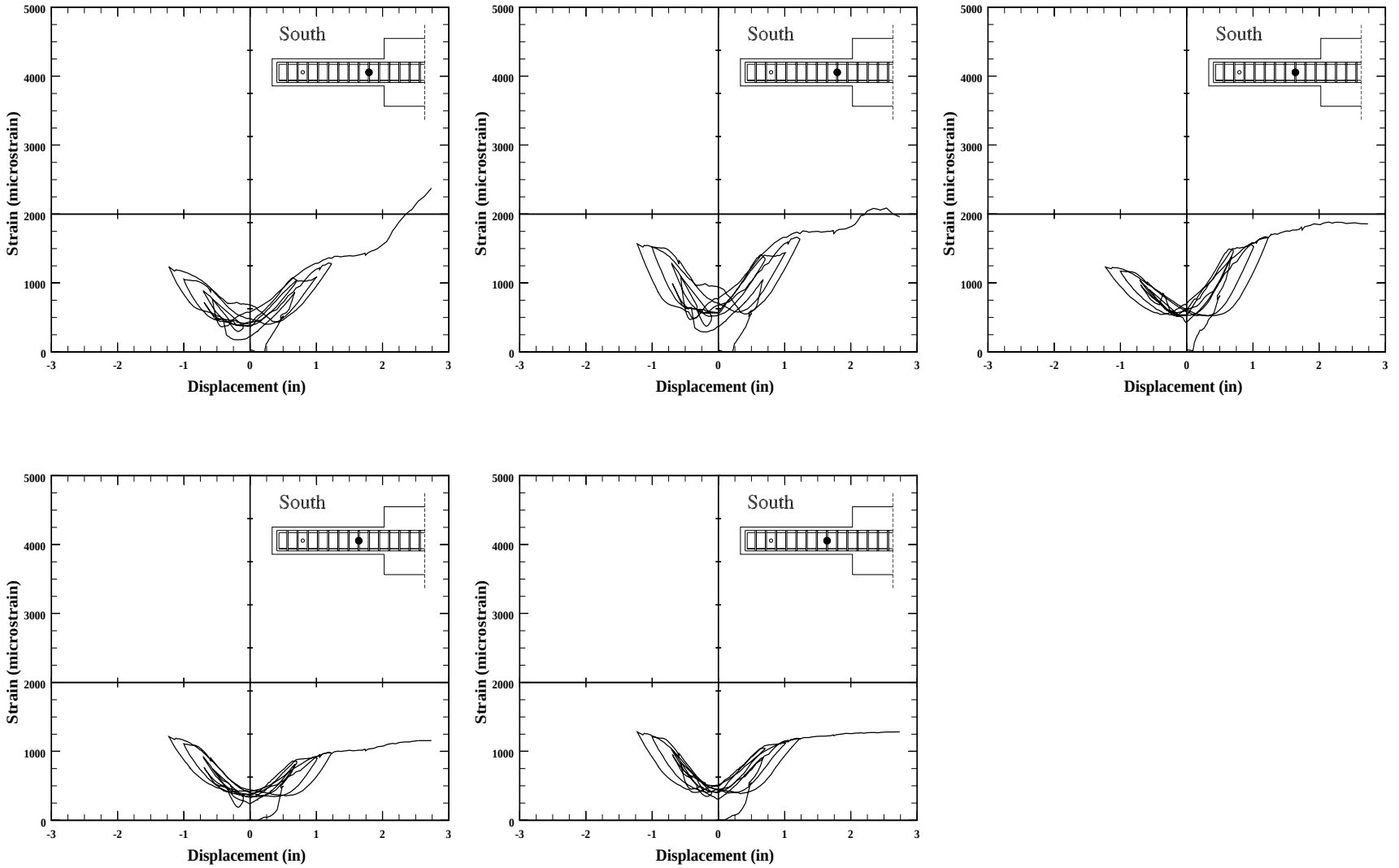

Figure 3.84. Measured stirrup strain vs load-point displacement for specimen C5-10, south element.

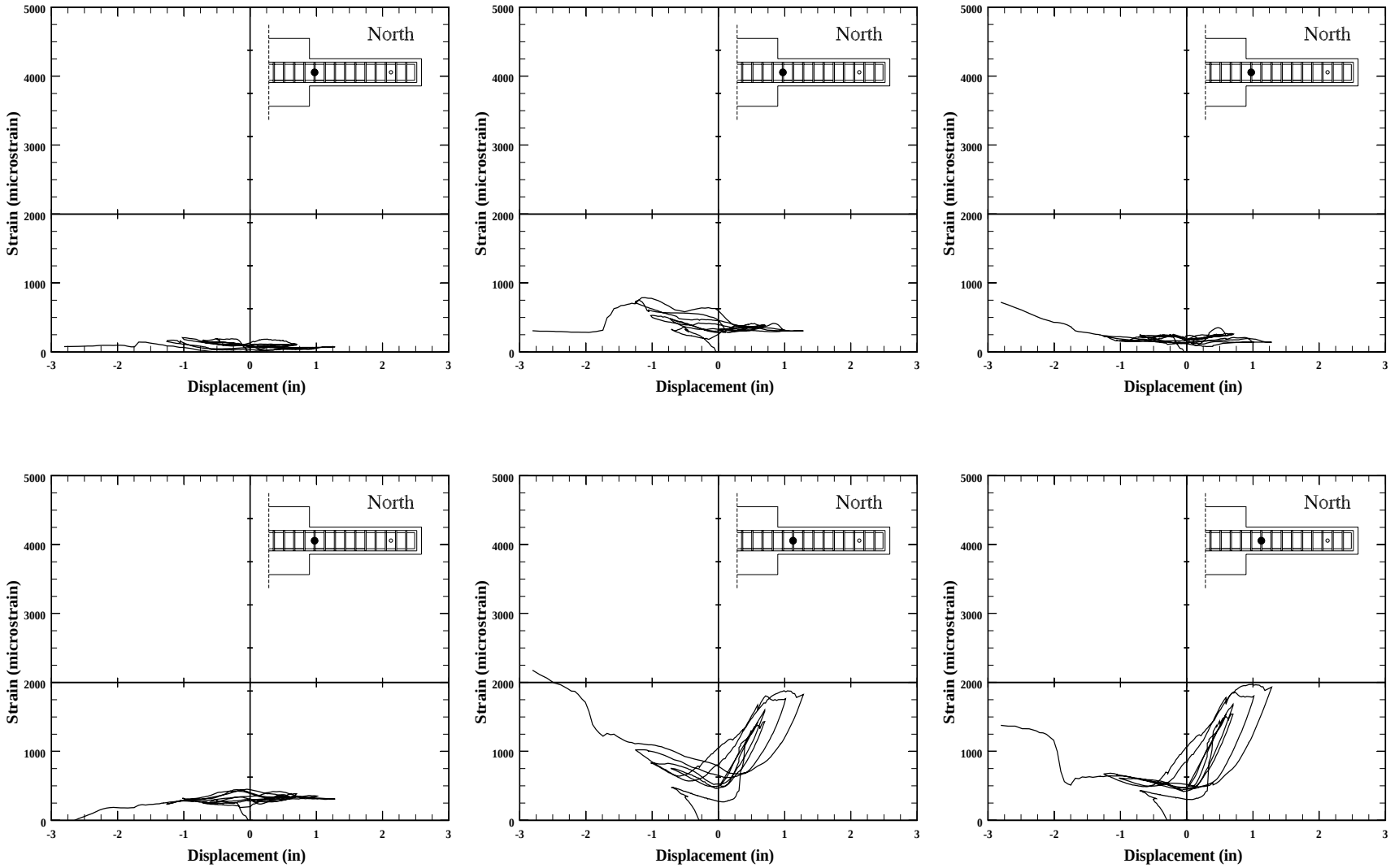

Figure 3.85. Measured stirrup strain vs load-point displacement for specimen C5-10, north element.

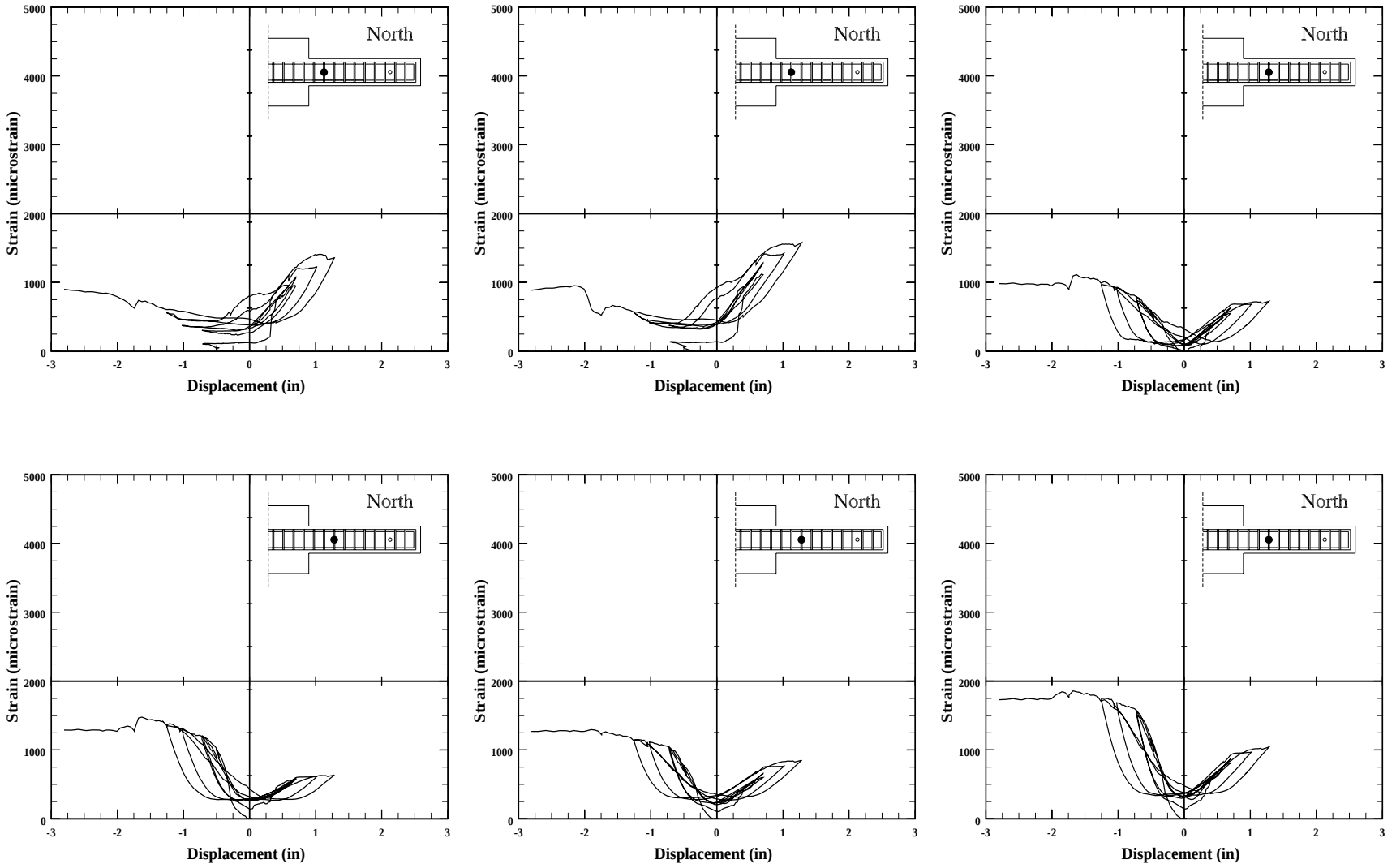

Figure 3.86. Measured stirrup strain vs load-point displacement for specimen C5-10, north element.

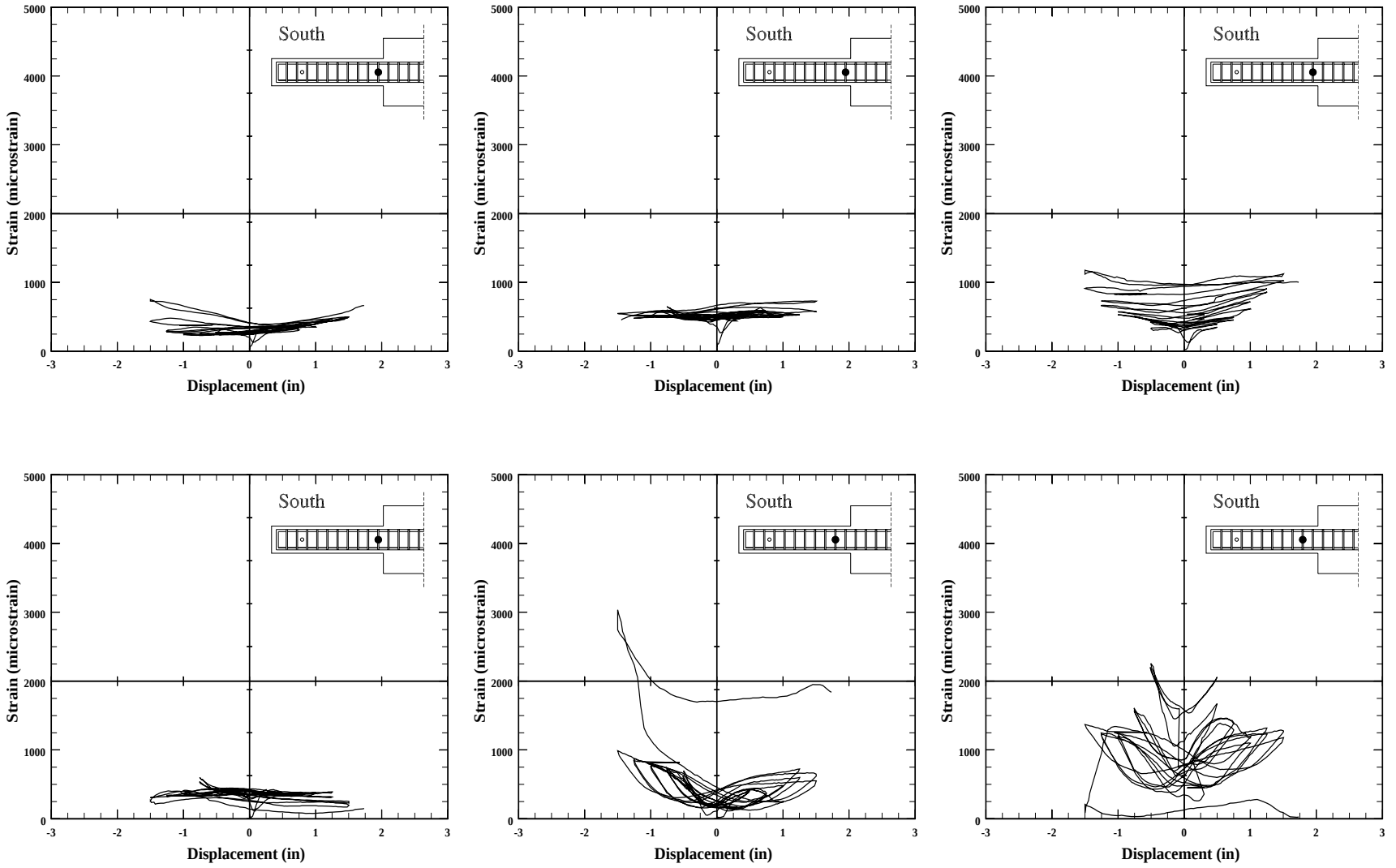

Figure 3.87. Measured stirrup strain vs load-point displacement for specimen C5-20, south element.

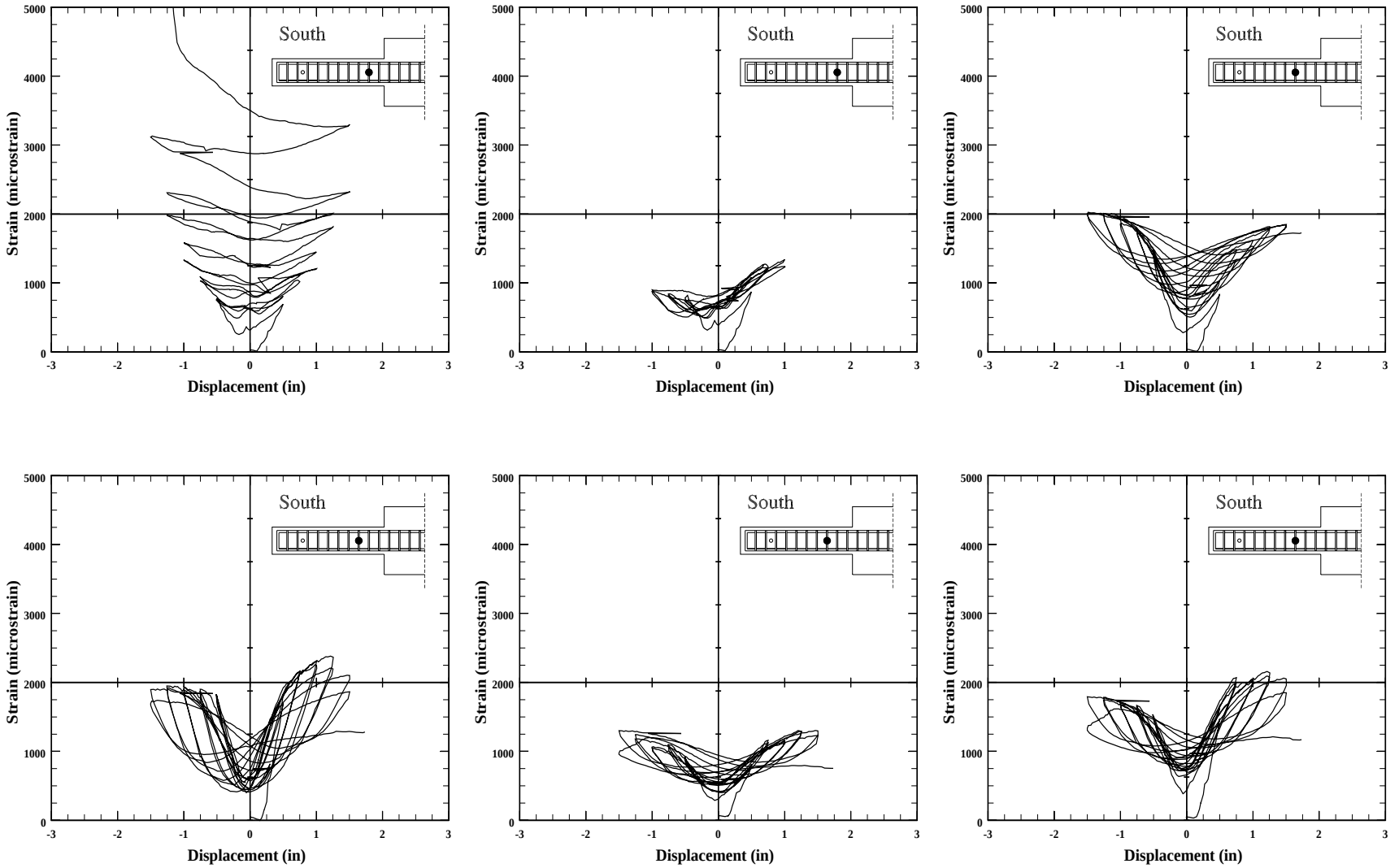

Figure 3.88. Measured stirrup strain vs load-point displacement for specimen C5-20, south element.

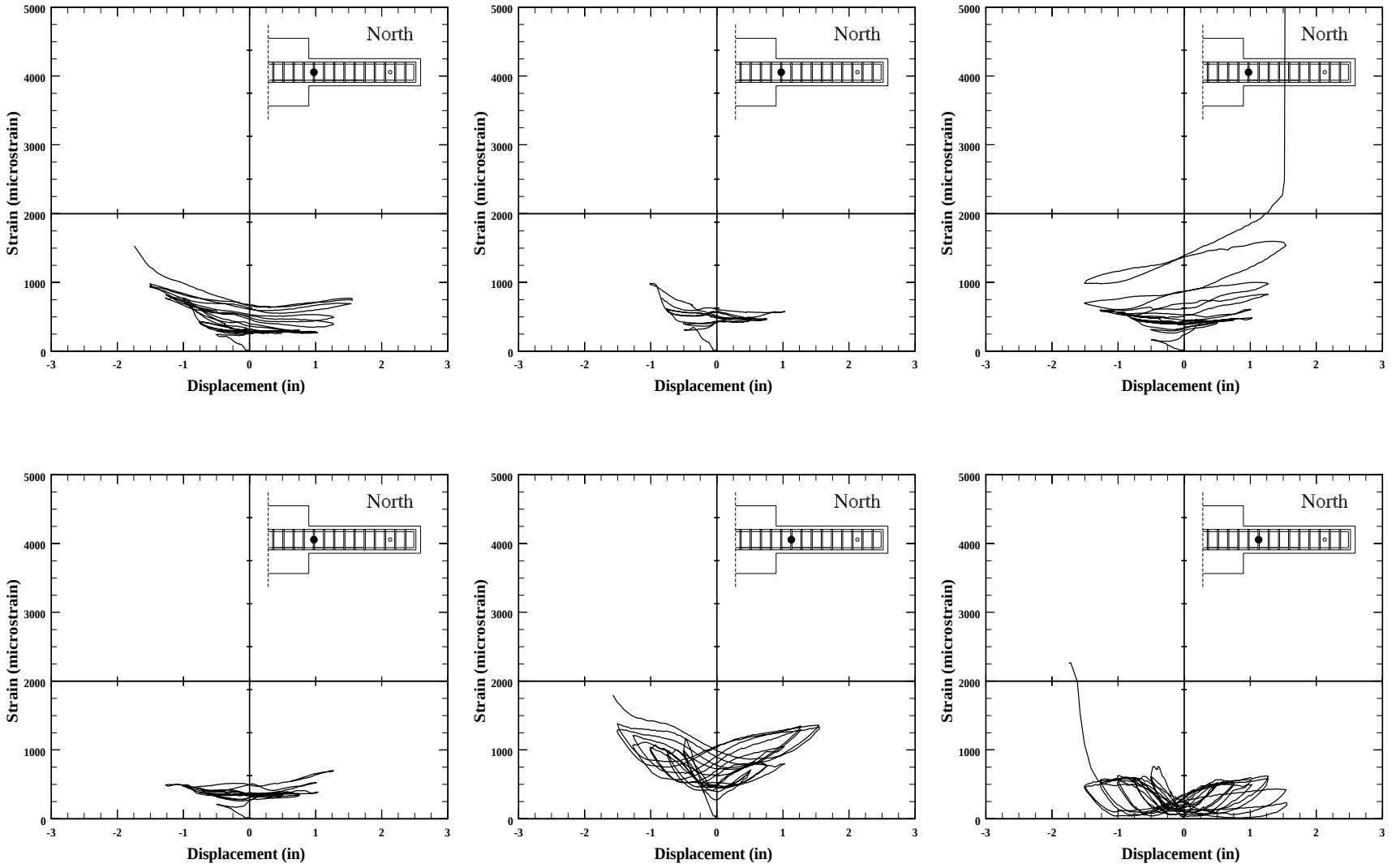

Figure 3.89. Measured stirrup strain vs load-point displacement for specimen C5-20, north element.

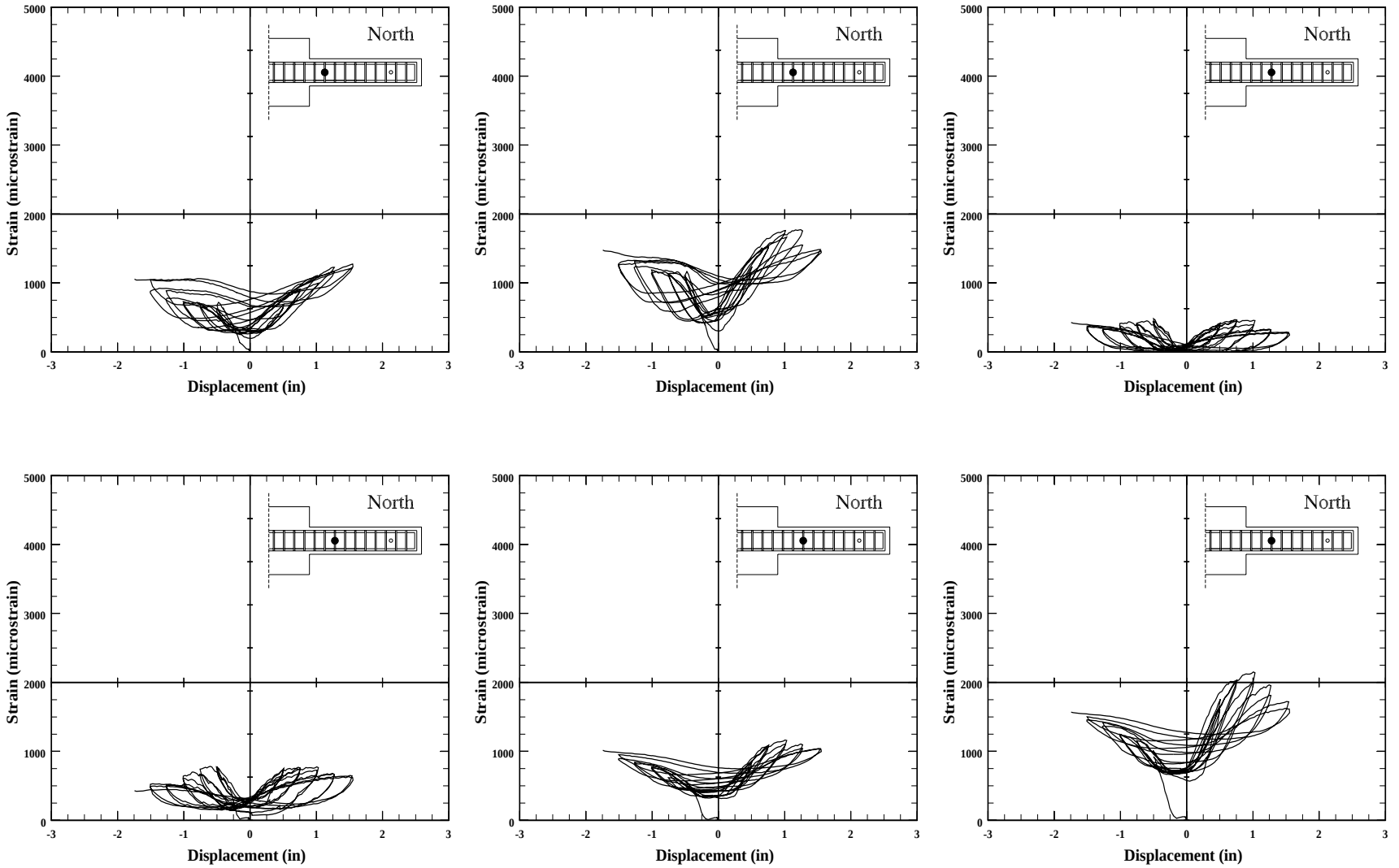

Figure 3.90. Measured stirrup strain vs load-point displacement for specimen C5-20, south element.

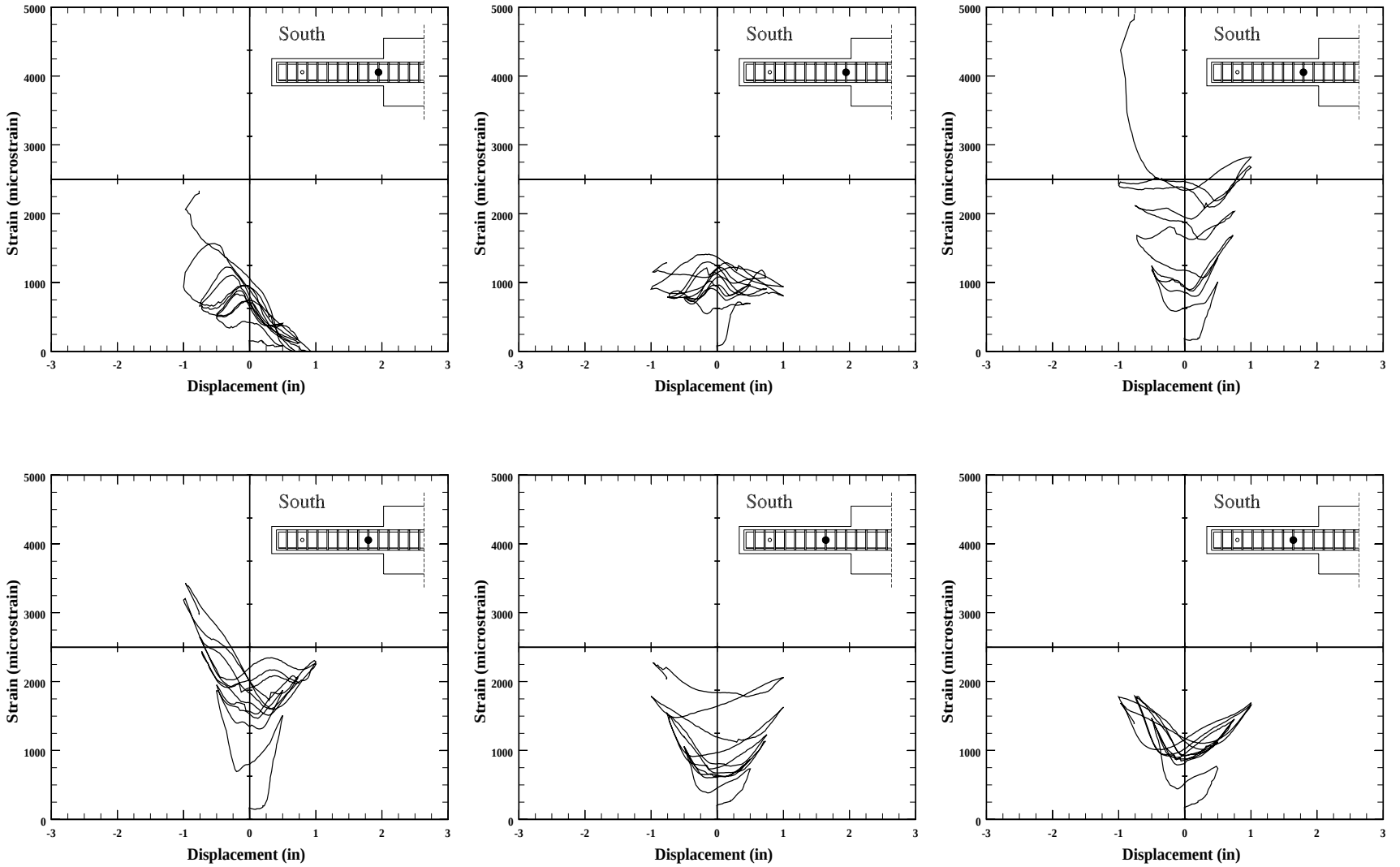

Figure 3.91. Measured stirrup strain vs load-point displacement for specimen C5-40, south element.

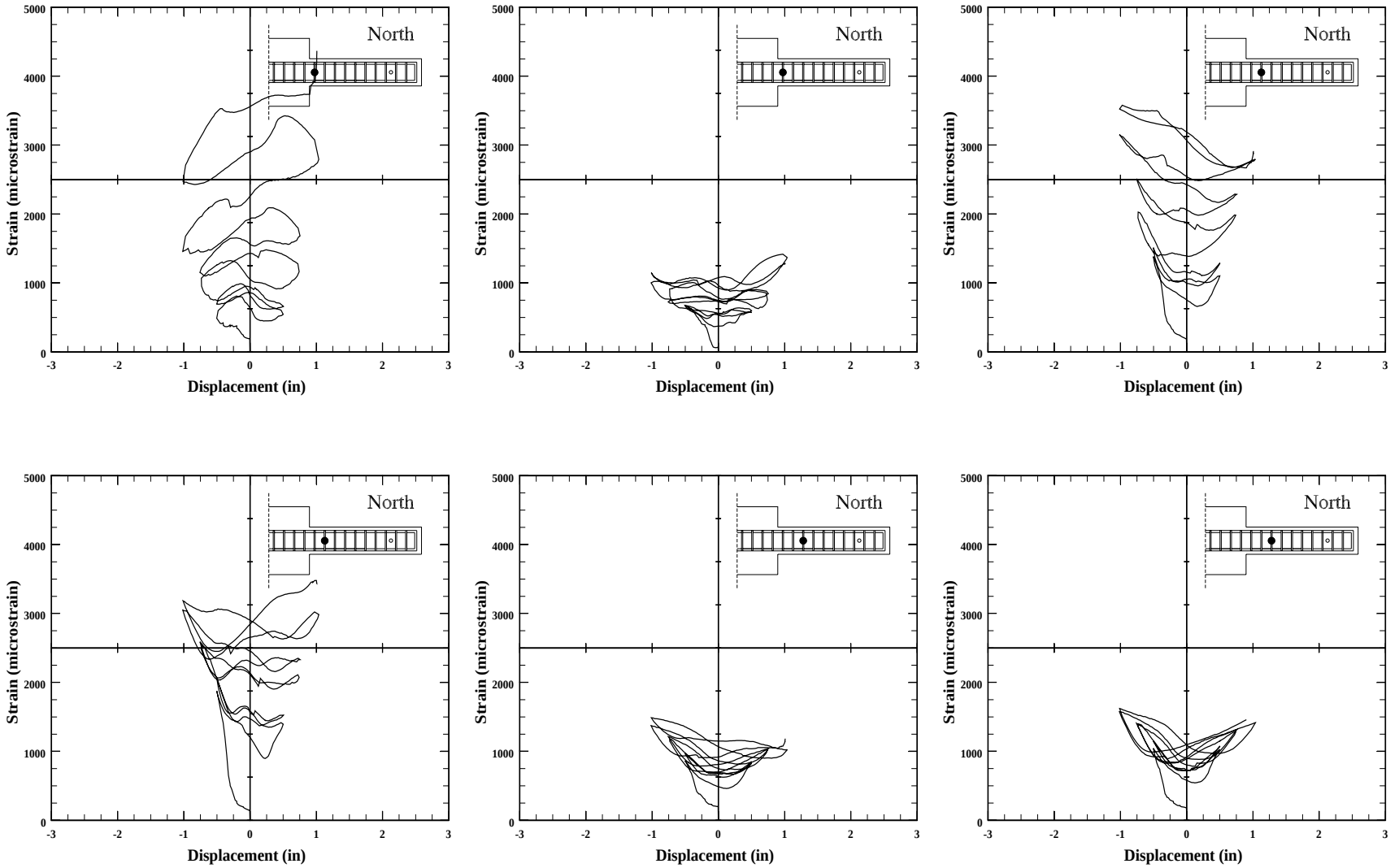

Figure 3.92. Measured stirrup strain vs load-point displacement for specimen C5-40, north element.

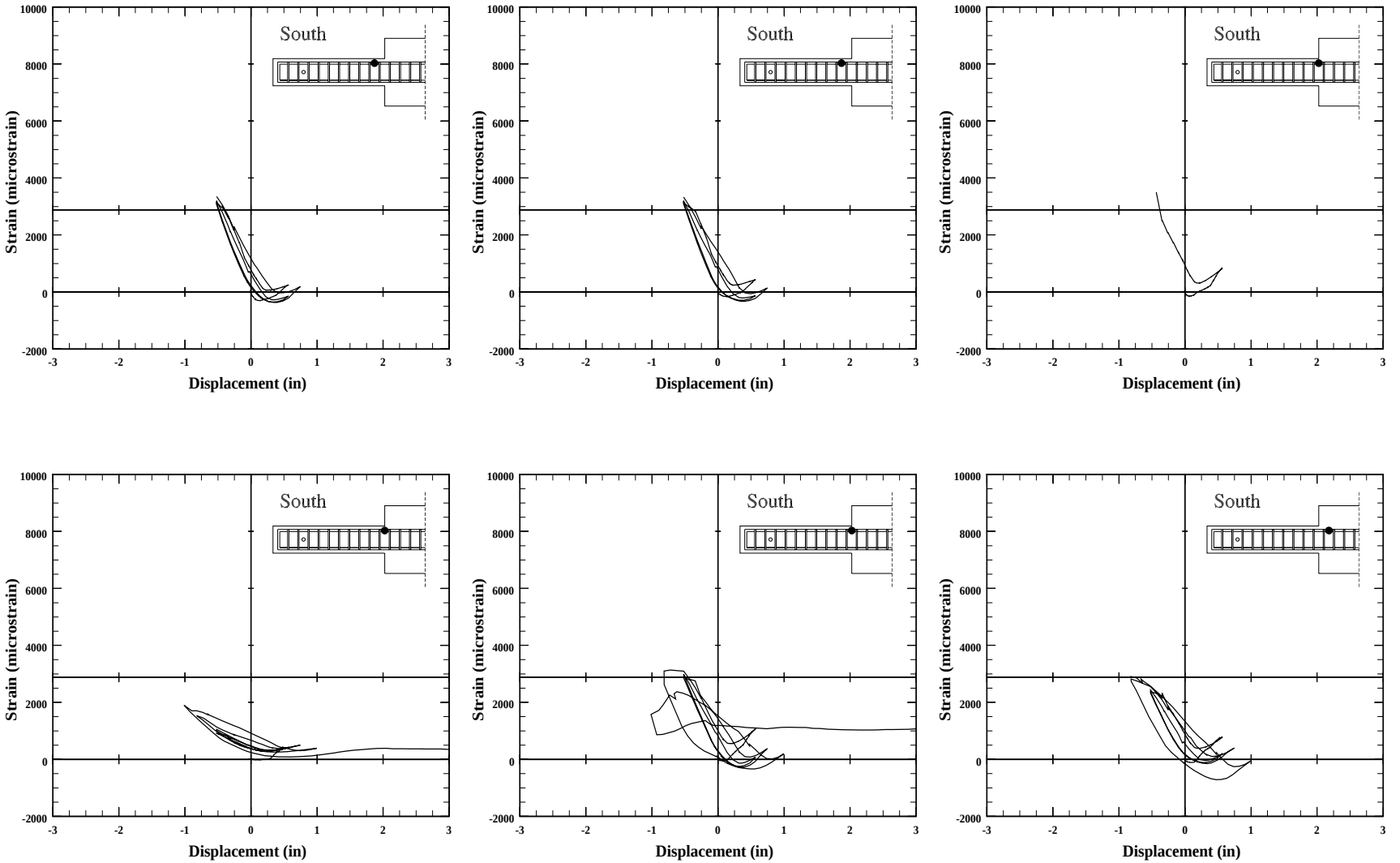

Figure 3.93. Measured longitudinal-bar strain vs load-point displacement for specimen C10-00, top bars.

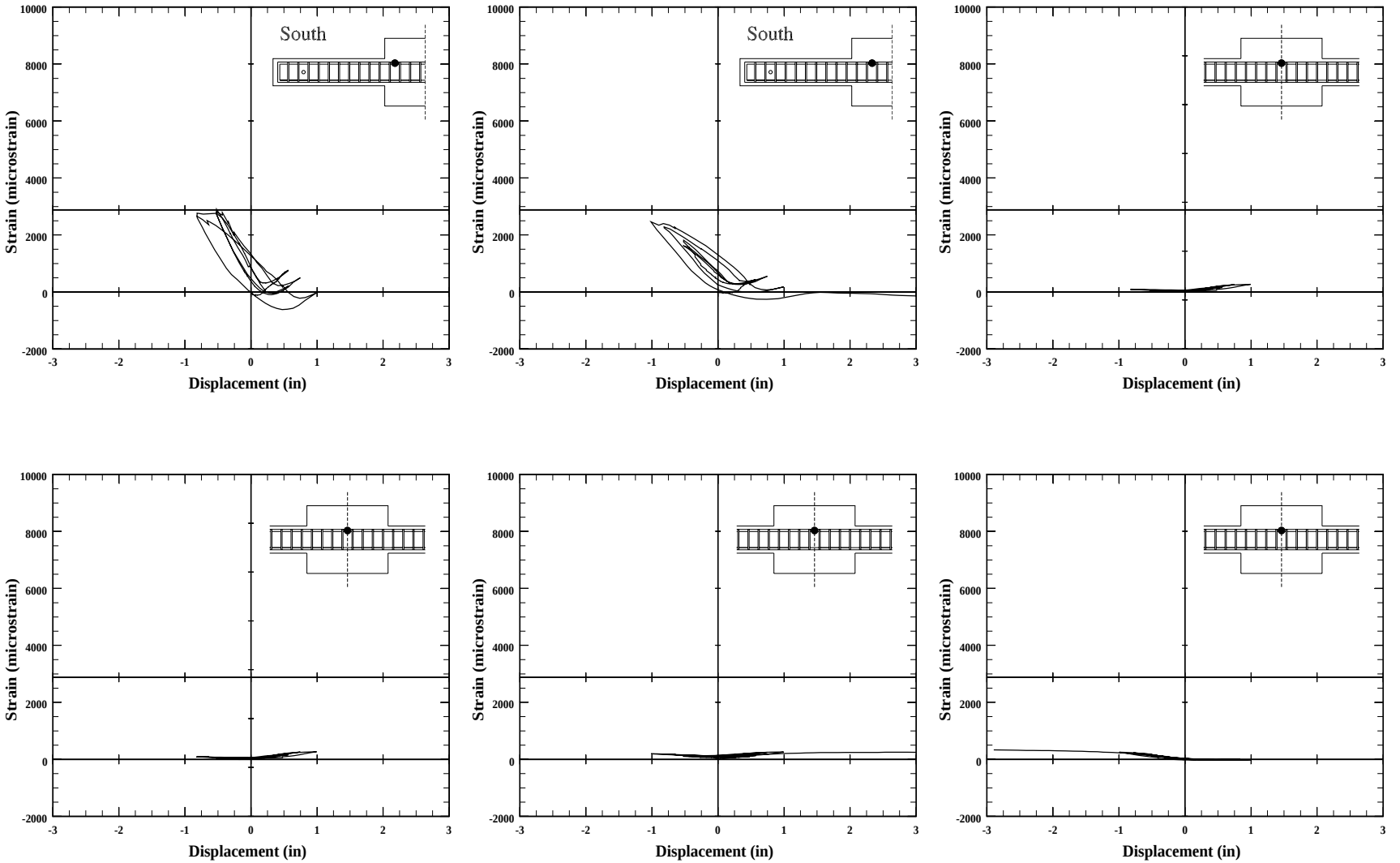

Figure 3.94. Measured longitudinal-bar strain vs load-point displacement for specimen C10-00, top bars.

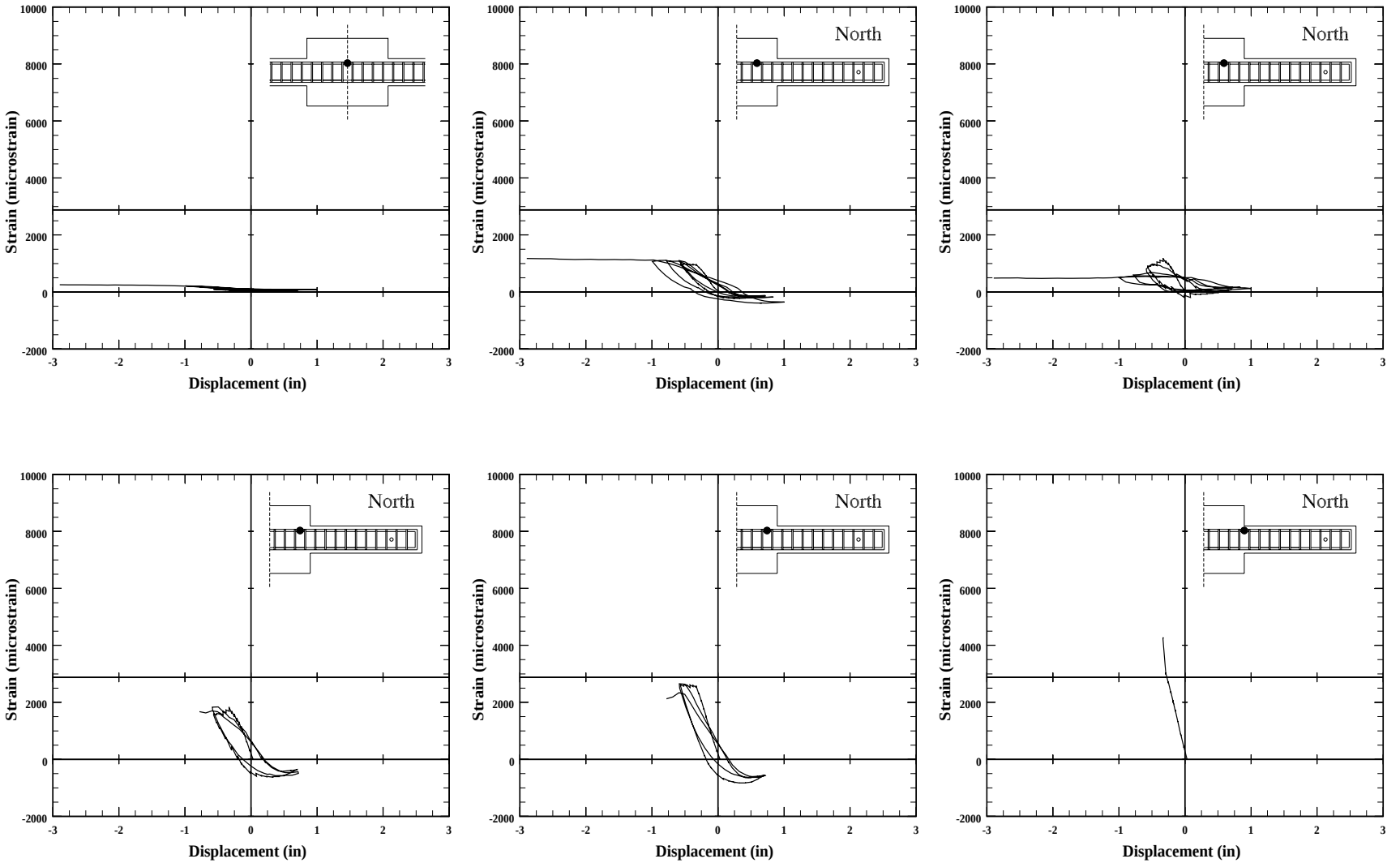

Figure 3.95. Measured longitudinal-bar strain vs load-point displacement for specimen C10-00, top bars.

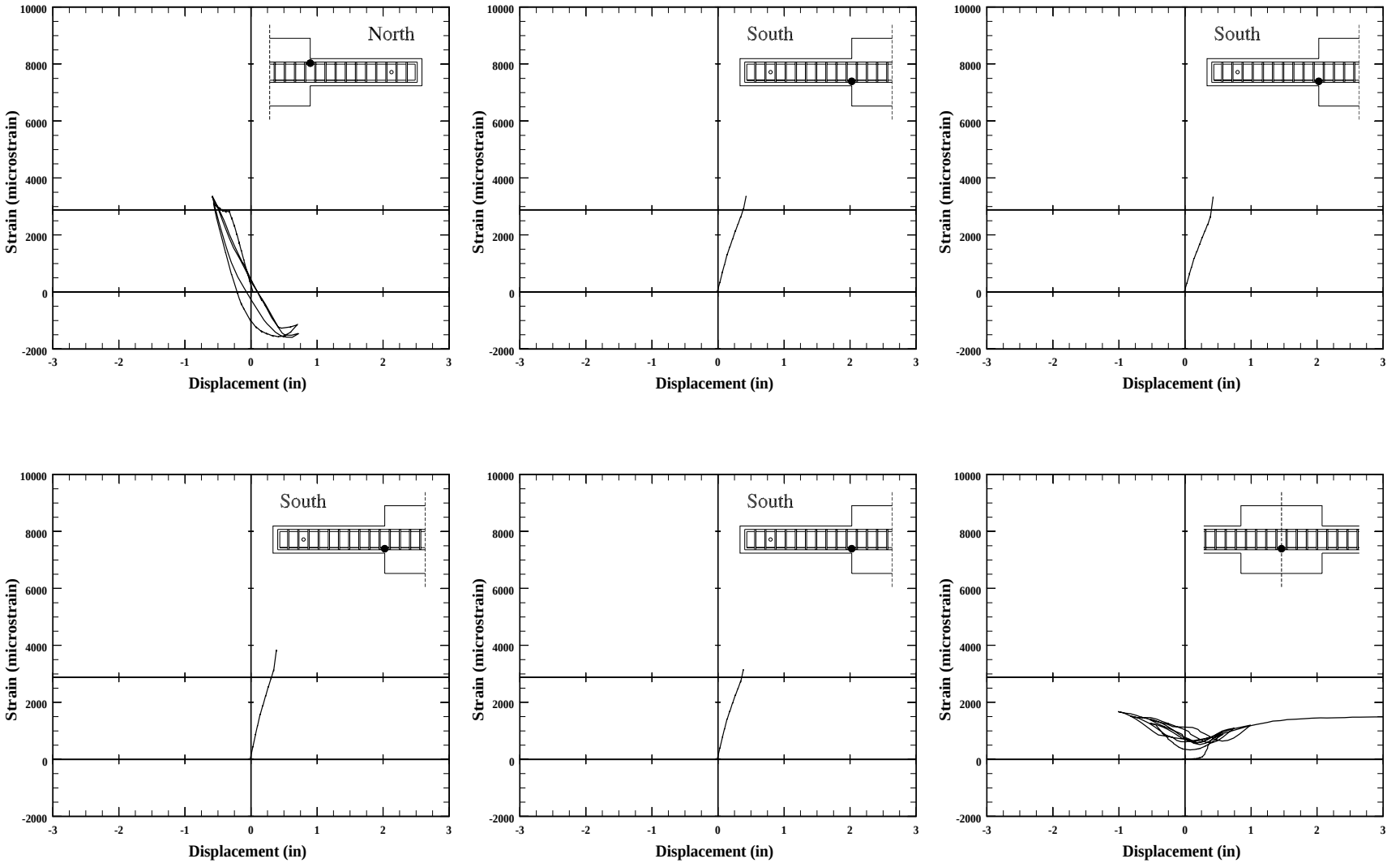

Figure 3.96. Measured longitudinal-bar strain vs load-point displacement for specimen C10-00, top and bottom bars.

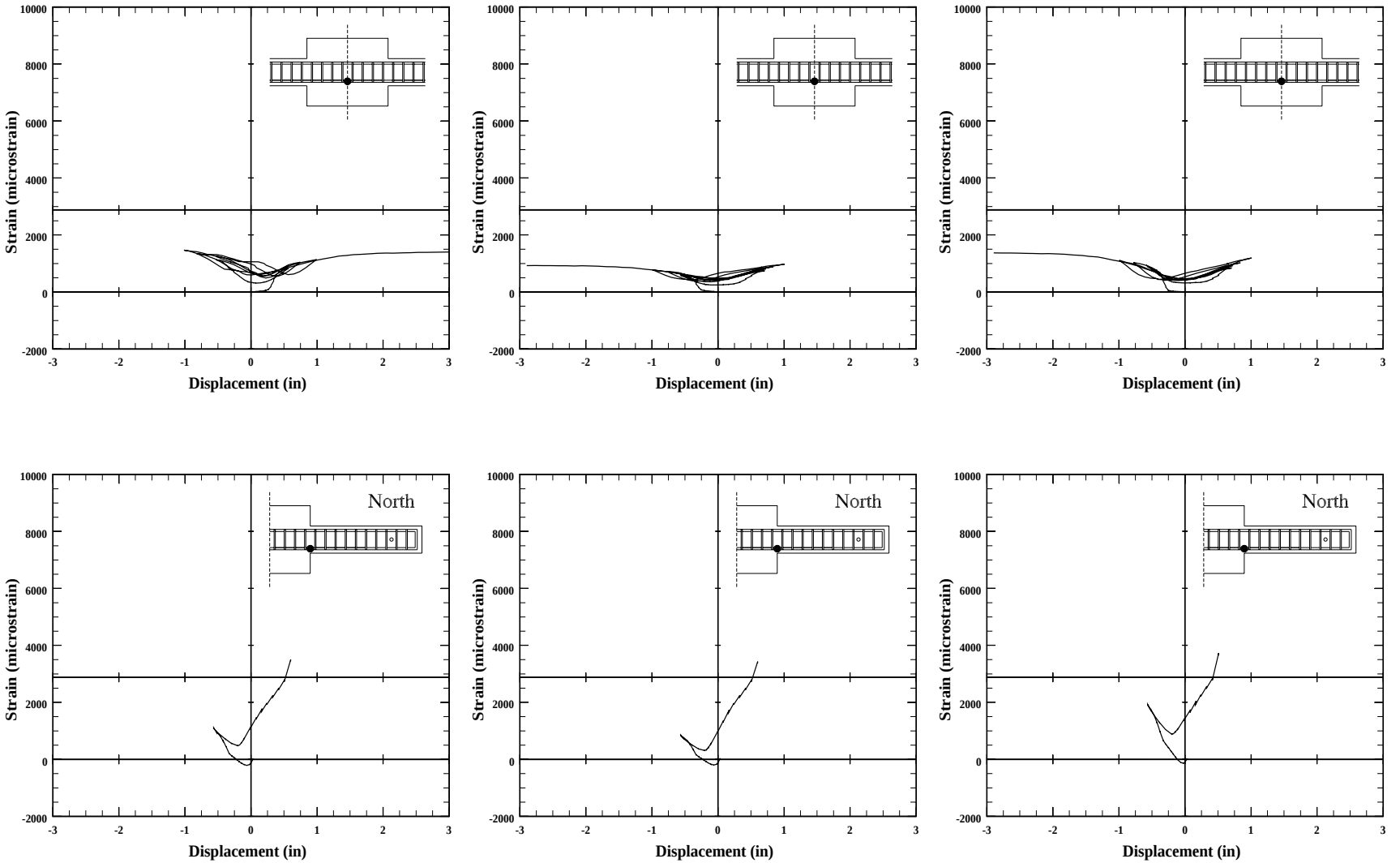

Figure 3.97. Measured longitudinal-bar strain vs load-point displacement for specimen C10-00, bottom bars.

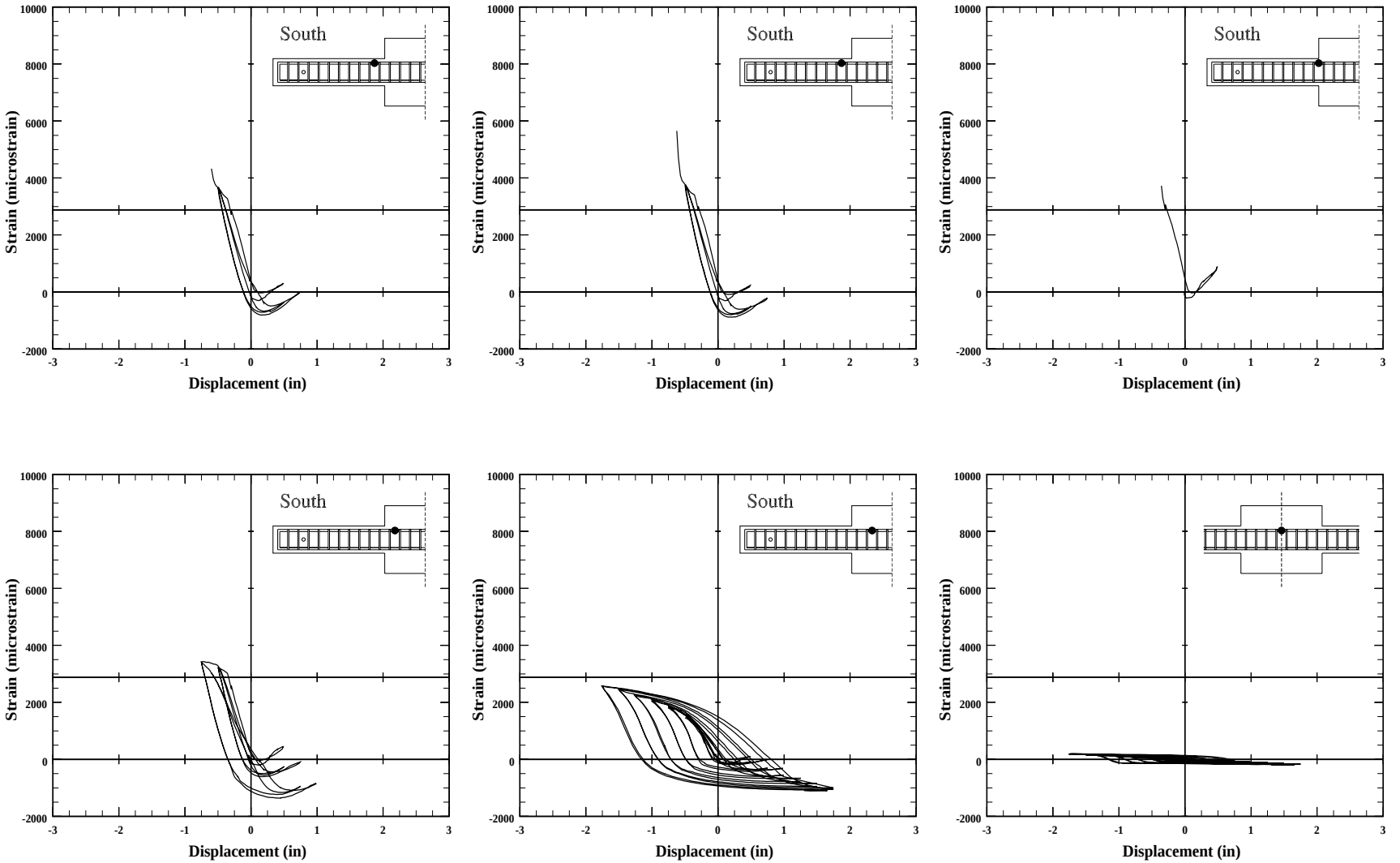

Figure 3.98. Measured longitudinal-bar strain vs load-point displacement for specimen C10-05, top bars.

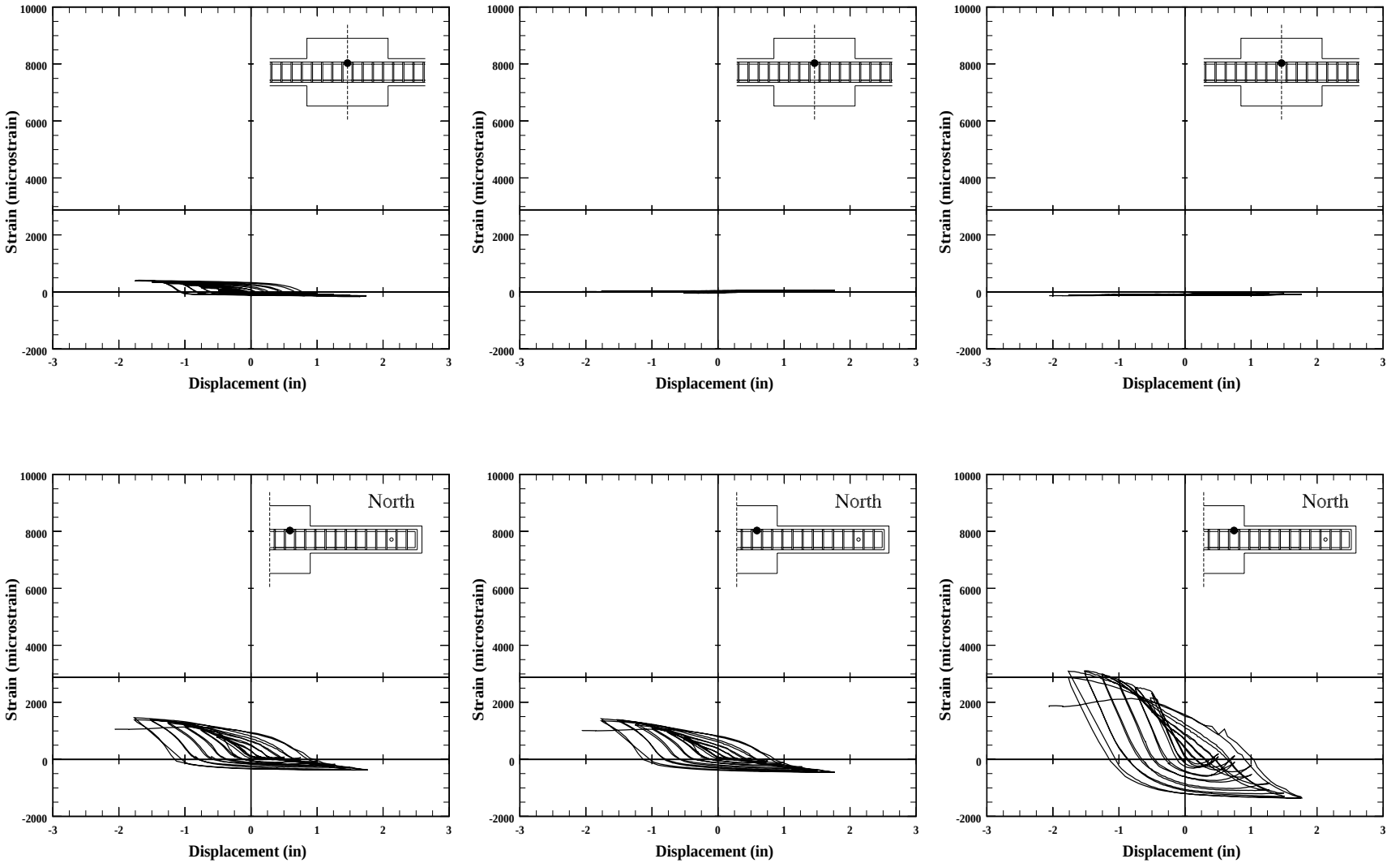

Figure 3.99. Measured longitudinal-bar strain vs load-point displacement for specimen C10-05, top bars.

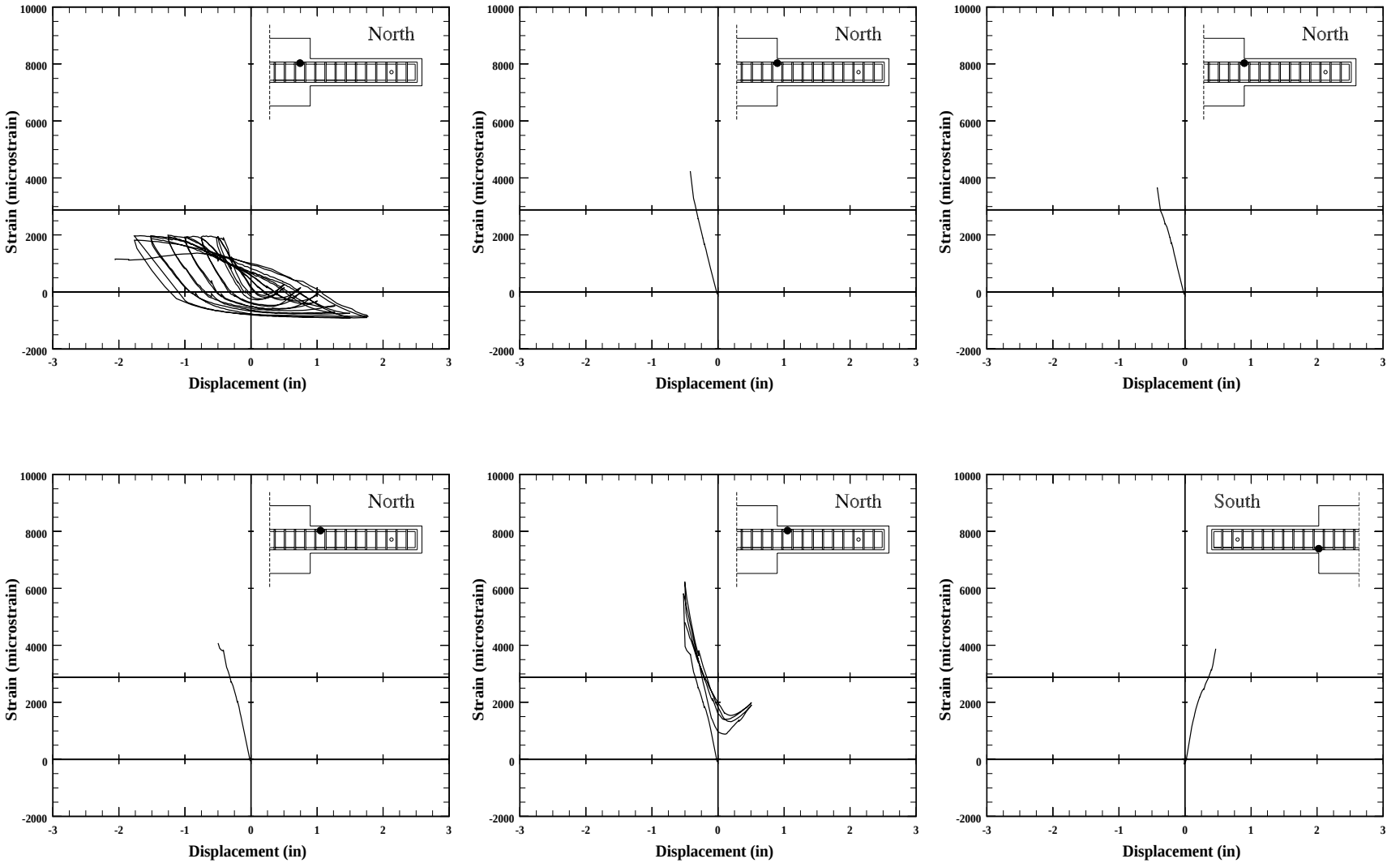

Figure 3.100. Measured longitudinal-bar strain vs load-point displacement for specimen C10-05, top and bottom bars.

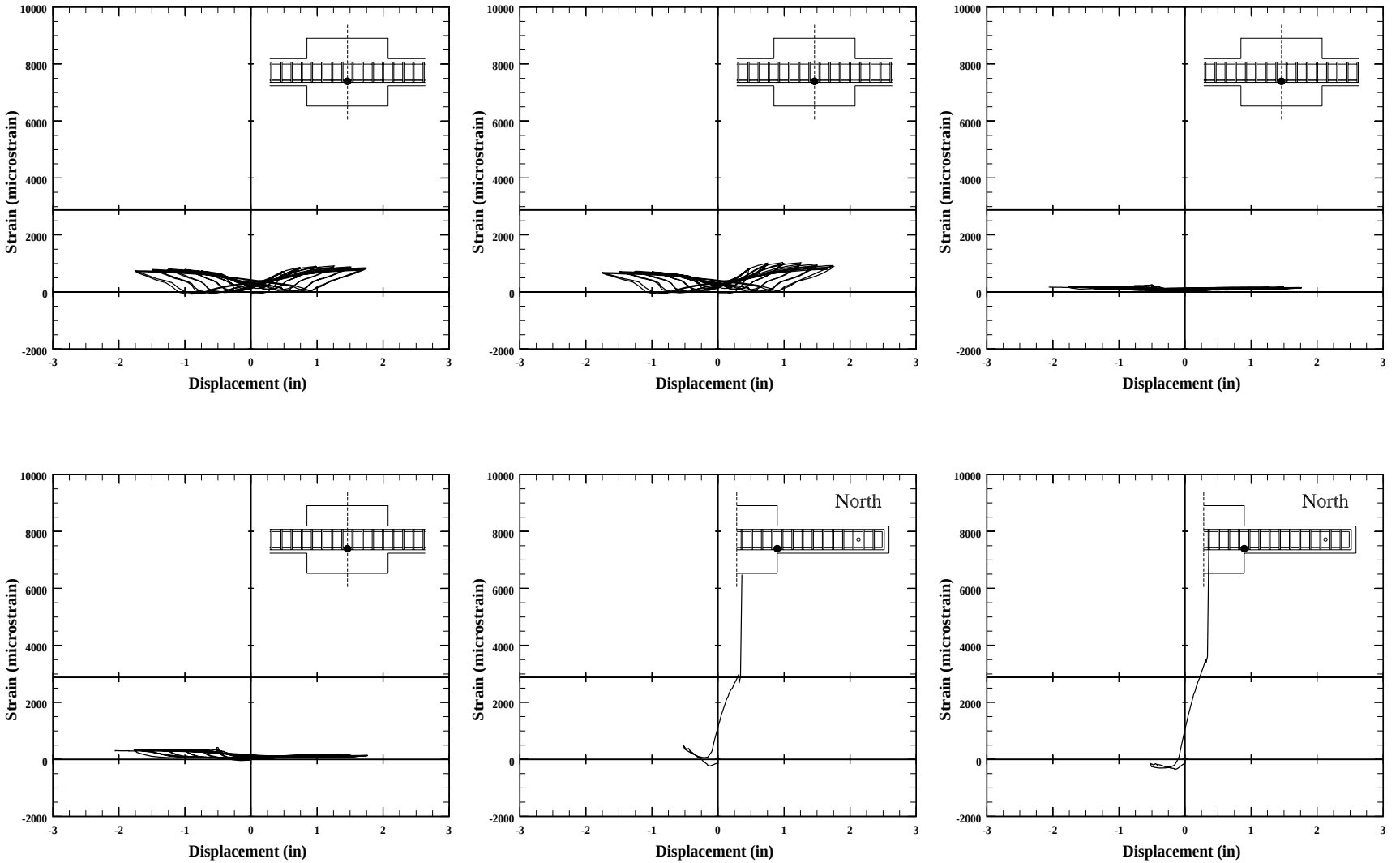

Figure 3.101. Measured longitudinal-bar strain vs load-point displacement for specimen C10-05, bottom bars.

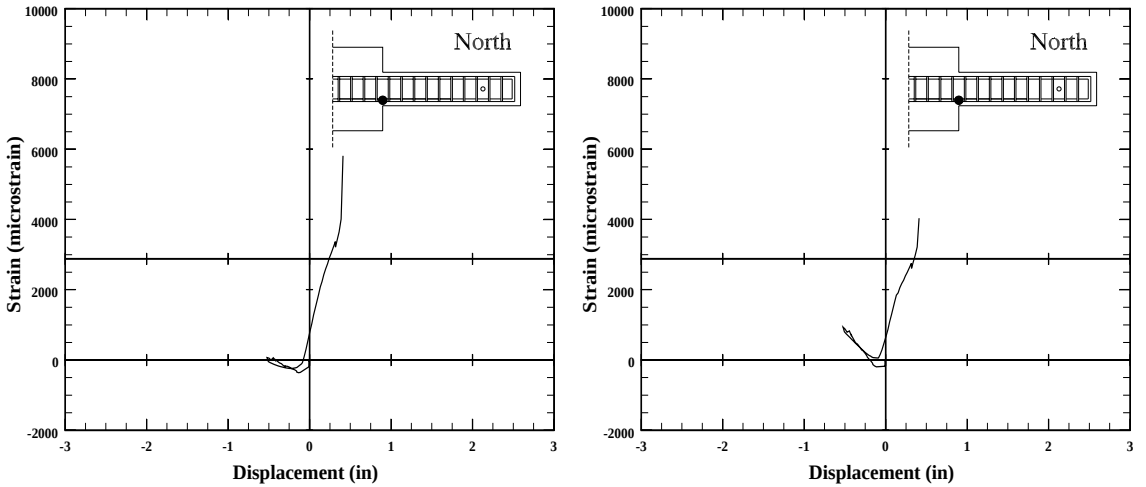

Figure 3.102. Measured longitudinal-bar strain vs load-point displacement for specimen C10-05, bottom bars.

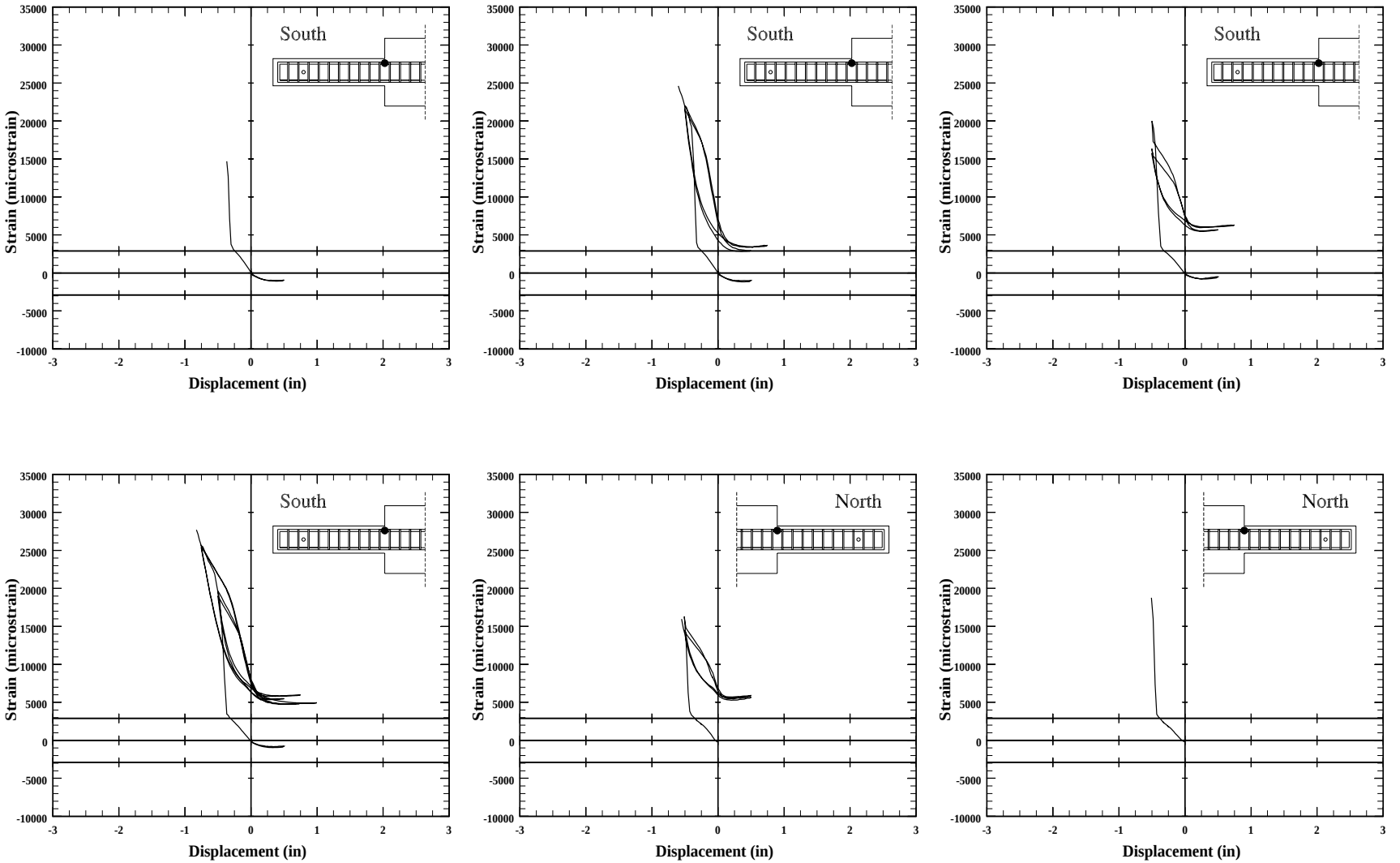

Figure 3.103. Measured longitudinal-bar strain vs load-point displacement for specimen C10-10, top bars.

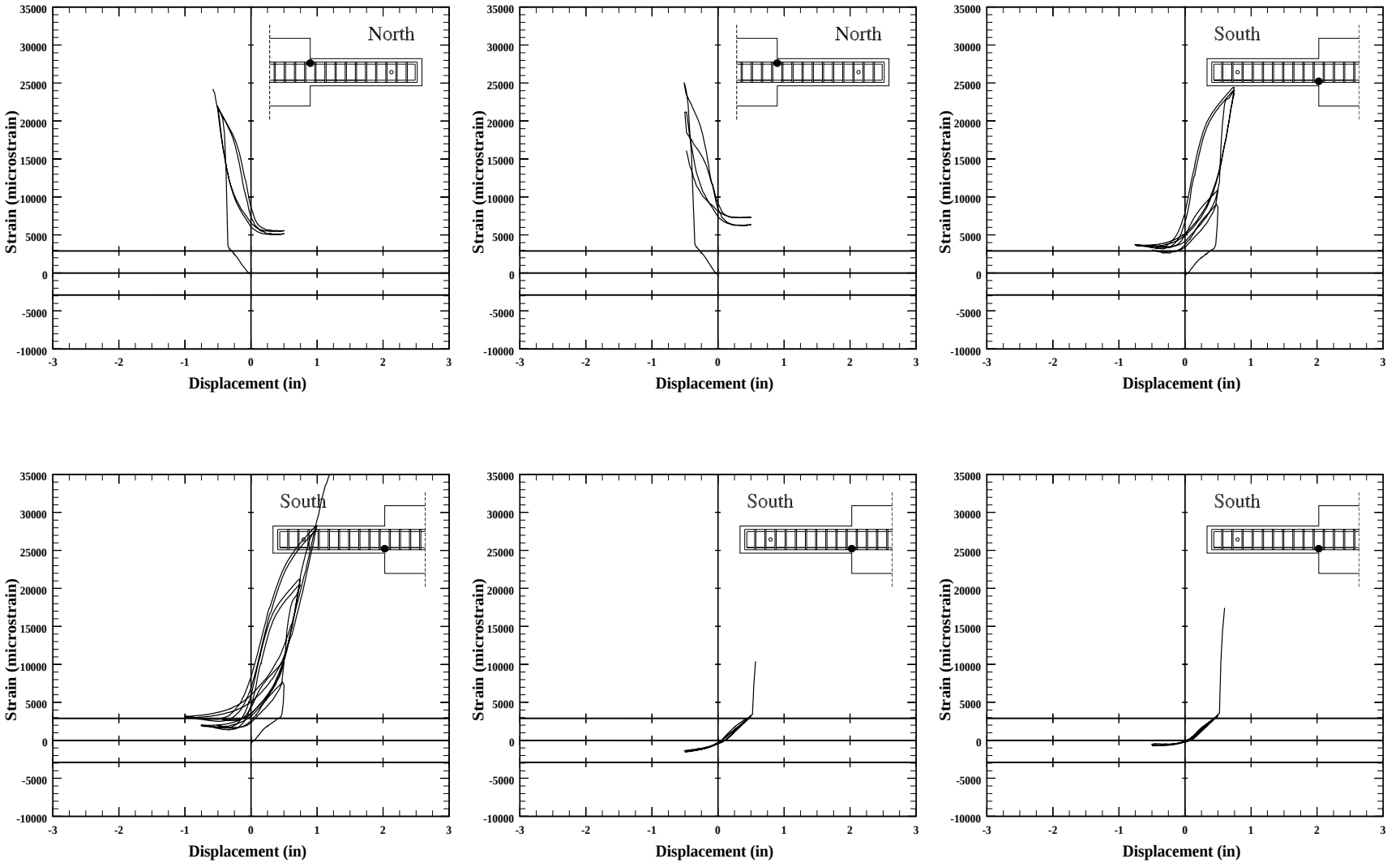

Figure 3.104. Measured longitudinal-bar strain vs load-point displacement for specimen C10-10, top and bottom bars.

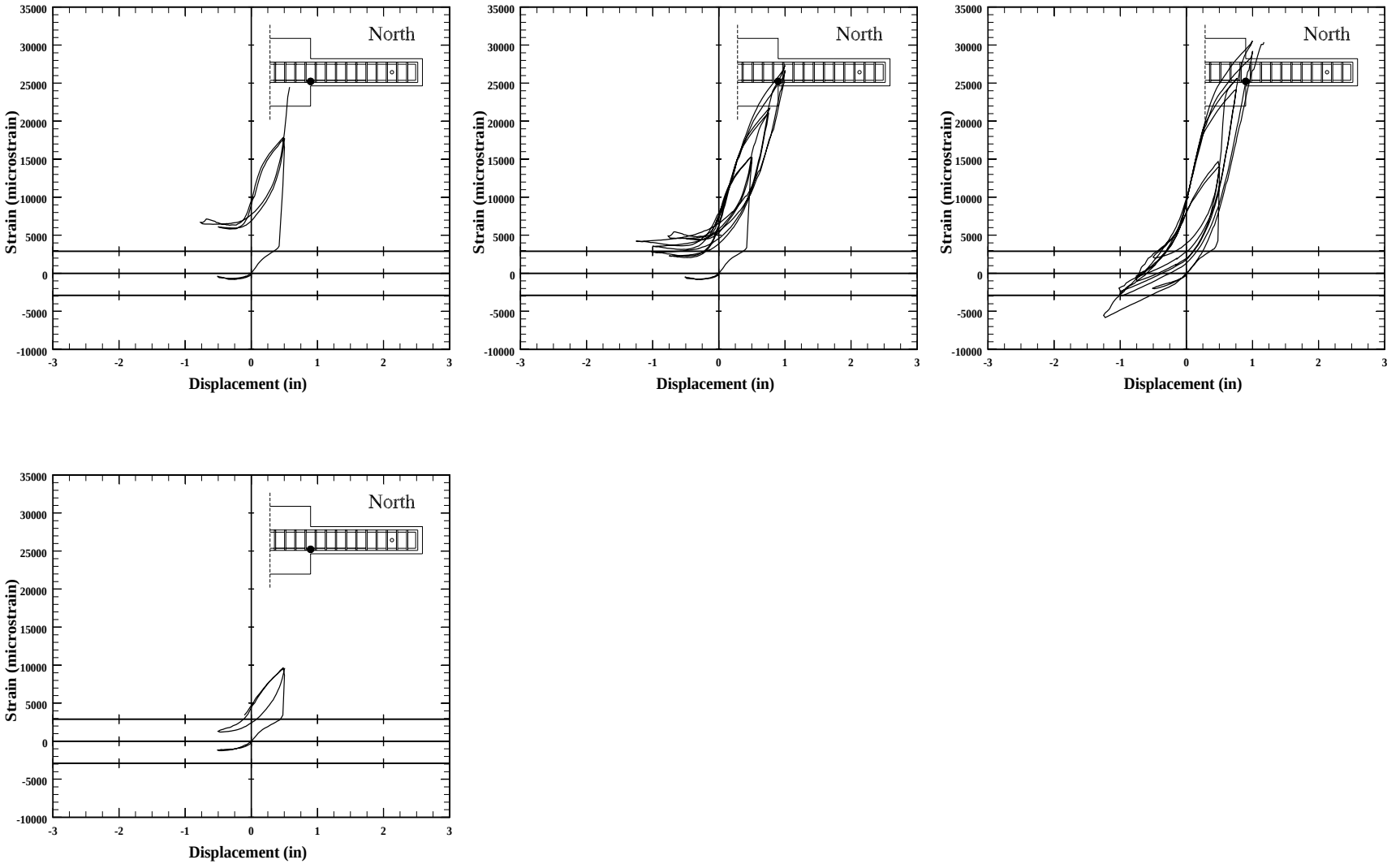

Figure 3.105. Measured longitudinal-bar strain vs load-point displacement for specimen C10-10, bottom bars.

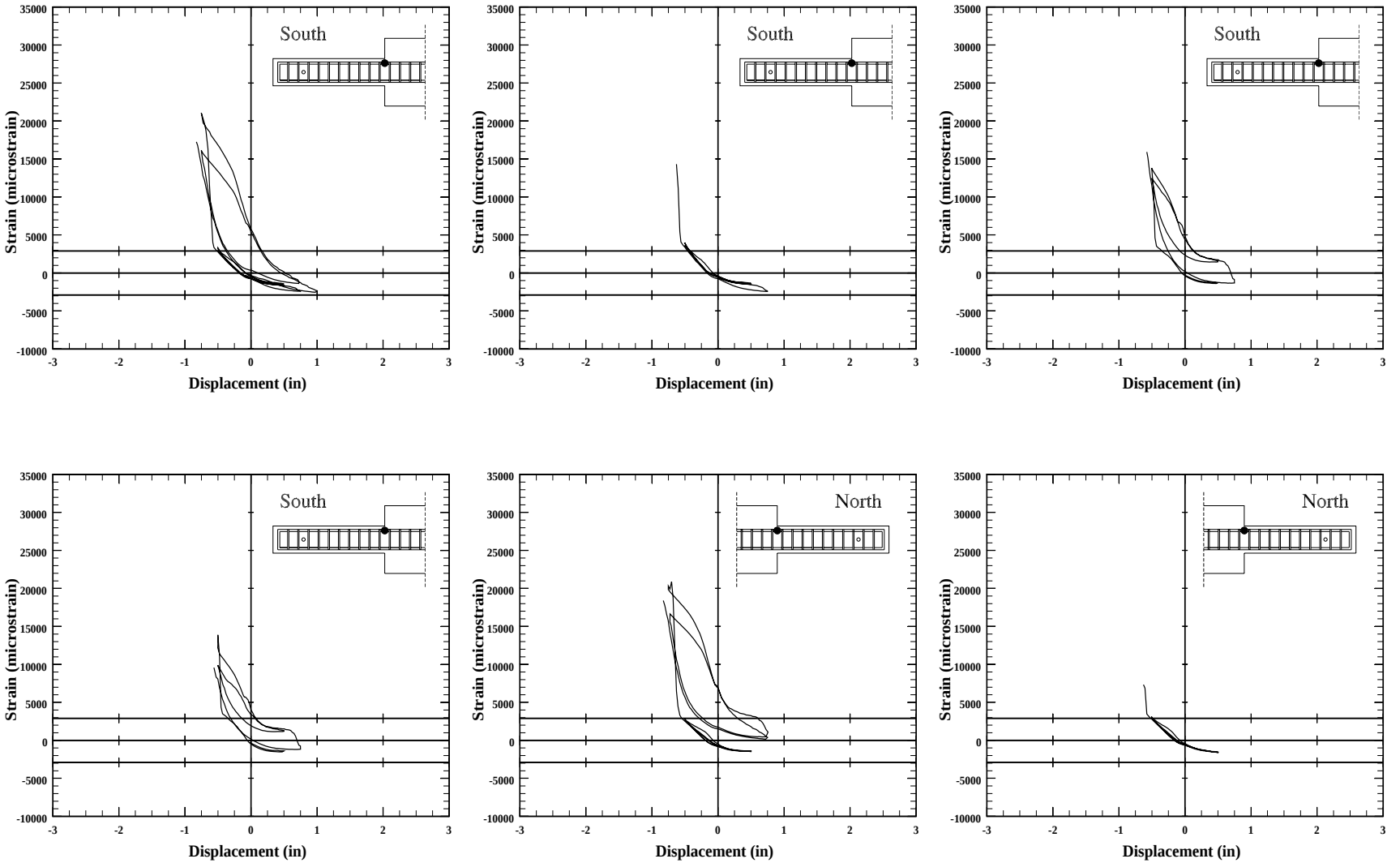

Figure 3.106. Measured longitudinal-bar strain vs load-point displacement for specimen C10-20, top bars.

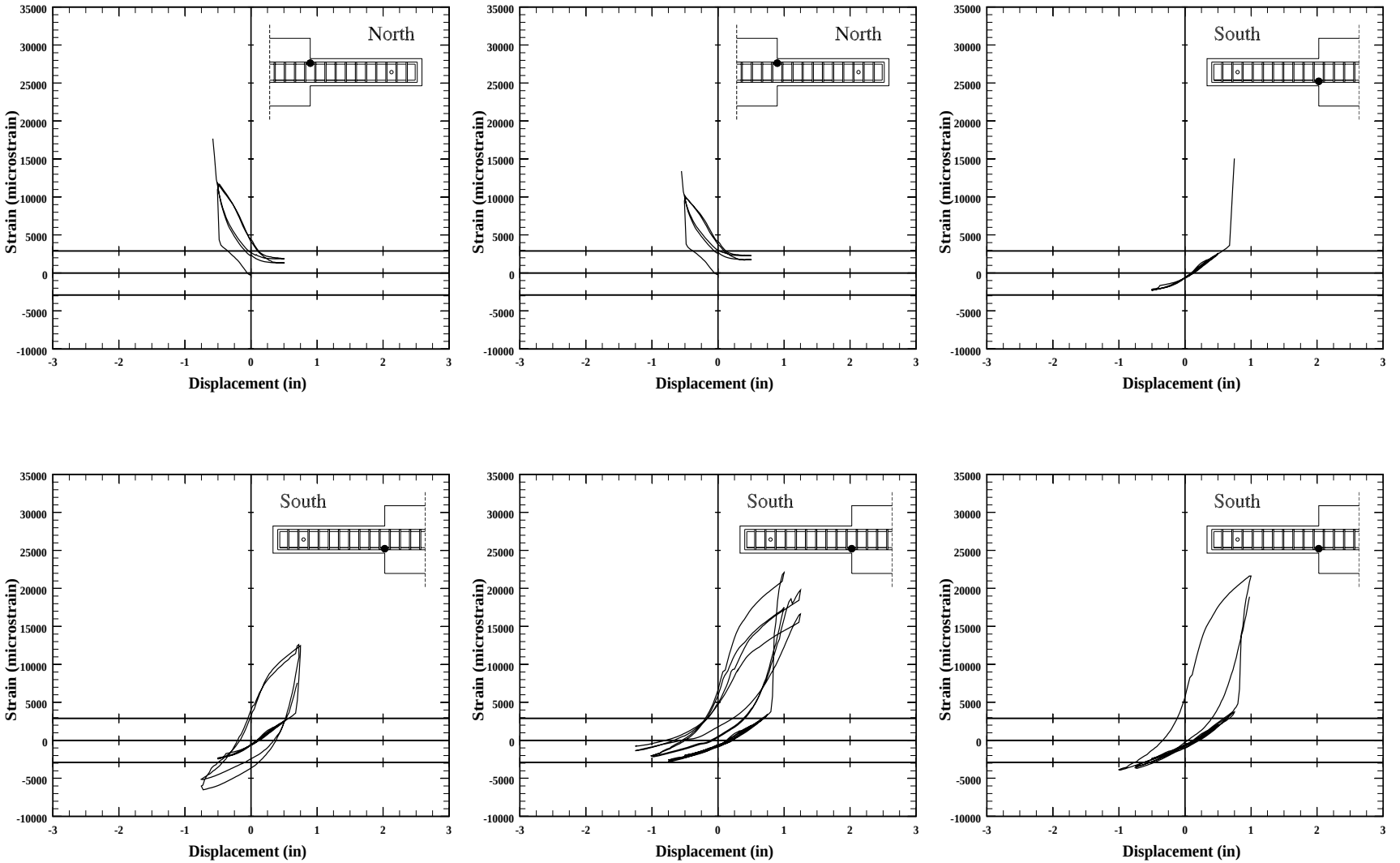

Figure 3.107. Measured longitudinal-bar strain vs load-point displacement for specimen C10-20, top and bottom bars.

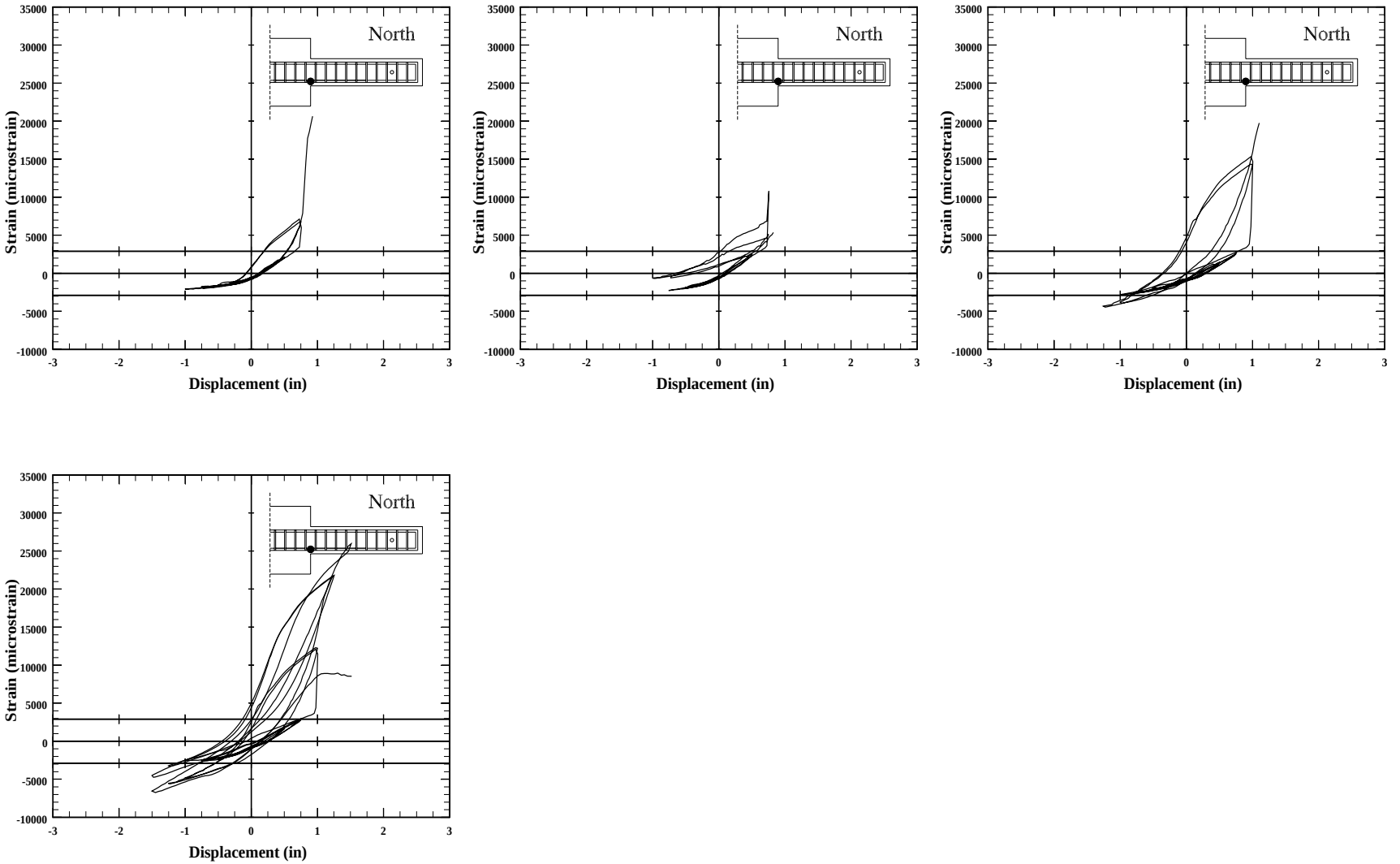

Figure 3.108. Measured longitudinal-bar strain vs load-point displacement for specimen C10-20, bottom bars.

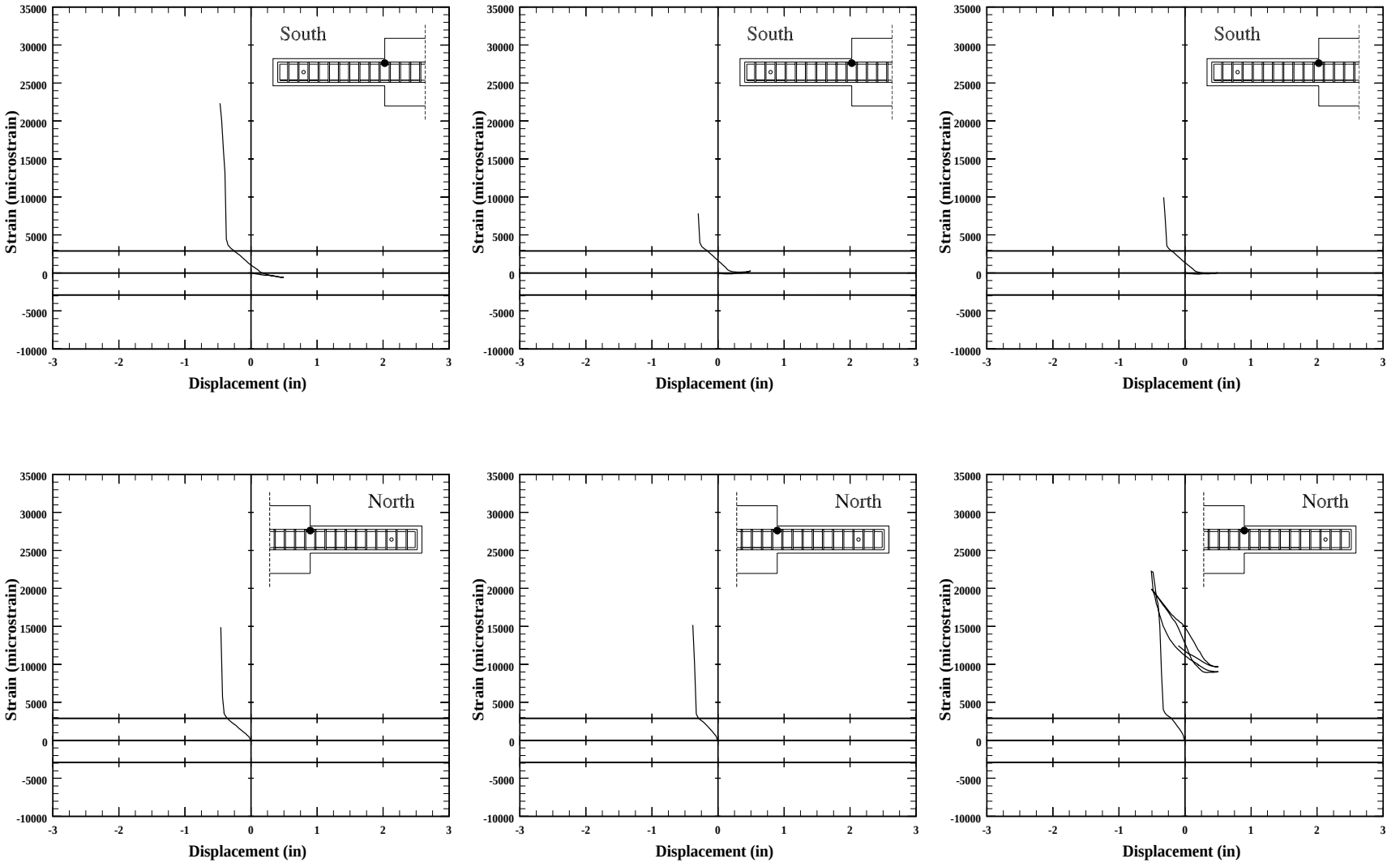

Figure 3.109. Measured longitudinal-bar strain vs load-point displacement for specimen C5-00, top bars.

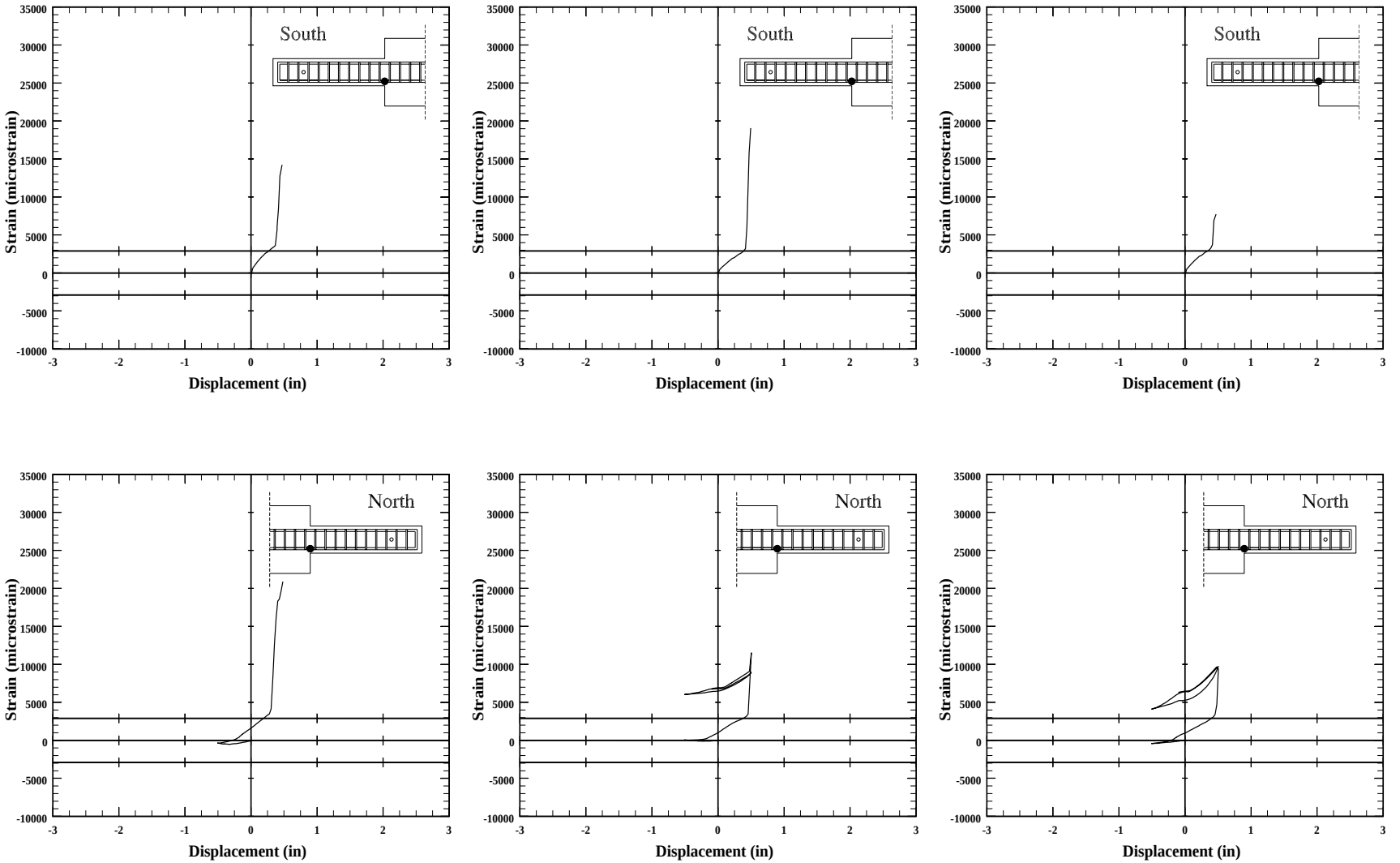

Figure 3.110. Measured longitudinal-bar strain vs load-point displacement for specimen C5-00, bottom bars.

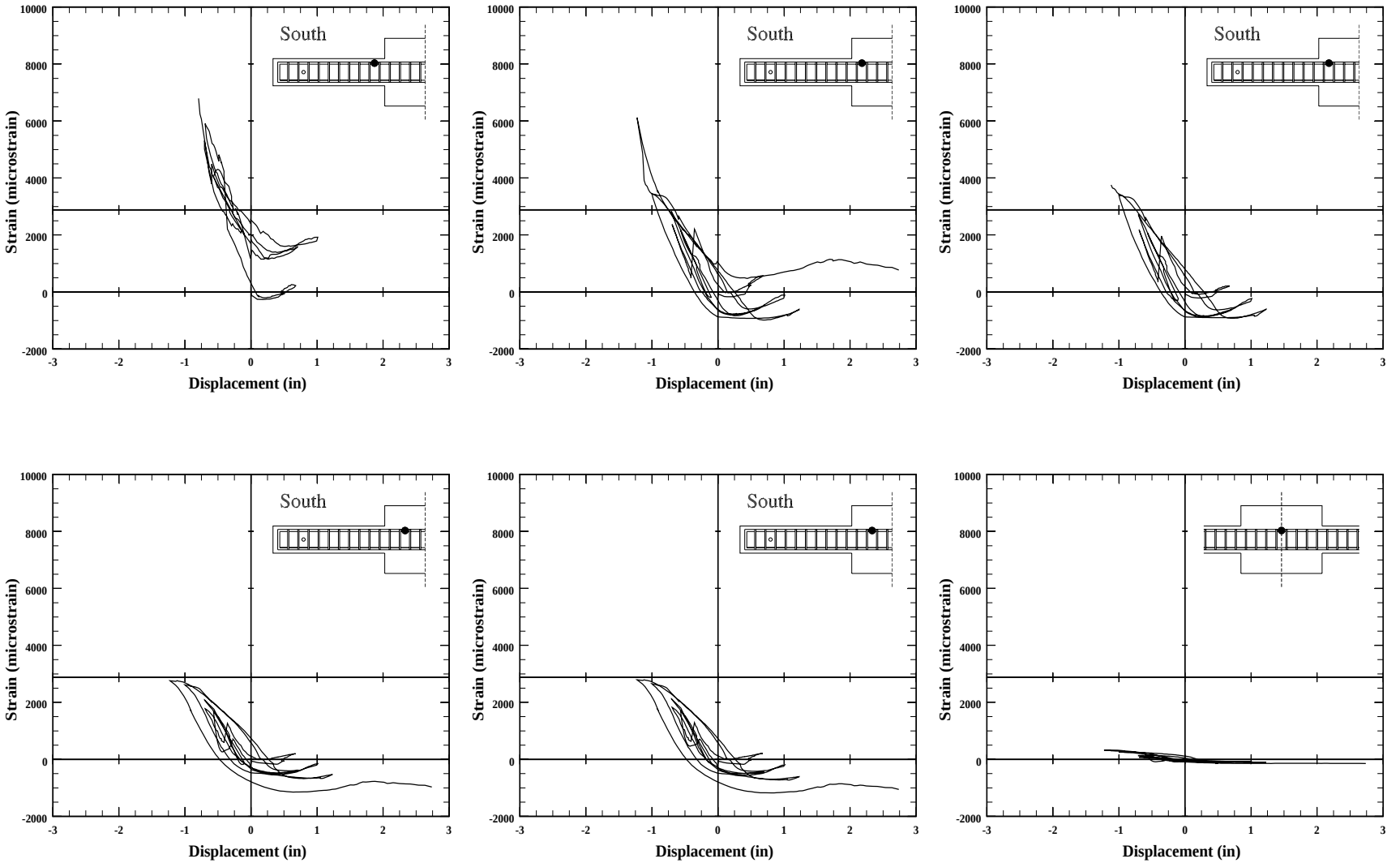

Figure 3.111. Measured longitudinal-bar strain vs load-point displacement for specimen C5-10, top bars.

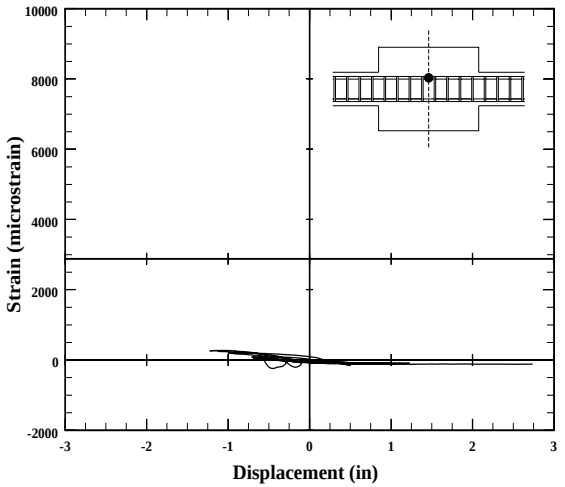
Strain (microstrain)
Displacement (in)

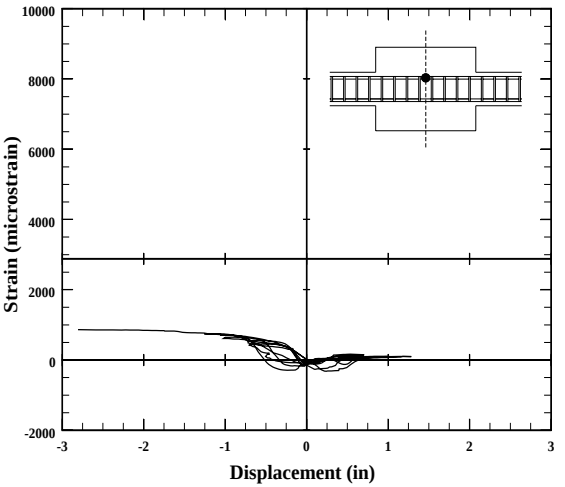
Strain (microstrain)
Displacement (in)

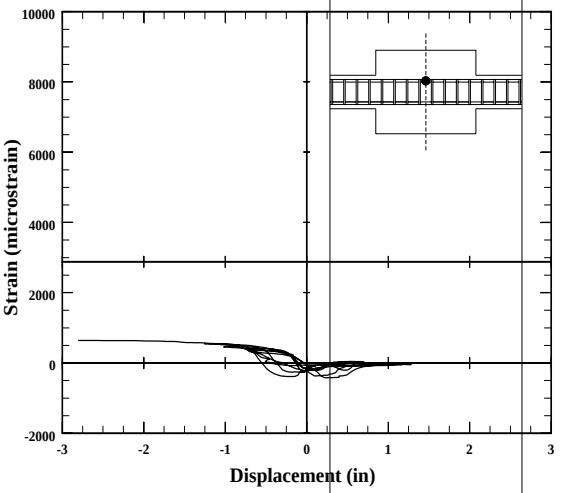
Strain (microstrain)
Displacement (in)

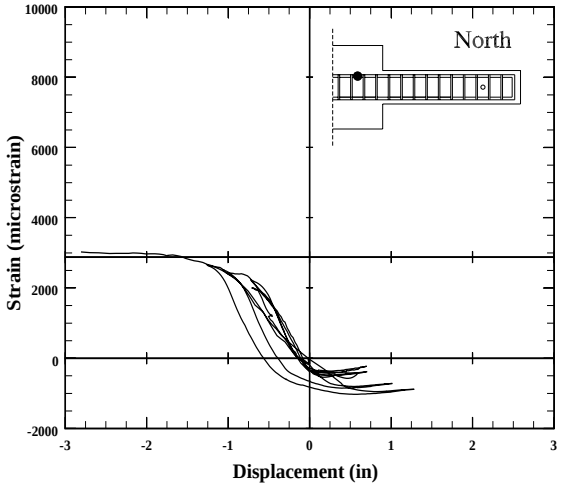
North
Strain (microstrain)
Displacement (in)

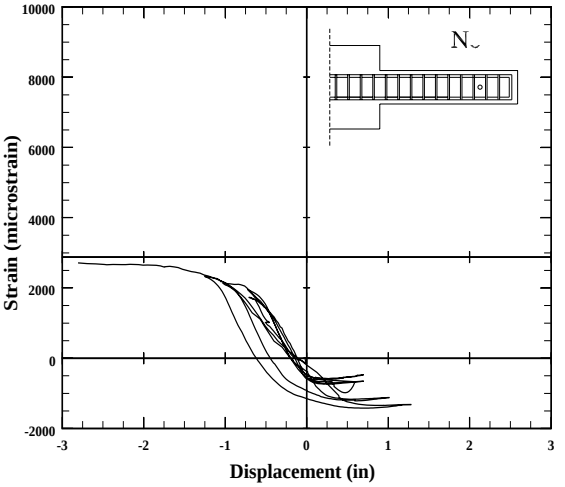
Strain (microstrain)
Displacement (in)

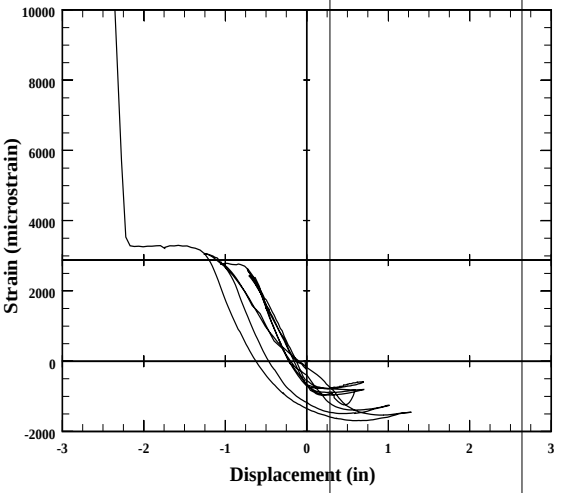
Strain (microstrain)
Displacement (in)

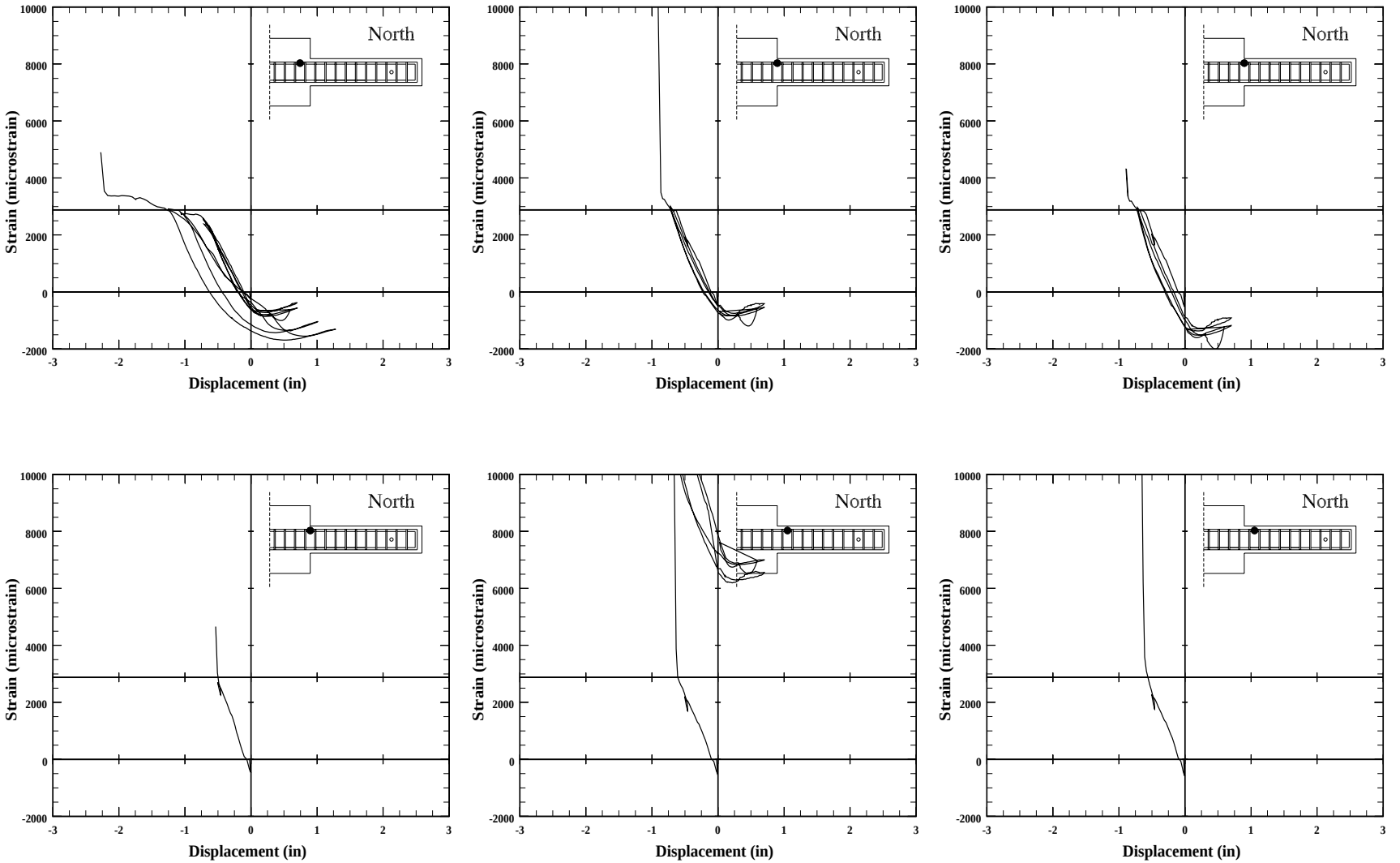

Figure 3.113. Measured longitudinal-bar strain vs load-point displacement for specimen C5-10, top bars.

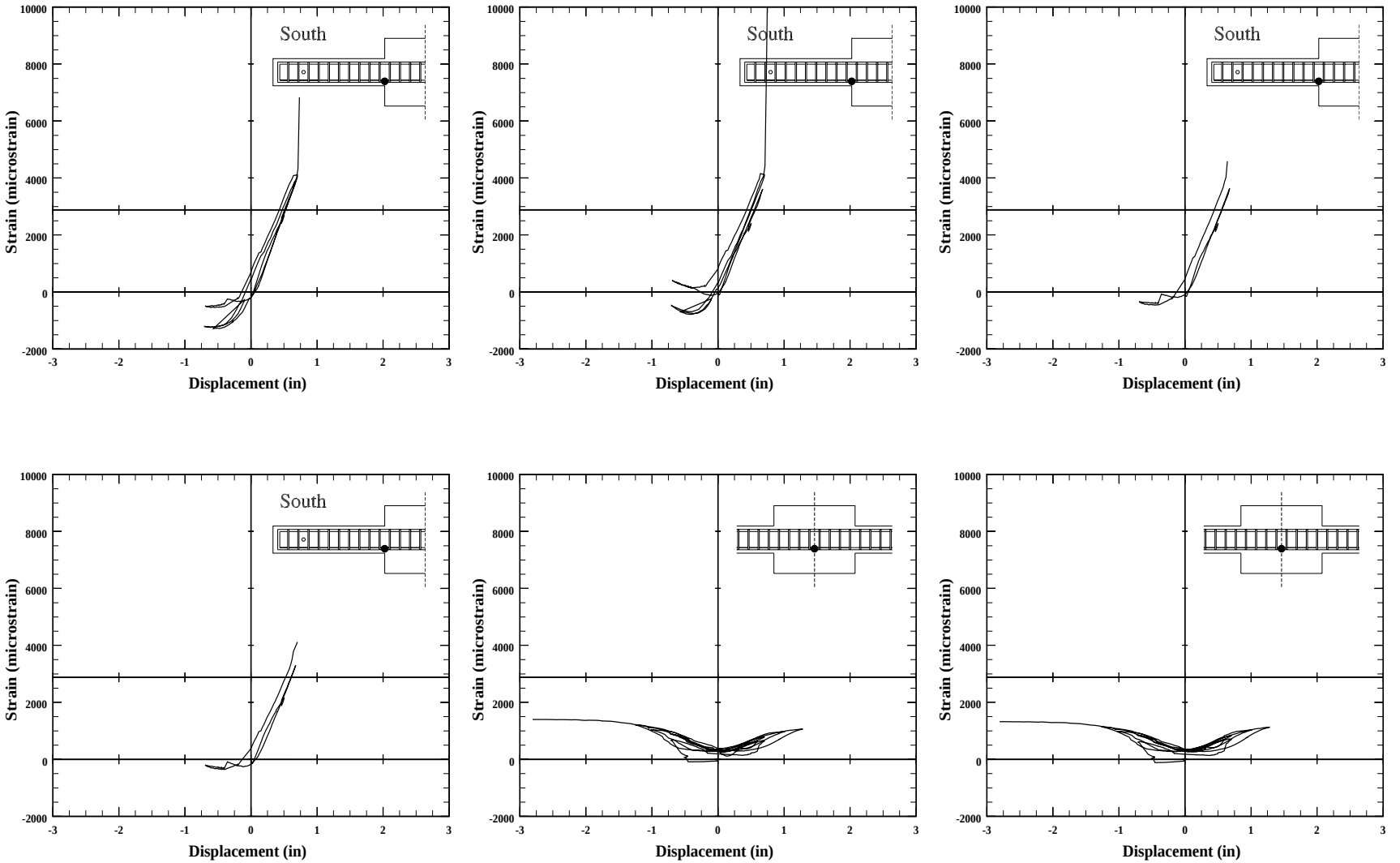

Figure 3.114. Measured longitudinal-bar strain vs load-point displacement for specimen C5-10, bottom bars.

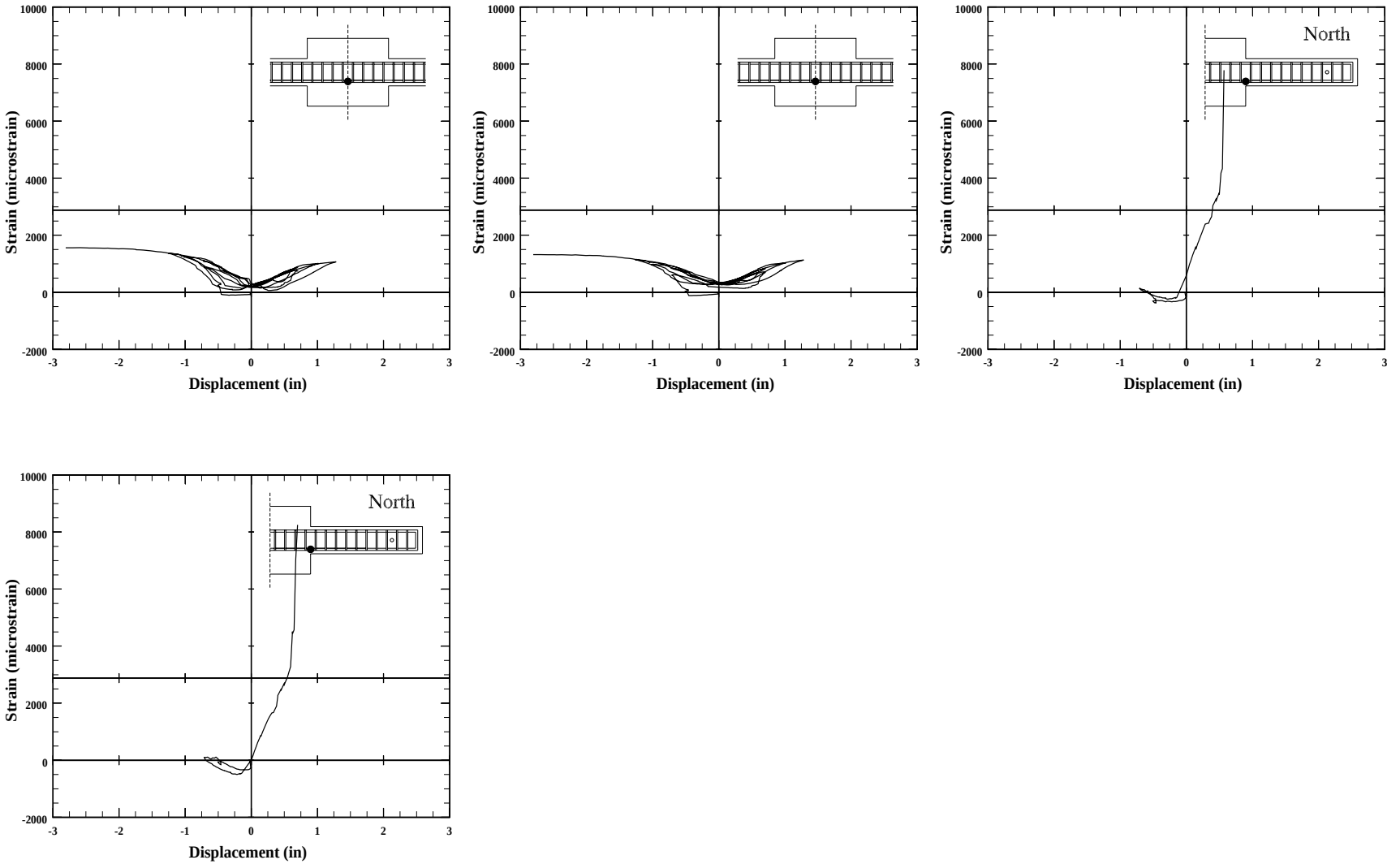

Figure 3.115. Measured longitudinal-bar strain vs load-point displacement for specimen C5-10, bottom bars.

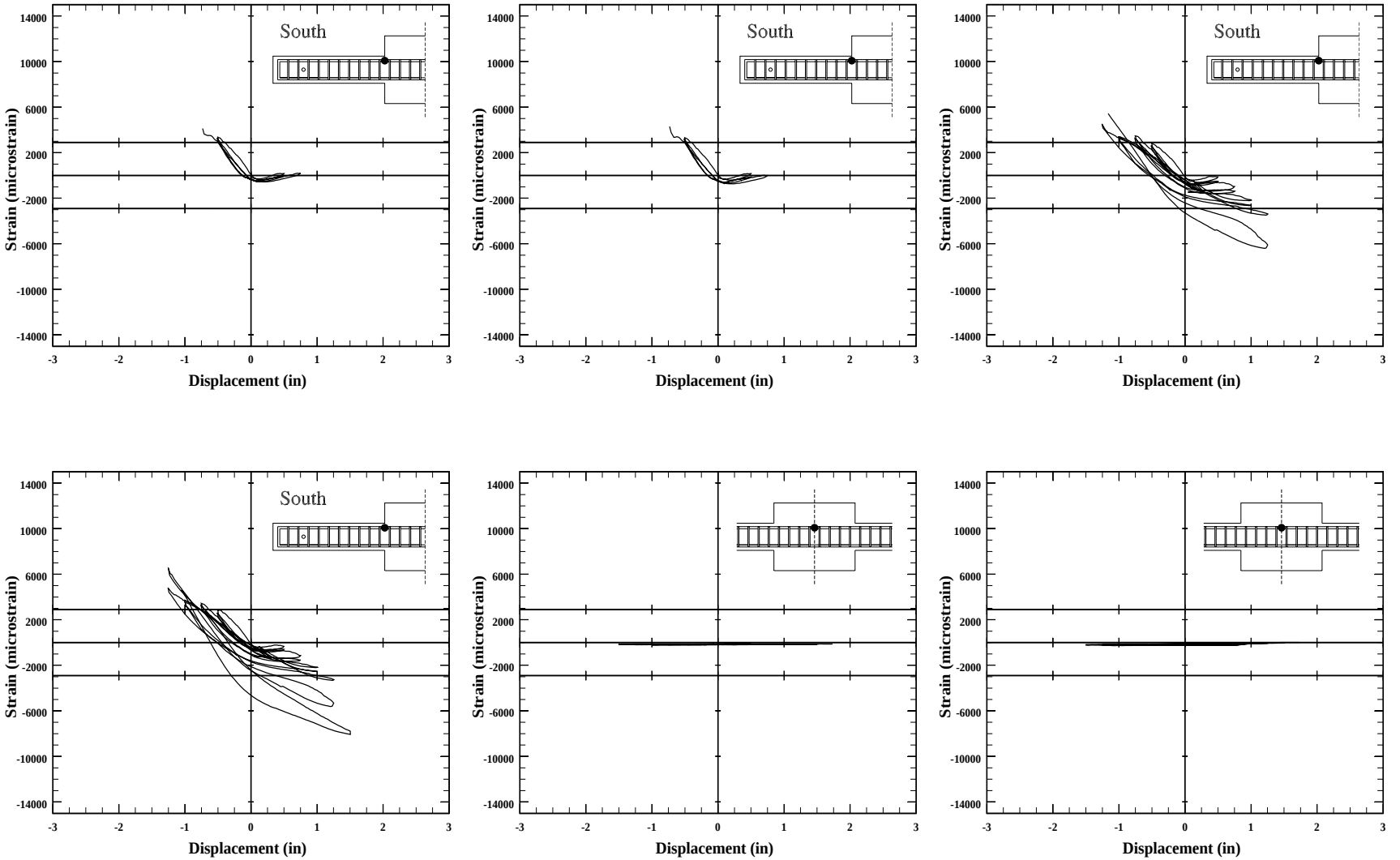

Figure 3.116. Measured longitudinal-bar strain vs load-point displacement for specimen C5-20, top bars.

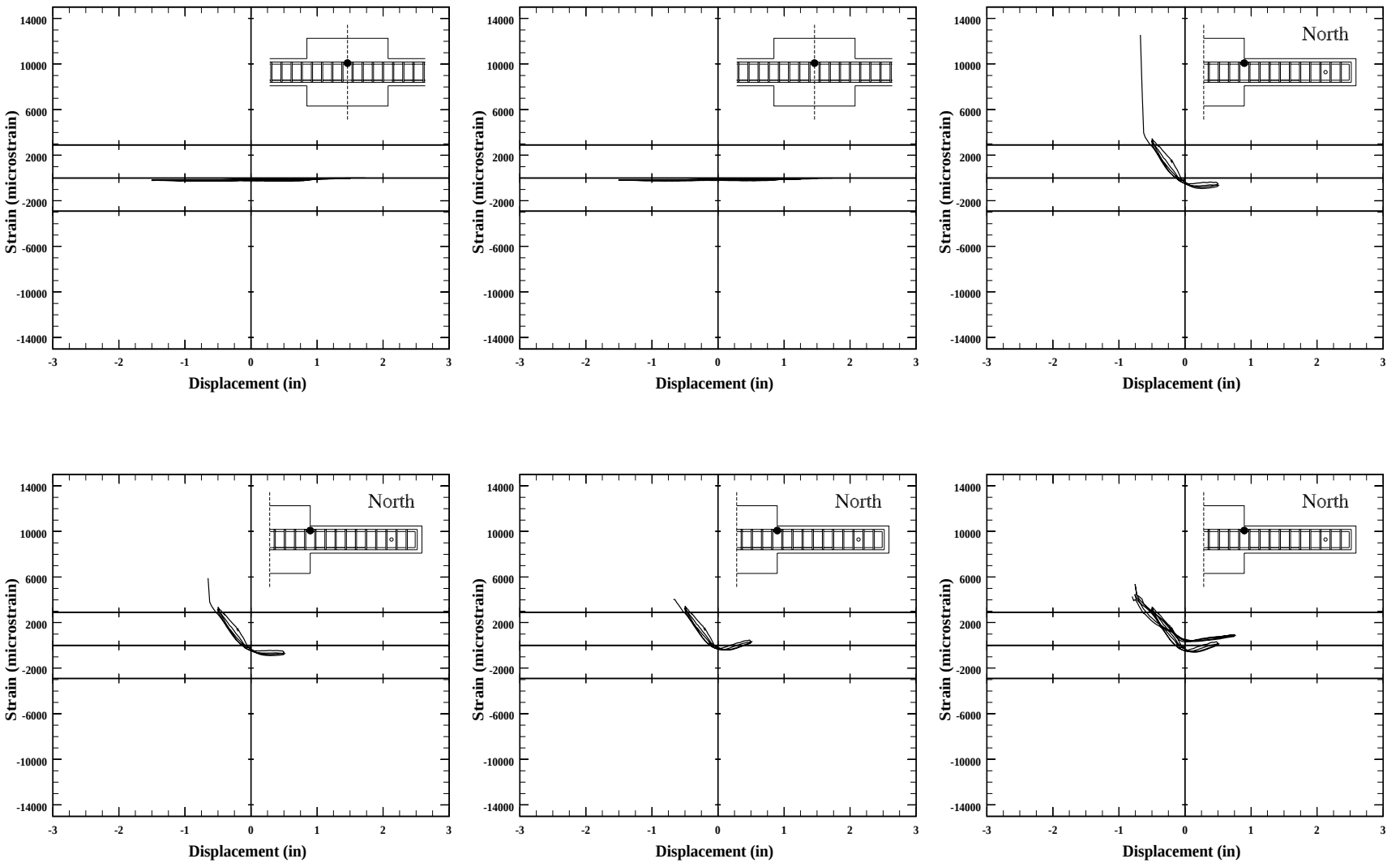

Figure 3.117. Measured longitudinal-bar strain vs load-point displacement for specimen C5-20, top bars.

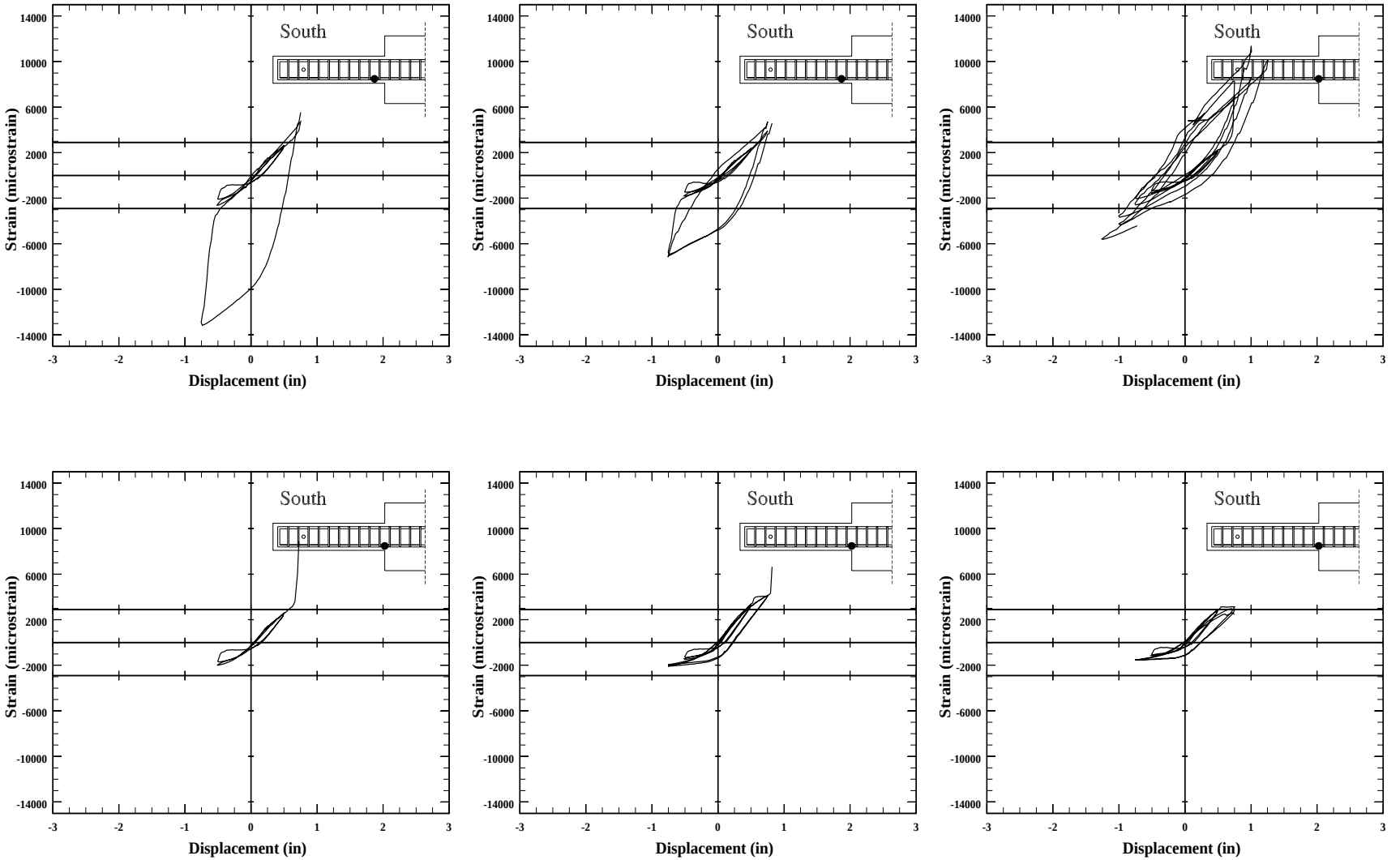

Figure 3.118. Measured longitudinal-bar strain vs load-point displacement for specimen C5-20, bottom bars.

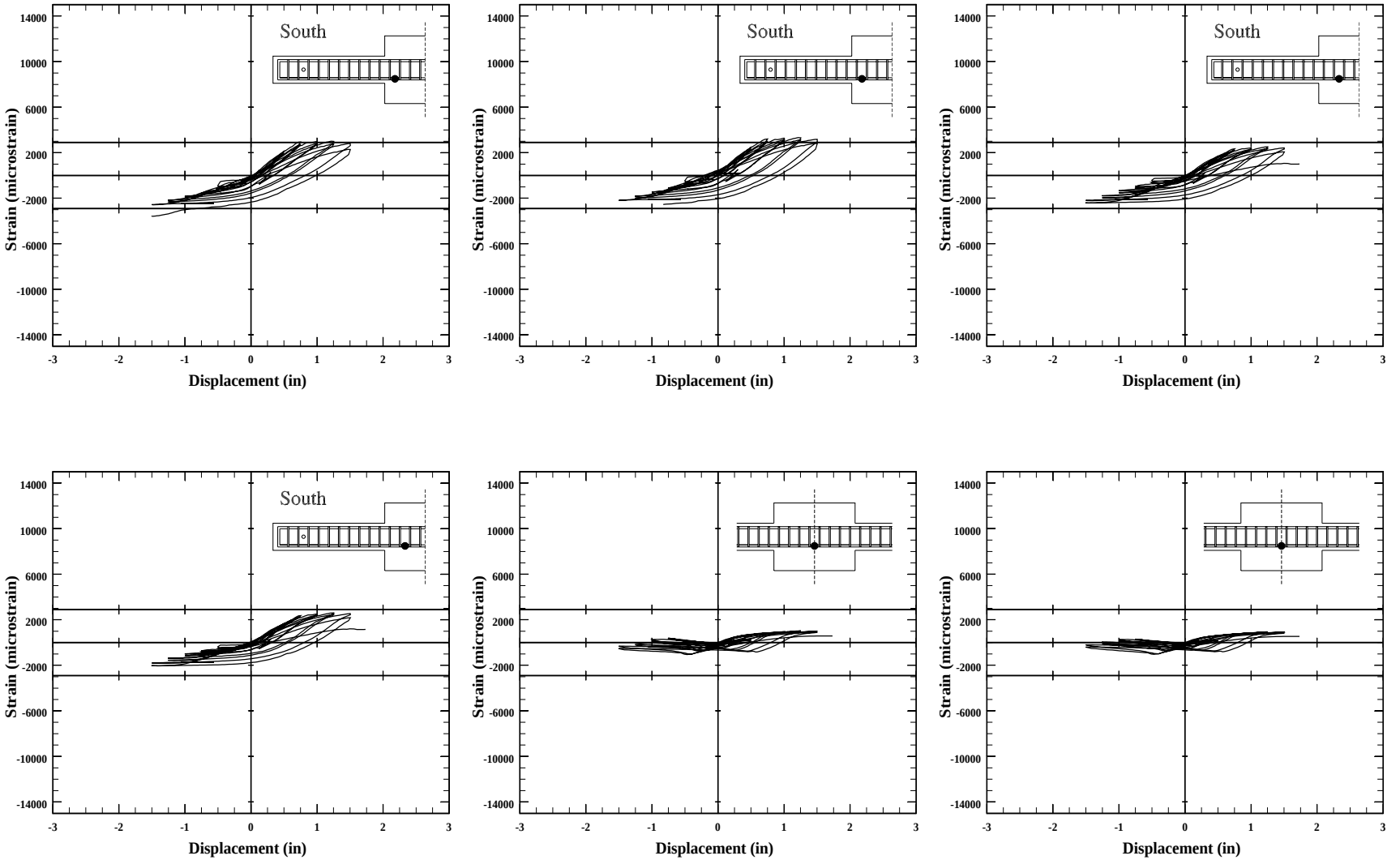

Figure 3.119. Measured longitudinal-bar strain vs load-point displacement for specimen C5-20, bottom bars.

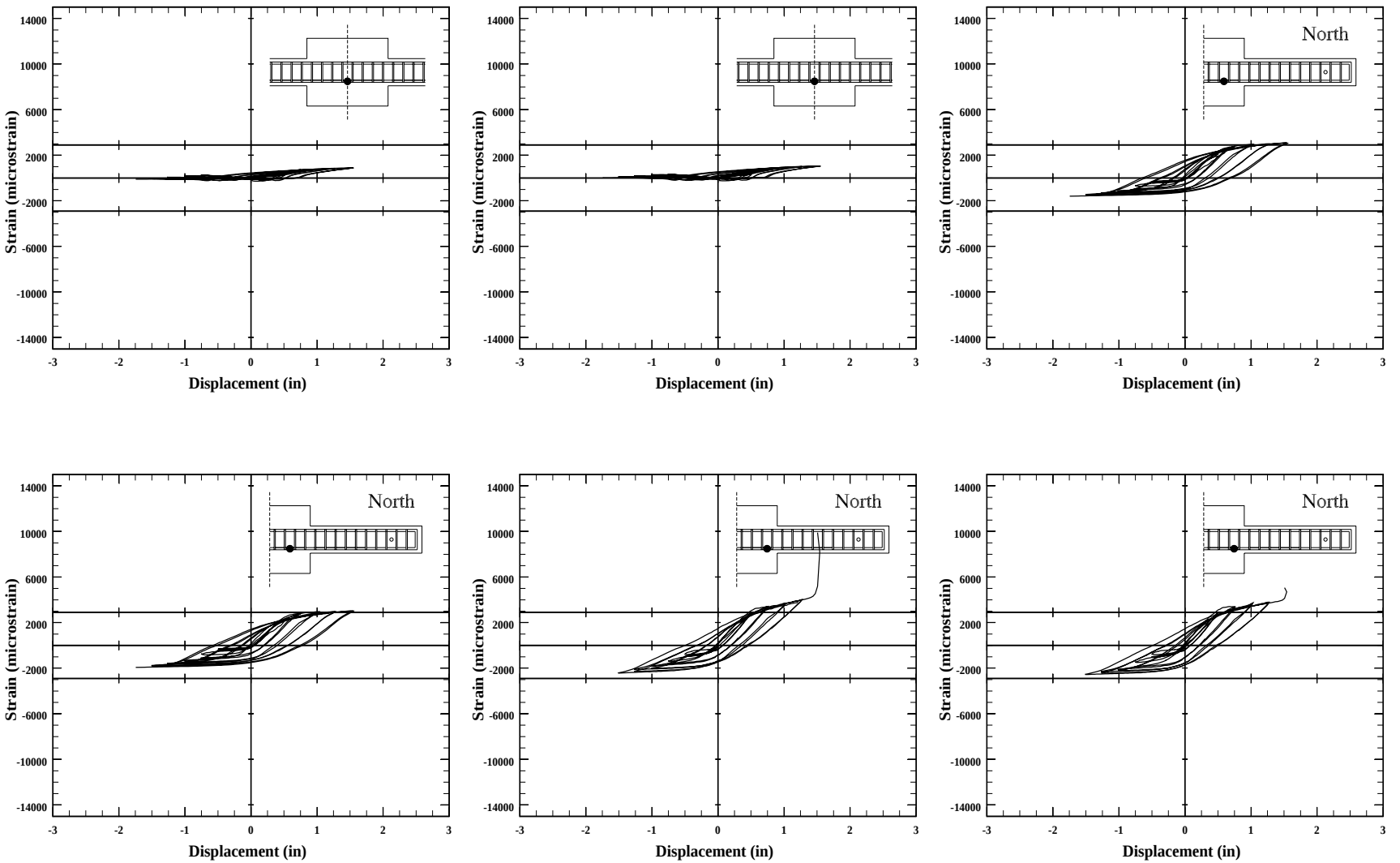

Figure 3.120. Measured longitudinal-bar strain vs load-point displacement for specimen C5-20, bottom bars.

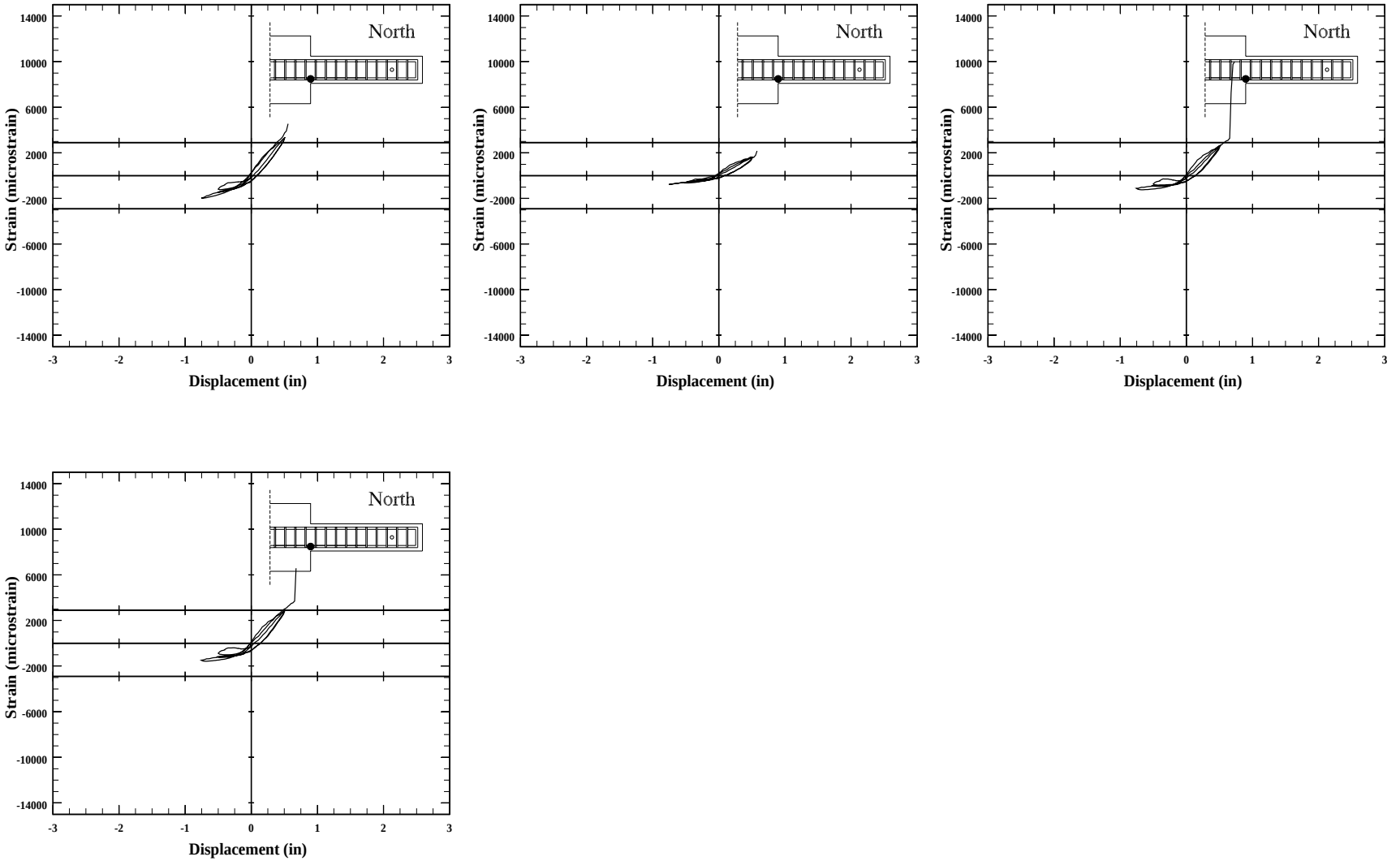

Figure 3.121. Measured longitudinal-bar strain vs load-point displacement for specimen C5-20, bottom bars.

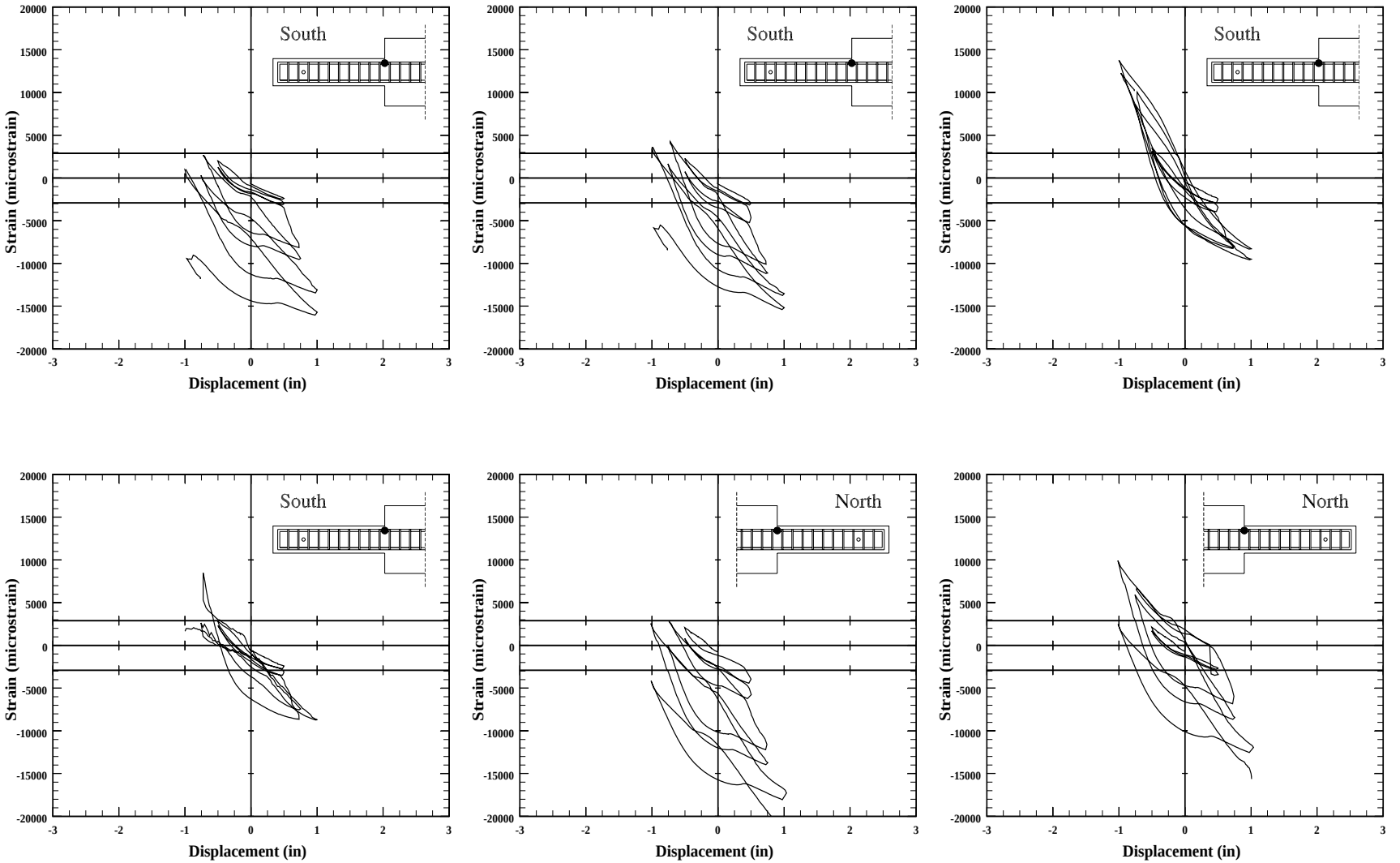

Figure 3.122. Measured longitudinal-bar strain vs load-point displacement for specimen C5-40, top bars.

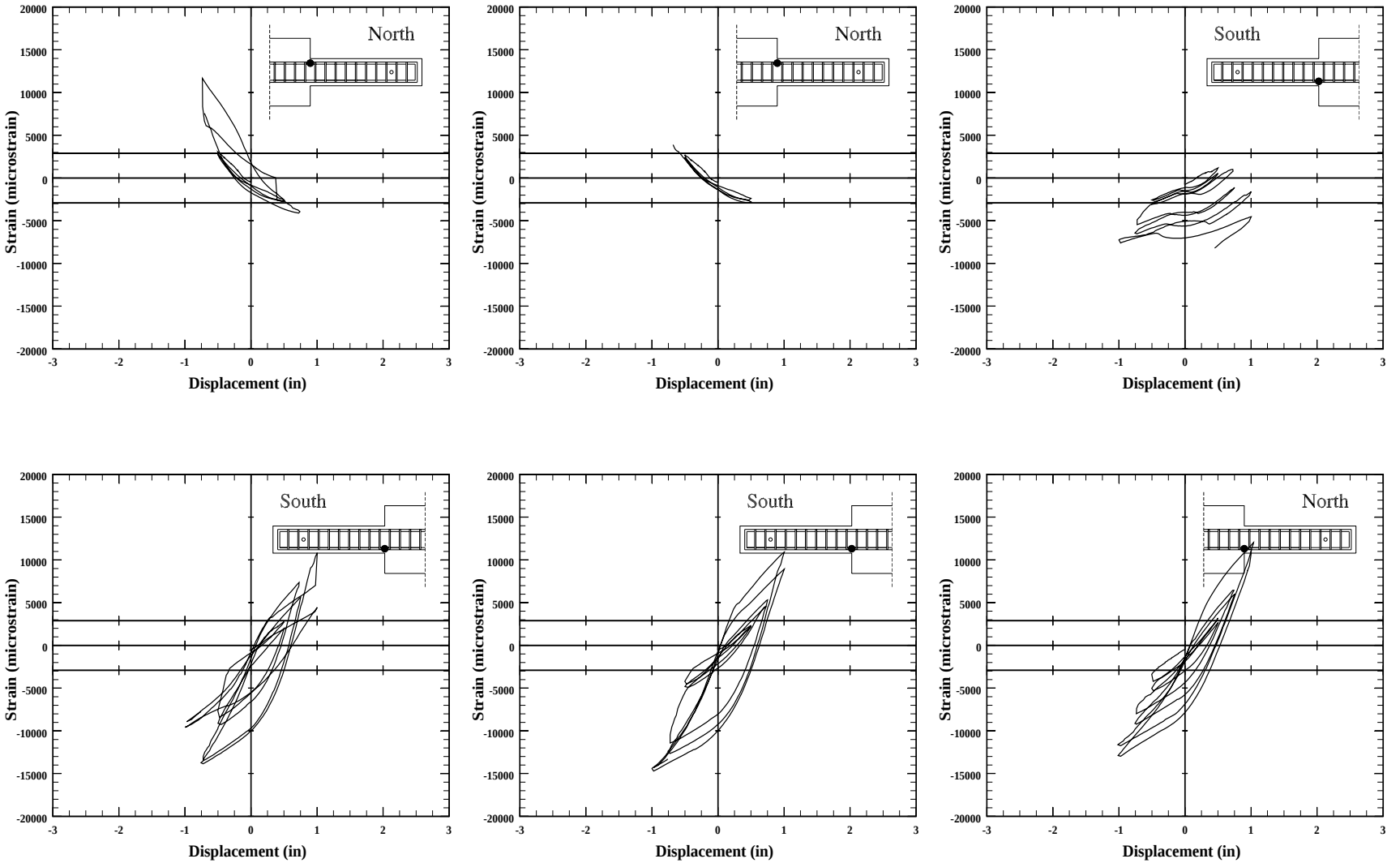

Figure 3.123. Measured longitudinal-bar strain vs load-point displacement for specimen C5-40, top and bottom bars.

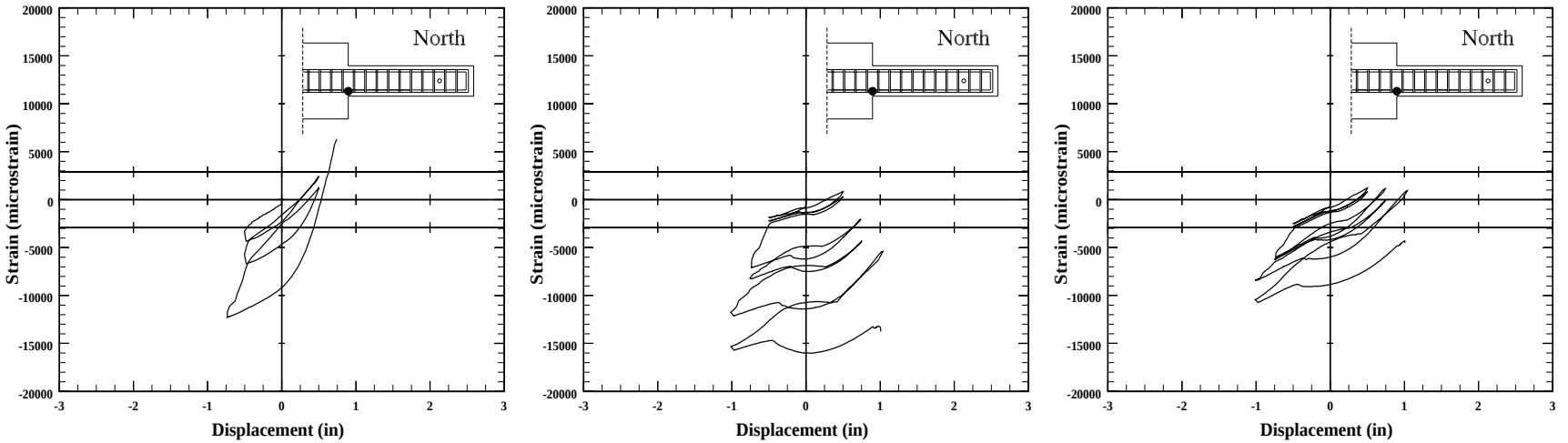

Figure 3.124. Measured longitudinal-bar strain vs load-point displacement for specimen C5-40, top bottom bars.

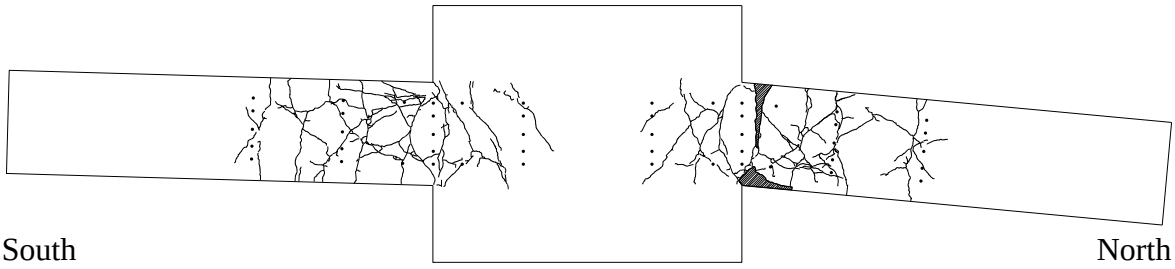

Figure 3.125. Location of cracks in specimen C10-00 at the end of the test.

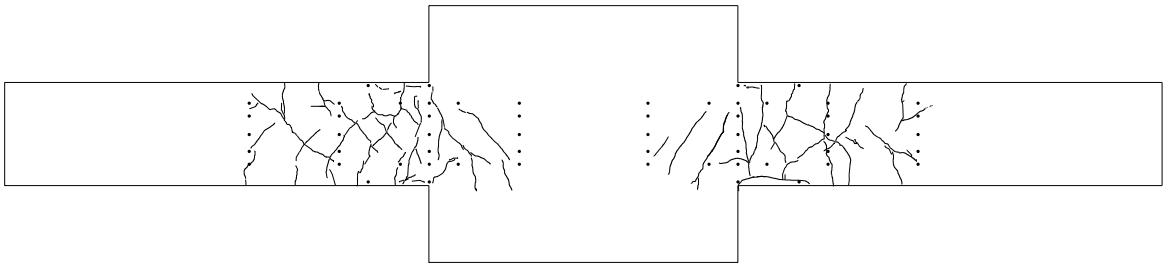

Figure 3.126. Location of cracks in specimen C10-05 after two cycles to a maximum deformation of 0.5 in.

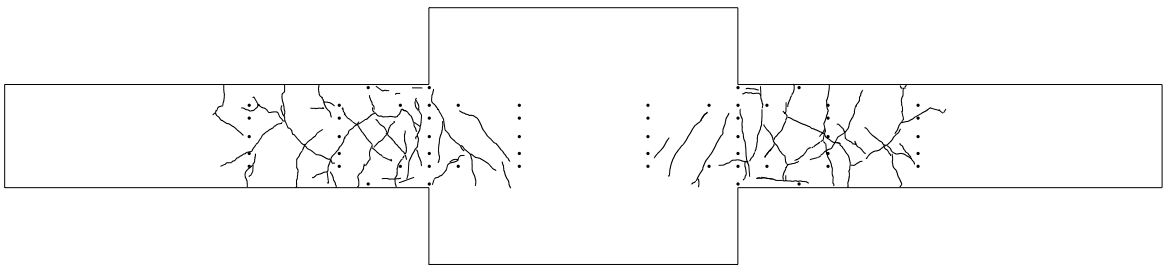

Figure 3.127. Location of cracks in specimen C10-05 after two cycles to a maximum deformation of 0.75 in.

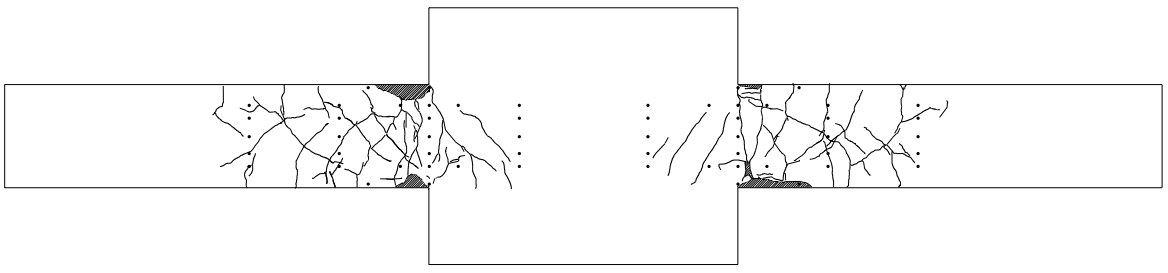

Figure 3.128. Location of cracks in specimen C10-05 after two cycles to a maximum deformation of 1.0 in.

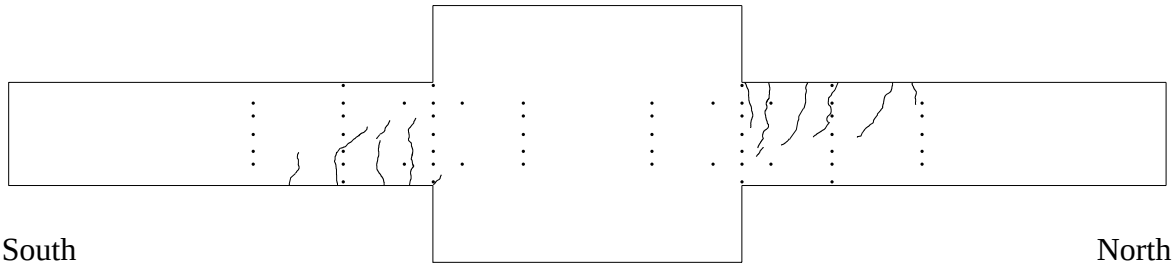

Figure 3.129. Location of cracks in specimen C10-10 at a deformation of 0.25 in. in the positive direction.

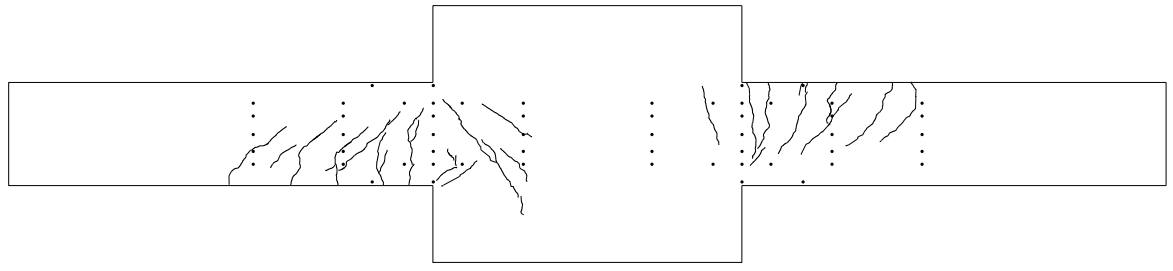

Figure 3.130. Location of cracks in specimen C10-10 at a deformation of 0.50 in. in the positive direction (at end of first quarter cycle).

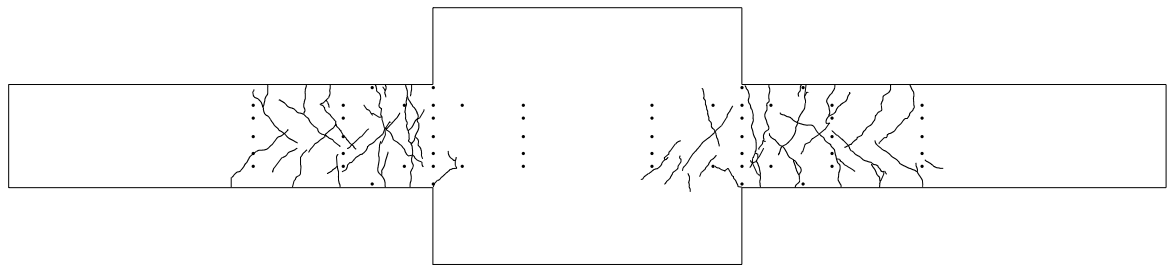

Figure 3.131. Location of cracks in specimen C10-10 at a deformation of 0.25 in. in the negative direction.

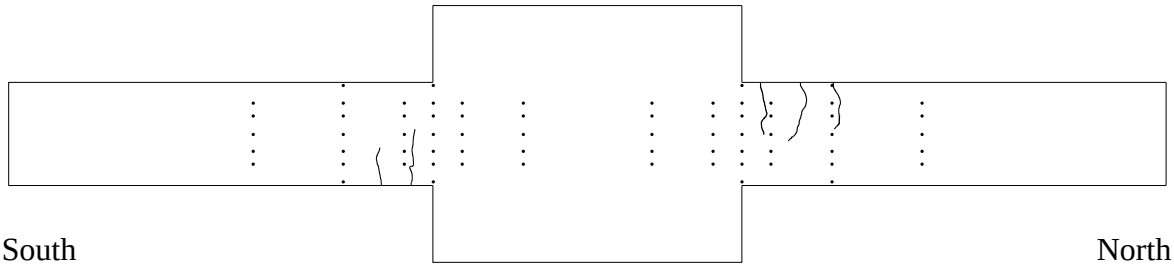

Figure 3.132. Location of cracks in specimen C10-20 at a deformation of 0.25 in. in the positive direction.

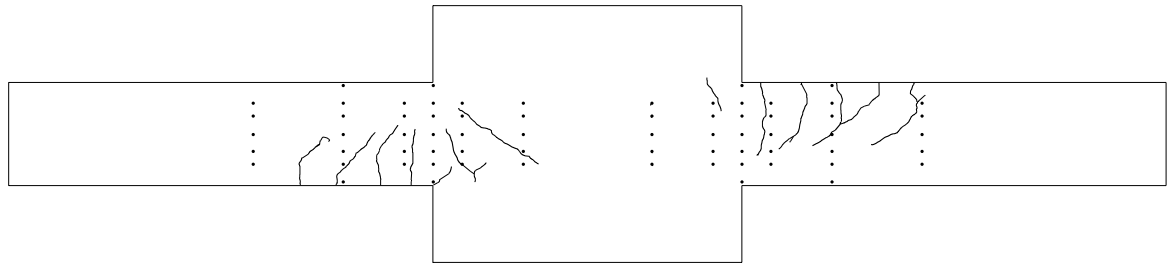

Figure 3.133. Location of cracks in specimen C10-20 at a deformation of 0.50 in. in the positive direction (at end first quarter cycle).

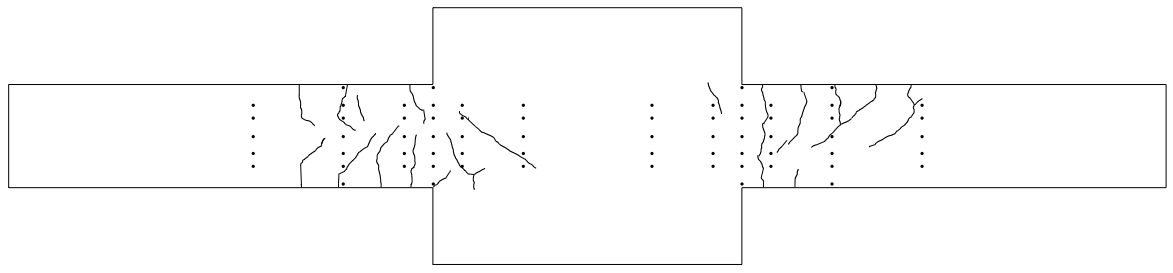

Figure 3.134. Location of cracks in specimen C10-10 at a deformation of 0.25 in. in the negative direction.

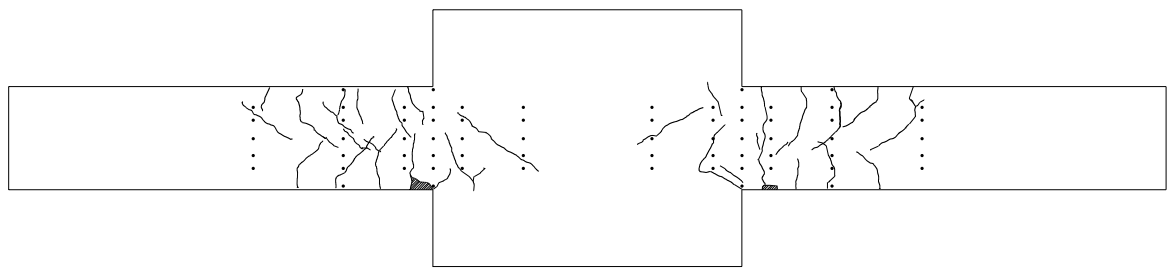

Figure 3.135. Location of cracks in specimen C10-10 at a deformation of 0.5 in. in the negative direction (at third quarter of first cycle).

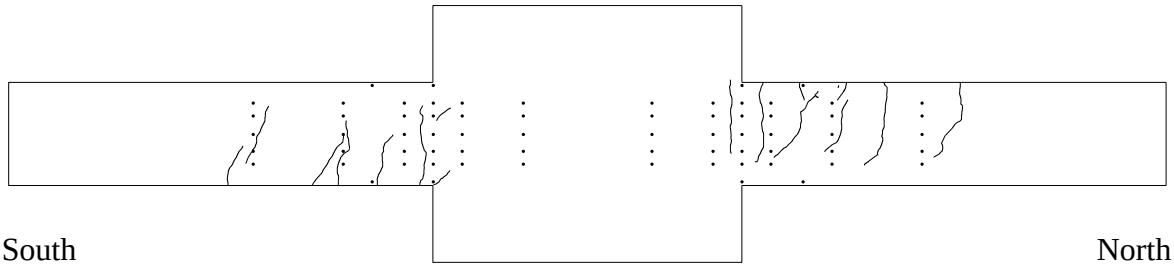

Figure 3.136. Location of cracks in specimen C5-00 at a deformation of 0.25 in. in the positive direction.

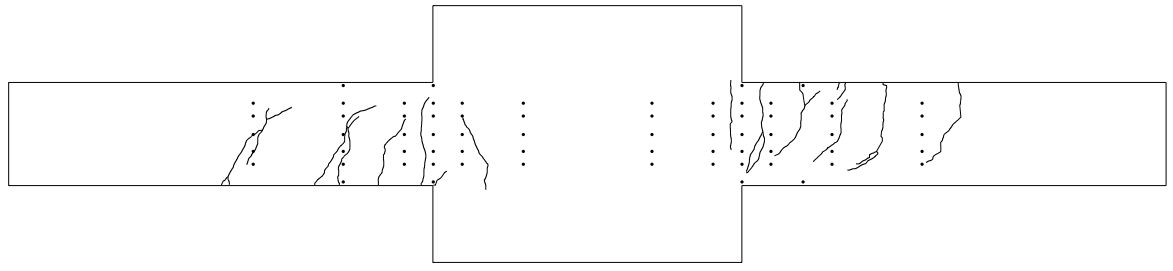

Figure 3.137. Location of cracks in specimen C5-00 at a deformation of 0.50 in. in the positive direction (at end first quarter cycle).

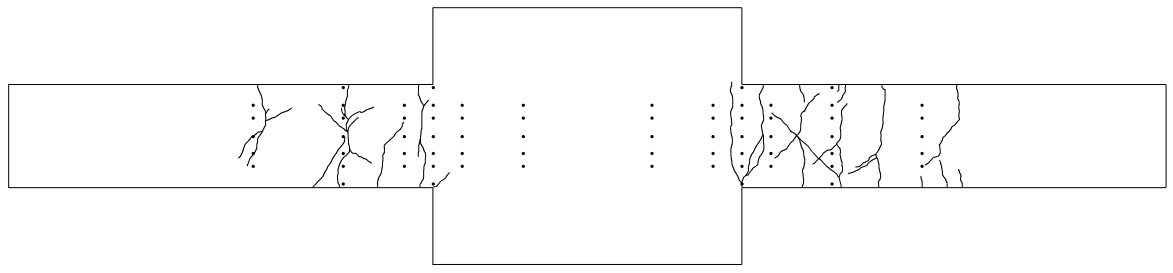

Figure 3.138. Location of cracks in specimen C5-00 at a deformation of 0.25 in. in the negative direction.

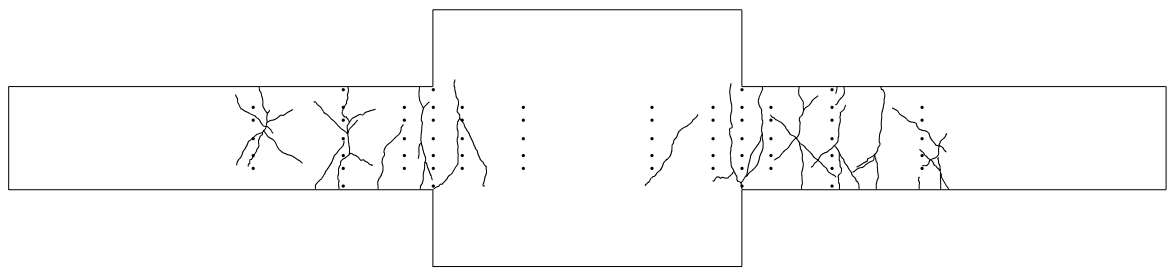

Figure 3.139. Location of cracks in specimen C5-00 at a deformation of 0.5 in. in the negative direction (at third quarter of first cycle).

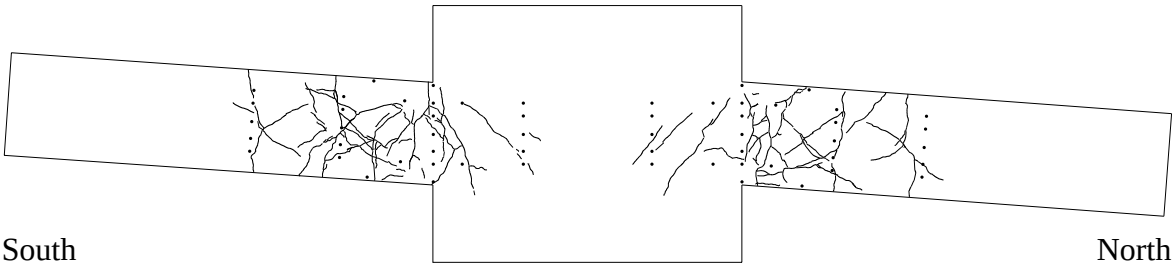

Figure 3.140. Location of cracks in specimen C5-10 at the end of the test.

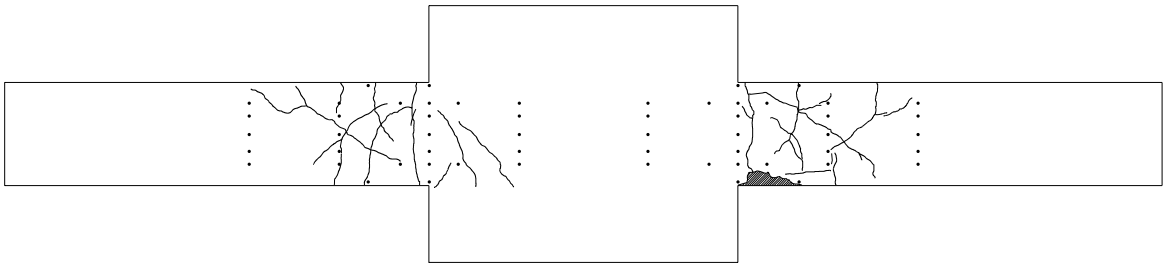

Figure 3.141. Location of cracks in specimen C5-20 at the end of the second cycle.

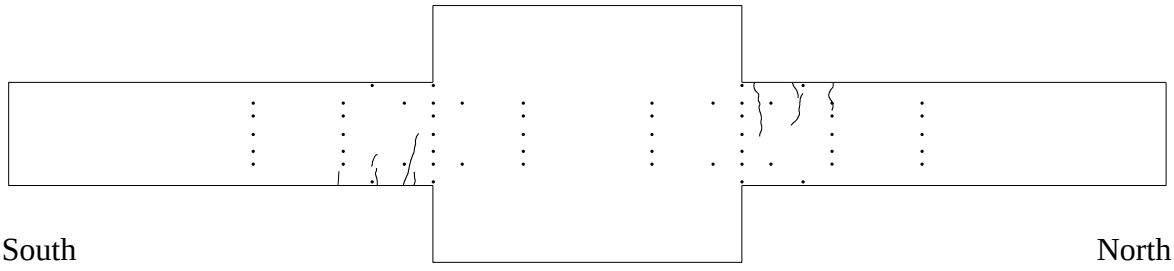

Figure 3.142. Location of cracks in specimen C5-40 at a deformation of 0.25 in. in the positive direction.

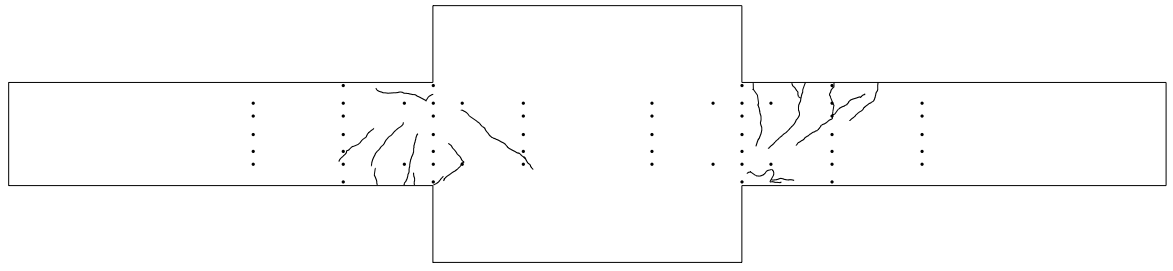

Figure 3.143. Location of cracks in specimen C5-40 at a deformation of 0.50 in. in the positive direction (at end first quarter cycle).

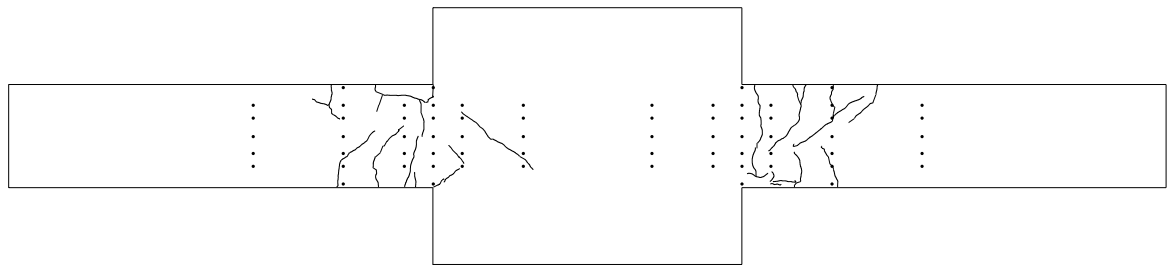

Figure 3.144. Location of cracks in specimen C5-40 at a deformation of 0.25 in. in the negative direction.

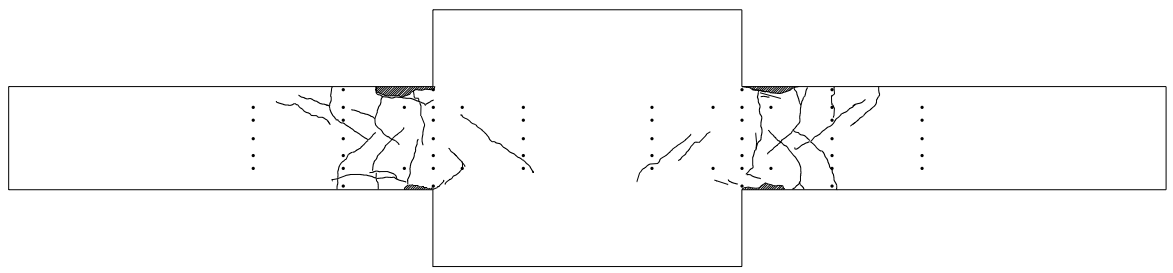

Figure 3.145. Location of cracks in specimen C5-40 at the end of the second cycle.

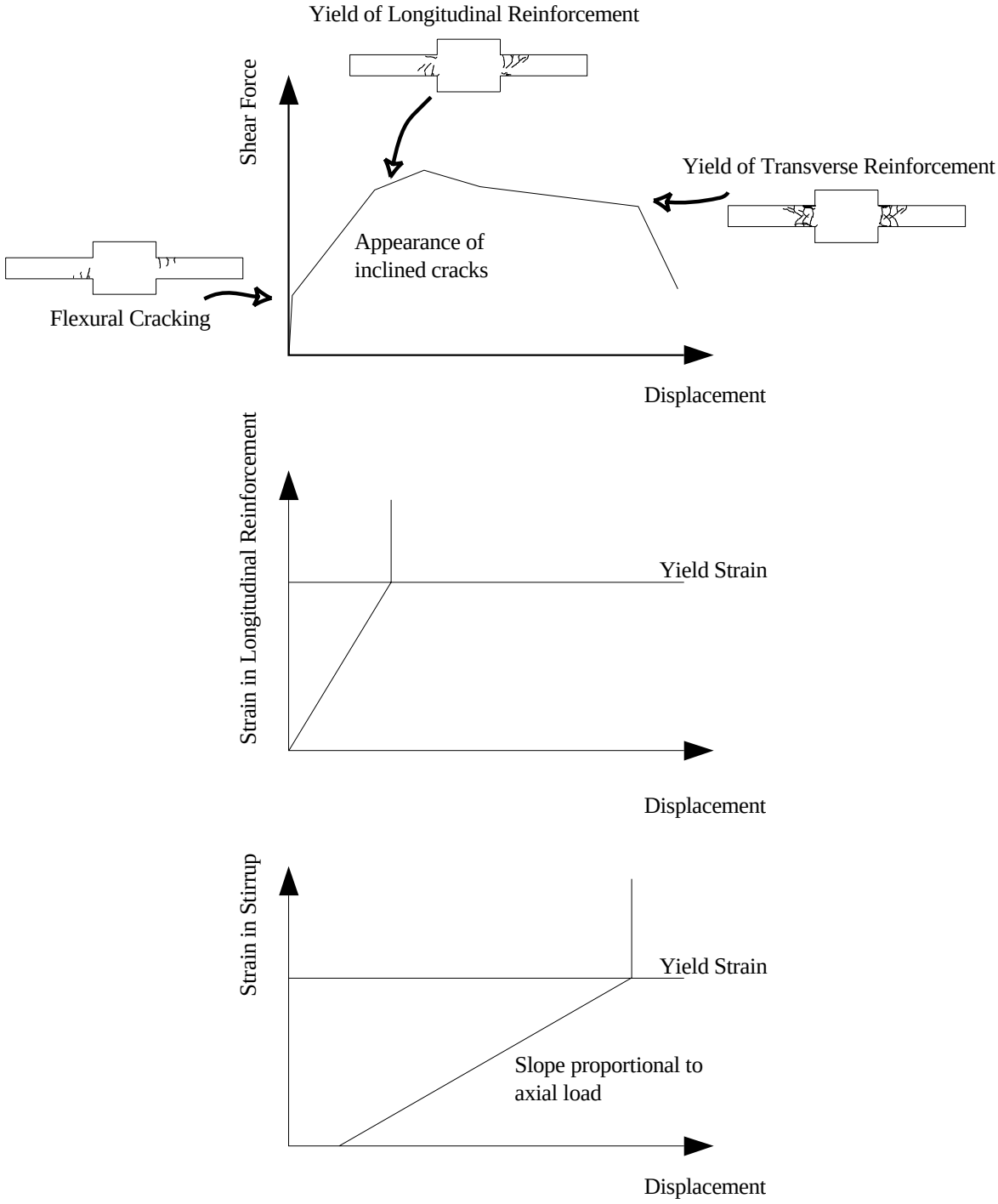

Figure 3.146. Summary of observed behavior.

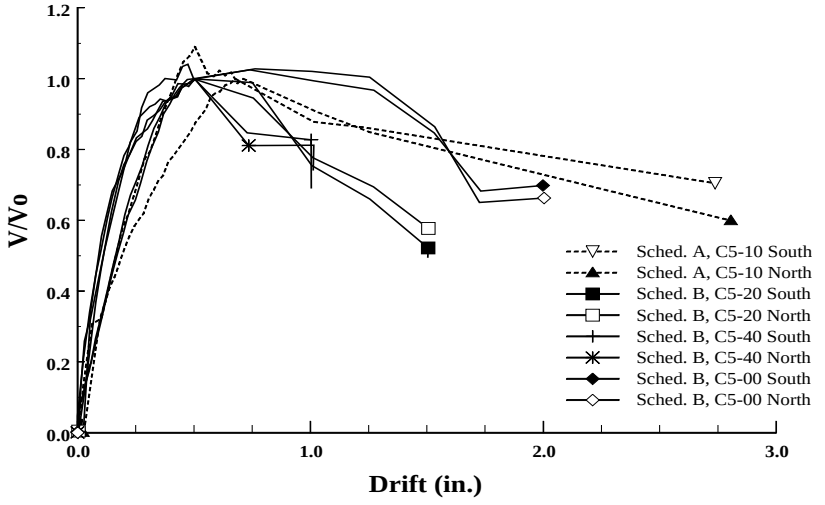

Figure 3.147. Comparison of Shear-Displacement envelope curves for normal-strength specimens.

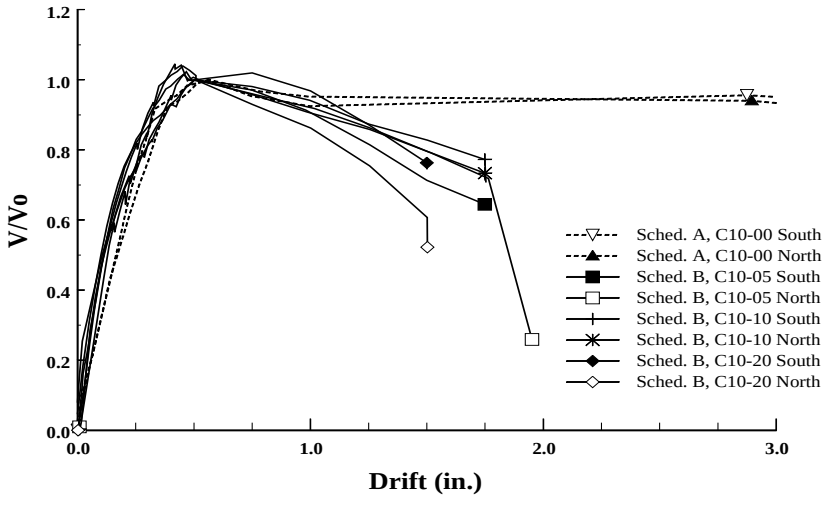

Figure 3.148. Comparison of Shear-Displacement envelope curves for high-strength specimens.

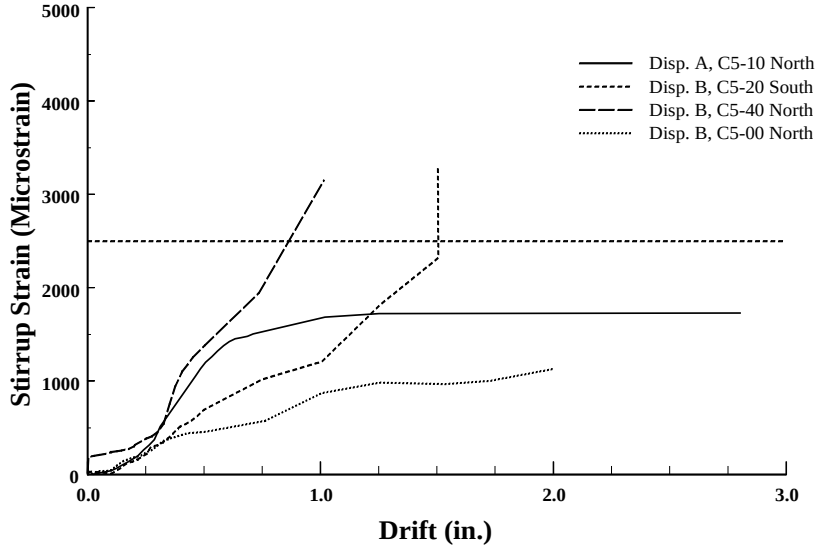

Figure 3.149. Comparison of Strain-Displacement envelope curves for critical stirrup of normal-strength specimens.

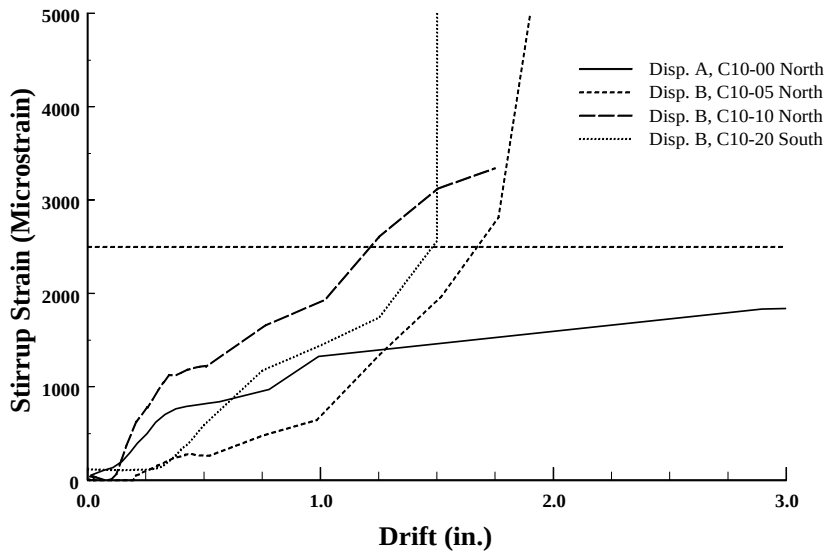

Figure 3.150. Comparison of Strain-Displacement envelope curves for critical stirrup of high-strength specimens.

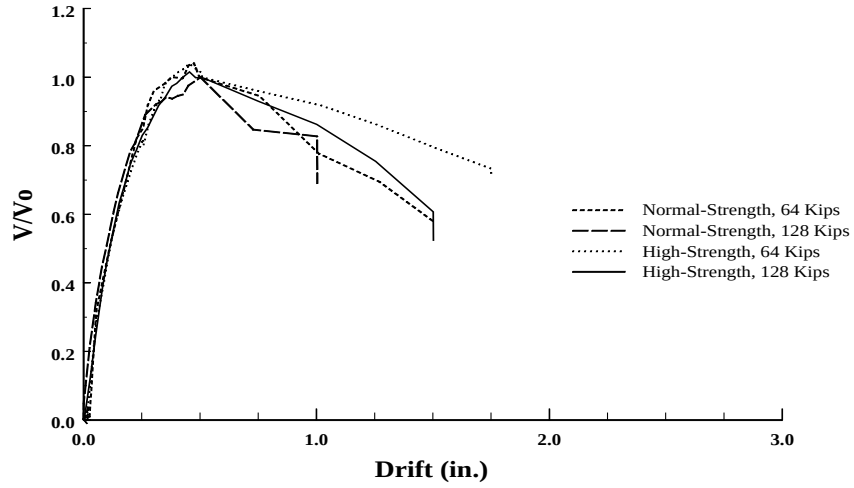

Figure 3.151. Comparison of Shear-Displacement envelope curves for specimens with similar axial loads.

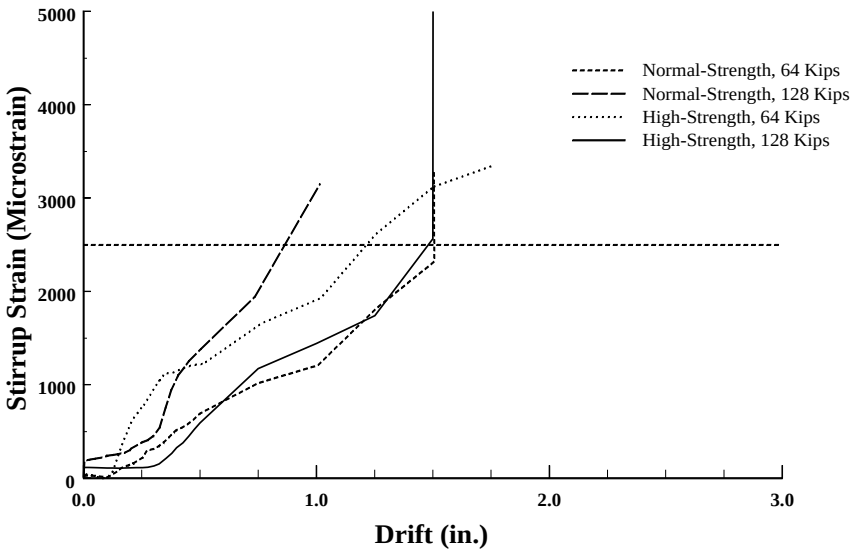

Figure 3.152. Comparison of Strain-Displacement curves for critical stirrup of specimens with similar axial loads.

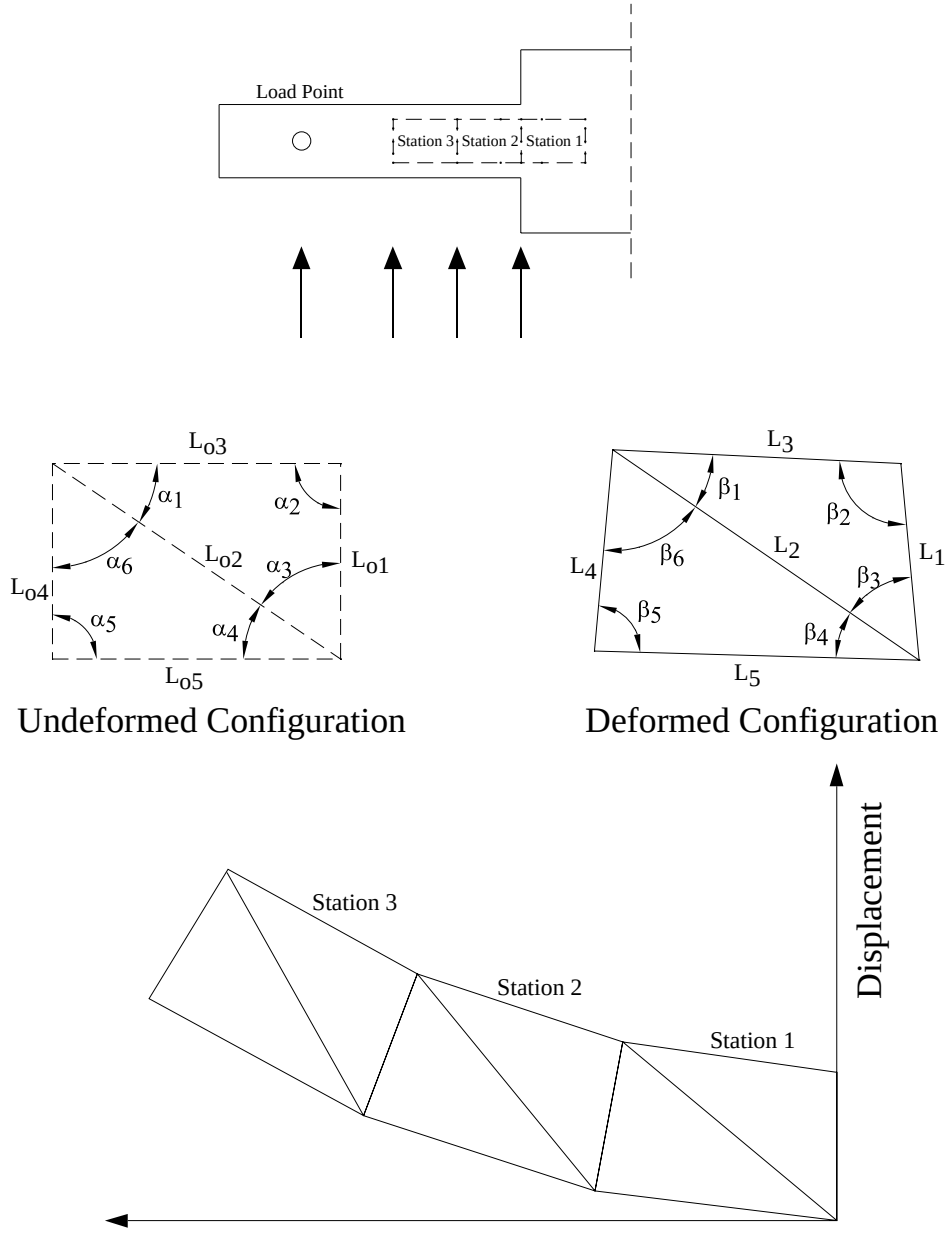

Figure 4.1. Parameters to calculate vertical deflections based on electronic Whittemore gage readings.

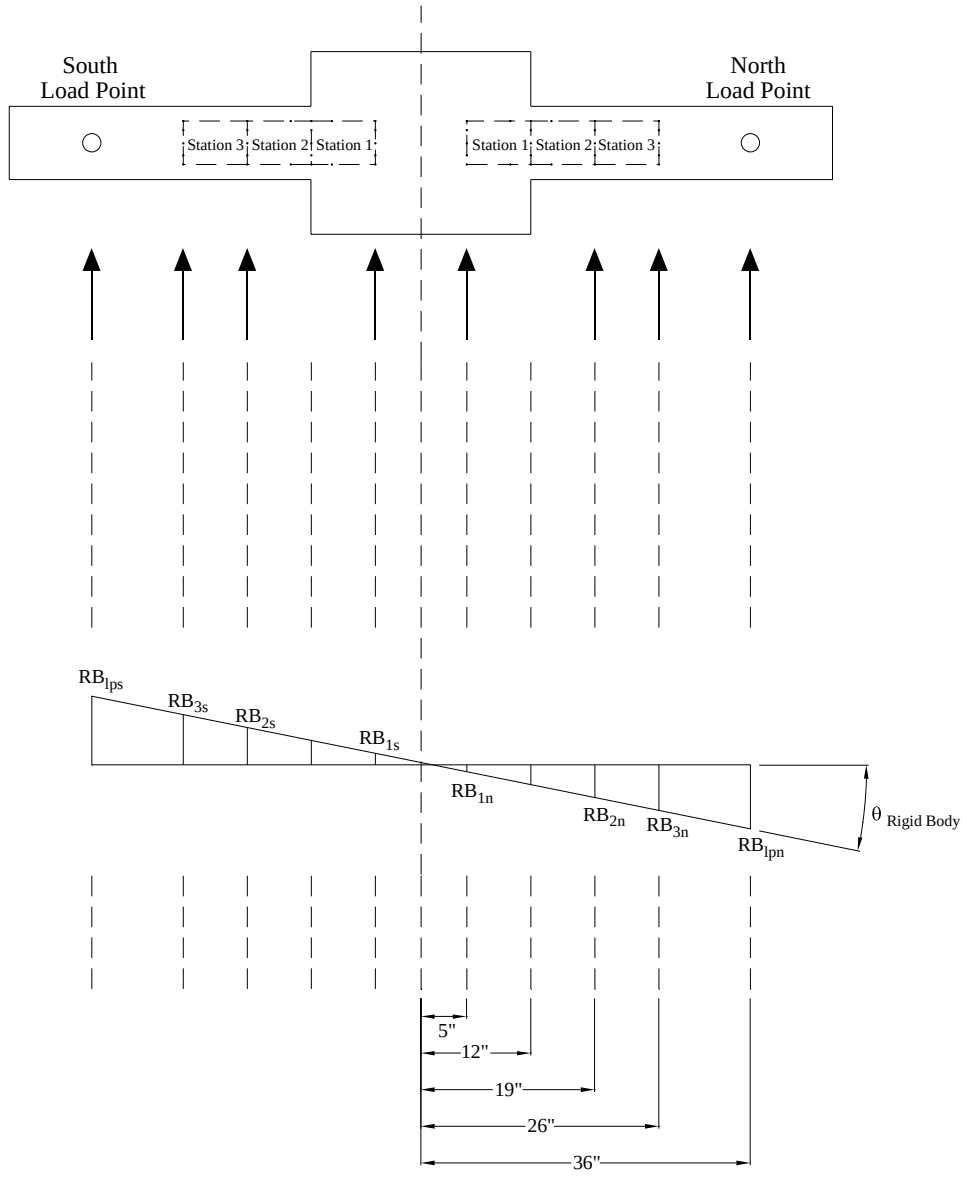

Figure 4.2. Model used to calculate the rigid body displacements.

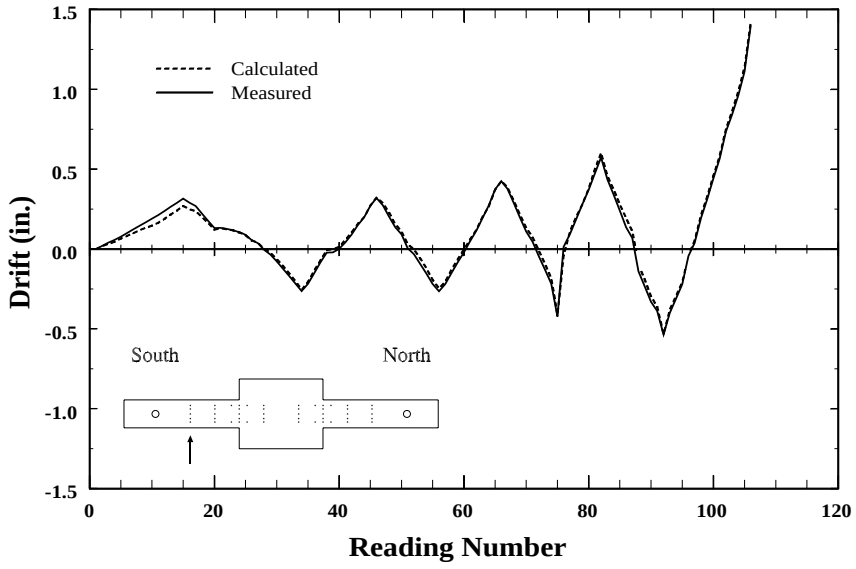

Figure 4.3. Comparison between measured and calculated displacements related to shear, flexure, and slip. Specimen C10-00, south element, station3.

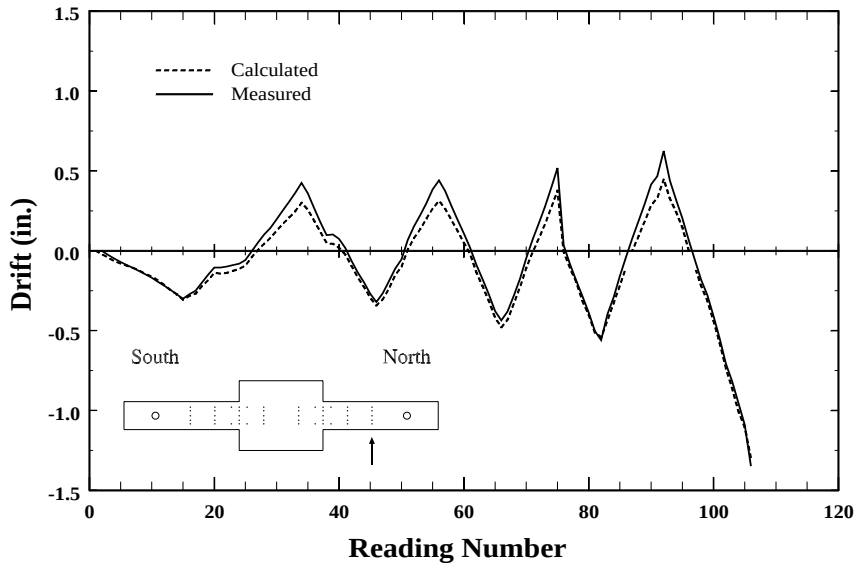

Figure 4.4. Comparison between measured and calculated displacements related to shear, flexure, and slip. Specimen C10-00, north element, station3.

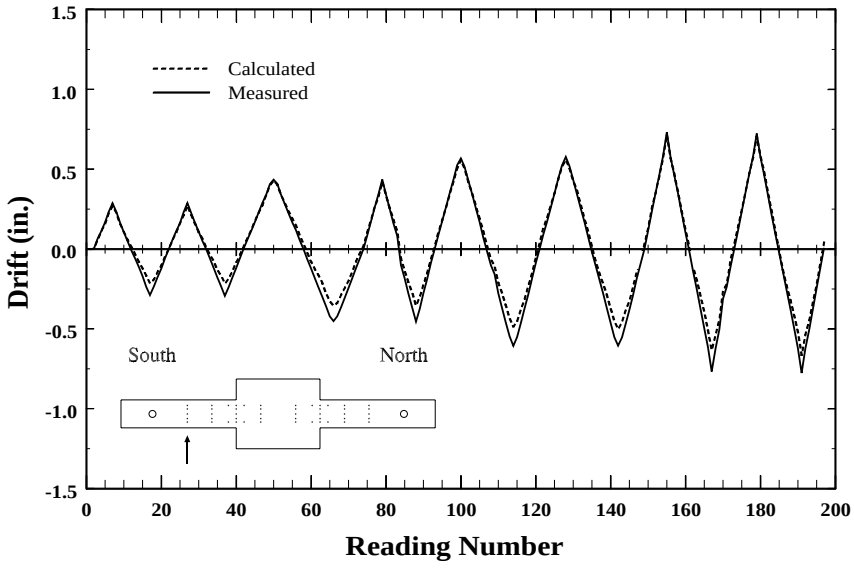

Figure 4.5. Comparison between measured and calculated displacements related to shear, flexure, and slip. Specimen C10-05, south element, station3.

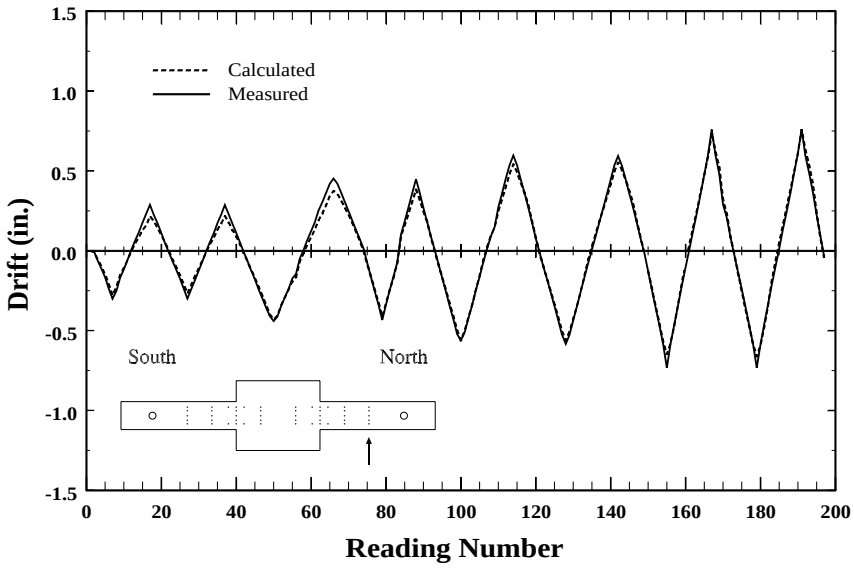

Figure 4.6. Comparison between measured and calculated displacements related to shear, flexure, and slip. Specimen C10-05, north element, station3.

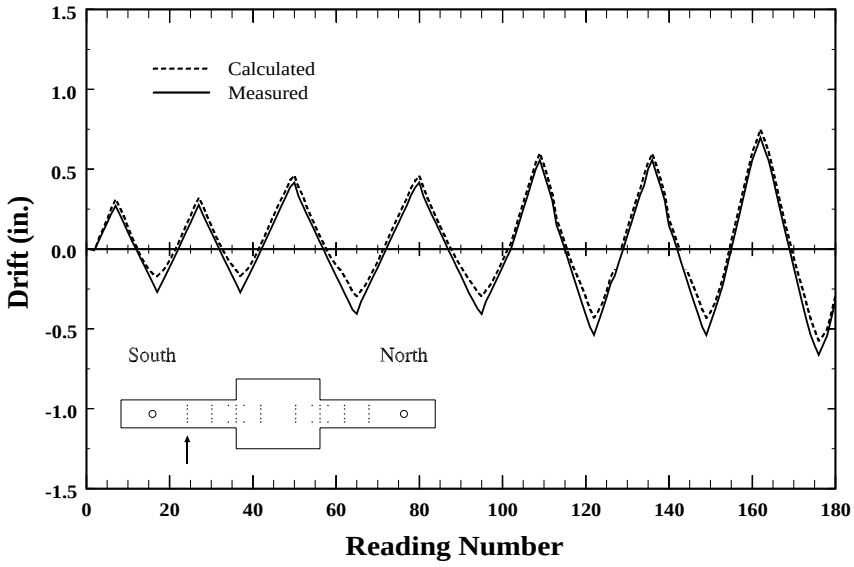

Figure 4.7. Comparison between measured and calculated displacements related to shear, flexure, and slip. Specimen C10-10, south element, station3.

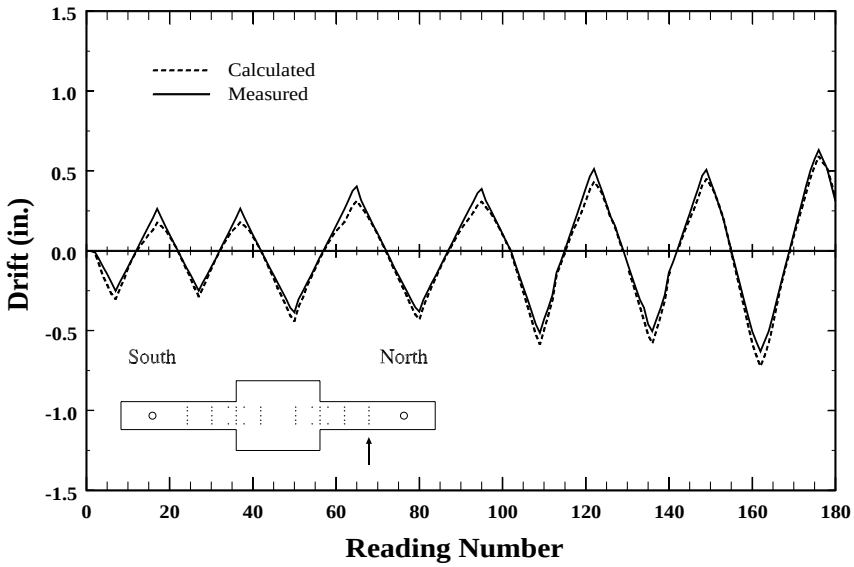

Figure 4.8. Comparison between measured and calculated displacements related to shear, flexure, and slip. Specimen C10-10, north element, station3.

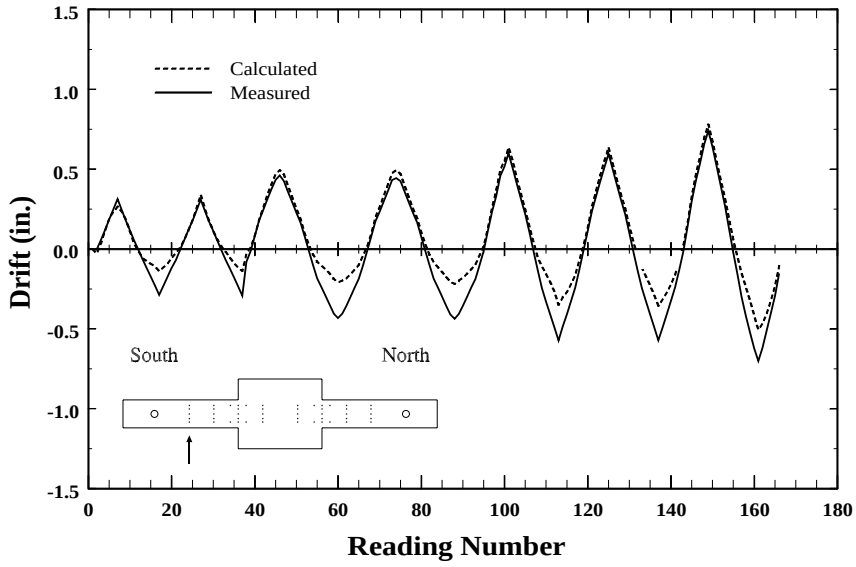

Figure 4.9. Comparison between measured and calculated displacements related to shear, flexure, and slip. Specimen C10-20, south element, station3.

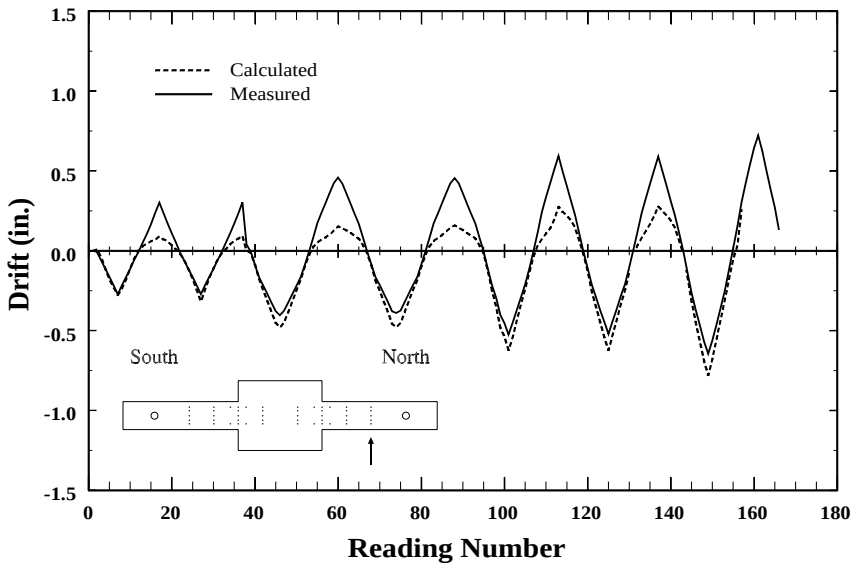

Figure 4.10. Comparison between measured and calculated displacements related to shear, flexure, and slip. Specimen C10-20, north element, station3.

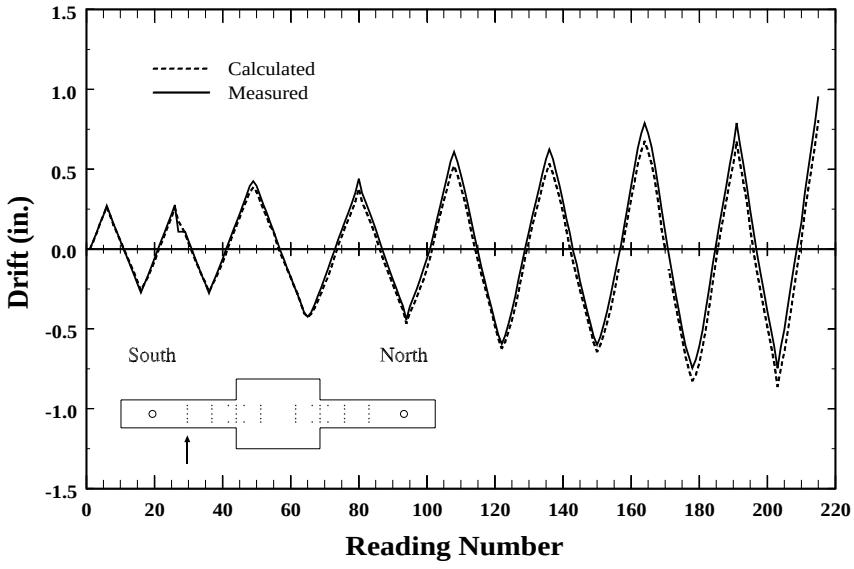

Figure 4.11. Comparison between measured and calculated displacements related to shear, flexure, and slip. Specimen C5-00, south element, station3.

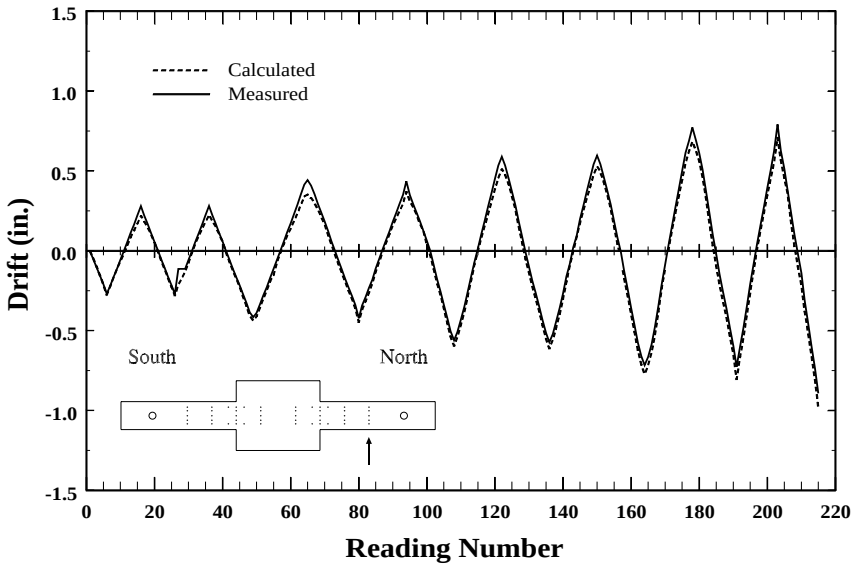

Figure 4.12. Comparison between measured and calculated displacements related to shear, flexure, and slip. Specimen C5-00, north element, station3.

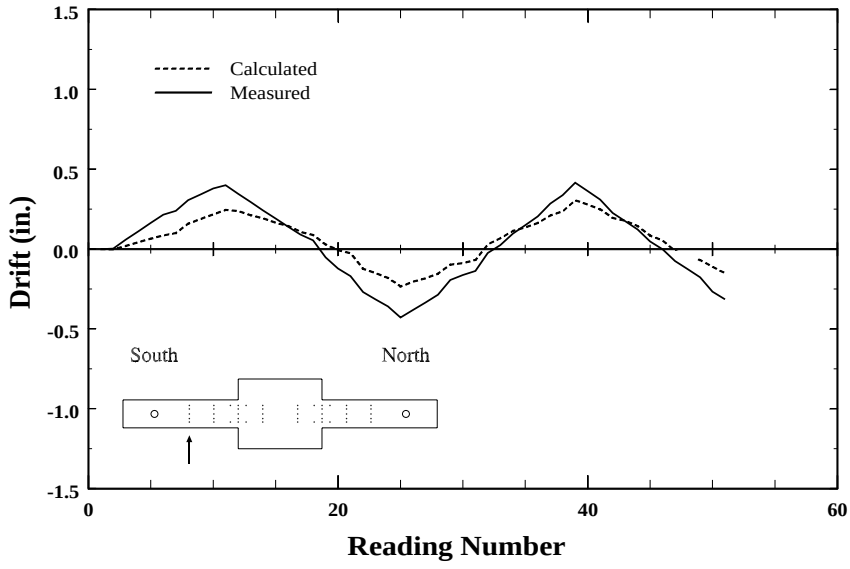

Figure 4.13. Comparison between measured and calculated displacements related to shear, flexure, and slip. Specimen C5-10, south element, station3.

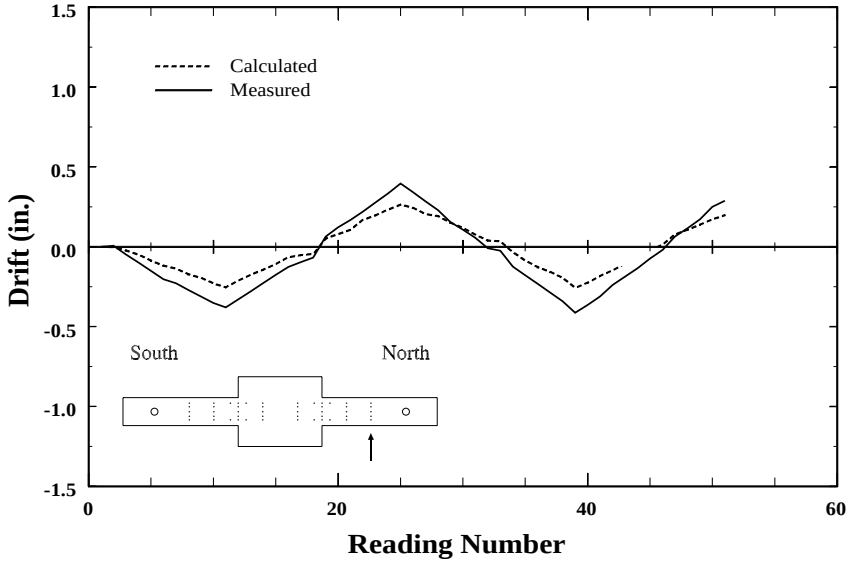

Figure 4.14. Comparison between measured and calculated displacements related to shear, flexure, and slip. Specimen C5-10, north element, station3.

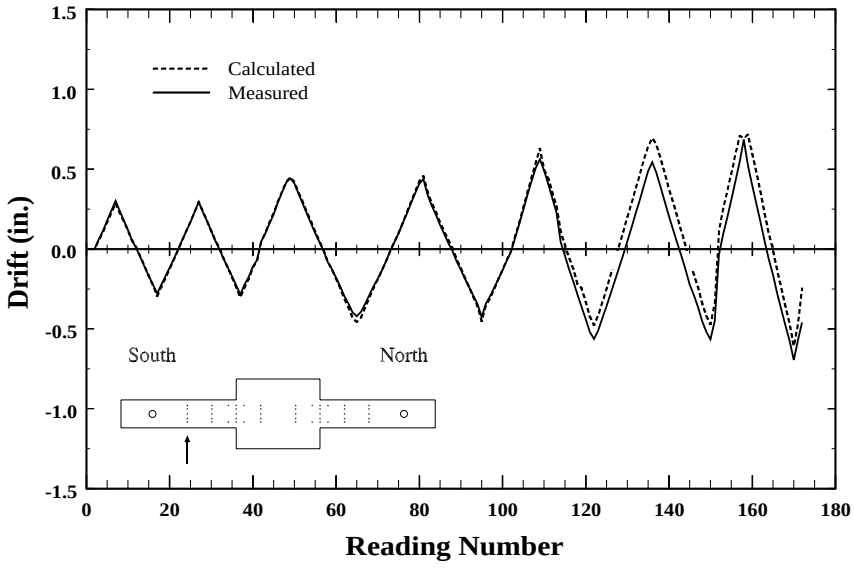

Figure 4.15. Comparison between measured and calculated displacements related to shear, flexure, and slip. Specimen C5-20, south element, station3.

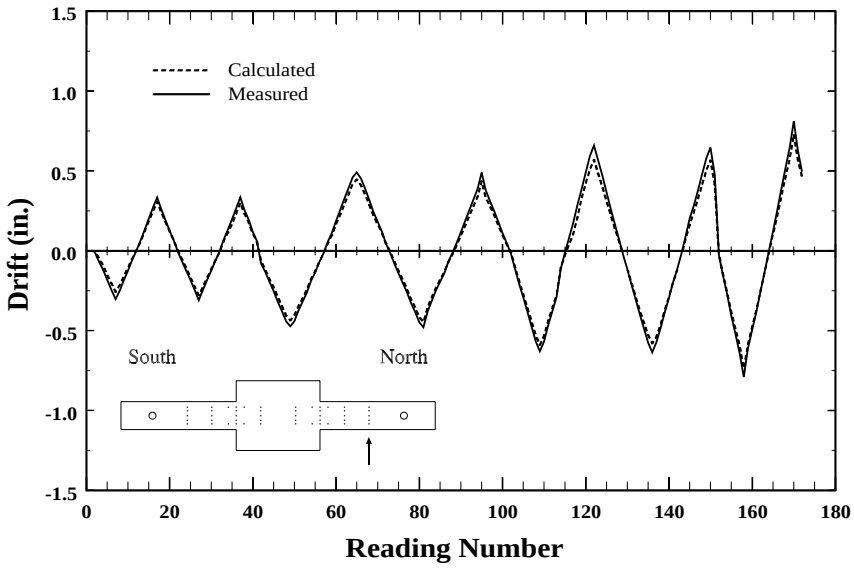

Figure 4.16. Comparison between measured and calculated displacements related to shear, flexure, and slip. Specimen C5-20, north element, station3.

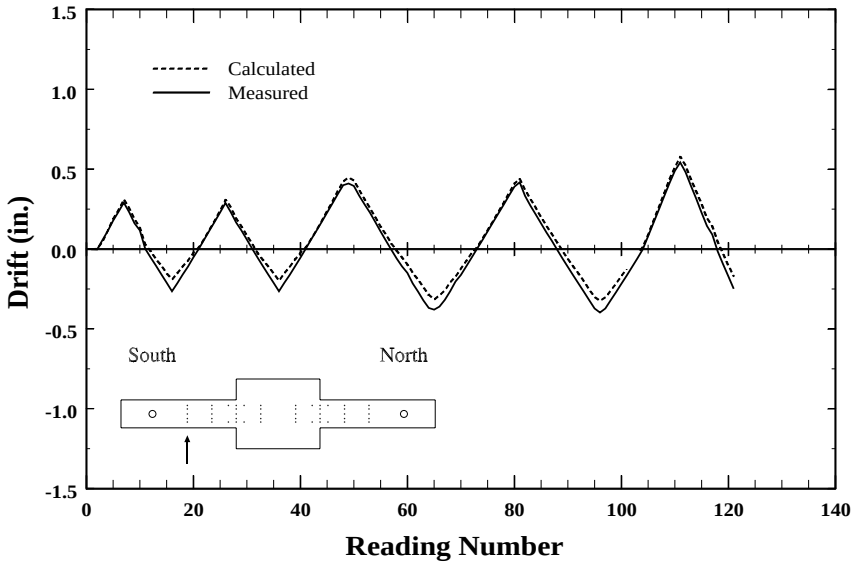

Figure 4.17. Comparison between measured and calculated displacements related to shear, flexure, and slip. Specimen C5-40, south element, station3.

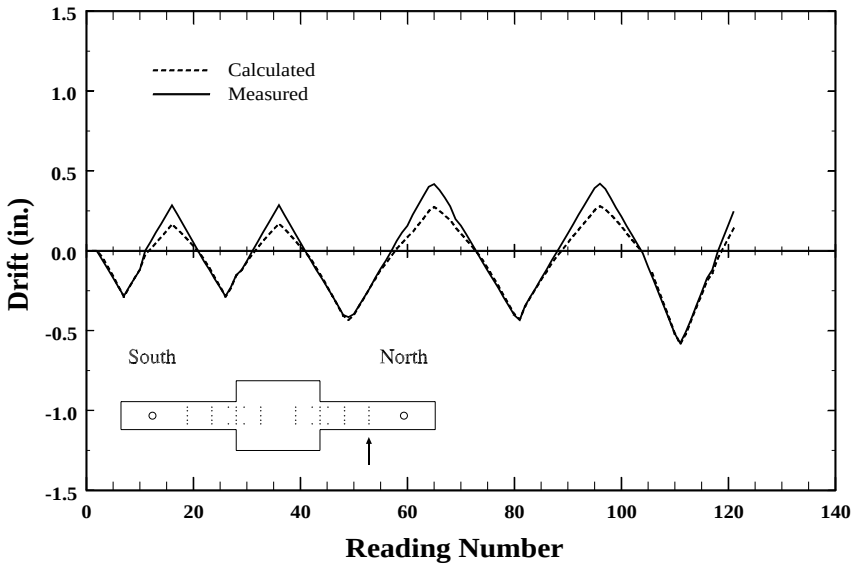

Figure 4.18. Comparison between measured and calculated displacements related to shear, flexure, and slip. Specimen C5-40, north element, station3.

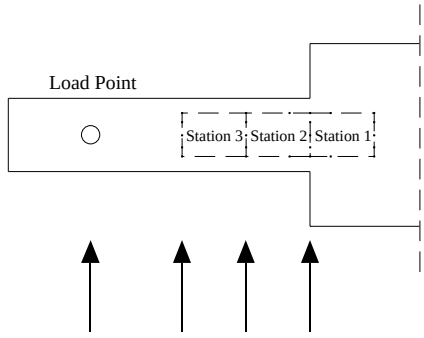

Specimen

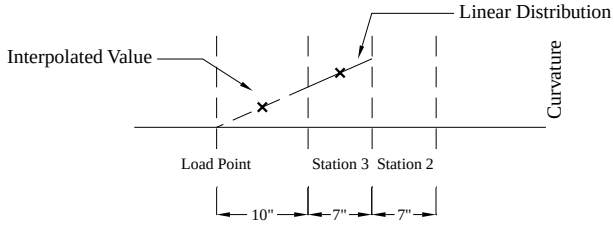

Flexural Deformations

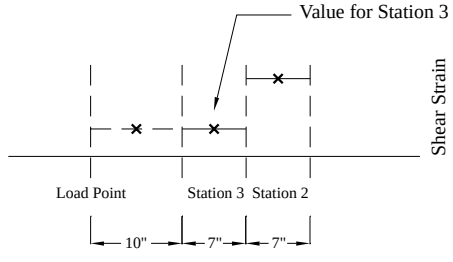

Shear Deformations

Figure 4.19. Procedure to extrapolate deformation components related to shear and flexure to the load-point.

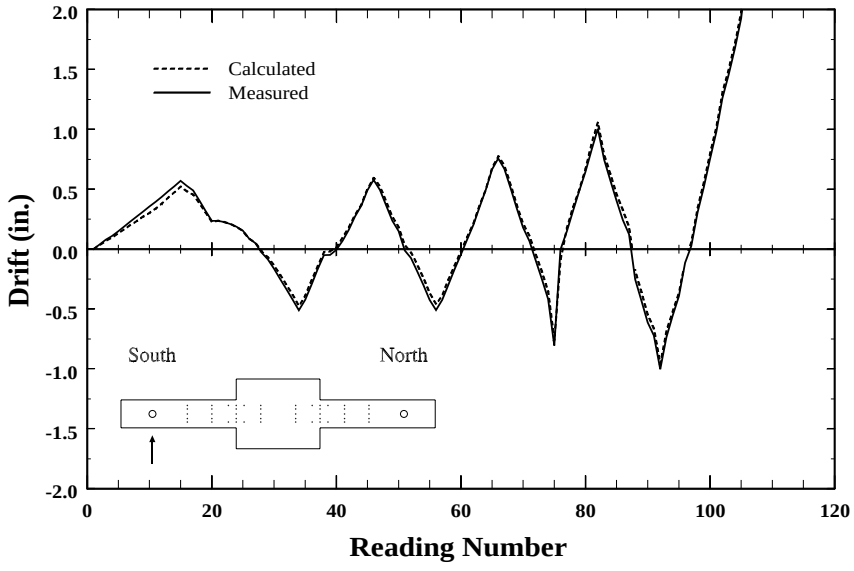

Figure 4.20. Comparison between measured and calculated displacements related to shear, flexure, and slip. Specimen C10-00, south element, load-point.

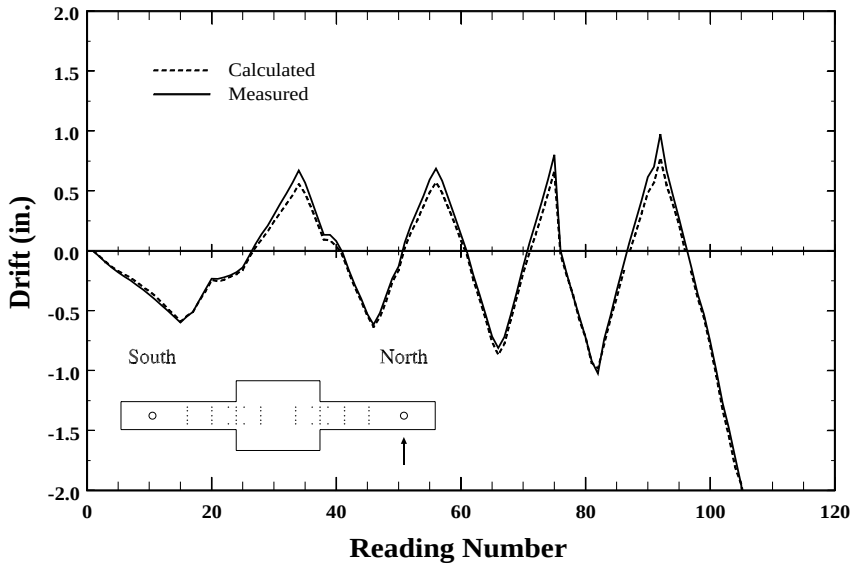

Figure 4.21. Comparison between measured and calculated displacements related to shear, flexure, and slip. Specimen C10-00, north element, load-point.

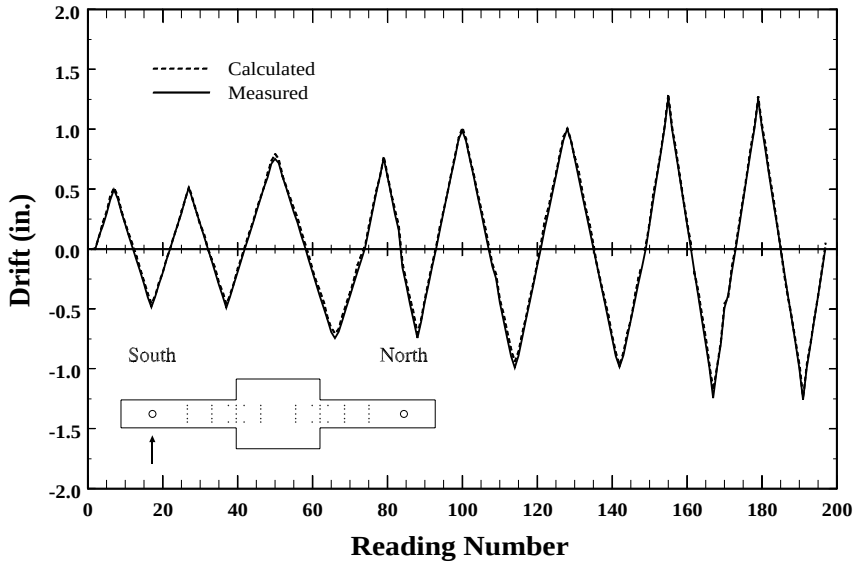

Figure 4.22. Comparison between measured and calculated displacements related to shear, flexure, and slip. Specimen C10-05, south element, load-point.

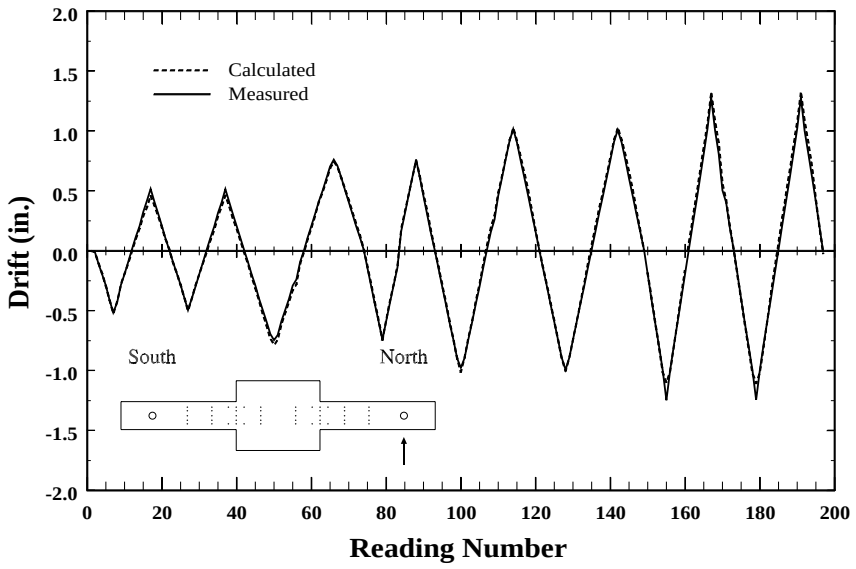

Figure 4.23. Comparison between measured and calculated displacements related to shear, flexure, and slip. Specimen C10-05, north element, load-point.

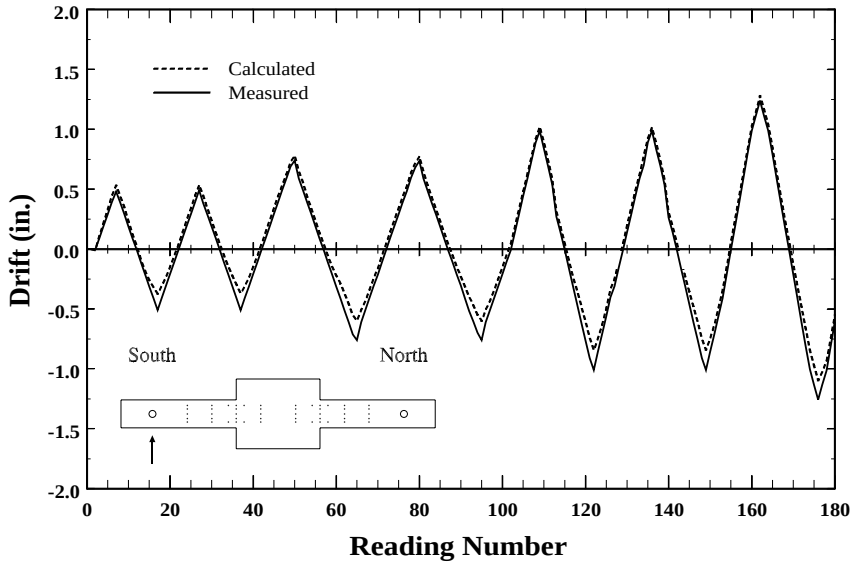

Figure 4.24. Comparison between measured and calculated displacements related to shear, flexure, and slip. Specimen C10-10, south element, load-point.

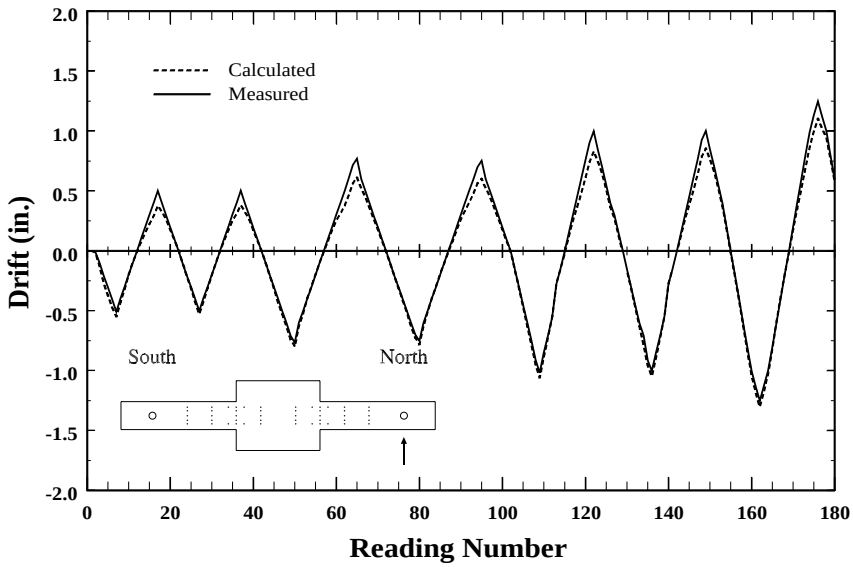

Figure 4.25. Comparison between measured and calculated displacements related to shear, flexure, and slip. Specimen C10-10, north element, load-point.

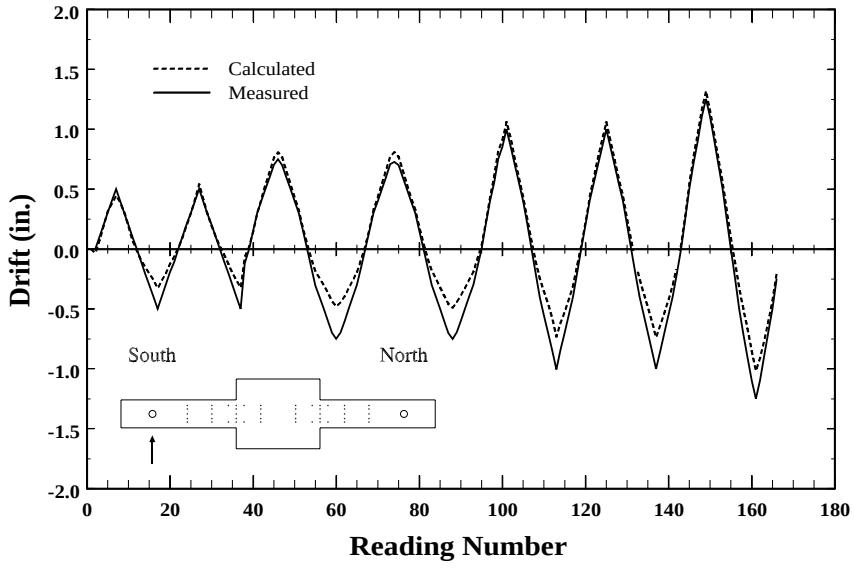

Figure 4.26. Comparison between measured and calculated displacements related to shear, flexure, and slip. Specimen C10-20, south element, load-point.

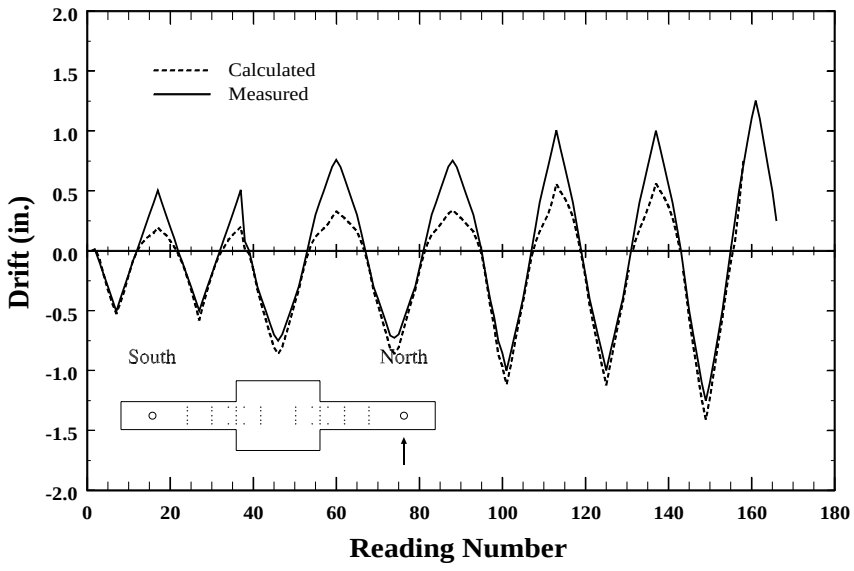

Figure 4.27. Comparison between measured and calculated displacements related to shear, flexure, and slip. Specimen C10-20, north element, load-point.

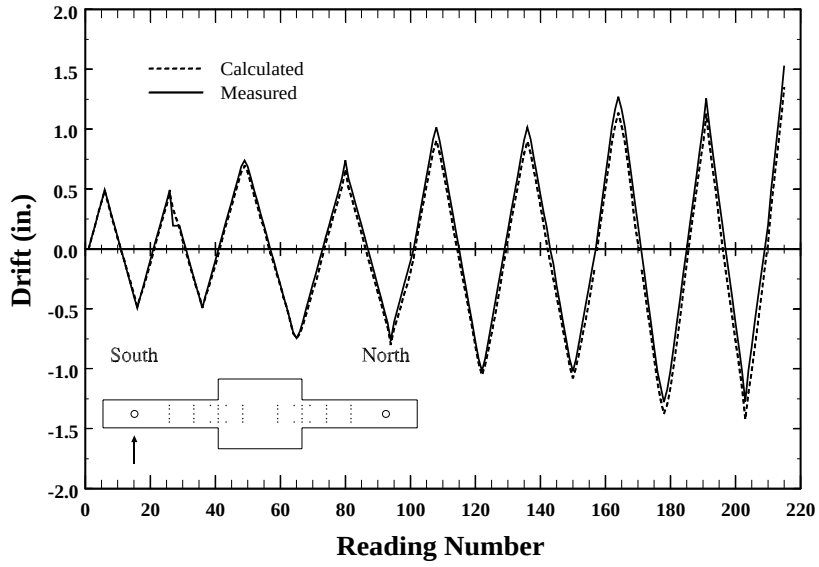

Figure 4.28. Comparison between measured and calculated displacements related to shear, flexure, and slip. Specimen C5-00, south element, load-point.

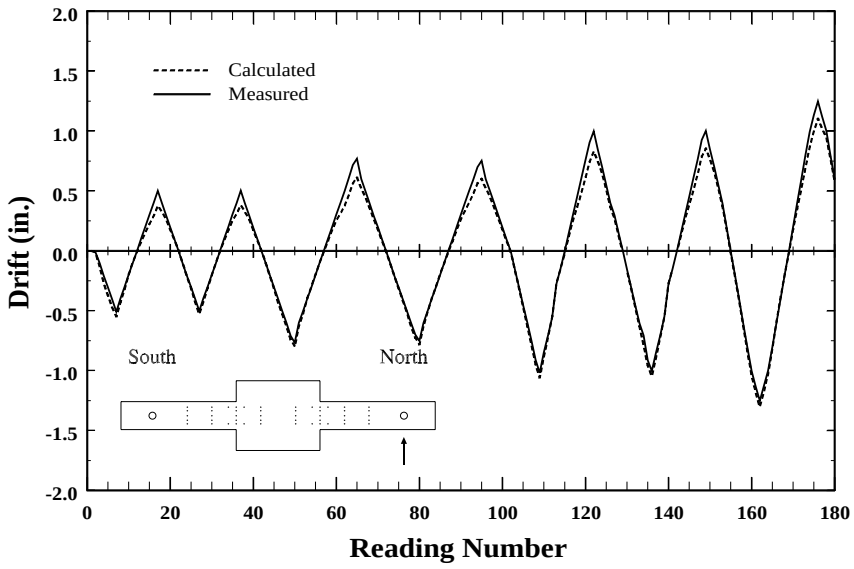

Figure 4.29. Comparison between measured and calculated displacements related to shear, flexure, and slip. Specimen C5-00, north element, load-point.

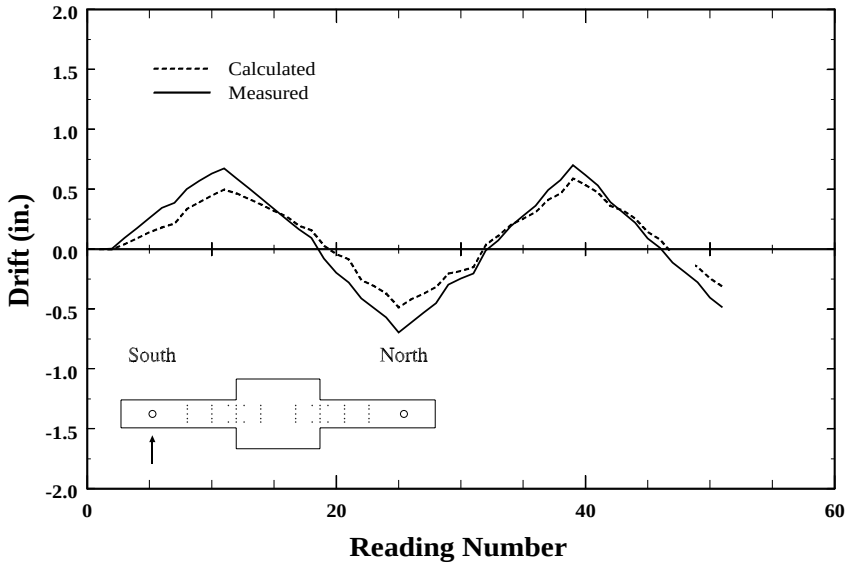

Figure 4.30. Comparison between measured and calculated displacements related to shear, flexure, and slip. Specimen C5-10, south element, load-point.

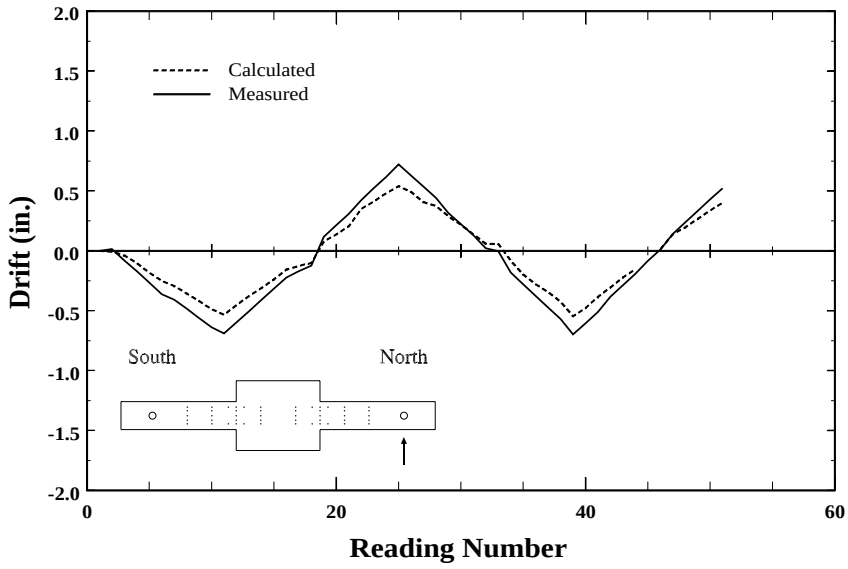

Figure 4.31. Comparison between measured and calculated displacements related to shear, flexure, and slip. Specimen C5-10, north element, load-point.

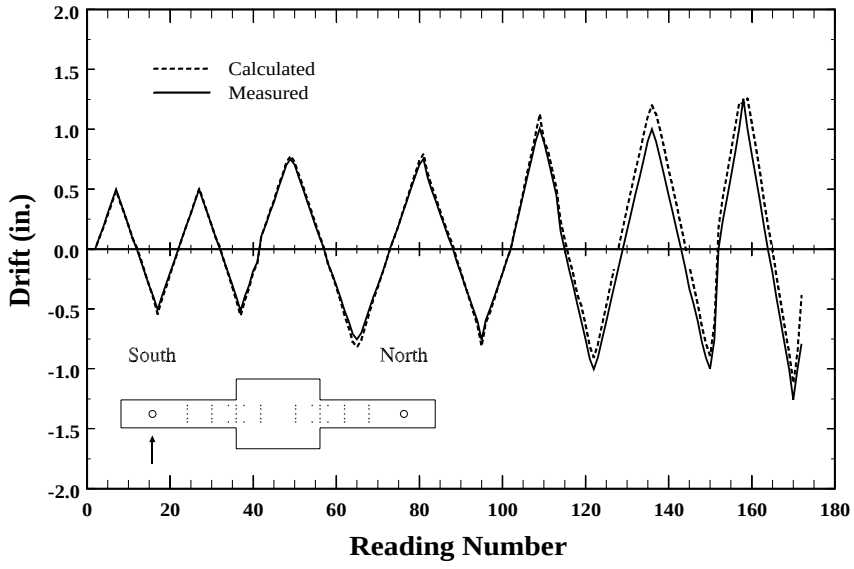

Figure 4.32. Comparison between measured and calculated displacements related to shear, flexure, and slip. Specimen C5-20, south element, load-point.

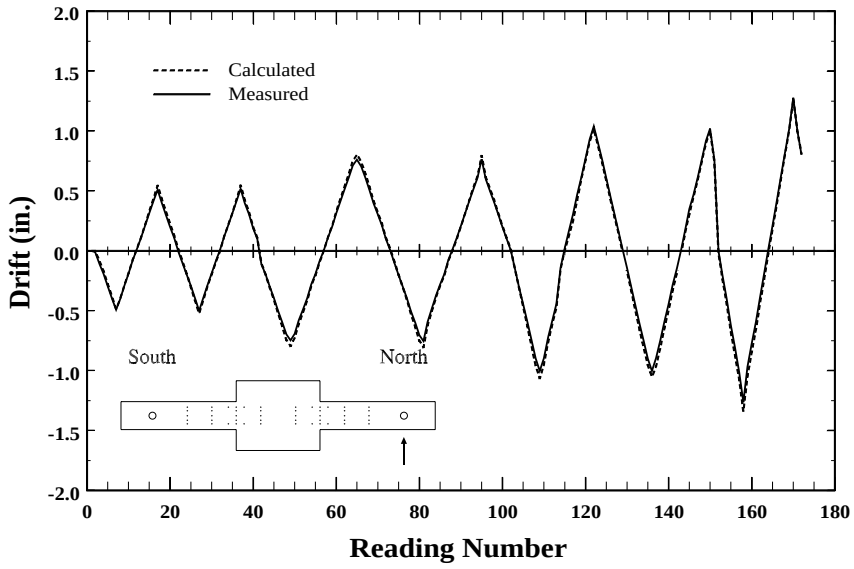

Figure 4.33. Comparison between measured and calculated displacements related to shear, flexure, and slip. Specimen C5-20, north element, load-point.

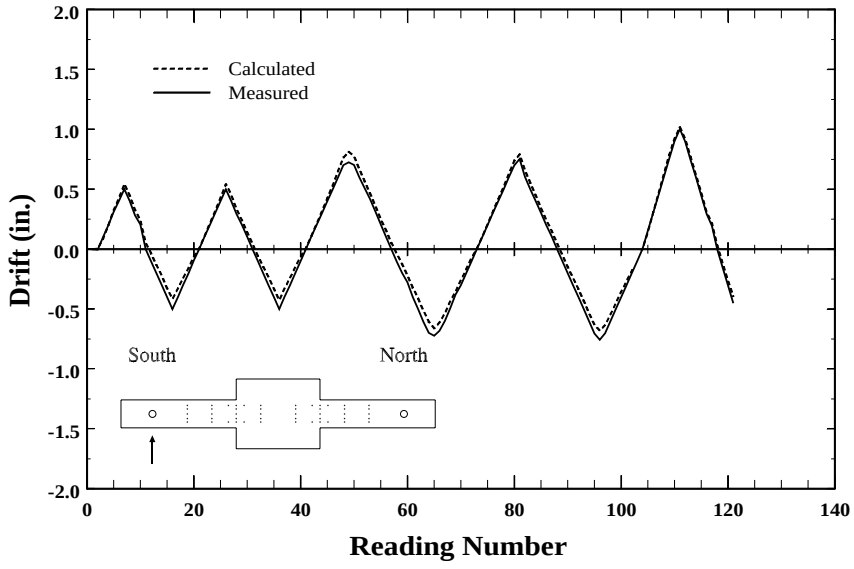

Figure 4.34. Comparison between measured and calculated displacements related to shear, flexure, and slip. Specimen C5-40, south element, load-point.

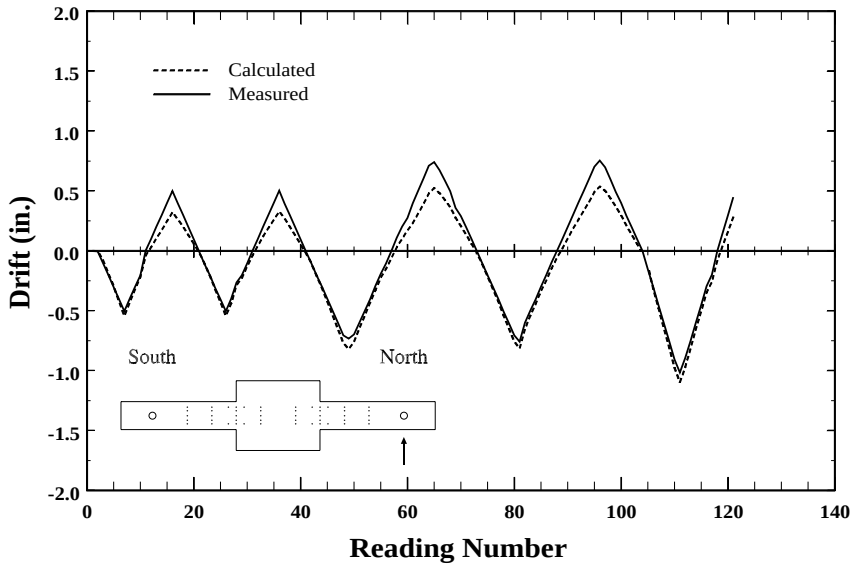

Figure 4.35. Comparison between measured and calculated displacements related to shear, flexure, and slip. Specimen C5-40, north element, load-point.

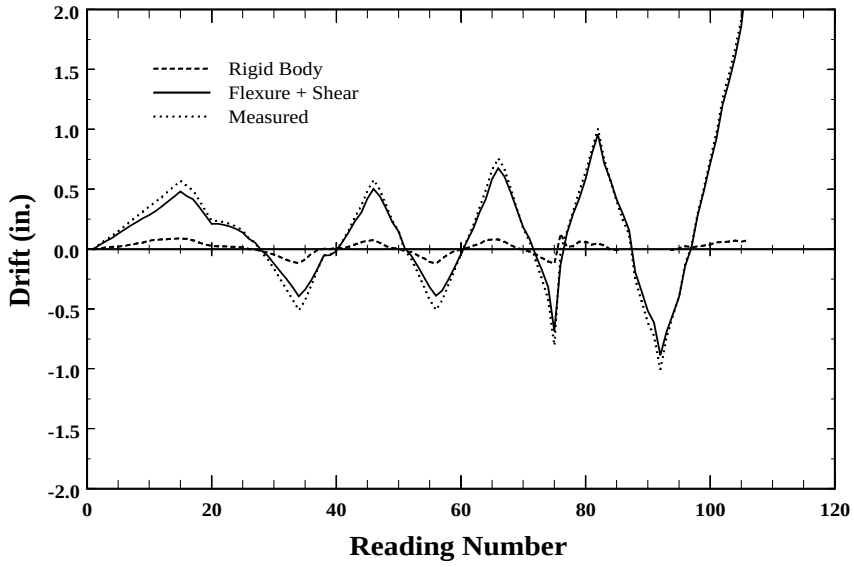

Figure 4.36. Displacement components related to shear and flexure + slip. Specimen C10-00, south element, load-point.

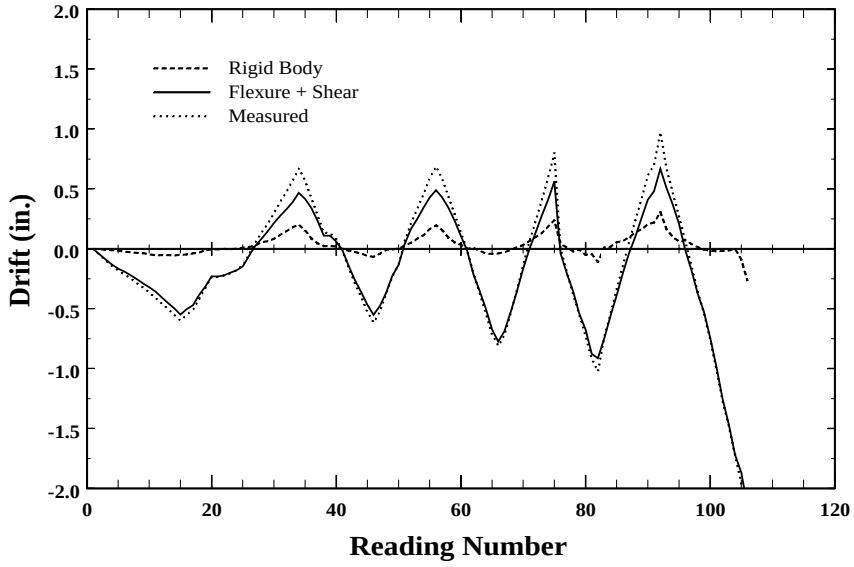

Figure 4.37. Displacement components related to shear and flexure + slip. Specimen C10-00, north element, load-point.

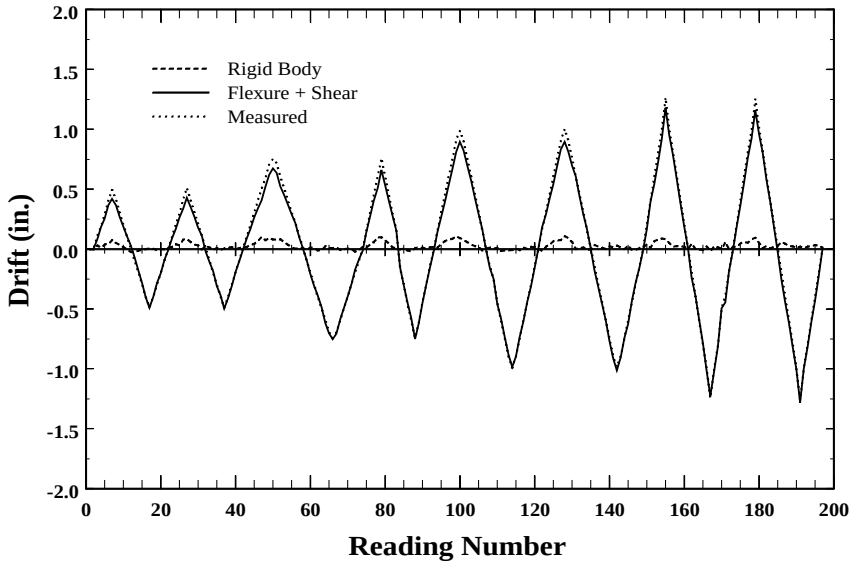

Figure 4.38. Displacement components related to shear and flexure + slip. Specimen C10-05, south element, load-point.

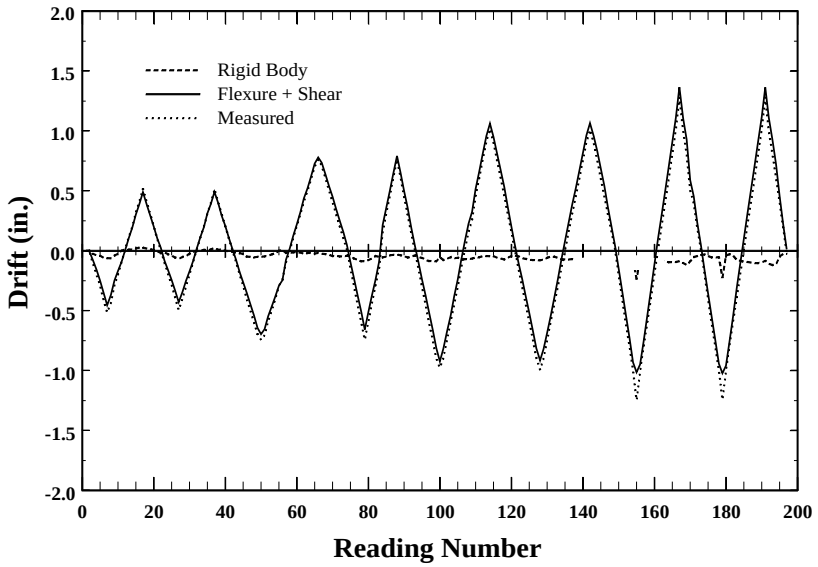

Figure 4.39. Displacement components related to shear and flexure + slip. Specimen C10-05, north element, load-point.

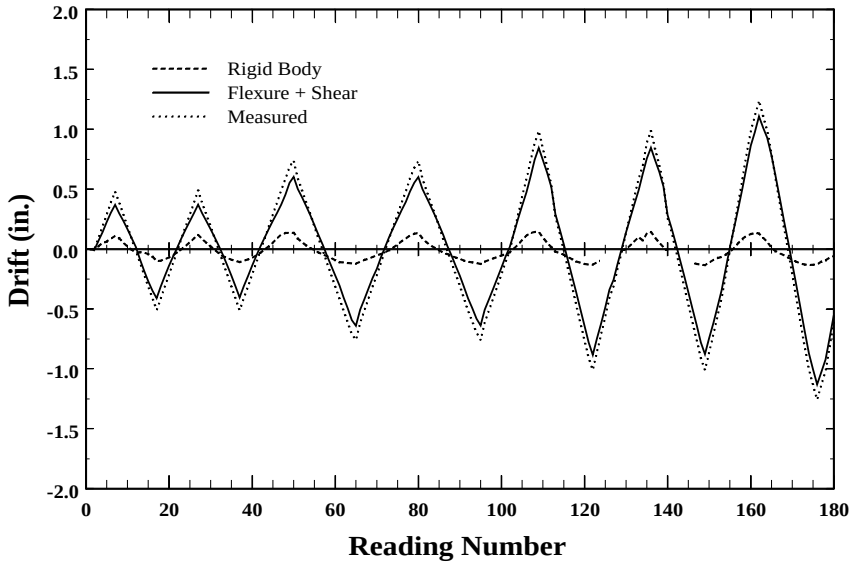

Figure 4.40. Displacement components related to shear and flexure + slip. Specimen C10-10, south element, load-point.

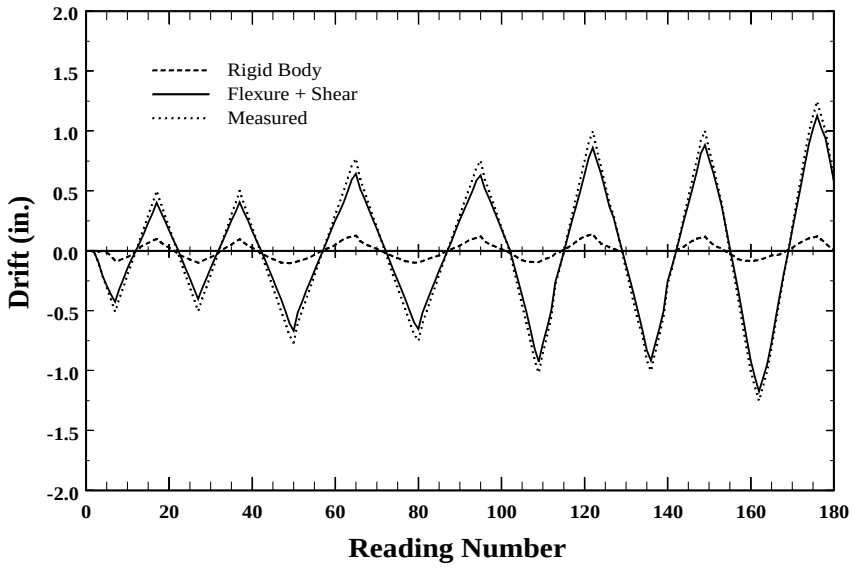

Figure 4.41. Displacement components related to shear and flexure + slip. Specimen C10-10, north element, load-point.

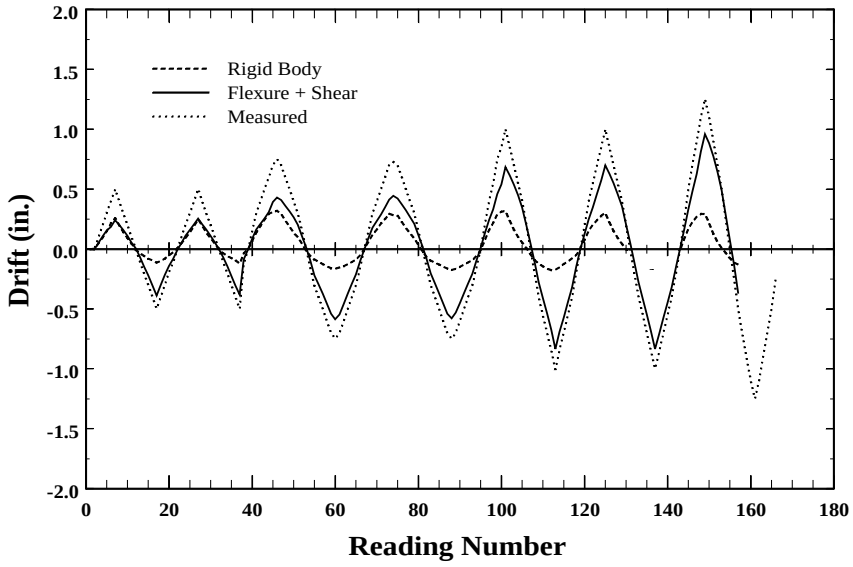

Figure 4.42. Displacement components related to shear and flexure + slip. Specimen C10-20, south element, load-point.

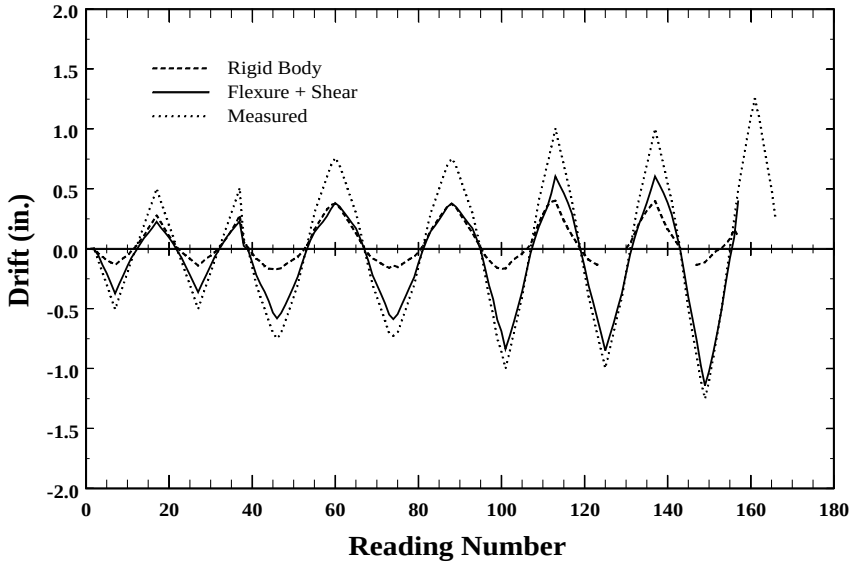

Figure 4.43. Displacement components related to shear and flexure + slip. Specimen C10-20, north element, load-point.

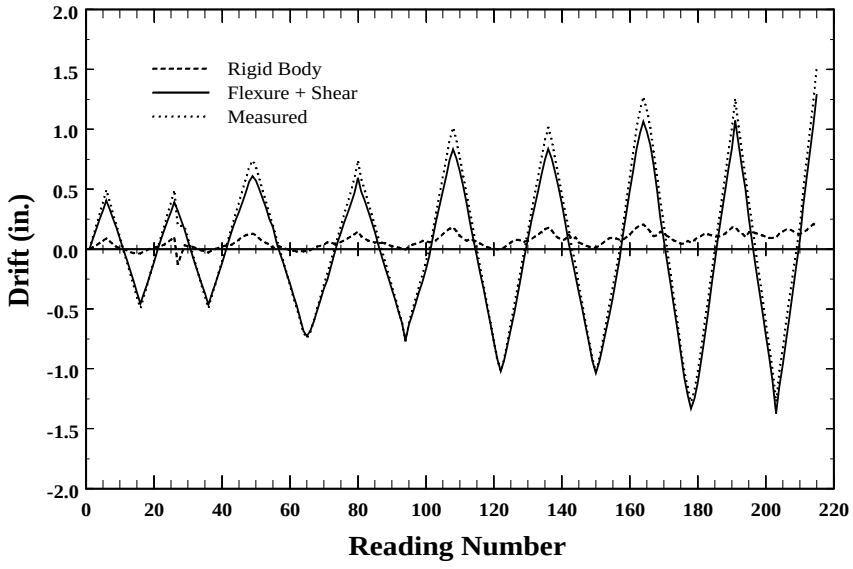

Figure 4.44. Displacement components related to shear and flexure + slip. Specimen C5-00, south element, load-point.

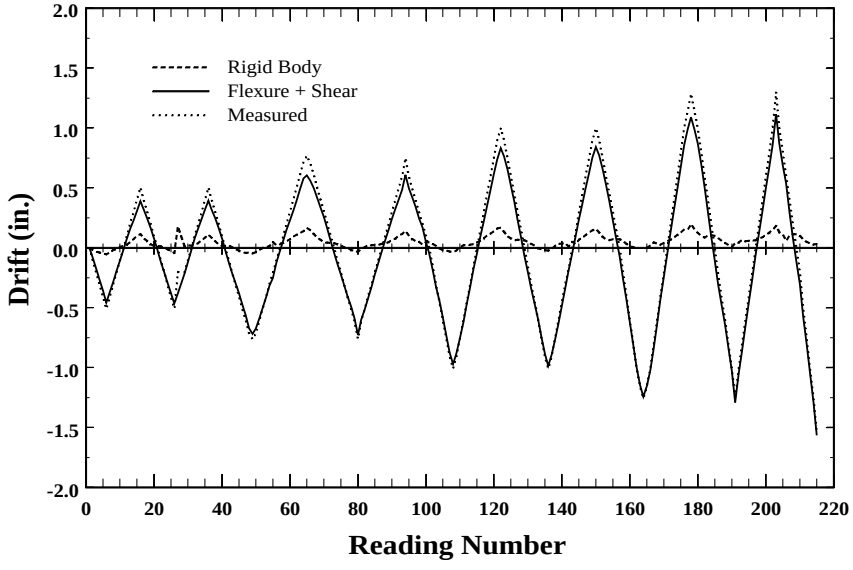

Figure 4.45. Displacement components related to shear and flexure + slip. Specimen C5-00, north element, load-point.

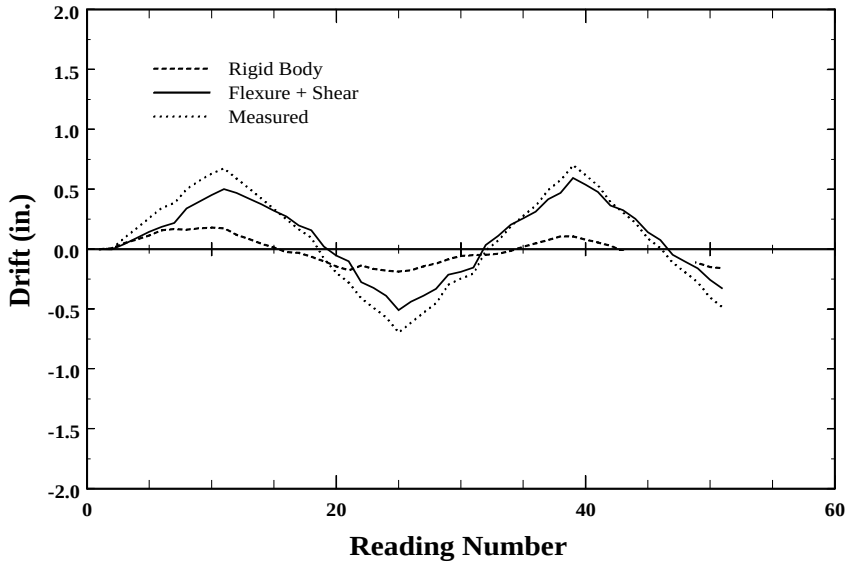

Figure 4.46. Displacement components related to shear and flexure + slip. Specimen C5-10, south element, load-point.

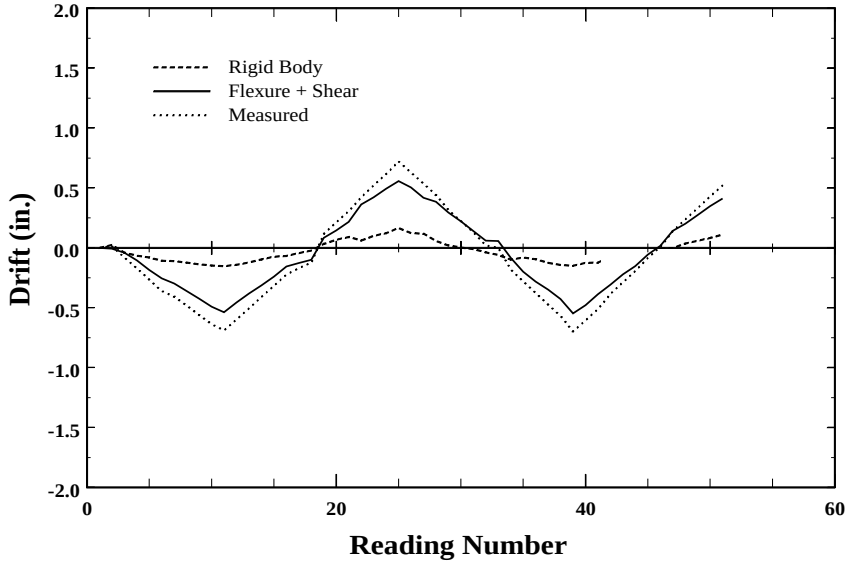

Figure 4.47. Displacement components related to shear and flexure + slip. Specimen C5-10, north element, load-point.

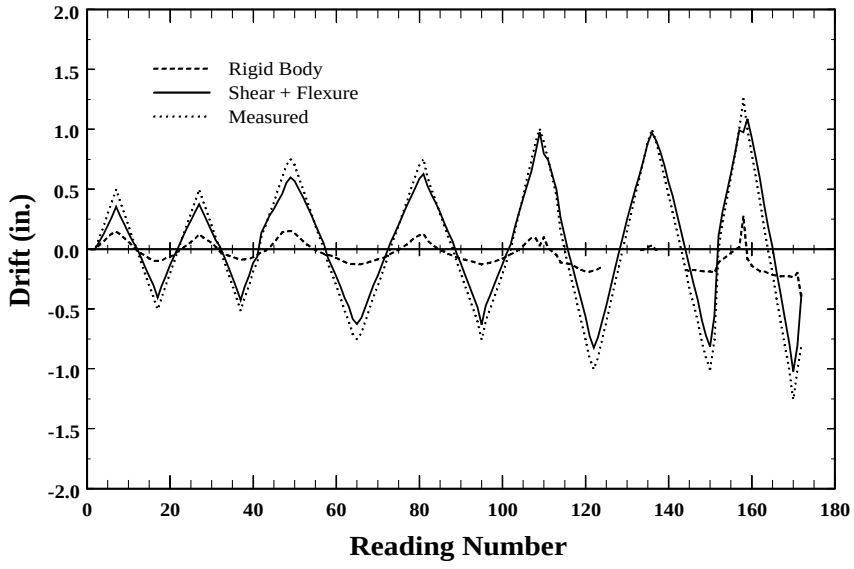

Figure 4.48. Displacement components related to shear and flexure + slip. Specimen C5-20, south element, load-point.

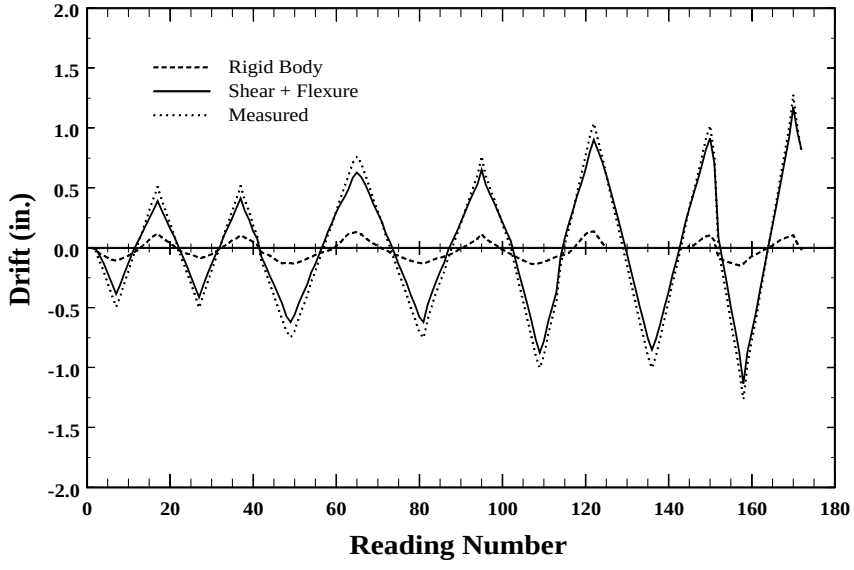

Figure 4.49. Displacement components related to shear and flexure + slip. Specimen C5-20, north element, load-point.

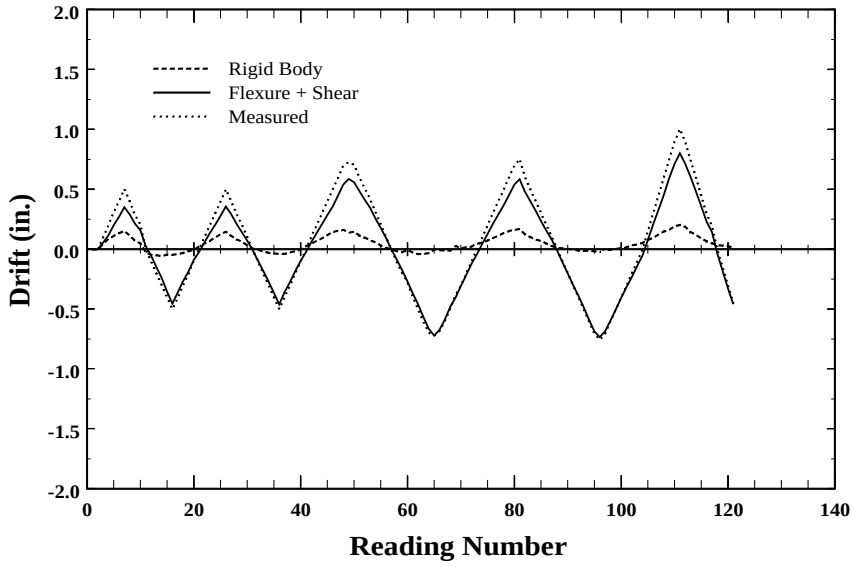

Figure 4.50. Displacement components related to shear and flexure + slip. Specimen C5-40, south element, load-point.

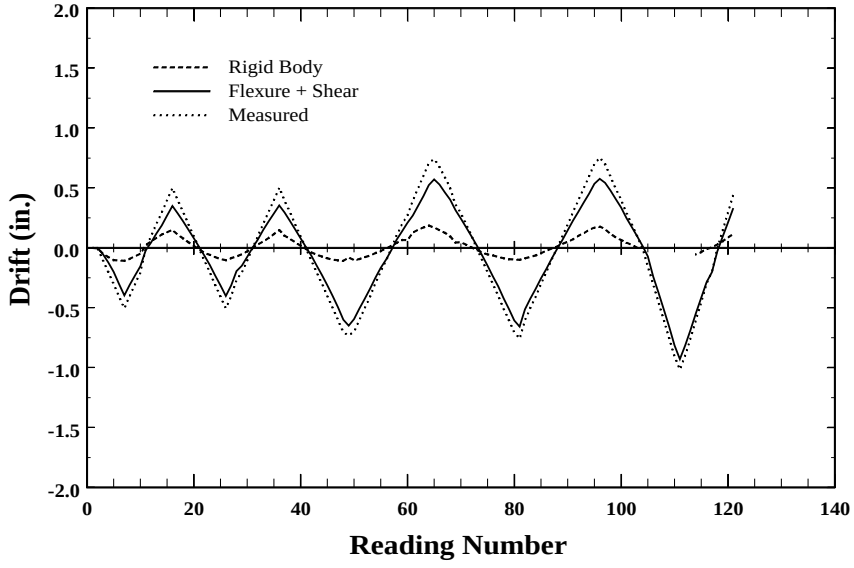

Figure 4.51. Displacement components related to shear and flexure + slip. Specimen C5-40, north element, load-point.

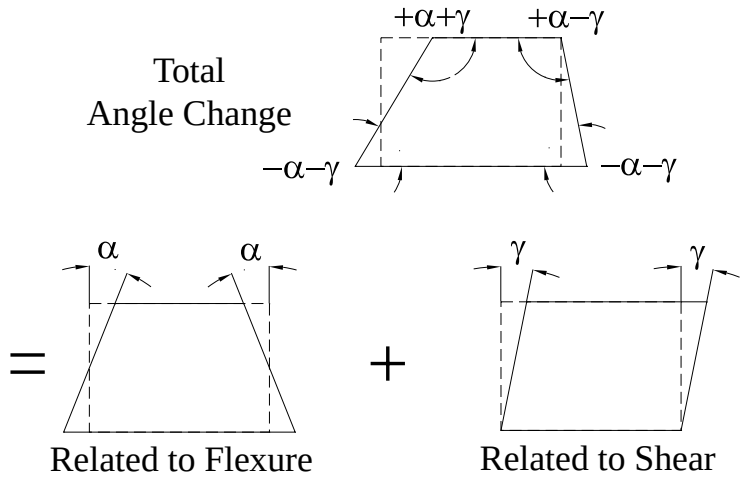

Figure 4.52. Deformation components related to shear and flexure.

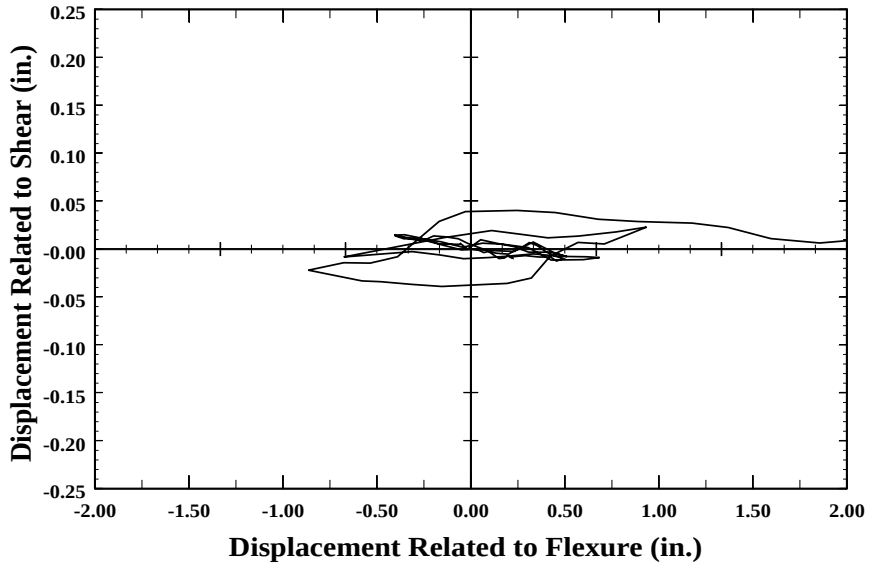

Figure 4.53. Displacement component related to shear vs displacement component related to flexure+slip. Specimen C10-00, south element, load-point.

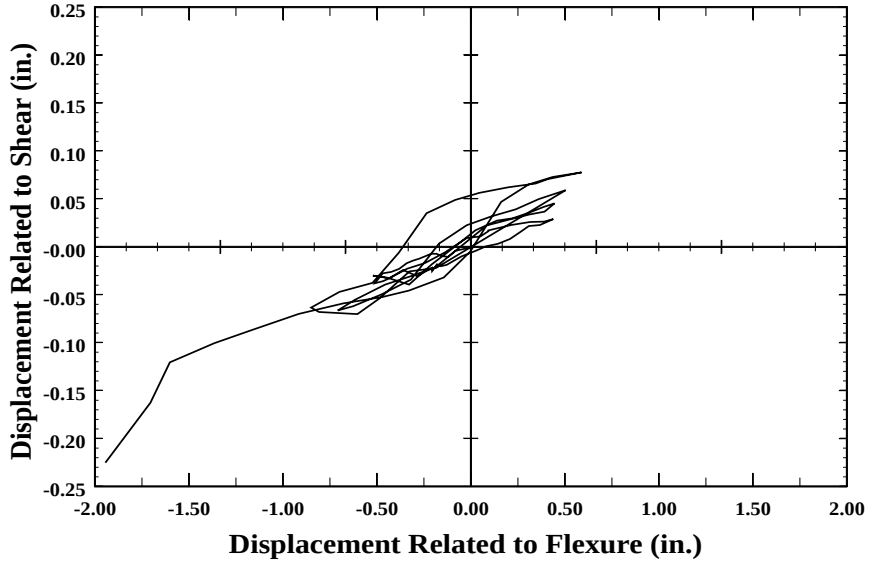

Figure 4.54. Displacement component related to shear vs displacement component related to flexure+slip. Specimen C10-00, north element, load-point.

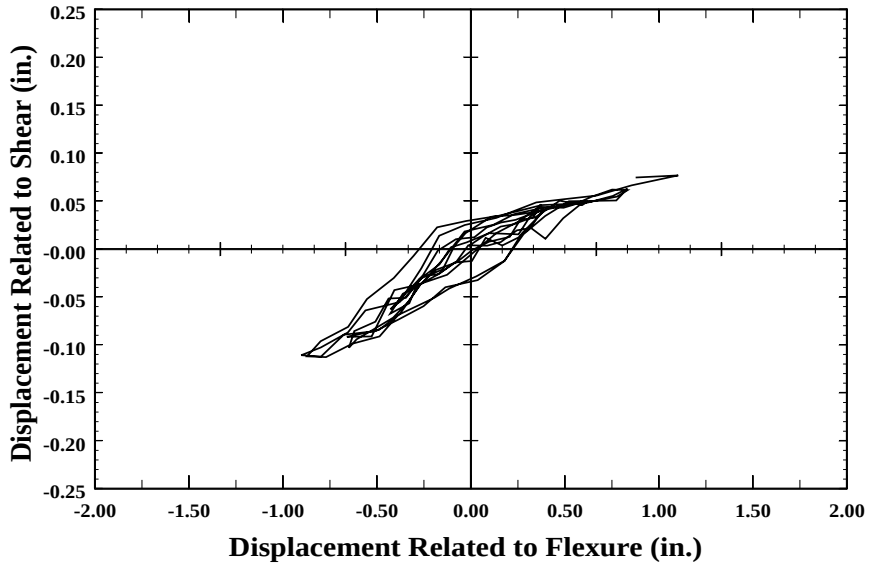

Figure 4.55. Displacement component related to shear vs displacement component related to flexure+slip. Specimen C10-05, south element, load-point.

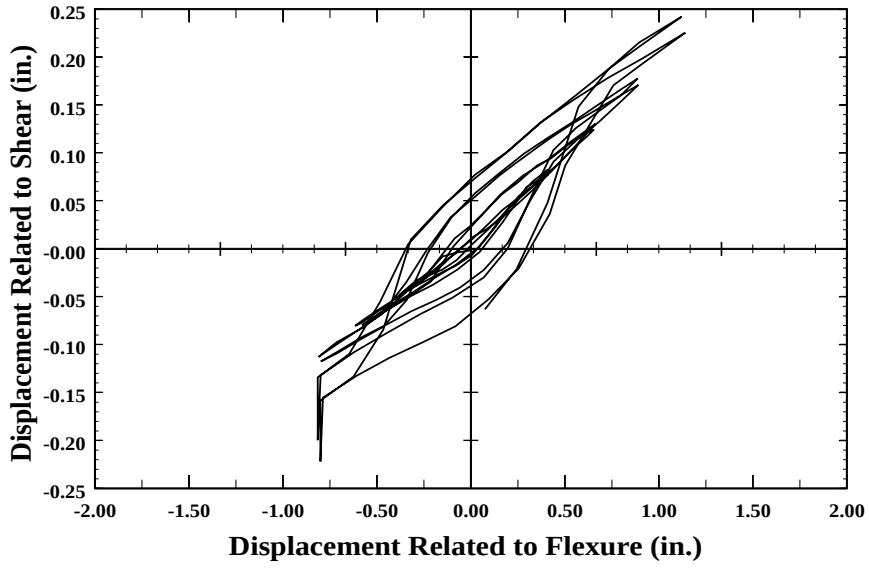

Figure 4.56. Displacement component related to shear vs displacement component related to flexure+slip. Specimen C10-05, north element, load-point.

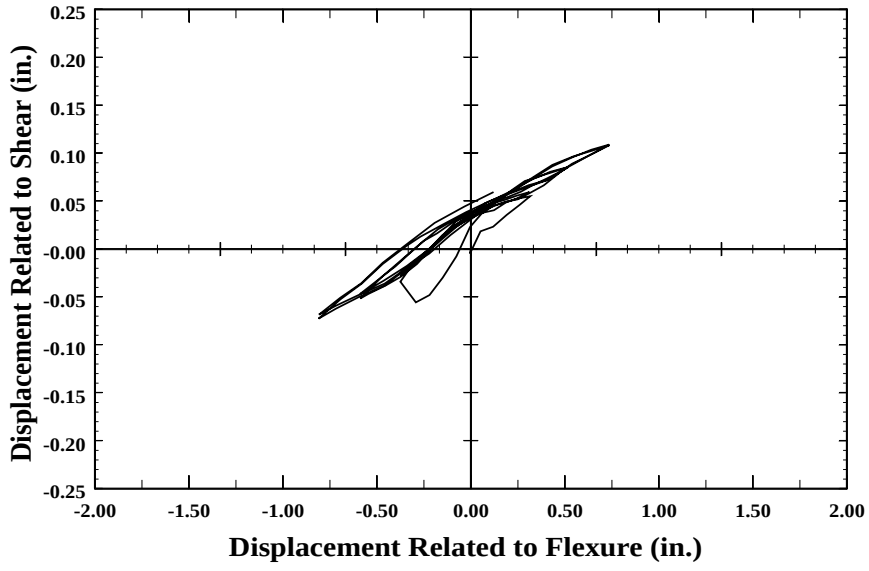

Figure 4.57. Displacement component related to shear vs displacement component related to flexure+slip. Specimen C10-10, south element, load-point.

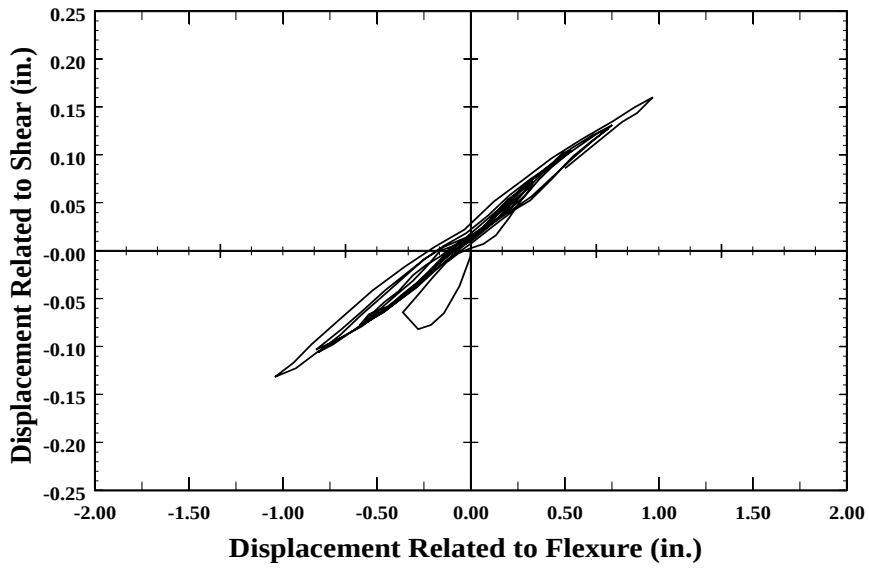

Figure 4.58. Displacement component related to shear vs displacement component related to flexure+slip. Specimen C10-10, north element, load-point.

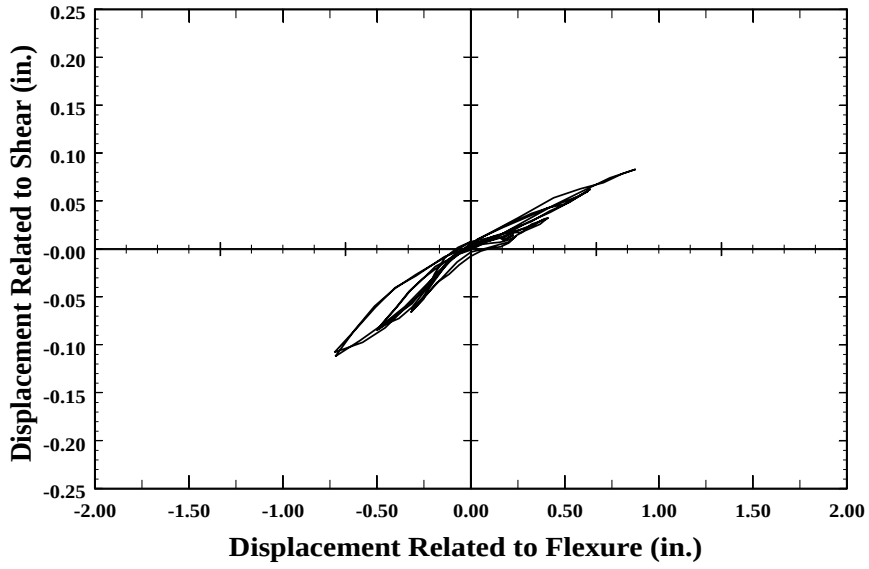

Figure 4.59. Displacement component related to shear vs displacement component related to flexure+slip. Specimen C10-20, south element, load-point.

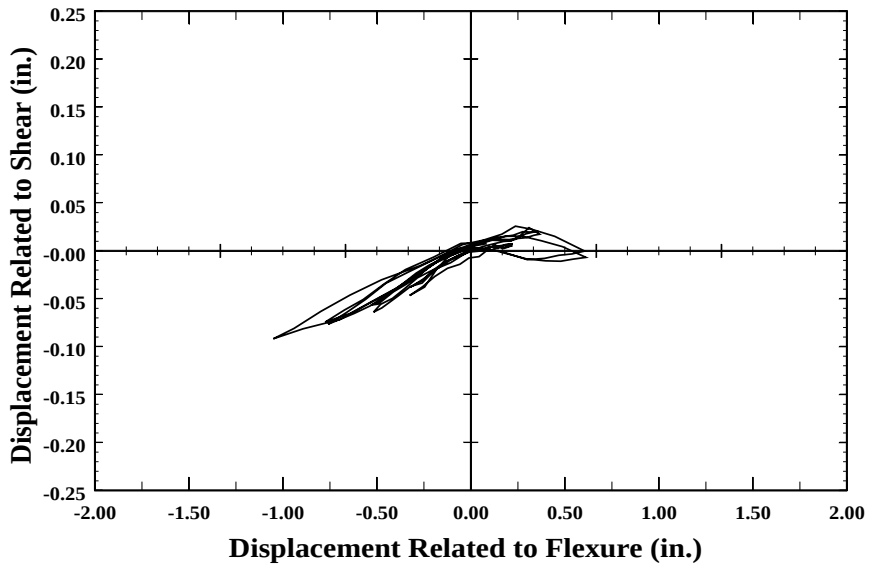

Figure 4.60. Displacement component related to shear vs displacement component related to flexure+slip. Specimen C10-20, north element, load-point.

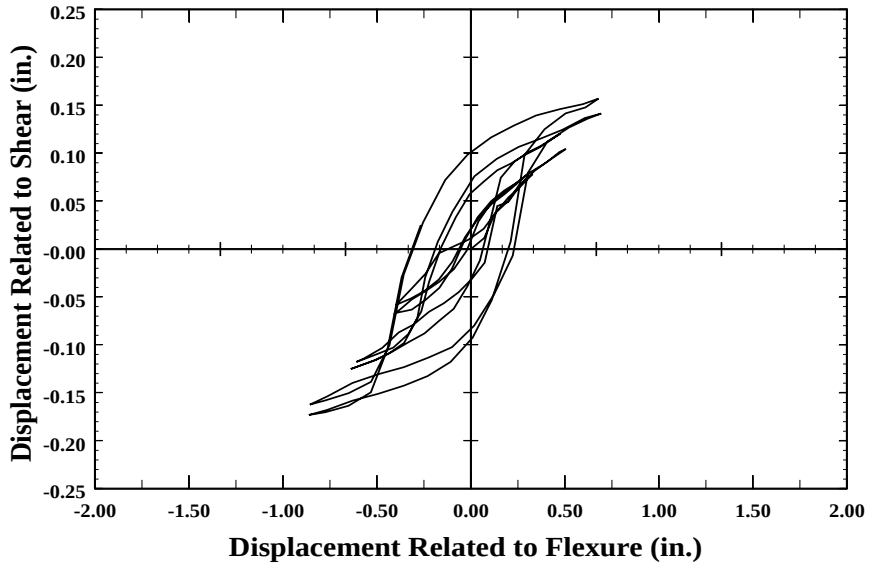

Figure 4.61. Displacement component related to shear vs displacement component related to flexure+slip. Specimen C5-00, south element, load-point.

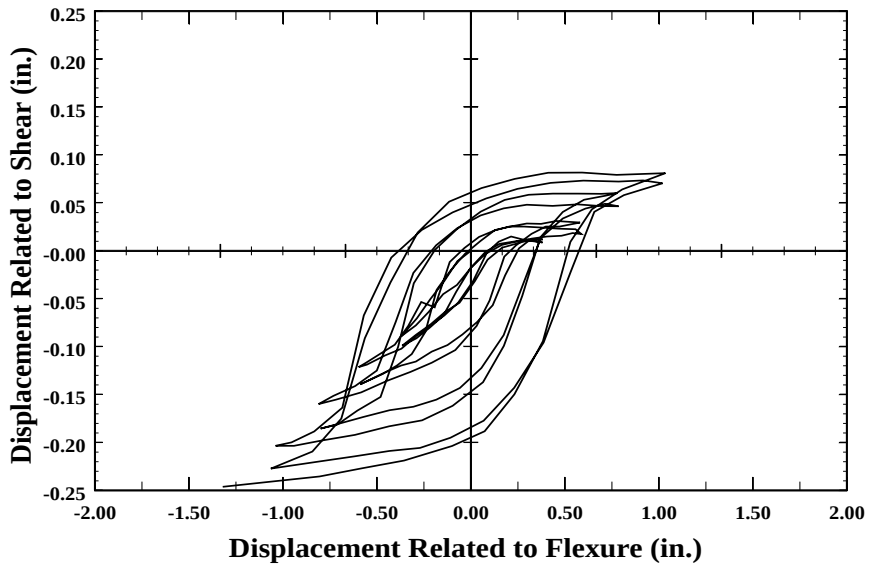

Figure 4.62. Displacement component related to shear vs displacement component related to flexure+slip. Specimen C5-00, north element, load-point.

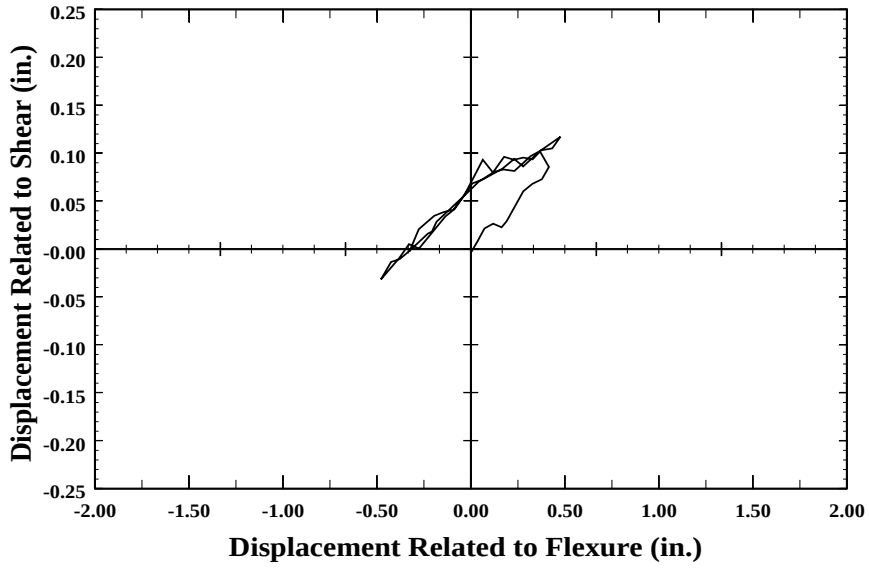

Figure 4.63. Displacement component related to shear vs displacement component related to flexure+slip. Specimen C5-10, south element, load-point.

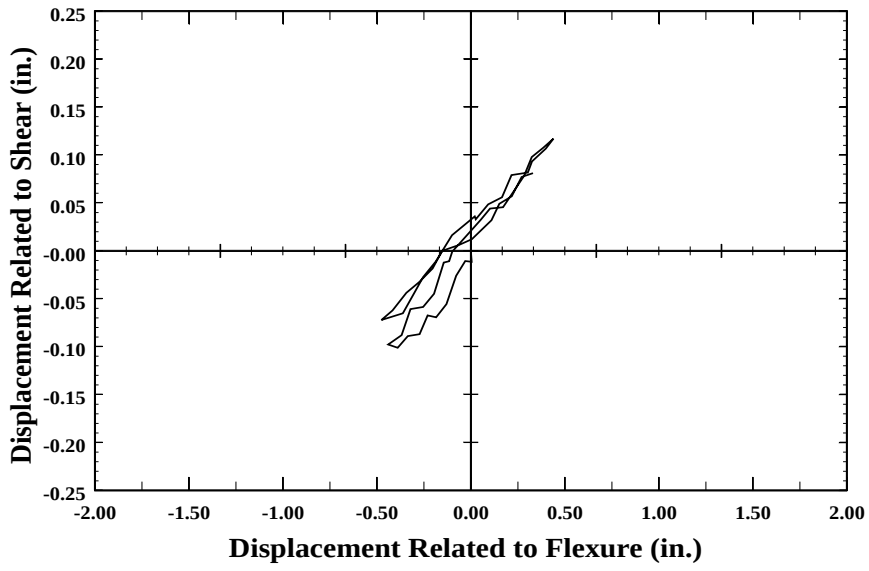

Figure 4.64. Displacement component related to shear vs displacement component related to flexure+slip. Specimen C5-10, north element, load-point.

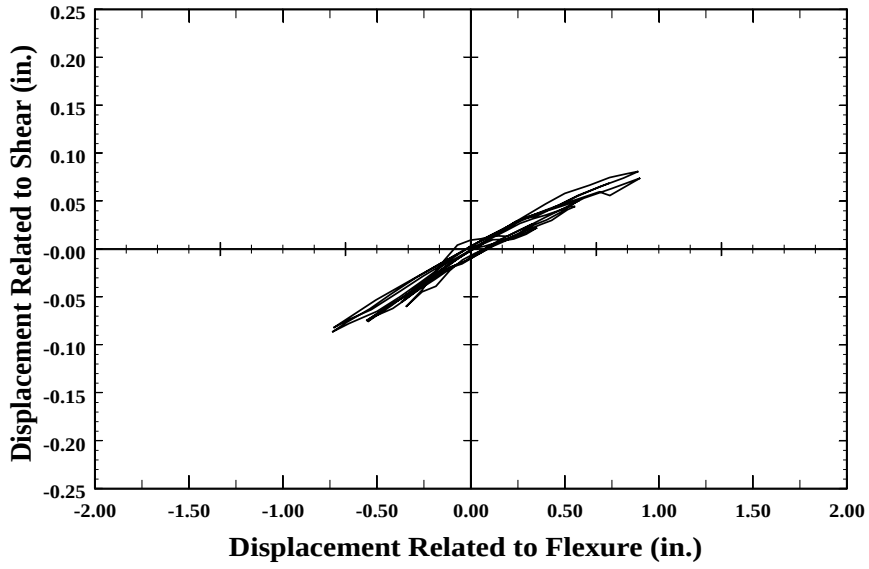

Figure 4.65. Displacement component related to shear vs displacement component related to flexure+slip. Specimen C5-20, south element, load-point.

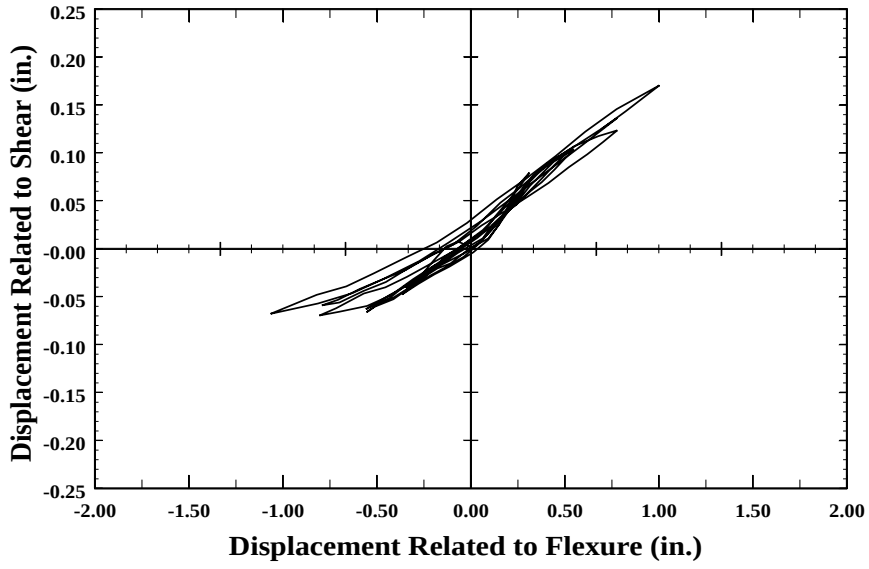

Figure 4.66. Displacement component related to shear vs displacement component related to flexure+slip. Specimen C5-20, north element, load-point.

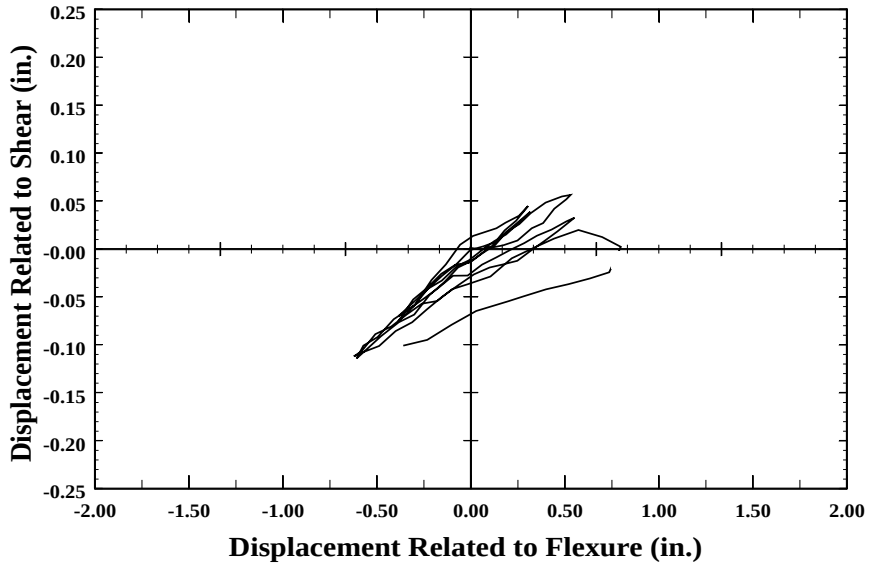

Figure 4.67. Displacement component related to shear vs displacement component related to flexure+slip. Specimen C5-40, south element, load-point.

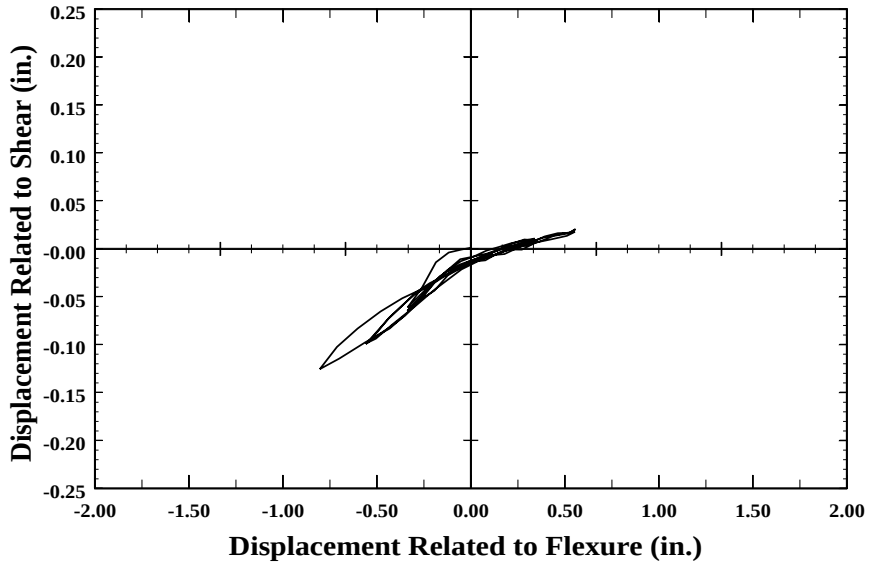

Figure 4.68. Displacement component related to shear vs displacement component related to flexure+slip. Specimen C5-40, north element, load-point.

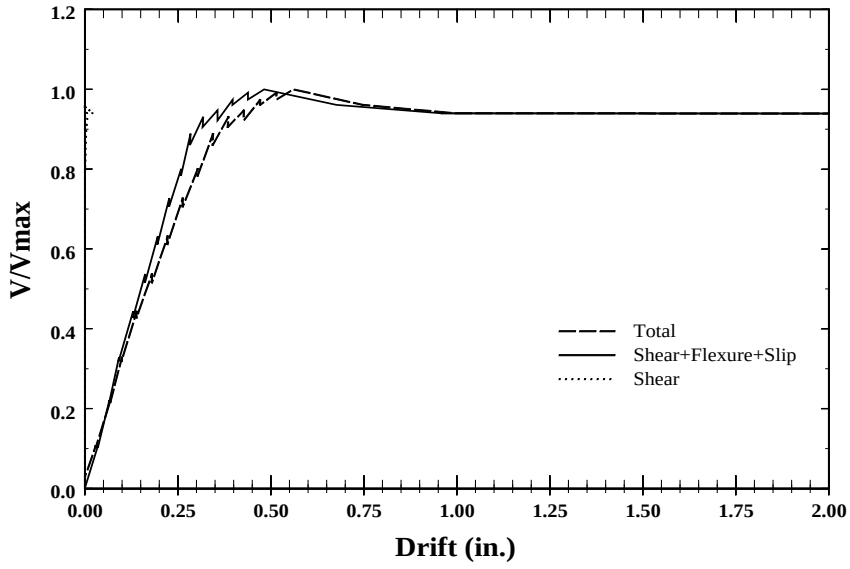

Figure 4.69. Envelope curve for displacement components at the load-point while loading with a positive couple. Specimen C10-00, south element.

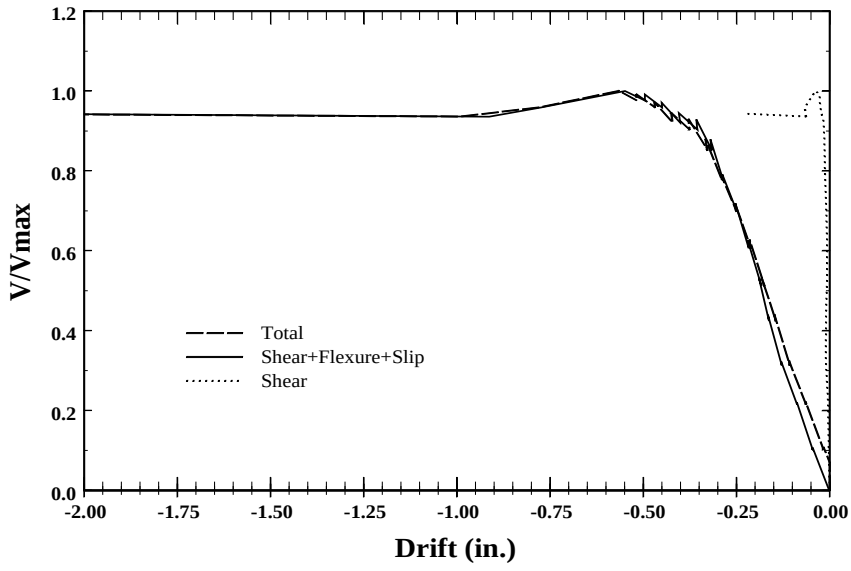

Figure 4.70. Envelope curve for displacement components at the load-point while loading with a positive couple. Specimen C10-00, north element.

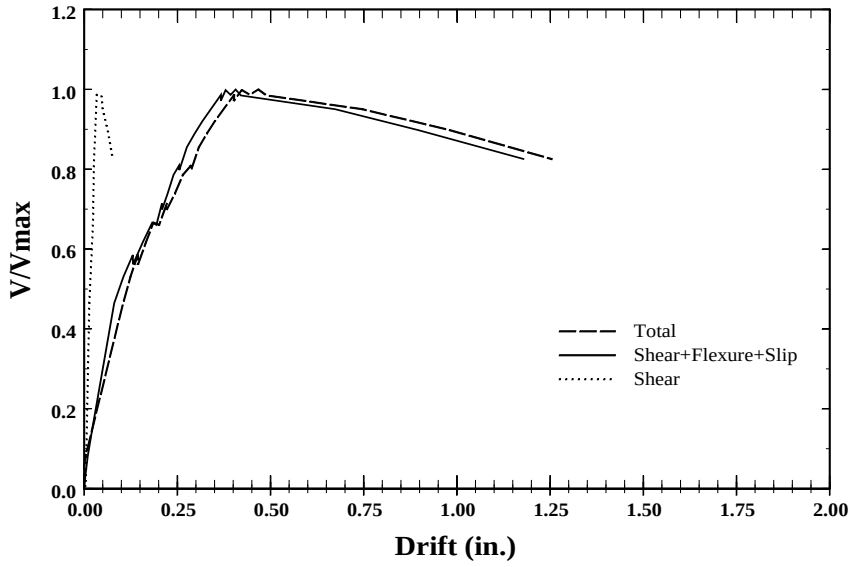

Figure 4.71. Envelope curve for displacement components at the load-point while loading with a positive couple. Specimen C10-05, south element.

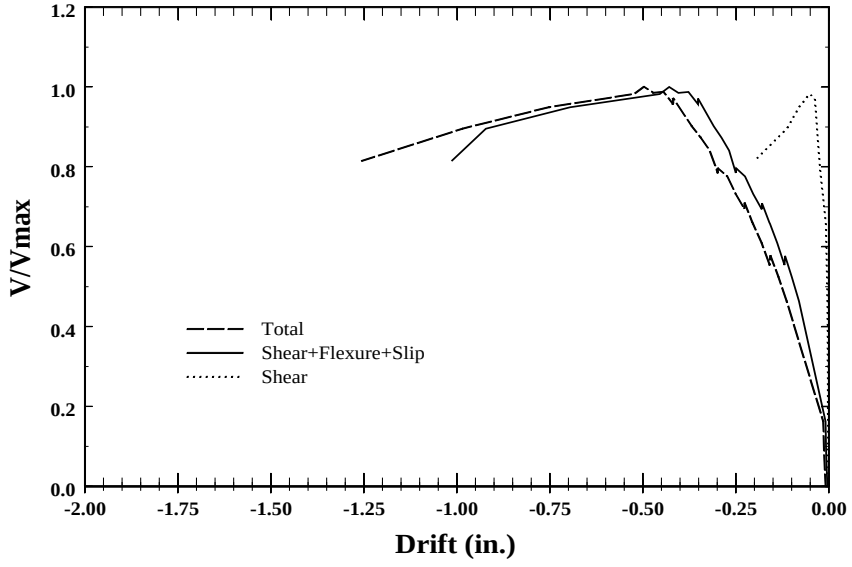

Figure 4.72. Envelope curve for displacement components at the load-point while loading with a positive couple. Specimen C10-05, north element.

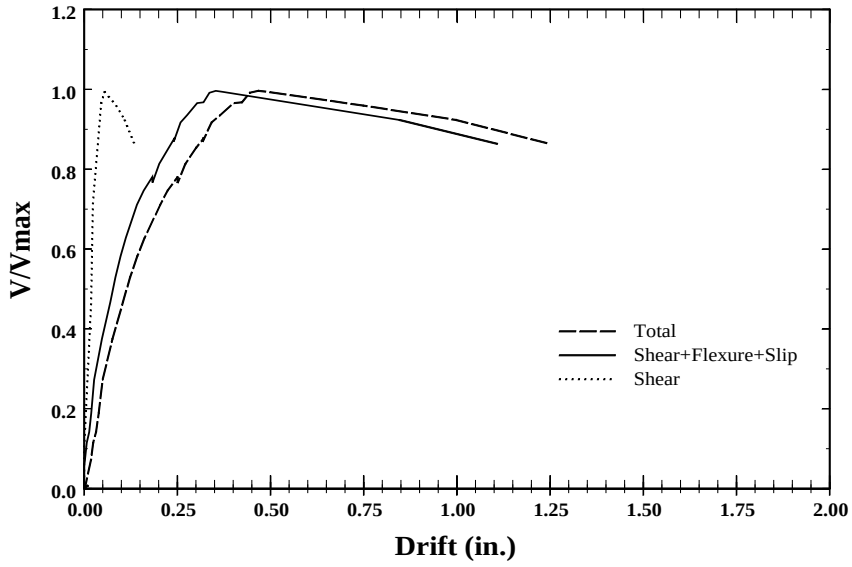

Figure 4.73. Envelope curve for displacement components at the load-point while loading with a positive couple. Specimen C10-10, south element.

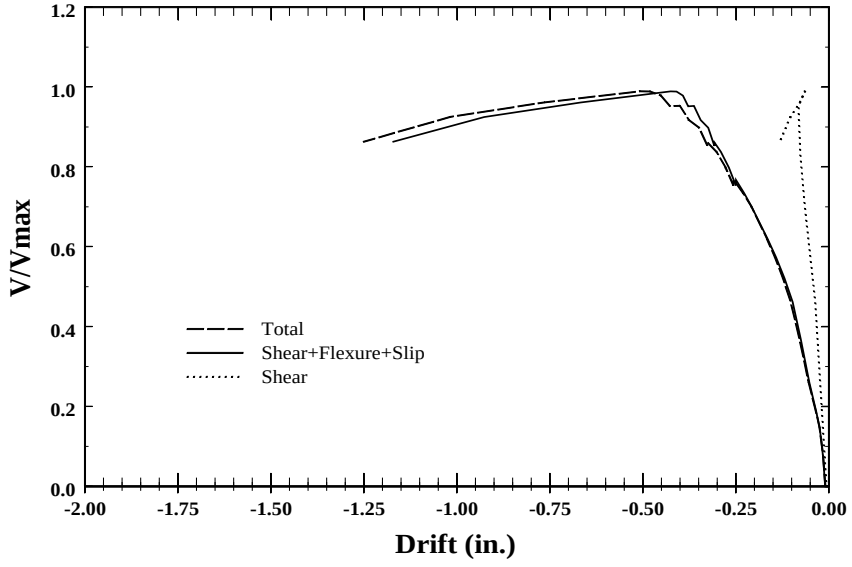

Figure 4.74. Envelope curve for displacement components at the load-point while loading with a positive couple. Specimen C10-10, north element.

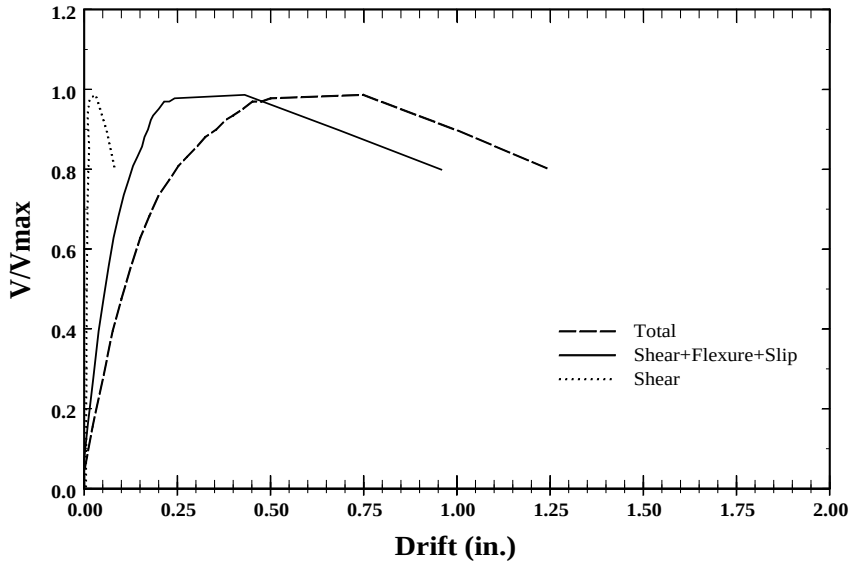

Figure 4.75. Envelope curve for displacement components at the load-point while loading with a positive couple. Specimen C10-20, south element.

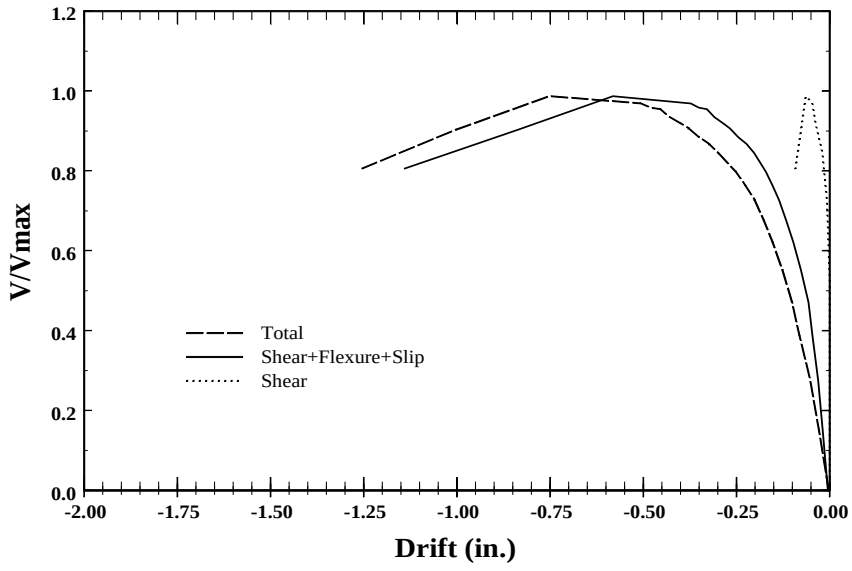

Figure 4.76. Envelope curve for displacement components at the load-point while loading with a positive couple. Specimen C10-20, north element.

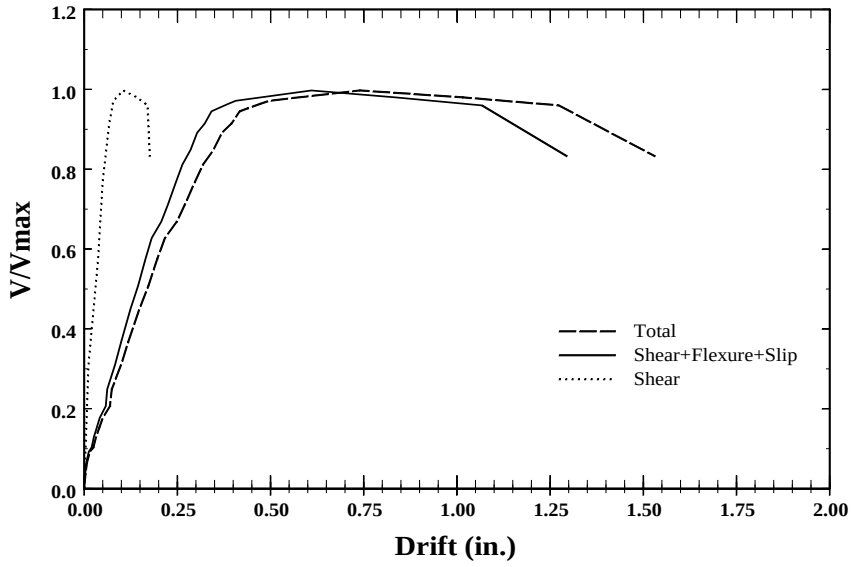

Figure 4.77. Envelope curve for displacement components at the load-point while loading with a positive couple. Specimen C5-00, south element.

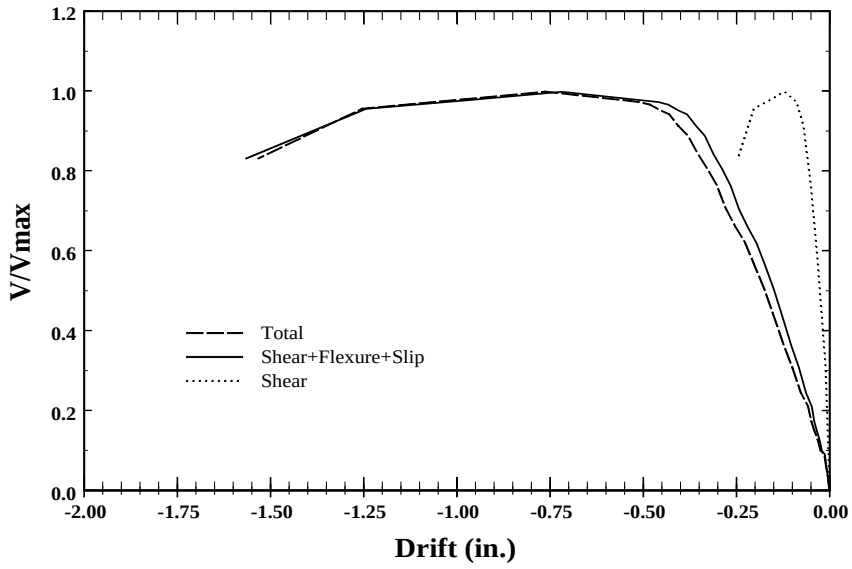

Figure 4.78. Envelope curve for displacement components at the load-point while loading with a positive couple. Specimen C5-00, north element.

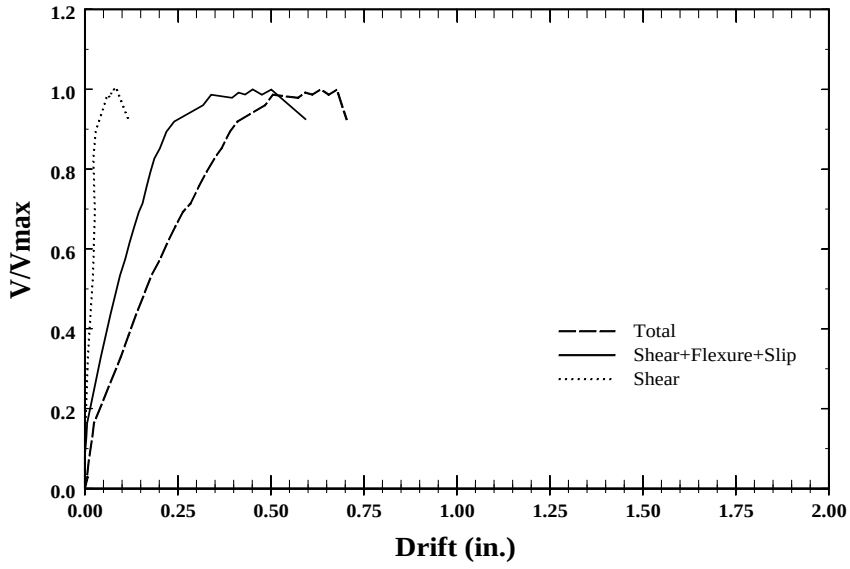

Figure 4.79. Envelope curve for displacement components at the load-point while loading with a positive couple. Specimen C5-10, south element.

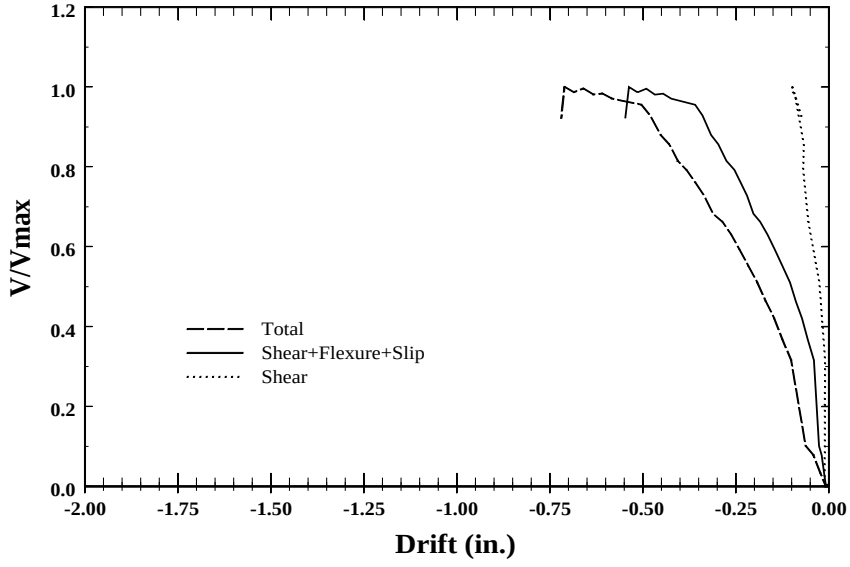

Figure 4.80. Envelope curve for displacement components at the load-point while loading with a positive couple. Specimen C5-10, north element.

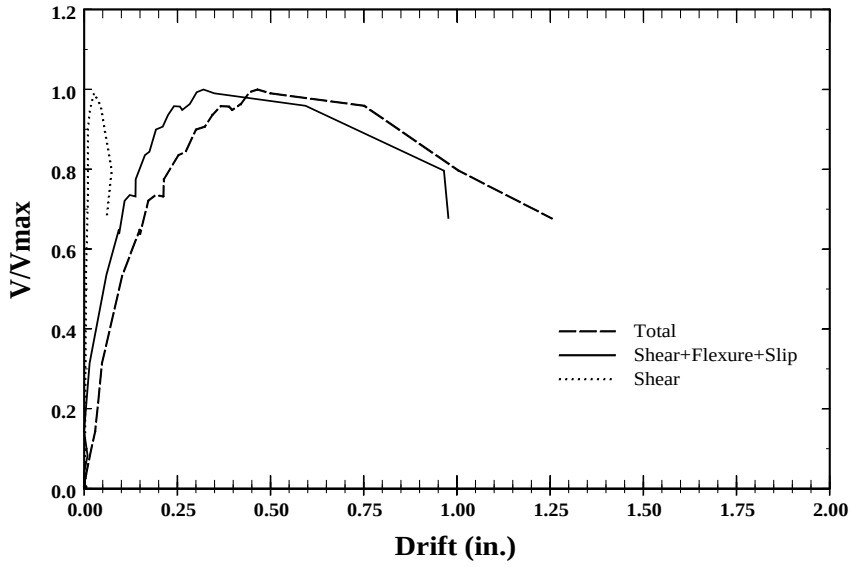

Figure 4.81. Envelope curve for displacement components at the load-point while loading with a positive couple. Specimen C5-20, south element.

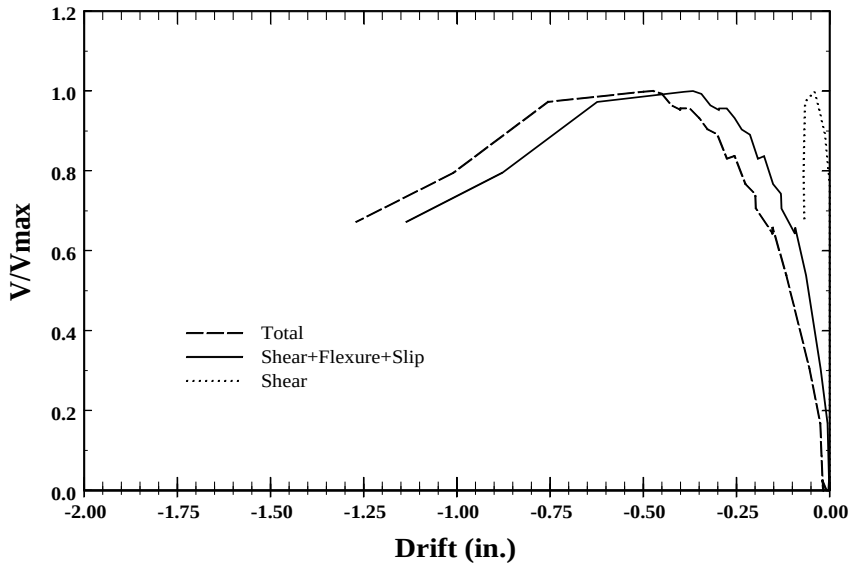

Figure 4.82. Envelope curve for displacement components at the load-point while loading with a positive couple. Specimen C5-20, north element.

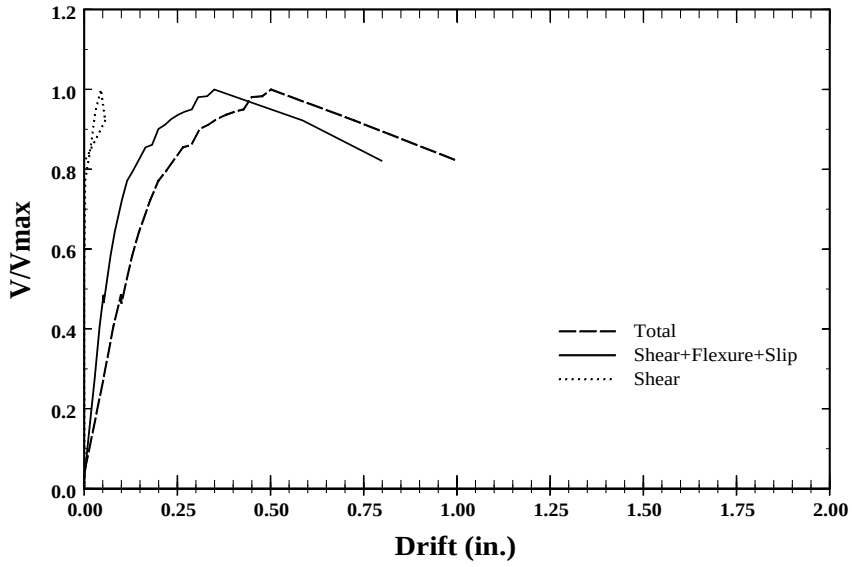

Figure 4.83. Envelope curve for displacement components at the load-point while loading with a positive couple. Specimen C5-40, south element.

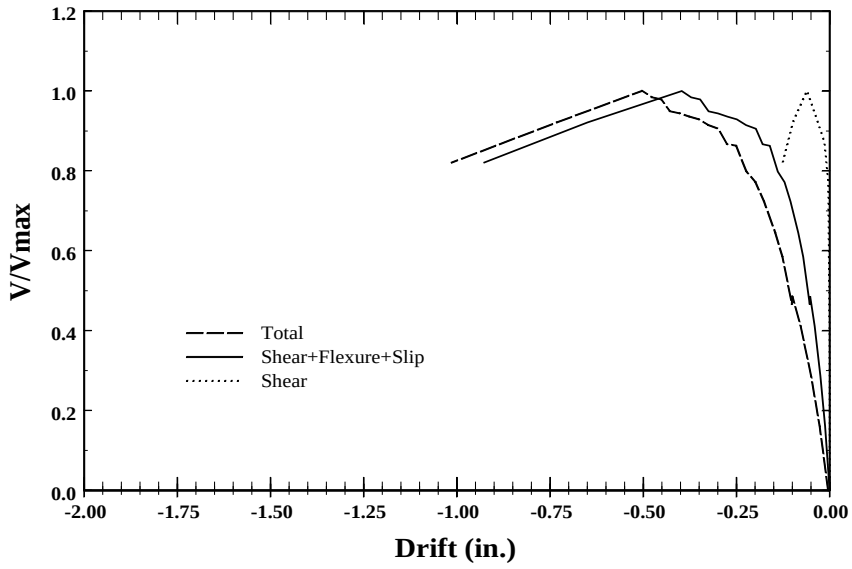

Figure 4.84. Envelope curve for displacement components at the load-point while loading with a positive couple. Specimen C5-40, north element.

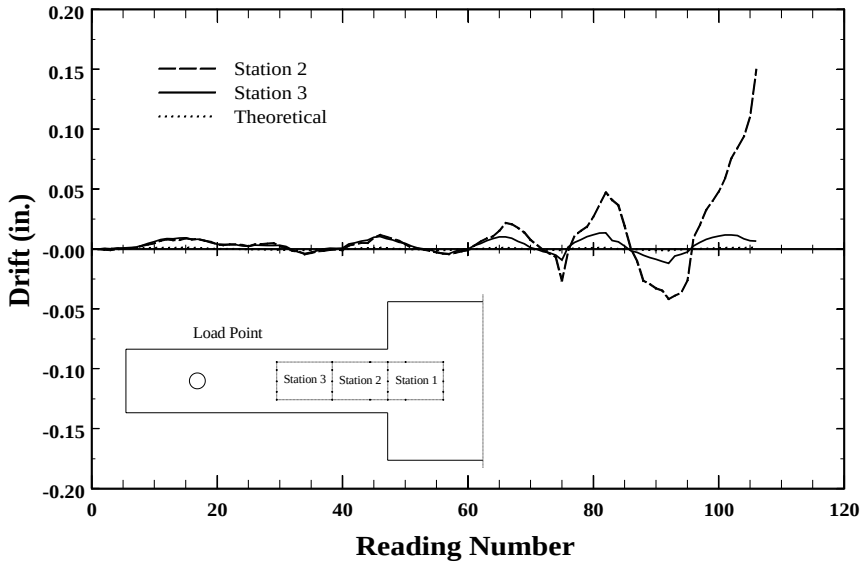

Figure 4.85. Displacement related to shear. Increment inferred from electronic Whittemore gage readings at stations 2 and 3 vs calculated. Specimen C10-00, south element.

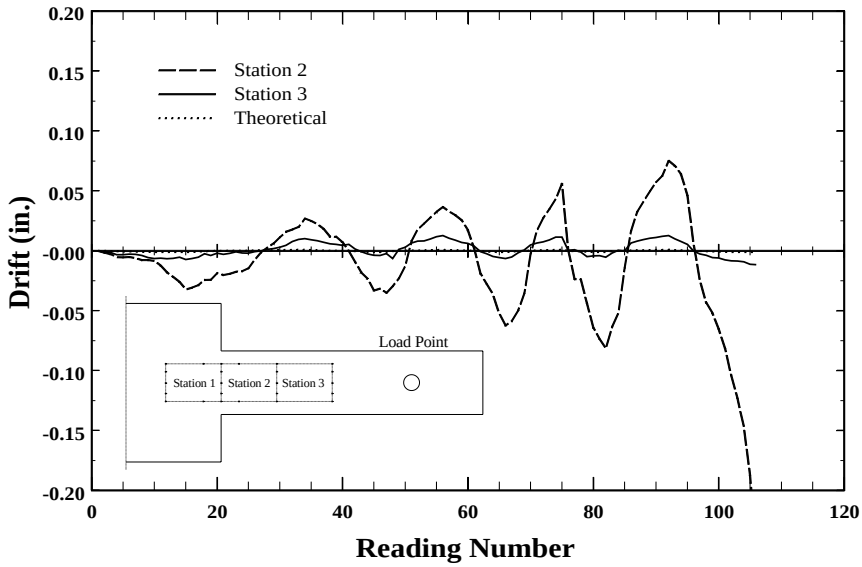

Figure 4.86. Displacement related to shear. Increment inferred from electronic Whittemore gage readings at stations 2 and 3 vs calculated. Specimen C10-00, north element.

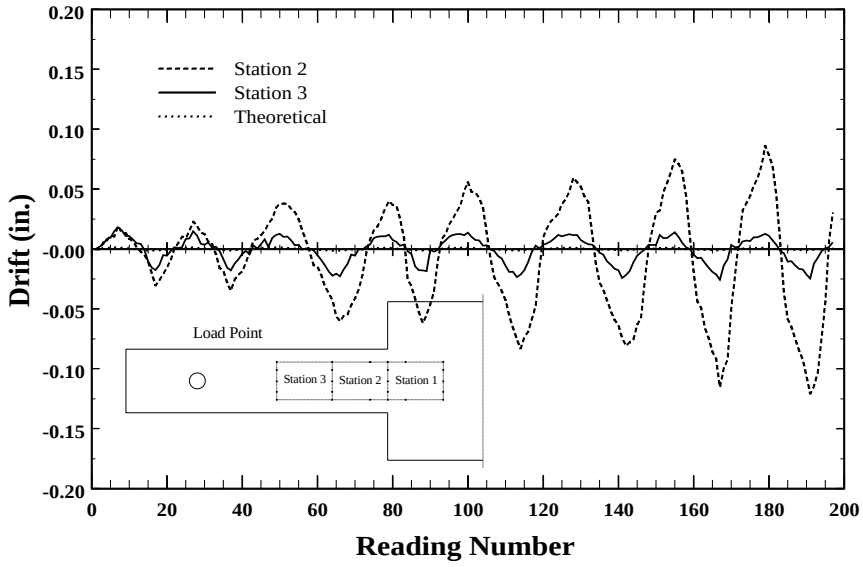

Figure 4.87. Displacement related to shear. Increment inferred from electronic Whittemore gage readings at stations 2 and 3 vs calculated. Specimen C10-05, south element.

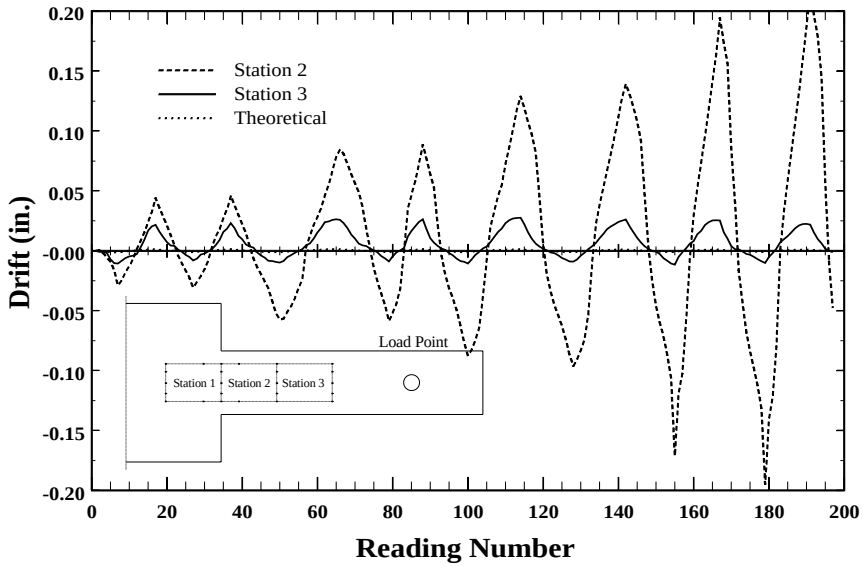

Figure 4.88. Displacement related to shear. Increment inferred from electronic Whittemore gage readings at stations 2 and 3 vs calculated. Specimen C10-05, north element.

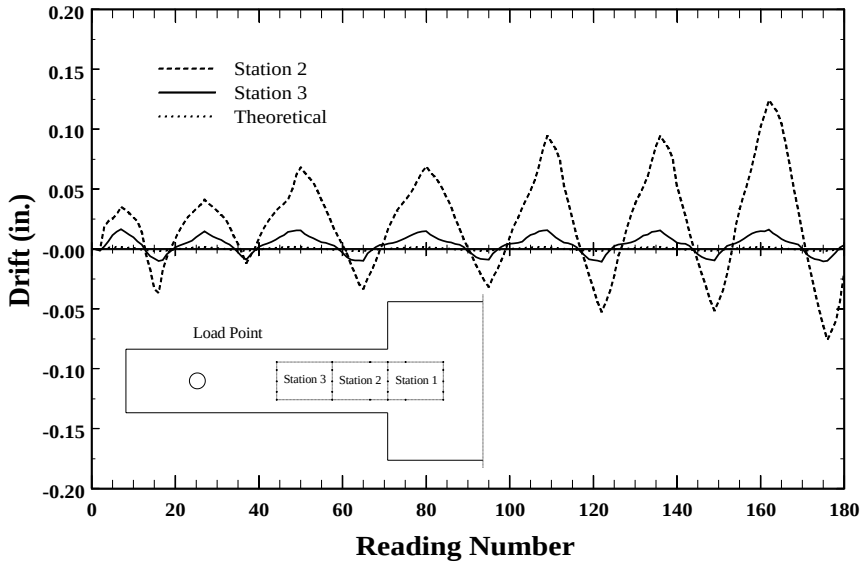

Figure 4.89. Displacement related to shear. Increment inferred from electronic Whittemore gage readings at stations 2 and 3 vs calculated. Specimen C10-10, south element.

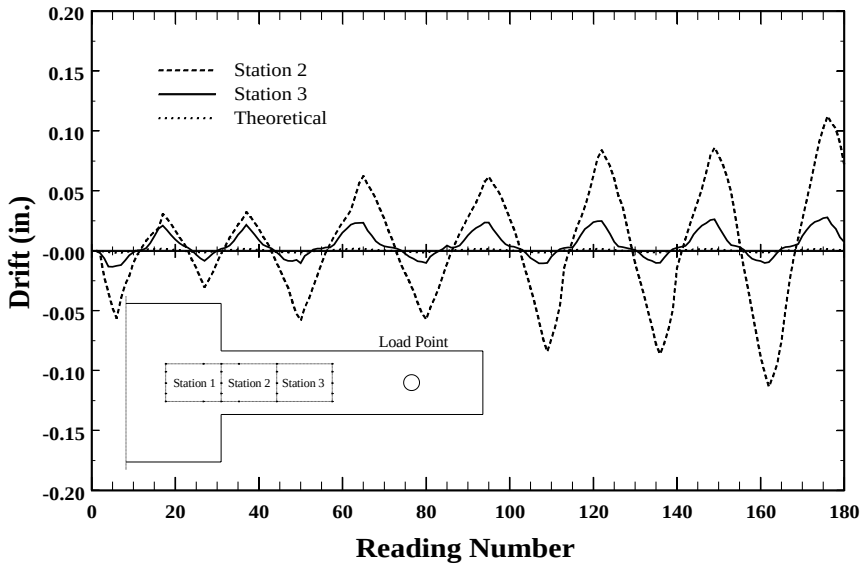

Figure 4.90. Displacement related to shear. Increment inferred from electronic Whittemore gage readings at stations 2 and 3 vs calculated. Specimen C10-10, north element.

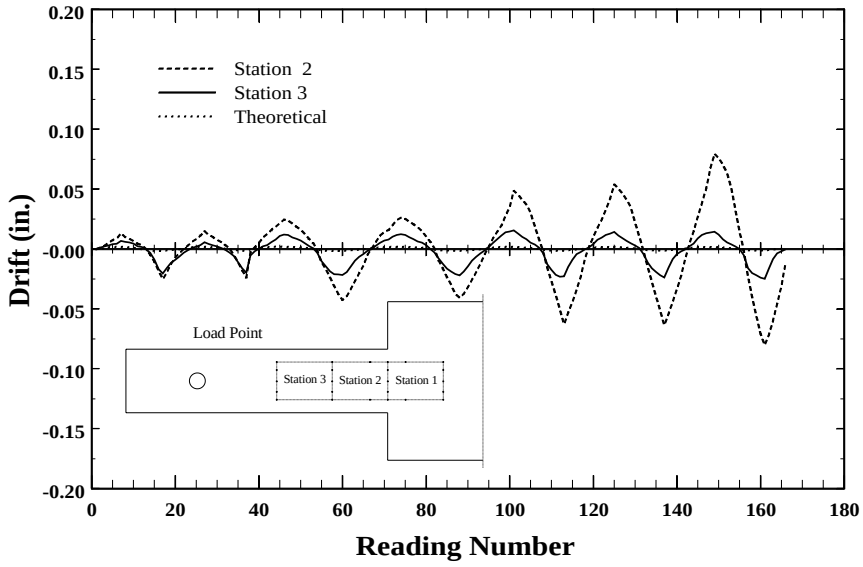

Figure 4.91. Displacement related to shear. Increment inferred from electronic Whittemore gage readings at stations 2 and 3 vs calculated. Specimen C10-20, south element.

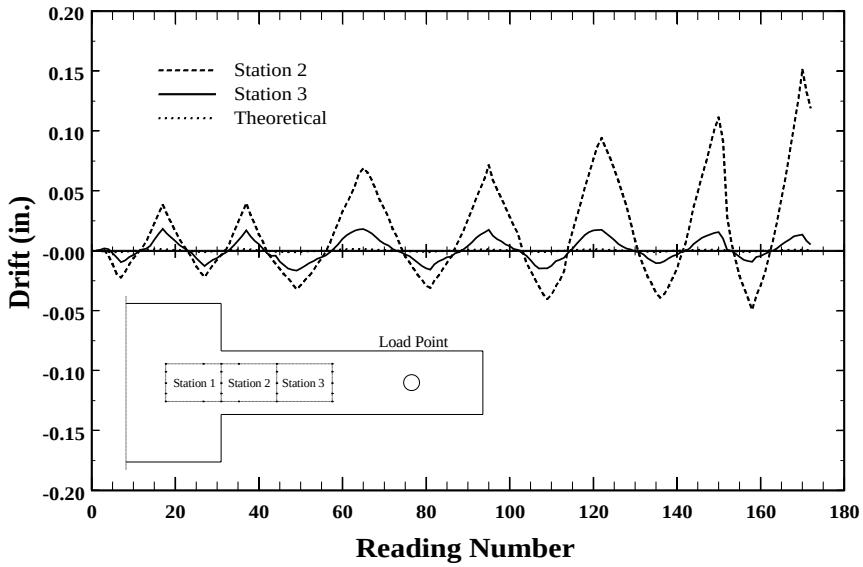

Figure 4.92. Displacement related to shear. Increment inferred from electronic Whittemore gage readings at stations 2 and 3 vs calculated. Specimen C10-20, north element.

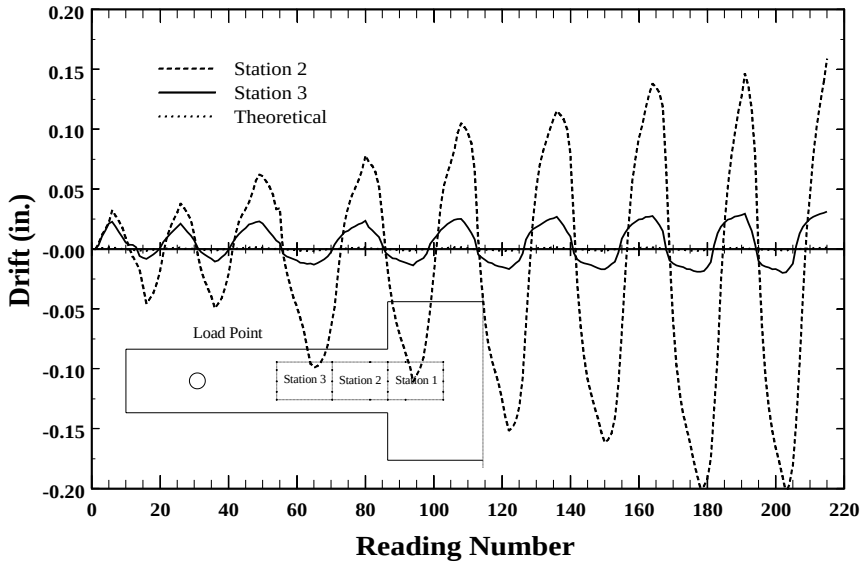

Figure 4.93. Displacement related to shear. Increment inferred from electronic Whittemore gage readings at stations 2 and 3 vs calculated. Specimen C5-00, south element.

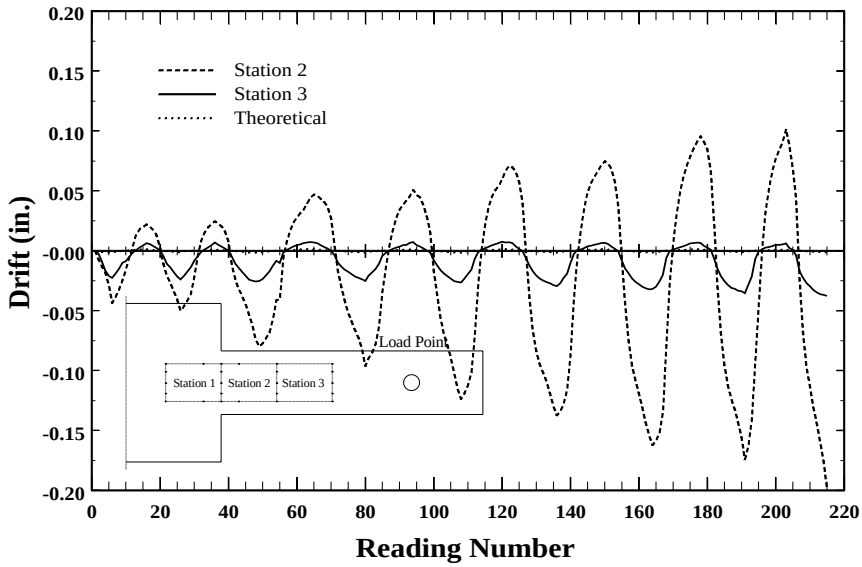

Figure 4.94. Displacement related to shear. Increment inferred from electronic Whittemore gage readings at stations 2 and 3 vs calculated. Specimen C5-00, north element.

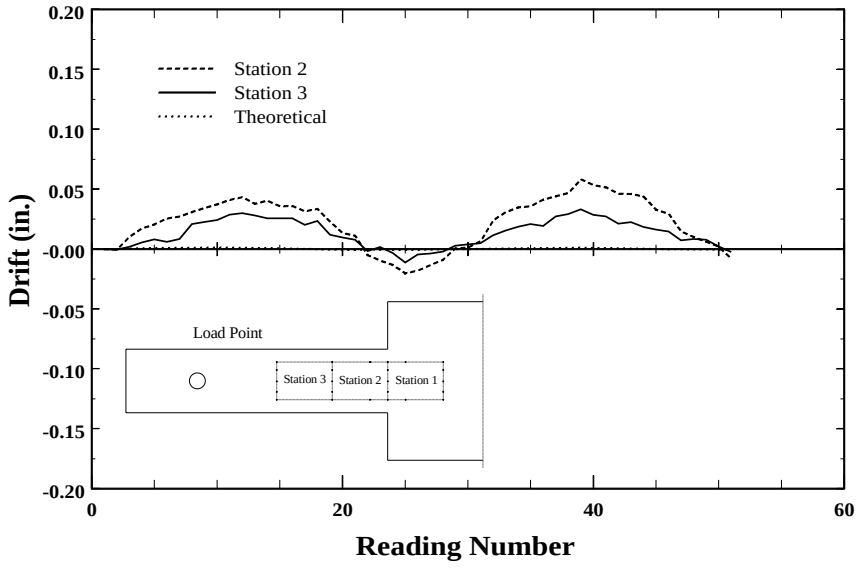

Figure 4.95. Displacement related to shear. Increment inferred from electronic Whittemore gage readings at stations 2 and 3 vs calculated. Specimen C5-10, south element.

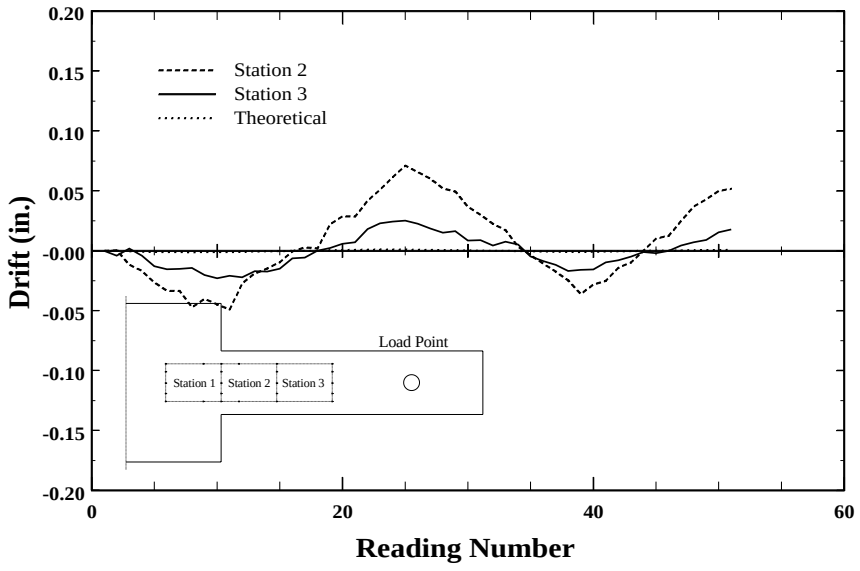

Figure 4.96. Displacement related to shear. Increment inferred from electronic Whittemore gage readings at stations 2 and 3 vs calculated. Specimen C5-10, north element.

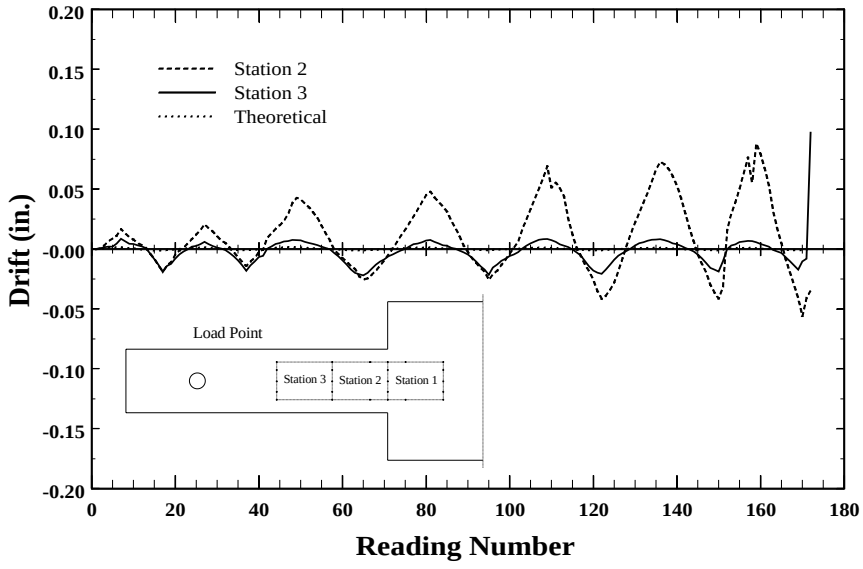

Figure 4.97. Displacement related to shear. Increment inferred from electronic Whittemore gage readings at stations 2 and 3 vs calculated. Specimen C5-20, south element.

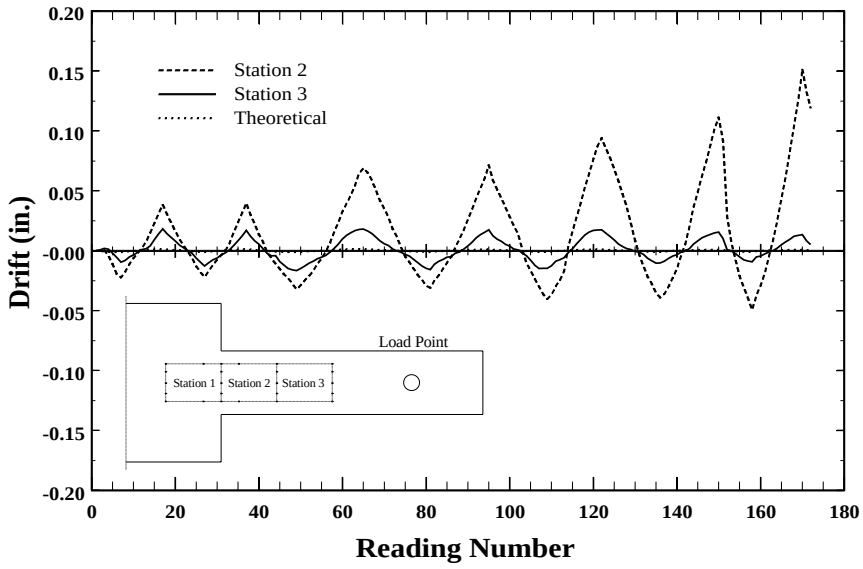

Figure 4.98. Displacement related to shear. Increment inferred from electronic Whittemore gage readings at stations 2 and 3 vs calculated. Specimen C5-20, north element.

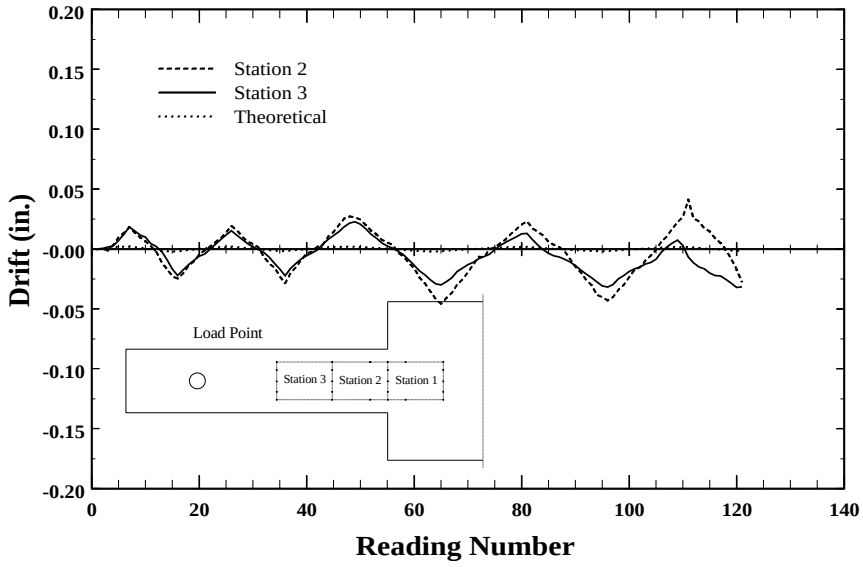

Figure 4.99. Displacement related to shear. Increment inferred from electronic Whittemore gage readings at stations 2 and 3 vs calculated. Specimen C5-40, south element.

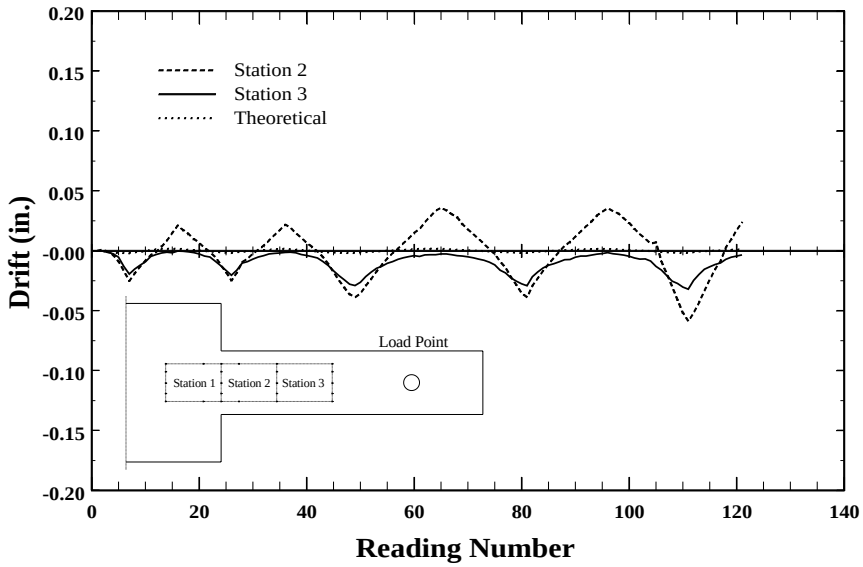

Figure 4.100. Displacement related to shear. Increment inferred from electronic Whittemore gage readings at stations 2 and 3 vs calculated. Specimen C5-40, north element.

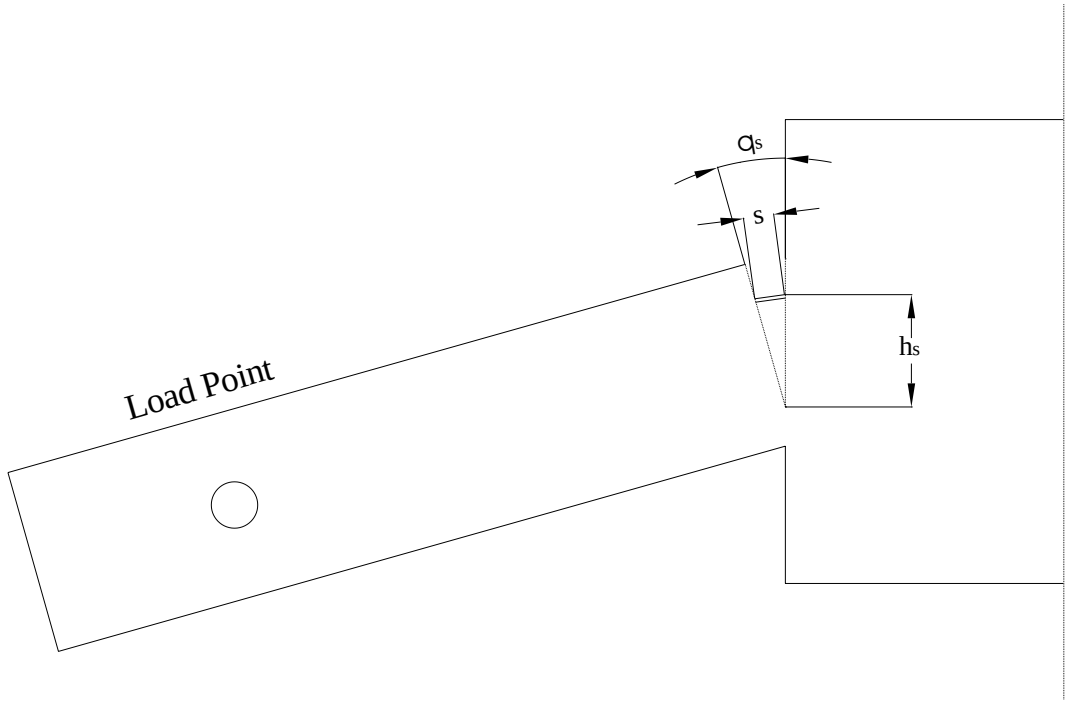

Figure 4.101. Deformation component related to slip.

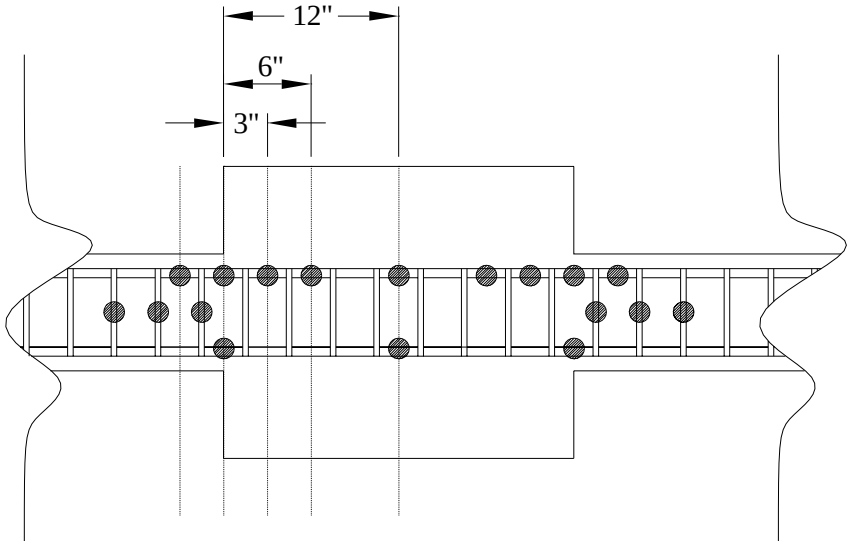

Figure 4.102. Location of strain gages in the joint area.

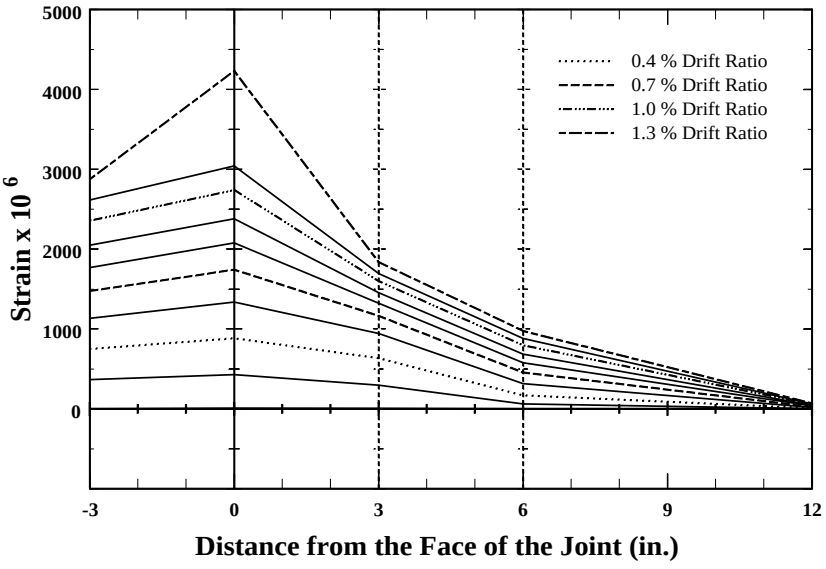

Figure 4.103. Tensile strain distribution in top north bar along the anchorage zone. Specimen C10-00.

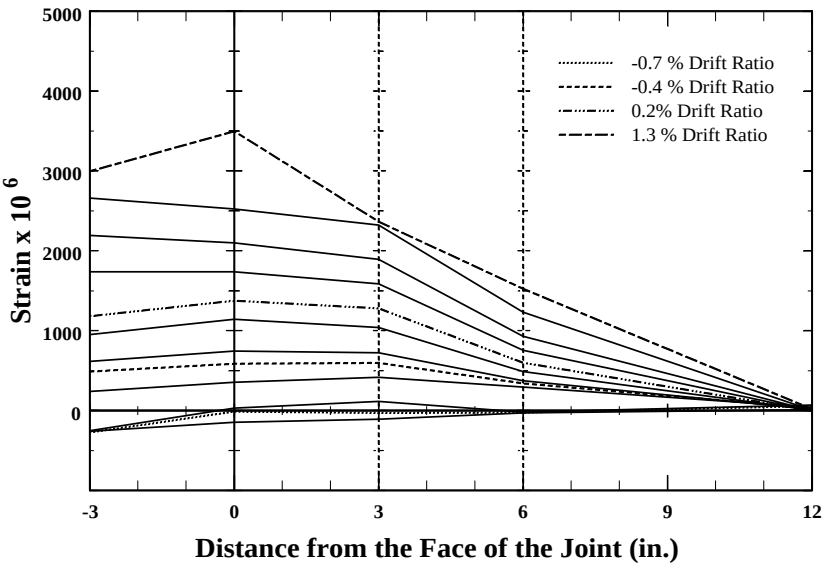

Figure 4.104. Tensile strain distribution in top south bar along the anchorage zone. Specimen C10-00.

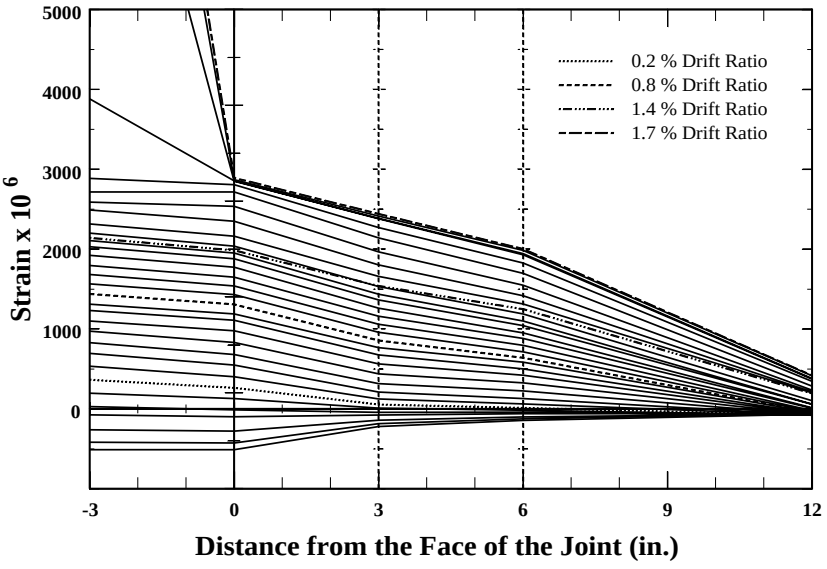

Figure 4.105. Tensile strain distribution in top north bar along the anchorage zone. Specimen C5-10.

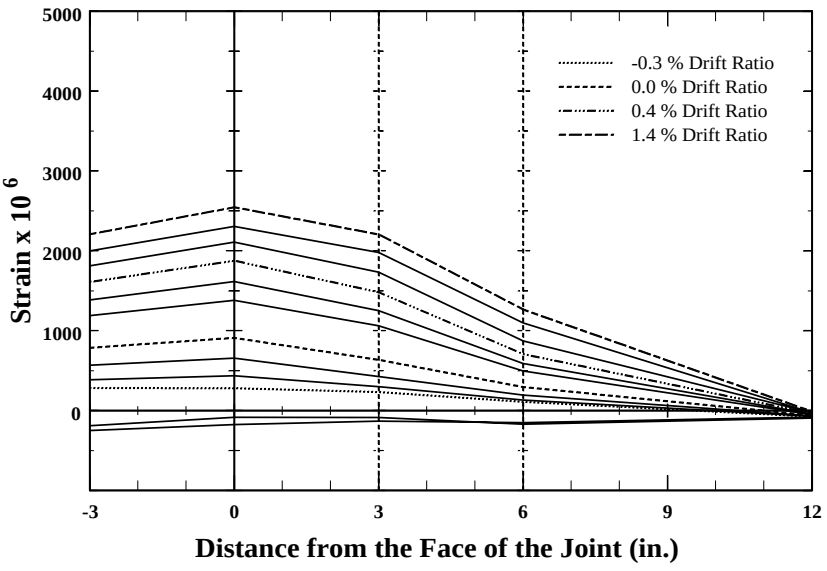

Figure 4.106. Tensile strain distribution in top south bar along the anchorage zone. Specimen C5-10.

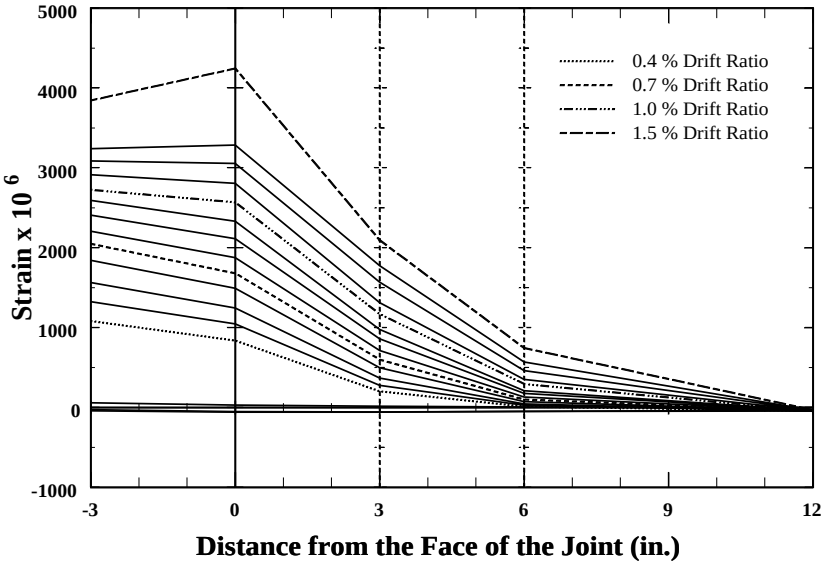

Figure 4.107. Tensile strain distribution in top north bar along the anchorage zone. Specimen C10-05.

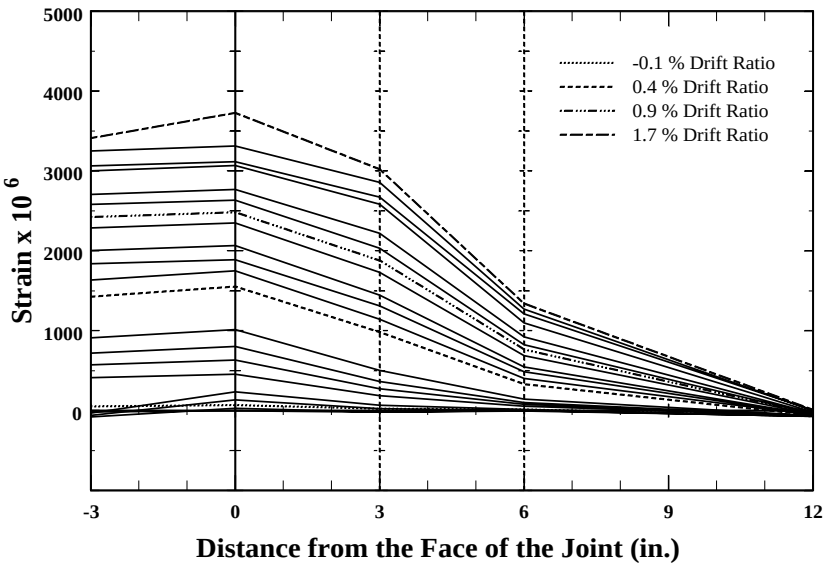

Figure 4.108. Tensile strain distribution in top south bar along the anchorage zone. Specimen C10-05.

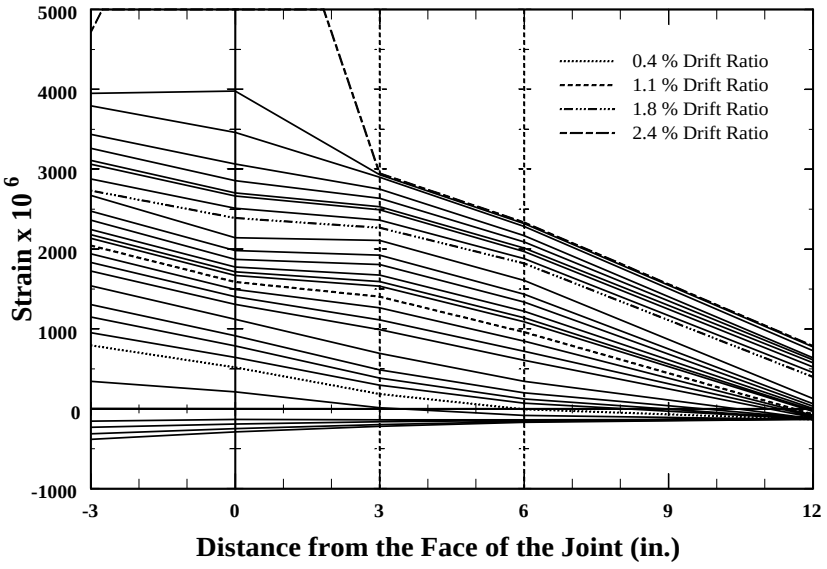

Figure 4.109. Tensile strain distribution in bottom north bar along the anchorage zone. Specimen C5-20.

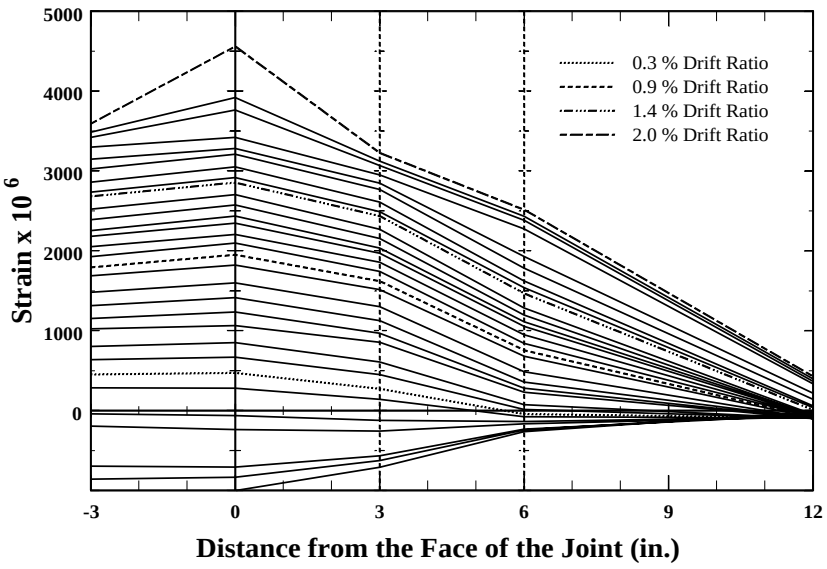

Figure 4.110. Tensile strain distribution in bottom south bar along the anchorage zone. Specimen C5-20.

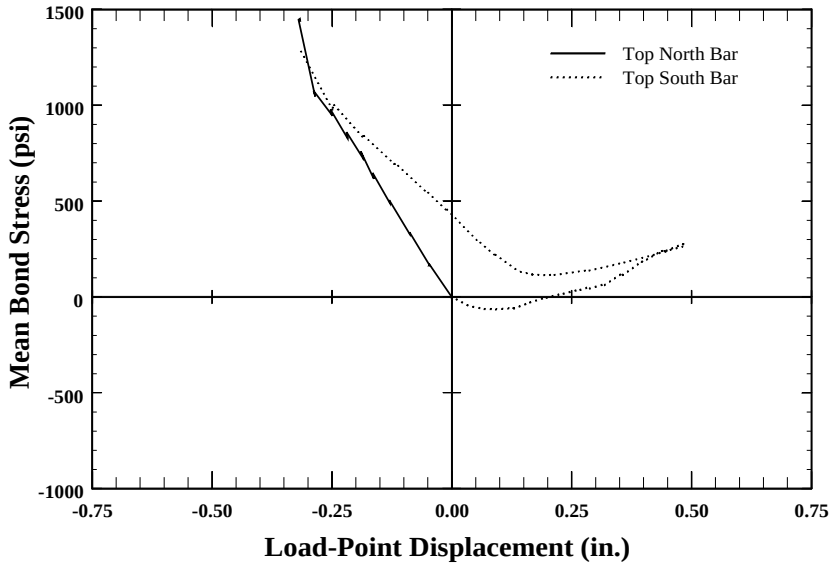

Figure 4.111. Mean bond stress for top bars of specimen C10-00.

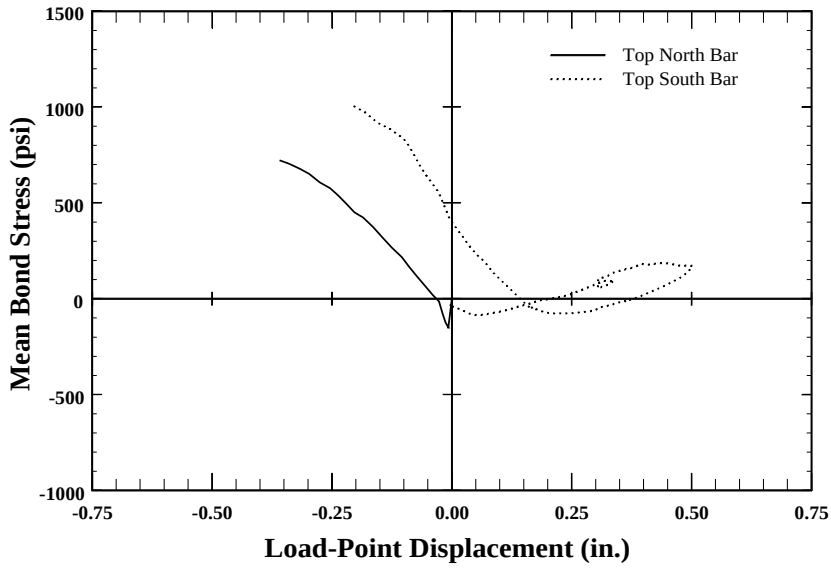

Figure 4.112. Mean bond stress for top bars of specimen C5-10.

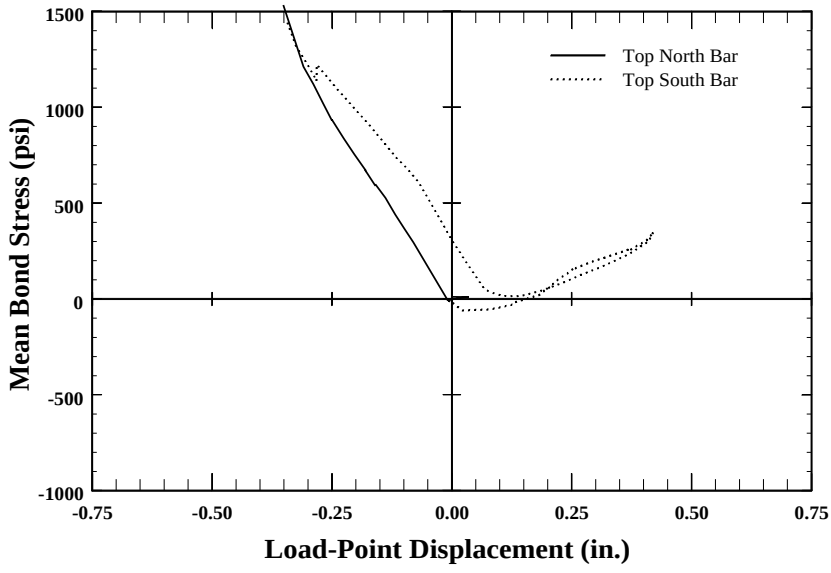

Figure 4.113. Mean bond stress for top bars of specimen C10-05.

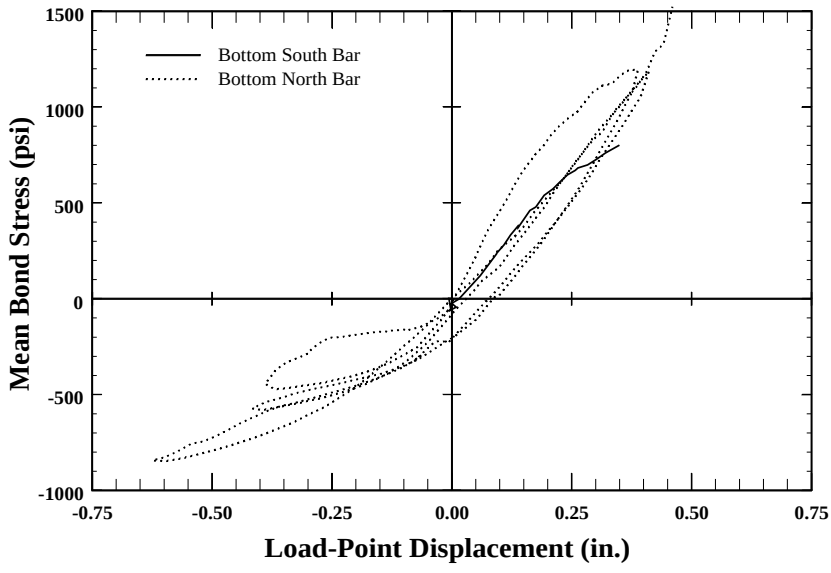

Figure 4.114. Mean bond stress for bottom bars of specimen C5-20.

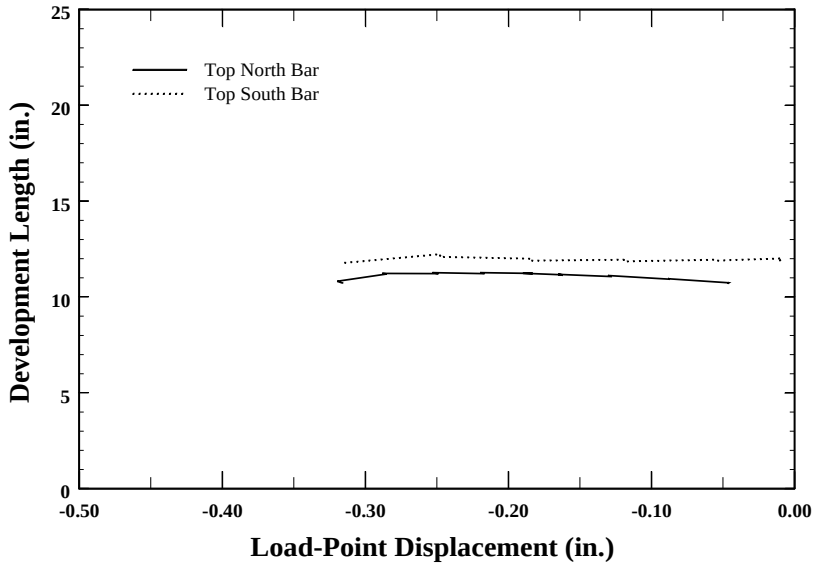

Figure 4.115. Calculated development length for Specimen C10-00.

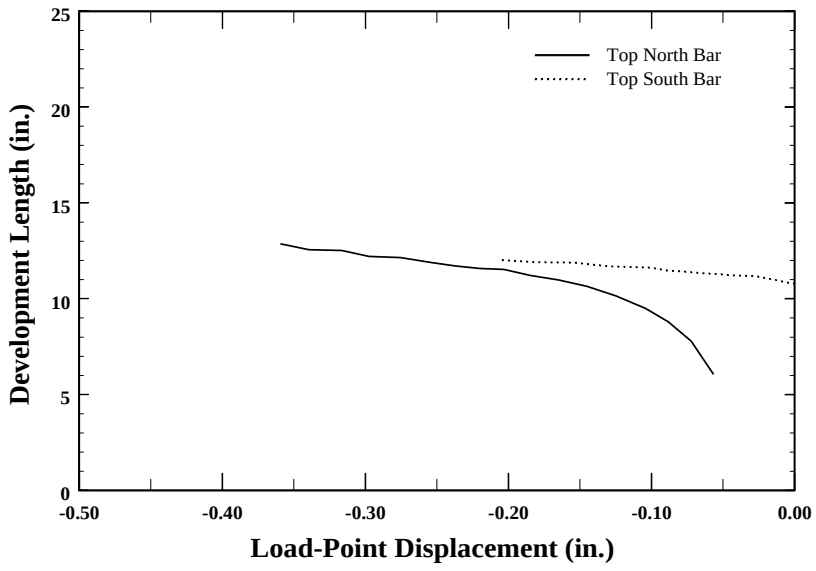

Figure 4.116. Calculated development length for Specimen C5-10.

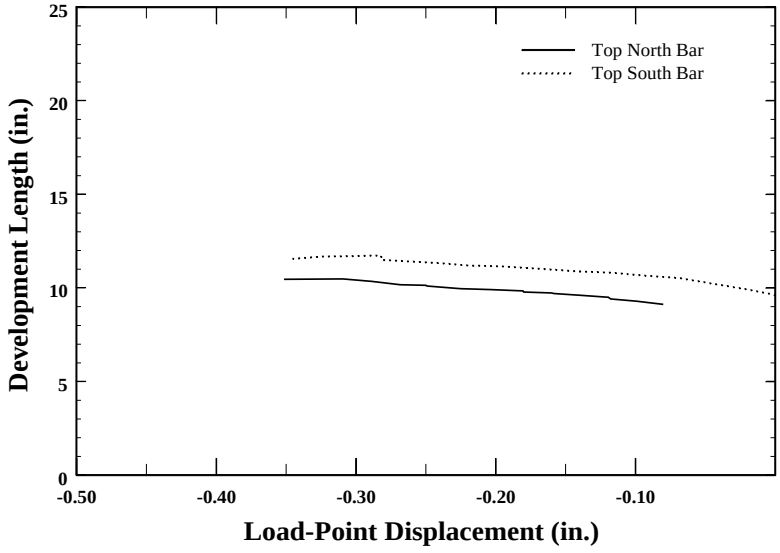

Figure 4.117. Calculated development length for Specimen C10-05.

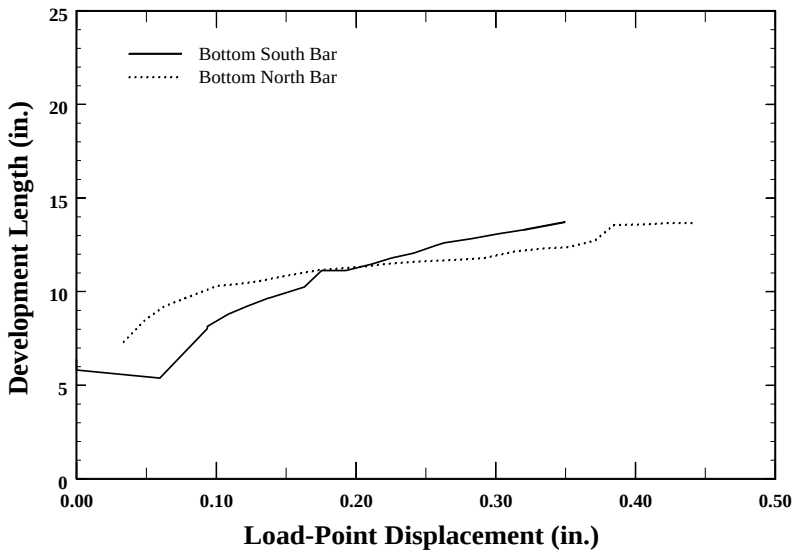

Figure 4.118. Calculated development length for Specimen C5-20.

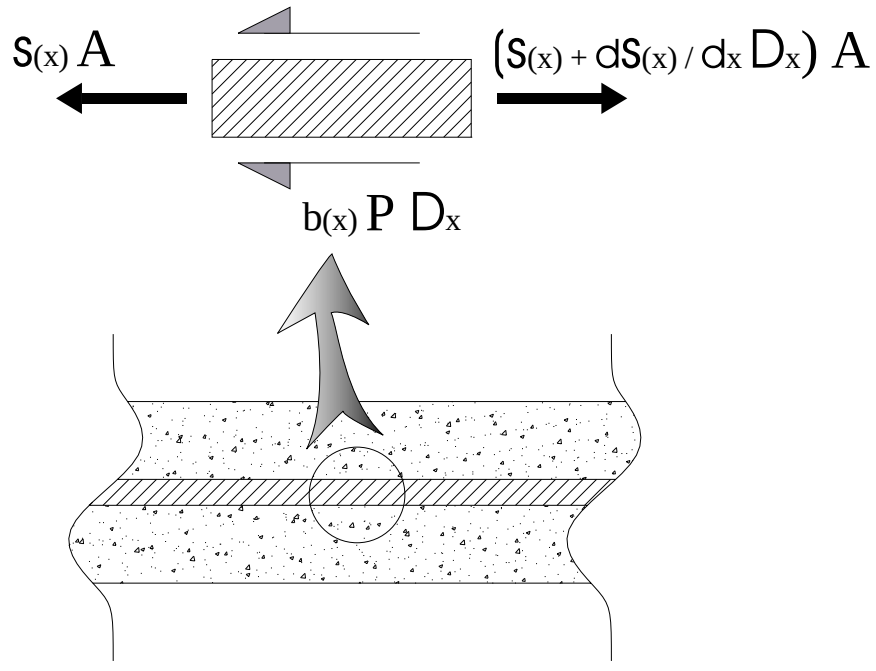

Figure 5.1. Free body diagram for section of reinforcing bar.

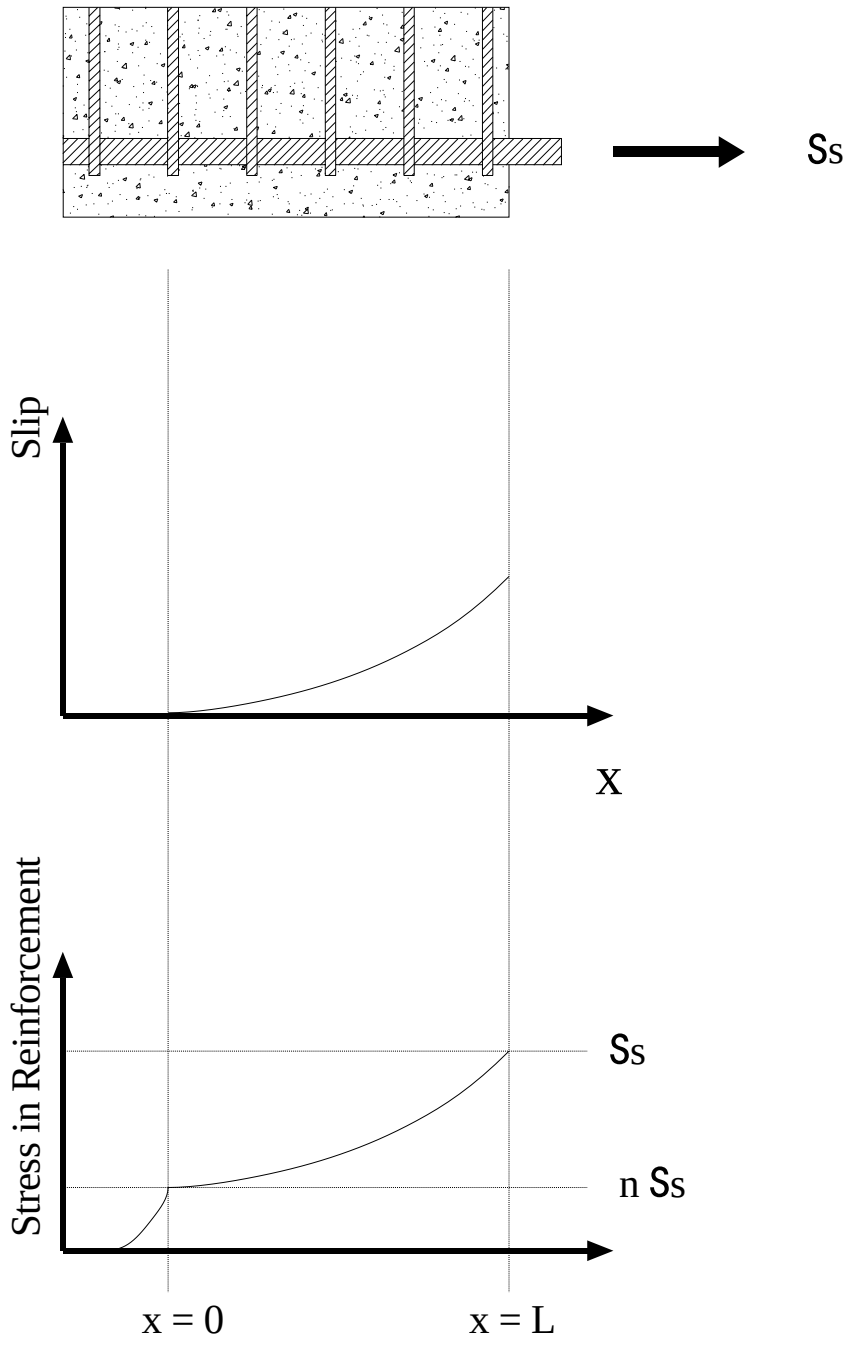

Figure 5.2. Distribution of slip and stress along the anchored length of the bar for the case of b_o= 0.

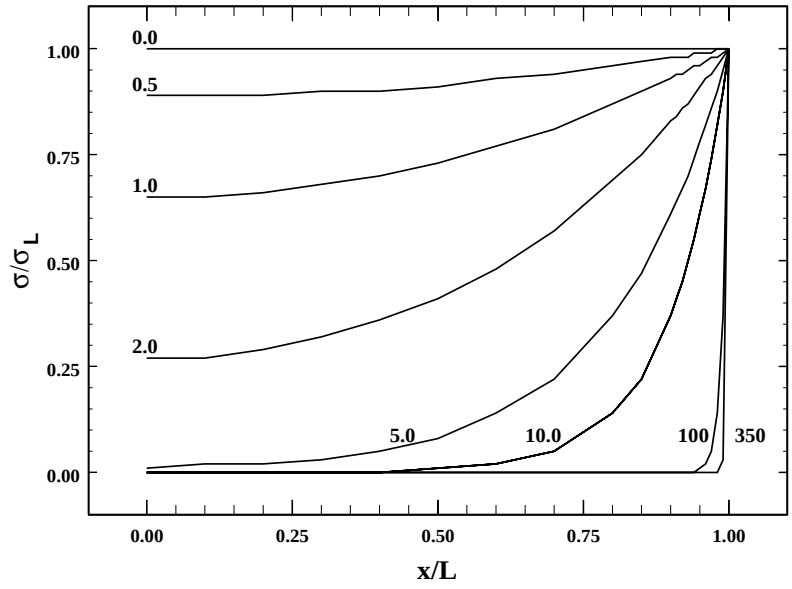

Figure 5.3. Distribution of stress along the anchored length of the bar for different values of k_pL. Case of $b_o = 0$.

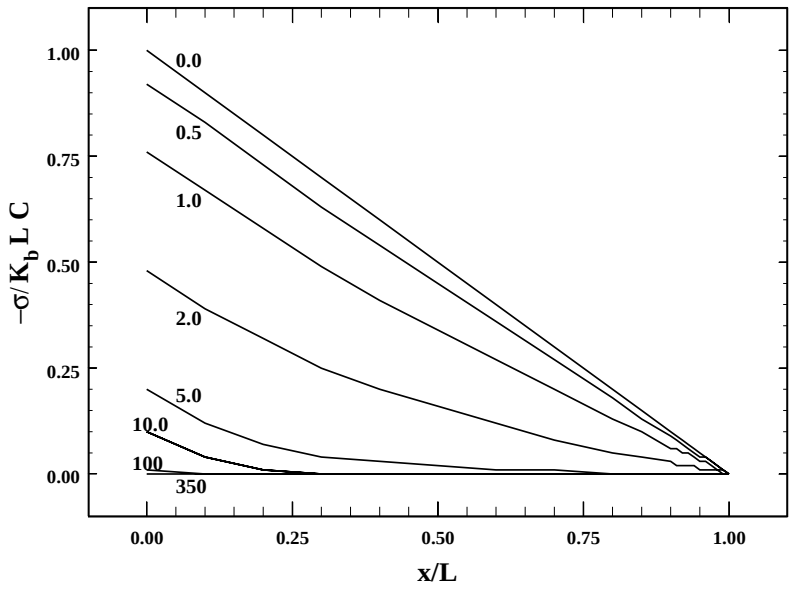

Figure 5.4. Contribution of the term related to k_b to the stress along the anchored length of the bar.

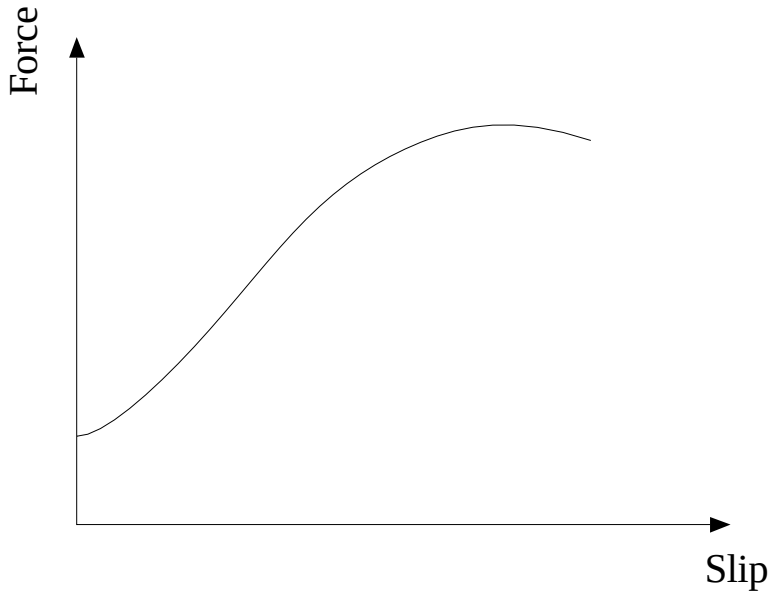

Figure 5.5. Typical stress vs. slip relationship for a deformed bar as reported by Abrams (Abrams, 1913).

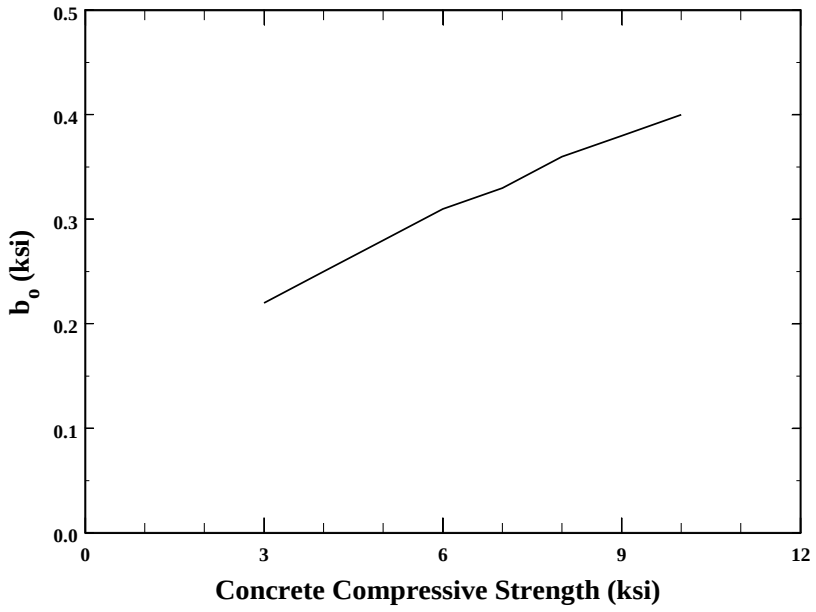

Figure 5.6. Suggested relationship between b_o and compressive strength of the concrete for the test series.

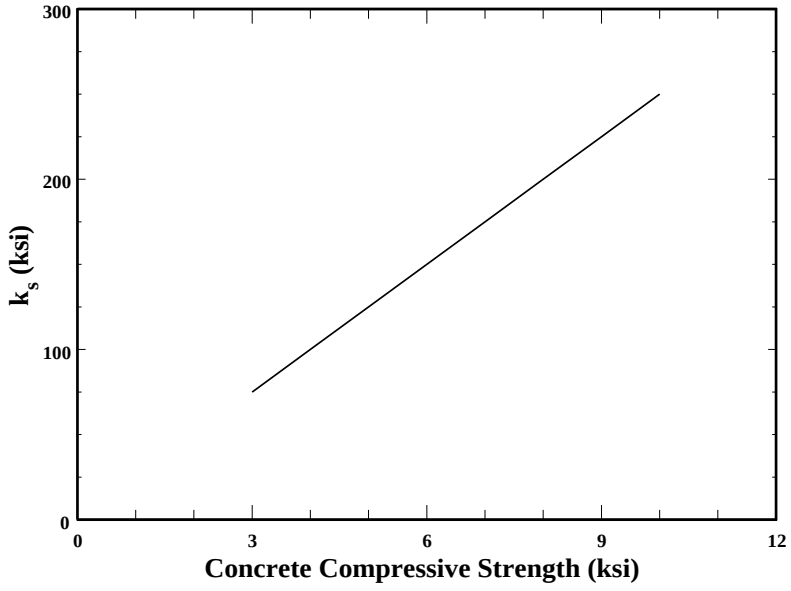

Figure 5.7. Suggested relationship between k_s and compressive strength of the concrete for the test series.

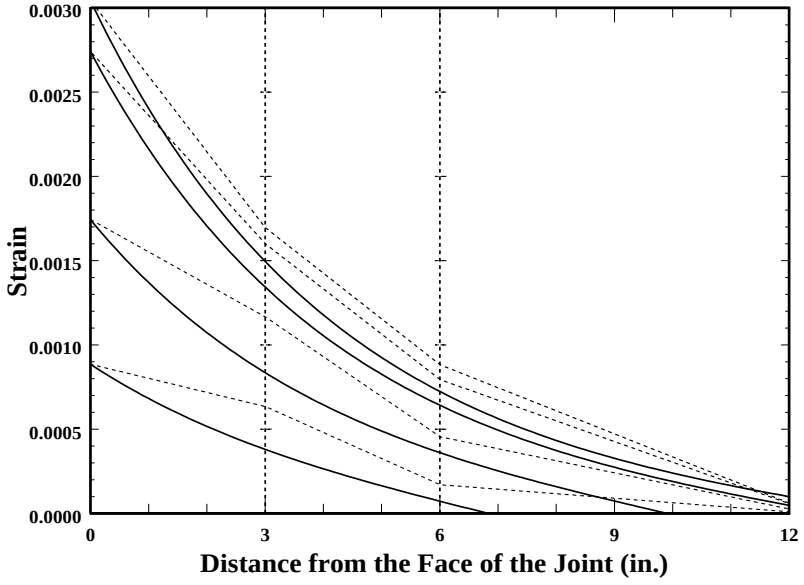

Figure 5.8. Calculated and measured strains along the anchorage length, specimen C10-00.

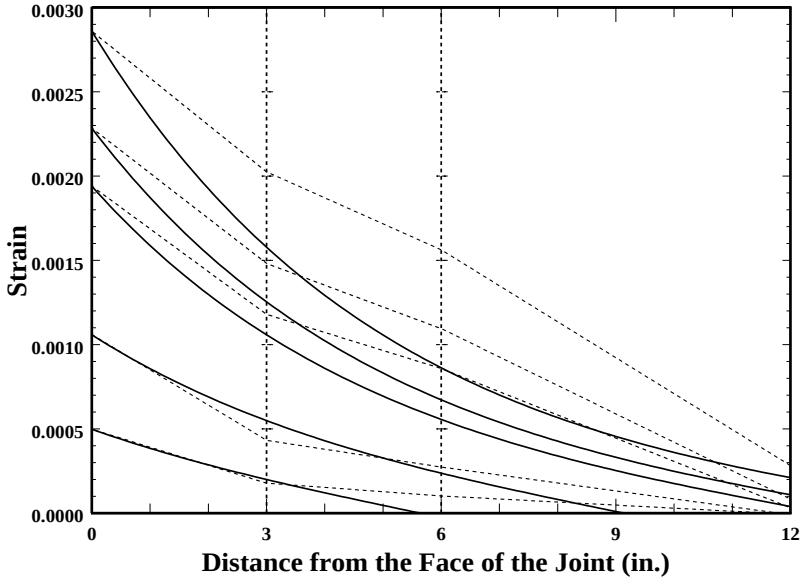

Figure 5.9. Calculated and measured strains along the anchorage length, specimen C5-10.

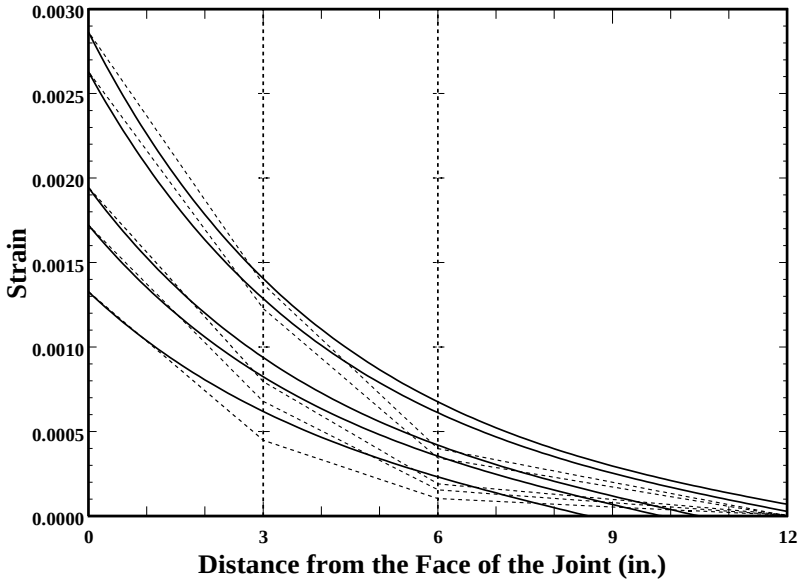

Figure 5.10. Calculated and measured strains along the anchorage length, specimen C10-05.

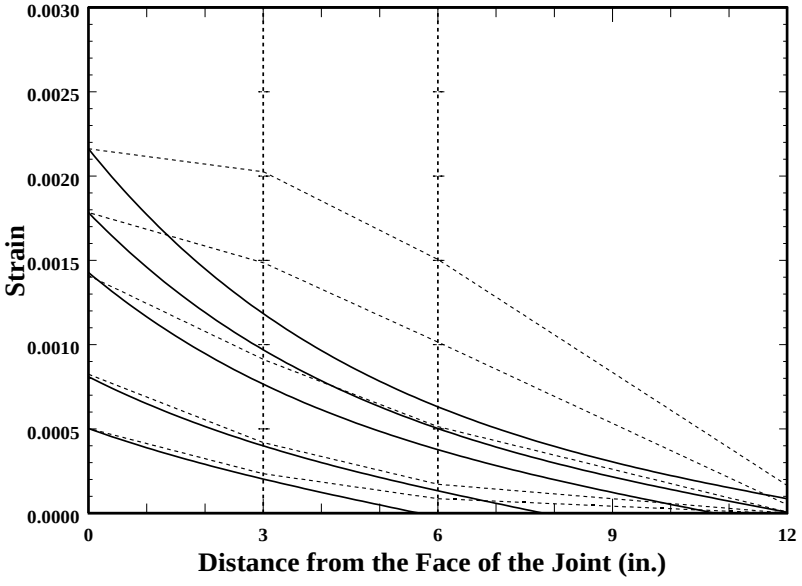

Figure 5.11. Calculated and measured strains along the anchorage length, specimen C5-20.

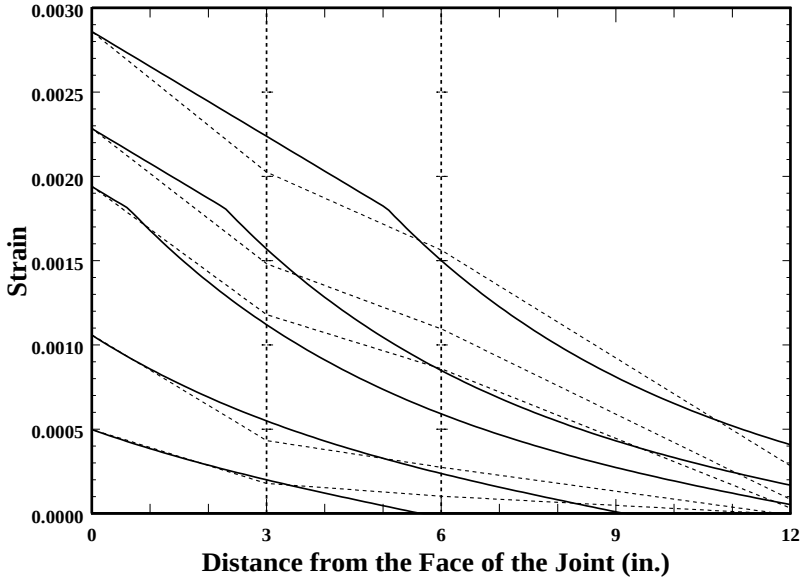

Figure 5.12. Calculated and measured strains along the anchorage length, specimen C5-10.

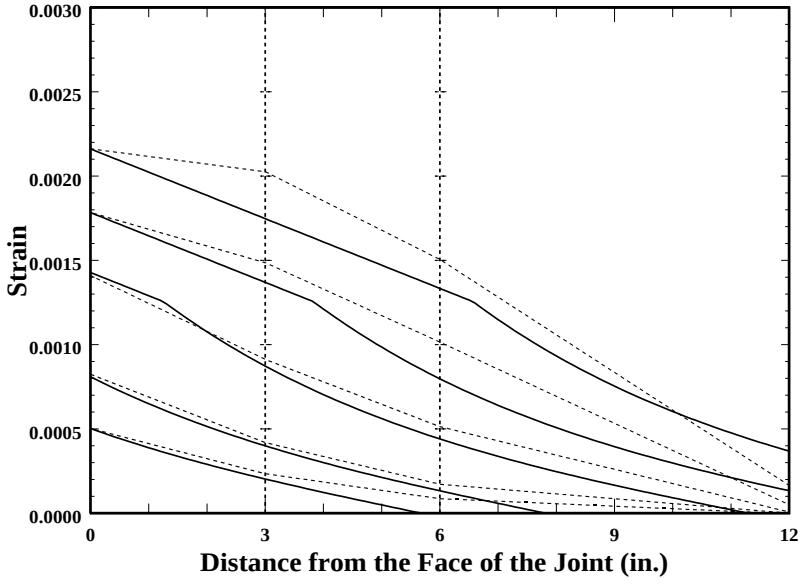

Figure 5.13. Calculated and measured strains along the anchorage length, specimen C5-20.

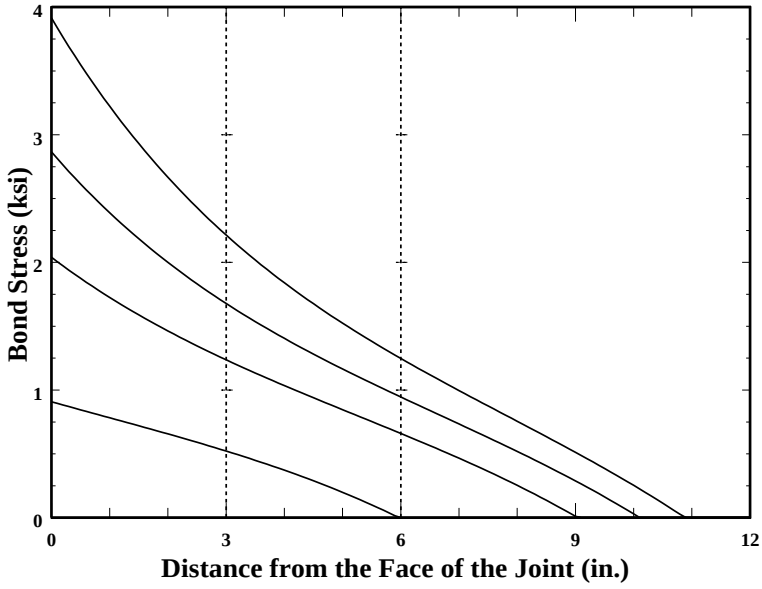

Figure 5.14. Calculated bond stress along the anchorage length, specimen C10-00.

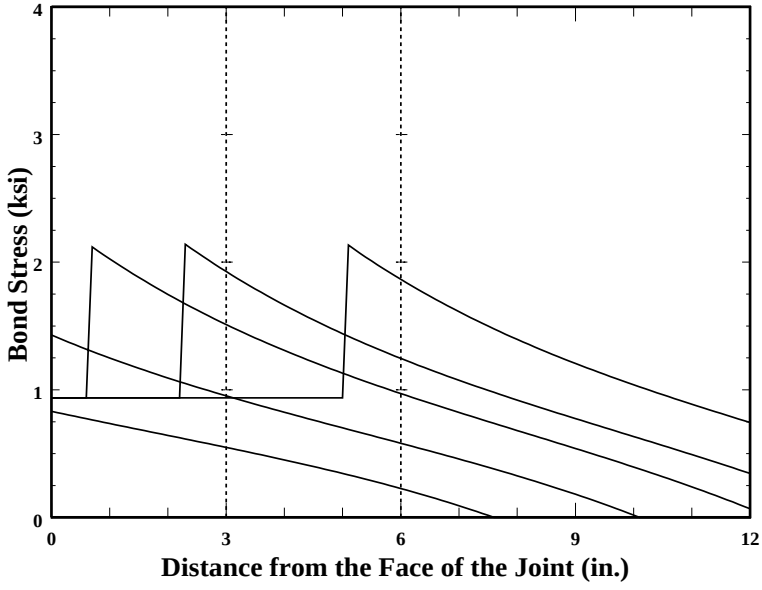

Figure 5.15. Calculated bond stress along the anchorage length, specimen C5-10.

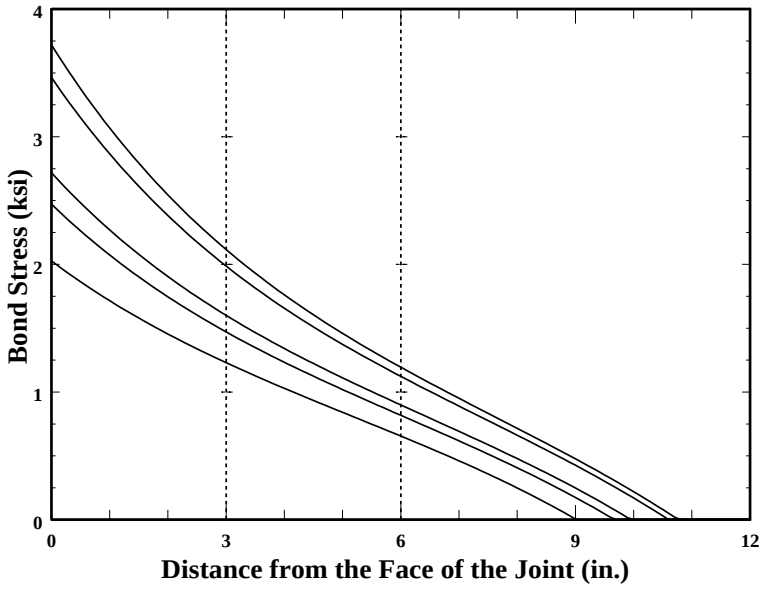

Figure 5.16. Calculated bond stress along the anchorage length, specimen C10-05.

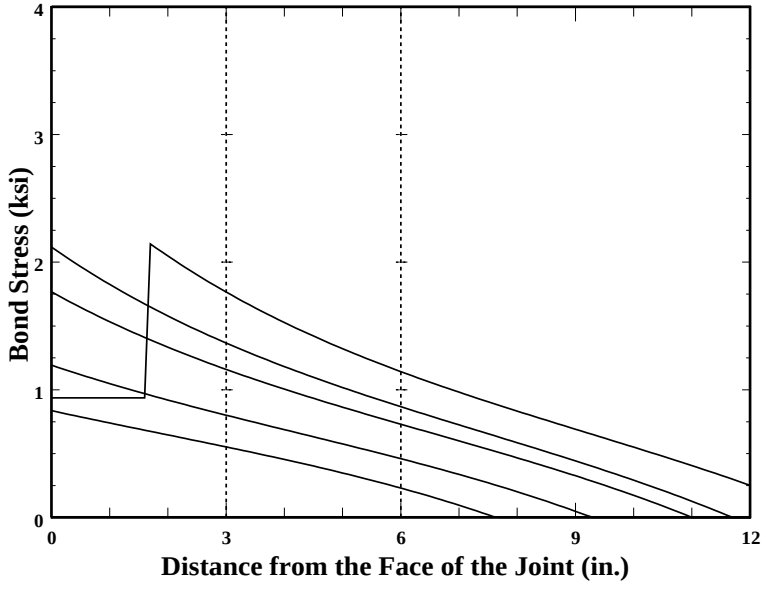

Figure 5.17. Calculated bond stress along the anchorage length, specimen C5-20.

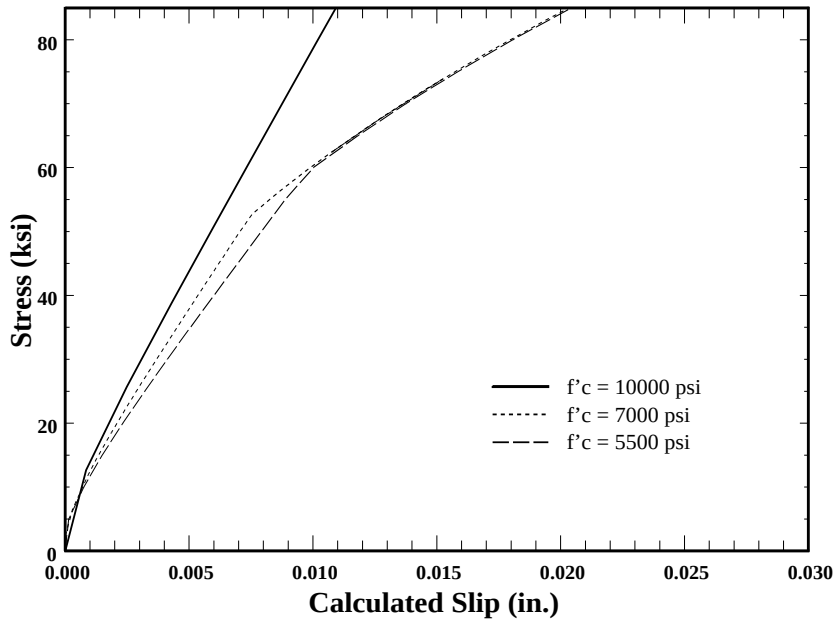

Figure 5.18. Calculated relationships between stress at the face of the joint and slip for different compressive strengths.

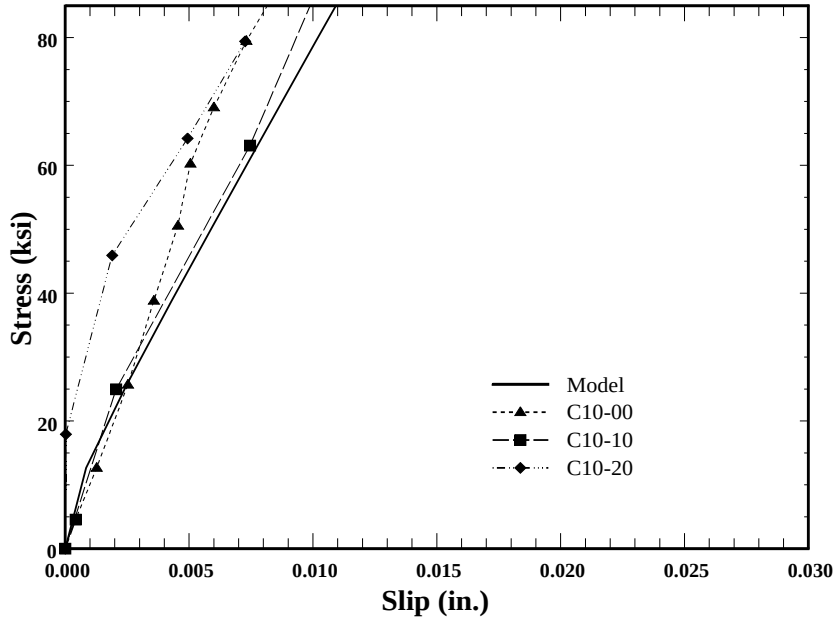

Figure 5.19. Calculated and measured relationship between stress at the face of the joint and slip for specimens C10-00 and C10-05.

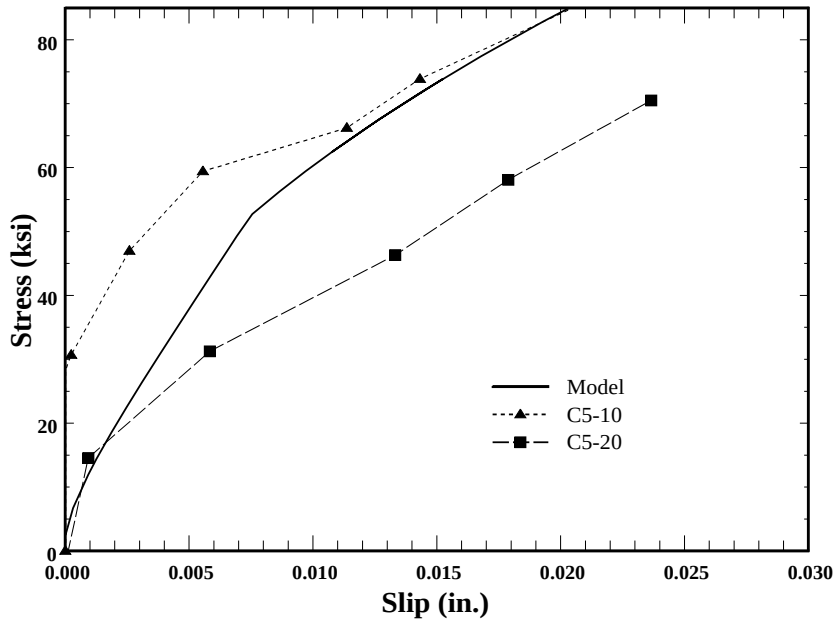

Figure 5.20. Calculated and measured relationship between stress at the face of the joint and slip for specimens C5-10 and C5-20.

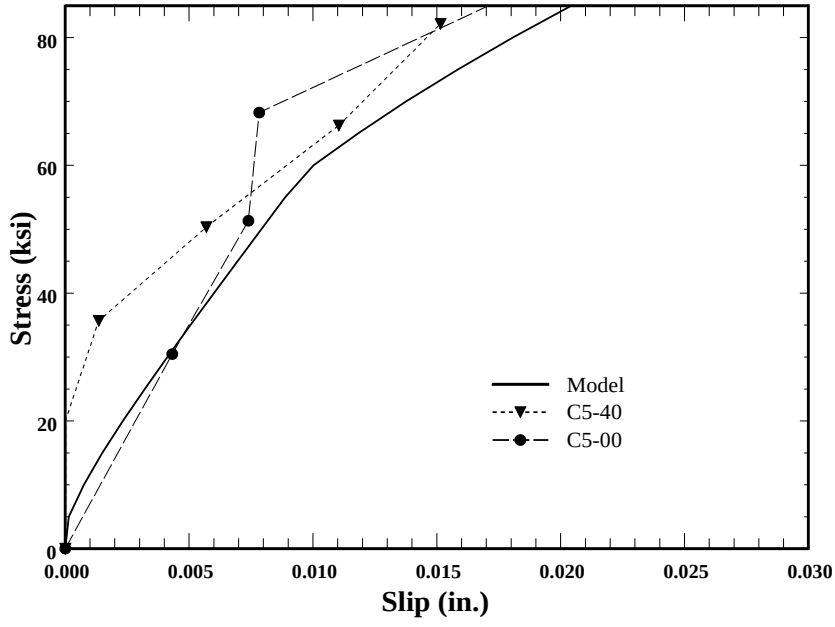

Figure 5.21. Calculated and measured relationship between stress at the face of the joint and slip for specimens C5-00 and C5-40.

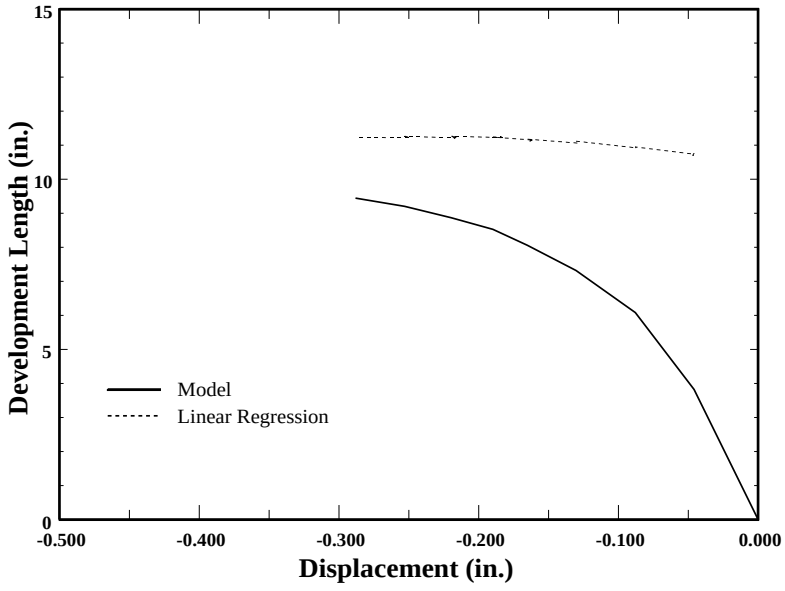

Figure 5.22. Calculated development length for specimen C10-00.

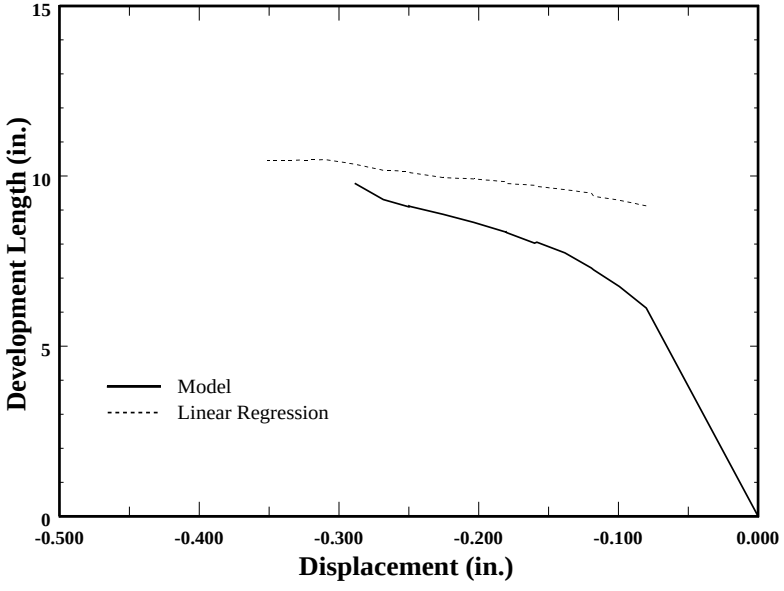

Figure 5.23. Calculated development length for specimen C10-05.

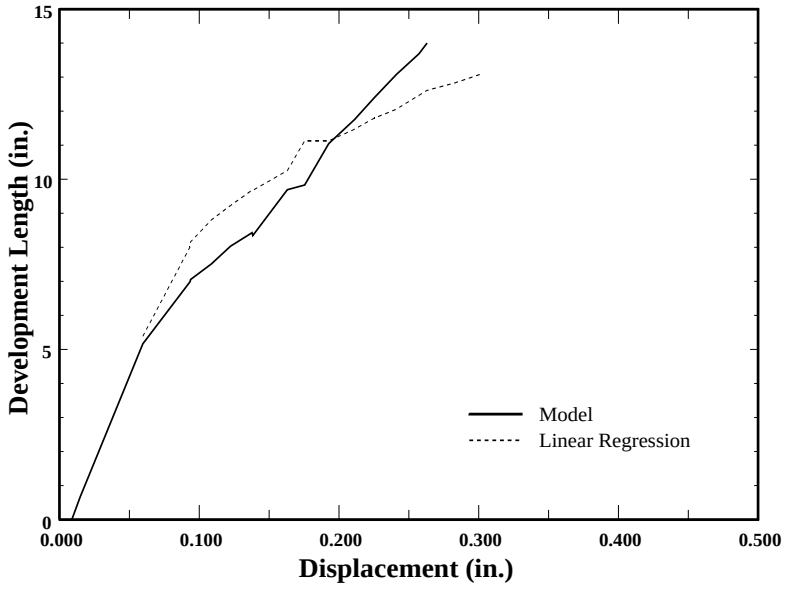

Figure 5.24. Calculated development length for specimen C5-20.

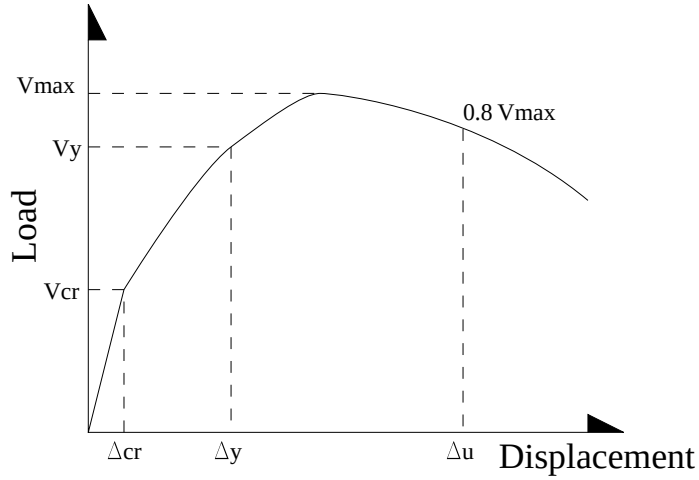

Figure 6.1. Typical measured load-displacement curve.

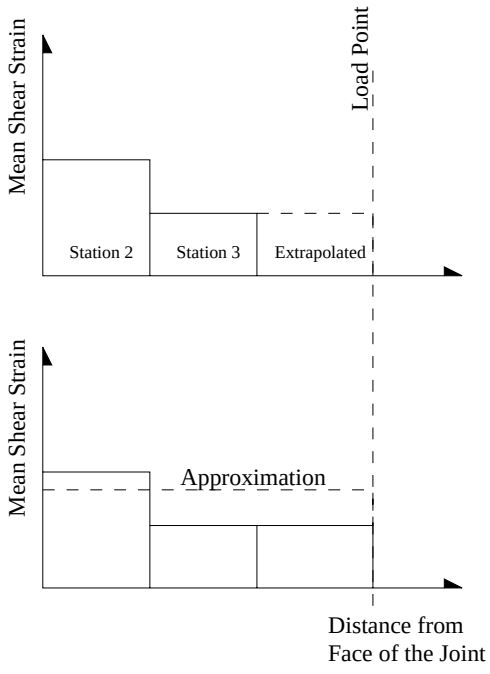

Figure 6.2. Procedure to calculated load-displacement response.

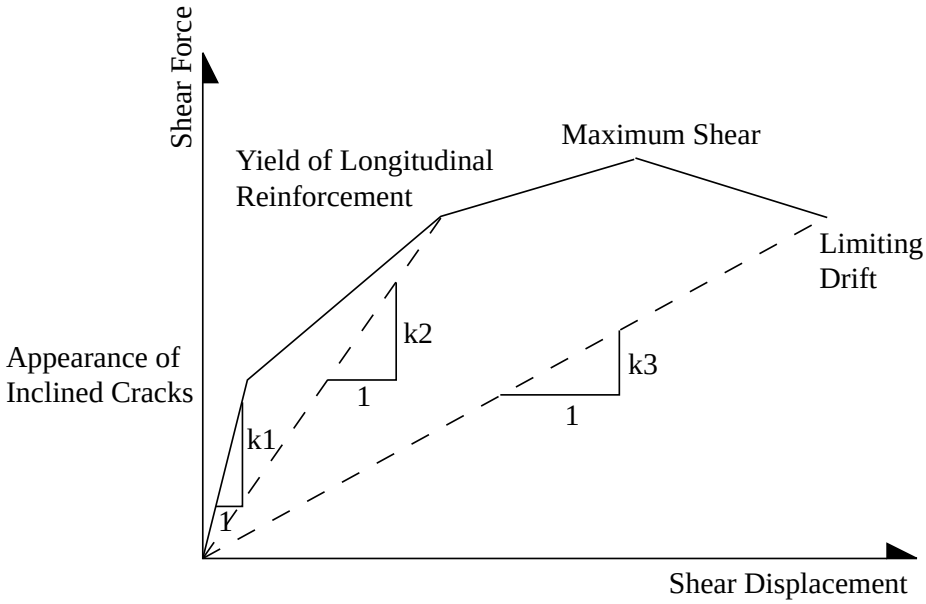

$$k1 = \frac{5\,A\,G}{6\,L} \qquad k2 = \frac{A\,G}{12\,L} \qquad k3 = \frac{A\,G}{36\,L}$$

Figure 6.3. Simplified relationship between shear force and shear displacement used to calculate the displacement component related to shear.

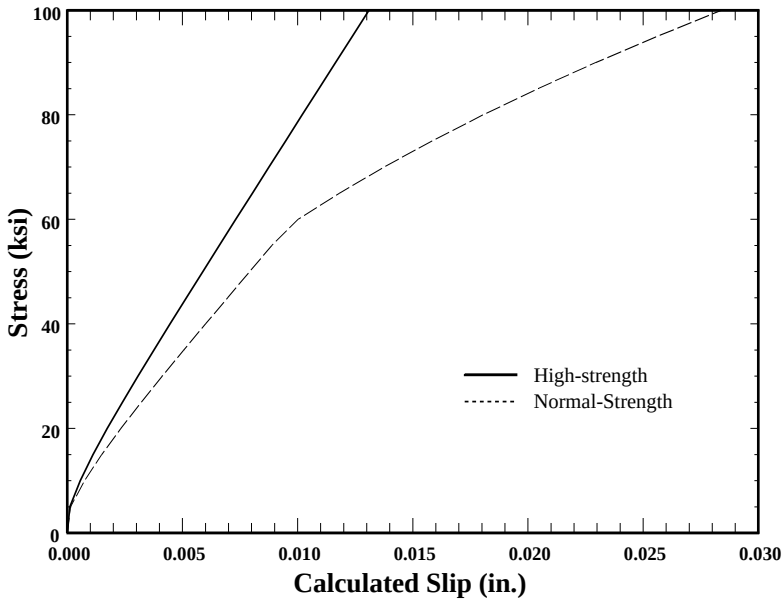

Figure 6.4. Relationship between stress in the longitudinal reinforcement and slip.

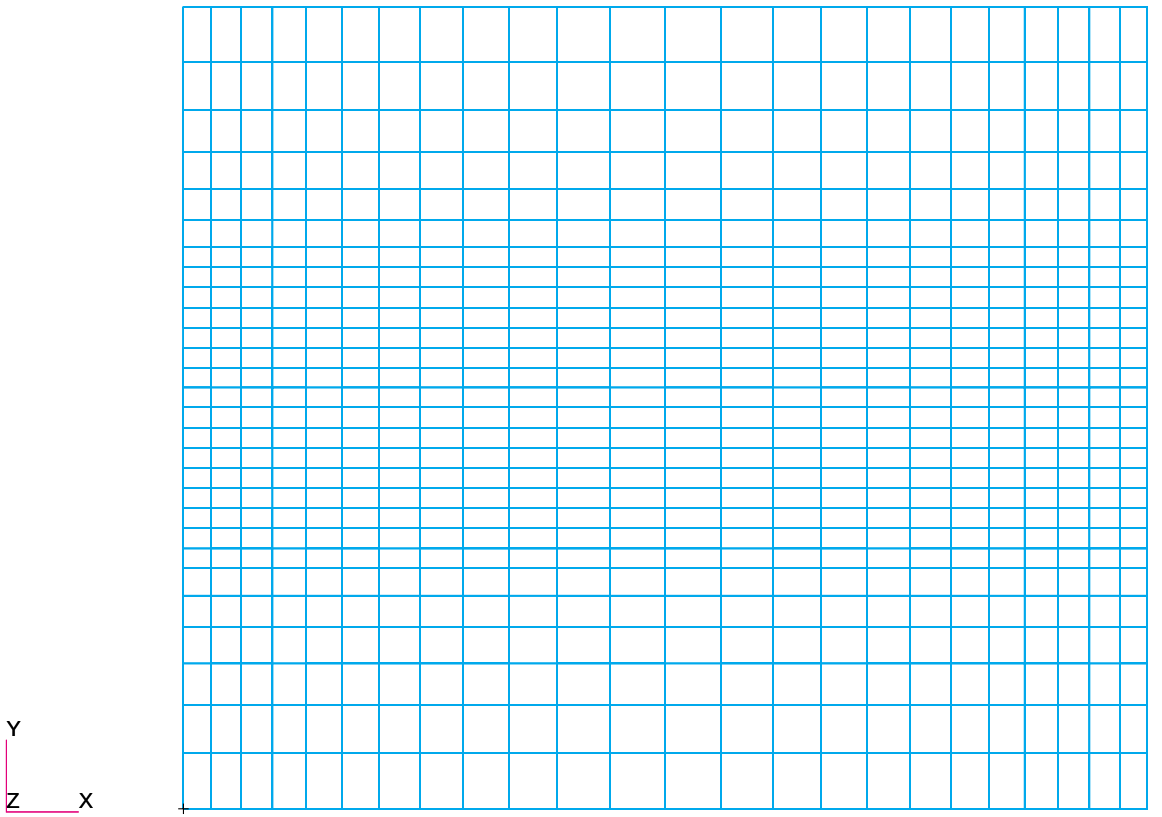

Figure 6.5. Frontal view of finite element mesh for the model used to analyze the deformation of the joint.

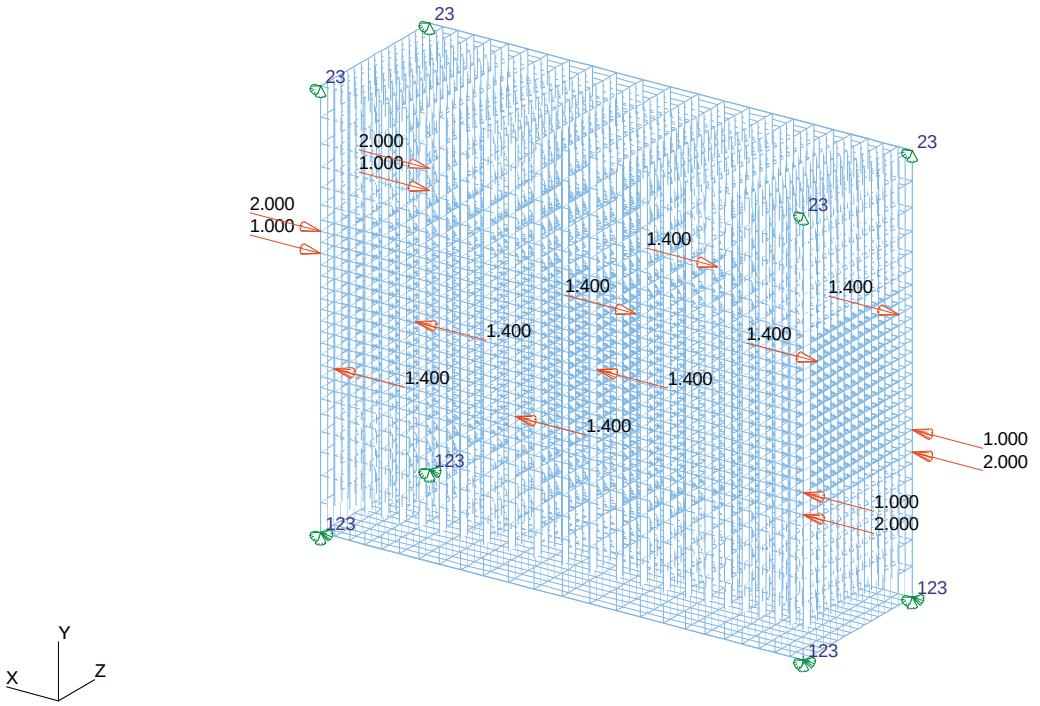

Figure 6.6. Loads and boundary conditions of the finite element model used to analyze the deformation of the joint.

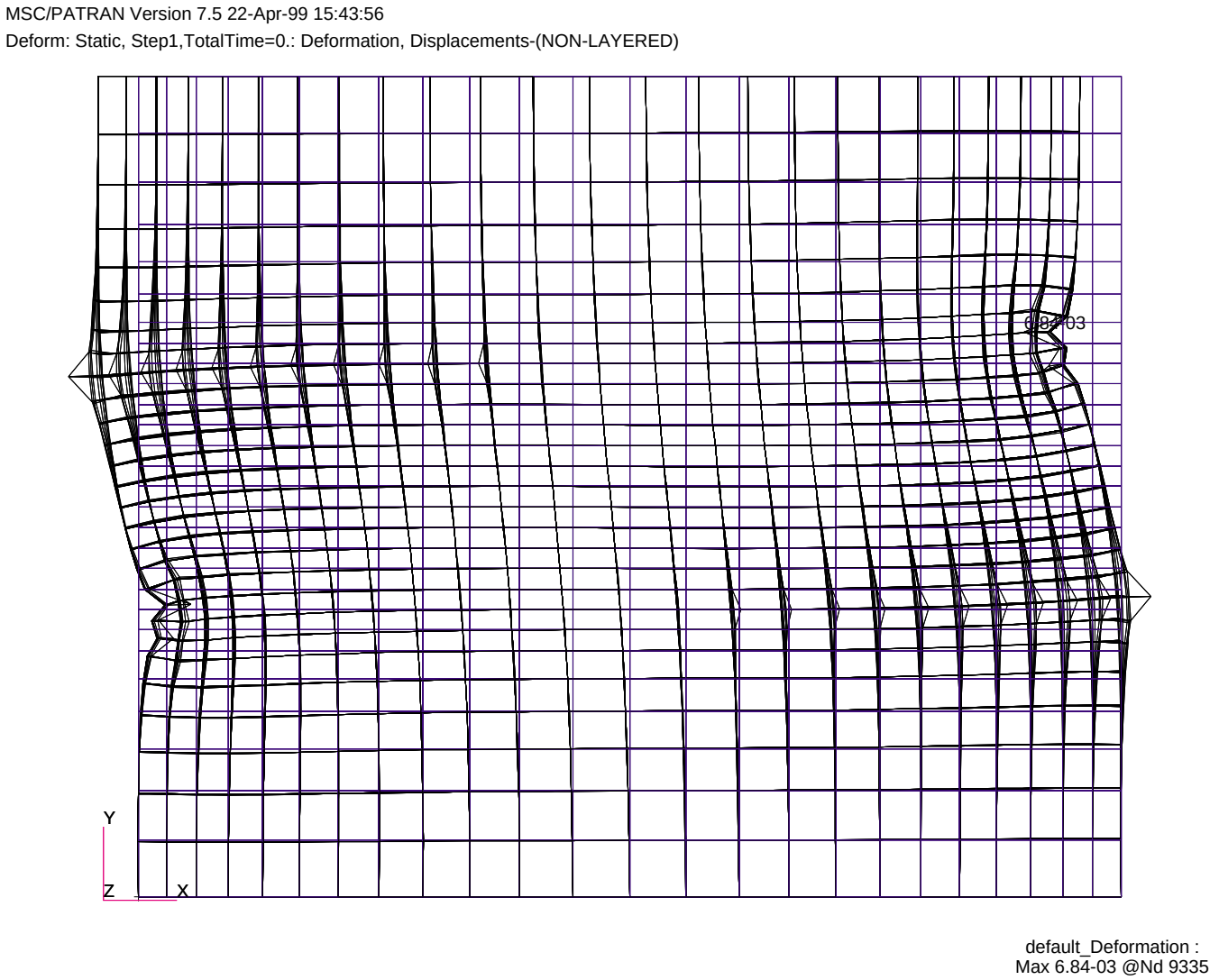

Figure 6.7. Frontal view of deformed mesh for the finite element model used to analyze the joint.

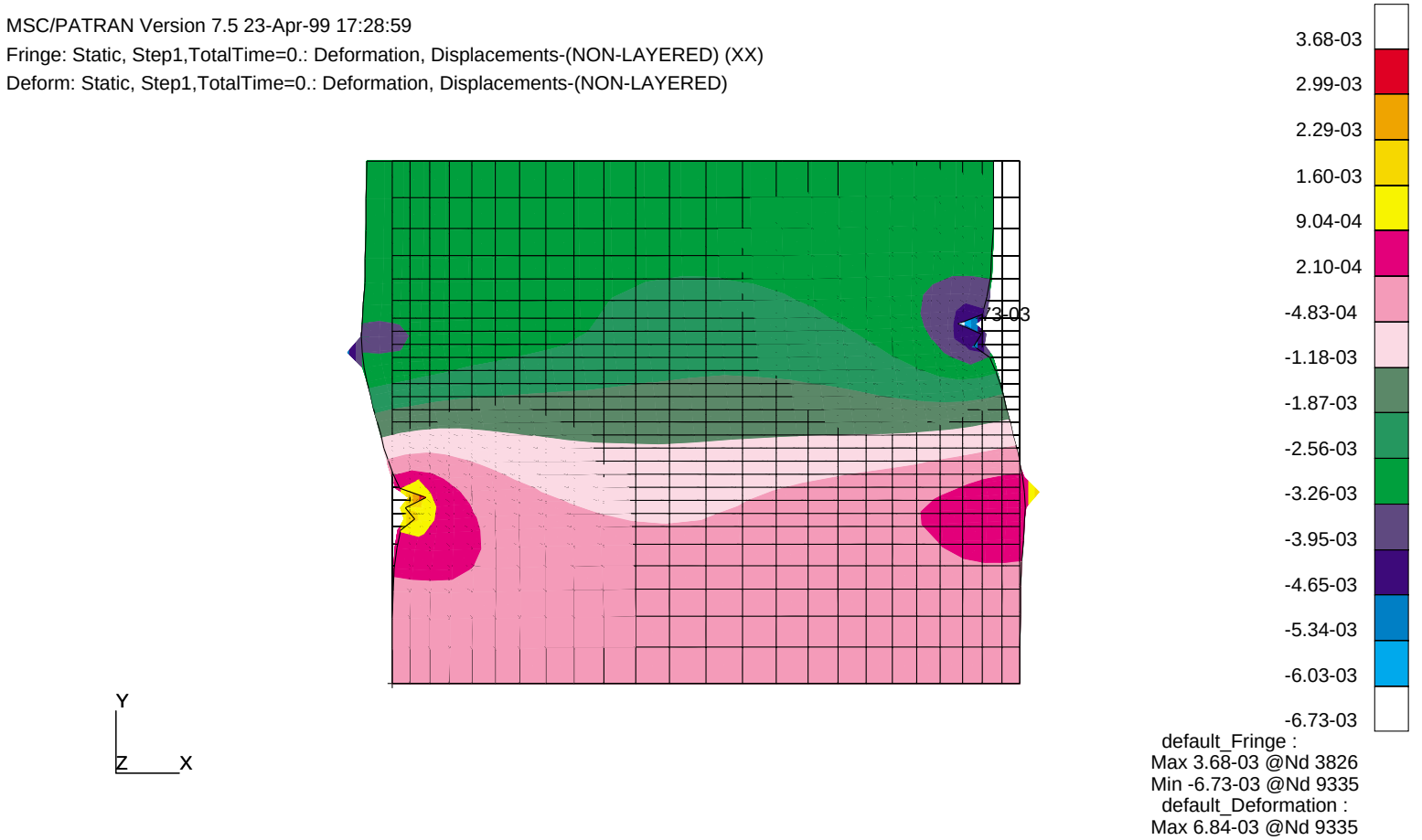

Figure 6.8. Calculated deformations in the surface of the joint, along the longitudinal direction, obtained from the finite element analysis.

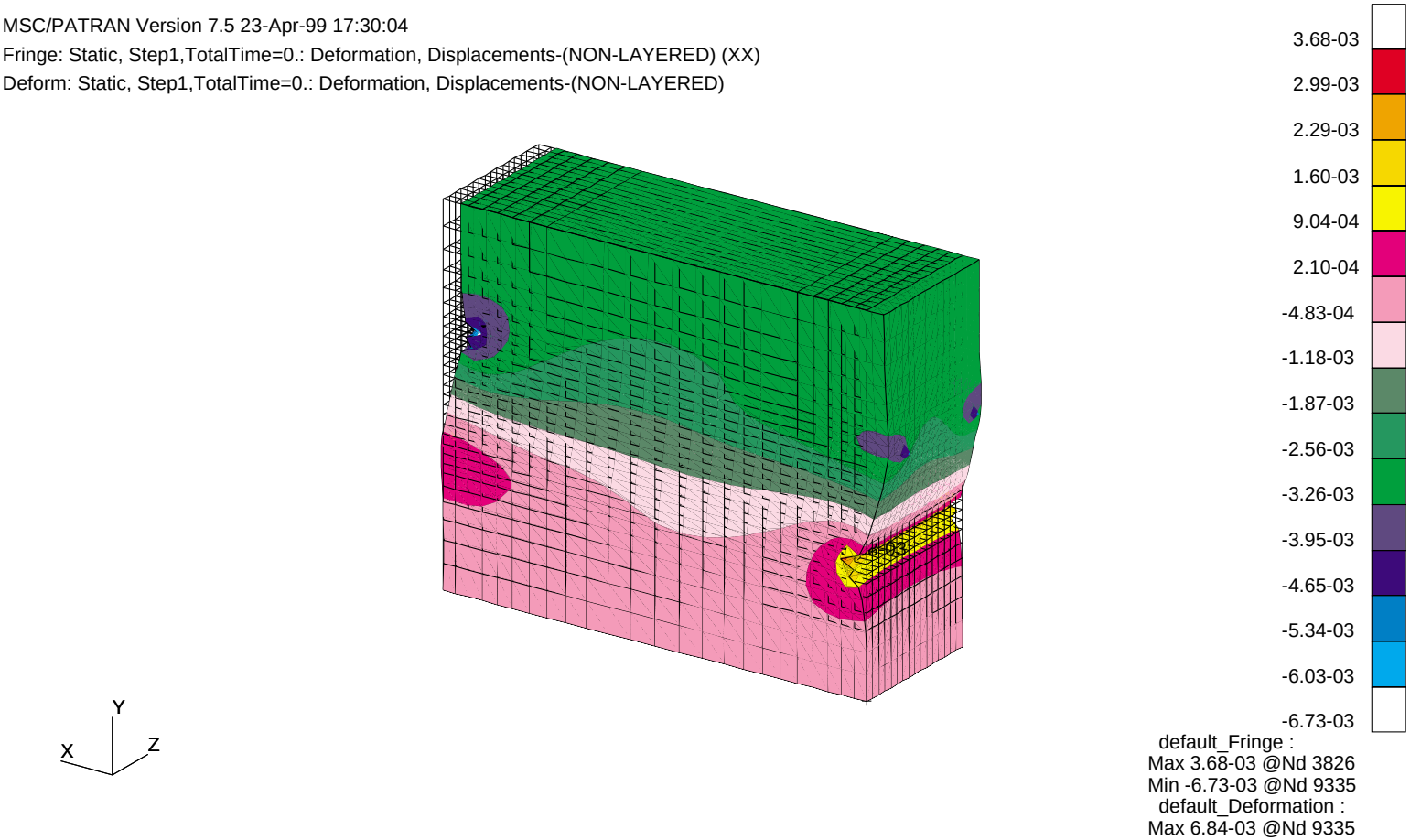

Figure 6.9. Calculated deformations, along the longitudinal direction, obtained from the finite element analysis.

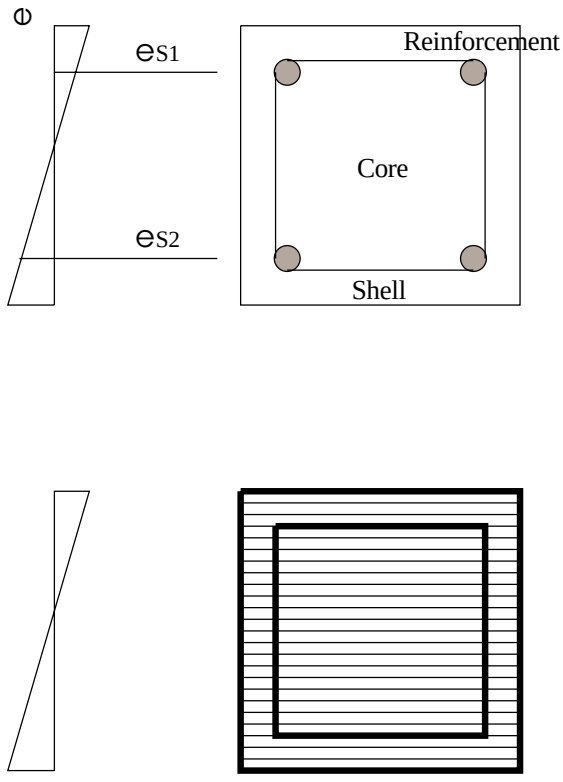

Figure 6.10. Procedure to calculate moment-curvature relationship

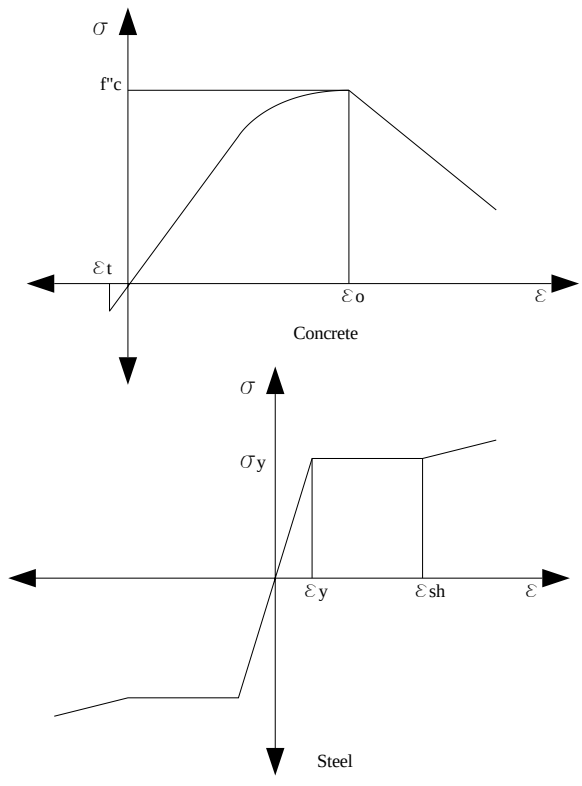

Figure 6.11. Material models.

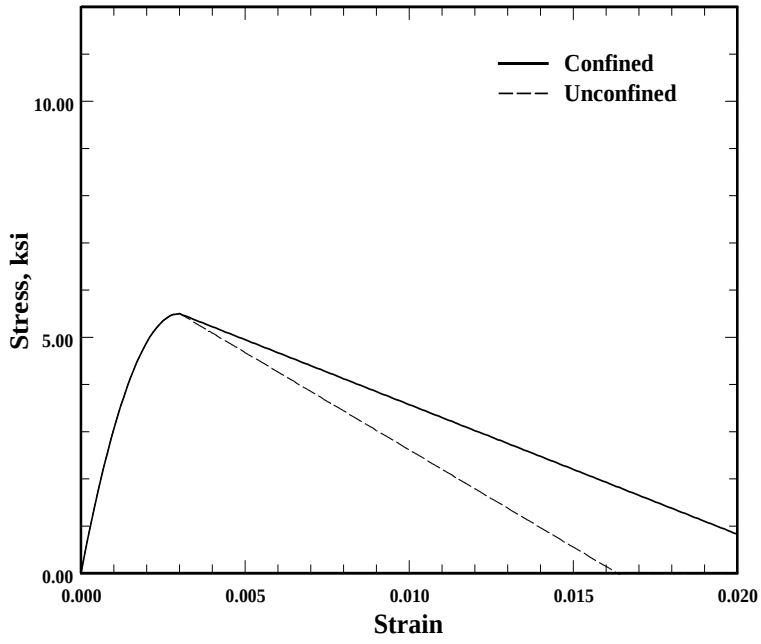

Figure 6.12. Stress-strain relationship for concrete, 5,500 psi compressive strength.

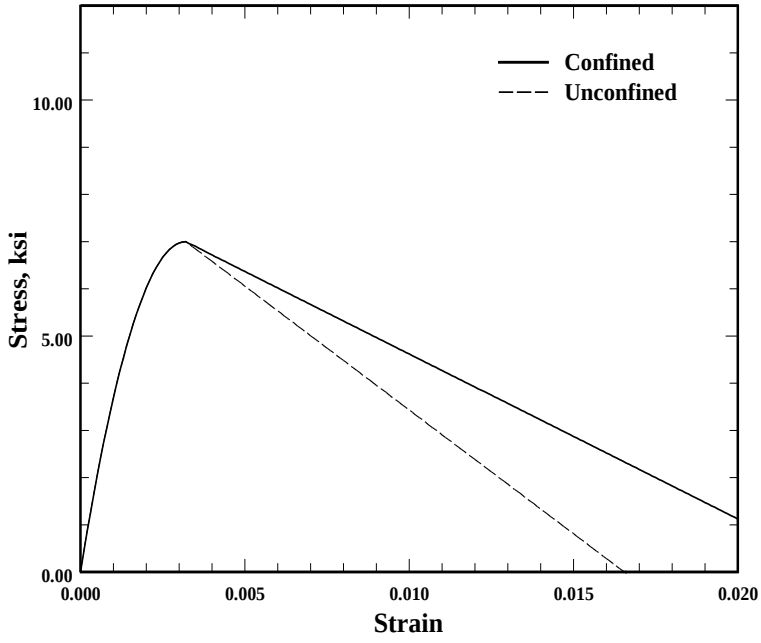

Figure 6.13. Stress-strain relationship for concrete, 7,000 psi compressive strength.

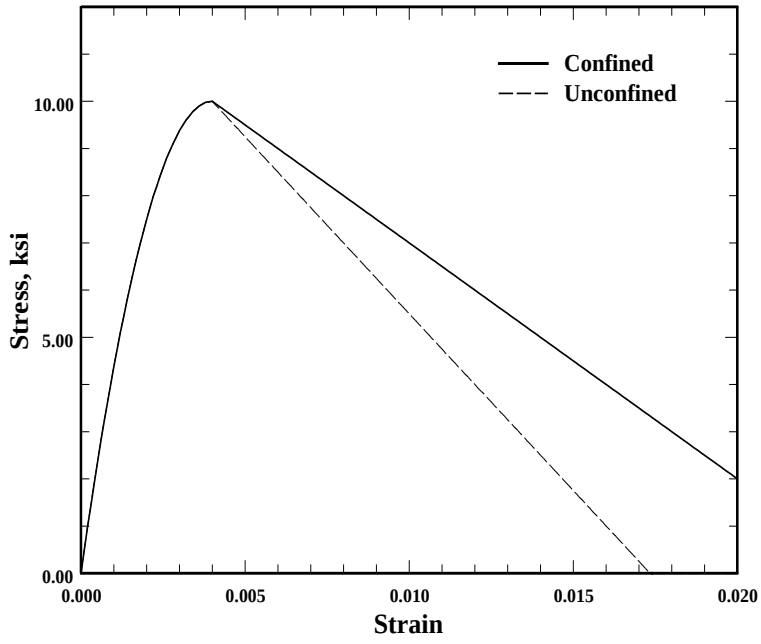

Figure 6.14. Stress-strain relationship for concrete, 10,000 psi compressive strength.

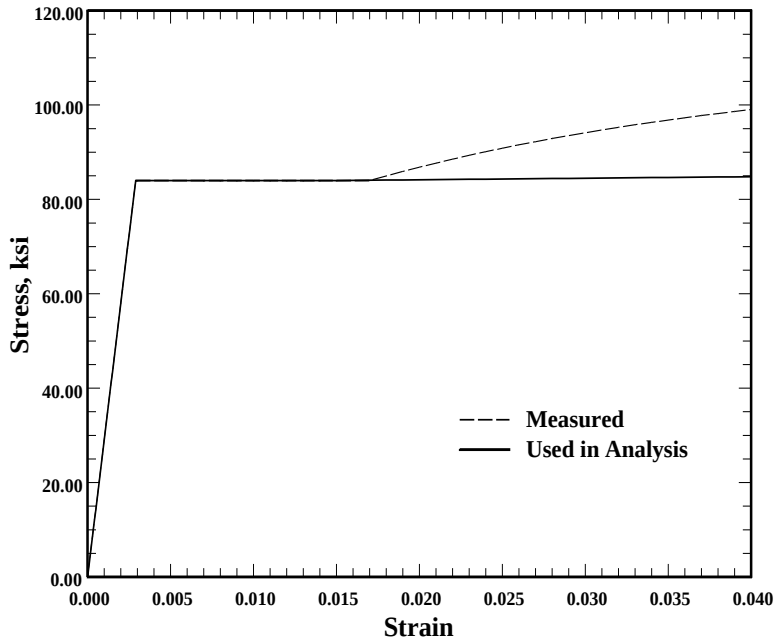

Figure 6.15. Stress-strain relationship for steel.

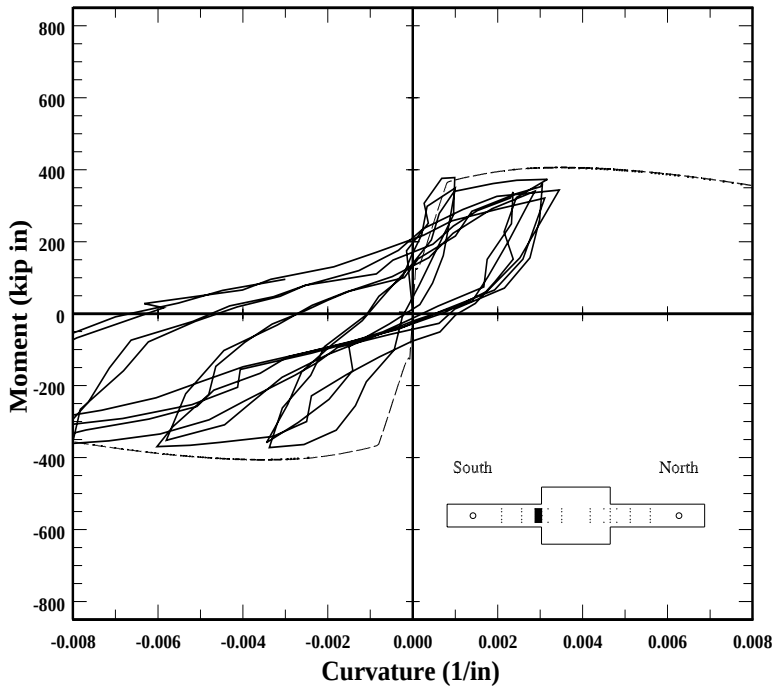

Figure 6.16. Calculated and measured moment-curvature relationship for specimen C10-05, south member.

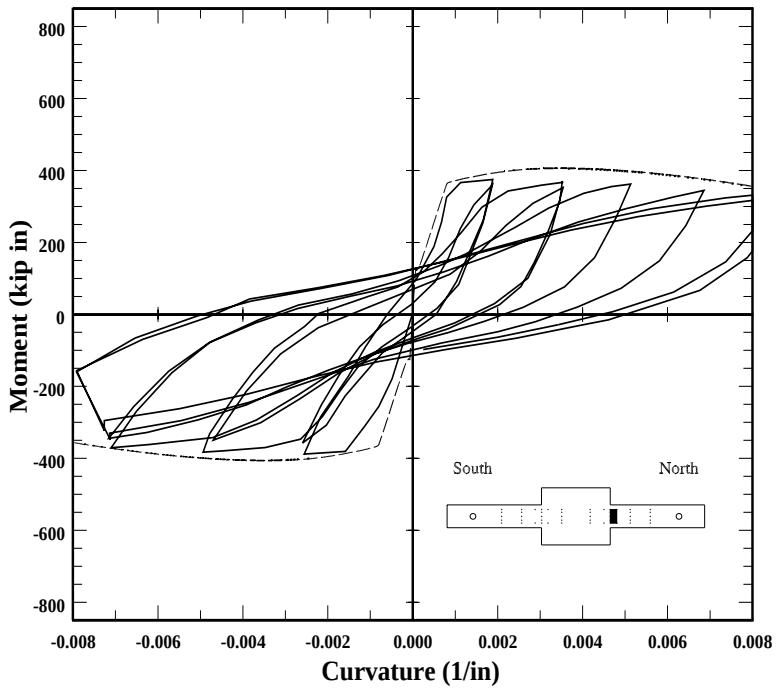

Figure 6.17. Calculated and measured moment-curvature relationship for specimen C10-05, north member.

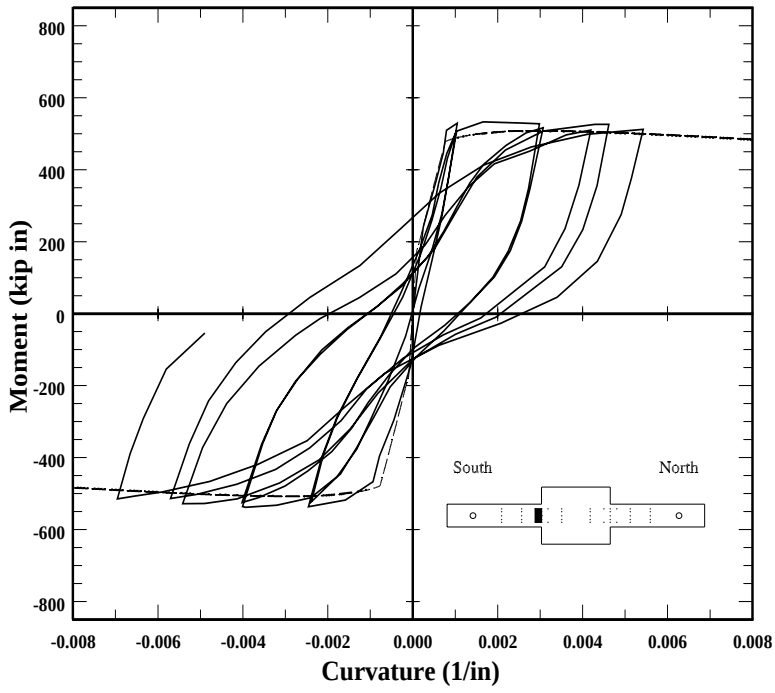

Figure 6.18. Calculated and measured moment-curvature relationship for specimen C10-10, south member.

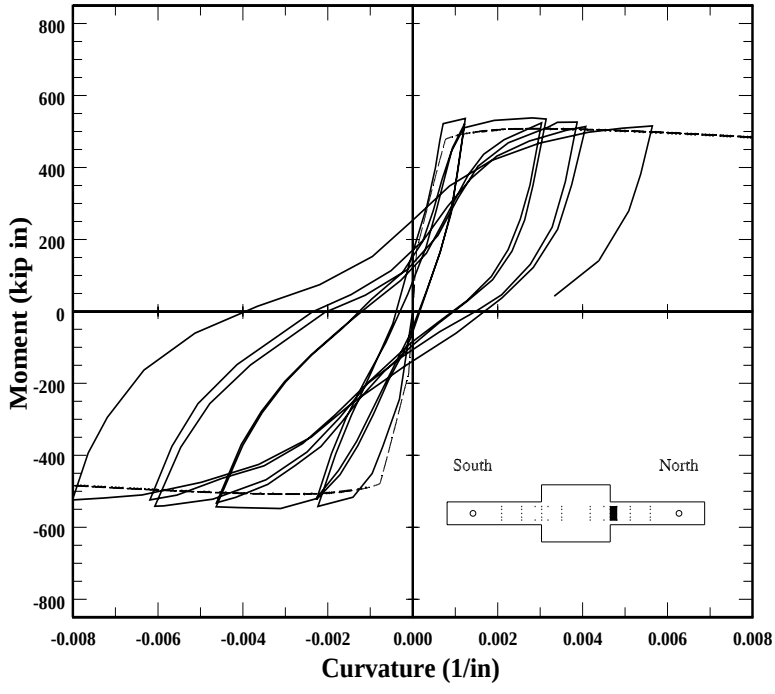

Figure 6.19. Calculated and measured moment-curvature relationship for specimen C10-10, north member.

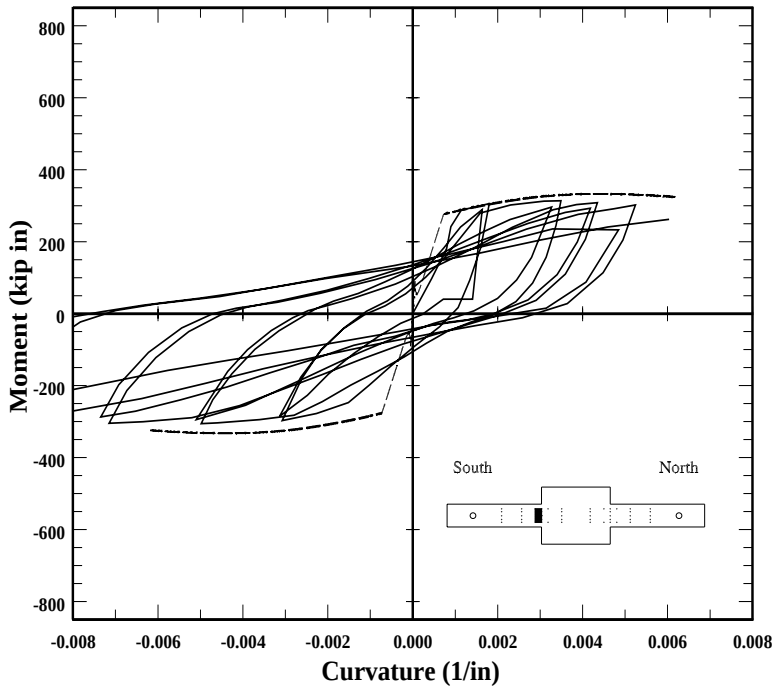

Figure 6.20. Calculated and measured moment-curvature relationship for specimen C10-20, south member.

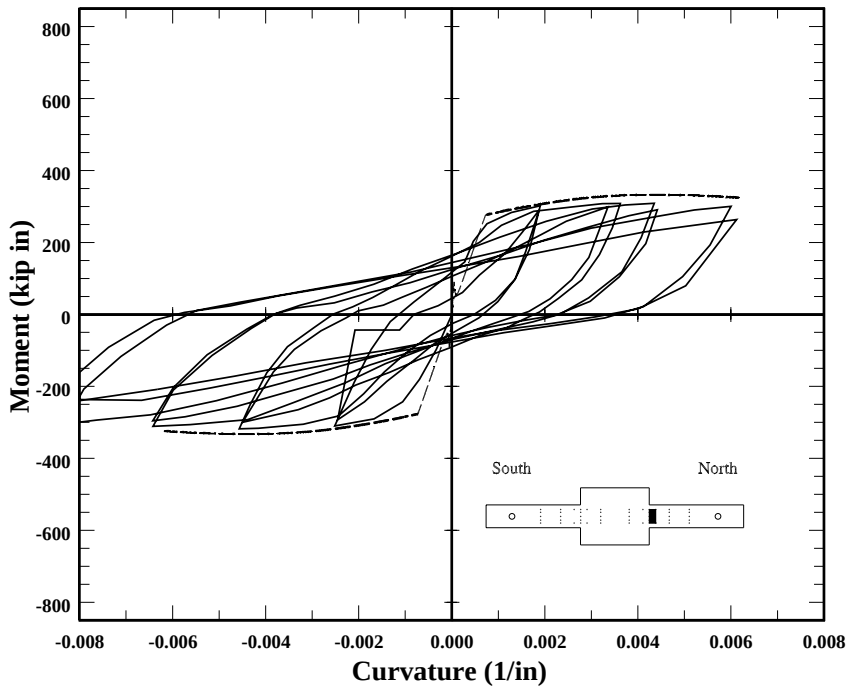

Figure 6.21. Calculated and measured moment-curvature relationship for specimen C10-20, north member.

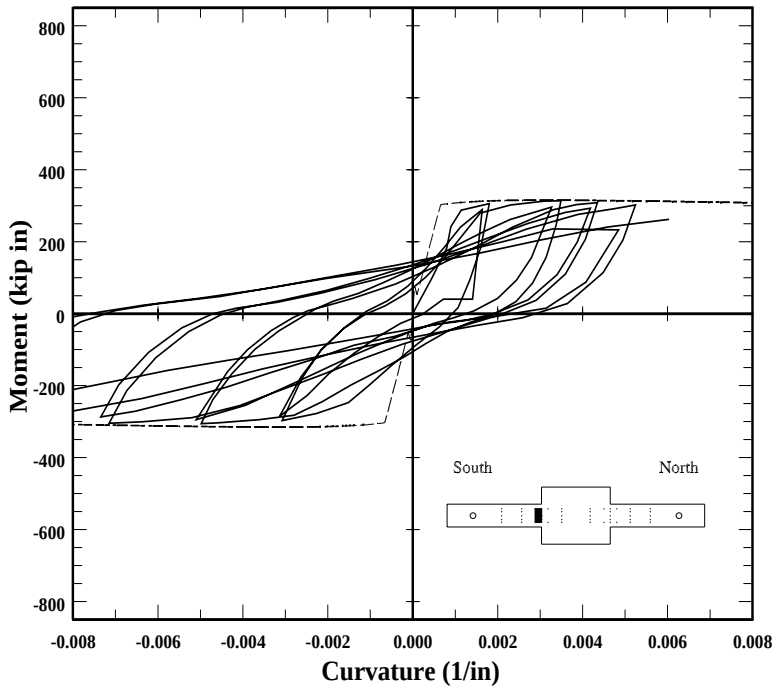

Figure 6.22. Calculated and measured moment-curvature relationship for specimen C5-00, south member.

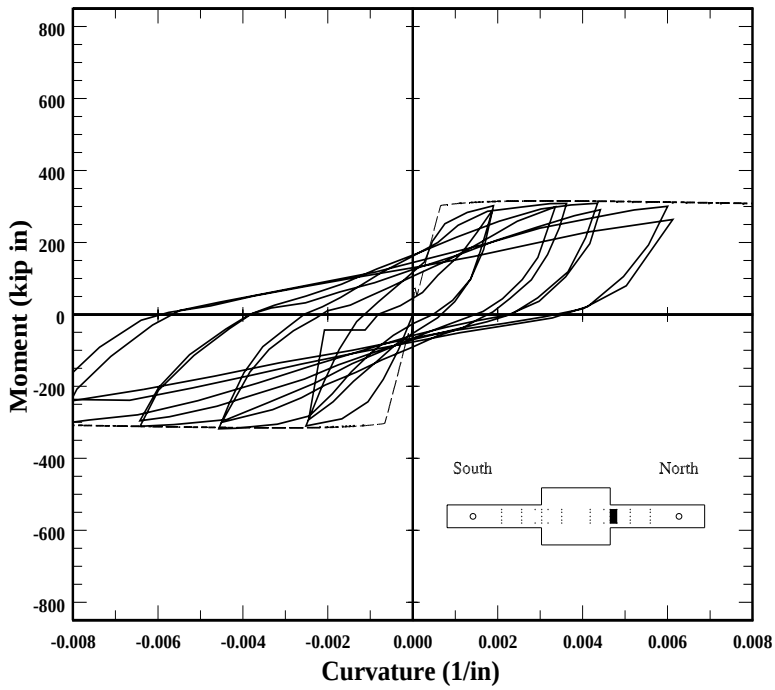

Figure 6.23. Calculated and measured moment-curvature relationship for specimen C5-00, north member.

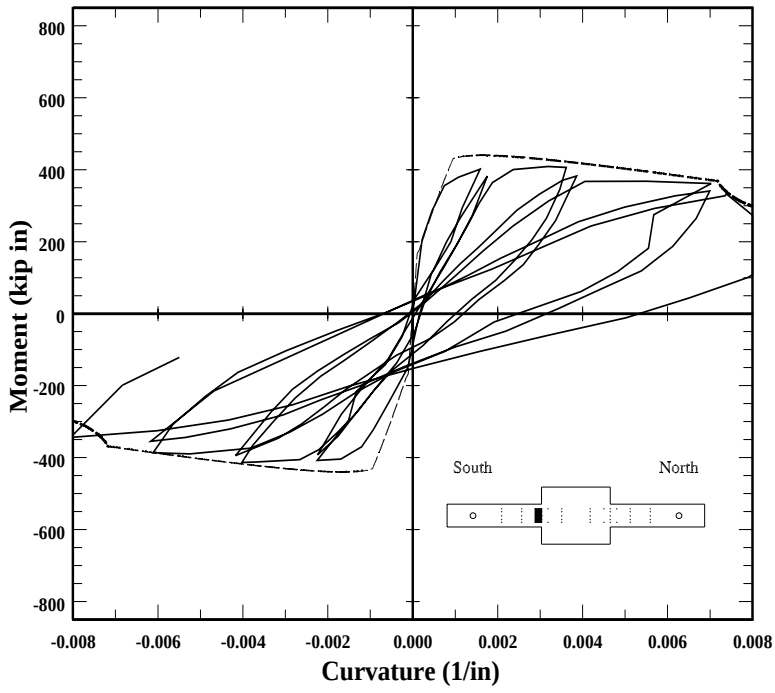

Figure 6.24. Calculated and measured moment-curvature relationship for specimen C5-20, south member.

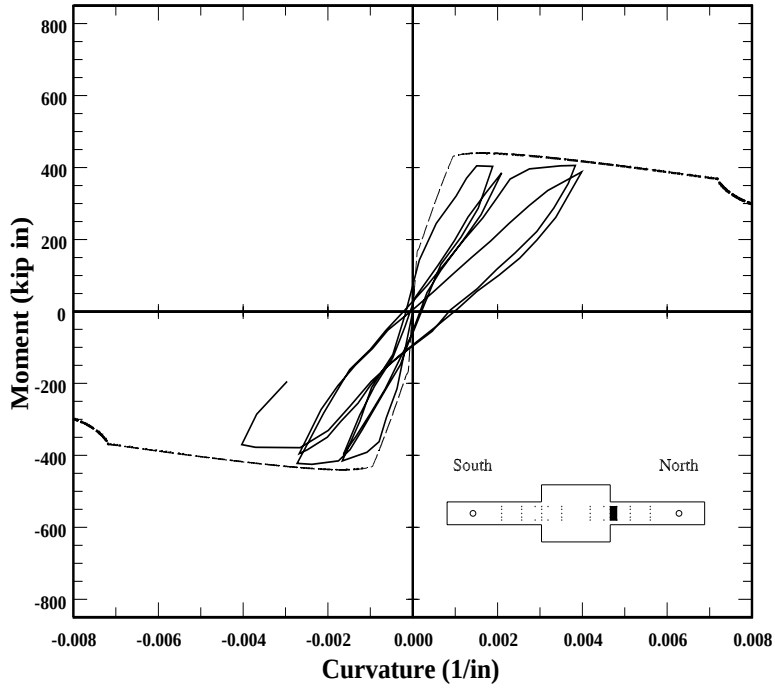

Figure 6.25. Calculated and measured moment-curvature relationship for specimen C5-20, north member.

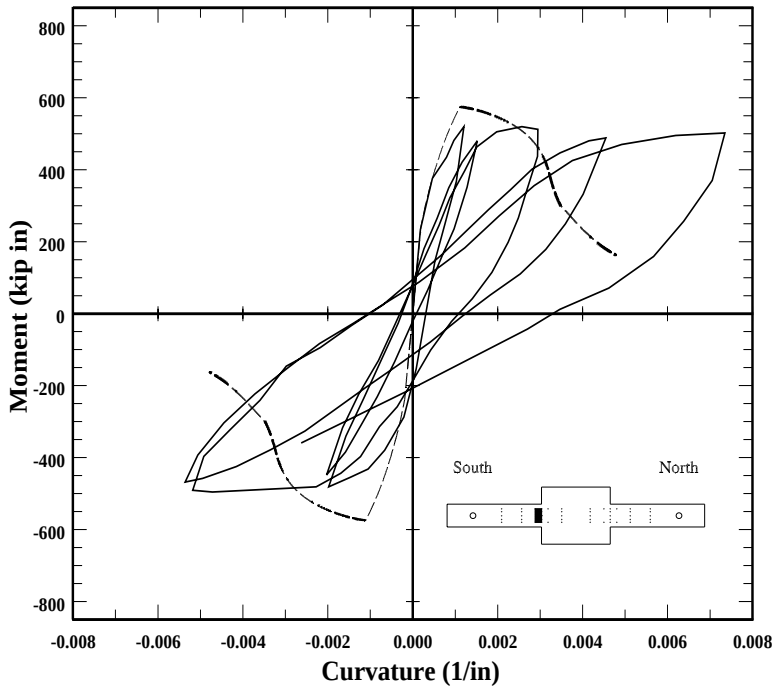

Figure 6.26. Calculated and measured moment-curvature relationship for specimen C5-40, south member.

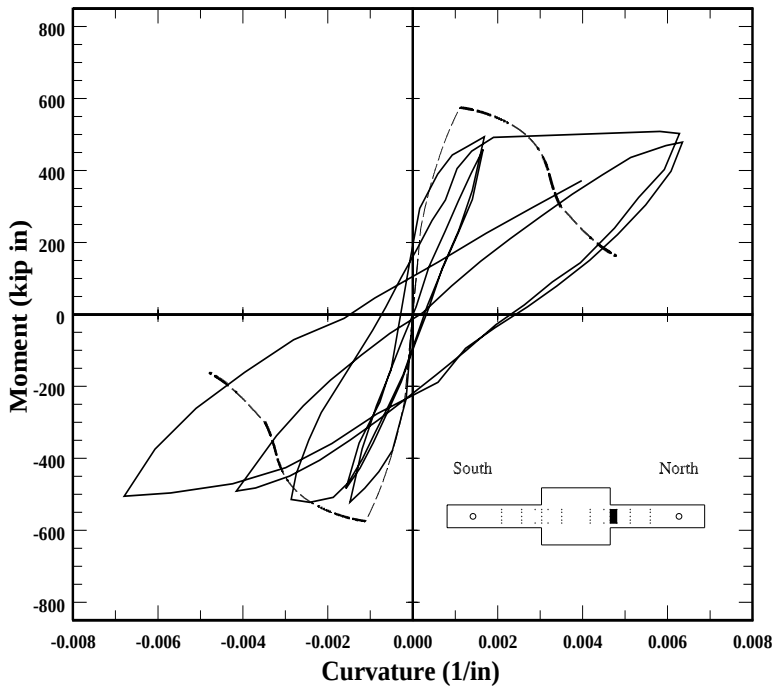

Figure 6.27. Calculated and measured moment-curvature relationship for specimen C5-40, north member.

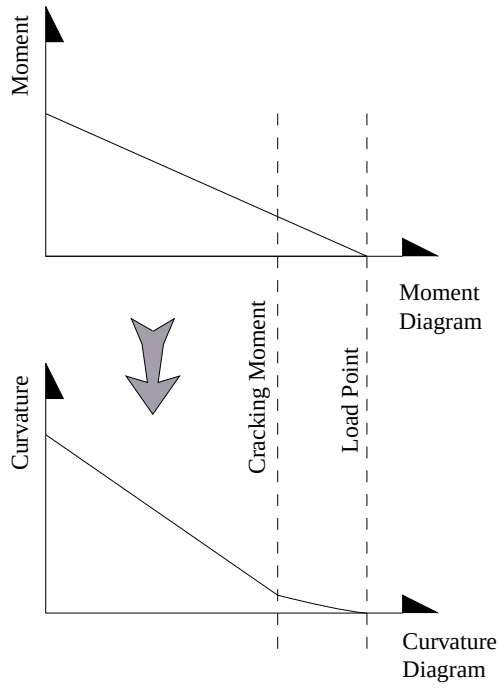

Figure 6.28. Procedure to calculate displacement related to flexure based on the moment-curvature relationship.

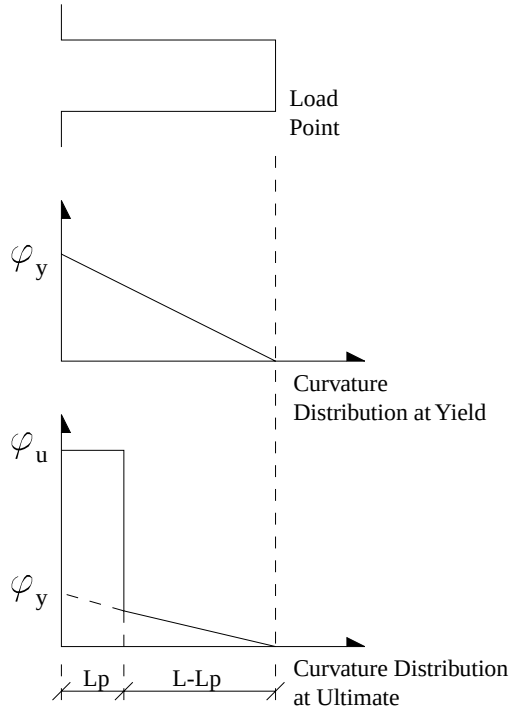

Figure 6.29. Assumed curvature distributions for the displacement at yield and the limiting drift.

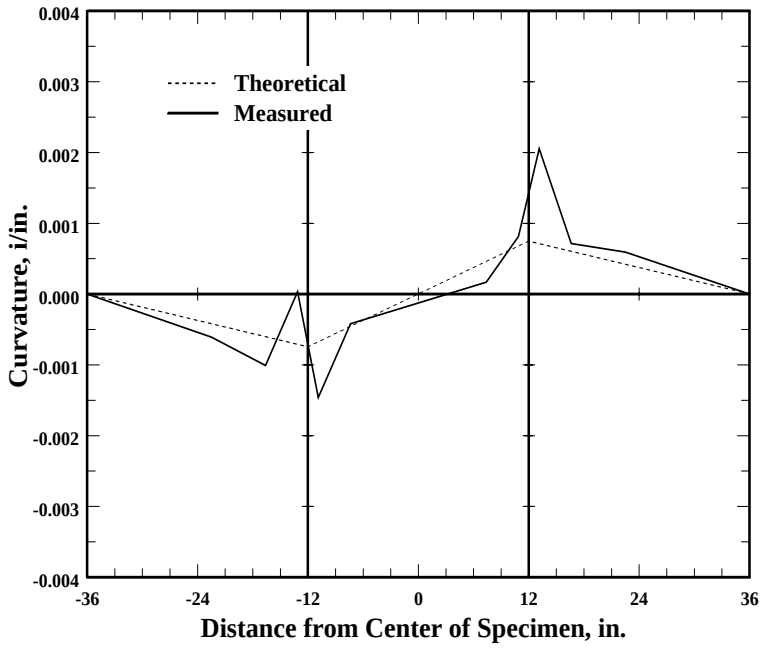

Figure 6.30. Curvature distribution along the length of specimen C10-00 near yield.

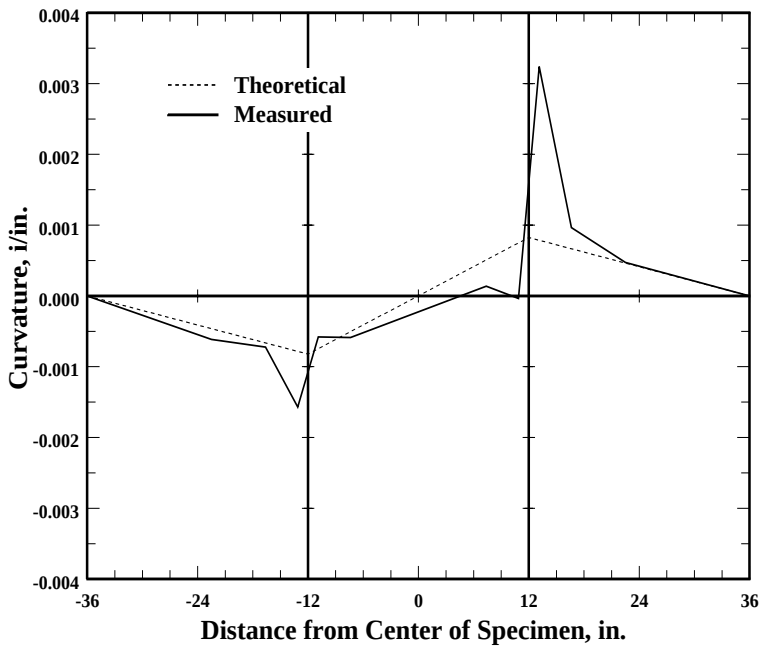

Figure 6.31. Curvature distribution along the length of specimen C10-05 near yield.

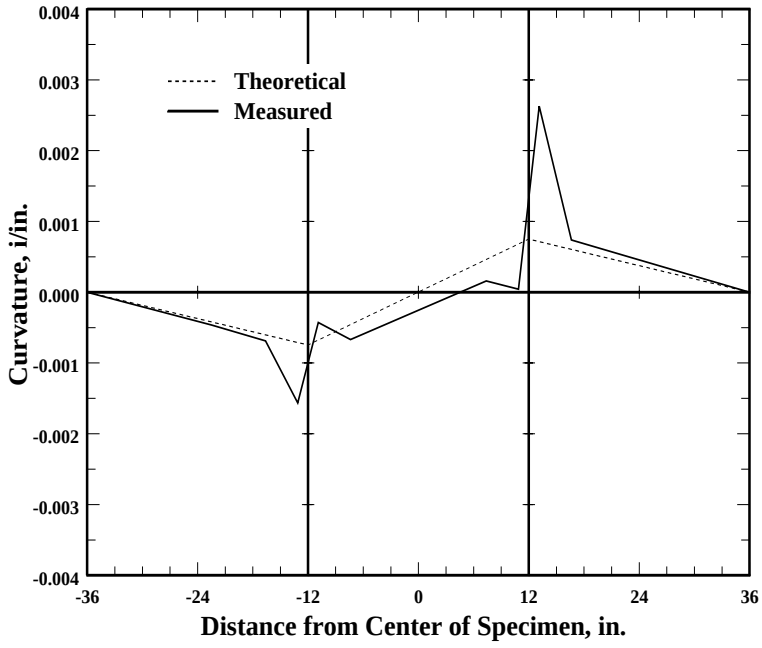

Figure 6.32. Curvature distribution along the length of specimen C10-10 near yield.

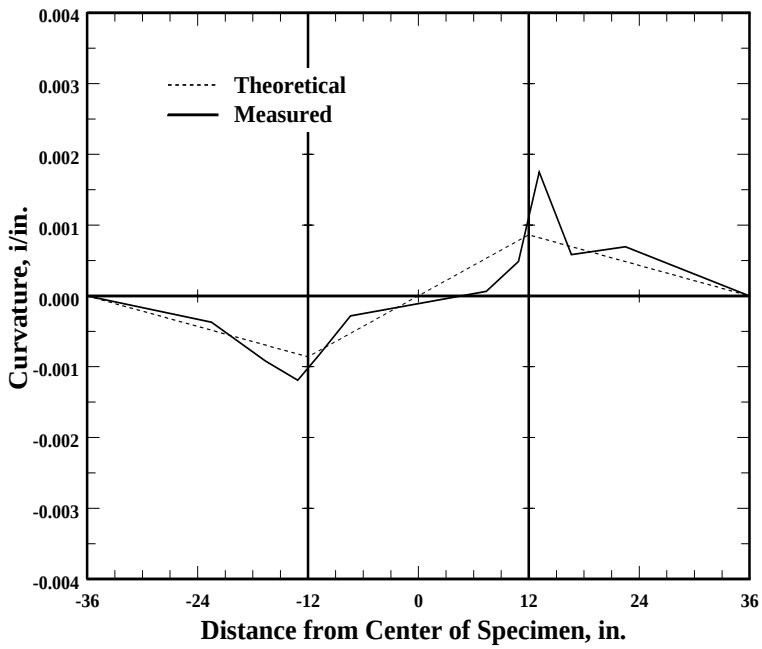

Figure 6.33. Curvature distribution along the length of specimen C10-20 near yield.

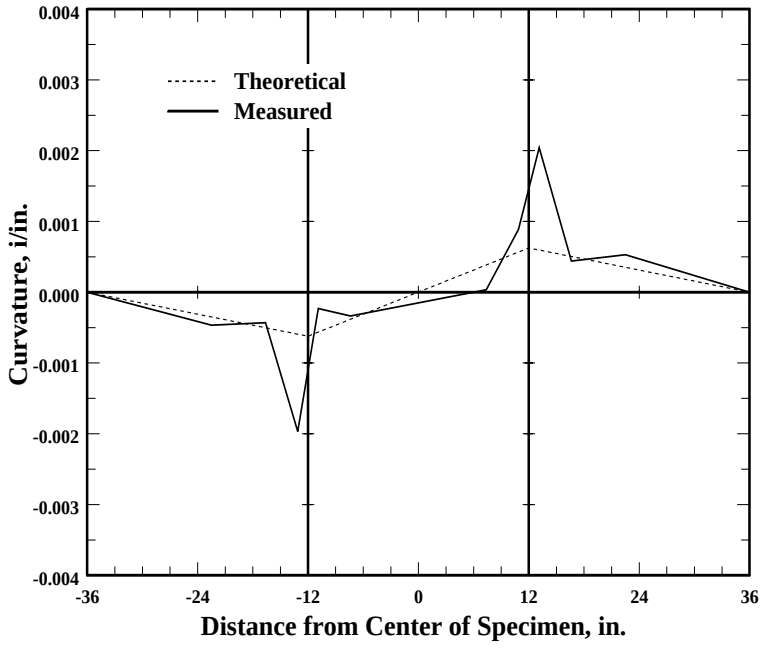

Figure 6.34. Curvature distribution along the length of specimen C5-00 near yield.

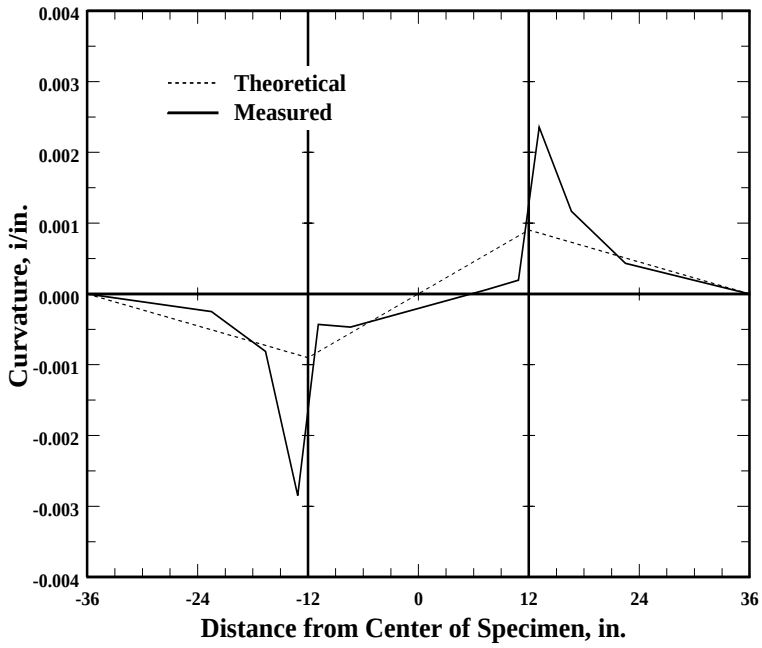

Figure 6.35. Curvature distribution along the length of specimen C5-20 near yield.

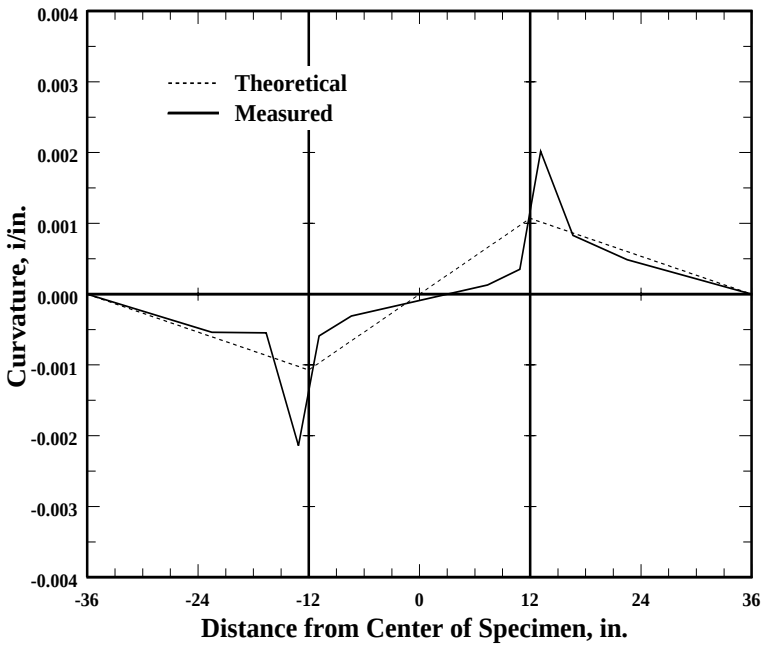

Figure 6.36. Curvature distribution along the length of specimen C5-40 near yield.

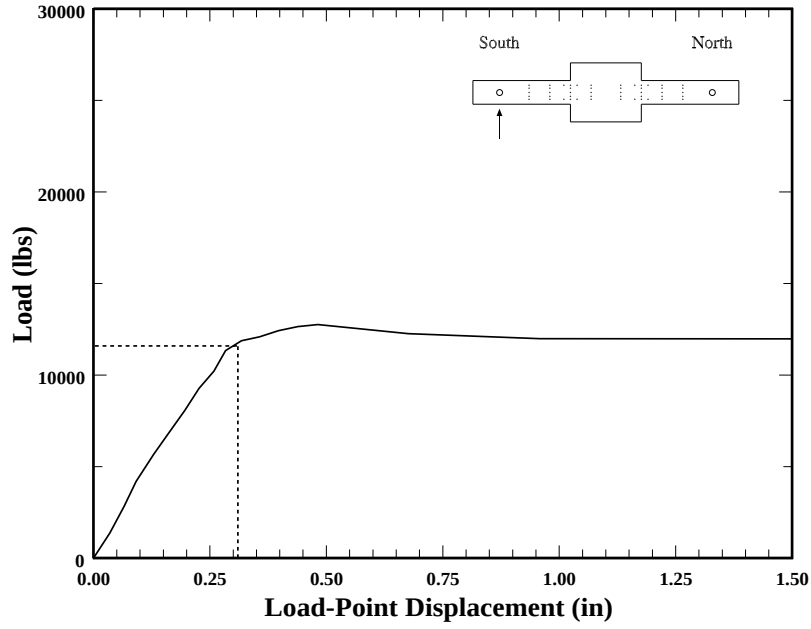

Figure 6.37. Yield displacement and load for specimen C10-00, south member.

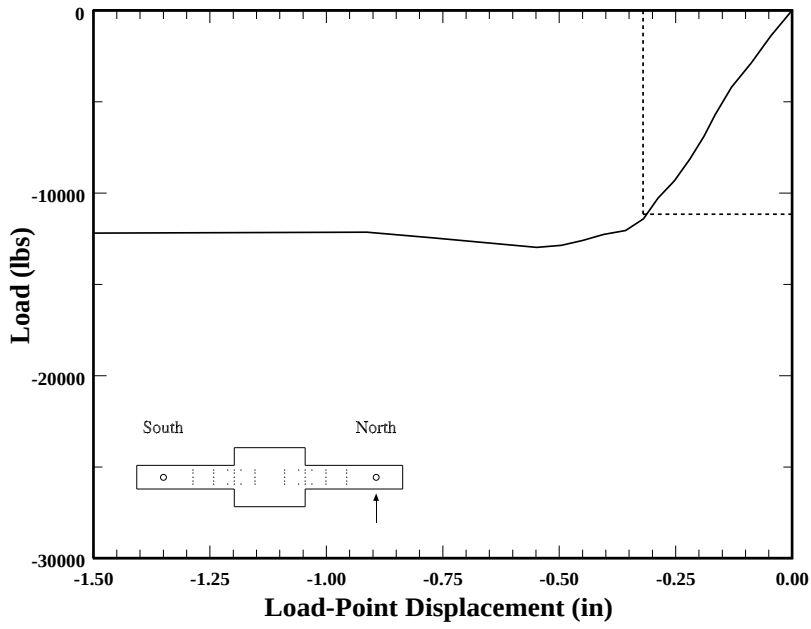

Figure 6.38. Yield displacement and load for specimen C10-00, north member.

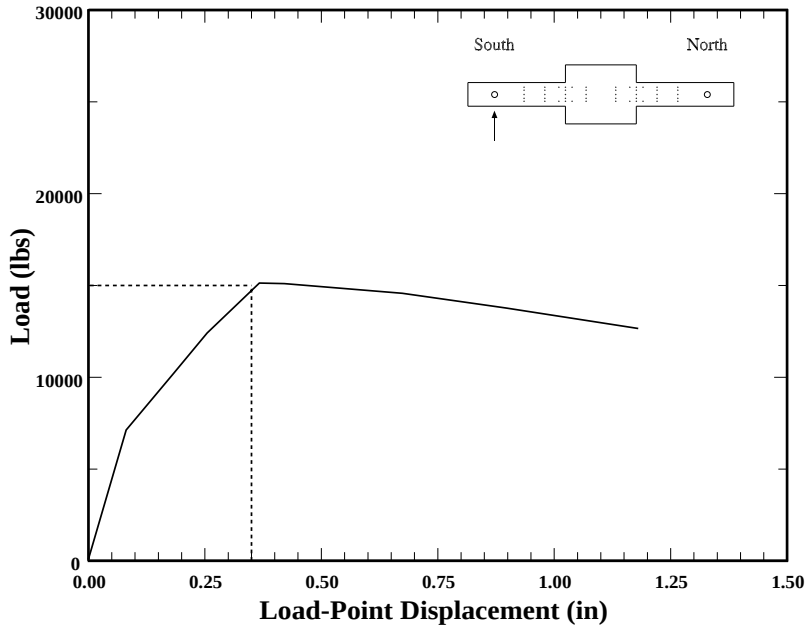

Figure 6.39. Yield displacement and load for specimen C10-05, south member.

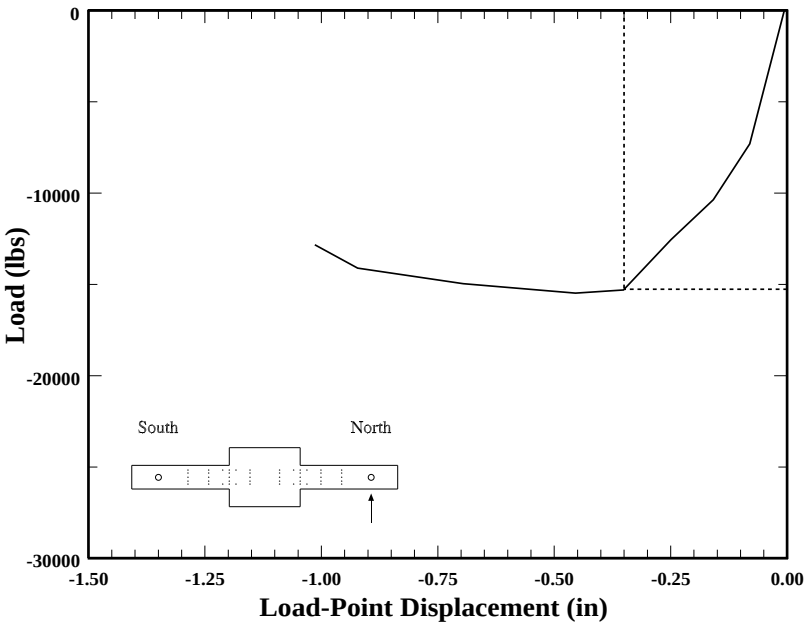

Figure 6.40. Yield displacement and load for specimen C10-05, north member.

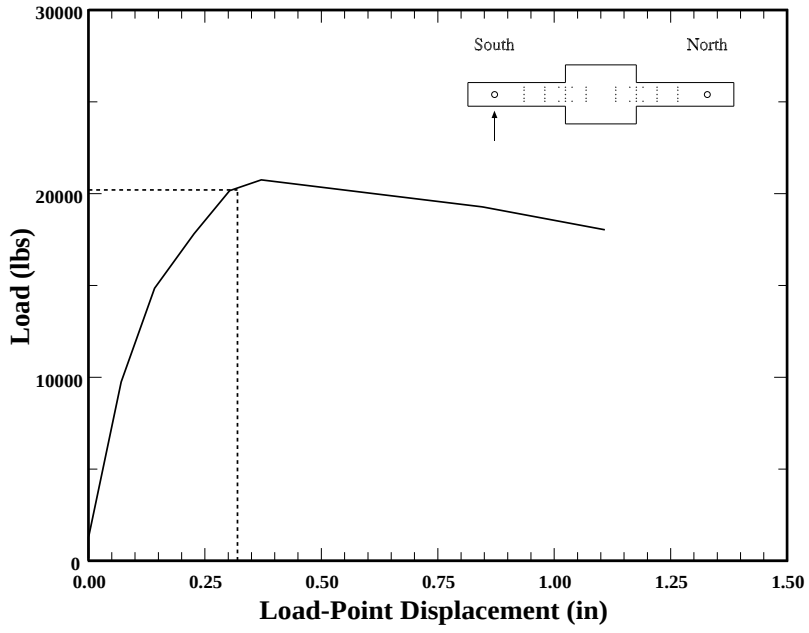

Figure 6.41. Yield displacement and load for specimen C10-10, south member.

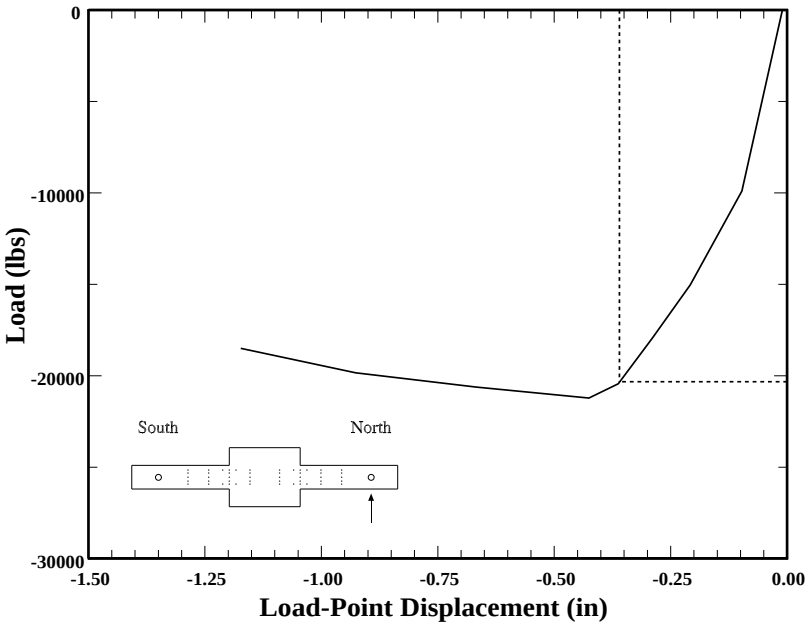

Figure 6.42. Yield displacement and load for specimen C10-10, south member.

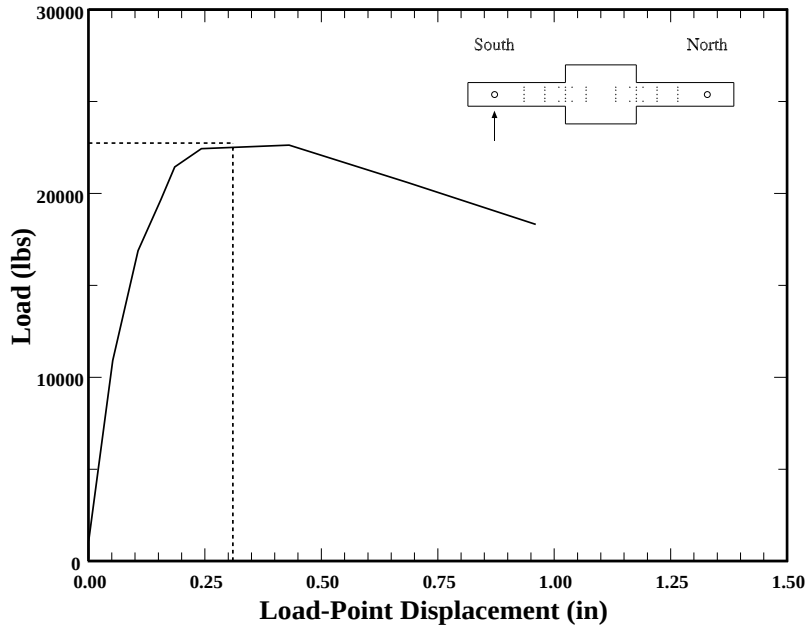

Figure 6.43. Yield displacement and load for specimen C10-20, south member.

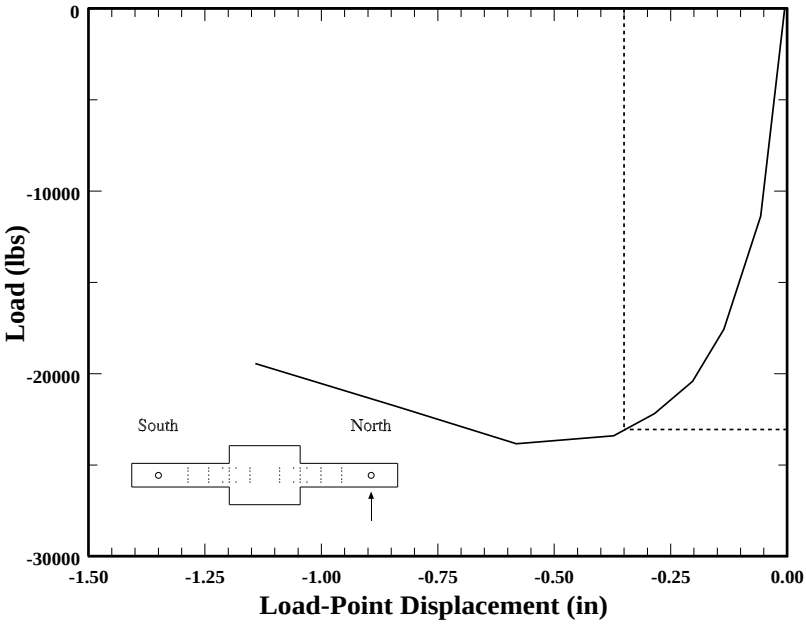

Figure 6.44. Yield displacement and load for specimen C10-20, north member.

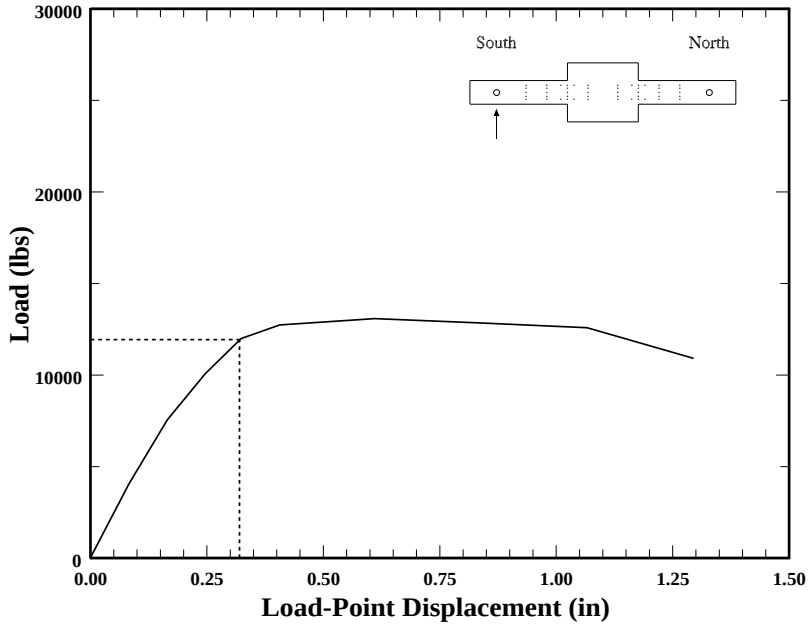

Figure 6.45. Yield displacement and load for specimen C5-00, south member.

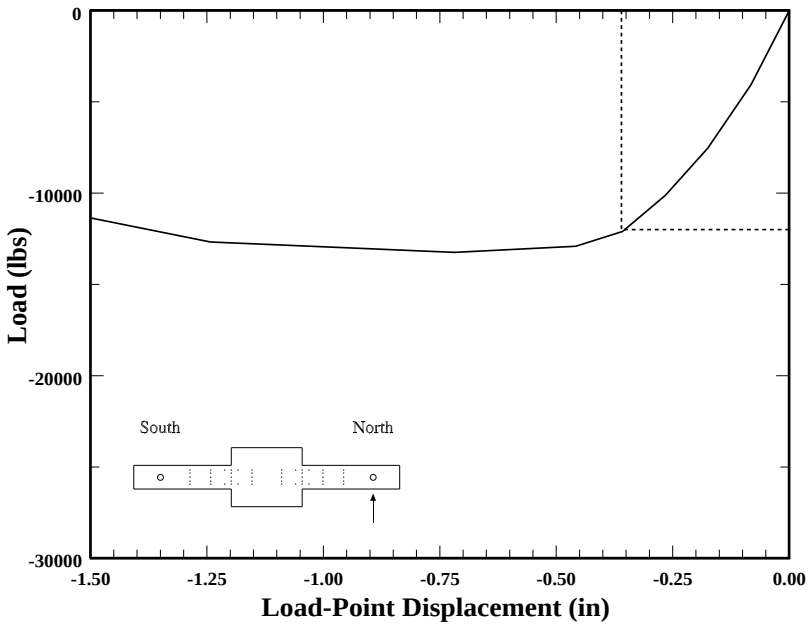

Figure 6.46. Yield displacement and load for specimen C5-00, north member.

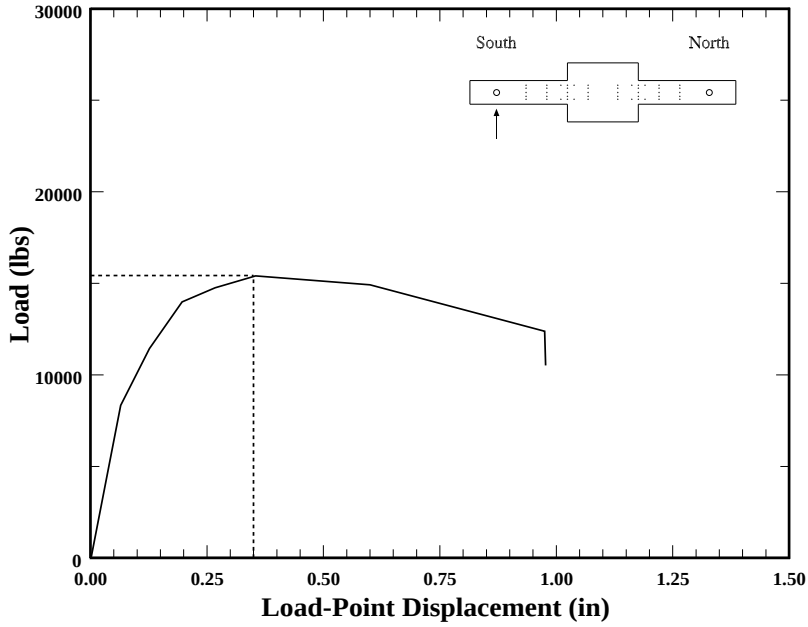

Figure 6.47. Yield displacement and load for specimen C5-20, south member.

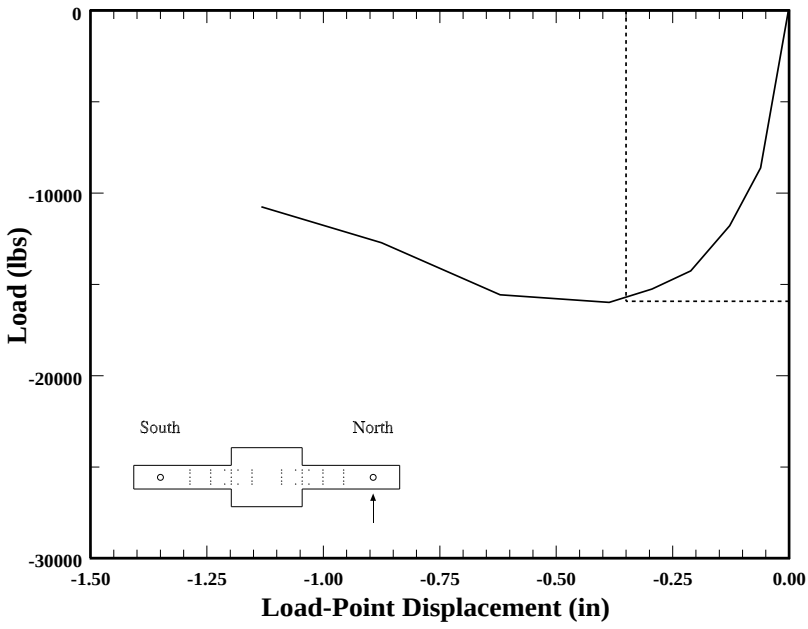

Figure 6.48. Yield displacement and load for specimen C5-20, north member.

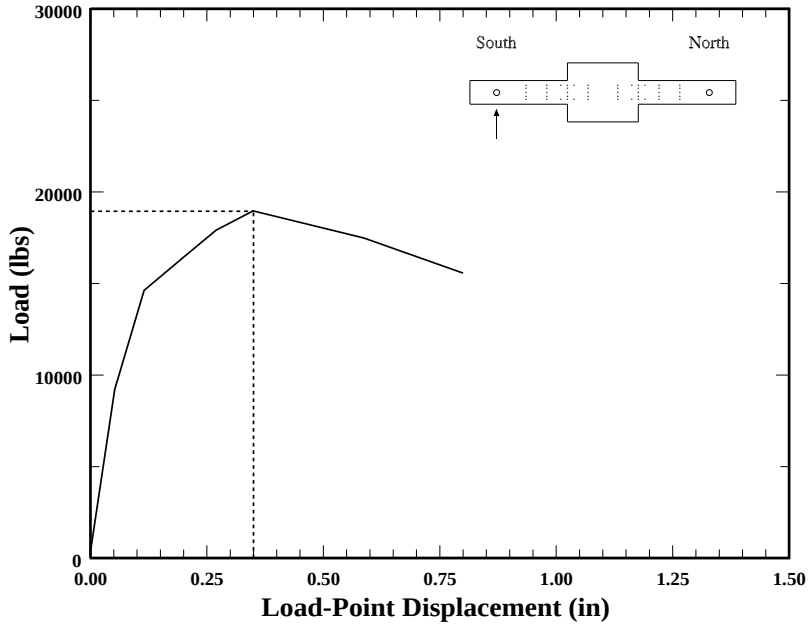

Figure 6.49. Yield displacement and load for specimen C5-40, south member.

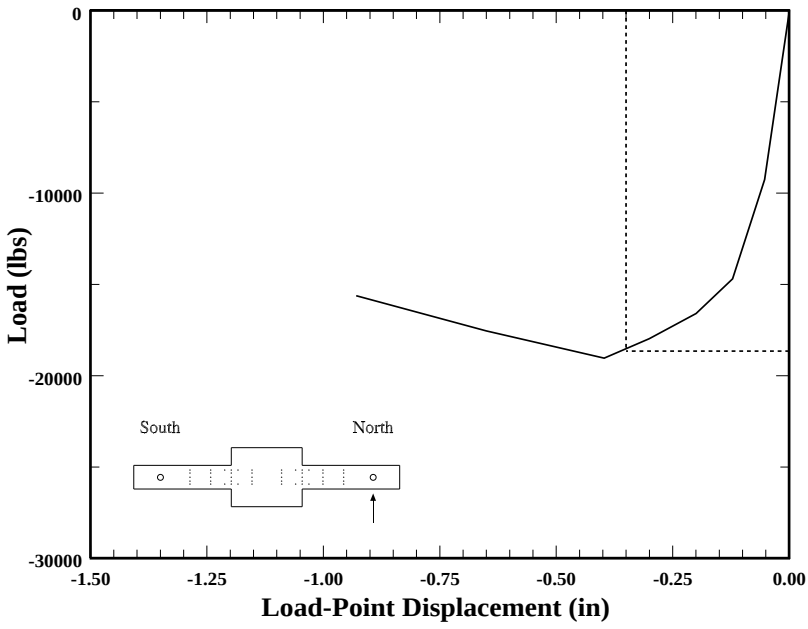

Figure 6.50. Yield displacement and load for specimen C5-40, north member.

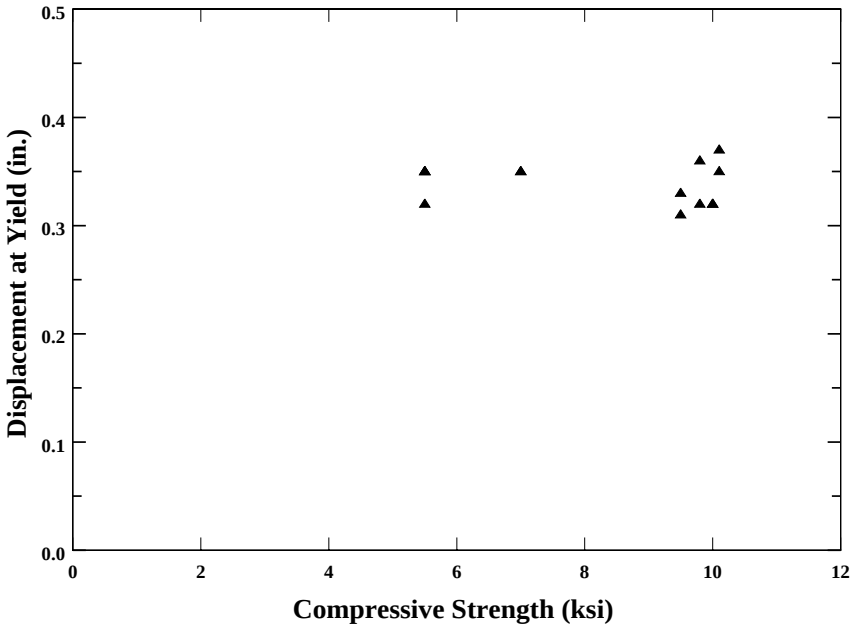

Figure 6.51. Measured displacement at yield vs. compressive strength of member.

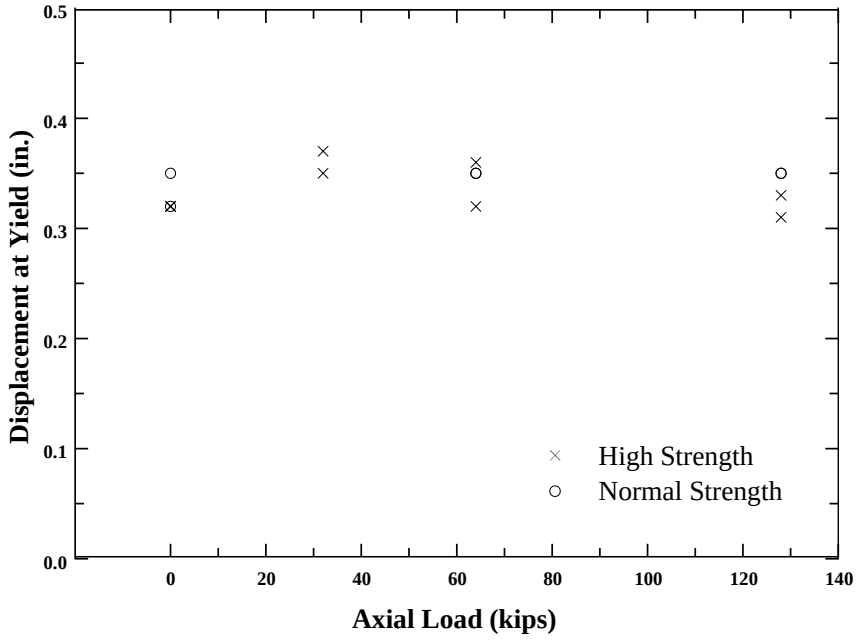

Figure 6.52. Measured displacement at yield vs. axial load applied to member.

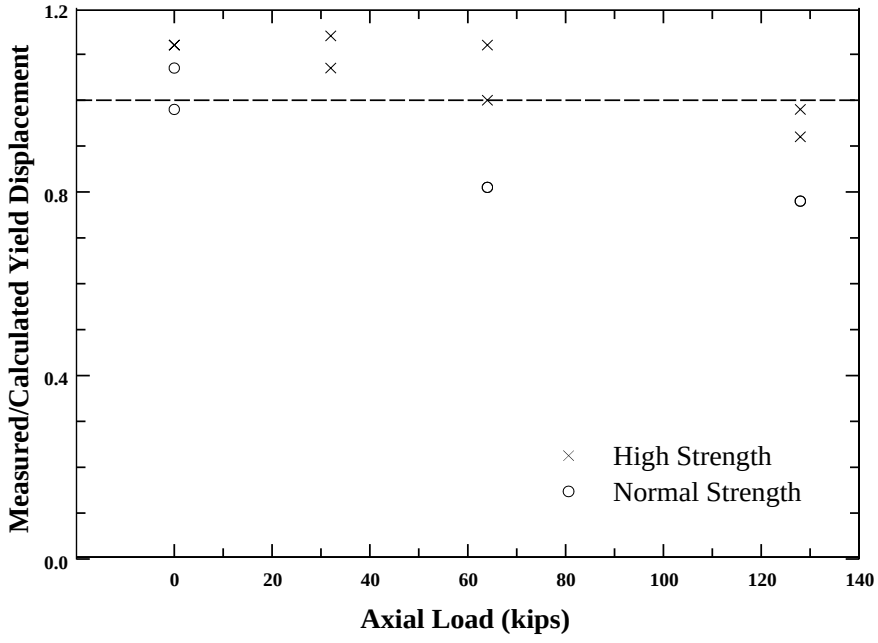

Figure 6.53. Ratio of measured to calculated yield displacement.

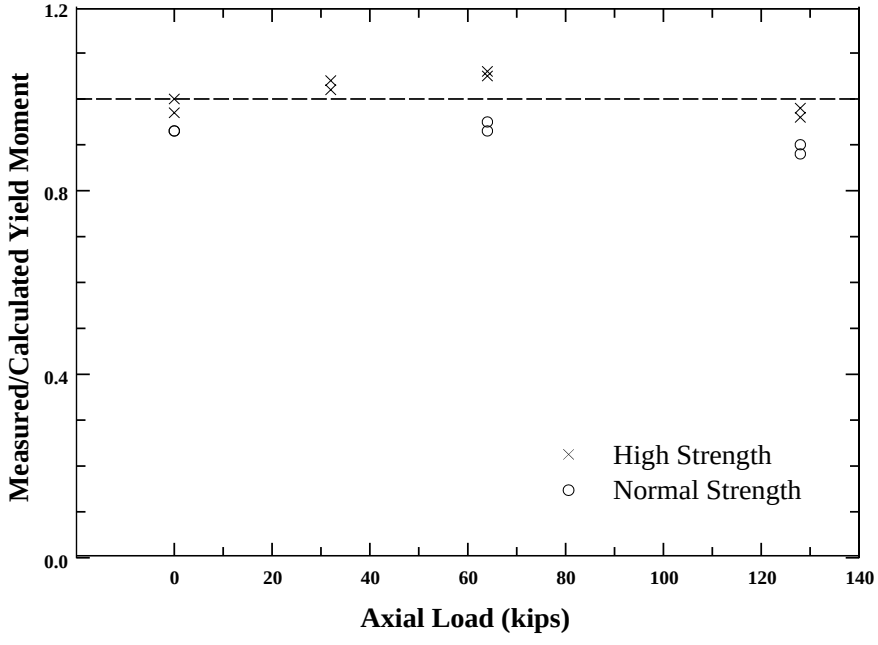

Figure 6.54. Ratio of measured to calculated displacement at yield vs axial load applied to member.

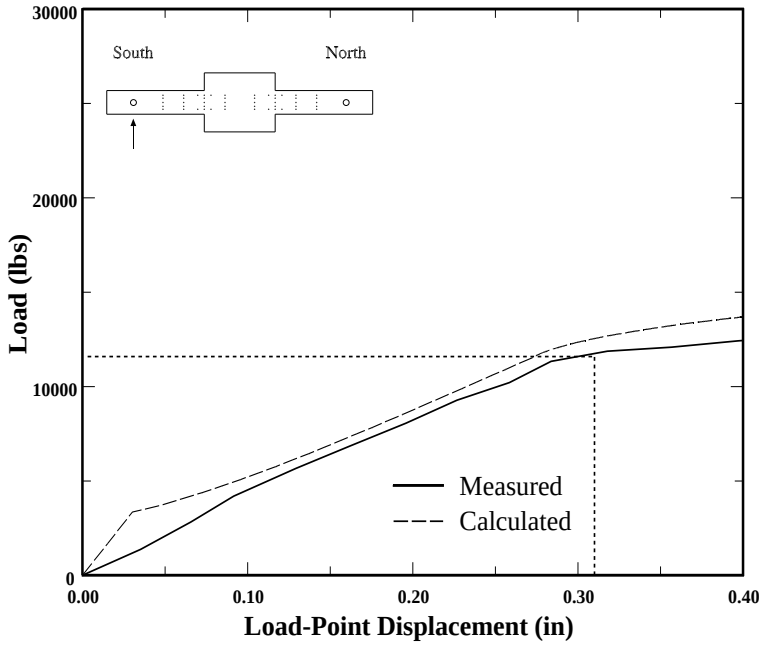

Figure 6.55. Calculated and measured load-displacement relationship for specimen C10-00, south member. (The test specimen was cracked during the pilot test).

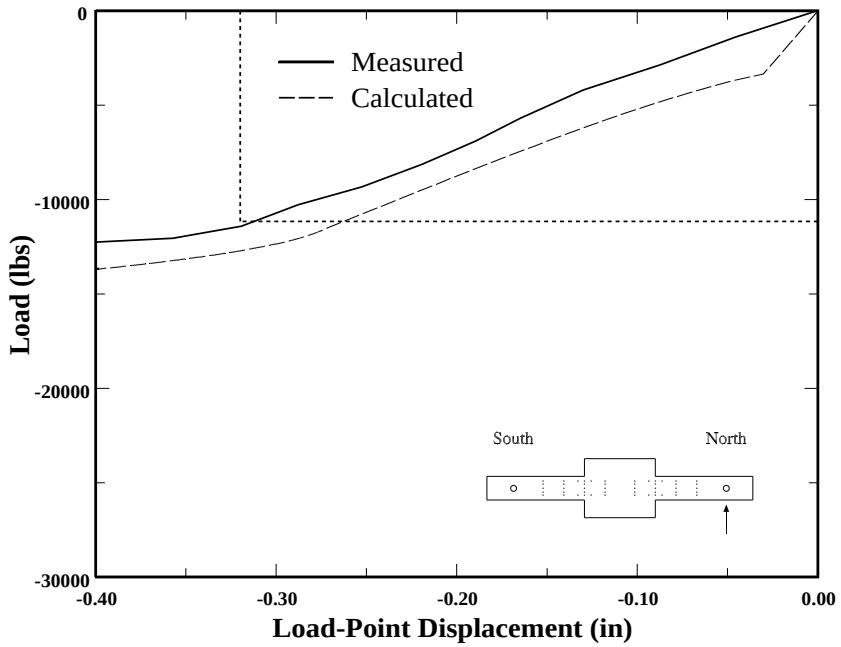

Figure 6.56. Calculated and measured load-displacement relationship for specimen C10-00, north member. (Test specimen was cracked during the pilot test).

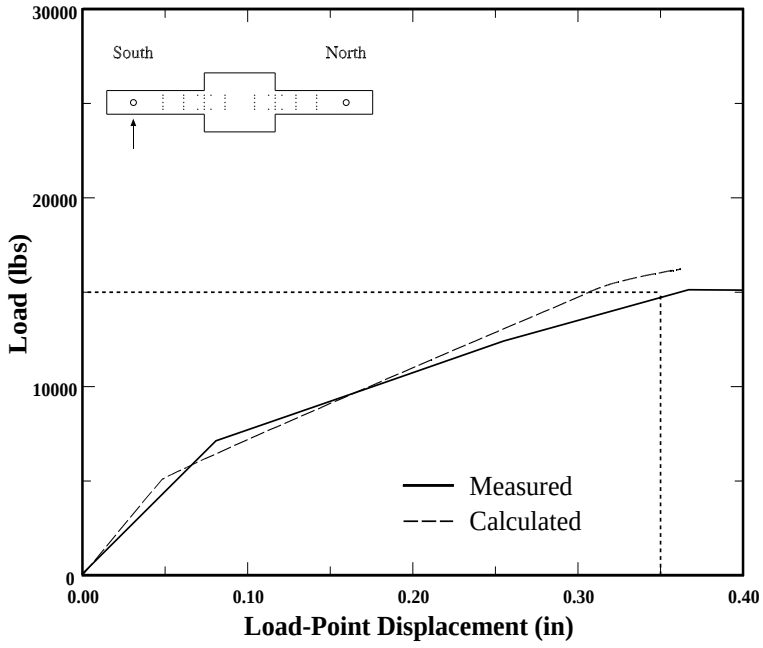

Figure 6.57. Calculated and measured load-displacement relationship for specimen C10-05, south member.

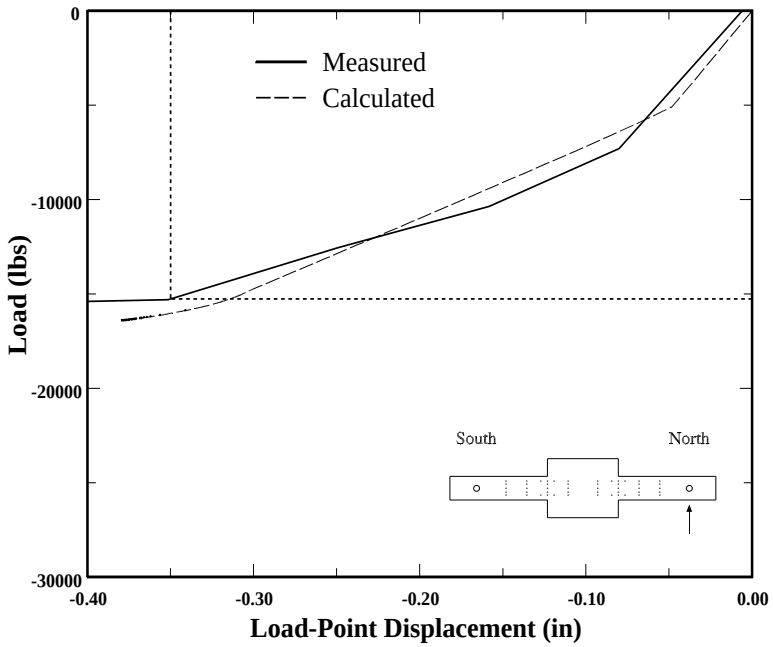

Figure 6.58. Calculated and measured load-displacement relationship for specimen C10-05, north member.

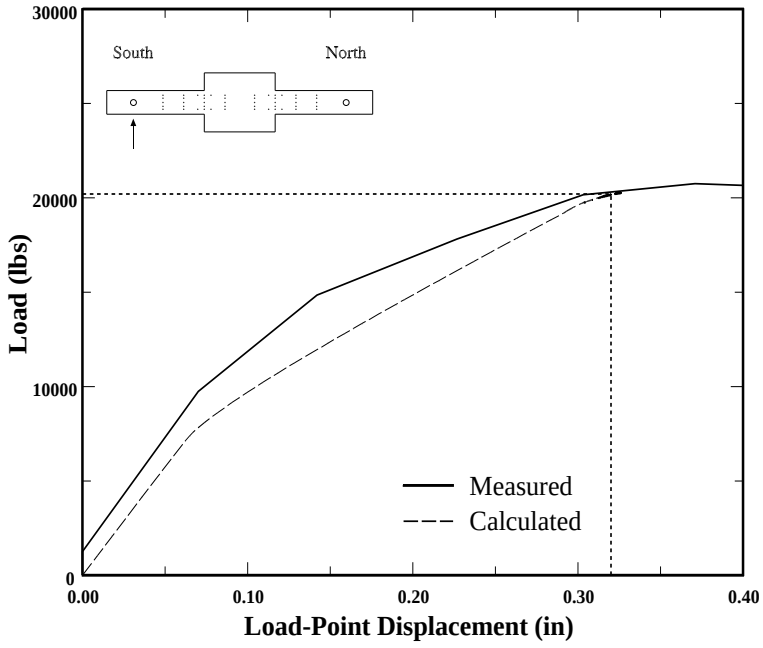

Figure 6.59. Calculated and measured load-displacement relationship for specimen C10-10, south member.

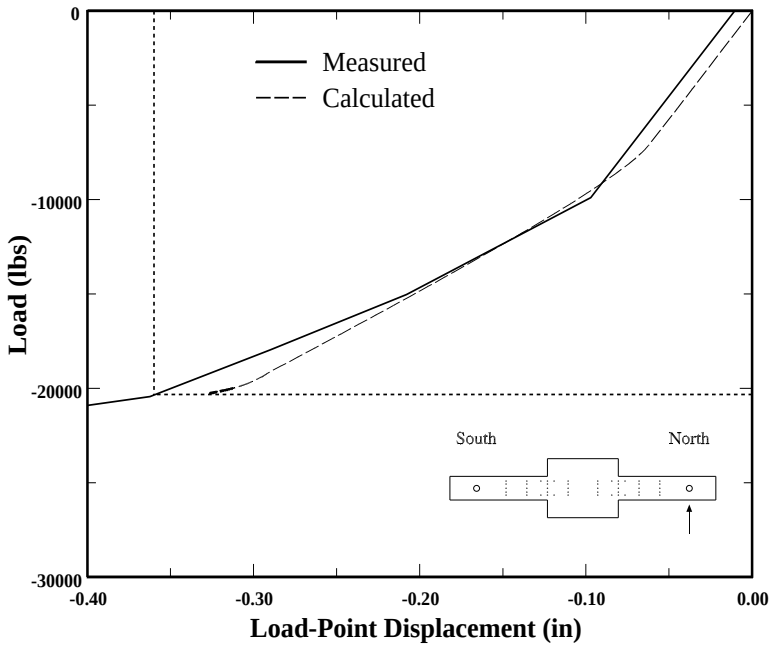

Figure 6.60. Calculated and measured load-displacement relationship for specimen C10-10, north member.

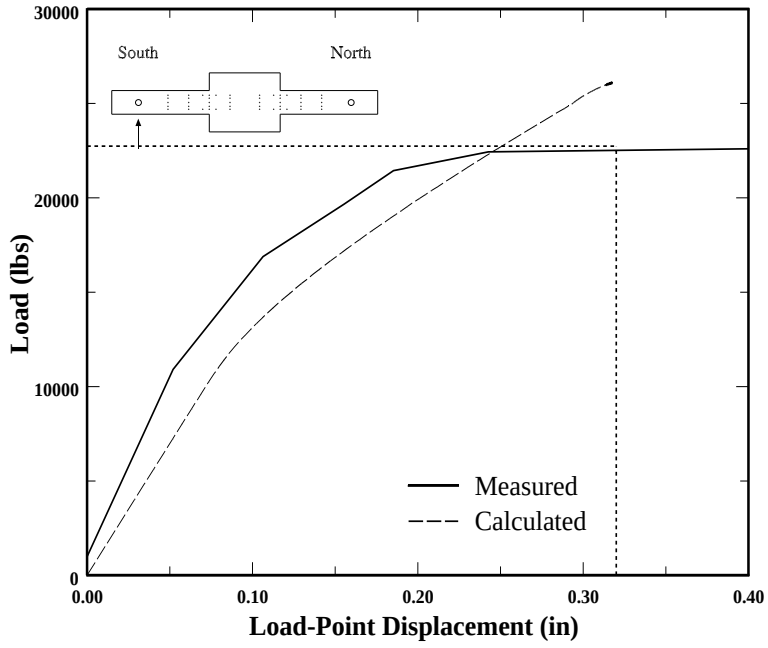

Figure 6.61. Calculated and measured load-displacement relationship for specimen C10-20, south member.

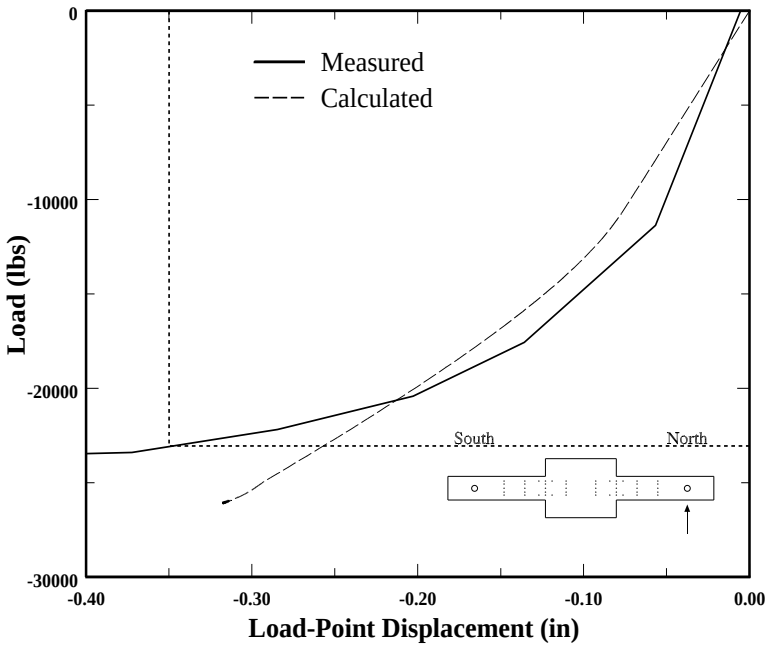

Figure 6.62. Calculated and measured load-displacement relationship for specimen C10-20, north member.

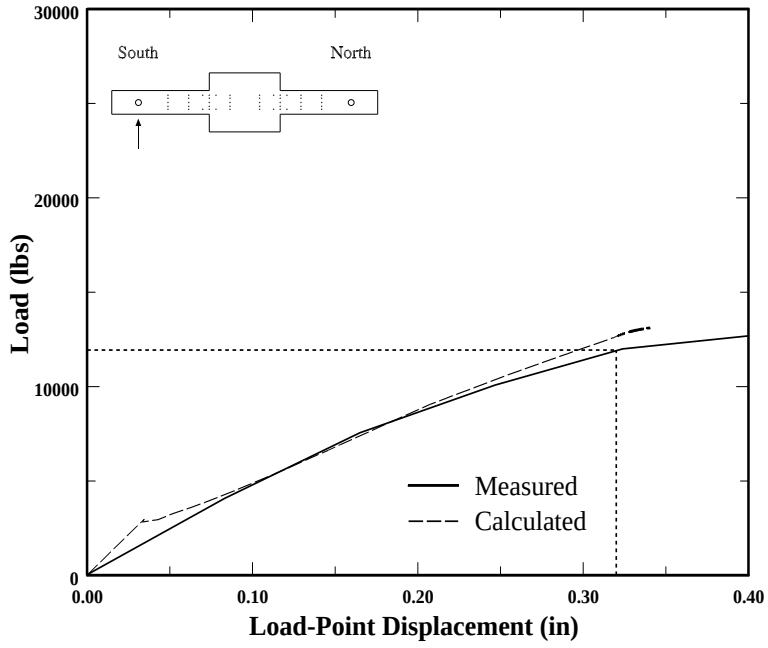

Figure 6.63. Calculated and measured load-displacement relationship for specimen C5-00, south member.

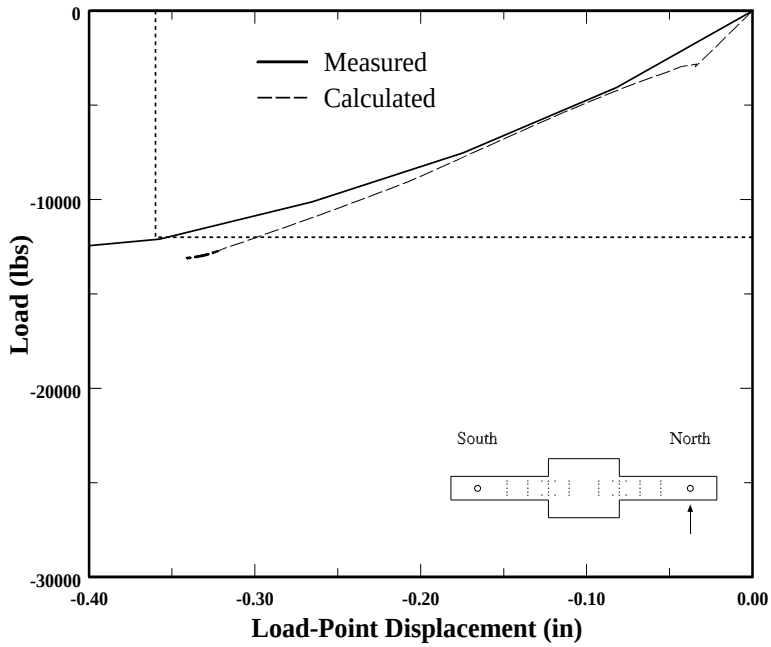

Figure 6.64. Calculated and measured load-displacement relationship for specimen C5-00, north member.

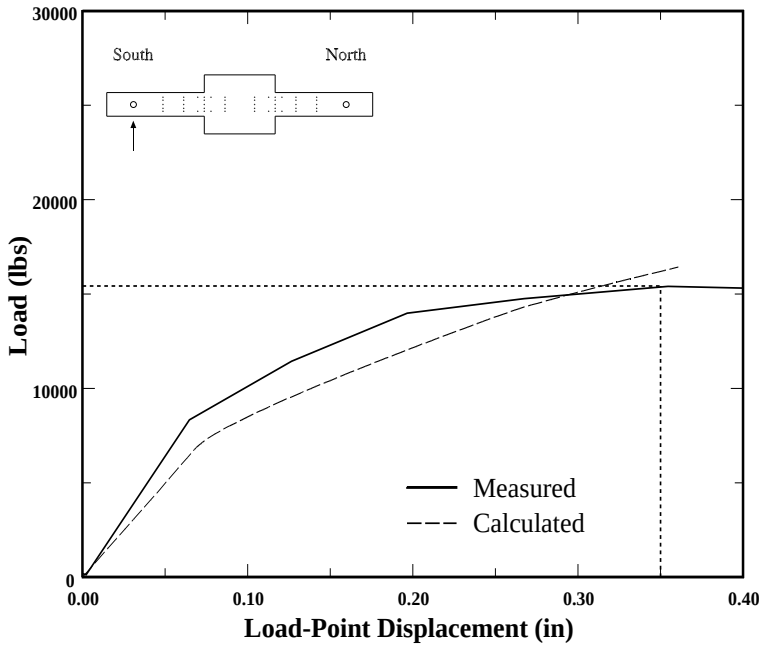

Figure 6.65. Calculated and measured load-displacement relationship for specimen C5-20, south member.

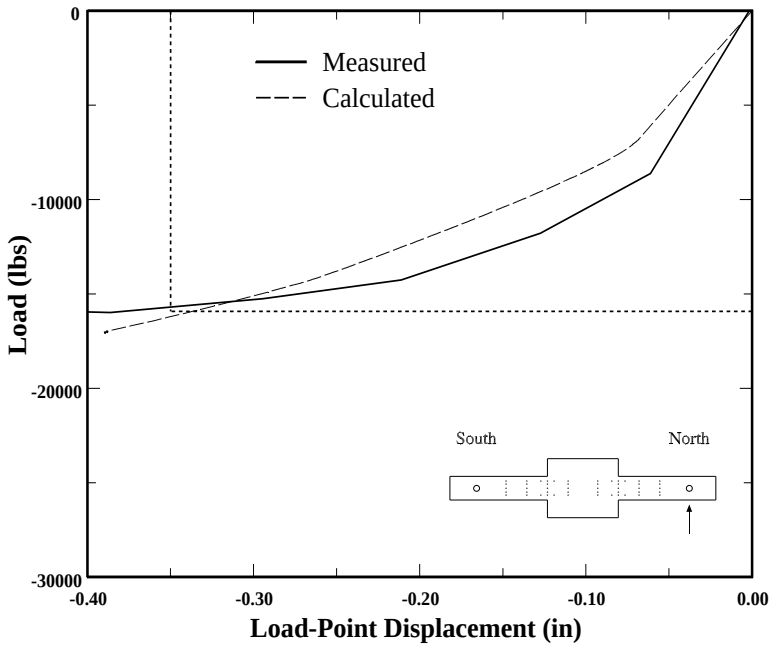

Figure 6.66. Calculated and measured load-displacement relationship for specimen C5-20, north member.

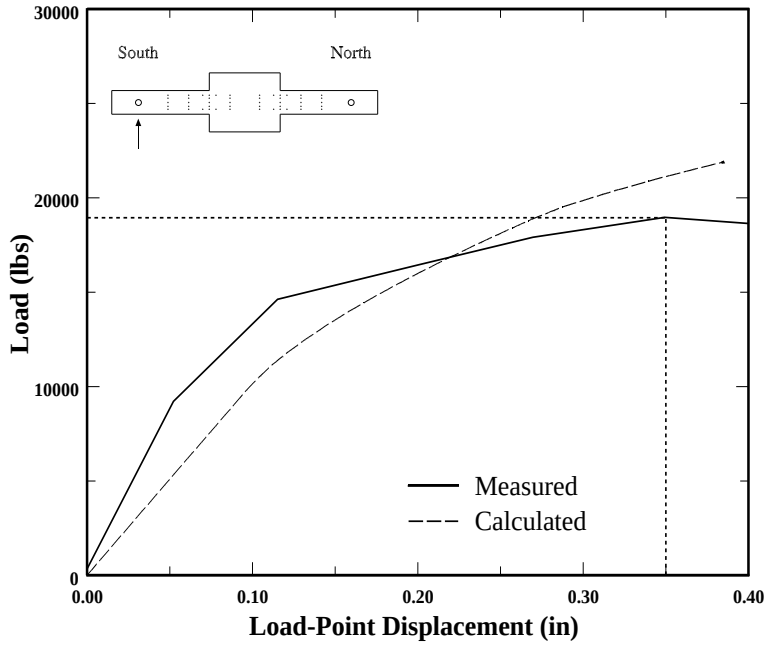

Figure 6.67. Calculated and measured load-displacement relationship for specimen C5-40, south member.

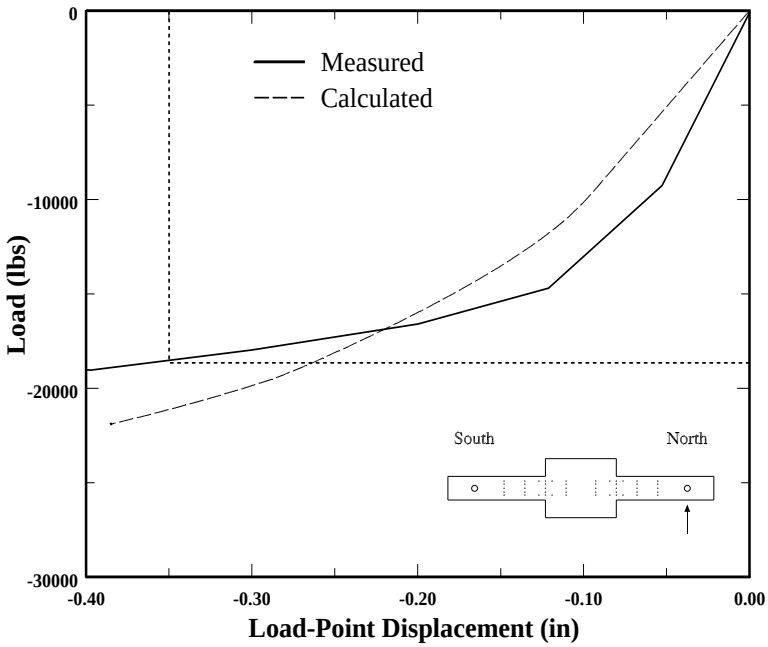

Figure 6.68. Calculated and measured load-displacement relationship for specimen C5-40, north member.

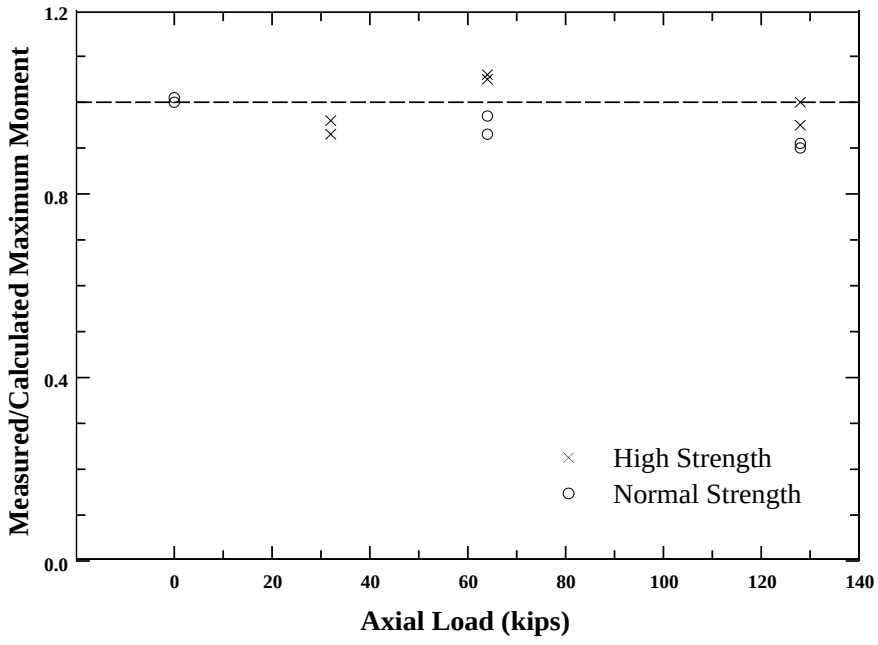

Figure 6.69. Ratio of measured to calculated maximum moment vs axial load applied to member.

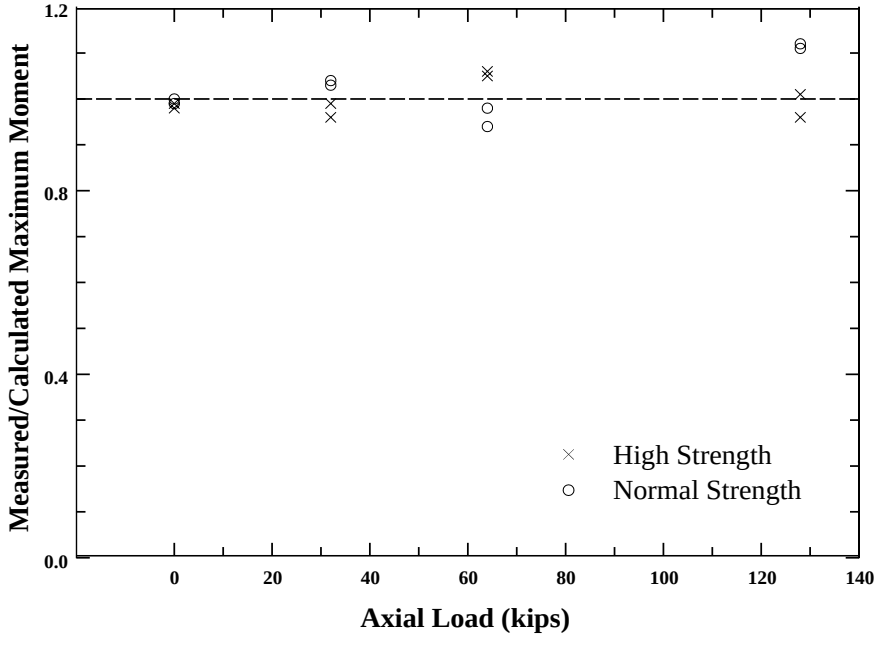

Figure 6.70. Ratio of measured to calculated maximum moment vs axial load applied to member. Strength calculated according to ACI Building Code (ACI, 1995).

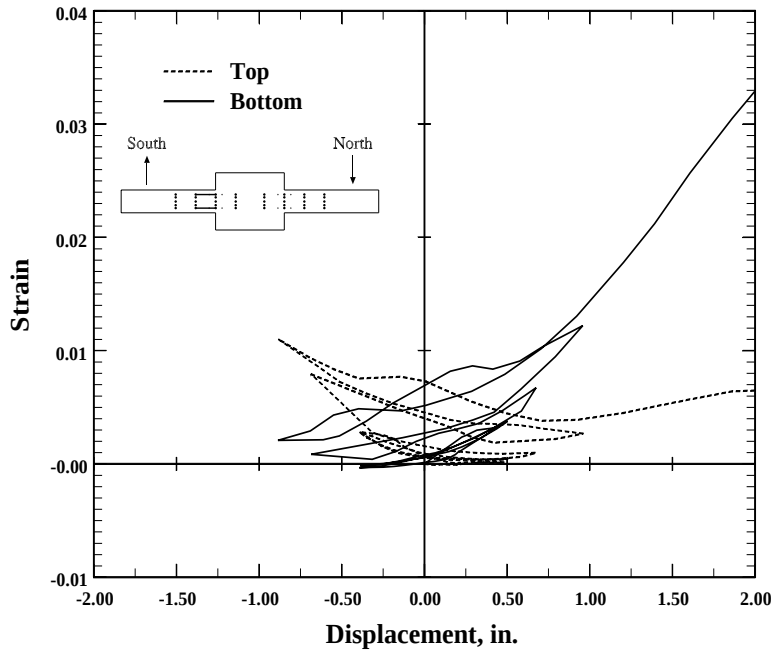

Figure 6.71. Strain at the level of the reinforcement. Specimen C10-00, south member.

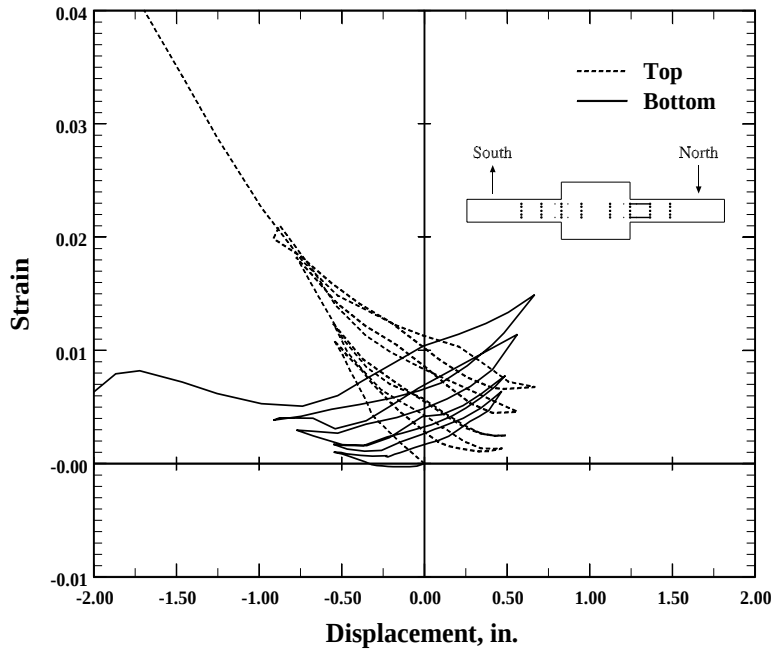

Figure 6.72. Strain at the level of the reinforcement. Specimen C10-00, north member.

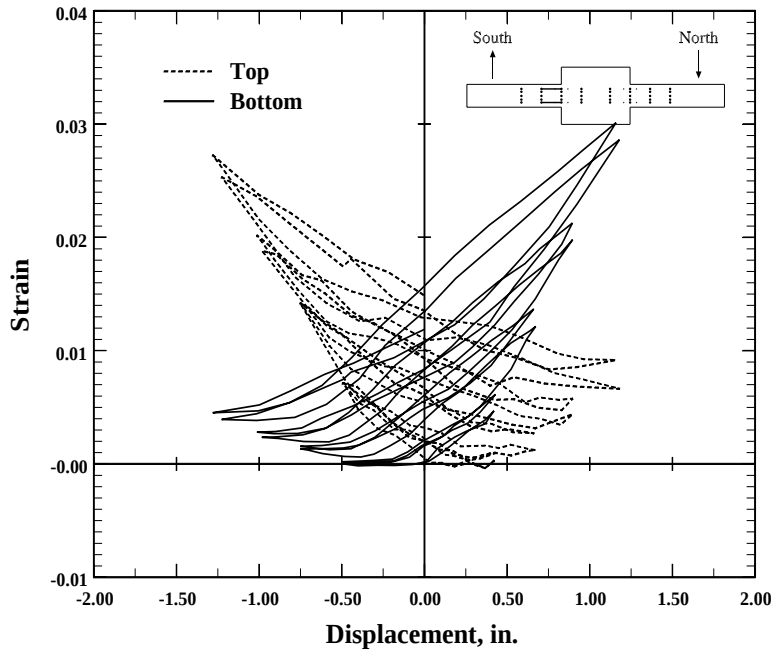

Figure 6.73. Strain at the level of the reinforcement. Specimen C10-05, south member.

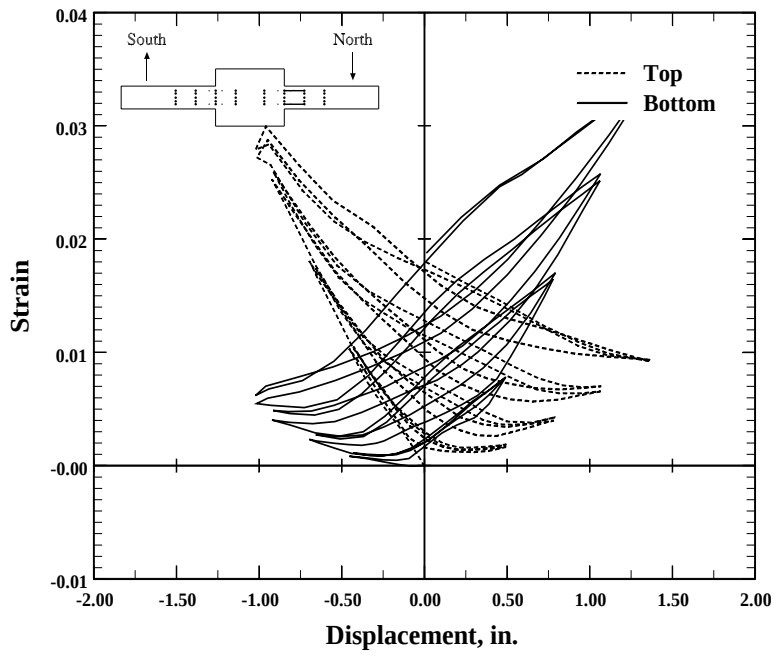

Figure 6.74. Strain at the level of the reinforcement. Specimen C10-05, north member.

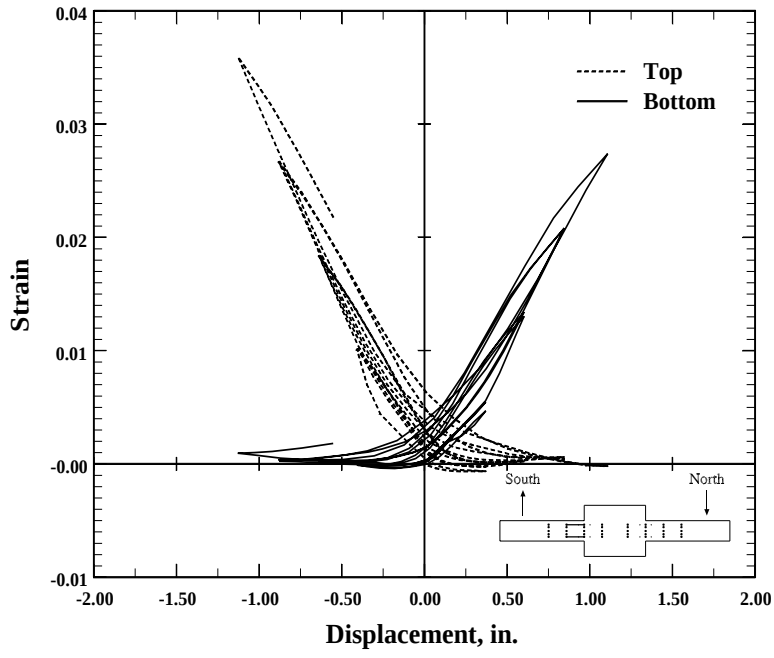

Figure 6.75. Strain at the level of the reinforcement. Specimen C10-10, south member.

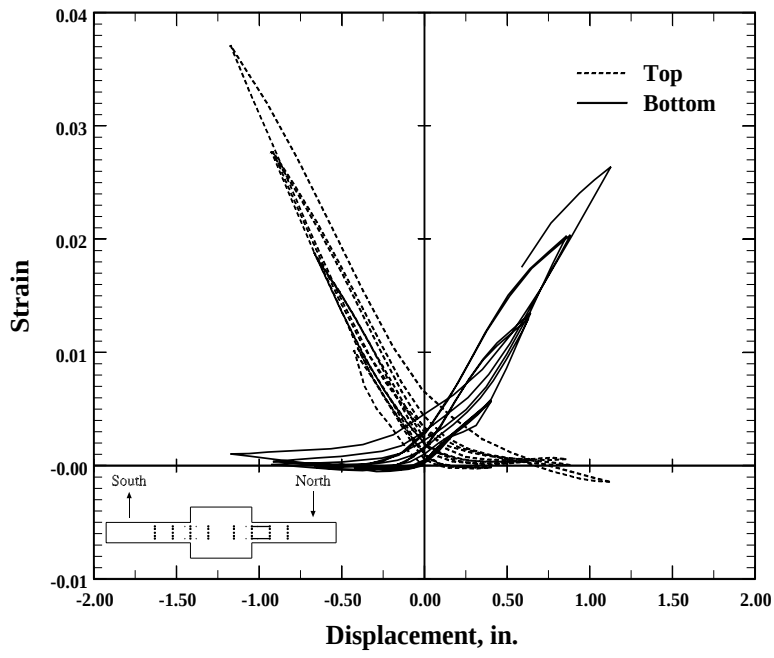

Figure 6.76. Strain at the level of the reinforcement. Specimen C10-10, north member.

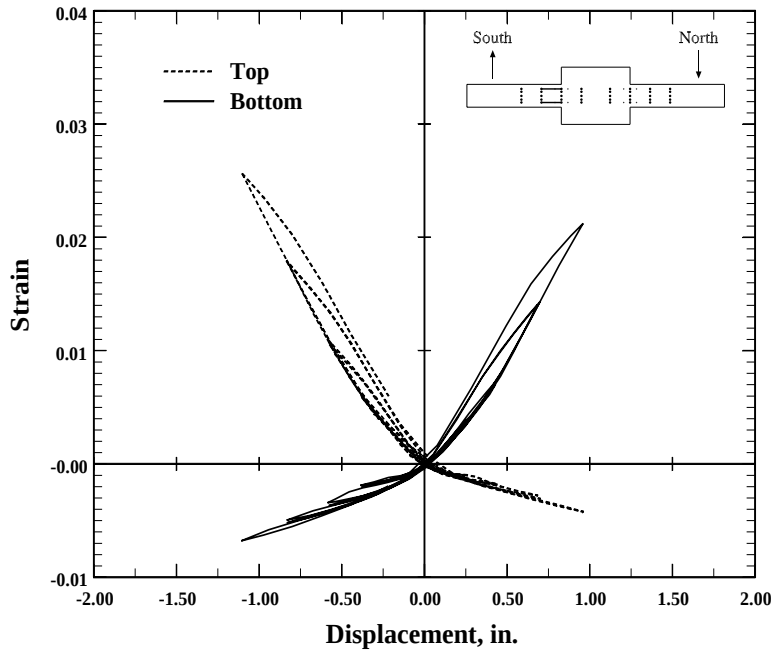

Figure 6.77. Strain at the level of the reinforcement. Specimen C10-20, south member.

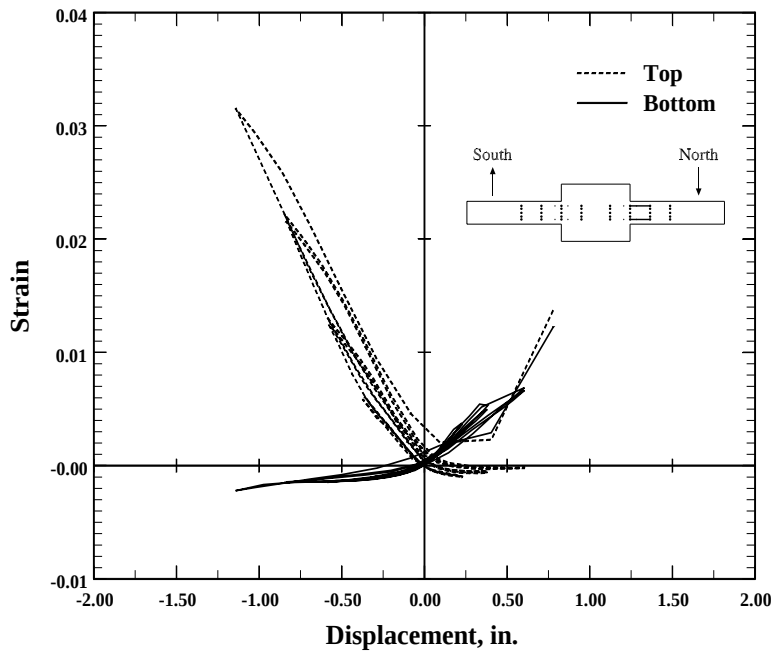

Figure 6.78. Strain at the level of the reinforcement. Specimen C10-20, north member.

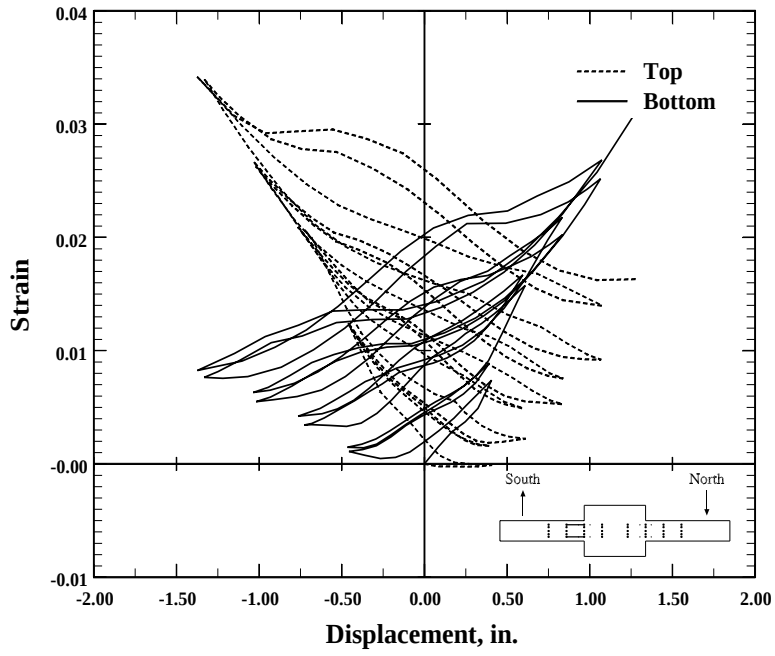

Figure 6.79. Strain at the level of the reinforcement. Specimen C5-00, south member.

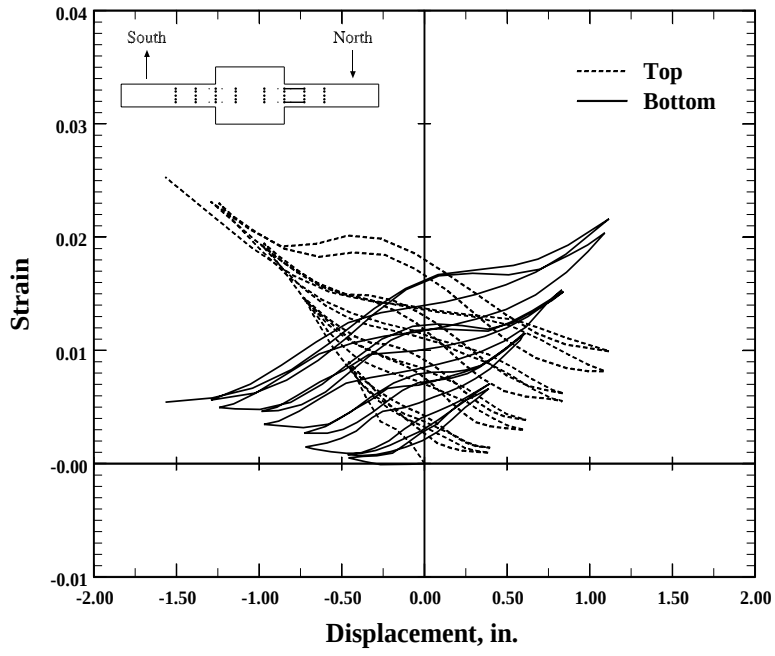

Figure 6.80. Strain at the level of the reinforcement. Specimen C5-00, north member.

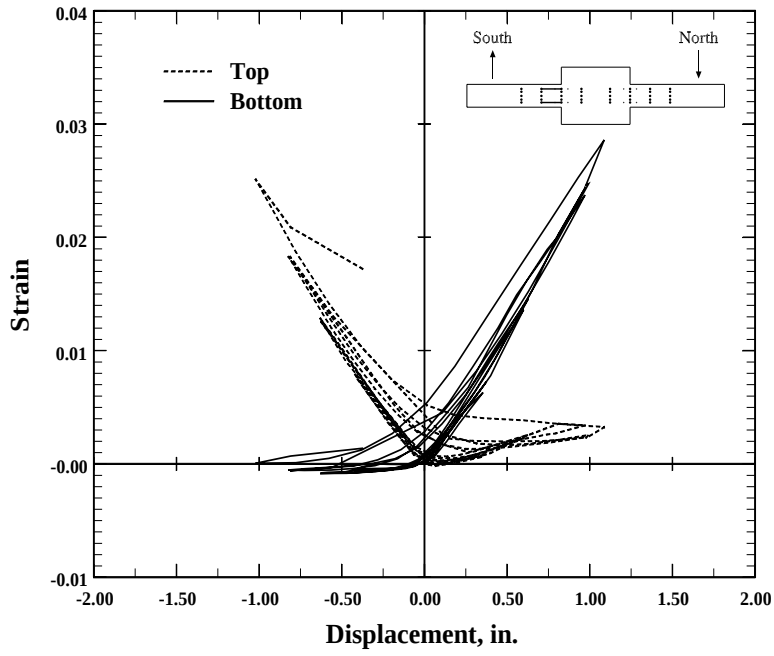

Figure 6.81. Strain at the level of the reinforcement. Specimen C5-20, south member.

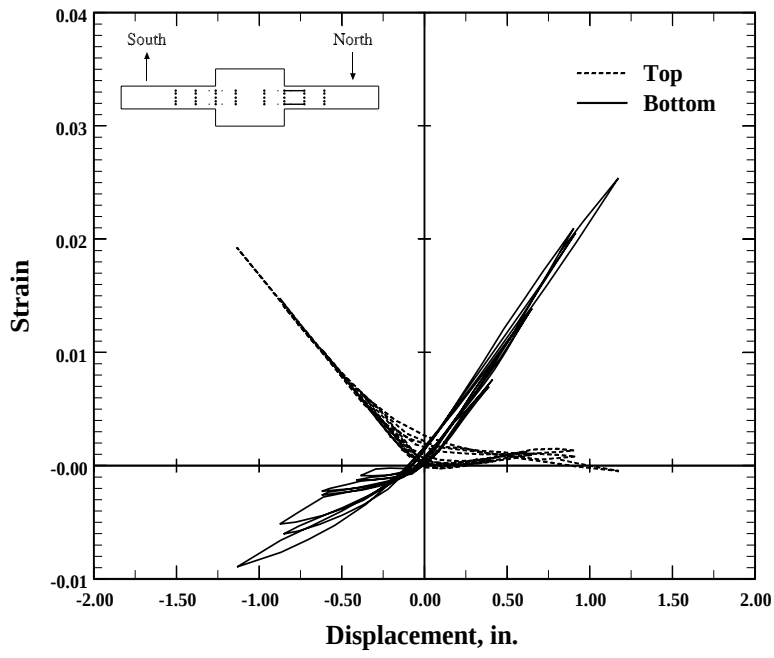

Figure 6.82. Strain at the level of the reinforcement. Specimen C5-20, north member.

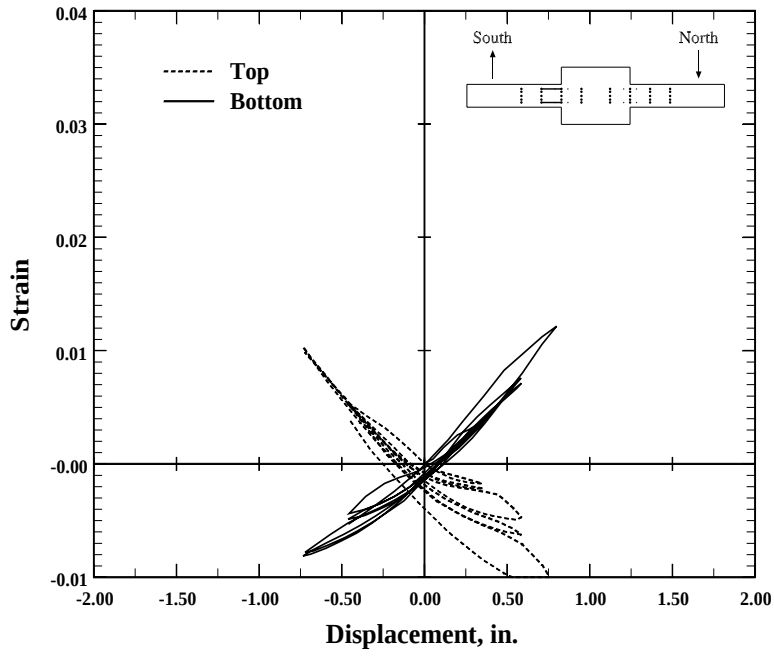

Figure 6.83. Strain at the level of the reinforcement. Specimen C5-40, south member.

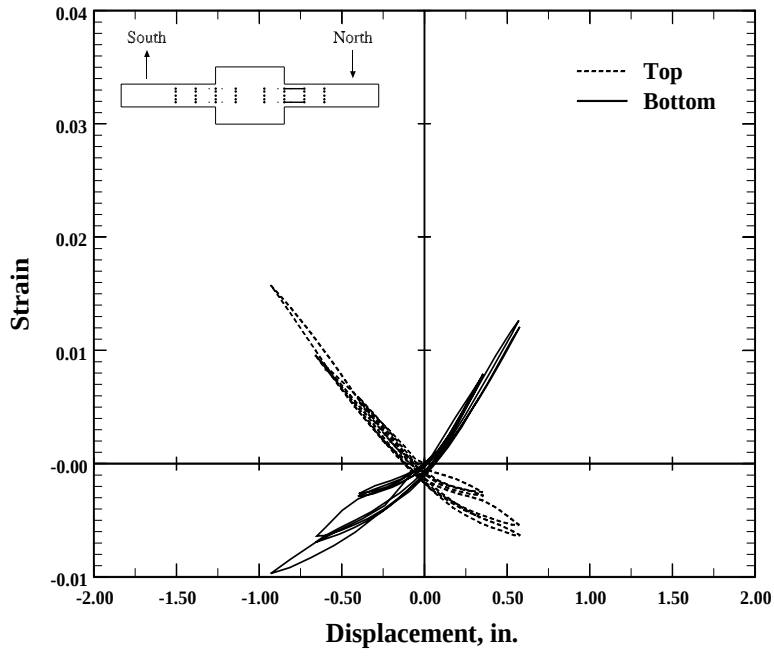

Figure 6.84. Strain at the level of the reinforcement. Specimen C5-40, north member.

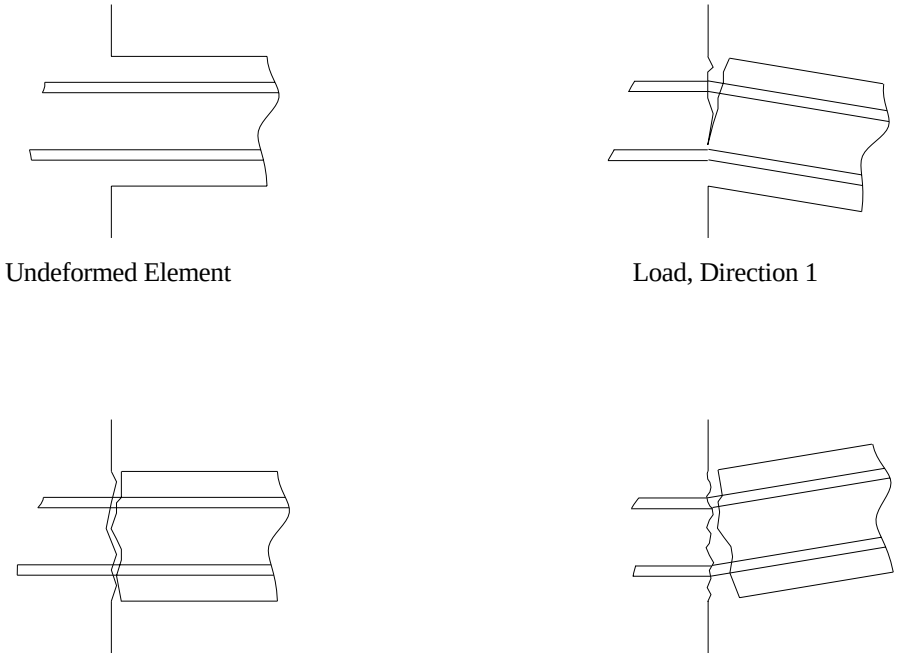

Figure 6.85. Behavior of specimen under cyclic loading.

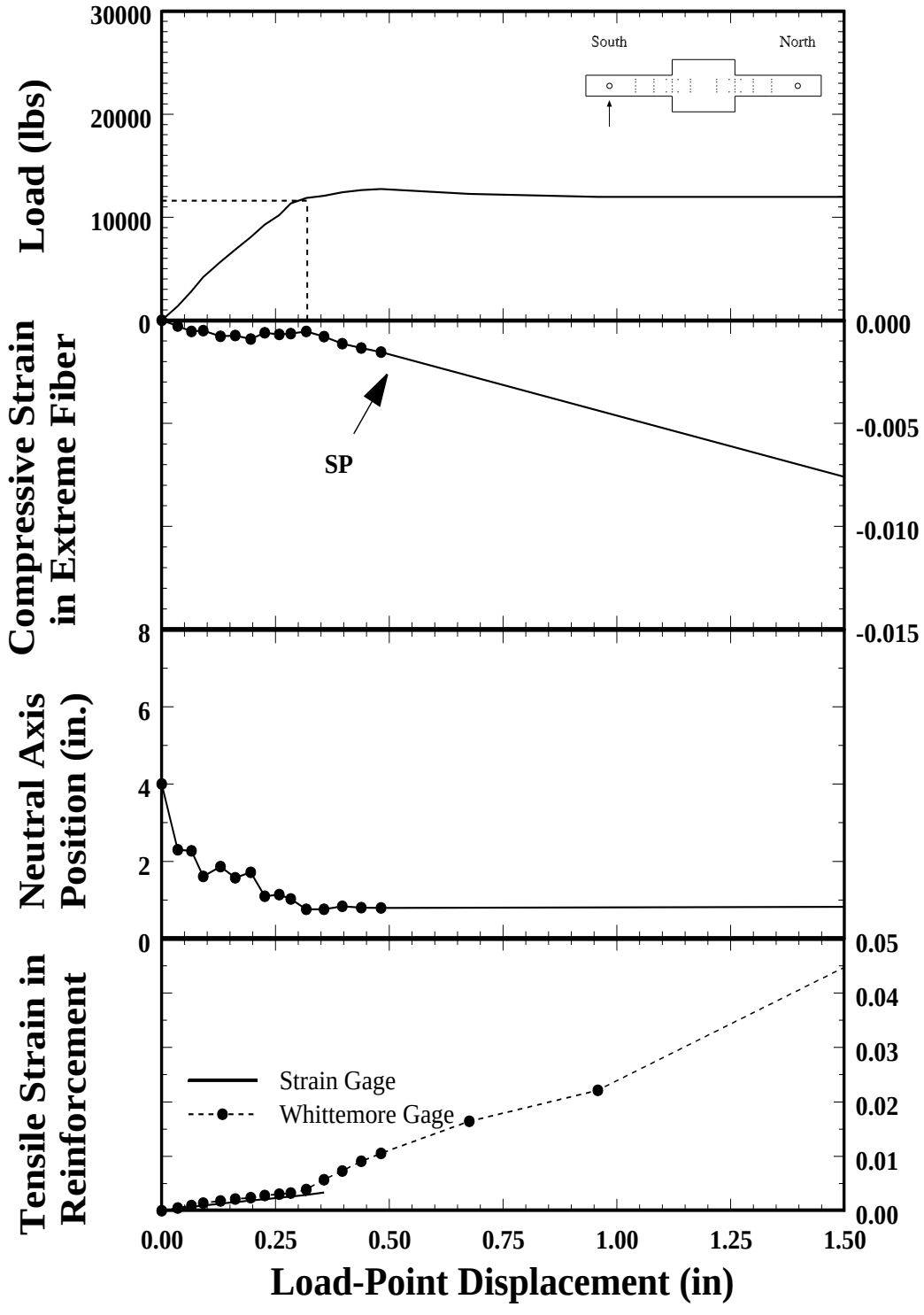

Figure 6.86. Envelope curves for the measured response of specimen C10-00, south member.

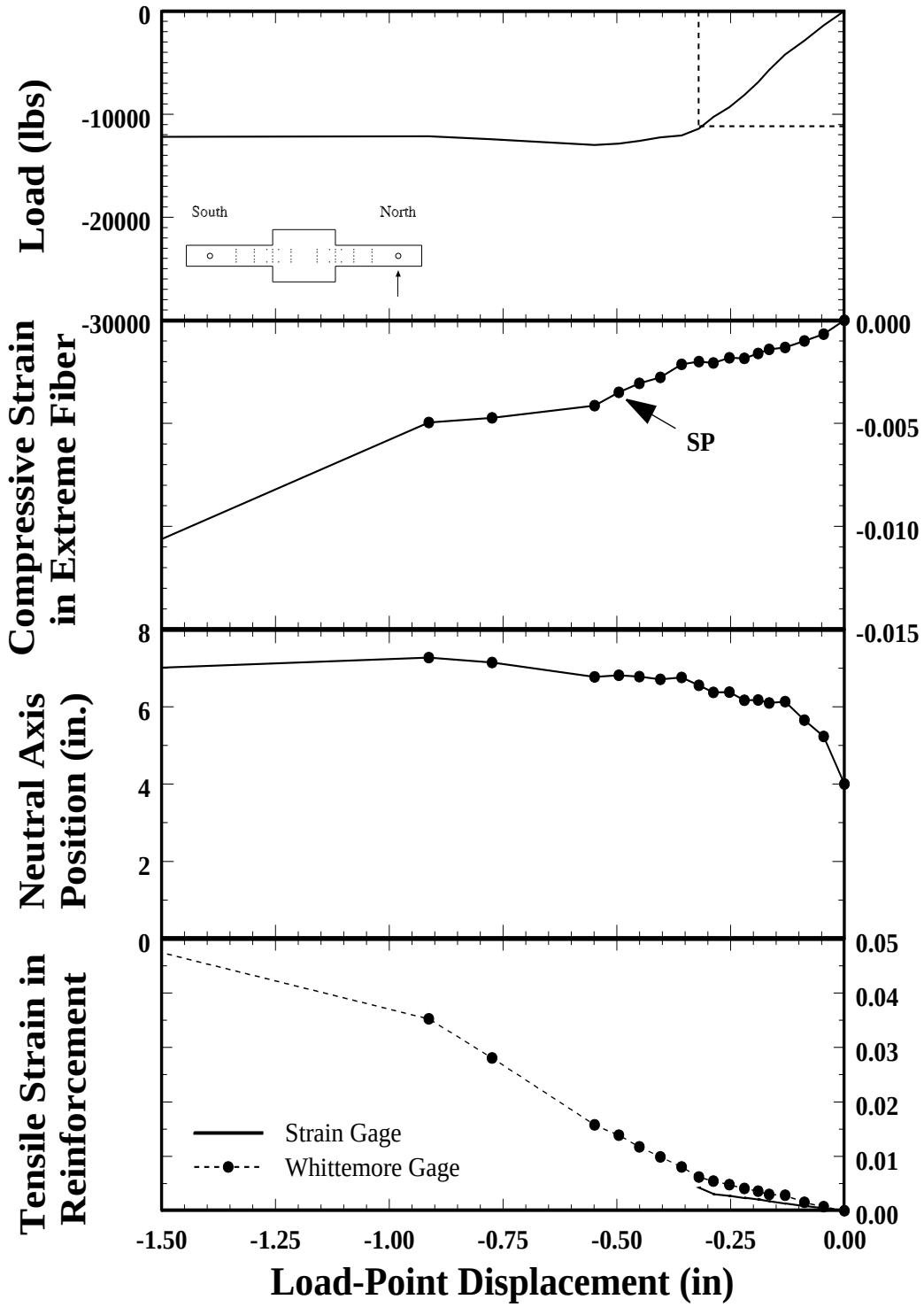

Figure 6.87. Envelope curves for the measured response of specimen C10-00, north member.

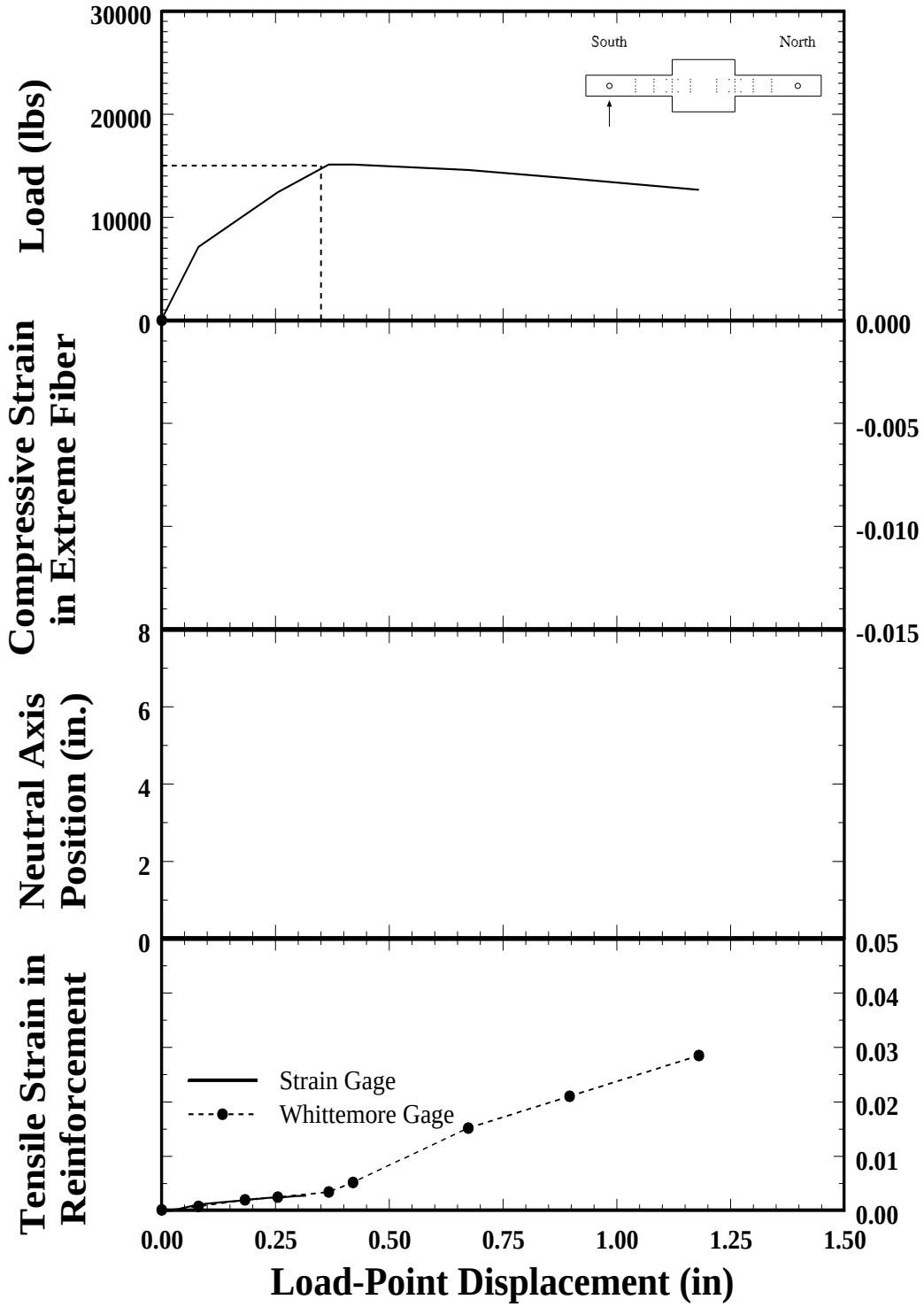

Figure 6.88. Envelope curves for the measured response of specimen C10-05, south member.

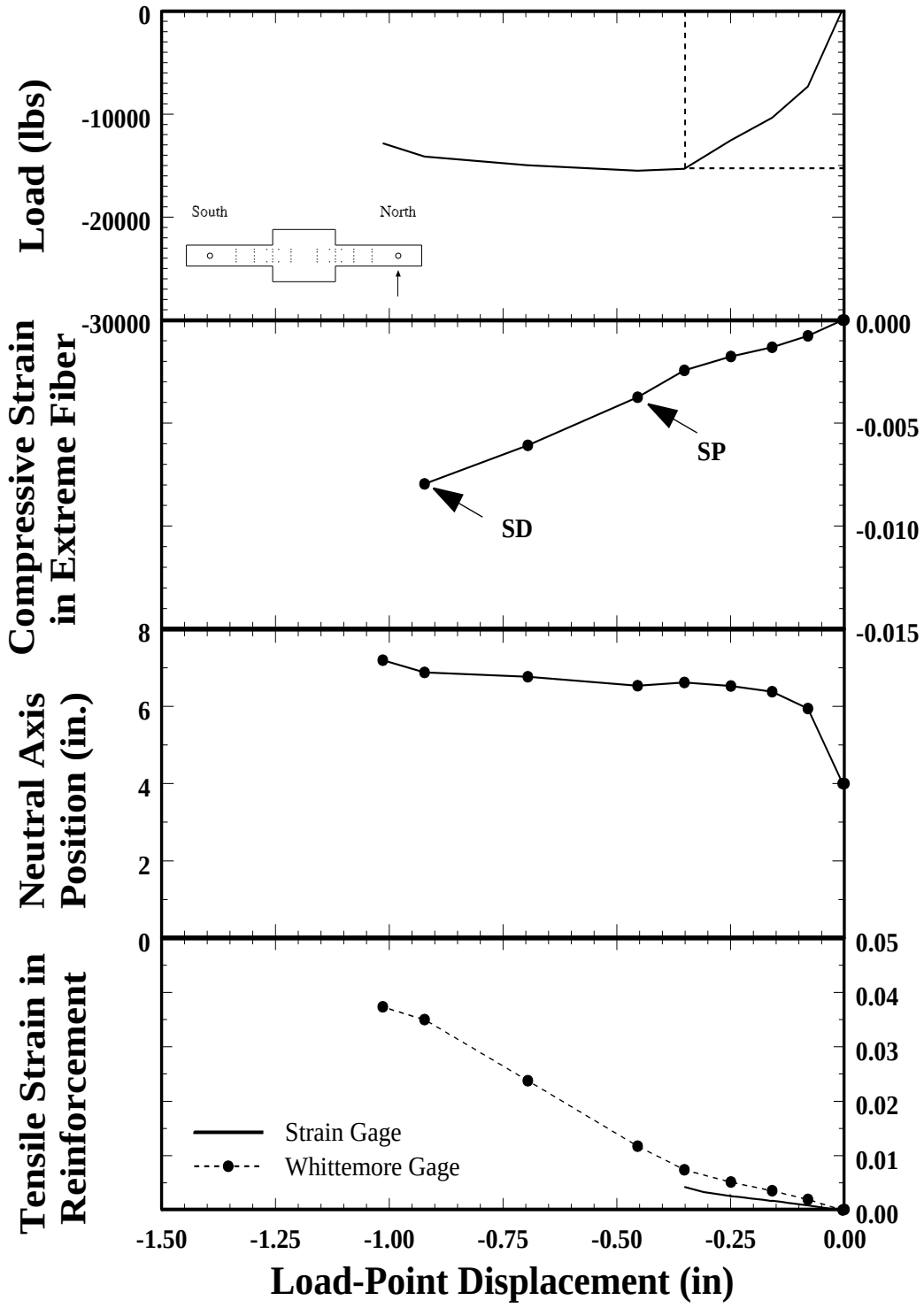

Figure 6.89. Envelope curves for the measured response of specimen C10-05, north member.

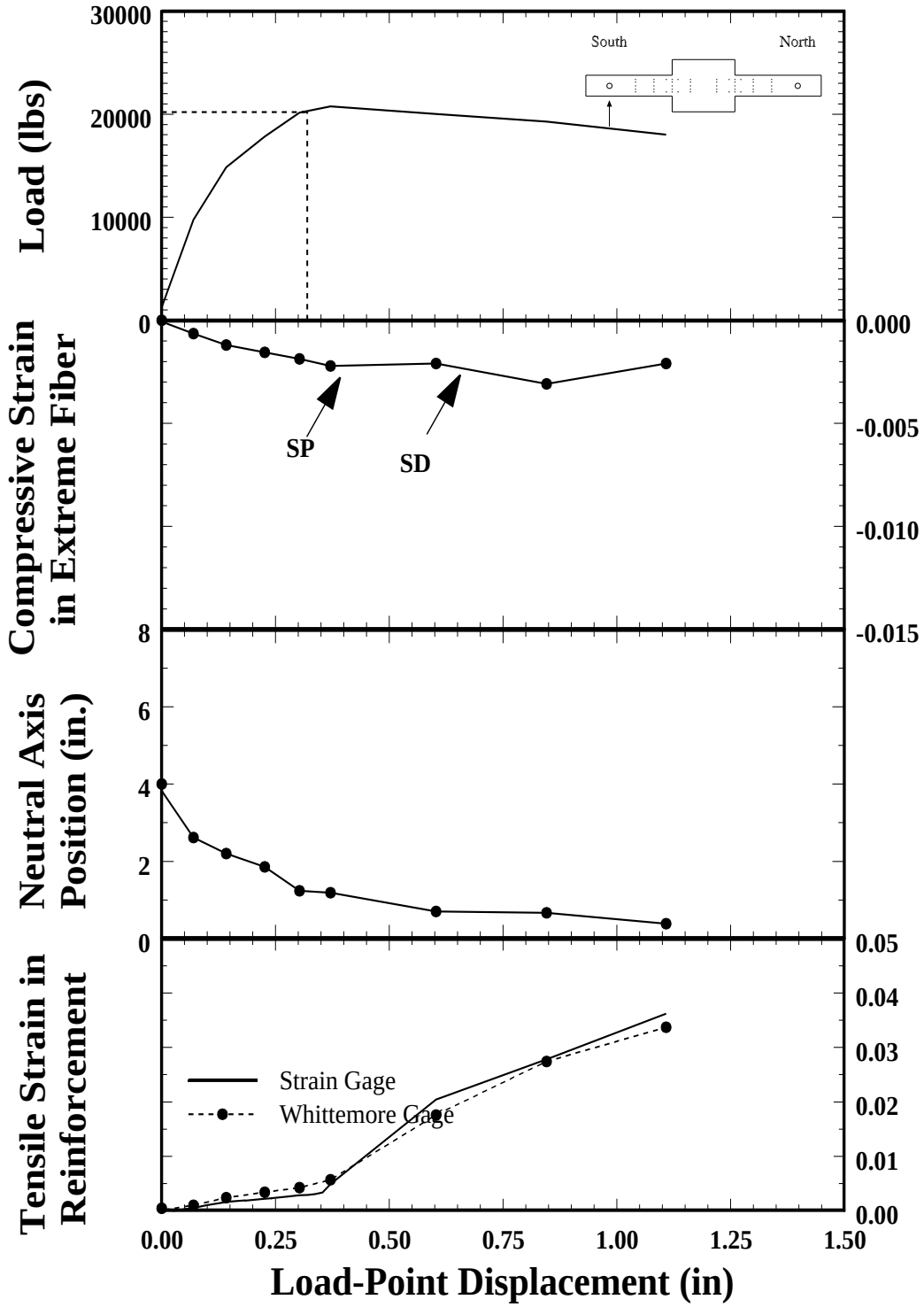

Figure 6.90. Envelope curves for the measured response of specimen C10-10, south member.

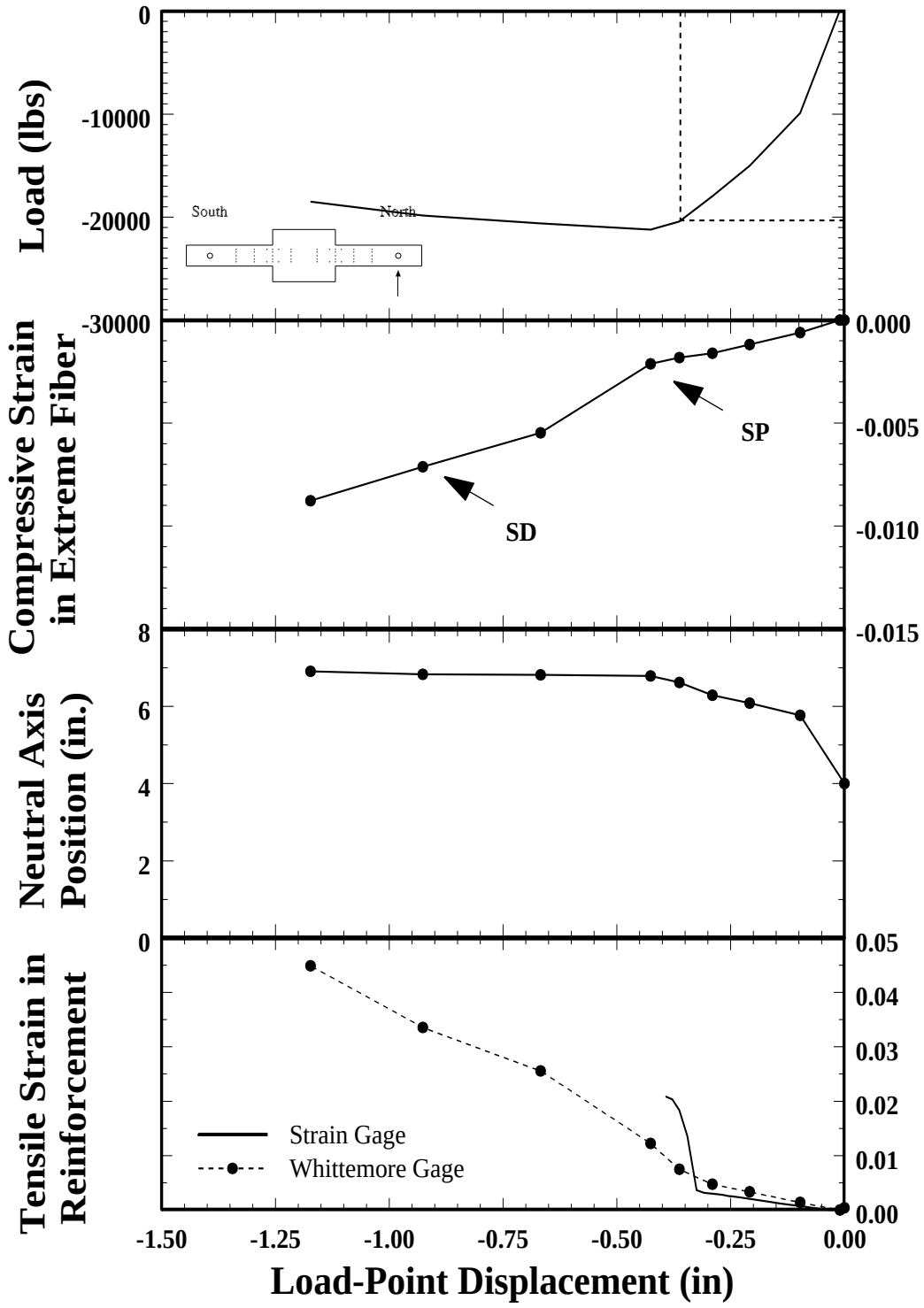

Figure 6.91. Envelope curves for the measured response of specimen C10-10, north member.

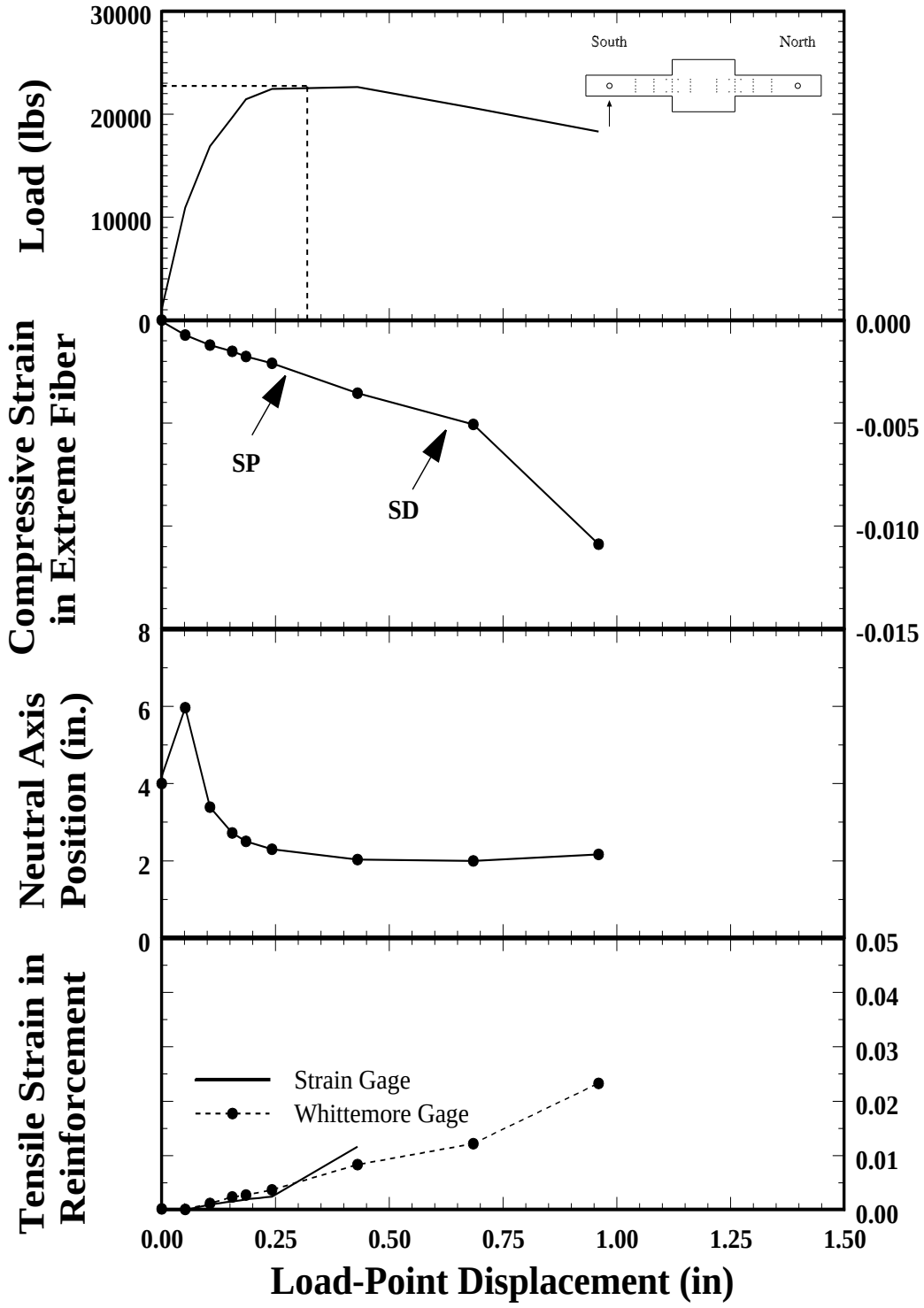

Figure 6.92. Envelope curves for the measured response of specimen C10-20, south member.

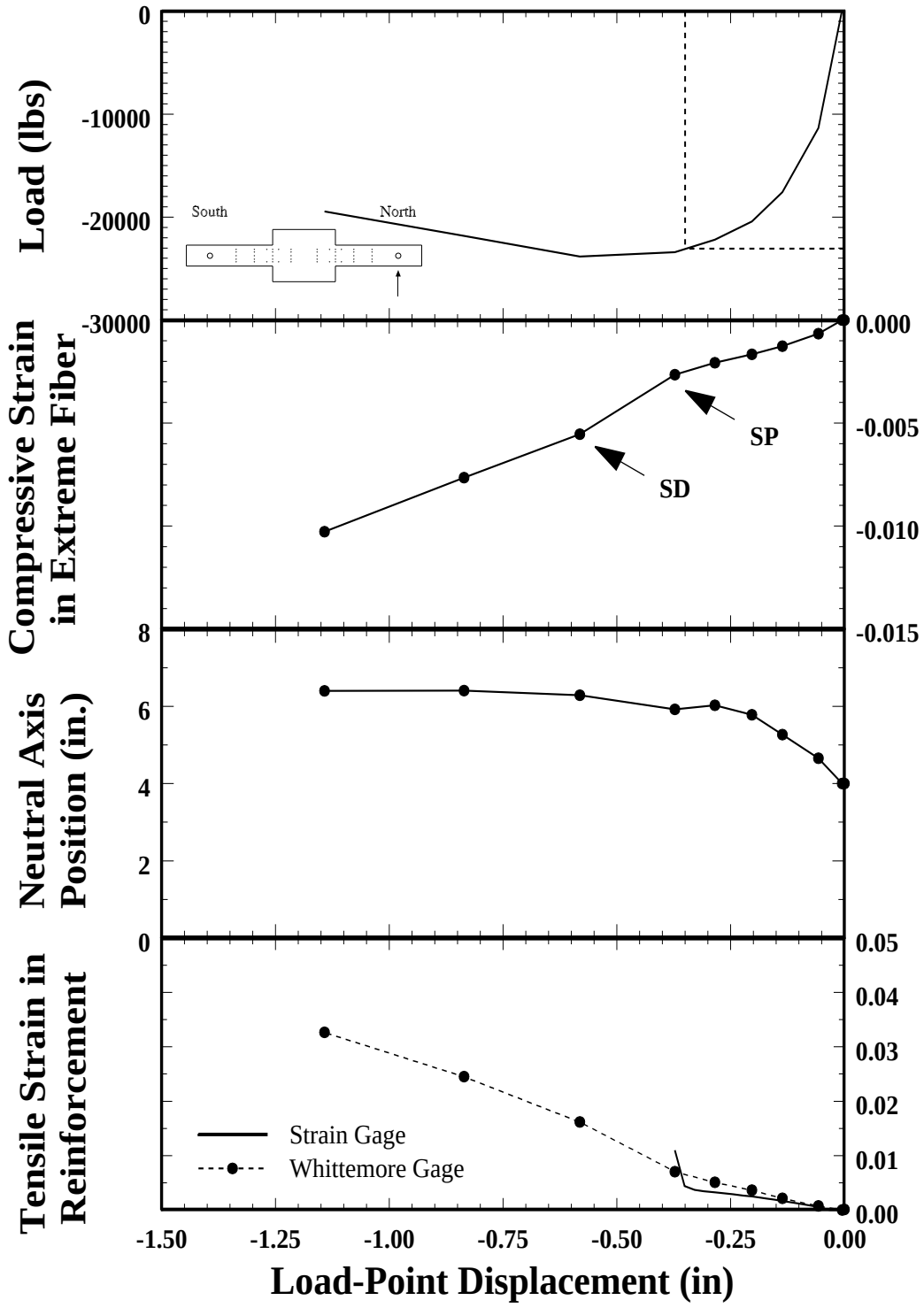

Figure 6.93. Envelope curves for the measured response of specimen C10-20, north member.

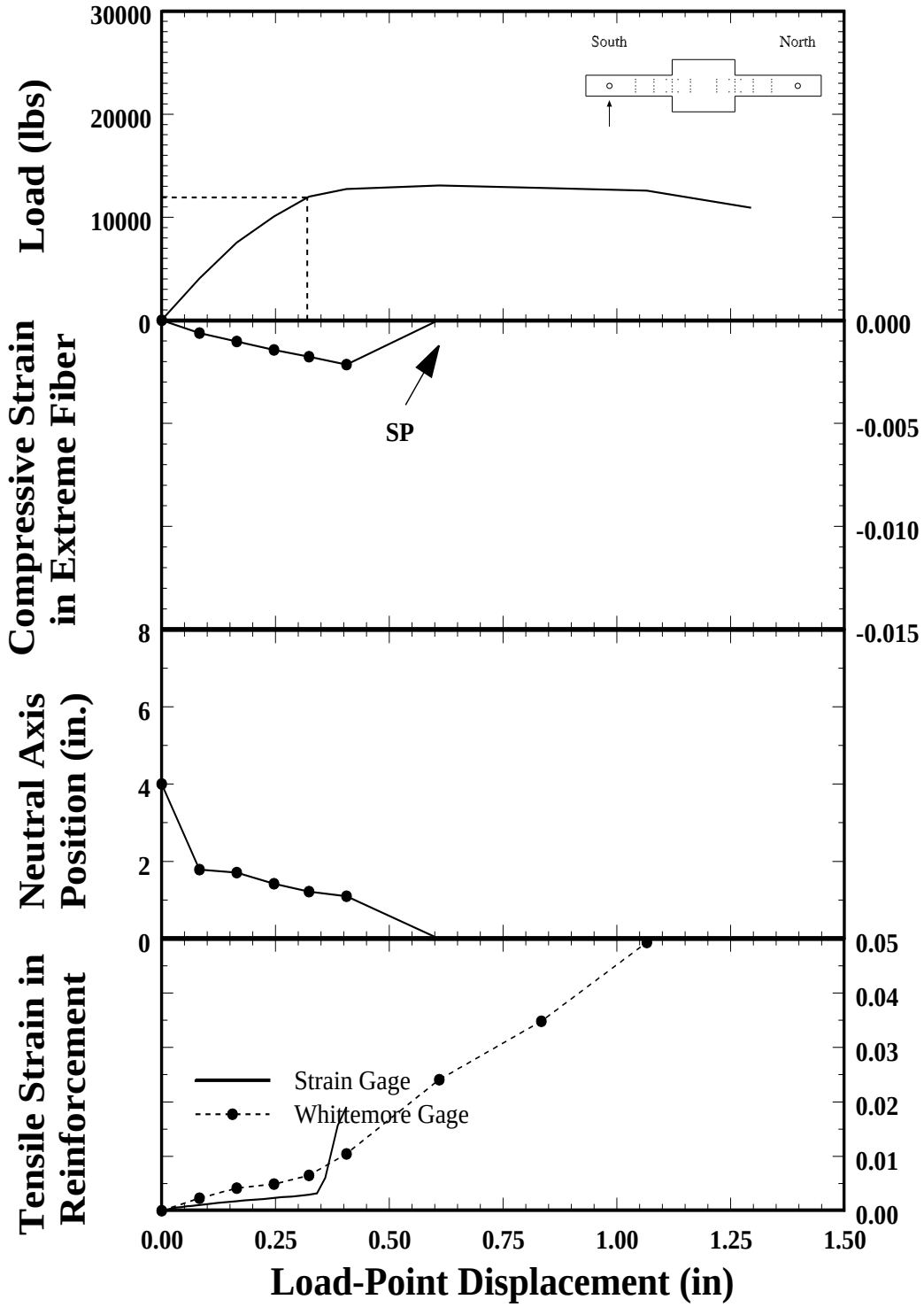

Figure 6.94. Envelope curves for the measured response of specimen C5-00, south member.

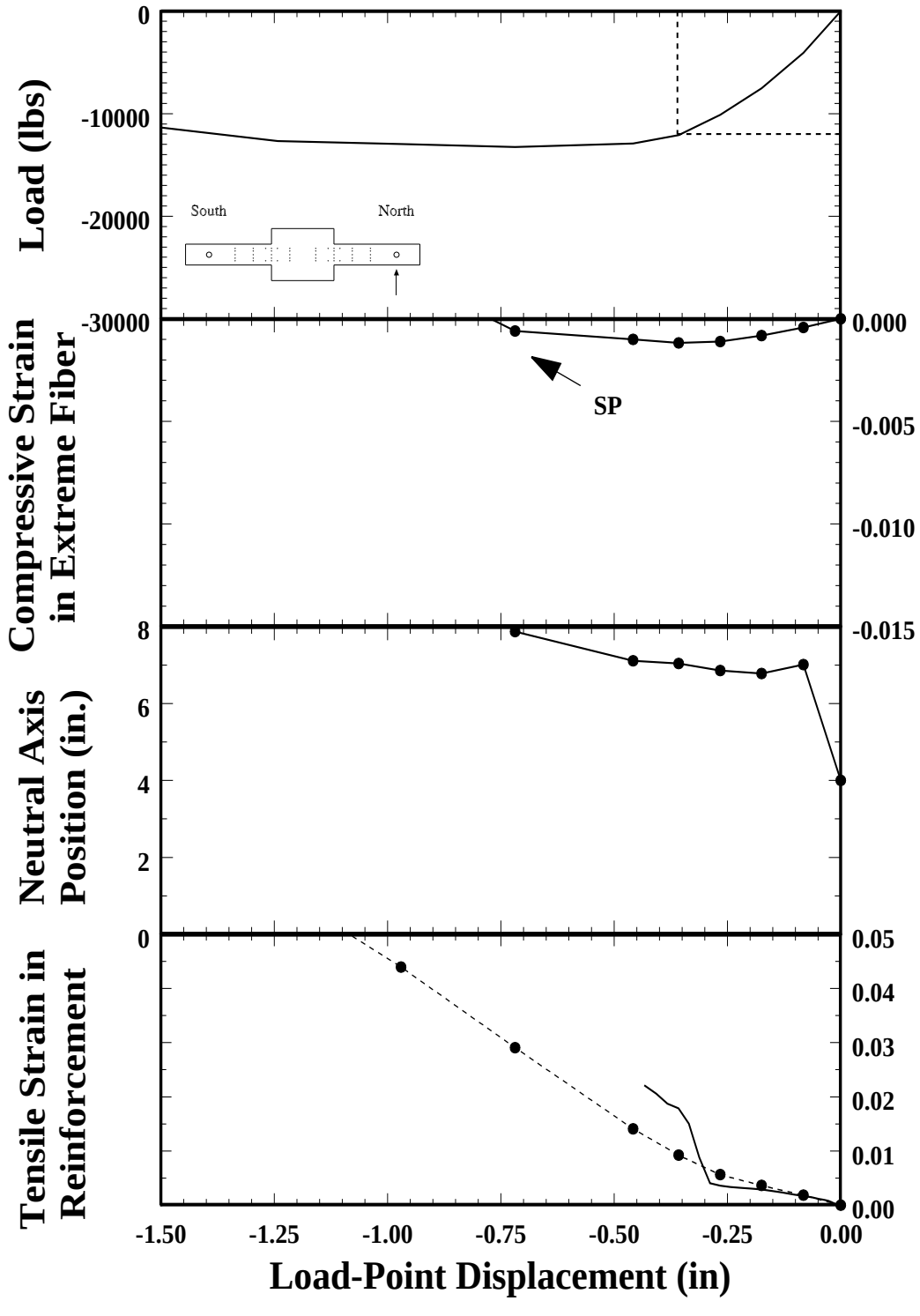

Figure 6.95. Envelope curves for the measured response of specimen C5-00, north member.

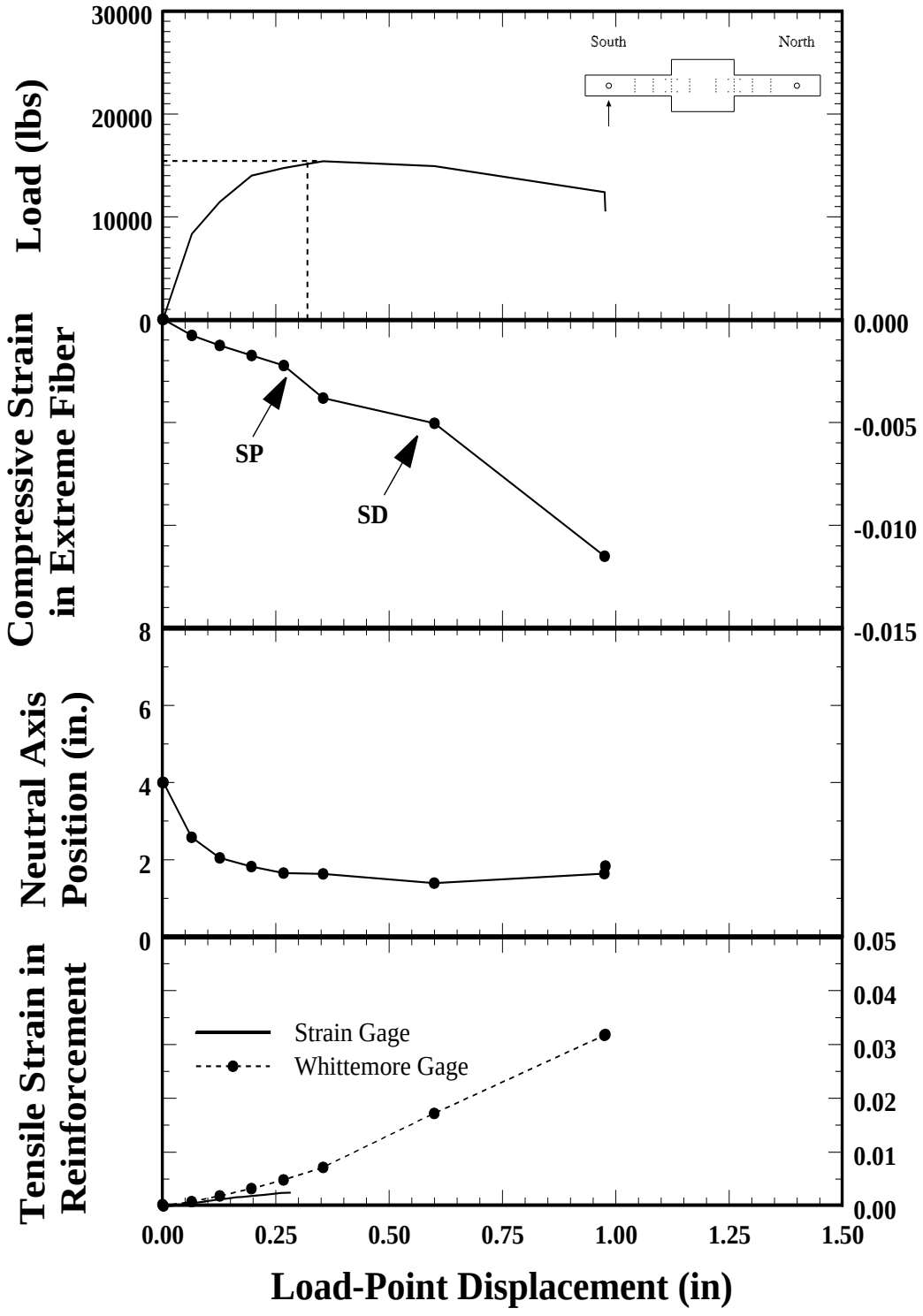

Figure 6.96. Envelope curves for the measured response of specimen C5-20, south member.

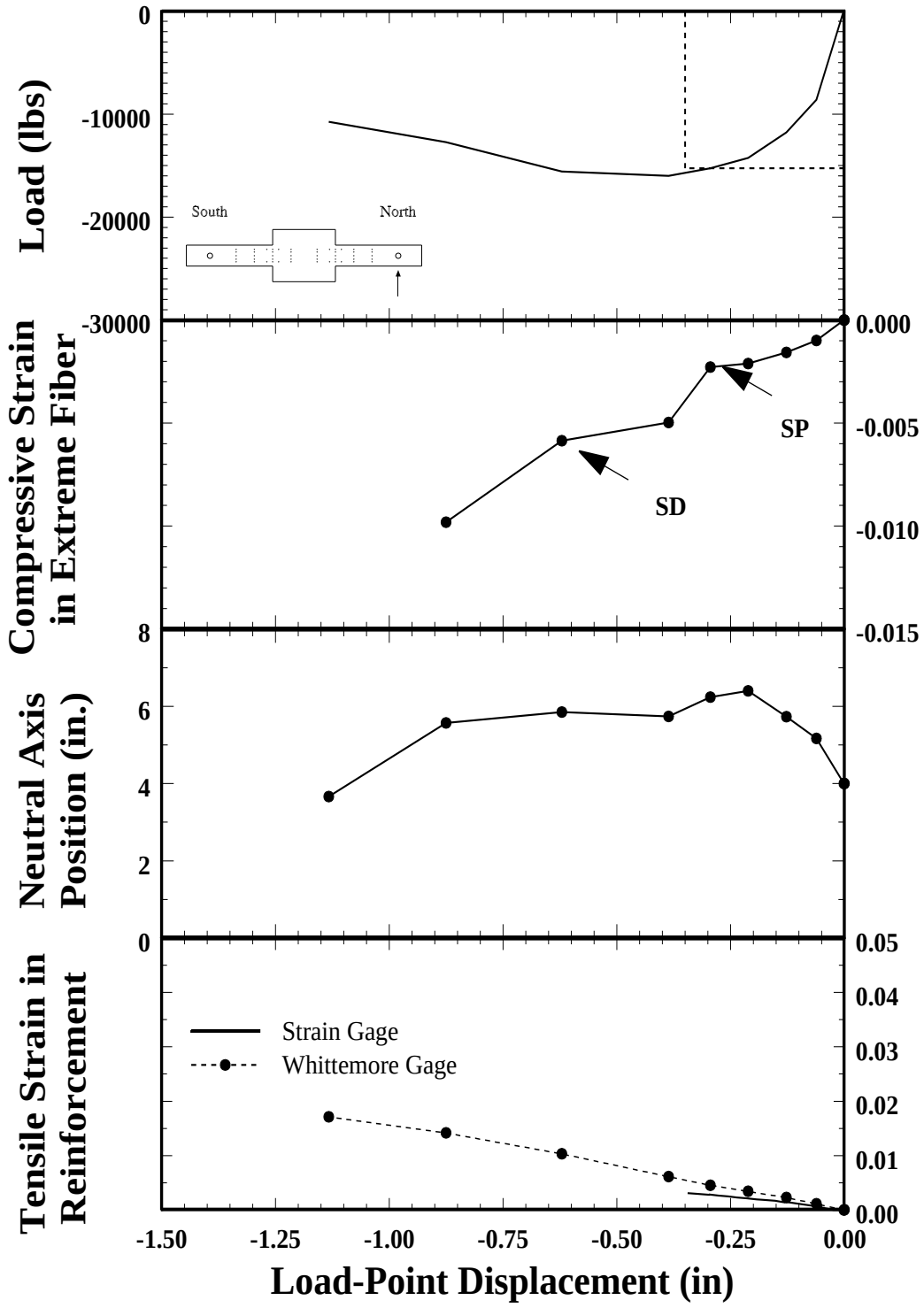

Figure 6.97. Envelope curves for the measured response of specimen C5-20, north member.

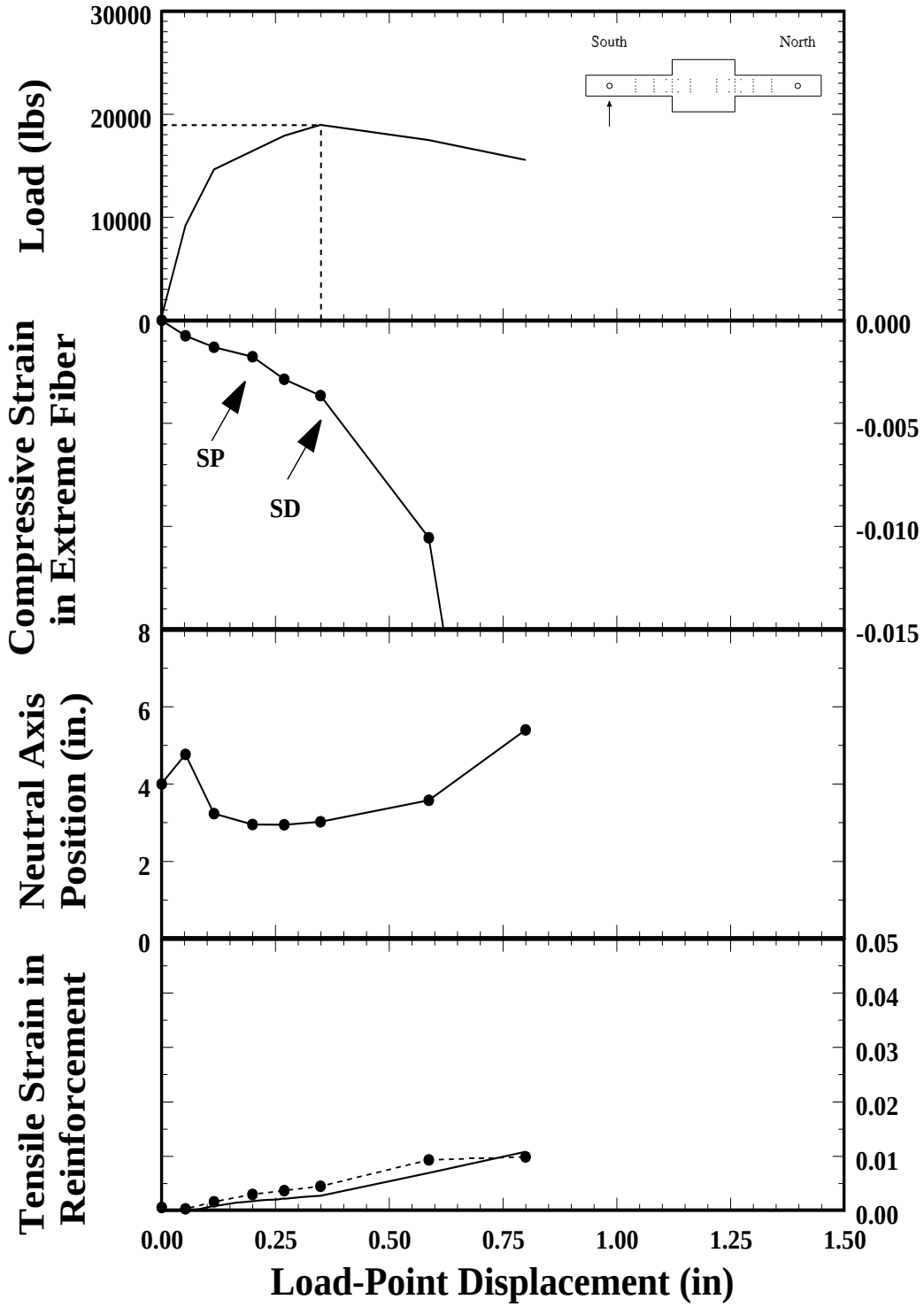

Figure 6.98. Envelope curves for the measured response of specimen C5-40, south member.

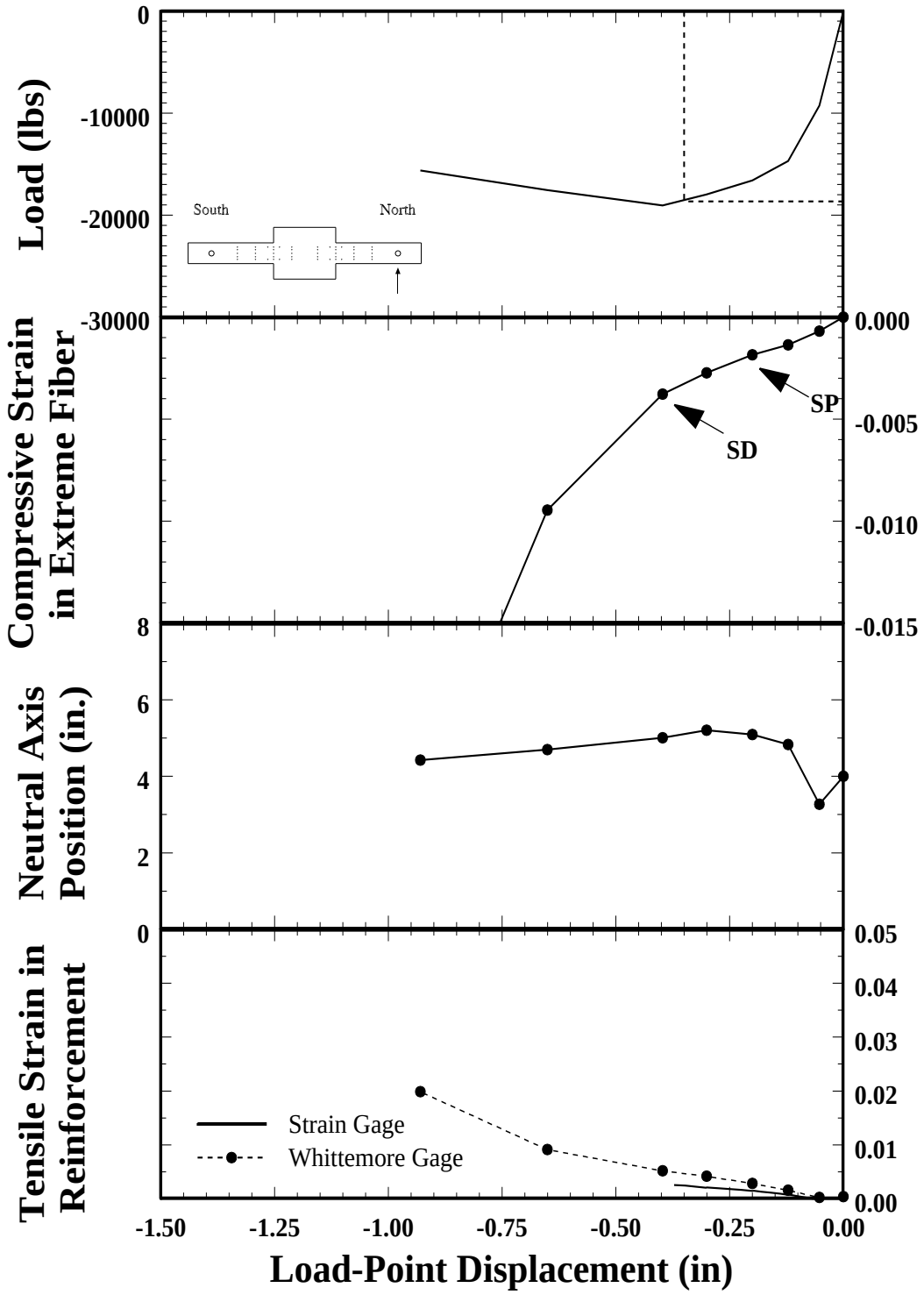

Figure 6.99. Envelope curves for the measured response of specimen C5-40, north member.

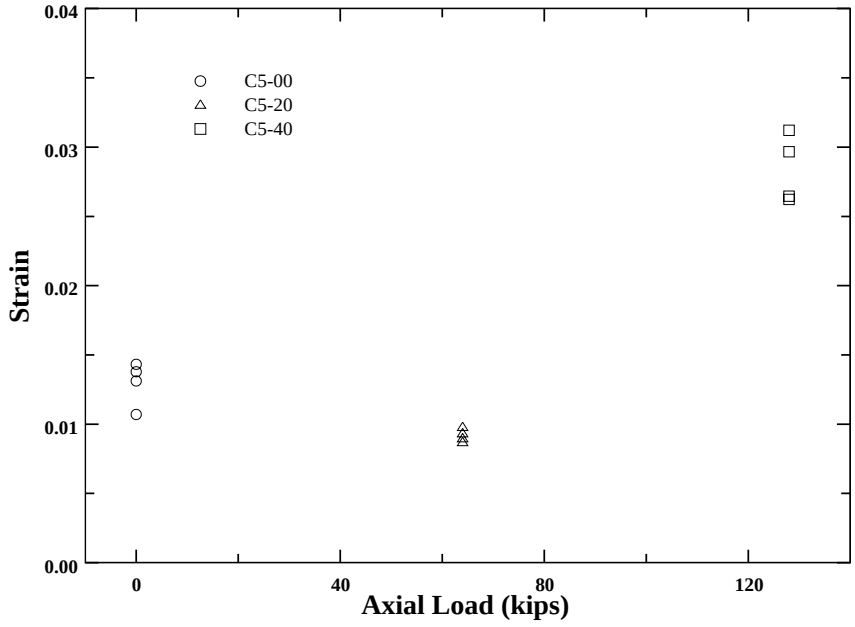

Figure 6.100. Calculated strain at the extreme compression fiber of the shell vs. axial load, for the inferred curvature at ultimate. Normal-strength specimens.

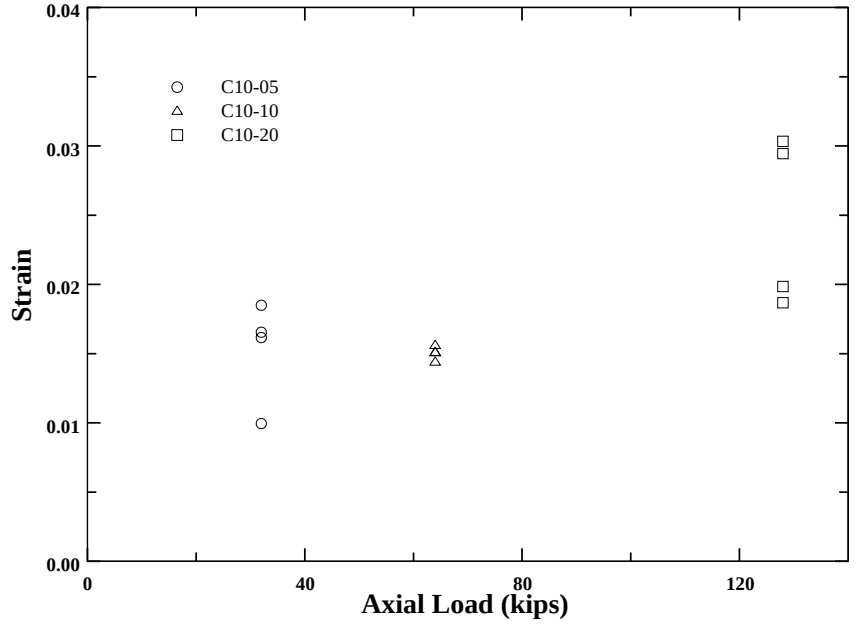

Figure 6.101. Calculated strain at the extreme compression fiber of the shell vs. axial load, for the inferred curvature at ultimate. High-strength specimens.

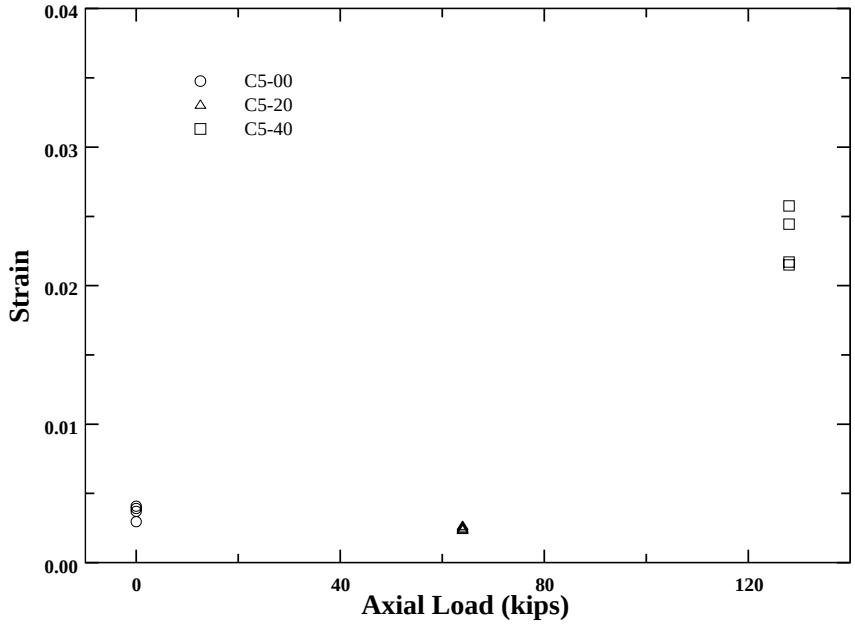

Figure 6.102. Calculated strain at the extreme compression fiber of the confined core vs. axial load, for the inferred curvature at ultimate. Normal-strength specimens.

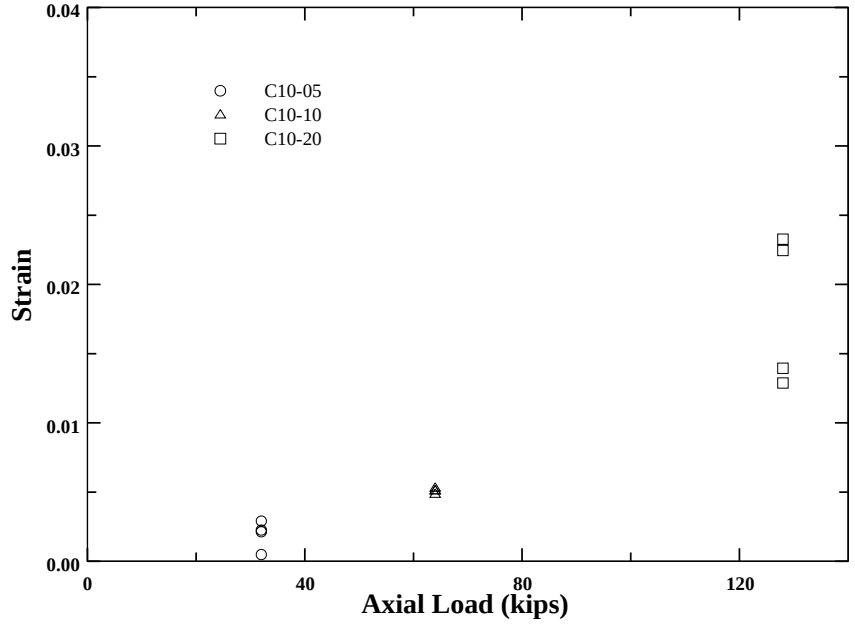

Figure 6.103. Calculated strain at the extreme compression fiber of the confined core vs. axial load, for the inferred curvature at ultimate. High-strength specimens.

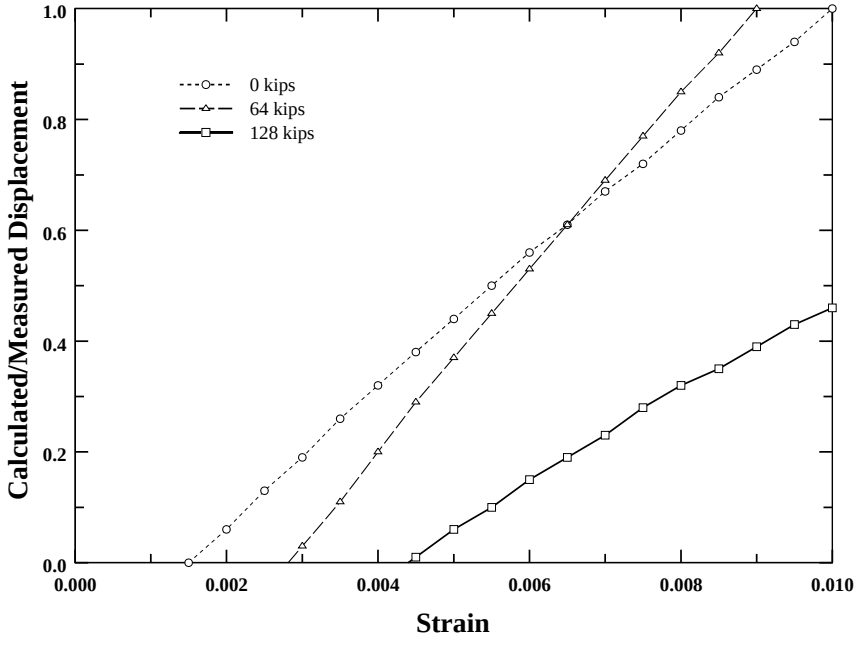

Figure 6.104. Ratio of calculated to measured displacement vs strain at the extreme compression fiber. Normal-strength specimens.

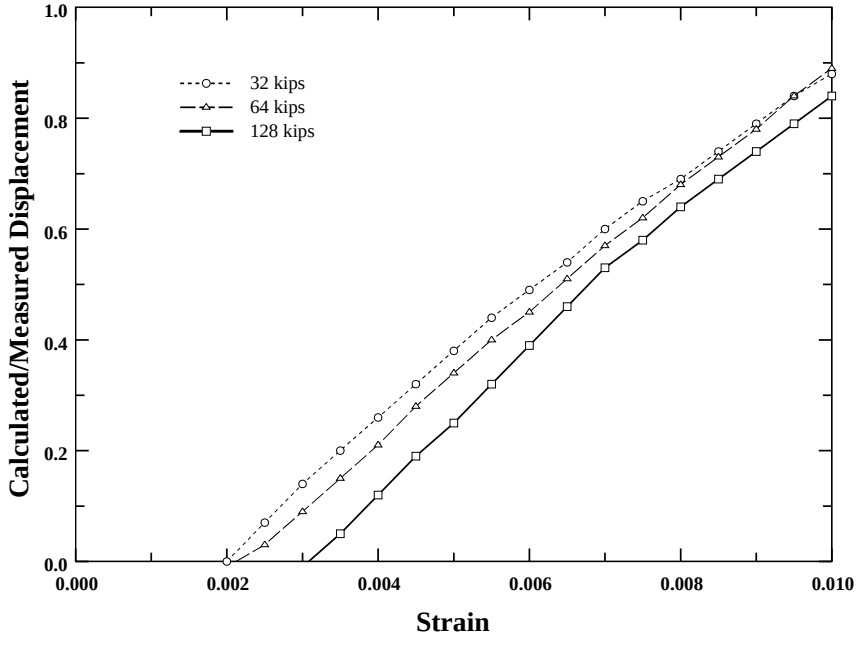

Figure 6.105. Ratio of calculated to measured displacement vs strain at the extreme compression fiber. High-strength specimens.

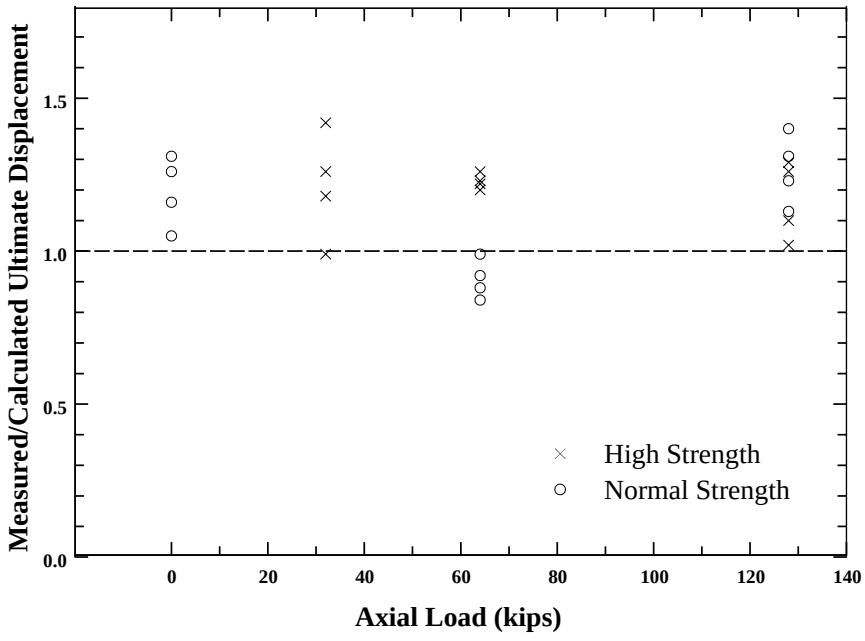

Figure 6.106. Ratio of measured to calculated limiting drift.

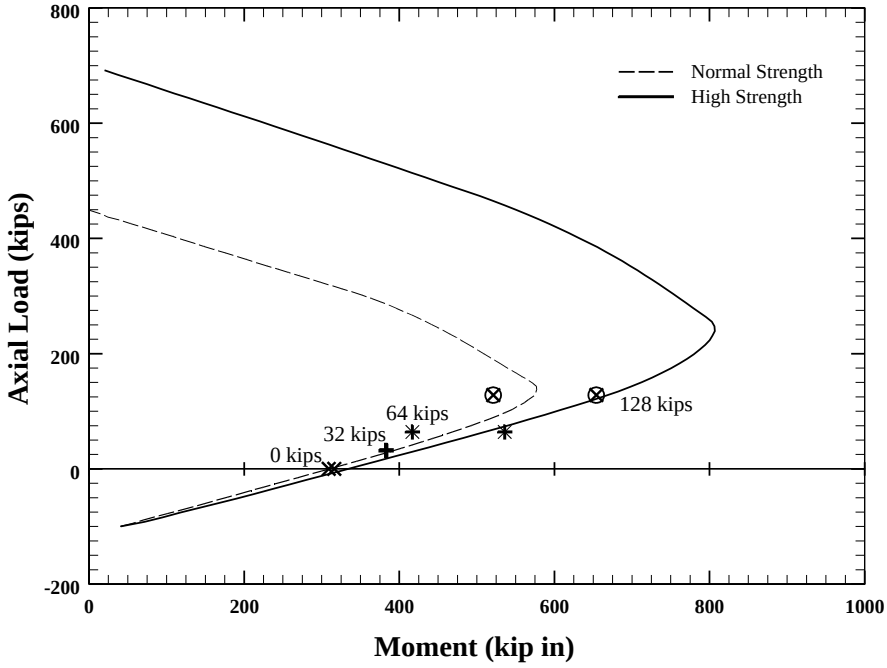

Figure 7.1. Calculated and measured moment-axial load relationships for specimens.

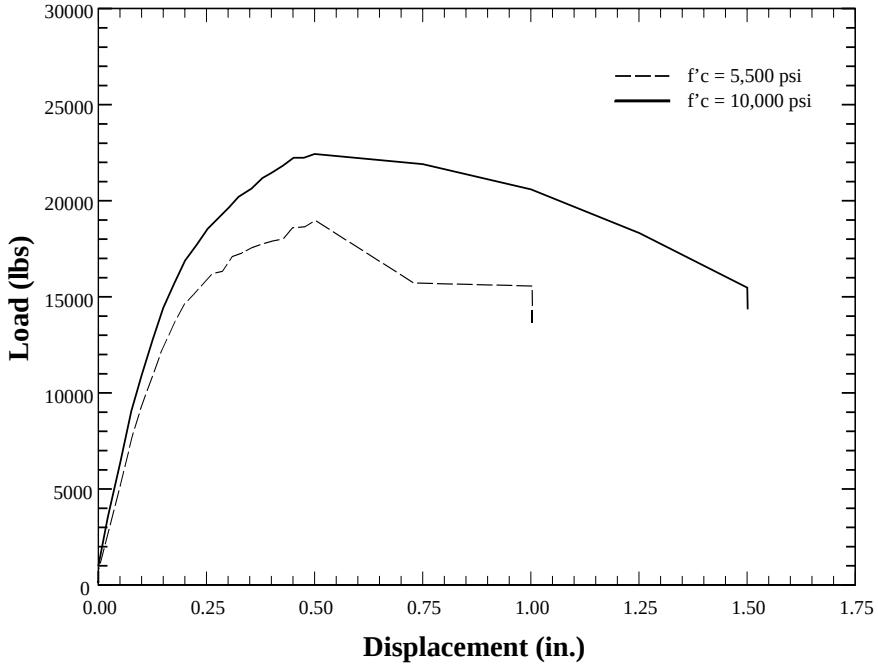

Figure 7.2. Measured load-displacement relationships for specimens C5-40 and C10-20.

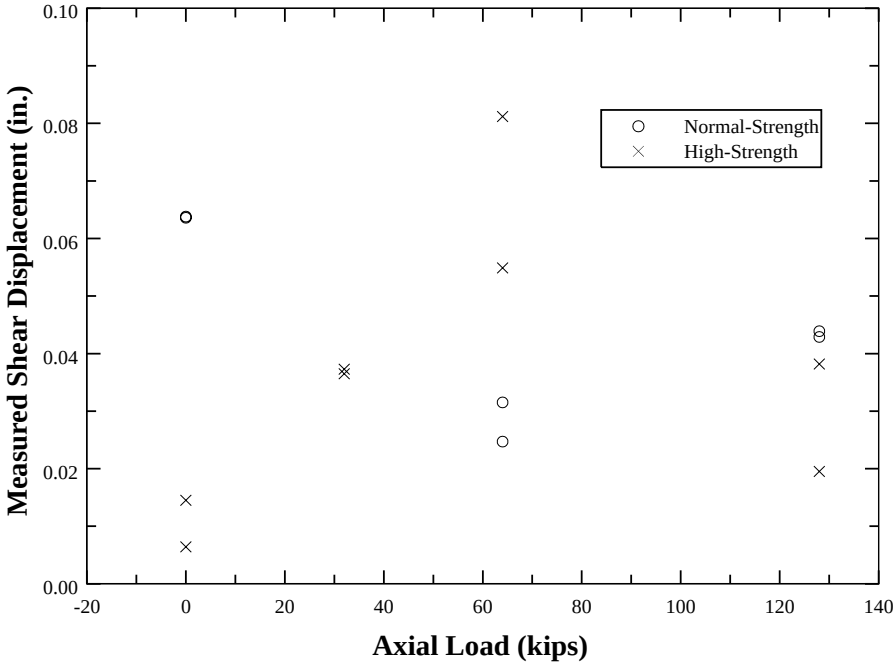

Figure 7.3. Measured shear displacement at yield vs axial load.

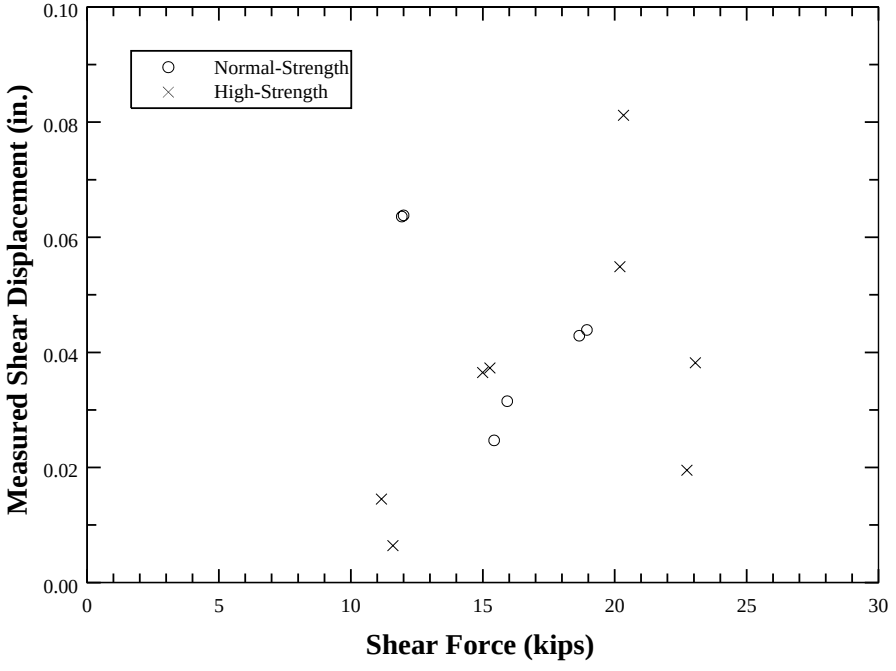

Figure 7.4. Measured shear displacement at yield vs shear force.

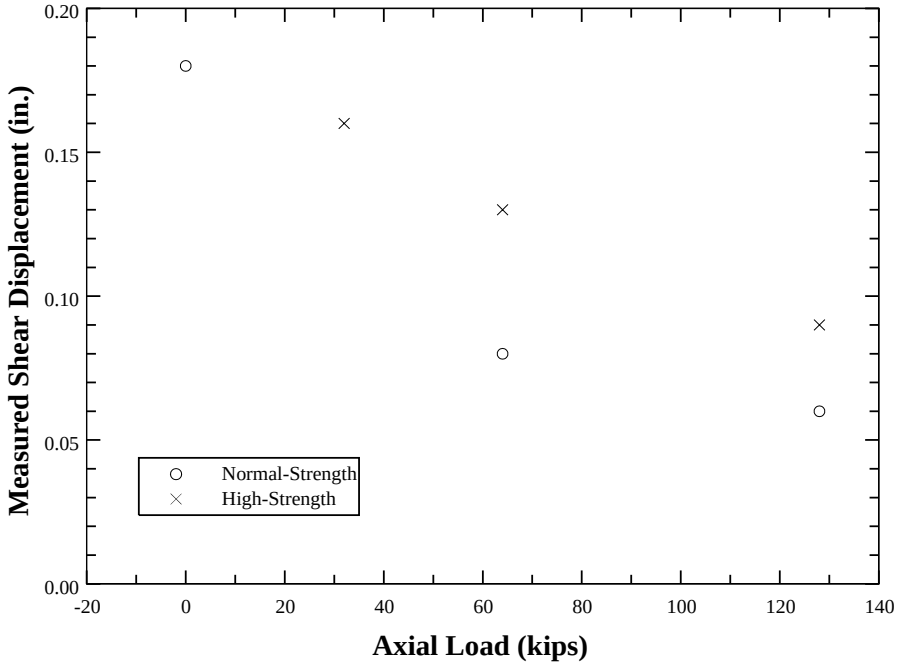

Figure 7.5. Measured shear displacement at ultimate vs axial load.

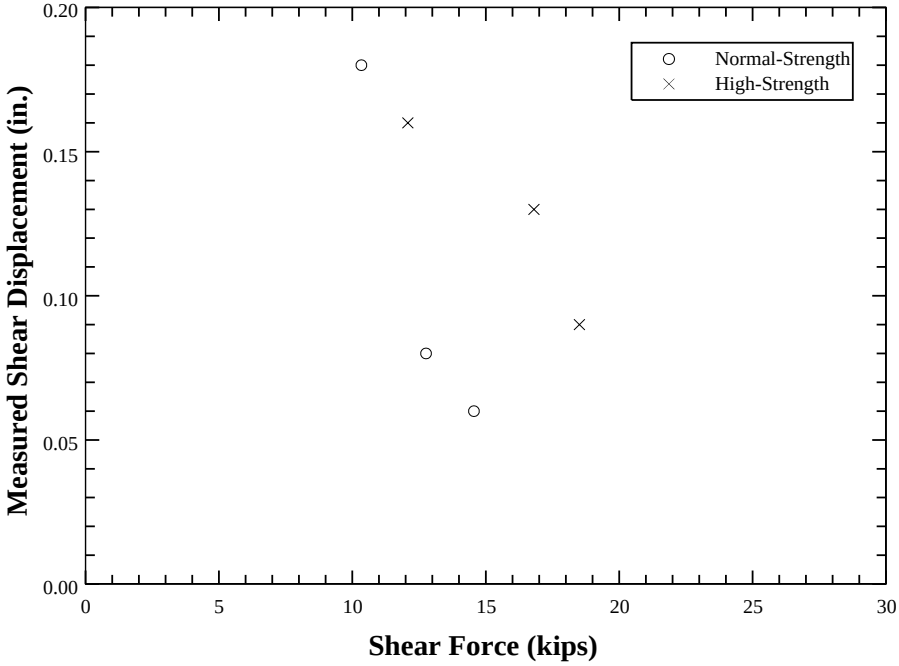

Figure 7.6. Measured shear displacement at ultimate vs shear force.

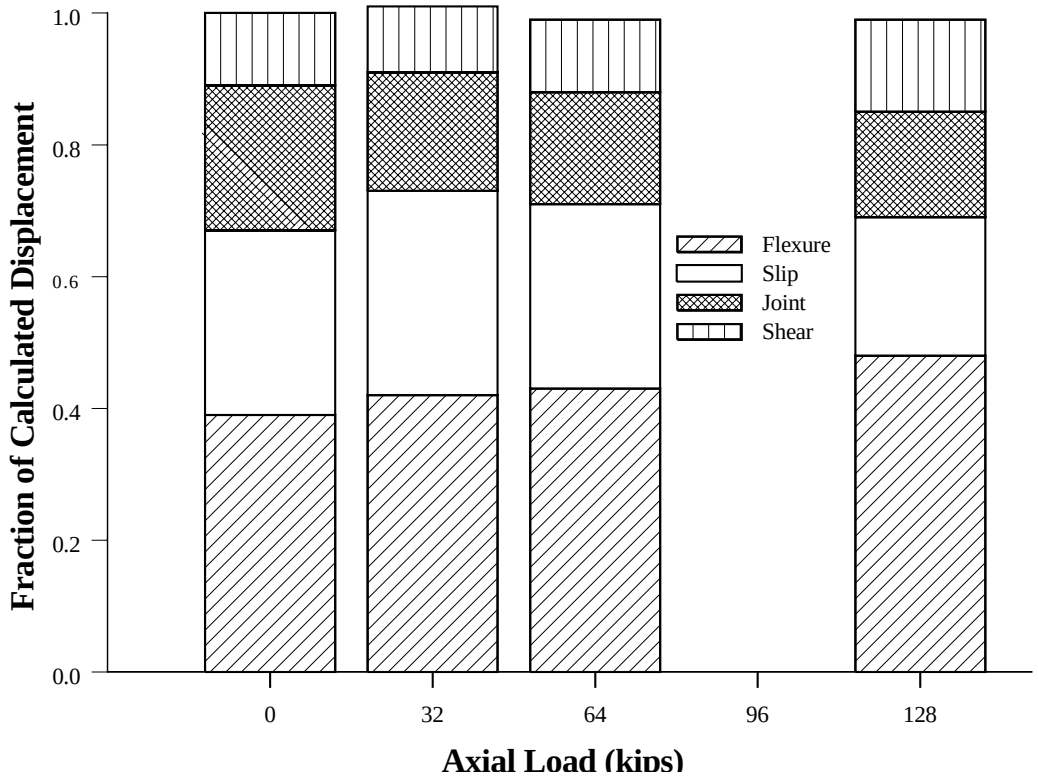

Figure 7.7. Components of the calculated yield displacement for normal-strength specimens.

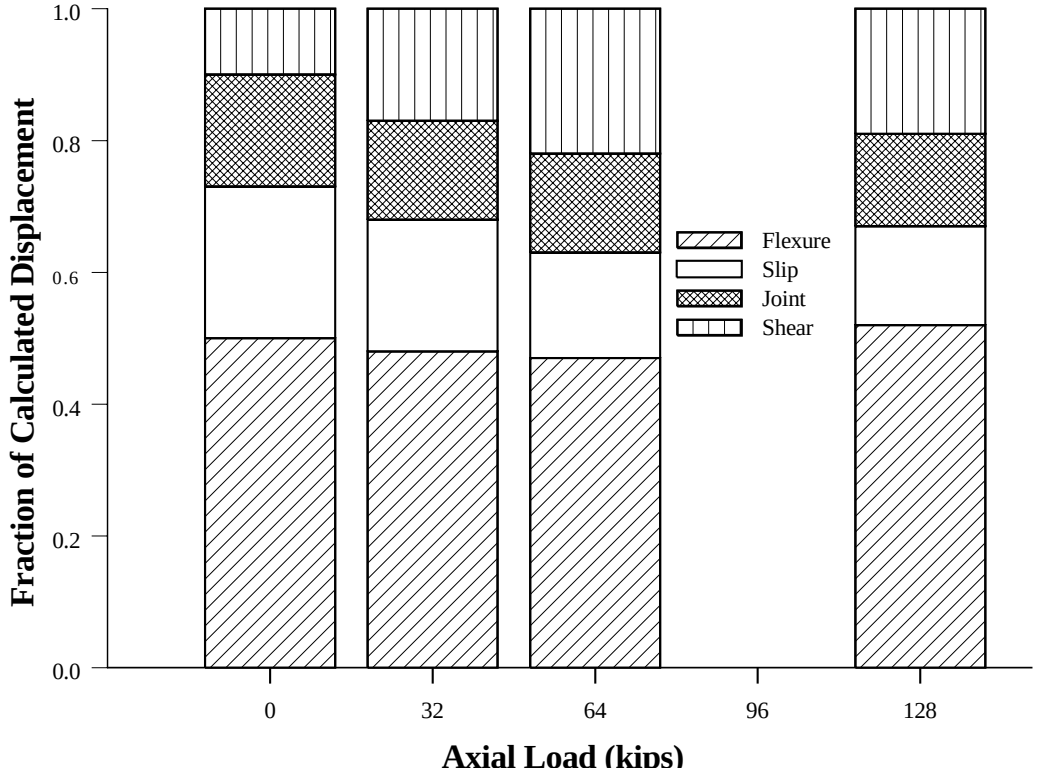

Figure 7.8. Components of the calculated yield displacement for high-strength specimens.

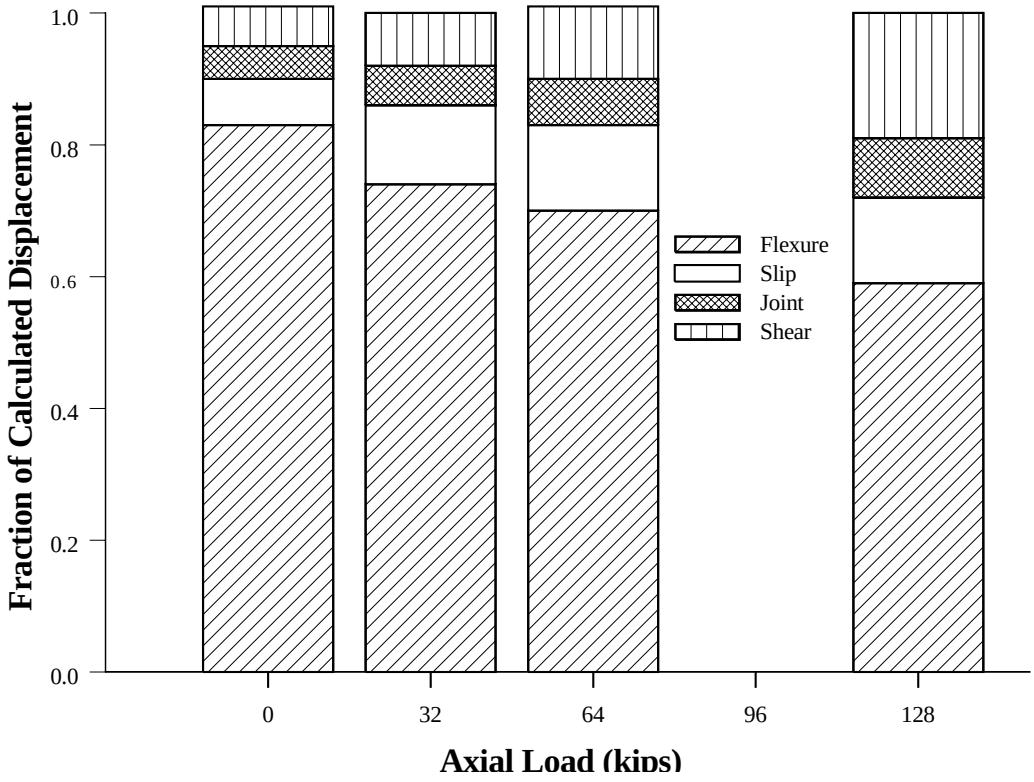

Figure 7.9. Components of the calculated limiting drift for normal-strength specimens.

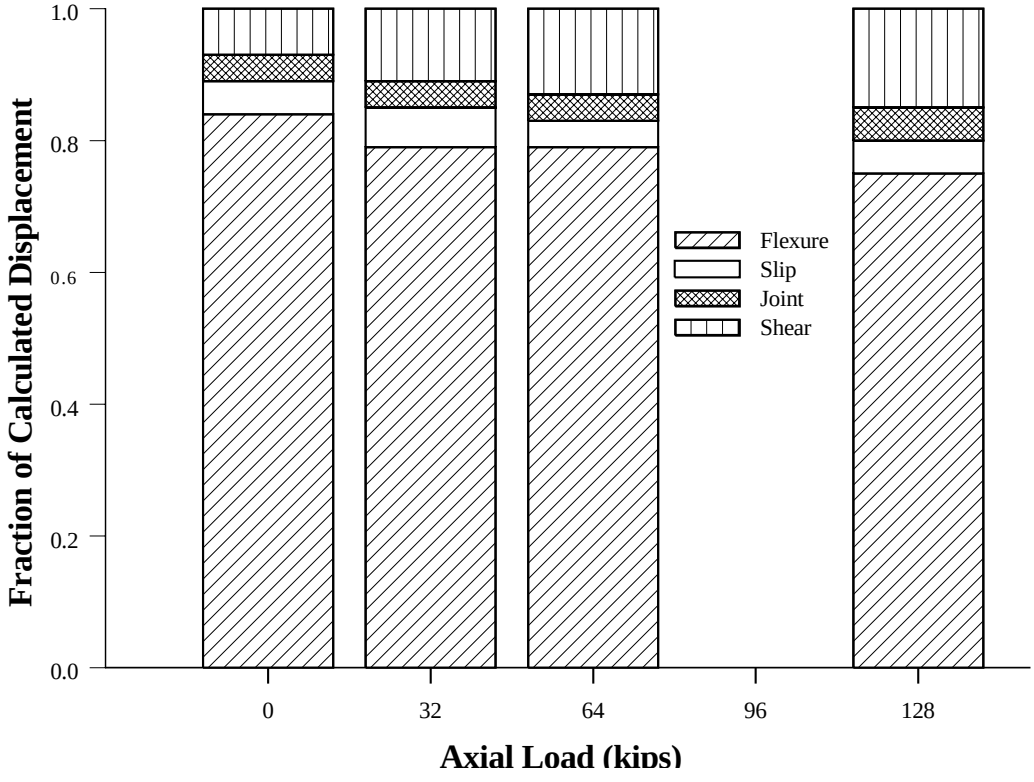

Figure 7.10. Components of the calculated limiting drift for high-strength specimens.

Appendix

Experimental Investigation

A. 1 Introduction

This Appendix includes information about the material properties, the test setup and the dimensions of the test specimens. It also describes the procedures followed during each test.

A. 2 Materials

A. 2. 1 Concrete

Concrete for the eight column specimens was obtained from Irving Materials Inc., a ready mix supplier from West Lafayette, Indiana. Specimens were cast in groups of two, resulting in four different batches. Designations for test specimens, steel samples and concrete mixes are summarized in Table A.1.

Concrete was cast using two mix designs. Batches 1 and 3 (Table A.2) were cast using the same proportions of Cement, Fly ash, sand, #12 gravel, water and Water Reducer. The mixes for batches 2 and 4 (Table A.2) also included an air entrainment agent. Batches # 1 and # 3 had a target strength of 10,000 psi. Batches # 2 and # 4 were used for control specimens with a target strength of 5000 psi. Proportions for both mixes are shown in Table A.2. Sand and No. 12 gravel came from the Vulcan Materials Plant in Battleground, Indiana, near the Wabash river.

Compressive strength of the concrete was measured by means of compressive tests of 4 by 8-in. cylinders, capped with neoprene pads. The variation of strength with time for each batch is presented in Figures A.1 through A.4. Typically, there was a noticeable increase in strength immediately after the moist-curing period ended.

Table A.3 shows a comparison between the average compressive strength of 4 x 8 in. and 6 x 12 in. cylinders. Data presented in Table A.3 is for three of the eight specimens and it indicates that average compressive strength was similar. Specimen C10-10 was tested at 42 days, while specimens C10-20 and C5-00 were tested at 177 and 123 days respectively. These results show that the ratio of 4 x 8 in. to 6 x 12 in. cylinder compressive strength decreased with time.

A special procedure was used to determine the initial Young's modulus for the concrete. A 6 x 12 in. cylinder was loaded initially to approximately 30% of its expected strength, with deformation readings taken after increments of 175 psi. Then the cylinder was unloaded and the same process repeated two more times.

The deformation readings were made using a mechanical concrete cylinder compressometer, model CT-170, from Elle International. It had a gage length of six in. The sensitivity of the dial was 0.0001 in. The device amplified the deformation along the axis of the cylinder by a factor of two. Young's modulus was calculated by performing linear regression on the measured unit stresses and strains. Reported values represent the mean of all measurements made. Individual standard deviations ranged from 7,000 to 168,000 psi.

Figures A.5 and A.6 show modulus of elasticity test results for specimens C5-40 (compressive strength of 5,000 psi) and C10-20 (compressive strength of 10,000 psi). Each graph shows unit stress vs unit strain for all three measurements, indicating that there was uniformity between readings.

Figure A.7 shows the variation of the modulus of elasticity with respect to average compressive strength. Also presented in the graph are expressions included in the ACI-318 Building Code (American Concrete Institute, 1995) and the ACI Committee 363 report on high-strength concrete (American Concrete Institute, Committee 363, 1984). Both expressions overestimated the measured modulus of elasticity for the 10,000 psi mixes.

Tensile strength was measured from flexure-beam tests. Dimensions for the flexure- beam specimens were 6 x 6 x 22 in. They were loaded at two points symmetrically located about the midspan, separated by 6 in. The bottom supports were 18 in. apart,

leaving an additional 2 in. on each end of the beam. Flexure-beam tests were carried out at a loading rate of 1,800 lb. per minute using a 120-kip Baldwin testing machine. The dial on the testing machine was set to the intermediate load range setting, with a sensitivity of 10 lbs.

Figure A.8 shows the variation of the modulus of rupture with compressive strength. The trend may be represented approximately by the expression 10 $\sqrt{f'c}$, with the exception of the result from specimen C10-10. Although they were tested at 42 days, flexure beams for specimen C10-10 had a modulus of rupture lower than all other specimens. Flexure beams from the same batch were tested again for specimen C10-20 at an age of 177 days, resulting in a higher modulus of rupture, which was consistent with measurements for batch 1. The mix design for batch 1 was the same as that used in specimens C10-20 and C10-20, with a target compressive strength of 10000 psi.

Table A.4 summarizes mean values for the concrete test results.

A.2.2 **Reinforcement**

Reinforcing cages were built using ASTM A615 grade 60 steel. The cages consisted of No. 5 bars for longitudinal reinforcement and No. 3 bars for stirrups. Samples from each size of bar (12 samples for No. 5 bars and 10 samples for No. 3 bars) were instrumented with a Measurements Group model CEA-06-125UN-350 strain gage and an MTS 634.25E-54 extensometer with a 2 in. gage length. Tensile tests were conducted on the instrumented samples using a 120-kip Baldwin test frame with a sensitivity of 100 lbs. Measured steel properties are summarized in Tables A.5 and A.6.

All No. 5 bars came from the same shipment. Random samples taken from different bars were designated SG1 and tested (Fig. A.9). For specimens 5 through 8 samples were taken from the bars that were actually used to build the specimens. These samples were designated SG3 (Fig. A.10) and SG4 (Fig. A.11). Tensile tests showed uniformity among the properties of No. 5 bar samples.

Bars of size No. 3 bars were bought in two different shipments. The first group of bars, designated SG1S (Fig. A.12), was used to build the hoops for specimens 1 through 4. A second shipment of bars, designated SG3S (Fig. A.13), was used in specimens 5 through

8. Samples were taken randomly from each group of bars and tested. As opposed to the No. 5 bars, measured material properties for No. 3 bars varied considerably.

A.3 Specimens

Test specimens were designed to simulate a beam-column connection, with the assumption that the point of contraflexure in the column was stationary.

Figure A.14 shows a schematic drawing of the idealized frame structure and the test specimen. In order to simplify the construction of the reaction frames, the specimens were tested horizontally.

Test specimens consisted of a joint with two columns spanning out of it in opposite directions. Dimensions of the joint were increased with the intent of minimizing deformations inside the joint area and anchorage problems. The motion of the joint was constrained by post-tensioning it to the test base, so that most deformation would occur in the columns.

Because of the large forces required to test high-strength concrete, specimens were constructed using a scale of approximately 2/3.

A.3.1 Dimensions

Overall specimen dimensions are presented in Figure A.15. The total distance between inflection points was 6 ft. The distance between each column face and inflection point was 2 ft., leaving the remaining 2 ft. for the joint. The columns were extended 9 in. beyond the inflection points to facilitate applying the axial load.

The columns had a square cross section, 8 by 8 in (Fig. A.15). The shear span to depth ratio was approximately 3.4.

Designations for as-built dimensions are shown in Figure A.16 and reported in tables A.7 to A.22.

A. 3. 2 **Reinforcement Details**

All specimens had similar reinforcing details. The longitudinal reinforcement consisted of 4 No. 5 bars for a reinforcement ratio ρ of 1.9%.

The amount and distribution of confining steel was the same for all tests. The transverse reinforcement ratio ρ_w was chosen to be 1% because it was deemed representative of current construction practice. This resulted in No. 3 stirrups at 3 in. Spacing.

Reinforcement details are presented in Figure A.17.

A. 3. 3 **Casting and Curing**

Specimens were cast into two sets of steel forms. Figures A.18, A 19 and A.20 show the metal forms assembled before casting. Figures A.21 and A.22 show a close up of the south joint for specimen 7, also before casting. Concrete from the delivery truck (Figure A.23) was deposited on wheelbarrows and vibrated into the forms (Figure A.24). Each batch consisted of two specimens, 4x8 in. cylinders, 6 x 12 in. cylinders and flexure beams as shown in Figure A.25.

Forms were stripped after one day and all pieces cast were covered with burlap and plastic and moist cured for two weeks (Figures A.28 and A.29). After the curing period, the specimens were kept in the laboratory until they were tested.

A. 4 **Test Procedure**

The load history was intended to induce deformations in the columns well into the nonlinear range, while providing the effect of cyclic loading typical of earthquakes. Drawings showing the test apparatus are presented in Figures A.31 and A.32.

A. 4. 1 **Loading Frame**

To simulate the effect of earthquake loading, specimens were loaded anti-symmetrically using two MTS 55-kip actuators. Each actuator was attached to a

reaction steel frame which was anchored to the strong floor of the laboratory (Figs A.31 and A.32).

Each specimens was aligned on top of a high-strength concrete pedestal and a layer of hydrostone was cast to fix them in place. The hydrostone mix was proportioned by volume, four parts of hydrostone to one part of water. Once the hydrostone set, the specimen was post-tensioned to the high-strength concrete base using four one-in. diameter high-strength steel bolts. The bolts were all-thread and had a nominal yield strength of 110 ksi. The concrete base was tied to the reaction frames with steel angles in order to prevent it from lifting (Figure A.32).

Axial load was applied by post-tensioning the specimens externally with four one-in. diameter high-strength Dwidag bars. The bars were grade 150 with a nominal area of 0.85 in. Tension on the bars was applied with four 70-kip center-hole rams, as shown in Figure A.33, and monitored individually with load cells. The load in the rams was controlled manually.

A.4.2 **Measurements**

One of the objectives of the tests was to study deformations that occur in columns subjected to lateral loading both before and after yield. In order to obtain data relevant to this objective it was essential to monitor both the deformations within the column and the absolute deflections of the elements with respect to a fixed reference point.

The lateral load-deflection history was monitored at four different points throughout the length of the column. The first point was located 5 in. from the center of the specimen (Fig. A.34) and it was intended to provide information about any rigid body motion. Displacements were also recorded at points located at distances d and 2d from the face of the column. The fourth and final control point for lateral deflections was located at the inflection point (Fig. A.34).

Deformations within the column were recorded in a predefined grid shown in Figure A.34. To capture the effect of deformations related to flexure and shear, it was necessary to record the horizontal, vertical and diagonal distances within the grid throughout the duration of the tests.

To provide additional information, deformations in the column were also recorded using electronic Whittermore gages, according to the pattern shown in Figure A.35.

The strain in the longitudinal bars (Fig. A.36) was recorded at several points inside the joint region trying to capture the effect of slip, although this is somewhat limited by the disturbances created by the attachment of the strain gages.

Strain in the transverse reinforcement near the joint region was also measured. These measurements were intended to provide insight as to the fraction of the total shear force carried by the transverse reinforcement at different levels of deformation throughout the load history.

A.4.3 **Instrumentation**

Three different types of physical quantities were measured throughout the series of tests: strain, displacement, and force.

Displacements within grid points were recorded by means of linear variable-differential transformers (LVDT's) manufactured by Schaevitz, with ranges varying from ±0.25 in. to ±0.50 in. They were fixed to the specimen with anchor bolts attached to the reinforcing cage before casting (Figs. A.21, A.22 and A.26). Instruments with ranges up to ±5.00 in. were used to measure the lateral displacement histories.

On the opposite face of the column a grid was laid out using metal contact points glued with epoxy cement to the concrete surface, as indicated in Figures A.30 and A.35. The distance between points was measured using electronic Whittemore gages which were designed and built for this series of tests. Three different instruments were built for gage lengths of 4.75, 7.0 and 8.5 in. The main components in these instruments were an external metal case fabricated with aluminum tubing, a frictionless sliding table and a displacement transducer (Fig. A.36). The range of the displacement transducer was ±0.25 in.

The reinforcing cage was instrumented with ¼-in. strain gages from Measurements Group Inc., model CEA-06-125UN-350 (Fig. A.36), rated for a maximum strain of 5%. Bars were prepared by first grinding off deformations to provide a smooth surface, and then dry abrading using 220-grit paper. A conditioner was applied (mild phosphoric acid

compound) to wet the bar, which was again abraded using 400-grit paper. Final preparation consisted of cleaning the surface using a conditioner and neutralizer.

Strain gages were attached to the bars using epoxy cements M-Bond 200 or AE-10 (Measurements Group Inc., 1979) and coated with wax to protect them against moisture. A second coating with a two part polysulfide liquid polymer compound (Measurements Group Inc., MCoat-J) was applied for added protection against moisture and mechanical protection during casting. Strain gages attached with M-Bond AE-10 were cured at normal room temperature for a period of two days, during which pressure was applied using clamps.

Lateral loads were obtained using 55-kip MTS 661.22C-01 load cells mounted on the MTS series 244 actuator assemblies. Axial loads on the post-tensioning bars were measured with 50-kip hollow load cells that were fabricated at the University of Illinois, Urbana (Fig. A.32).

A.4.4 Test Procedure

At the beginning of each test the following procedure was observed:

1) Align the specimen on top of the high-strength pedestal and cast a layer of hydrostone to fix it in place.

2) Post-tension the specimen to pedestal using high-strength all-thread bolts.

3) Take initial deformation and strain readings to map undeformed configuration.

4) Apply axial loads with center-hole rams.

5) Take deformation, strain and load readings.

6) Attach both actuators to the inflection points of the specimen using a pin connector.

7) Take deformation, strain and load readings.

Once the lateral loading was started, deformation, load and strain readings were taken after increments of approximately 0.025 in. For each increment, lateral loading was stopped and the axial load adjusted before scanning all instruments.

Every four increments the test was stopped to map deformations in the specimen with electronic Whittemore gages. The first cycle was intended to deform the specimen up to yield. During this first loading cycle a larger number of Whittemore readings were taken to provide greater detail about the strain distribution near the joint.

Given the spacing between readings, the first cycle resulted in approximately 80 sets of scans and 20 deformation maps taken with the electronic Whittemore gages. For subsequent cycles to larger displacements the spacing between scans was maintained resulting in an increased number of readings per cycle.

In order to limit the duration of the test, the number of Whittemore deformation maps was kept similar for all cycles. This implied larger deformations between each map as the maximum displacement of the cycles increased.

At points of maximum deflection the test was stopped to mark cracks and take photographs. Typically, the duration of each cycle varied between 6 and 8 hours when Whittemore readings were taken.

Near the end of the tests, deformations became so large that the electronic Whittemore gages went out of range. On other occasions, in specimens with higher axial loads, the anchor points were lost when the shell was crushed. Whenever either condition appeared, electronic Whittemore gage readings were stopped and the test continued while scanning only the remaining sensors.

Table A.1

Materials

Specimen	Designation	Concrete Batch	Target Strength	Axial Load	Steel-Sample Group Designation	
			psi	Kips	No. 3	No. 5
1	C10-00	1	10,000	0	SG1S	SG1
3	C10-05	1	10,000	32	SG1S	SG1
5	C10-10	3	10,000	64	SG3S	SG4
8	C10-20	3	10,000	128	SG3S	SG4
7	C5-00	4	5,000	0	SG3S	SG3
2	C5-10	2	5,000	32	SG1S	SG1
4	C5-20	2	5,000	64	SG1S	SG1
6	C5-40	4	5,000	128	SG3S	SG3

Table A.2

Mix Proportions

Proportions	Units	Batch 1	Batch 2	Batch 3	Batch 4
Target Strength	psi	10,000	5,000	10,000	5,000
Cement	lb.	752	658	752	658
Fly Ash	lb.	150	0	150	0
Sand	lb.	1,100	1,300	1,100	1,300
#12 Gravel	lb.	1,700	1,700	1,700	1,700
Water	lb.	288	208	288	208
HRWR	oz	162	100	162	100
Air	%	0	5	0	5
$\frac{\text{Water}}{\text{Cementitious Materials}}$	ratio	0.32	0.32	0.32	0.32

Quantities given are per cubic yard of concrete.

Table A.3

Compressive Strength of 4 x 8 in. and 6 x 12 in. Cylinders

Specimen	Mean Compressive Strength (psi)		Ratio
	4 x 8 in. Cylinders	6 x 12 in. Cylinders	$\frac{\text{4 x 8 in. Strength}}{\text{6 x 12 in. Strength}}$
C10-10	9,830	9,650	1.02
C10-20	9,500	9,930	0.96
C5-00	5,500	5,990	0.92

Table A.4

Measured Concrete Properties

Specimen	Batch	Days	Slump	Compressive Strength	Tensile Strength	Modulus of Elasticity
			in	psi	psi	psi
C10-00	1	343	$3\text{-}^{1}/_{2}$	10,000	1,010	4.3×10^{6}
C10-05	1	450	$3\text{-}^{1}/_{2}$	10,100	990	4.5×10^{6}
C10-10	3	42	$3\text{-}^{7}/_{8}$	9,830	540	4.9×10^{6}
C10-20	3	177	$3\text{-}^{7}/_{8}$	9,500	925	5.2×10^{6}
C5-00	4	123	6	5,500	780	3.5×10^{6}
C5-10	2	300	$1\text{-}^{1}/_{4}$	6,900	1,050	4.7×10^{6}
C5-20	2	379	$1\text{-}^{1}/_{4}$	7,000	995	4.6×10^{6}
C5-40	4	102	6	5,520	830	3.5×10^{6}

Table A.5

Steel Properties, Specimens 1 through 4

Reinforcing Bar Size	Designation for Samples	Used in Specimens	Coupon	σ_y ksi	ε_{sh}	σ_u ksi
3	SG1S	1 to 4	1	62	0.002	103
3	SG1S	1 to 4	2	58	0.002	89
3	SG1S	1 to 4	3	58	0.002	90
3	SG1S	1 to 4	4	58	0.002	89
5	SG1	1 to 4	1	85	0.016	108
5	SG1	1 to 4	2	85	0.015	107
5	SG1	1 to 4	3	85	0.016	107
5	SG1	1 to 4	4	85	0.019	107

Table A.6

Steel Properties, Specimens 5 through 8

Reinforcing Bar Size	Designation for Samples	Used in Specimens	Coupon	σ_y ksi	ε_{sh}	σ_u ksi
3	SG3S	3 & 4	1	69	0.014	107
3	SG3S	3 & 4	2	70	0.002	113
3	SG3S	3 & 4	3	77	0.008	119
3	SG3S	3 & 4	4	73	0.009	111
3	SG3S	3 & 4	5	73	0.006	110
3	SG3S	3 & 4	6	75	0.009	101
5	SG3	4	1	83	0.015	106
5	SG3	4	2	83	0.016	106
5	SG3	4	3	83	0.014	105
5	SG3	4	4	83	0.016	106
5	SG4	3	1	83	0.016	106
5	SG4	3	2	83	0.015	106
5	SG4	3	3	83	0.016	106
5	SG4	3	4	83	0.016	106

Table A.7

As Built Dimensions for Specimen C5-00

Cross Section Dimensions (in.)				
Position	THh	BHh	EVh	WVh
N2	8	8-1/16	7-15/16	7-15/16
N3	8	8-1/16	8	7-15/16
S2	8-1/16	8	7-7/8	7-15/16
S3	8	8	7-15/16	8
Bar Spacing (in.)				
	THd	BHd	EVd	WVd
N1	4-7/8	4-11/16	5-7/16	5-3/8
N2	4-7/8	4-5/8	5-7/16	5-1/2
N3	4-7/8	4-5/8	5-1/2	5-9/16
S1	4-7/8	4-13/16	5-5/8	5-1/2
S2	4-5/8	4-13/16	5-5/8	5-1/2
S3	4-5/8	4-7/8	5-5/8	5-5/8

Table A.8

Cover Dimensions for Specimen C5-00

Top Cover (in.)				
Position	EVtc	EHtc	WVtc	WHtc
N1	1-1/4	1-5/16	1-1/8	1-1/4
N2	1-1/8	1-3/8	15/16	1-1/8
N3	1-1/8	1-1/2	15/16	1
S1	1	1-7/16	1	1-1/8
S2	1	1-1/2	15/16	1-5/16
S3	1	1-1/2	7/8	1-1/4
Bottom Cover (in.)				
	EVbc	EHbc	WVbc	WHbc
N1	3/4	1-7/16	15/16	1-3/16
N2	3/4	1-1/2	7/8	1-5/16
N3	3/4	1-1/2	7/8	1-5/16
S1	3/4	1-5/8	13/16	1-1/4
S2	5/8	1-3/4	7/8	1-1/4
S3	11/16	1-3/4	7/8	1-1/4

Table A.9

As Built Dimensions for Specimen C5-10

Cross Section Dimensions (in.)				
Position	THh	BHh	EVh	WVh
N2	8	8	7-7/8	8
N3	8	8	7-15/16	7-15/16
S2	8	8	8	7-15/16
S3	8	8-1/16	8	8-1/16
Bar Spacing (in.)				
	THd	BHd	EVd	WVd
N1	3-7/8	3-3/8	3-7/8	4
N2	3-7/8	3-1/2	4	4
N3	3-7/8	3-1/2	4-1/8	3-15/16
S1	3-1/2	3-1/4	3-7/8	4-3/16
S2	3-1/2	3-3/8	4	4-3/16
S3	3-1/2	3-7/16	4-1/16	4-3/8

Table A.10

Cover Dimensions for Specimen C5-10

Top Cover (in.)				
Position	EVtc	EHtc	WVtc	WHtc
N1	1-3/4	2	1-5/8	1-1/2
N2	1-5/8	2-1/8	1-5/8	1-3/8
N3	1-9/16	2-1/4	1-5/8	1-1/4
S1	2-1/8	1-7/8	1-3/4	2
S2	2-1/8	1-3/4	1-3/4	2-1/8
S3	2-1/16	1-3/4	1-3/4	2-1/8
Bottom Cover (in.)				
	EVbc	EHbc	WVbc	WHbc
N1	1-5/8	2-1/8	1-3/4	1-7/8
N2	1-5/8	2-1/8	1-3/4	1-3/4
N3	1-5/8	2-3/16	1-3/4	1-11/16
S1	1-3/8	2-1/4	1-3/8	1-7/8
S2	1-1/4	2-1/8	1-3/8	1-7/8
S3	1-1/4	2-1/8	1-5/16	1-7/8

Table A.11

As Built Dimensions for Specimen C5-20

Cross Section Dimensions (in.)				
Position	THh	BHh	EVh	WVh
N2	8	7-7/8	8	8-1/16
N3	8-1/8	8	8	8-1/8
S2	7-15/16	8	8-1/16	8-1/16
S3	8	8	8-1/8	8-1/8
Bar Spacing (in.)				
	THd	BHd	EVd	WVd
N1	3-1/2	3-7/8	4-1/8	3-15/16
N2	3-1/2	3-13/16	4-1/8	4
N3	3-1/2	3-7/8	4-1/16	4-1/16
S1	3-5/16	3-7/8	4-1/8	3-7/8
S2	3-5/16	3-3/4	4-1/16	3-15/16
S3	3-1/4	3-3/4	4-1/8	4-1/16

Table A.12

Cover Dimensions for Specimen C5-20

Top Cover (in.)				
Position	EVtc	EHtc	WVtc	WHtc
N1	1-3/4	1-7/8	1-3/4	2-1/8
N2	1-3/4	1-7/8	1-9/16	2-3/16
N3	1-3/4	1-3/4	1-9/16	2-1/4
S1	1-7/8	2-1/8	2	1-7/8
S2	1-7/8	2-1/8	2	1-7/8
S3	1-7/8	2-1/4	1-15/16	1-7/8
Bottom Cover (in.)				
	EVbc	EHbc	WVbc	WHbc
N1	1-1/2	2	1-3/4	1-1/2
N2	1-1/2	1-15/16	1-7/8	1-1/2
N3	1-9/16	2	1-7/8	1-1/2
S1	1-1/2	2-1/16	1-9/16	1-7/16
S2	1-1/2	2-1/16	1-1/2	1-9/16
S3	1-1/2	2-1/16	1-1/2	1-9/16

Table A.13

As Built Dimensions for Specimen C5-40

Cross Section Dimensions (in.)				
Position	THh	BHh	EVh	WVh
N2	8	8-1/16	8-1/8	8-1/16
N3	8-1/16	8-1/16	8-1/8	8-1/16
S2	8	8	7-15/16	8
S3	8-1/8	8	8	8-1/16
Bar Spacing (in.)				
	THd	BHd	EVd	WVd
N1	4-13/16	5-1/4	5-3/8	5-1/4
N2	4-13/16	5-1/4	5-3/8	5-1/4
N3	4-13/16	5-1/4	5-3/8	5-1/4
S1	4-7/8	5-1/8	5-5/16	5-1/8
S2	4-7/8	5-1/8	5-5/16	5-1/8
S3	5	5-1/8	5-1/4	5-1/4

Table A.14

Cover Dimensions for Specimen C5-40

Top Cover (in.)				
Position	EVtc	EHtc	WVtc	WHtc
N1	1-1/4	1-7/16	1-1/8	1-1/8
N2	1-1/4	1-7/16	1-3/16	1-1/8
N3	1-1/4	1-1/2	1-3/16	1-1/8
S1	1-1/4	1-1/4	1-3/16	1-1/4
S2	1-1/4	1-1/4	1-3/16	1-1/4
S3	1-1/4	1-1/4	1-3/16	1-1/4
Bottom Cover (in.)				
	EVbc	EHbc	WVbc	WHbc
N1	7/8	1-3/8	1	3/4
N2	7/8	1-7/16	1	3/4
N3	7/8	1-7/16	1	3/4
S1	3/4	1-3/8	1-1/16	15/16
S2	3/4	1-5/16	1-1/16	15/16
S3	15/16	1-5/16	1	15/16

Table A.15

As Built Dimensions for Specimen C10-00

Cross Section Dimensions (in.)				
Position	THh	BHh	EVh	WVh
N2	7-15/16	8	7-13/16	7-15/16
N3	7-7/8	8	7-7/8	8
S2	7-15/16	8	7-7/8	7-7/8
S3	8	8	8	8
Bar Spacing (in.)				
	THd	BHd	EVd	WVd
N1	3-3/8	3-3/4	4-1/8	3-13/16
N2	3-3/8	3-3/4	4-1/8	3-13/16
N3	3-3/8	3-3/4	4-3/16	4
S1	3-3/16	3-9/16	4-1/8	4-1/16
S2	3-1/8	3-7/16	4-1/8	4-1/16
S3	3-3/16	3-3/8	4-3/16	4-5/16

Table A.16

Cover Dimensions for Specimen C10-00

Top Cover (in.)				
Position	EVtc	EHtc	WVtc	WHtc
N1	1-13/16	2-1/8	1-3/4	1-7/8
N2	1-5/8	2-1/8	1-3/4	1-13/16
N3	1-9/16	2-1/8	1-3/4	1-3/4
S1	1-11/16	2-3/16	1-11/16	2
S2	1-11/16	2-3/16	1-11/16	2
S3	1-3/4	2-1/8	1-9/16	2-1/16
Bottom Cover (in.)				
	EVbc	EHbc	WVbc	WHbc
N1	1-7/16	2-1/8	1-3/4	1-1/2
N2	1-7/16	2-1/8	1-3/4	1-1/2
N3	1-1/2	2-1/8	1-5/8	1-1/2
S1	1-7/16	2-1/16	1-1/2	1-3/4
S2	1-7/16	2-1/16	1-1/2	1-7/8
S3	1-7/16	2-1/16	1-1/2	2-15/16

Table A.17

As Built Dimensions for Specimen C10-05

Cross Section Dimensions (in.)				
Position	THh	BHh	EVh	WVh
N2	8	7-7/8	8	8
N3	8-1/16	7-15/16	8	8
S2	8	8	8-1/16	8
S3	8	8	8-1/8	8
Bar Spacing (in.)				
	THd	BHd	EVd	WVd
N1	3-3/8	3-1/2	4	4-1/8
N2	3-5/16	3-1/2	4	4-1/8
N3	3-3/8	3-9/16	4	4-1/8
S1	3-1/2	3-1/2	3-7/8	4-1/16
S2	3-1/2	3-1/2	3-15/16	4-1/16
S3	3-1/2	3-1/2	4	4

Table A.18

Cover Dimensions for Specimen C10-05

Top Cover (in.)				
Position	EVtc	EHtc	WVtc	WHtc
N1	1-5/8	1-7/8	1-5/8	2-1/8
N2	1-7/8	1-7/8	1-3/4	2-3/16
N3	1-7/8	1-7/8	1-3/4	2-3/16
S1	2	1-3/8	1-13/16	2-1/2
S2	2	1-3/8	1-13/16	2-1/2
S3	2	1-3/8	1-7/8	2-1/2
Bottom Cover (in.)				
	EVbc	EHbc	WVbc	WHbc
N1	1-3/4	2-1/8	1-5/8	1-5/8
N2	1-1/2	2-1/8	1-1/2	1-5/8
N3	1-1/2	2-1/8	1-1/2	1-5/8
S1	1-1/2	1-3/4	1-1/2	2-1/8
S2	1-1/2	1-3/4	1-1/2	2-1/8
S3	1-1/2	1-3/4	1-1/2	2-1/8

Table A.19

As Built Dimensions for Specimen C10-10

Cross Section Dimensions (in.)				
Position	THh	BHh	EVh	WVh
N2	8-1/16	8	8-1/16	8-1/16
N3	8-1/16	8	8	8
S2	7-15/16	8	8	8
S3	8	8	8-1/16	8-1/16
Bar Spacing (in.)				
	THd	BHd	EVd	WVd
N1	4-1/2	4-3/4	5-5/16	5-1/4
N2	4-1/2	4-3/4	5-5/16	5-5/16
N3	4-1/2	4-3/4	5-5/16	5-1/4
S1	4-9/16	4-7/8	5-3/8	5-3/16
S2	4-9/16	4-7/8	5-5/16	5-3/16
S3	4-5/8	4-7/8	5-5/16	5-1/4

Table A.20

Cover Dimensions for Specimen C10-10

Top Cover (in.)				
Position	EVtc	EHtc	WVtc	WHtc
N1	7/8	1-11/16	1-1/8	1-1/4
N2	7/8	1-11/16	1-1/8	1-1/4
N3	13/16	1-13/16	1-1/8	1-1/8
S1	15/16	1-3/8	1-1/16	1-3/8
S2	1	1-3/8	1-1/16	1-3/8
S3	1	1-3/8	1-1/16	1-3/8
Bottom Cover (in.)				
	EVbc	EHbc	WVbc	WHbc
N1	1-1/4	1-1/8	1-1/16	1-1/2
N2	1-1/4	1-1/8	1	1-1/2
N3	1-1/4	1-1/8	1	1-1/2
S1	1	1-1/4	1-1/8	1-1/4
S2	1-1/16	1-1/4	1-1/8	1-1/4
S3	1-1/8	1-1/4	1-1/8	1-1/4

Table A.21

As Built Dimensions for Specimen C10-20

Cross Section Dimensions (in.)				
Position	THh	BHh	EVh	WVh
N2	8	8-1/16	8	8
N3	8	8-1/16	7-15/16	8
S2	8-1/16	8	7-7/8	7-15/16
S3	8	8	7-7/8	8
Bar Spacing (in.)				
	THd	BHd	EVd	WVd
N1	4-13/16	5-1/16	5-5/16	5-1/2
N2	4-3/4	5-1/8	5-5/16	5-1/2
N3	4-5/8	5-1/8	5-3/8	5-1/2
S1	4-7/8	4-5/8	5-3/8	5-1/2
S2	4-13/16	4-5/8	5-1/4	5-1/2
S3	4-3/4	4-11/16	5-1/4	5-1/2

Table A.22

Cover Dimensions for Specimen C10-20

Top Cover (in.)				
Position	EVtc	EHtc	WVtc	WHtc
N1	1	1-5/16	1	1-1/4
N2	1	1-3/8	1	1-1/4
N3	1	1-1/2	1	1-1/4
S1	1	1-3/8	1-1/16	1-3/16
S2	1	1-3/8	1-1/16	1-1/4
S3	1	1-3/8	1-1/8	1-1/4
Bottom Cover (in.)				
	EVbc	EHbc	WVbc	WHbc
N1	1	1-1/4	13/16	1-1/16
N2	1-1/16	1-1/4	7/8	1-1/16
N3	15/16	1-1/4	7/8	1-1/16
S1	7/8	1-1/4	3/4	1-1/2
S2	1	1-1/4	3/4	1-1/2
S3	1	1-3/16	3/4	1-1/2

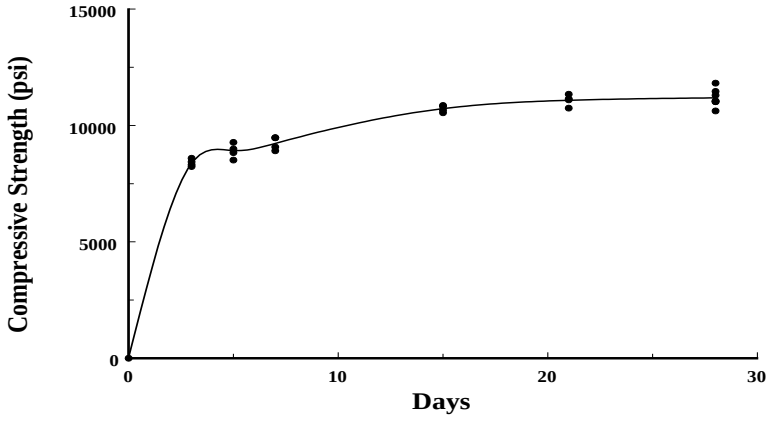

Figure A.1. Variation of mean compressive strength with time for batch 1.

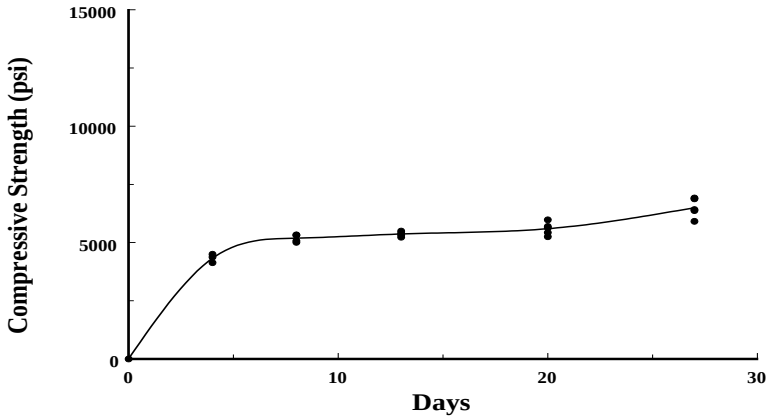

Figure A.2. Variation of mean compressive strength with time for batch 2.

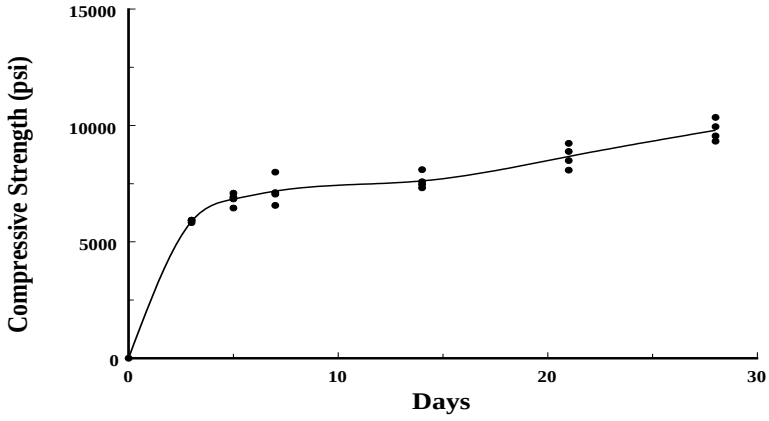

Figure A.3. Variation of mean compressive strength with time for batch 3.

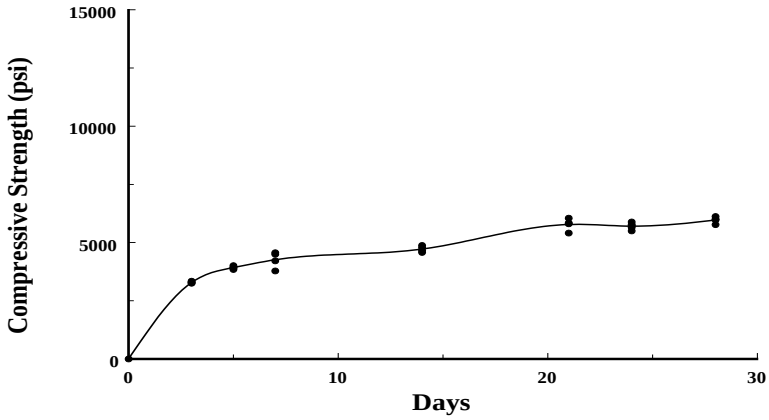

Figure A.4. Variation of mean compressive strength with time for batch 4.

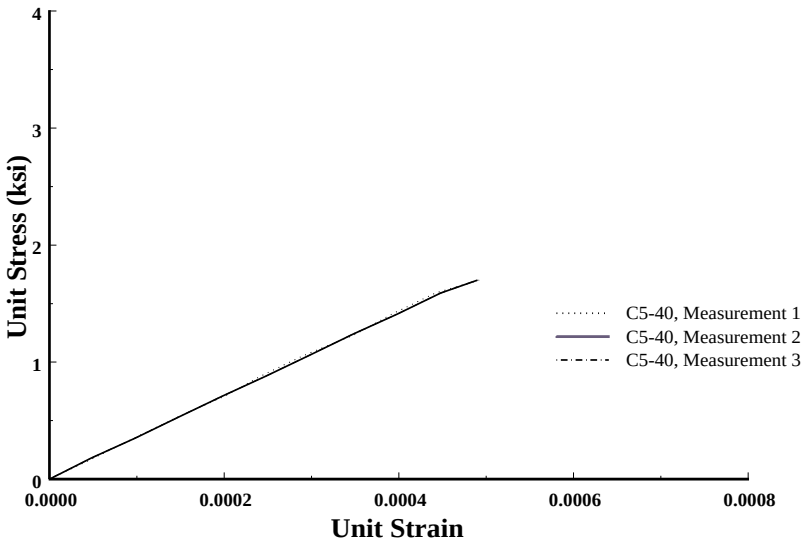

Figure A.5. Unit stress vs unit strain for modulus of elasticity tests, specimen 6.

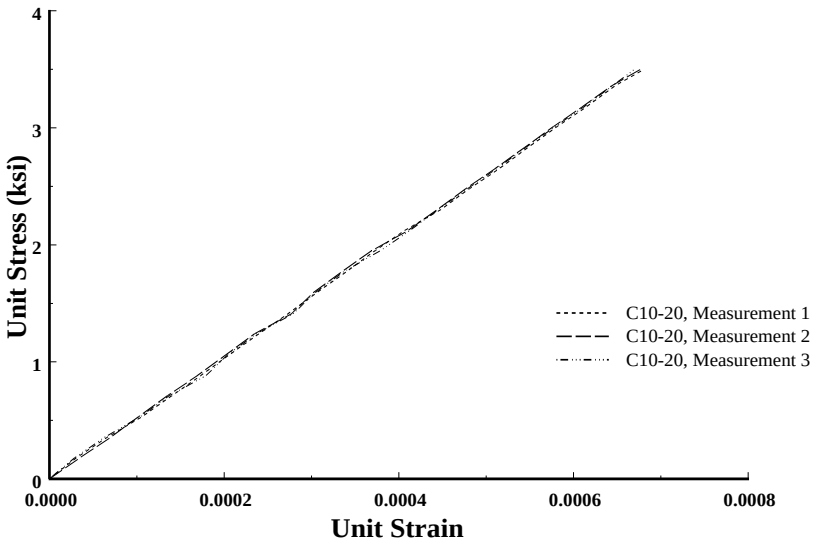

Figure A.6. Unit stress vs unit strain for modulus of elasticity tests, specimen 8.

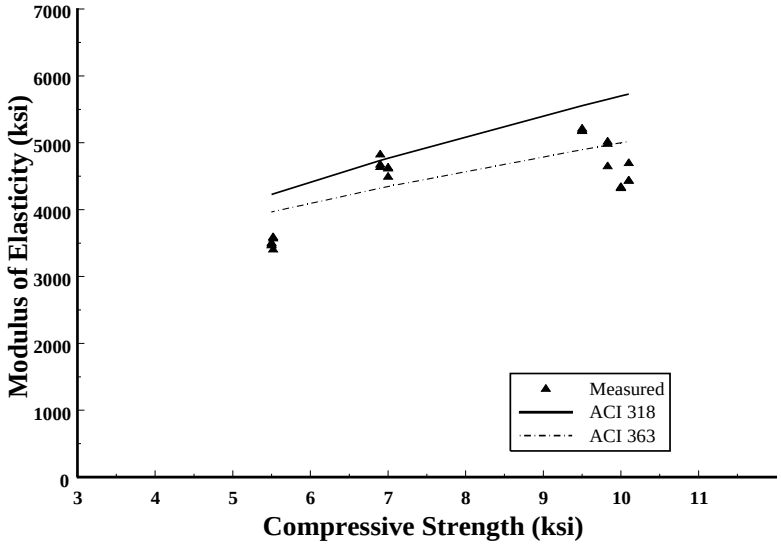

Figure A.7. Variation of modulus of elasticity with respect to mean compressive strength for all specimens.

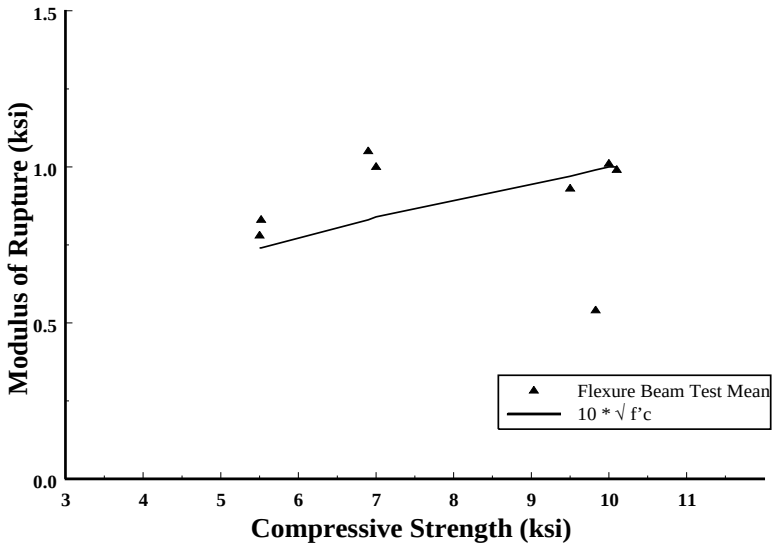

Figure A.8. Variation of modulus of rupture with respect to mean compressive strength for all specimens.

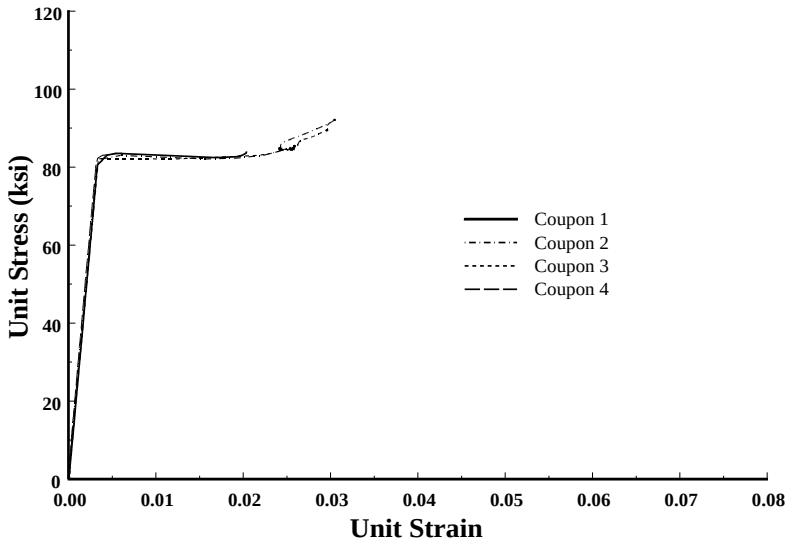

Figure A.9. Unit stress-unit strain relationship for steel samples SG1.

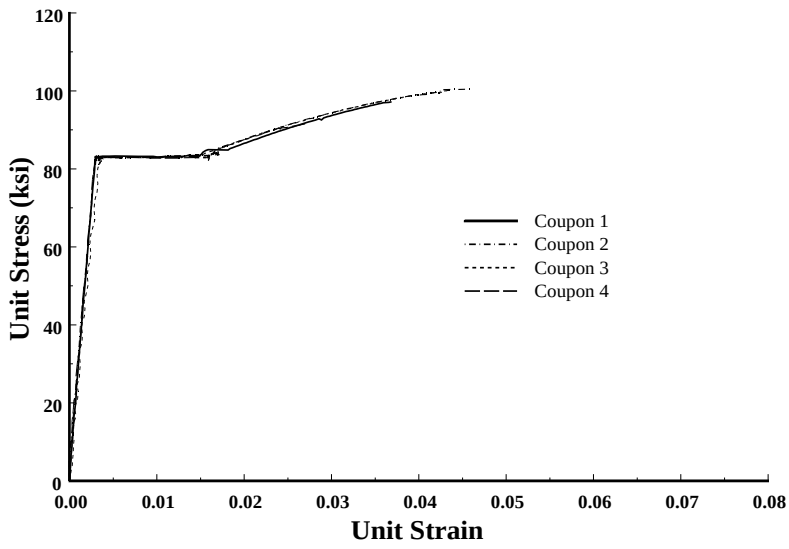

Figure A.10. Unit stress-unit strain relationship for steel samples SG3.

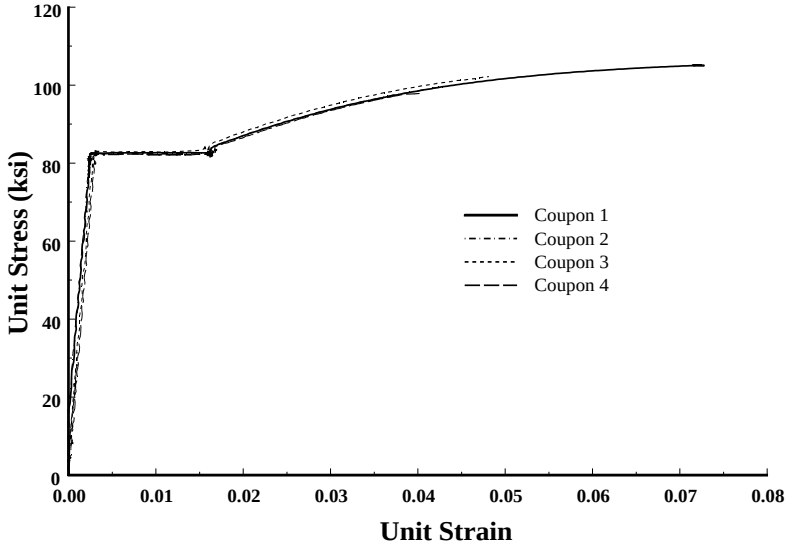

Figure A.11. Unit stress-unit strain relationship for samples SG4.

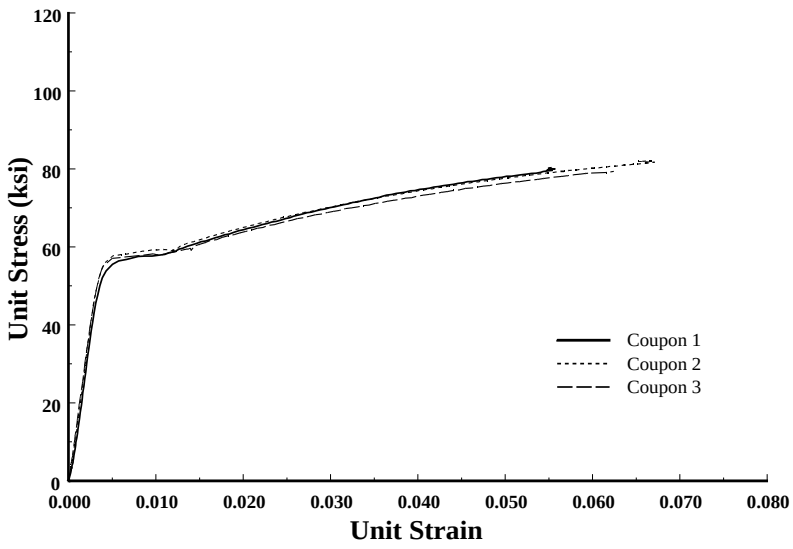

Figure A.12. Unit stress-unit strain relationship for samples SG1S.

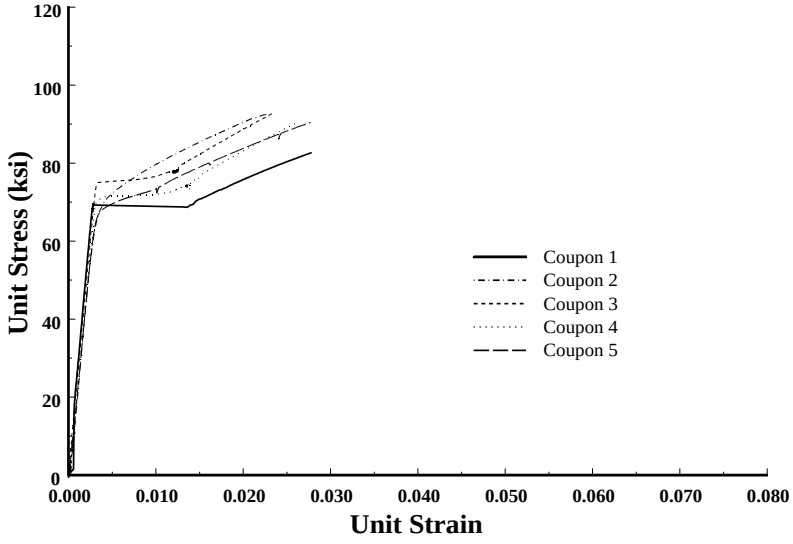

Figure A.13. Unit stress-unit strain relationship for samples SG3S.

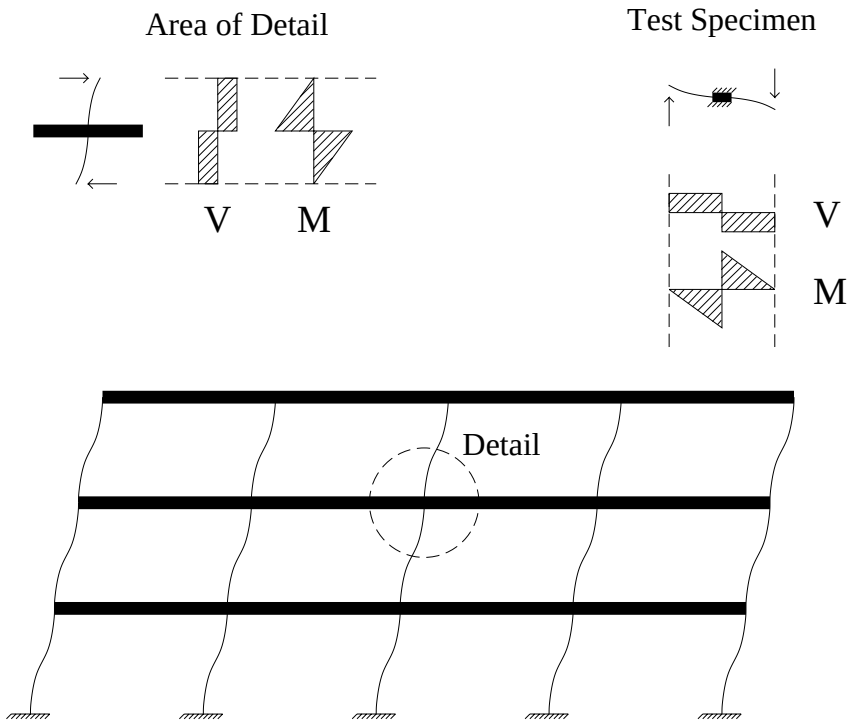

Figure A.14. Idealized moment resisting frame and test specimen.

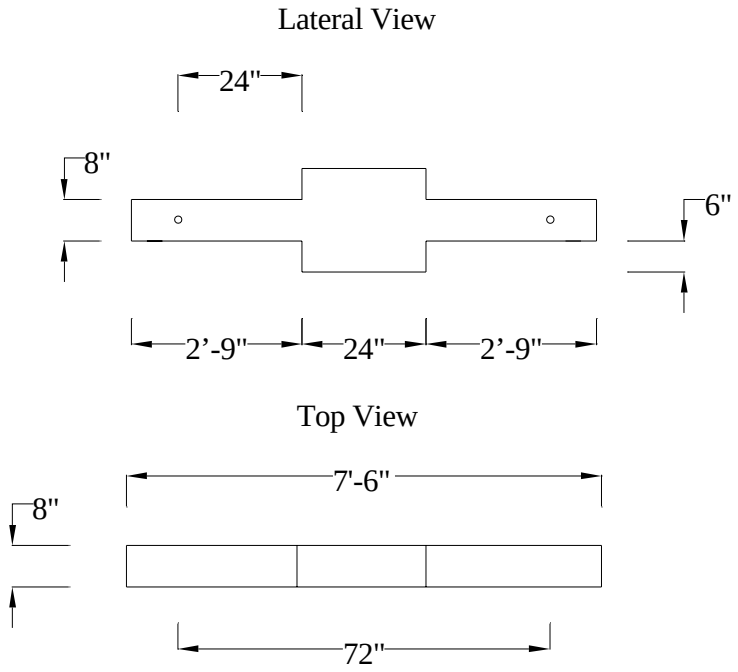

Figure A.15. Dimensions of test specimen.

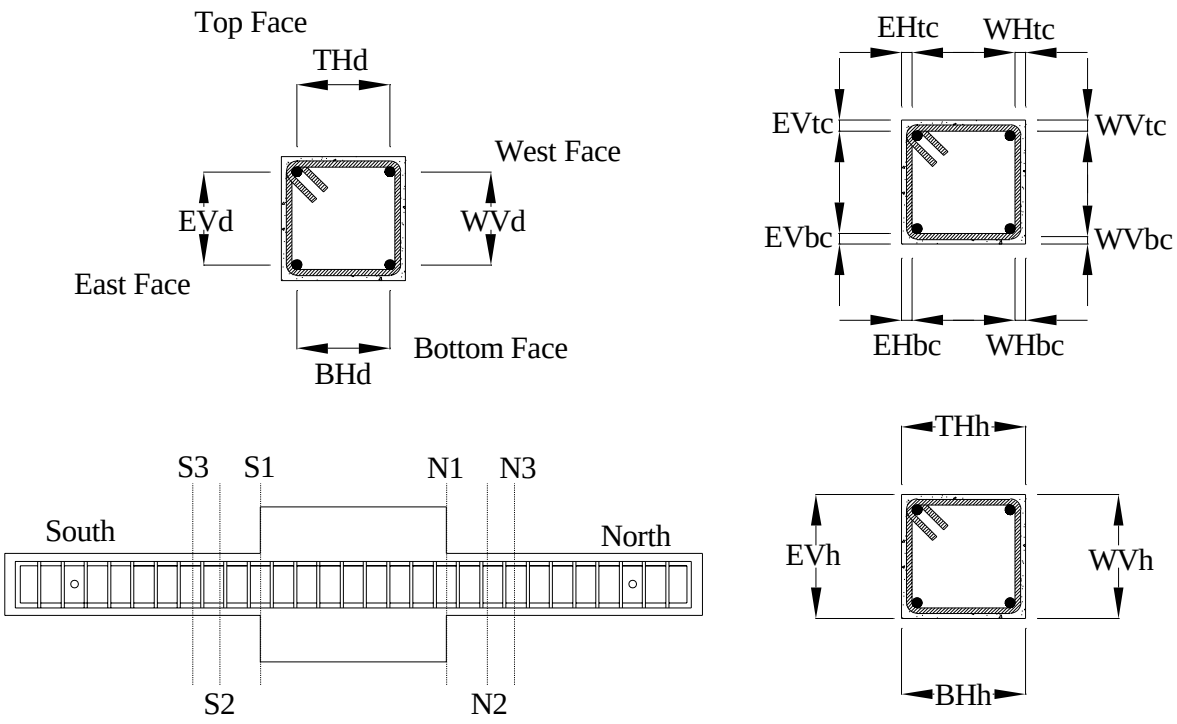

Figure A.16. Designation for as-built dimensions reported in Tables A.7 to A.22.

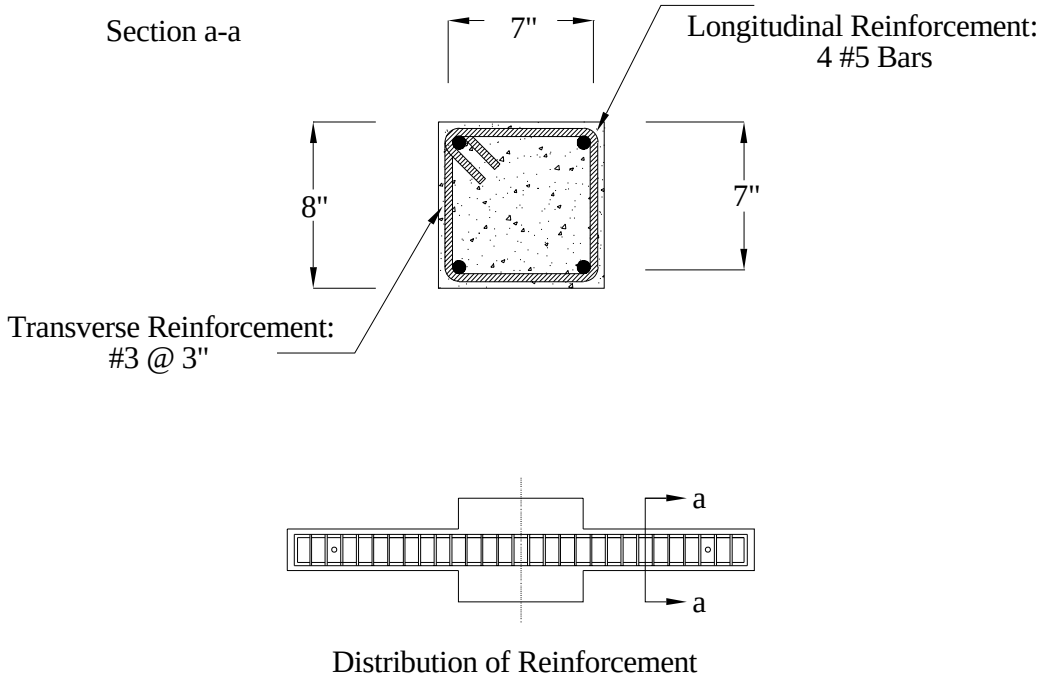

Figure A.17. Reinforcement for test specimens.

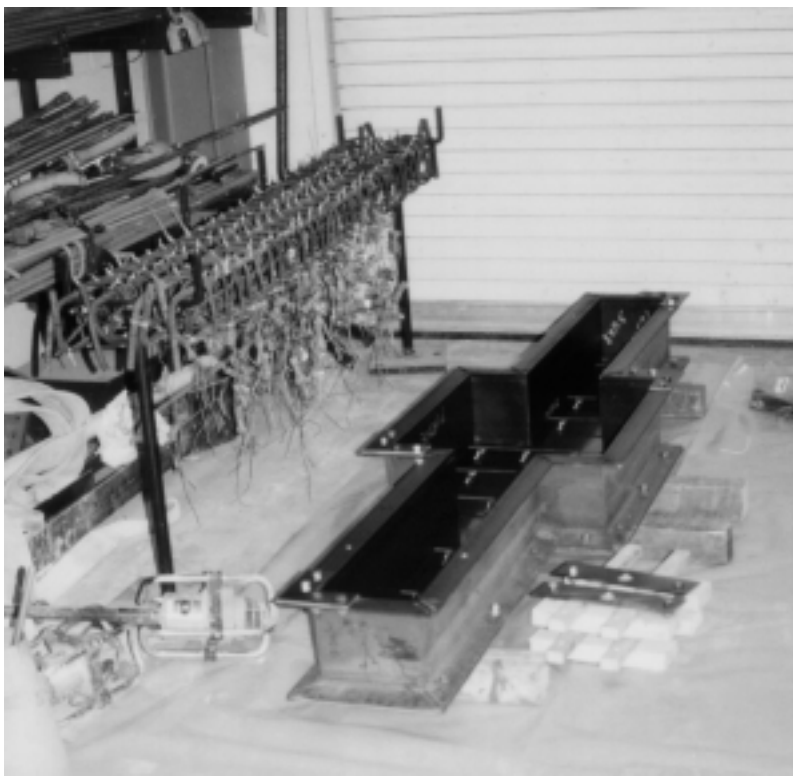

Figure A.18. Metal form and reinforcing cages before casting.

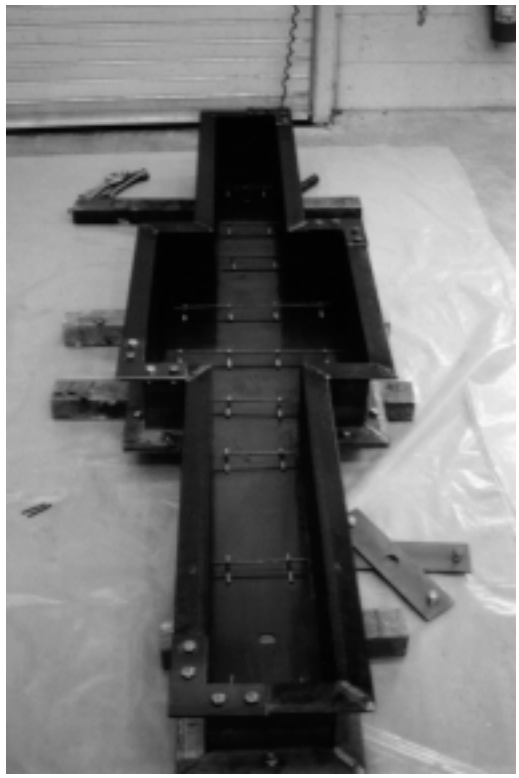

Figure A.19. Metal form assembled and covered with form oil.

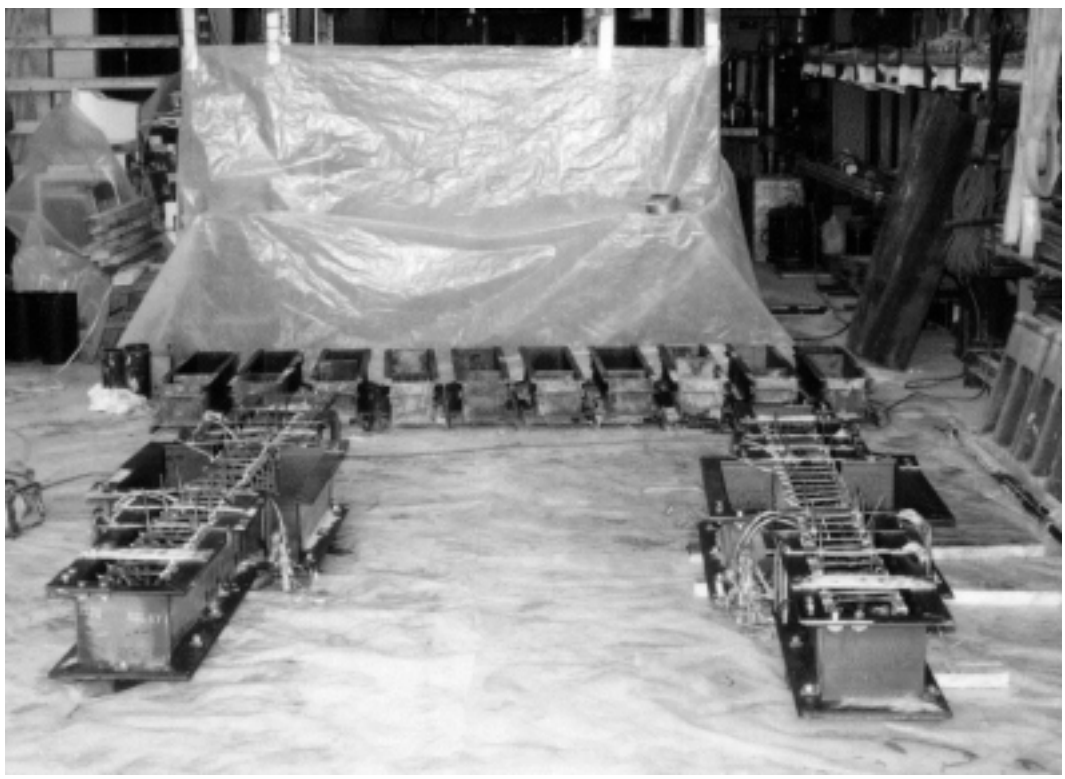

Figure A.20. Metal forms with cages and anchoring bolts in place, immediately before casting.

Figure A.21. Detail of south joint for specimen 7 showing stirrup spacing, prior to casting.

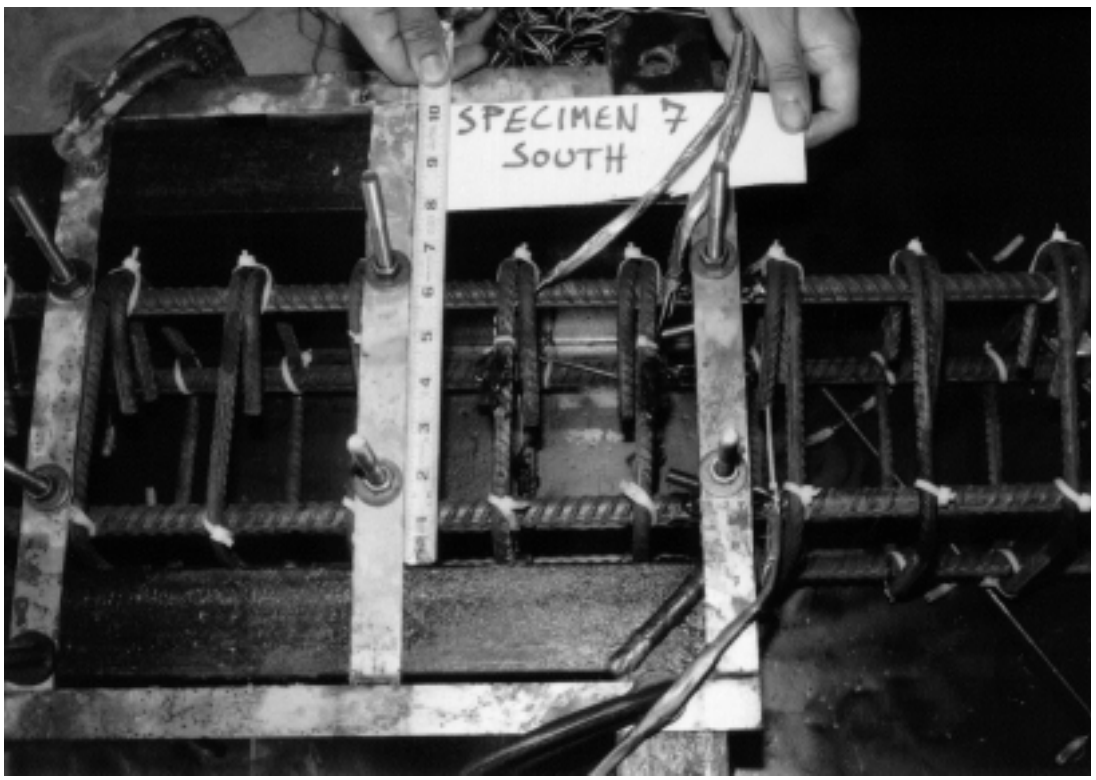

Figure A.22. Detail of south joint for specimen 7 showing the effective depth, prior to casting.

Figure A.23. Concrete being delivered by mixer truck.

Figure A.24. Concrete being vibrated inside the metal forms.

Figure A.25. Finishing the surfaces for specimens and flexure beams.

Figure A.26. Finished specimen.

Figure A.27. Slump test for batch 2.

Figure A.28. Specimen covered with wet burlap during the curing period.

Figure A.29. Specimens, flexure beams and cylinders covered with wet burlap and plastic.

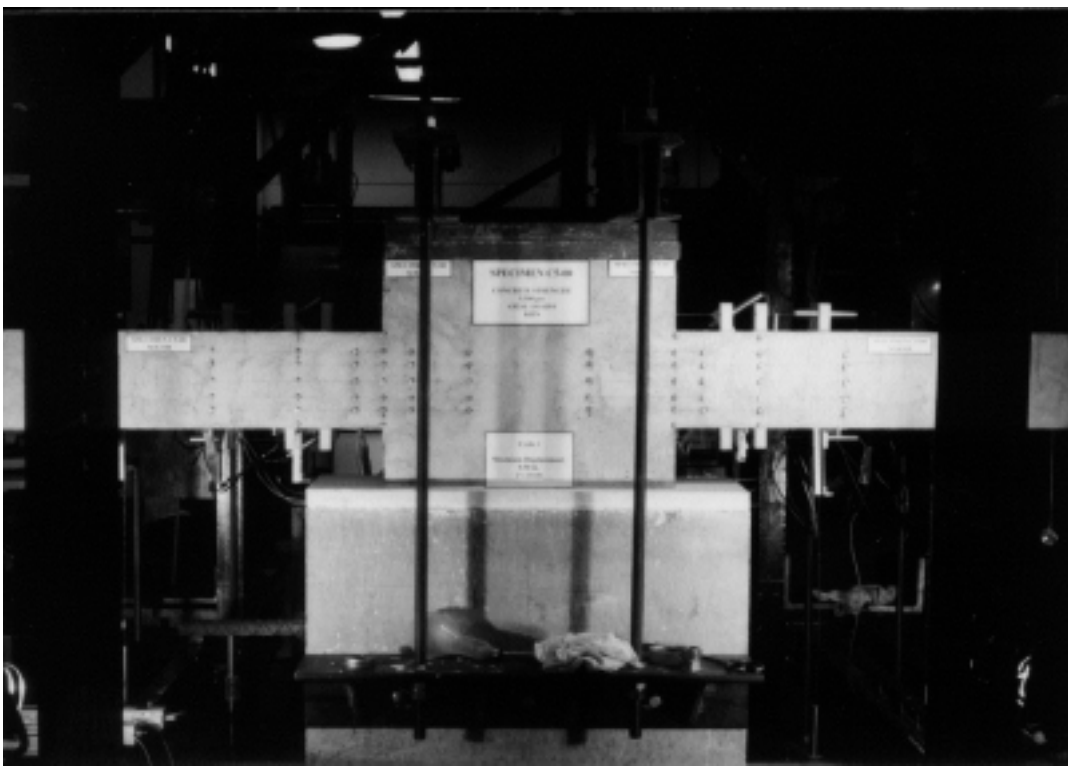

Figure A.30. Specimen fixed to test base and instrumented.

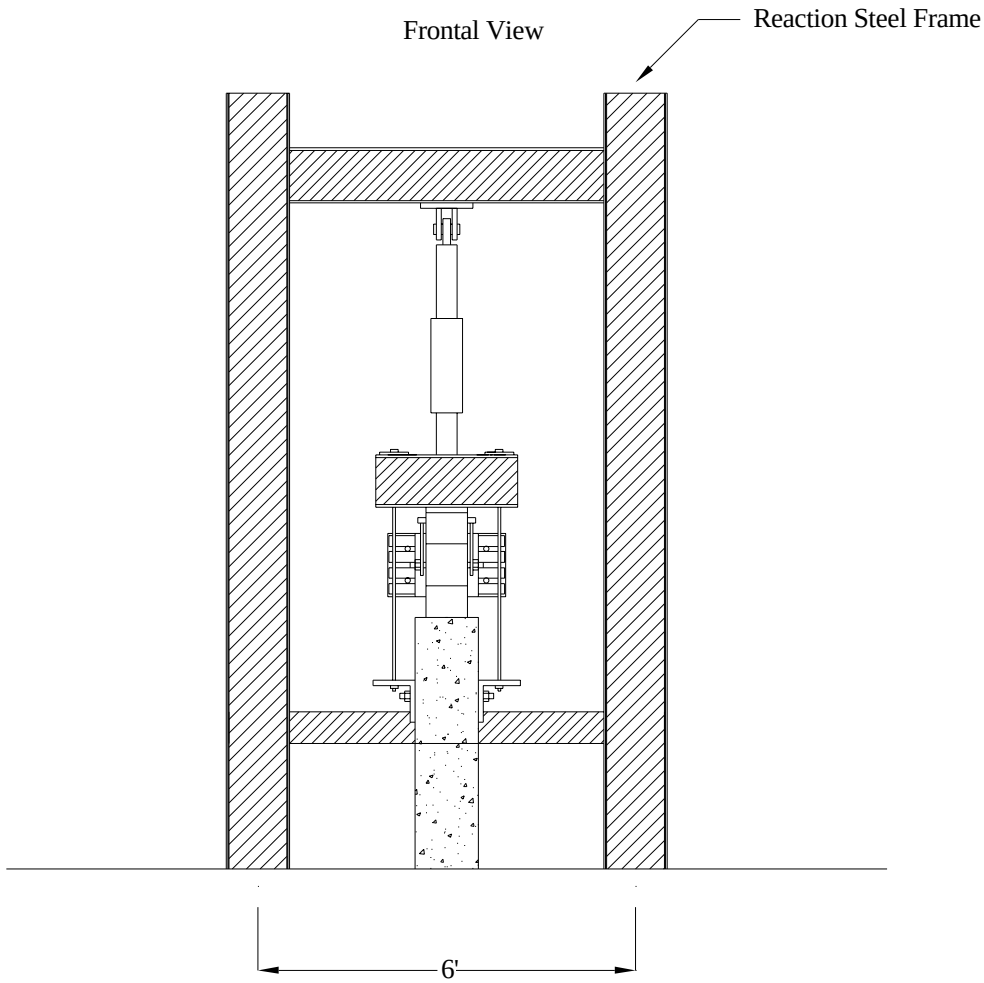

Figure A.31. Frontal view of test setup.

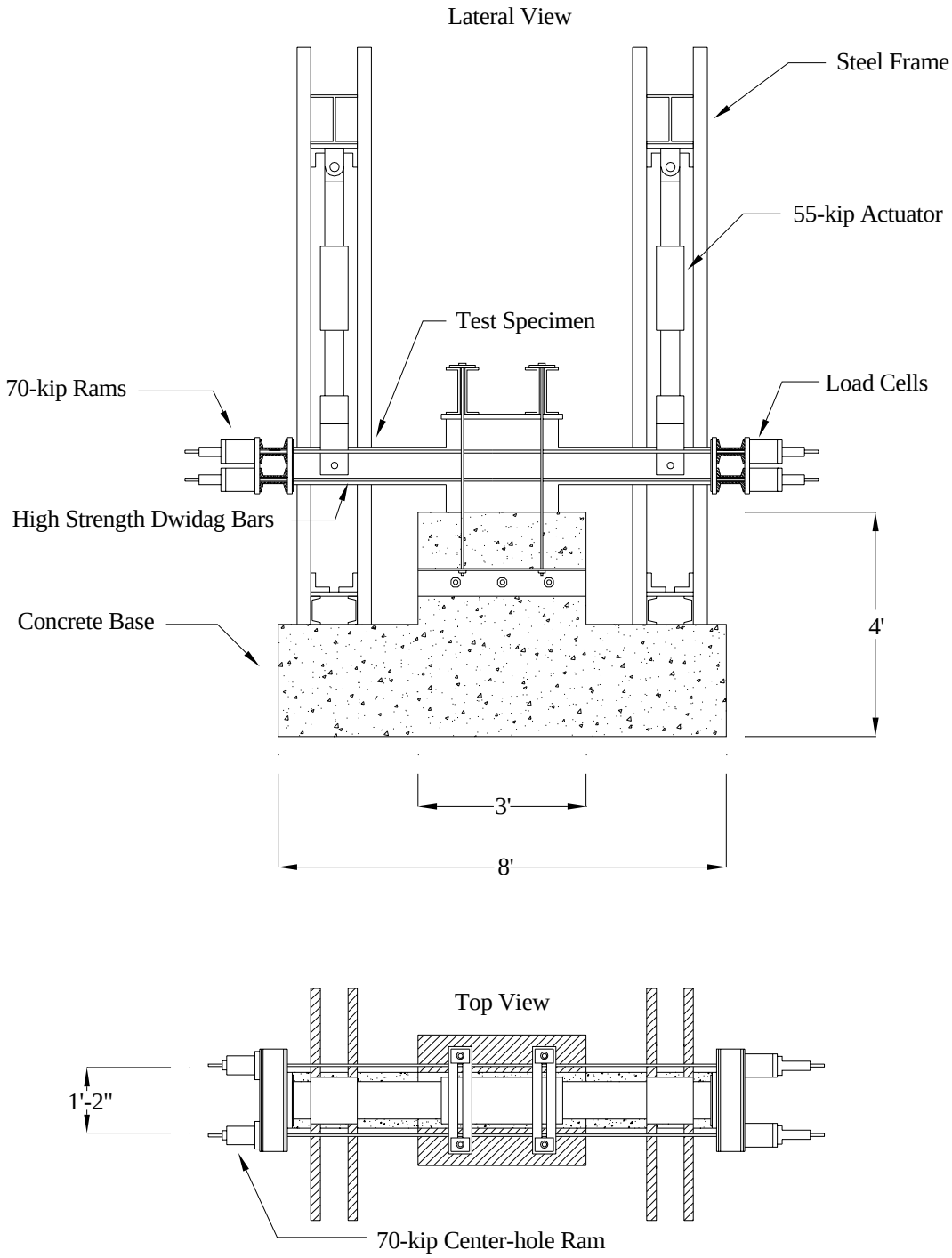

Figure A.32 Test apparatus

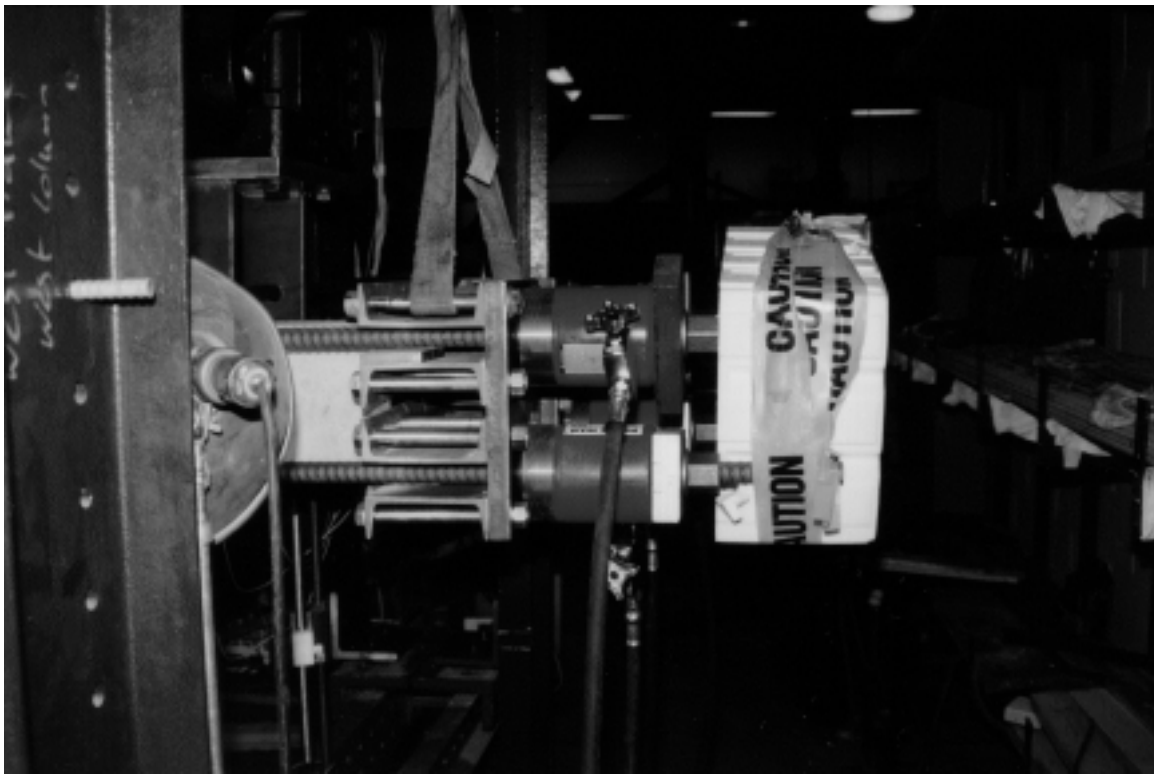

Figure A.33. Center-hole rams used to apply the axial load.

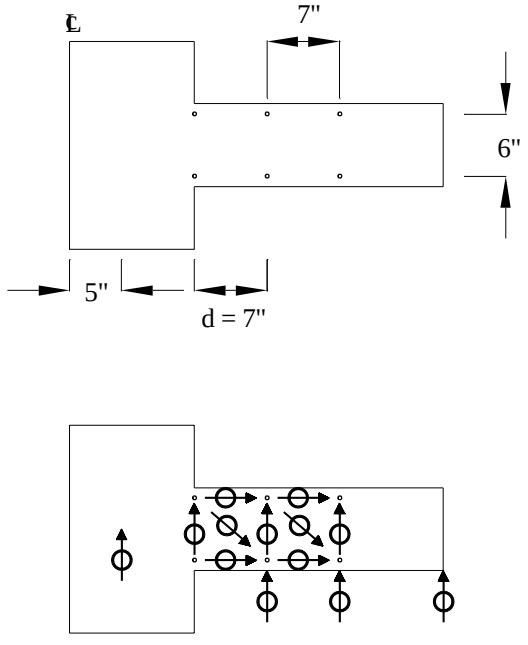

Figure A.34. Location of displacement measurements taken with displacement transducers.

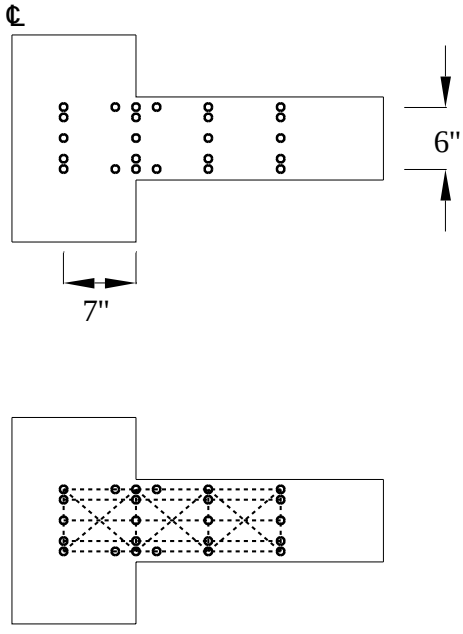

Figure A.35. Location of displacement readings taken with electronic Whittemore gages.

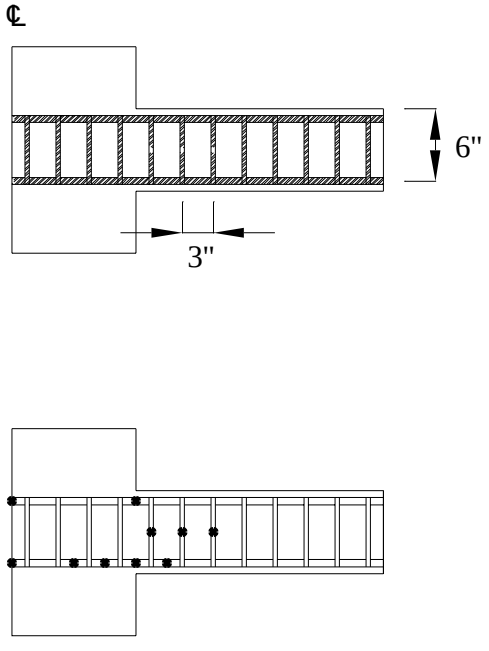

Figure A.36. Position of strain gages in the reinforcing cage.

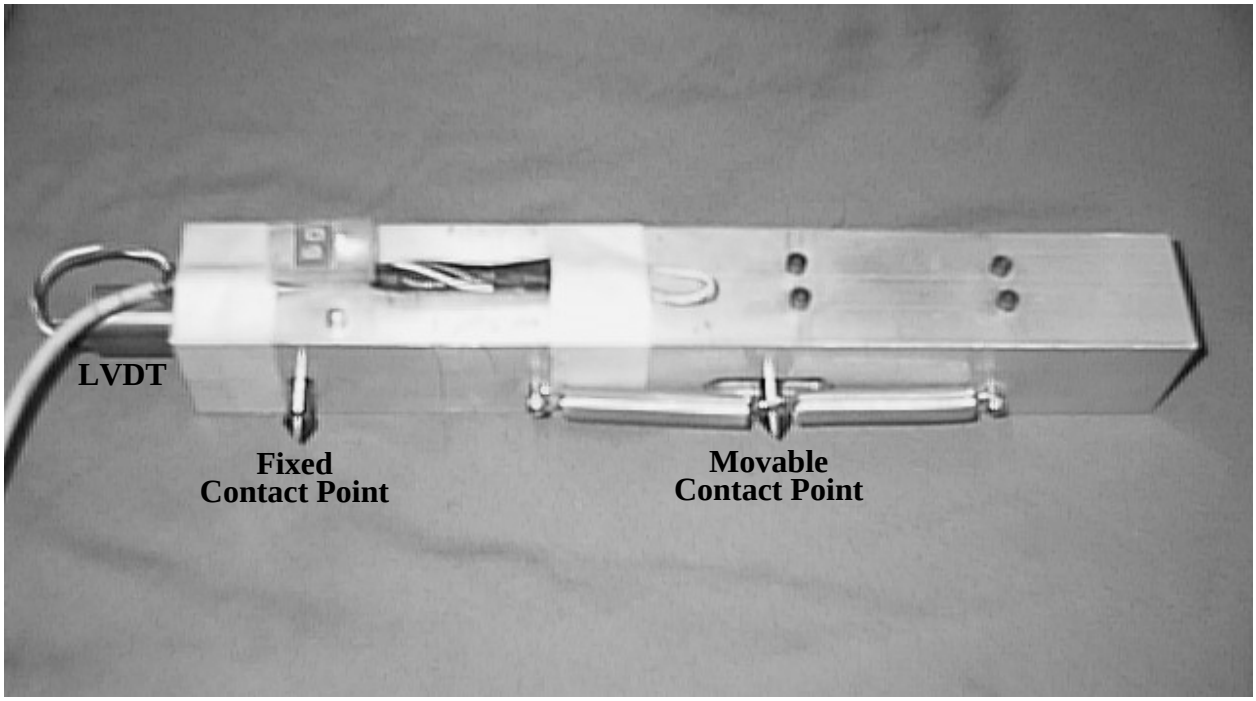

Figure A.37. Electronic Whittemore Gage.

Vita

Adolfo Benjamin Matamoros was born in Alajuela, Costa Rica on 21 February 1967. He graduated with the degree of “Licenciado en Ingeniería Civil” from the University of Costa Rica in 1989. While attending the University of Costa Rica as an undergraduate, he worked for a structural engineering firm in San José, as an engineering assistant.

Upon completing his undergraduate studies, he worked as a private consultant in structural engineering. He returned to the University of Costa Rica in 1989, where he worked as a Civil Engineer at the Earthquake Engineering Laboratory. He enrolled in the Master of Science program at the University of Costa Rica in 1991, and was admitted to the University of Illinois at Urbana-Champaign in 1992, where he obtained the degree of Master of Science in Civil Engineering in 1994.